UNIVERSITY OF BIRMINGHAM

Simulation and Fabrication of a Microtubular Solid Oxide Fuel Cell Stack with Novel Anode Current Collection and Enhanced Thermofluidynamics

by

Oujen Gwythyr Hodjati-Pugh

(Student ID: 1163599)

A Thesis Submitted to the University of Birmingham for the

Degree of Doctor of Philosophy

Supervisor:

Prof Robert Steinberger-Wilckens

Co-supervisor:

Dr Aman Dhir

This work was performed at:

Centre for Fuel Cell and Hydrogen Research

School of Chemical Engineering

College of Engineering and Physical Sciences

University of Birmingham

September 2020

Abstract

This PhD deals with the development of Microtubular Solid Oxide Fuel Cells (µT-SOFC) at the cell and sub-stack level. The study provides a body of work as a basis for future development in the field. The information has been acquired and interpreted empirically and numerically.

µT-SOFCs are suited to a broad range of applications with power demands ranging from a few watts to several hundred watts. µT-SOFCs possess inherently favourable characteristics over alternate configurations such as high thermo-mechanical stability, high volumetric power density and rapid start-up times, lending them for particular value use in portable applications. Efficient current collection and interconnection constitute a bottleneck in the progression of the technology and addressing this was the focus of this study. An empirical study to determine the effect of varying current collector position and number was conducted. A mathematical model with its underpinnings in a resistance path model was constructed to interpret the empirical findings. A multiphysics CFD model mirroring the experimental setup was constructed to build on the insight provided by the mathematical model. The model was validated and fitted with experimental data and was reliable for prediction of µT-SOFC performance within set parameters.

Contacting of each electrode is most simply and most typically achieved from the cell exterior at the expense of available active cell area and durability. Building on the knowledge gained in the empirical and numerical studies, a novel method of internal current collection was proposed; collecting current from multiple points along the inner wall of the anode supported cell. The current collector also acted as a flow turbuliser, enhancing the flow and thermal distribution within the fuel cell. To reduce the contact resistance of the internal current collector, a contacting technique was identified, namely brazing. Brazing enabled the formation of multiple, physical joints along the interior of the µT-SOFC. The brazing improved the current collector performance and durability. The study featured the development of a novel braze and braze application technique.

CAD and CFD were used for the optimisation of a 4-cell µT-SOFC manifold, stack, and operating conditions. The stack design used data from the experimental testing of cells with the novel, brazed internal current collector. Two 4-cell stacks with two current collector variations, both using the novel, brazed internal current collector design, were fabricated and electrochemically tested. Data from performance and durability testing of the stacks was presented and the best design identified.

Acknowledgements

First and foremost, I would like to express my profound gratitude to Prof. Robert Steinberger-Wilckens for giving me this opportunity and for his support and wisdom throughout the journey. His faith and positive attitude was a great motivation for me, inspiring me to work hard and complete my PhD.

I would like to express my appreciation to Dr Aman Dhir (School of Chemical Engineering, University of Wolverhampton), my co-supervisor for imparting great knowledge and technical know-how to ensure that the research progress was smooth. His suggestions in difficult times and critical analysis improved my work throughout.

I would like to thank Dr James Andrews for his time, patience and his willingness to share his extensive knowledge of mathematical modelling. I wish to thank Dr Bostjan Hari for his help with CFD modelling from the very beginning. I would also like to thank Dr Yousif Al-Sagheer for his help with the development of a fuel cell control system. I would like to thank Dr Artur-Majewski, Dr Lina Troskialina and Dr Tony Meadowcroft for their guidance on fuel cell and stack development. Indeed the thanks are extended to all of the lecturers and teachers who have shared knowledge throughout my formal education. The funding from the EPSRC (EP/L015749/1) through the CDT in Fuel Cells and their Fuels is also greatly acknowledged.

I want to express my gratitude to Bob Sharpe, Steve Brookes and Bill for sharing just a small amount of their vast practical engineering knowledge. Their help with rig building and maintenance, fabrication and welding were immeasurable. The cups of tea and biscuits went a great length in boosting morale.

I would also like to thank the staff at CalGavin Ltd, in particular Martin Gough, Dr Peter Drögemüller, Stephen Perkins and Steve. Their willingness to share knowledge, time and support was truly heartwarming. I would like to express my kindest regards and appreciation to the staff at Kepston Ltd. In particular Chris Marsh, Tony Smith and Chrissy for imparting wisdom in brazing and braze application, and for their time and enthusiasm to progress my studies. Also, thanks go to Pat Rogers from VBC Ltd for his insight in braze materials. Thanks to Seamus Bourke from Frost Electroplating Ltd for his support with electroless plating. I would like to thank Leslie Curtis from Birmingham City

University (School of Jewellery) for his support with electroplating. I would also like to thank Dr Tom Heenan from UCL for his time and support with XRCT imaging and processing.

I would like to thank my friends and colleagues throughout the journey. A special mention to Mel, Sathish and Kun. Together went through the pain and reward of the PhD process. Also to Pete, Alan, Liam, Bernardo, Ahmed, Elias, Brogan and Abby for the fun times we had and the memories shared.

Last and most importantly I would like to express my heartfelt gratitude to my mum and dad, my wider family, present and departed, for their relentless and everlasting encouragement, support, knowledge and love that sustains me. It is them to whom I dedicate this work.

Publications

- O. Hodjati-Pugh, A. Dhir, R. Steinberger-Wilckens, Three-Dimensional Modelling of a Microtubular SOFC: A Multiphysics Approach, ECS Trans. 78 (2017) 2659–2672.doi:10.1149/07801.2659ecst.
- O. Hodjati-Pugh, A. Dhir, R. Steinberger-Wilckens, Internal Current Collection in Microtubular SOFCs : Minimisation of Contact Resistance via Brazing and Plating, ECS Trans. 91 (2019) 553–548.doi:doi.org/10.1149/09101.0533ecst.
- O. Hodjati-Pugh, A. Dhir, R. Steinberger-Wilckens, The development of current collection in micro-tubular solid oxide fuel cells—a review, Appl. Sci. 11 (2021) 1–27.doi:10.3390/app11031077.
- O. Hodjati-pugh, J. Andrews, A. Dhir, R. Steinberger-Wilckens, Analysis of current collection in micro-tubular solid oxide fuel cells: An empirical and mathematical modelling approach for minimised ohmic polarisation, J. Power Sources. 494 (2021) 229780.doi:10.1016/j.jpowsour.2021.229780.
- O. Hodjati-Pugh, A. Dhir, R. Steinberger-Wilckens, Internal current collection and thermofluidynamic enhancement in a microtubular SOFC, Int. J. Heat Mass Transf. 173 (2021).doi:10.1016/j.ijheatmasstransfer.2021.121255.

Conferences Attended

- FCH2 2015 [Birmingham, UK] - (Poster) Tubular SOFC Cell Design and Stack Development for Portable Applications
- H2FC SUPREGEN 2016 [Belfast, UK] - (Poster) Three-dimensional Modelling of a Microtubular SOFC: A Multiphysics Approach
- FCH2 2017 [Birmingham, UK] - (Poster) Tubular SOFC Cell Design and Stack Development for Portable Applications
- SOFC XV [Miami, USA] 2017 – (Presentation) Three-dimensional Modelling of a Microtubular SOFC: A Multiphysics Approach
- FCH2 2018 [Birmingham, UK] – (Presentation) A Study of Microtubular SOFC Interconnect Configuration: A Modelling and Experimental approach
- ModVal 2018 [Aarau, Switzerland] – (Poster) Multiphysics Modelling of a Segmented Microtubular SOFC: A Study of Interconnect Configuration
- H2FC SUPERGEN 2018 [Birmingham, UK] – (Poster) A Study of Microtubular SOFC Interconnect Configuration: A Modelling and Experimental approach
- EUA Low Carbon Forum 2019 [Kenilworth, UK] – (Presentation) SOFC Technology for Hot Water and Heating
- SOFC XVI 2019 [Kyoto, Japan] – (Presentation) Current Collection in Microtubular SOFCs: Minimisation of Contact Resistance via Brazing and Plating

Awards

- Best Poster Award – H2FC 2016 - Three-dimensional Modelling of a Microtubular SOFC: A Multiphysics Approach

Technical Courses

- Joint European Summer School 2015 [Athens] – Introduction to SOFC Technology
- ECST European SOFC & SOE Forum 2016 [Switzerland] – Fuel Cell Technology
- Joint European Summer School 2016 [Athens] – Modelling Masterclass

‘The man who moves a mountain begins by carrying away small stones.’

Confucius (551-479 BC)

‘Success is not final, failure is not fatal: It is the courage to continue that counts.’

Winston Churchill (1874-1965)

‘Perseverance is the hard work you do after you get tired of doing the hard work you already did.’

Newt Gingrich (1943-)

Table of Contents

List of Figures

List of Tables

Chapter 1 Introduction

1.1 Energy Dilemma – Motivation for Sustainable Development

The detrimental effects of global warming are becoming ever-present [1]. Figure 1.1 a) shows the increasing trend in average land-sea temperature change between 1850 and 2019 compared to the 1961-1990 average [2]. It is widely accepted that human (anthropogenic) activities are a significant contributor to global warming and the sharp increase in temperature has been correlated to the rapid increase in energy consumption with the advent of the industrial revolution [3,4]. Machines of the industrial era increased productivity and economic development immeasurably, but the energy-hungry machines rely on the consumption of fossil fuels. Combustion of fossil-based fuels, which are still heavily relied on to support economic activity to date, emit greenhouse gases (GHG) such as CO_2 and other pollutants. Such GHGs warm the Earth in a phenomenon known as the greenhouse effect [5]. While modern machines are more efficient at converting energy to work and emit fewer pollutants, the increase in population size, productivity (GDP per person), economic development, technological advancement and more widespread adoption of energy-intensive technology means that the increasing global energy consumption and GHG emission is set to continue [6]. The historical global CO_2 concentration is seen in Figure 1.1 b) [2].

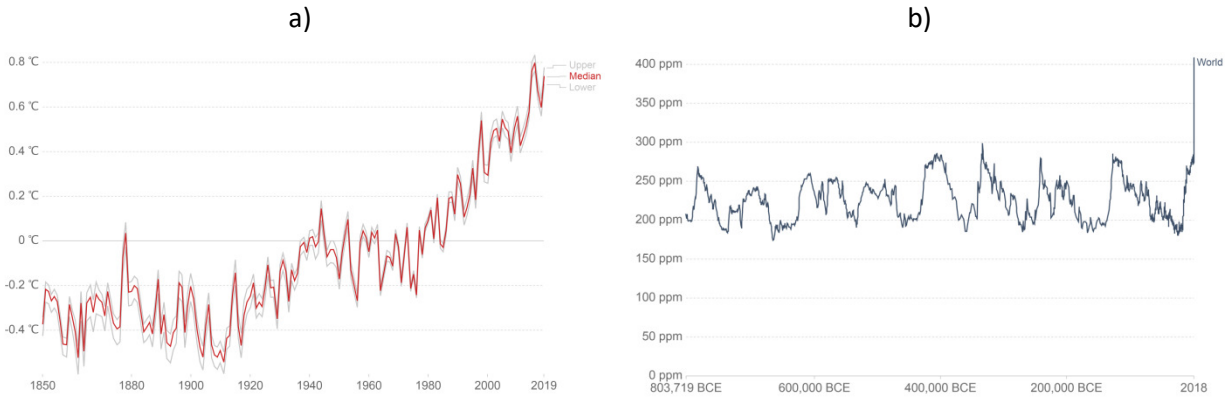

Figure 1.1 - a) Global average land-sea temperature relative to 1961-1990 average, b) historical global atmospheric CO_2 concentration [2].

The scientific community, industry and the general public are looking towards renewable energy technologies to enable a divergence from greenhouse emitting fossil fuels, whose finite supply is inherently unsustainable [7,8]. This divergence from the exploitation of the Earth's resources promotes the ethos of sustainable development, meeting the needs of today, without compromising the needs of future generations [9]. Notable reports such as the Stern Review detail the

environmental costs expected on the current growth trajectory [10], which, alongside pressure from the 1998 Kyoto Protocol [11], 2015 Paris Agreement (194 Countries Participating) [12,13], and governmental level emission policies has led to a significant increase in recent and projected renewable energy deployment [14]. These efforts to reduce emissions, increase the efficiency of energy usage while improving global energy security are all to contribute to the common goal of holding global warming to well below 2°C and 'pursue efforts' to limit it to 1.5°C to avoid irreversible damage [13].

Global primary energy consumption increased by 1.3% in 2019. This increase was driven by renewables which accounted for 40% of the increase. Also, the share of renewables in primary energy mix increased from 3% in 2015 to a record 5% share in 2019, overtaking nuclear. This is expected to further increase to 10% by 2035 [15]. By inspection of global GHG emissions by sector, seen in Figure 1.2 [2], electricity and heat is the biggest sector to be decarbonised. This sector accounts for 30% of the emissions, nearly twice than the next highest sector which is transport. The increasing electrification of the world economy accounts for nearly two-thirds of the increase in global energy consumption with the share predicted to be 47% by 2035, up from 42% in 2015 [3]. Transportation is another key sector to be targeted for emission reduction, accounting for 14% of global GHG emissions, with 95% of the transportation energy coming from fossil fuel resources.

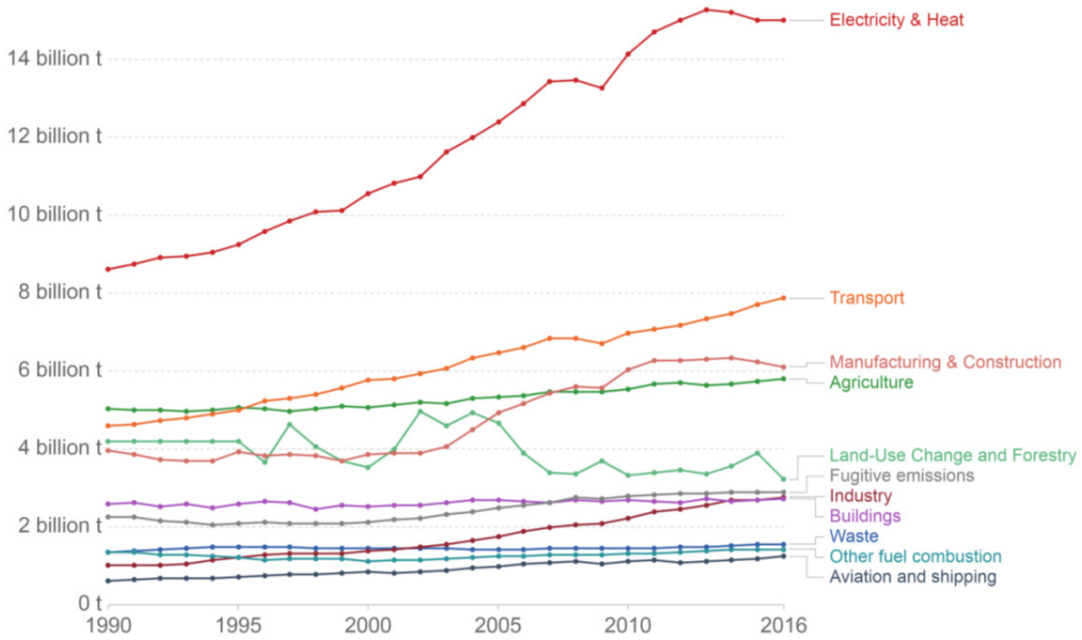

Figure 1.2 – World greenhouse gas emissions by sector measured in tonnes of CO_2e [2].

Efforts must also be made to reduce the overall energy consumption, limiting the energy consumed without sacrificing the quality of life or economic development. Concepts have been developed to curb energy consumption, such as the sustainable 2 kW society by ETH Zurich (Switzerland) that proposed a 2 kW cap on energy consumption per capita [16]. Current technologies alone cannot meet the energy demands, improve energy efficiency and adhere to ever-tightening emission regulations. Research and development must focus on technologies capable of fulfilling the requirements in multiple applications and spanning several sectors. For instance, fuel cells which can be used for heat and power on a domestic to industrial scale, as well as mobile auxiliary power units and also powering vehicles of any scale on land, water and air [17]. It is the prospects offered by such technologies, combined with the environmental impacts of the transport and energy sectors that have been key driving forces for the advent of the hydrogen economy.

1.2 The Hydrogen Economy

The hydrogen economy is a system of production, distribution, storage and use of hydrogen as an energy carrier, much like electricity [18]. Not to be confused as a primary fuel like oil or gas, hydrogen is a secondary form of energy. While elemental hydrogen is the most abundant element on Earth, molecular hydrogen does not occur naturally in convenient reservoirs and so must be produced from primary sources. A fundamental asset of the hydrogen economy is that hydrogen conversion to electricity and heat has zero point-of-use emissions, particularly significant in the transport sector for reducing GHGs and pollution in urban areas. The majority of the associated emissions, if any, are centralised at the source of production, meaning targeted emission reduction can be conducted on a large scale by the producer, shifting them away from the point of use to be more easily and affordably addressed at a large scale. A schematic of the current hydrocarbon and the future hydrogen-based economies are seen in Figure 1.3. Hydrogen can be used to decarbonise multiple, heavily polluting sectors such as transport, heat, and power.

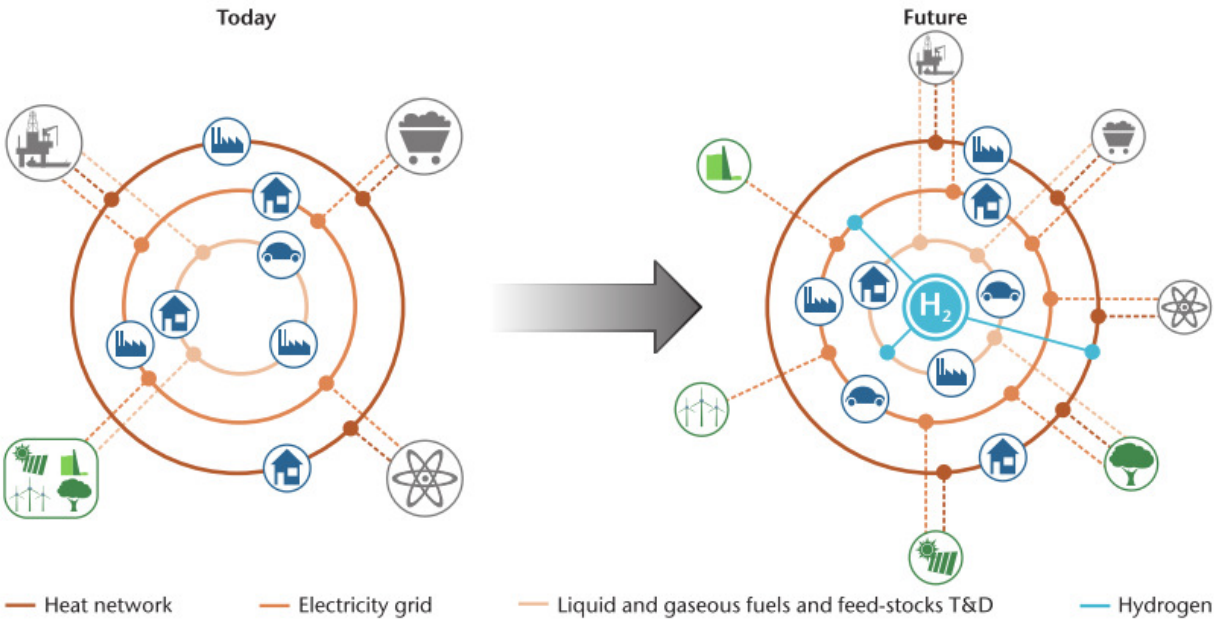

Figure 1.3 – Transition from a hydrocarbon economy to a sustainable hydrogen economy [18].

The rapid and widespread adoption of renewables such as wind and solar poses a problem in that the supply of electricity generated fluctuates and does not sync well with the existing supply and demand profile of the grid infrastructure [19]. Surplus renewably energy can be used to generate 'green hydrogen' from the electrolysis of water with zero associated emissions [20]. The hydrogen is stored and transported to be converted back to produce work, electricity or otherwise, when there is a demand. This hydrogen grid buffer can smooth the electricity supply/demand profile to alleviate the increasing stress on the electricity grid e.g. with the increasing adoption of electric vehicles. Fuel cell vehicles can run directly off the hydrogen produced from renewables with no tailpipe emissions [3]. Such vehicles can be used to reduce the emissions in the transport sector including rail, aviation and shipping. Hydrogen can also be used to decarbonise the heat and power networks. Trials of hydrogen blending (<20%) in the gas grid have been proven successful with minimal to no modification of existing infrastructure and appliances such as cookers and boilers [21]. While hydrogen can be burnt to produce a useful output for example in a boiler or combustion engine and still produce no emissions except water, fuel cells pose a much more efficient way of extracting the chemical energy stored in hydrogen [22].

1.3 Fuel Cell Technology Overview

The underlying fuel cell principles were discovered by Christian Friedrich Schönbein and principally demonstrated by Sir William Grove in 1839 [23]. Fuel cells are highly efficient electrochemical conversion devices that directly extract electrical energy from hydrogen, and hydrogen-enriched fuels [17]. All fuel cells consist of an electrolyte, a positively charged electrode, a negatively charged electrode and a current collecting electrical circuit. The electrolyte, a gas-tight, electrically insulating barrier separates the electrodes. Electrochemical oxidation and reduction reactions occur at the anode and cathode, mobilised ions from the reaction pass through the ionically permeable, gas-tight electrolyte. The charge balancing electrons produced/consumed in the reduction/oxidation (RedOx) reactions respectively are forced around the electrically insulating electrolyte into an external circuit. The flow of these electrons is called charge and is used to produce electrical work.

Fuel cells are categorised by their electrolyte (by which they are named), operating temperature and geometric configuration. There are six common types of fuel cells: solid oxide fuel cells (SOFC), molten carbonate fuel cells (MCFC), alkaline fuel cells (AFC), phosphoric acid fuel cells (PAFC), proton exchange fuel cells (PEFC) and direct methanol fuel cells (DMFC) which are a specific type of PEFC [24]. Low temperature fuel cells operate below 220°C while high temperature variants such as the MCFC and SOFC operate above 550°C. While all fuel cells except the DMFC can operate on H_2, some can operate on hydrocarbons (HCs) such as the SOFC that can directly reform carbonaceous fuels at the anode to produce hydrogen and other byproducts (of which some can also contribute to electron production) [25]. Compared to low temperature fuel cells, high temperature fuel cells are more tolerant to fuel impurities and particulates such as CO, CO_2 and H_2S. This alleviates issues surrounding H_2 infrastructure needed to produce high purity H_2 required for PEFCs [26]. This flexibility facilitates the integration of fuel cells globally, using the existing hydrocarbon supply chain of the fossil fuel based economy including the gas grid. A schematic of the key operating principles and features of the most common fuel cells including operating temperature range, feedstock, mobile ion and typical electrical efficiency is seen in Figure 1.4.

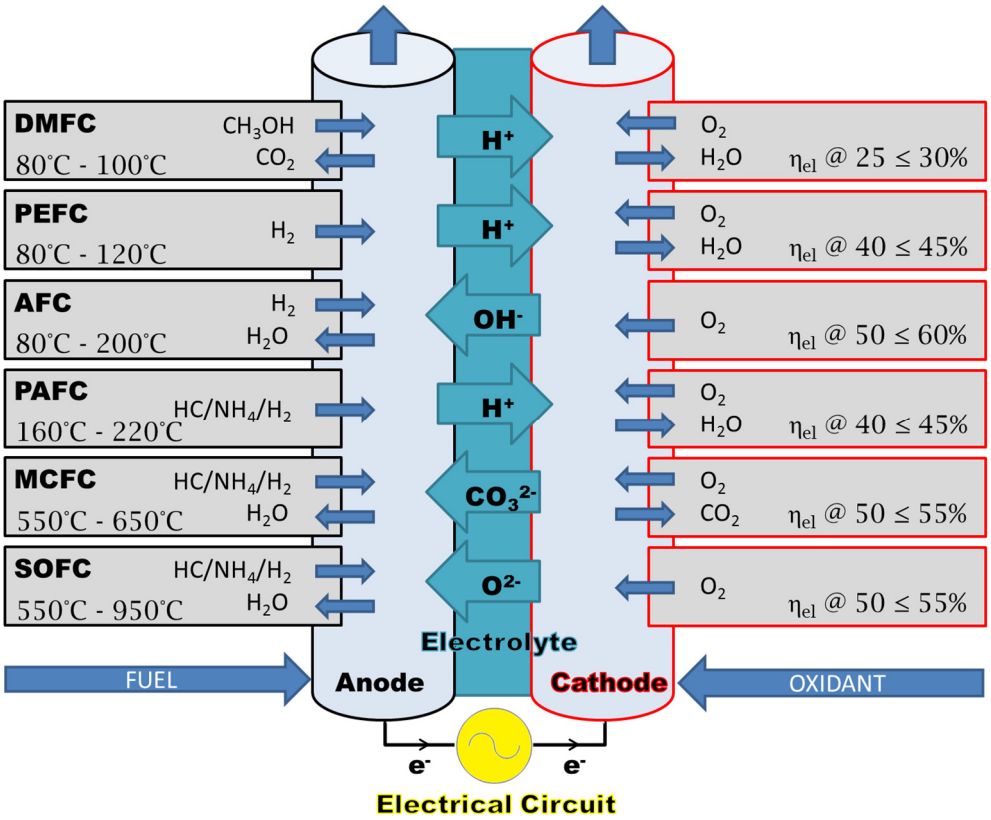

Figure 1.4 - Fuel cell schematic with operating temperature and electrical efficiency.

1.4 Fuel Cell Market

The stackable/scalable, modular nature of fuel cells suits them to a broad spectrum of applications ranging from a few watts in portable power devices to several megawatts in backup and peaking power units. The first commercial fuel cells were AFCs used by the NASA space exploration programmes for providing power to satellites and space capsules [27]. Since then fuel cells have been used in many applications, broadly categorised into portable, stationary and transport markets. Low temperature fuel cells can use lightweight, low temperature materials such as plastics and polymers. The fast start-up time and simple heating system required to reach the low operating temperatures of around 80°C has favoured them in the automotive and portable power sector for on-demand power. PAFC, MCFC and SOFC are typically employed for stationary applications such as power generation, grid backup and combined heat and power (CHP). This is due to the increasing time and system complexity/size required to reach the higher operating temperatures and the benefit of having higher efficiency and higher fuel flexibility. However, SOFC technology has been proven to also be functional in the portable and transport sectors [28,29].

The number of units shipped over the last five years (2019 included as a partial forecast) for each sector is seen in Figure 1.5 a) [30]. In 2018, 68,500 fuel cell units were shipped, 76% of which were in the stationary sector, 16% were employed in transport and 8% were for portable applications. Out of the units shipped in 2018, 75% were in Asia. Japan contributes strongly to the fuel cell Asia market. In particular, the stationary sector, where SOFC fuel cells are increasingly being adopted for domestic and commercial CHP and more than 100,000 units have been installed within Japan in the EneFarm project [31]. The next largest markets with respect to units shipped are North America followed by Europe.

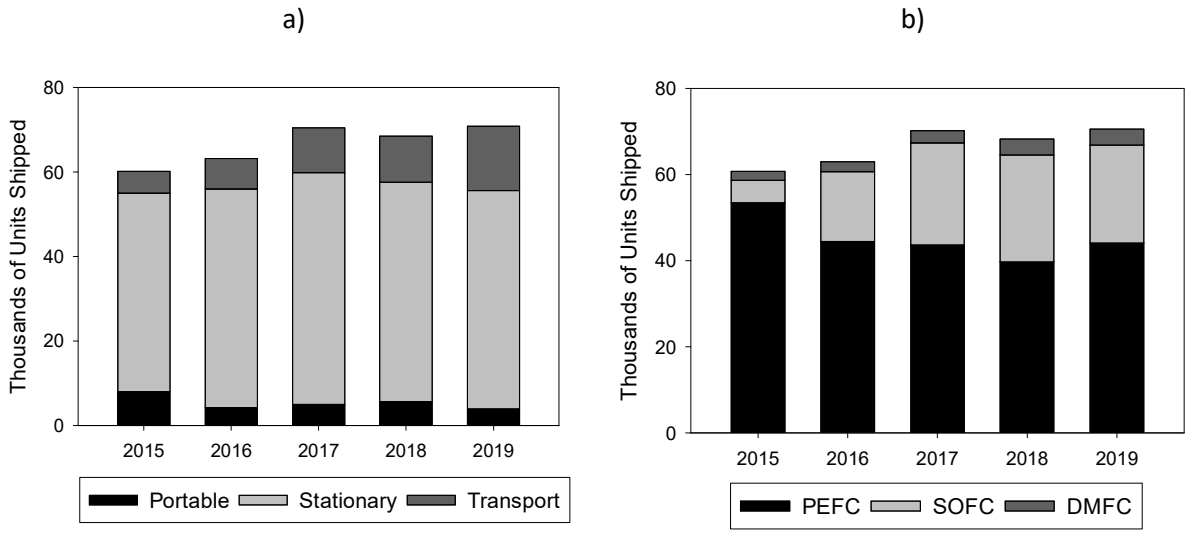

Figure 1.5 - Thousands of fuel cell units shipped between 2015 and 2019 (2019 includes a partial forecast) by a) application, b) fuel cell type; reproduced from [30].

PEFC technology is increasingly being adopted in the transport sector in fuel cell/hybridised vehicles including forklifts, buses, boats, trams, trains, planes, drones, motorcycles, submarines and automobiles such as the Toyota Mirai or Hyundai ix35 [32–37]. PEFC are the most widely adopted fuel cell technology in terms of units shipped over the last five years as seen in Figure 1.5 b) [30]. Of the 68,500 units shipped in 2018, 58% were PEFC, 36% were SOFC, 5.4% were DMFC and the rest PAFC.

1.5 Fuel Cell Thermodynamics

From the first law of thermodynamics:

$$dU = dQ - dW \quad (1)$$

the change in internal energy of a closed system (dU) is equal to the heat transferred to the system (dQ) minus the work done by the system (dW) [22]. From the second law of thermodynamics:

$$dS = \frac{dQ_{rev}}{T} \quad (2)$$

we can infer the entropy change of a system based on how heat transfer causes the system to change, for a constant pressure process. Based on equation (1) and (2), we can define thermodynamic potentials, which, with mathematical manipulation via Legendre transforms can be described with respect to easily measurable quantities such as temperature, pressure and volume. The thermodynamic potential for the Gibbs free energy, the exploitable energy potential is given by equation (3) and in its differential form by (4). The thermodynamic potential for enthalpy is given in equation (5) and in its differential form in (6). Equation (5) is substituted into (3) to form (7), another expression for the Gibbs free energy which in its differential is given by equation (8) [17]:

$$G = U - TS + pV \quad (3) \qquad dG = dU - TdS - SdT + pdV + Vdp \quad (4)$$

$$H = U + pV \quad (5) \qquad dH = dU + pdV + Vdp \quad (6)$$

$$G = H - TS \quad (7) \qquad dG = dH - TdS - SdT \quad (8)$$

From equation (1) and (2) we get:

$$dU = TdS - dW \quad (9)$$

The work done (dU) is defined as the sum of the mechanical work of the system (pdV), the expansion of the system against pressure, plus the electrical work done by the system (dW_{elec}):

$$dU = TdS - (pdV + dW_{elec}) \quad (10)$$

Substituting (10) into (4) we get:

$$dG = -SdT + Vdp - dW_{elec} \quad (11)$$

Which for an isothermal and isobaric process ($dT, dP = 0$) we get equation (12) in differential form and (13) in molar quantities:

$$dG = -dW_{elec} \quad (12) \qquad W_{elec} = -\Delta g_{rxn} \quad (13)$$

The potential to do electrical work is defined by the electric potential difference, E [V}, through which a moving charge Q [C] passes as seen in equation (14). Considering the charge to be carried by electrons we get equation (15).

$$W_{elec} = EQ \quad (14) \qquad Q = nF \quad (15)$$

Substituting equation (15) into (14) we get equation (16) relating the Gibbs free energy of a reaction to the electric potential of that reaction:

$$\Delta \hat{g} = -nFE \quad (16)$$

At standard conditions (S.T.P) the electric potential difference/ideal standard potential which is the maximum available electrical work is given by equation (17) in differential form and in molar quantities at the same conditions in equation (18) [38]:

$$E^0 = -\frac{\Delta G^0}{nF} \quad (17) \qquad E^0 = -\frac{\Delta \hat{g}^0{}_{rxn}}{nF} \quad (18)$$

For the reaction of pure H_2 and O_2 at atmospheric pressure and at 298 K (R.T.P) the Gibbs free energy of formation is -237.1 [kJ.mol^{-1}]. Substituting values into equation (17) we get (19), a reversible open circuit voltage/standard reversible potential of 1.23 V.

$$E^0 = \frac{237.1}{2 * 96485} = 1.23\ V \quad (19)$$

However, to consider real-world operation of a fuel cell, we use the Nernst equation which accounts for the deviance from the ideal standard potential. The Nernst equation describes the relationship between the standard potential and the ideal equilibrium potential at other temperatures and pressures of reactants and products. Two common forms of the Nernst equation are given in (20) and (21).

$$E = -\frac{\Delta G}{NF} + \frac{RT}{nF}\ln\left(\frac{P_{O_2}^{\frac{1}{2}} * P_{H_2}}{P_{H_2O}}\right) \quad \textbf{(20)}$$

$$E = E^0 - \frac{RT}{2F}\ln\left(\frac{P_{O_2}^{\frac{1}{2}} * P_{H_2}}{P_{H_2O}}\right) \quad \textbf{(21)}$$

1.6 Fuel Cell Efficiency

Similarly to how we described the ideal reversible voltage, we can define the thermal voltage at a constant pressure:

$$E_{th} = -\frac{\Delta H}{nF} \quad \textbf{(22)}$$

which is the maximum available work assuming all of the potential chemical energy went into electrical work [17]. Taking equation (8) at isothermal conditions ($dT=0$) we get equation (23), or in terms of molar quantities at the same conditions, we get equation (24):

$$dG = dH - TdS \quad \textbf{(23)}$$

$$\Delta\hat{g} = \Delta\hat{h} - T\Delta\hat{S} \quad \textbf{(24)}$$

We can therefore define the maximum thermodynamic efficiency, also known as the fuel cell reversible fuel cell efficiency as the ratio of the maximum electrical work (the standard potential) to the thermal voltage, using equation (17), equation (22) and (23) to get equation (25).

$$\eta_{Fc,rev} = \frac{E^0}{E_{th}} = \frac{\Delta G}{\Delta H} = 1 - \frac{T\Delta S}{\Delta H} \quad \textbf{(25)}$$

For the simple hydrogen oxidation fuel cell reaction:

$$H_2 + \frac{1}{2}O_2 \rightarrow H_2O \quad \textbf{(26)}$$

(26)

at standard conditions, we substitute values of $\Delta G^0 = 237.1$ [kJ.mol^{-1}] and $\Delta H^0 = 285.8$ [kJ.mol^{-1}] into equation (25) to get the reversible fuel cell efficiency:

$$\frac{\Delta G^0}{\Delta H^0} = \frac{237.1}{285.8} = 0.83 = \eta_{FC,rev} \quad \textbf{(27)}$$

Evidently, fuel cells are not bound by the Carnot limit like other heat engines [39]. Figure 1.6 compares the Carnot efficiency and reversible fuel cell efficiencies defined in equation (25) versus operating temperate. A rejection temperature, T_L of 273.15 K is used. The higher heating value (HHV) considers the water produced in the reactions to be in the liquid phase. A gradient change is noticed at around 373K (100°C) for the fuel cell efficiency which is related to the water vaporisation (latent heat). The fuel cell has superior efficiency to the heat engine below 900K.

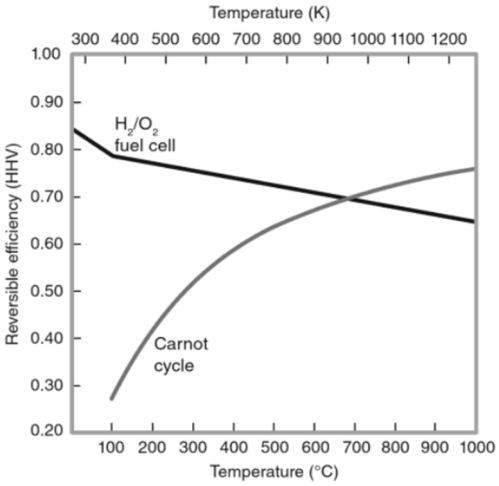

Carnot Efficiency

$$\eta_{carnot} = \frac{T_H - T_L}{T_H}$$

Reversible Fuel Cell Efficiency

$$\eta_{FC.rev} = \frac{\Delta G}{\Delta H_{HHV}}$$

Figure 1.6 - Carnot efficiency vs reversible fuel cell efficiency (HHV) where T_L = 273.15[K].

It is somewhat more convenient to describe fuel cell efficiency in a way as to avoid calculation of the enthalpy change of reactants and products which are hard to measure. Instead, a voltage efficiency, η_V, is defined:

$$\eta_V = \frac{V_{actual}}{V_{ideal}} \quad \textbf{(28)}$$

a ratio of the actual operating potential of the cell to the ideal voltage, defined and quantified in equation (17) and (19), respectively. Using this voltage efficiency we now define the actual efficiency (29), η_{actual}, as a product of the reversible fuel cell efficiency and voltage efficiency:

$$\eta_{actual} = \eta_{FC,rev}\eta_V \quad (29) \qquad \eta_{actual} = 0.83 * \frac{V_{actual}}{1.23} = 0.675 * V_{actual} \quad (30)$$

In order to account for the real world conversion efficiency of the chemical reactions within a fuel cell, we must consider the fuel utilisation. Excess fuel is typically fed to avoid starvation of the cell which can lead to accelerated degradation. The range of typical fuel utilisation range is large and is often between 40% and 80%. The fuel utilisation is defined by [40]:

$$F.U = \frac{iA}{nFv} \quad (31)$$

where *i* [A.cm^{-2}] is the current density, *A* [cm^2] is the active area, *n* is the number of participating electrons which is 2 for hydrogen, F is Faraday's constant, 96487 [C.mol^{-1}] which represents the charge per mole of equivalent electrons and *v* [mol.s^{-1}] is the molar flow rate of fuel supplied. Calculation in this way is useful for all fuel cell types and directly relates the fuel flow rate provided to the current produced. Fuel utilisation can also be calculated by considering the fuel cell from a chemical reactor viewpoint. To calculate the fuel utilisation in this way, knowledge of the inlet and outlet stream conditions are required. The conditions of the inlet streams such as flow rate, composition, temperature and pressure are often known, however, knowledge of the outlet conditions are more complex and costly to obtain. Nevertheless, calculating fuel utilisation in this way is useful, in particular for SOFCs as the energy contained in the exhaust fluids can be useful for CHP applications. The calculation is:

$$F.U = 1 - \frac{\dot{m}_{f,out}\Delta h_{f,out}}{\dot{m}_{f,in}\Delta h_{f,in}} \quad (32)$$

where $\dot{m}_{f,in}$ and $\dot{m}_{f,out}$ are the inlet and outlet mass flow rate from the cell, respectively [kg.s^{-1}]. The specific enthalpy associated with completely oxidising the inlet fuel and outlet/exhaust fuel is given by $\Delta h_{f,in}$ and $\Delta h_{f,out}$, respectively [kJ.kg^{-1}]. Finally, we can define the net efficiency of the fuel cell:

$$\eta_{net} = \eta_{actual} * F.U = 0.675 * V_{actual} * 0.7 \quad (33)$$

as a product of the actual efficiency and the fuel utilisation. Assuming a sensible fuel utilisation value of 70% and a typical operating potential of 0.7 V, the net efficiency is 33%.

1.7 Polarisation Plot

Applying an increasing potential difference on a cell (decreasing the operating potential from its OCV) acts to increase the driving force of electrochemical reactions to produce an increasing amount of current. The plot of the potential difference/operating voltage [V] of the cell versus current [A] or area adjusted current density [$A.cm^{-2}$] is known as a polarisation plot. A typical polarisation plot of a low temperature fuel cell at atmospheric pressure is seen in Figure 1.7. Labelled is the reversible open circuit voltage at 1.23 V and the lower actual open circuit potential (OCV) of the cell. The inverse relationship of the Gibbs free energy seen in equation (23) and OCV with temperature will see this value drop to nearer 1 V for a high temperature SOFC [17].

The curve can be split into three regions at low current density, medium current density and high current density in which different irreversibilities arising from real-world phenomenon are dominant [41]. In the low current density region, activation polarisation losses arising from sluggish electrode reactions (particularly at the cathode) which are dominant. In low temperature cells the high driving force for reactions results in a sharp voltage drop, however, high temperature operation such as that in SOFC promotes rapid kinetics and a very small drop is observed which can shift the curve upwards, increasing efficiency. The medium current density region is dominated by ohmic polarisation losses from the resistance to electron flow in the electrodes and current collectors and resistance to ion flow in the electrolyte. The ohmic region is characteristically linear. Increasing operating temperature acts to increase the ohmic resistance of typical anode and current collecting materials. However, typical SOFC electrolytes will have a decreasing resistance with temperature (between 500°C and 1000°C). The high current density region is dominated by mass transport losses associated with the poor supply of reactants to reaction sites and blockages of the sites with reaction products. The difference between the cell OCV and operating potential is called the overpotential, η. A lower overpotential for a given current density indicates a more efficient operation. Some cells incur additional fuel crossover and current leakage at the electrolyte. This describes the small difference between the theoretical maximum OCV at the cell operating parameters and the OCV observed.

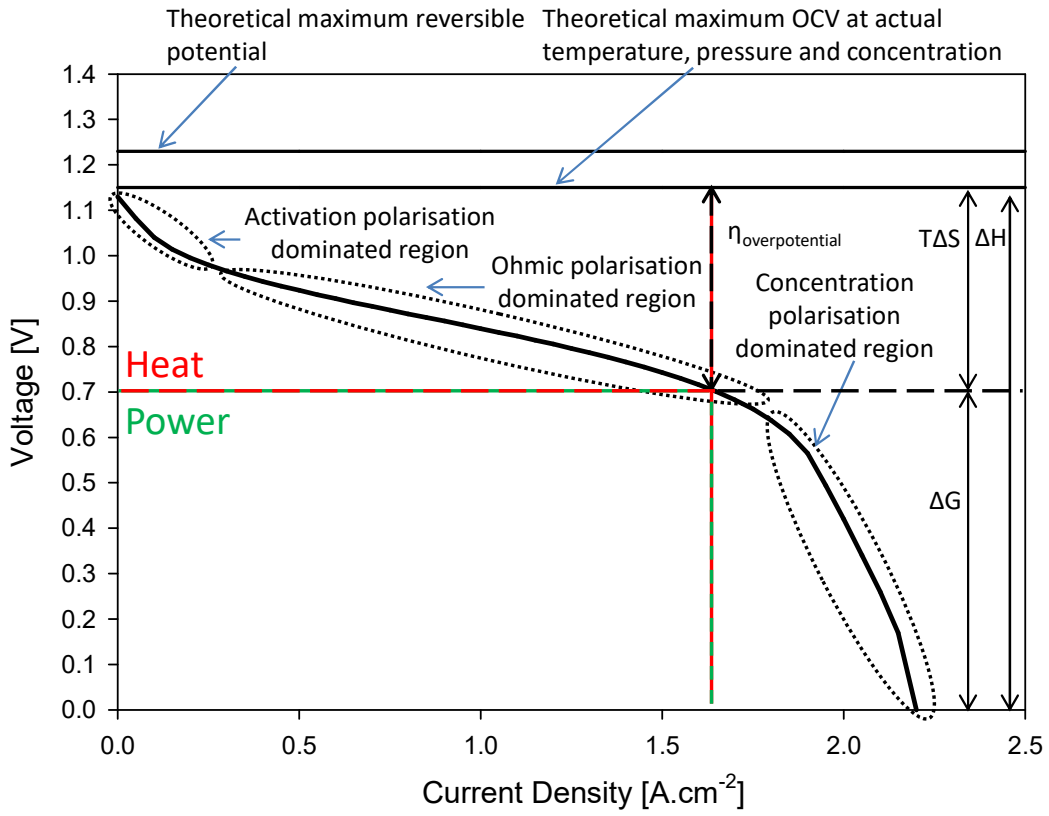

Figure 1.7 - Typical fuel cell polarisation plot with overlaid polarisation loss regions and thermodynamics.

The overpotential can be described with respect to the individual polarisation losses (which are well defined) incurred during operation and give an equation for the operating voltage of the cell [22]:

$$V = E^0 - \Delta V_{act} - \Delta V_{ohm} - \Delta V_{conc} = E^0 - \eta_{overpotential} \quad \textbf{(34)}$$

1.8 Solid Oxide Fuel Cells

Solid oxide fuel cells operate at high temperature and exhibit a typical electrical efficiency of between 50-60%, which is high when compared to other common fuel cells. If the heat generated by the high temperature SOFC is deemed useful, a combined heat and power (CHP) efficiency can be claimed at around and above 80-85%. The 'high quality' heat lends itself to integration into highly efficient steam and gas turbine power production systems [42]. Fuel is consumed (oxidised) at the anode seen in equation (35) while oxygen (typically from the air) is consumed (reduced) at the cathode as seen in equation (36). The mobile ion which is conducted through the ceramic electrolyte is an oxide ion, O^{2-}. The overall reaction seen in equation (37) produces water at the anode [26].

SOFC Anode:

$$2H_2 + 2O^{2-} \rightarrow 2H_2O + 4e^- \quad \textbf{(35)}$$

SOFC Cathode:

$$O_2 + 4e^- \rightarrow 2O^{2-} \quad \textbf{(36)}$$

Overall Reaction:

$$2H_2 + O_2 \rightarrow 2H_2O \quad \textbf{(37)}$$

SOFCs are available in several geometries, planar, tubular, and mixed types. Cells can either be self-supporting or externally supported. In the former, the electrode or electrolyte provides mechanical support for the cell [43]. In the latter, an external inert support may be used such as a porous ceramic material or the interconnect itself. Early tubular and planar cells were either cathode or electrolyte supported but now the standard is anode supported which allows for lower operating temperatures and ohmic polarisation coupled with improved mechanical stability. Relying on the relatively more conductive anode as a support also comes with issues surrounding mass transport losses through the porous structure, the potential for re-oxidation and loss of mechanical integrity and performance during operation. Externally supported cells are increasingly common in planar SOFCs, relying on the interconnect, typically a metal or an inert ceramic for mechanical support. The trend of SOFCs towards a lower operating temperature has widened the material selection for SOFC components [44]. Metal supported planar cells have a lower thermal mass and are less brittle than a ceramic supported cell and so can handle faster start-up times [45]. However, the operation is typically limited to lower temperatures (550 to 650°C) to avoid rapid degradation of the metallic components which restricts the use of internal reforming of hydrocarbons typically occuring above 650°C. In tubular devices, porous inert supports such as ceramics and metallic supports have been used. This allows for a segmented tubular cell design, essentially stacking cells along a support similar to integrated planar designs [46,47]. The externally supported SOFCs allow thinner electrode layers and electrolyte incurring lower ohmic loss and mass transport loss. Similarly to planar interconnects, tubular supports can contribute to improving/controlling gas flow to improve fuel utilisation. If electrically conductive, the support can also contribute to the current collection.

The planar geometry predates the tubular geometry and has been the most widely adopted. Planar cells typically have a higher power density than tubular cells at around 2 $W.cm^{-2}$ and are relatively easy to manufacture and stack [44]. However, homogenous gas supply and sealing are common issues. In addition, planar SOFC stacks have a high thermal mass, which combined with the gas supply issue make typical start-up times in the order of a few hours to avoid thermomechanically induced failure. A planar SOFC schematic is seen in Figure 1.8. The single cell is adjoined electrically and physically to adjacent cells by the interconnect [48]. The interconnect also functions as a barrier to chemically opposing electrode environments while controlling the flow of fuel and oxidant to the anode and cathode, respectively. The current direction is indicated by the yellow arrow. Planar stacks are typically heavy due to the large amount of interconnect material needed to separate each cell. The balance of plant (BoP) for planar stacks is often bulky, in particular, the gas supply and cooling system which combined with the slow start-up time and concern over mechanical durability typically restricts planar devices to stationary applications.

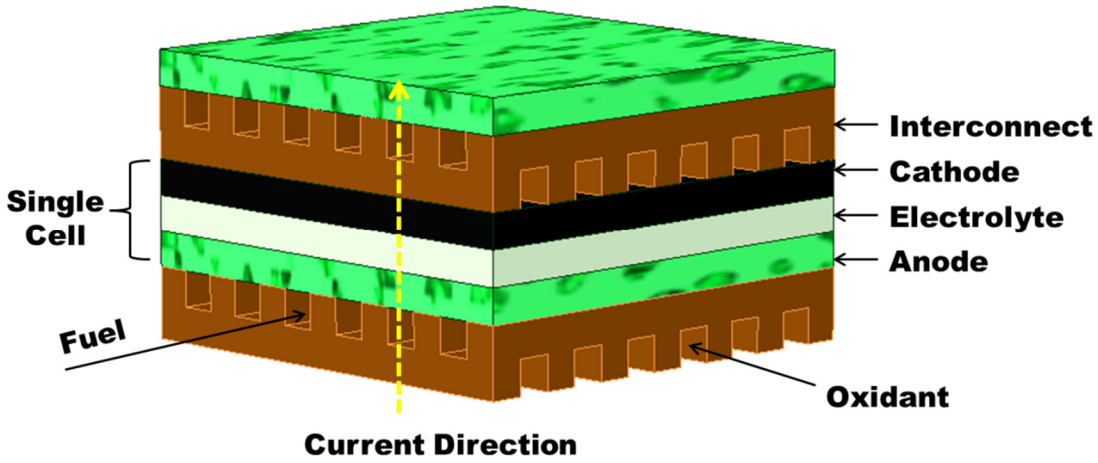

Figure 1.8 - Planar SOFC geometry.

Tubular cells are sub-divided by size, regular tubular SOFCs and microtubular SOFCs (µT-SOFC). Regular tubular were the first tubular SOFC, developed by Siemens Westinghouse, having a typical diameter of 1" and 2200 mm length [49]. Microtubular SOFCs developed by the Kendall family in the early '90s had diameters in the order of a few millimetres and length one or two orders of magnitude shorter than their larger predecessor [50]. The inverse proportionality of power density with tube radius means smaller cells have a relatively higher power density [51]. More recently, tubular SOFCs have been reported with larger diameters in the order of a few centimetres giving a higher total power per cell. This reduces the number of cells required in a stack for a given power output which

reduces complexity in manufacturing and assembling. Nevertheless, the larger size brings less mechanical stability.

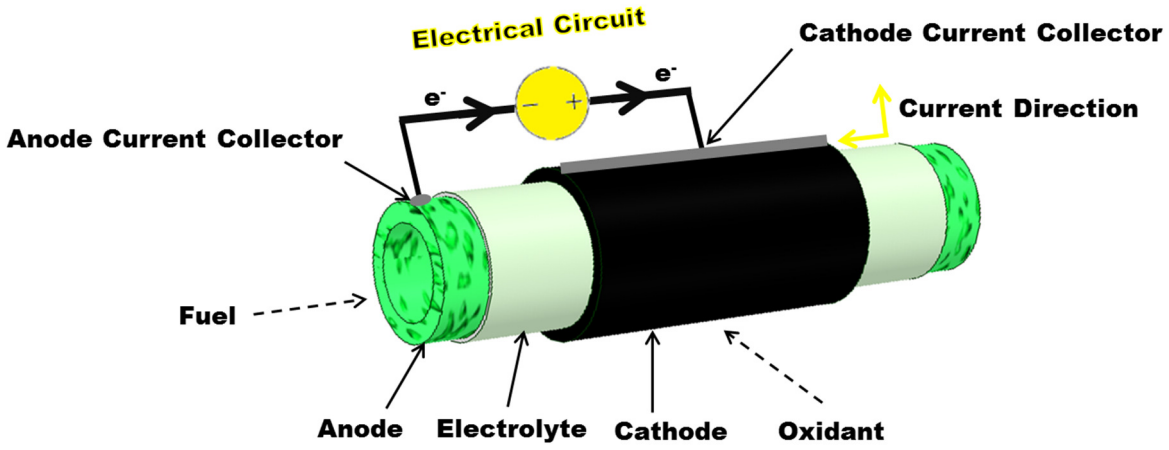

Figure 1.9 - Tubular SOFC geometry (anode supported) with current collectors and indicated current direction.

The distinguishing characteristics of planar versus microtubular SOFC cells are seen in Table 1.1. Microtubular fuel cells have inherently facile sealing and gas flow control, given that the dense electrolyte separates gas streams rather than an interconnect. A schematic of a tubular cell with current collectors and indicated current direction is seen in Figure 1.9. Tubular fuel cell designs exhibit similar power densities to planar devices at up to 1.5 $W.cm^{-2}$ [52,53]. The µT-SOFC concept lends itself to high mechanical strength and high thermomechanical durability. This strength and is inversely proportional to cell diameter. Smaller diameter cells have less material in a given length and so statistically speaking have a lower probability of crack formation and propagation. It was for this reason that the original Siemens Westinghouse (regular) tubular cells with larger cell diameter had a start-up time of more than 100 hours. The durability to mechanical shock and thermal cycling of µT-SOFC allows for rapid start-up times in the order of a few seconds [54]. The aforementioned enables near-instant, on-demand power permitting µT-SOFCs to be used for both stationary and portable power applications [55]. This widens the market for SOFC technology not typically accessible by planar devices. Several commercial companies have worked on µT-SOFC development including Adelan, Acumentrics, AMI, Ezelleron, Protonex, Komico, NGK, Toto, Tokyo Gas and others [50,56]. Tubular SOFC products have reached the commercial market globally, most widely adopted in Japan and Korea [57]. Portable devices have included the tubular Kraftwerk [58], a 5 V (10 W peak power) charging device (which was eventually never produced).

Table 1.1 - Characteristics of µT-SOFC and planar SOFC.

Characteristic	Tubular	Planar
Power Density	Medium	High
Mechanical Strength	High	Low
Start-up	Fast	Slower
Interconnect	Difficult/Cumbersome	Costly
Sealing	Facile	Mandatory
Manifold	Simple	Complex
Stack Power Density	Medium	High
System Compactness	High	Low
Manufacturing Cost	Medium-High	Low

The number of journal and conference articles in academic literature on tubular SOFCs has followed a declining trend over the past five years as seen in Figure 1.10 a). Instead, research has widened into more fundamental problems associated with µT-SOFC (and in most cases planar SOFC) such as sealing, manifolding and material development. Research in the field has been dominated by authors from China, showing nearly double the number from the USA which is the next largest contributor as seen in Figure 1.10 b). Materials development and testing, which are a common SOFC development area, are easier to conduct in planar form. Interconnection/current collection in tubular SOFCs is a critical area for development and is a bottleneck in the commercialisation of tubular cells and stacks.

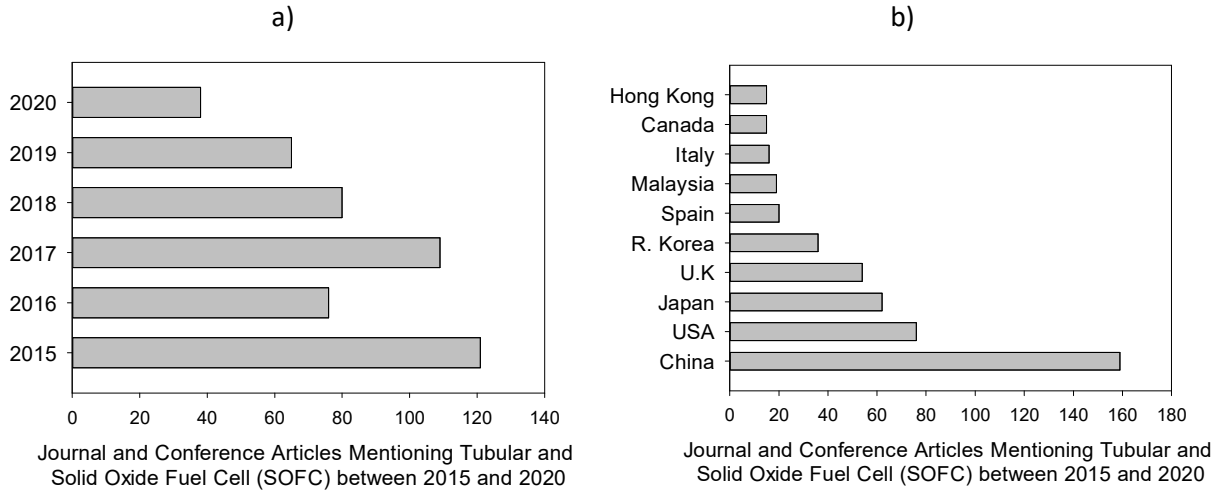

Figure 1.10 - Number of journal and conference articles between 2015 and 2020 mentioning tubular and solid oxide fuel cell (SOFC) from an Engineering Village search a) by year, b) by location.

1.9 Current Collection in µT-SOFC Cells and Stacks

To extract power from a tubular SOFC cell, current collectors must be used at each electrode. The low voltage characteristic of a fuel cell means cells are typically stacked to achieve a useful power output by interconnecting current collectors of adjacent cells. Current collection is one of the greatest problems for tubular SOFCs. Minimising current conduction pathways and thus minimising the resistance to electron flow is critical to reducing the ohmic resistance of interconnections. In planar configurations, the interconnect is in-plane with the electrodes of repeating cell units, contacting a large area of the electrochemically active region, resulting in short, mostly out-of-plane electron conduction pathways. In tubular configurations, however, cells are spaced apart. The minimum limit for cell spacing which is controlled by the manifold design is determined as a function of assembly logistics, wiring logistics and by the thermal management and gas supply design. These restrictions limit compactness, resulting in an interconnection network with a considerably higher pathway length. The cylindrical geometry plays a factor in the complexity, as current flows in the axial and radial dimension, increasing current conduction pathway length and leading to complexity in the interconnect design [41]. The direction of the current flow within each cell and throughout a stack will vary greatly with the current collector/interconnect configuration.

The early microtubular cells of the 1990s, developed by Kendall and Kilbride from Keele University (GB), had 'internal' anode current collection, typically nickel or silver, either as a spring-loaded coil or as a rolled mesh inserted within the cell fuel channel (on the bore side). Cathode current collection was typically achieved via silver wire wrapped/wound around the cell 'exterior' [59–62]. Anode current collection changed direction somewhat in the 2000s when research from AIST (Japan) such as Suzuki [63,64] and Dhir and K. Kendall (GB) [65–67] developed a technique to contact the anode from the cell exterior (external anode current collection) by either partially covering the anode support with electrolyte during fabrication, or by moving a portion of electrolyte to expose the anode interior (of an anode supported cell). A schematic of internal and external current collection of an anode supported tubular SOFC is seen in Figure 1.11.

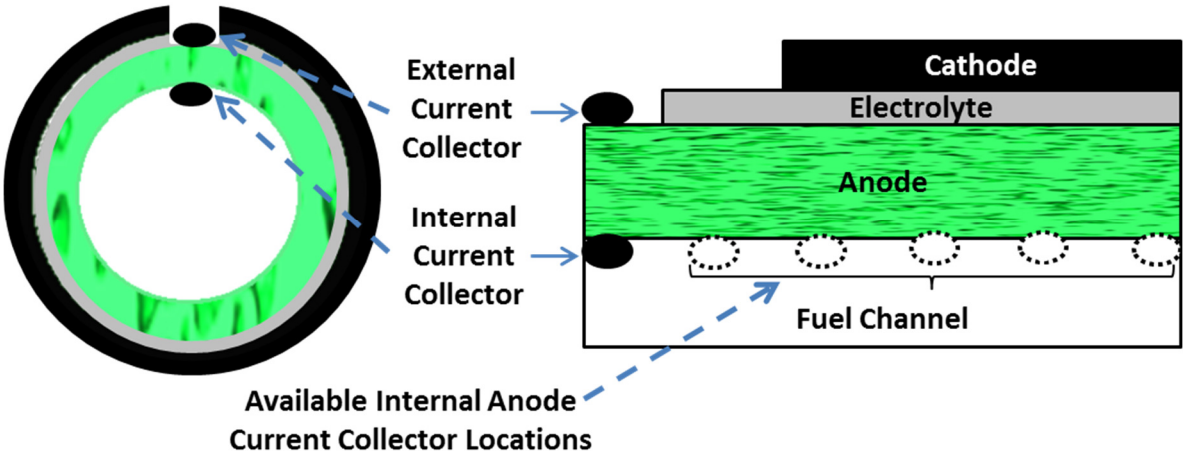

Figure 1.11 - Schematic of internal and external current collection in an anode supported µT-SOFC.

Results from the latter researchers showed that loss of contact between internal current collectors and the electrode due to thermal mismatch/shrinking and improper contacting led so severe degradation, indicating that R&D into a method for interconnect-electrode contacting for internal current collector designs was needed. The externally contacted anode showed enhanced electrochemical stability when tested and a reduced degradation rate. However, the new style necessitated sealing of the porous, exposed anode with high-temperature gas-tight sealants, another key area of development in SOFC technology [68]. For a given cell length, the internal current collector allows for a larger active area given the space requirement for an anode current collector allowing for a higher total power per cell. The method used for the current collection from the cathode of anode supported cells has remained largely unchanged from the aforementioned early 1990s research. Specifically, wrapping or hatching wire (most often silver) around the cathode surface, bound using mechanical force or by using adhesive pastes/sealing materials typically silver, gold or platinum based.

1.10 Interconnect Performance

Fundamentally, an SOFC interconnect must have a low ohmic resistance to minimise ohmic polarisation and thus must have a high electrical conductivity (bulk) and a low contact resistance. The resistance to electron flow or ion flow is governed by Ohm's law, from which we observe the proportional nature of voltage drop with current and resistance:

$$\Delta V = IR \tag{38}$$

where the voltage [V] is denoted by *V*, *I* is the current [A] and *R* is the resistance [Ω]. The resulting power loss can then be estimated:

$$P = \Delta V * I = I^2 R \quad \textbf{(39)}$$

from which we observe the proportional nature of voltage drop with resistance and the squared relationship with the current. However, it is more convenient to express equation (38) with a voltage drop, ΔV_{ohm} or ohmic polarisation with respect to the more familiar current density i [A.cm^{-2}] presented in polarisation plots (38). To do so, we introduce area specific resistance (ASR) measured in Ω.cm^2:

$$\Delta V_{ohm} = i * ASR \quad \textbf{(40)}$$

ASR is the key metric used to determine the ohmic performance of a cell. This normalised metric allows for comparison of different sized cells on an equivalent basis. The ASR of a cell can be derived from experimental data as an average over a potential range within the linear ohmic region from the gradient of a polarisation curve:

$$ASR\ [\Omega.cm^2] = \frac{\eta_{ohmic}[V]}{\Delta i\ [A.cm^{-2}]} \quad \textbf{(41)}$$

where the potential range should be the ohmic overpotential $\eta_{ohmic}[V]$, taken over the linear ohmic loss dominated region of the i-V curve, and Δi is the current density difference over that range. The ASR can be measured locally at a given potential or current by electrochemical impedance spectroscopy (EIS), where the total resistance R_T is measured and then adjusted by the active area [69]:

$$ASR\ [\Omega.cm^2] = A_{cell}[cm^2] * R_T[\Omega] \quad \textbf{(42)}$$

It should be noted that the ASR calculated in equation (41) and (42) are for the entire cell, and so the contribution from activation and mass transport polarisation is present, even though the data acquisition conditions are set so that the ohmic effects dominate the results. However, the ohmic polarisation, $R_{\Sigma\Omega}$ [Ω], which is cell specific be directly acquired from EIS data, yet still contains a contribution from ionic flow resistance in the electrolyte and electron flow in the electrodes and

interconnect. However, adjusting this value by the cell area does not give the ASR. The ASR of a virgin or tested material can be calculated ex-situ by measuring the resistivity, ρ, of known material thickness [48]:

$$ASR\ [\Omega.cm^2] = \mathrm{x}\ [m] *\ \rho\ [\Omega.\mathrm{cm}] \quad \textbf{(43)}$$

ASR targets for interconnect materials of the past (pre-2000s) were <100 mΩ.cm^2. With the more recent advancements in R&D, this target has been lowered by an order of magnitude within the last five years to <10 mΩ.cm^2 [70–72]. The target for overall cell resistance is <500 mΩ with <1000 mΩ deemed to be acceptable. The typical contribution of an SOFC interconnect to the ohmic polarisation is around 20 to 25%. The ohmic resistance of the interconnect itself can be broken down into contributions from the bulk material conductivity (which is the inverse of the resistivity) and the contact resistance:

$$\sigma\ [S.m^{-1}] = \frac{l}{RA} \quad \textbf{(44)}$$

Targets for values of the contact resistance are between 0.01 Ω.cm^2 and 0.05 Ω.cm^2 [73]. The three major factors related to interconnect contact resistance are (a) dimension tolerance and flatness of the interconnect, (b) non-uniform compression from the interconnect onto the electrode, and (c) the state of the contact surface (roughness, spallation, defects). While optimising the material for low resistance is important, it is common to test the performance of the material within a cell, which will better account for the real-world performance, hence why the cell ASR is a common metric in comparisons.

Given the intimacy of an interconnect to adjacent cell components, an interconnect must have similar thermal conductivity and thermal expansion coefficient to adjacent cell components and be chemically compatible in reducing and oxidising (RedOx) environments. Mechanical integrity and low weight must also be considered, particularly for portable applications, in addition to low cost and ease of manufacture/assembly [48,72]. In tubular configurations the interconnect does not always act as a barrier between the opposing anode and cathode environments, depending on the cell design. This opens up some degrees of freedom on interconnect requirements, and designs can be tailored to a specific electrode. Specifically, the requirement for gas-tightness and stability in both RedOx environments, when dropped, can widen the suitability of materials and interconnect design choices.

1.11 Thesis Objective

The goal of this thesis is the development of a high-performance, robust µT-SOFC stack with a low ohmic resistance for portable applications. The study will focus on current collection on a single cell level, addressing the minimisation of anode-current collector contact resistance to reduce the cell ASR. The optimised design on the single cell will be upscaled to the stack level, addressing the additional complexities from interconnection. Consideration to manifolding and sealing will be made before fabricating and testing stacks. Mathematical modelling and CFD modelling will be used throughout the study to aid understanding and for optimisation.

Chapter 2 Literature Review

This chapter presents a detailed literature survey of the empirical and modelling research regarding current collection and stack design in tubular solid oxide fuel cells and stacks. The chapter elaborates on research of the materials and methods used for current collection and the effects of current collector number, sizing, spacing and structure on cell performance. Research and research methods used for numerical and mathematical modelling of μT-SOFCs are studied. The chapter details the empirical and modelling research and research methods of μT-SOFC stack design with a focus on interconnection, manifolding and sealing. The aforementioned research is analysed and critiqued in order to ascertain solutions and a strategy for addressing the problems faced in the μT-SOFC field.

2.1 Materials for Current Collection

The trend in interconnect material selection, following the movement from high-temperature SOFC operation above 850°C to lower temperatures around 700°C to 750°C, has replaced the traditionally used ceramic perovskite-type materials such as $LaCrO_3$ as used in the original Westinghouse tubular designs, by nickel- or chromium-based steels and more recently ferritic stainless steels, as seen in Figure 2.1 [48,74]. Ceramic-based interconnects are brittle, costly and bring difficulties concerning their manufacture, shaping and cell assembly [75]. Metallic interconnects, however, are less brittle, potentially lower in cost, and possess inherent ductility, lending themselves to facile shaping. Metallic interconnects also have a much higher thermal conductivity than the traditional ceramic counterparts which leads to a favourable reduction in start-up/shut-down times of stacks, widening the scope for potential SOFC applications [48]. Typical metallic interconnect materials include ferritic stainless steels such as Crofer 22A/APU/H and ITM, chromium-based materials such as CFY [76], austenitic steels such as Alloy 310 [77] and nickel-based alloys such as Haynes 230, favoured for its corrosion resistance over Inconel and Hastelloy counterparts [78–80].

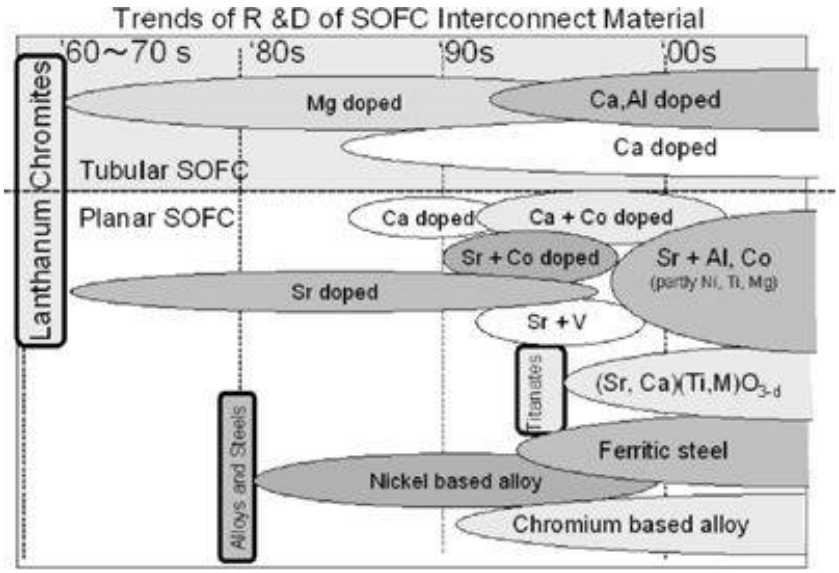

Figure 2.1 - Trend in R&D of SOFC interconnect materials [9].

Metallic interconnects come with their own problems to overcome, namely the increase in ASR and decrease in mechanical properties resulting from reactivity in redox environments through high-temperature corrosion mechanisms as seen in Figure 2.2 [81–83]. It should be noted that the ASR values of a current collector material are not the same as the ASR values of a cell using this material as a current collector. The ASR of a cell will be significantly higher given the additional contribution of the electrodes and electrolyte. The ASR of a material has a contribution from the bulk conductivity of the material and the contact resistance, the resistance at the interface of that material with the measuring device/adjacent materials. Chromium is typically used as an alloying element in metal interconnects to adjust the coefficient of thermal expansion (CTE) to adjacent fuel cell electrodes and the electrolyte. The chromium content is also important as it serves as a reservoir for the formation of a protective coating to prevent further oxidation. For an SOFC interconnect the ideal chromium range is between 18 and 22wt%, above which it contributes considerably to the ohmic resistance and below which it will not form the protective coating. Volatile chromium species migrate to the cathode causing poisoning [84]. Nevertheless, protective barrier layers can be applied to the exterior surface of the interconnect to minimise the effects and are in the development phase. Studies to mitigate such degradation have focused around optimisation of the composition and application techniques of the protective coatings such as $(Mn,Co)_3O_4$ and the control of naturally formed oxide layer growth, particularly in stainless steels [70,85–87].

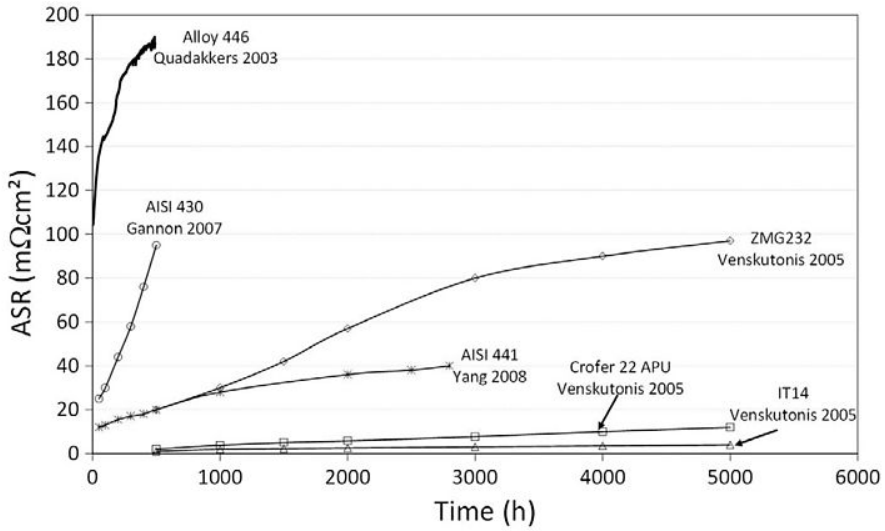

Figure 2.2 - ASR evolution of typical interconnect materials [72].

A key advantage of metallic current collectors is the ability to be joined to the electrodes, with other current collectors (interconnection), and to stack components with standard welding or brazing techniques [71,88]. A compressive load is applied to a planar stack to ensure intimate contact between fuel cell and interconnect components which is not possible in a tubular configuration, further highlighting the need for a secure interconnect-electrode and interconnect-interconnect joint able to withstand the thermally induced stresses and mechanical impacts incurred during operation [89]. Welding and brazing both use heat to melt a filler material that joins parent materials together. Welding is limited to metals and requires a higher temperature than brazing as the parent metal must also melt. Welding is suitable for exterior joints or where localised hot-spots caused by the welding flame are not an issue. Welded joints often have very high strength and can be fabricated at scale at a low cost. Brazing can be achieved at far lower temperatures than welding and both metals and non-metals such as ceramics can be brazed as only the filler material melts. Brazing can be done by induction, whereby a current passes through a magnetic metal braze causing it to flow and form a joint once cooled. Brazing can also be done in a furnace with a flame or electrical heating. The furnace can be used to carefully control the heating/cooling rate of the parent and braze materials which can alleviate CTE mismatches between components and avoid the formation of mechanical stress and failure in fuel cell components such as the electrolyte.

Gas tightness is an imperative interconnect property when acting as a barrier between opposing chemical environments as any leakage would lead to fuel combustion, fuel which will not be converted to electrons, leading to thermal hot spots which accelerate local degradation [90]. In

tubular configurations, solely the electrolyte provides the barrier between the fuel and oxidant atmospheres, giving an additional degree of freedom to interconnect material choice, potentially tailoring to suit either the anode or cathode side. This, combined with the lack of requirement for load-bearing/compressive strain has led to the use of highly conductive but costly precious metals, the most common being silver, followed by platinum, gold and palladium. These precious metals are known for their inertness and stability in high-temperature redox environments and do not form non-conductive oxide layers in air at elevated temperatures. Nickel, a non-precious, favourably low cost but relatively less conductive metal, is also frequently used as seen in Figure 2.3.

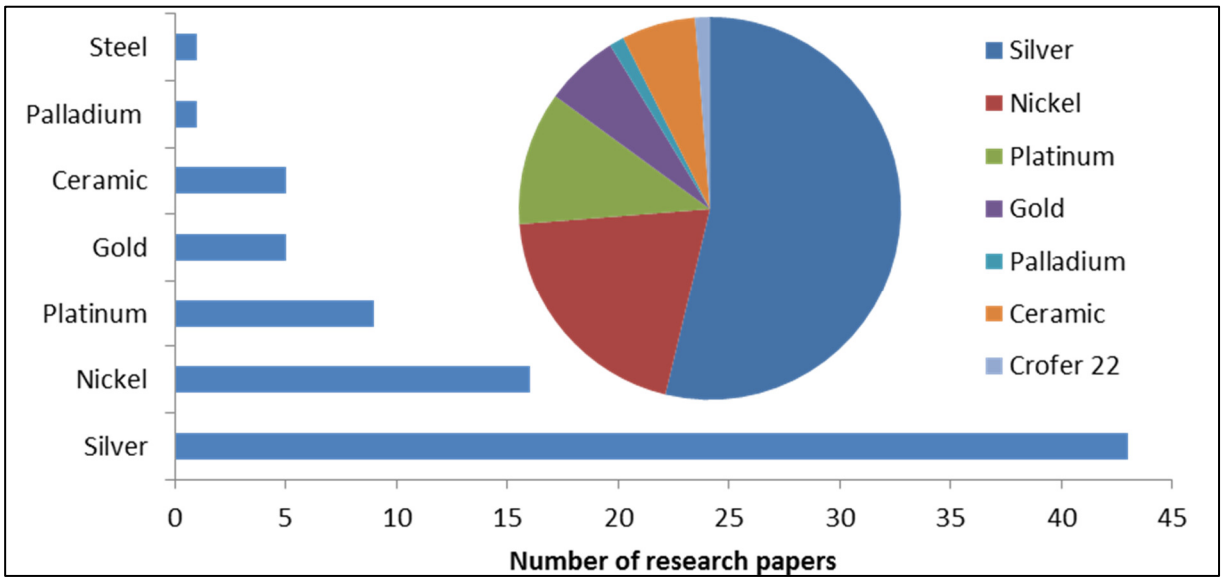

Figure 2.3 - Current collector materials used in µT-SOFC tests reported in literature, extracted from Table 2.2, for the 2015 to 2020 period.

While most frequently used, silver is not without fault. Compson et al. [91] suggested using silver as a SOFC interconnect at temperatures below 650°C to avoid loss of silver via sublimation, evaporation and diffusion. Degradation is particularly prevalent in silver under a dual atmosphere (redox) which may occur if silver is being used as a conductive paste on an externally accessed anode current collector or around fuel manifolds. Oxygen and hydrogen permeate the structure and form steam bubbles, leading to cavity nucleation and growth, and henceforth a loss of hermeticity [92]. Majewski et al. [93] observed the degradation of silver in a redox environment within 8 hours of operation when used as a µT-SOFC current collector at 700°C. They observed temperatures 100°C above the furnace temperature at the interface, indicating fuel crossover and resulting (spontaneous) combustion due to porosification of the originally gas-tight/dense silver sealant. Any silver migration could also lead to short-circuiting and reduced performance. While the melting temperature of silver

is 961°C, higher than typical SOFC operating temperatures, softening (annealing) of the wire and hence the loss of mechanical integrity occurs at far lower temperatures, a key factor for loss of interconnect-anode contact of silver-based internal current collectors [94]. Ding et al. [95] attributed the failure of their 4-cell stack to severed silver wires after only 4 hours of operation at 800°C and stated an urgency in finding an alternative current collector material for their tubular cells.

While nickel is somewhat stable in reducing environments, it undergoes high-temperature corrosion in oxidising environments, causing the formation of non-conductive oxide layers, hence its use on the anode side only (unless coated). Stable as it may be in reducing environments, nickel is a well-known reforming catalyst, which is employed in Ni-YSZ anodes for the electrochemical oxidation of hydrogen and in direct internal reforming. When used as an anode side interconnect with hydrocarbon fuels there will likely be a reduction in performance of the interconnect over time from carbon formation [96]. The metallic structure, high melting point and thermo-mechanical integrity of nickel across SOFC operating conditions favour it as an affinitive base metal to support well-adhered protective coatings. It is commonplace in the automotive and electronics sector. Coating with a more inert/corrosion resistant, more electrically conductive and hard/hard-wearing natured materials such as gold, silver, nickel-alloys and even perovskites can enhance the electrical performance and durability of nickel as a current collector for both the anode and cathode. Coatings can be achieved by simple painting/dipping techniques, by electroplating, a current-driven process, or by electroless plating, a chemically-driven process, of which the latter two can be produced at scale. Electroless plating achieves a more homogenous coating and finer control over layer thickness (proportional to exposure time for a given plating chemistry) than electroplating, particularly for intricate parts of differing thicknesses where an applied potential results in varying current densities, and thus differing rates of localised coating application [97–99].

A study by Hatchwell, Sammes and Kendall [59] looked at cathode side current collection methods from a materials perspective. The experiment determined whether a perovskite coated, nickel-based steel (Nimonic 90) could show comparable performance to the more commonly used silver wire. The coating suppressed chromium migration, but the electrical performance could not match that of the silver wires. They further discussed the limitations of using silver due to its high evaporation rates at typical SOFC operating temperatures, meaning unpredicted temperature spikes could inflict irreparable damage to the silver. Wire and strips of the silver were very close in performance, while a comparison of silver conductive ink covering the entire cathode versus a two-strip configuration

suggested the ink interference in cathode performance was negligible for this ink composition and cell geometry. The properties of typical SOFC interconnect materials and Ni-YSZ for a reference are given in Table 2.1.

Table 2.1 - Material properties of commonly used interconnect materials.

Material	CTE x 10^{-6} [K]	Conductivity [$S.cm^{-1}$]	Melting Point [°C]	Youngs Modulus [GPa]	Ref(s).
Ni-YSZ	11-13	$3x10^2$ (800°C)	-	57-58 (800)	[48,100,101]
$LaCrO_3$	9.5	0.34 (700°C)	2510	-	[89,101,102]
Crofer 22-APU (ferritic)	11.5-12.5	$8.3x10^4$ (1000°C) $8.7x10^3$ (800°C)	1510-1530	216 (750)	[100,103–105]
Haynes 230 (nickel-based)	15.2 (800°C)	$7.7x10^3$ (800°C)	1301-1371	159	[80,106]
Ducrolloy (Cr-based)	11.8-12 (800°C)	$1x10^4$ (1000°C)	1700	69	[107,108]
Silver (99.9%)	18.9,22 (800°C)	$1.6x10^5$ (800°C)	961	69	[102,109]
Nickel	13	$2.5x10^4$ (800°C)	1455	190	[110]
Platinum	10 (800°C)	$2.3x10^4$ (800°C)	1769	154-172	[102]
Gold	16.6 (800°C)	$1.1x10^5$ (800°C)	1064	79	[102]
Palladium	12.3(800°C)	$2.55x10^4$ (800°C)	1552	121	[102]

2.2 Current Collector Shape and Structure

Once the designer has chosen the optimal interconnect material, the thickness, shape and structure must be determined. For a planar device, this will be some sort of flat plate with an optimised corrugation/patterning for fuel and exhaust flow. In a tubular device, the decision is less clear and depends on whether current is collected on the bore side of the tube or the outer surface. The material will need to be formed to achieve intimate contact with the electrode and so a form that can be easily worked/shaped is preferable. The need to minimise electron pathway and maximise the contact area for current collection means designs can vary greatly. A study in planar SOFCs by Jiang et al. [111] showed that when current collector-electrode contact area was increased from 4.6% coverage to 27.2% the resistance of the cell decreased by 87% from 1.43 $\Omega.cm^2$ to 0.19 $\Omega.cm^2$ at 800°C. Consideration to preventing the current collector from impeding gas flow to and from the electrode must also be made remembering that an impermeable/non-porous current collector

covering the entire electrode surface would render the fuel cell useless. The tube dimension is a key factor in the design and problems can be common or specific to small/large bore and short/long variants. For example, in small-bore tubes (less than 2 to 3 mm ID), internal access is particularly difficult and the current collector size is limited, limiting the size and wire thickness and thus its current-carrying ability (w.r.t voltage loss), which is exacerbated if the length of the cell and contact wires are long. For larger bore tubes, achieving a suitable spring force (arising from the elasticity of the contact material), which is often relied on for smaller bores, becomes difficult due to the softening of the material at operating temperature which has a more significant impact on larger structures than smaller ones.

2.2.1 Wires

Wires are the most common choice of current collection and are used in some form in all but three of the publications reported in the literature (in Table 2.2) between 2015 and 2020, whether used for the anode and/or cathode current collection, as measurement probes, as the sole current collector, or in a combination with another design. In the last 5 years, the most common wire choice has been silver, followed by platinum, then gold and then nickel. Wires are readily available in most materials and dimensions and when chosen correctly achieve highly efficient current collection/conduction over long distances, an ideal candidate for interconnection between adjacent cells. Wires were the first μT-SOFC current collector to be used, published in the academic literature of the early 1990s [59,60,112]. Wires can be easily formed and shaped and can come in different profiles including round, flattened and triangular which can vary the available contact area, fitting and mechanical properties of the wire. Increasing the diameter of the wire reduces the voltage loss in the wire for a given current. Braiding is useful when the correct diameter of wire is not available and has the advantage of increasing the mechanical strength of the wire, important when a wire is operating at a temperature close to its softening/melting point. Wires can be easily shaped and are often coiled to fit the tube interior and exterior. Wires can be joined to create crisscrossed mesh-like structures, or into strips and bands. The cell with the highest power density reported in literature was recently published by Ren et al. [53] where silver wire and silver paste were used for both the anode and the cathode side of their alumina supported ‘microchannel structured’ cells. They achieved a current density of 1.4 $A.cm^{-2}$ at 0.7 V and a peak power density of 1.5 $W.cm^{-2}$ at 700°C although the cell did not supply an OCV of over 1 V which indicated either a severe fuel leakage and/or that the electrolyte was not complete and fully dense. When operated directly on methane the peak power

density was 1 $W.cm^{-2}$ and the ASR determined by EIS at OCV was 0.32 $\Omega.cm^2$ at 700°C. Rabuni et al. [20] achieved a current density of 1.25 $A.cm^{-2}$ at 0.7 V with a peak power density of 1.2 $W.cm^{-2}$ and an OCV greater than 1.1 V at 750°C. The cell reached 1.8 $A.cm^{-2}$ and 1.62 $W.cm^{-2}$ when operating at 800°C. The ASR determined by EIS was approximately 1 $\Omega.cm^2$ and 1.26 $\Omega.cm^2$ at 750°C and 800°C respectively. The authors used silver wire and silver paste for both anode and cathode current collection. The anode had 6 micro-channels as well as an optimised microstructure with finger-like structures for enhanced mass transport as seen in Figure 2.4.

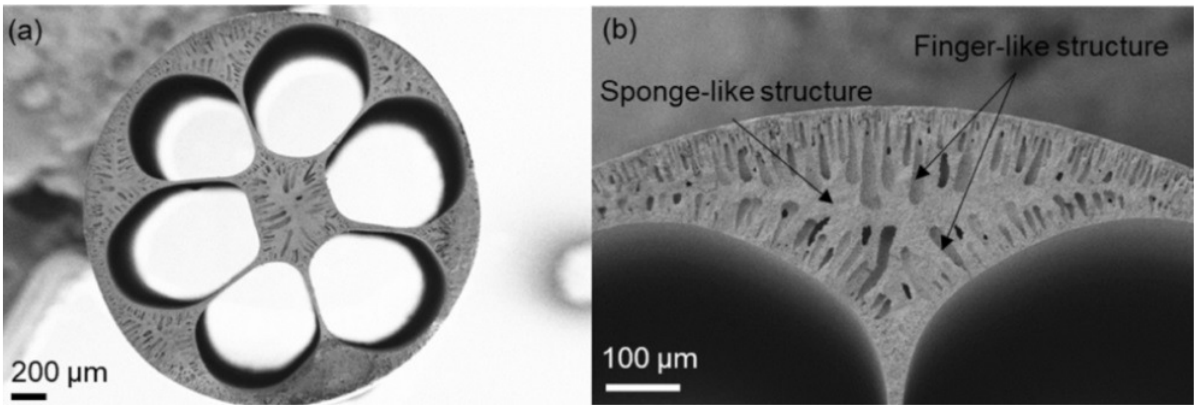

Figure 2.4 - 6-channel µT-SOFC cell with optimised microstructure a) cross-section, b) magnified microstructure [20].

2.2.2 Conductive Pastes, Paints and Inks

Wires (and other current collector types) are seldom used on their own, they are often used with the addition of conductive metal-based pastes/paints/inks (from here on jointly referred to as pastes). The pastes can be applied to the electrode, on the current collector or to both [113]. The paste acts to decrease the interfacial contact resistance between the electrode and current collector and acts as a bridge to ensure a continuous path for electron flow. The pastes are more conductive than typical anode cermets and cathode materials and so the paste will increase the overall conductivity of the cell in the axial and radial direction, acting as a current collector layer, which is particularly important for larger cells [25,114]. Pastes can also be used to secure the electrode to the current collector and are sintered to enhance their mechanical adhesion once applied [115]. Pastes are usually hand-painted which is a cause for concern with respect to reproducability and manufacturability [113].

The paste materials are most commonly silver, gold, platinum or nickel, the latter being reserved for the anode side [116,117]. Manufacturers offer variants with varying final porosity to control the gas

distribution and conductive properties. Denser variants are favoured when the contact patch is small in order to maximise the conductivity of the joint, or where sealing is also required, meaning the paste has dual functionality. More porous paints, which are typically less viscous (generally referred to as paints or inks) can be spread more liberally, covering the entirety of the active area if desired, which may lend itself to ease in manufacturing [52]. The conductive pastes can also infiltrate the electrodes and improve electron mobility in percolation pathways. Silver's functionality as a cathode material, acting as a catalyst for oxygen reduction, will contribute to electrochemical cell performance [93].

2.2.3 Current Collecting Layers

Somewhat similar to conductive pastes, current collecting layers can be used to improve the overall conductivity of an electrochemical cell. They can be an electrode or non-electrode materials, with properties biased towards current conduction rather than electrochemical/catalytic activity. The layers are typically formed in-situ during cell manufacture and can also provide mechanical support for the cell. Panthi et al. employed a nickel anode current collector layer in their porous zirconia supported tubular cells as seen in Figure 2.5 [118,119]. In their 2017 study, they achieved a current density of 0.8 $A.cm^{-2}$ at 0.7 V and a peak current density of 2 $A.cm^{-2}$ operating in H_2 at 750°C. The impedance at OCV operating under the same operating condition was 0.44 $\Omega.cm^2$.

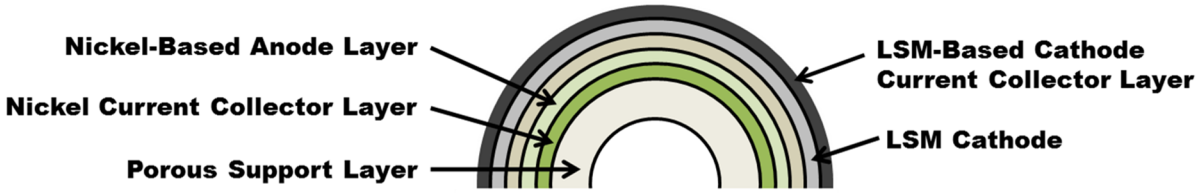

Figure 2.5 - Nickel anode current collecting layer in a porous YSZ supported cell reproduced from [118]**.**

Zhao et al. [120] also adopted a nickel current conduction layer in their 'inert-substrate-supported' cells. They studied the effect of increasing the current conducting layer thickness, finding that thickening the layer was favourable for the electrochemical performance but not for the redox stability of the cell. For their optimal design, they achieved a current density at 0.7 V of 0.63 $A.cm^{-2}$ with a peak power density of 2.5 $A.cm^{-2}$ in dry H_2 at 800°C. The ASR recorded at OCV at the same operating conditions was 0.75 $\Omega.cm^2$. The degradation rate was 4 mVh^{-1} over 11 redox cycles.

Kikuta et al. [121] looked into varying the ratio of thickness between a porous nickel anode current collecting layer and the anode, fixing the total thickness to 250 µm. The cell was a closed-end tube, single chamber design, meaning anode current collection was only possible from one end of the tube. They achieved a significant improvement with even the thinnest, 20 µm of current collecting layer, increasing the peak power density over four-fold from 0.12 $W.cm^{-2}$ to 0.52 $W.cm^{-2}$. This allowed them to reduce the thickness of their anode and current collector layer to 50 µm and 100 µm, achieving 0.6 $W.cm^{-2}$ from this design (recorded in Table 2.2).

Li et al. [122] developed a dual-layered, hollow fibre cell fabricated by a phase-inversion assisted co-extrusion methodology. They were able to achieve great control over the morphology of the nickel current conduction and Ni-YSZ anode microstructure. The objective was to improve the electrical conductivity and reduce the resistance to mass transfer throughout the cell; the former was quantified, observing a two-fold increase in electrical conductivity over a cell with no current collector layer as seen in Figure 2.6. They formed finger-like protrusions in the axial (seen in Figure 2.7) and radial dimension of the anode and current collector to generate a mesh-like 3D structure.

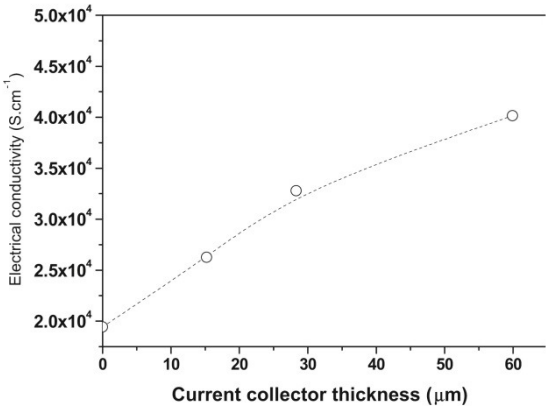

Figure 2.6 - Electrical conductivity as a function of current collector thickness [122]**.**

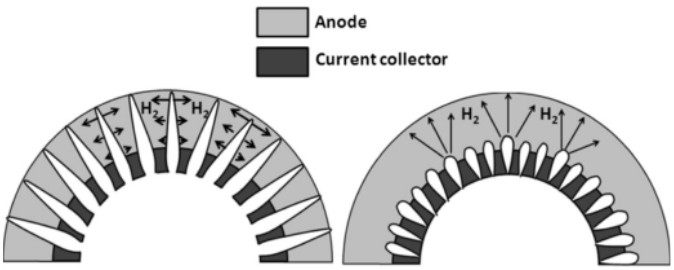

Figure 2.7- Cross-section schematic of dual-layer hollow fibre cell with mesh/finger-like protrusions for enhanced mass transport [122]**.**

2.2.4 Meshes

For nearly 15 years, metallic meshes have been successfully used for electrode contacting both µT-SOFC electrodes [123,124]. Meshes can be made by hatching wire into a network or bought pre-formed with a range of thicknesses and mesh aperture sizes available. Meshes achieve a high cross-sectional contacting area without considerably increasing the diameter of the cell. This is particularly

important on the outer electrode, allowing more compact spacing for cells in stacks. Bore side meshes must be selected carefully as not to block the flow of gas through the tube to the electrode surface.

Problems can occur on the anode side in anode-supported cells due to the metal sagging as a result of a reduction in elasticity with an increase in temperature. The sagging results in loss of contact with the anode wall at high temperature leading to a decrease in electrochemical performance, durability and reliability of the cell. Contact force, controlled by mechanical compression in planar devices, is known to be a key factor in optimising interconnect performance and is crucial for minimising contact resistance. To overcome these issues slide pins and other mesh supports are in development. Meshes can also be secured with conductive pastes and better integrated into the electrode surface itself with the likes of a metal oxide slurry, such as NiO on the anode, or with current collecting layers such as LSCF on the cathode side [125].

In 2017, Park et al. [126] used a nickel mesh secured by a nickel paste on the anode side, with a Crofer 22 mesh secured with an LSC paste on the cathode side. They compared the performance of the bare mesh with a 1.2 µm electrodeposited dual-layered coating. The mesh, with fine wires of 100 µm in diameter, was first applied with a Co_3O_4 spinel layer followed by a $LaMnO_3$ perovskite layer. The mesh achieved a current density at 0.7 V of 0.5 $A.cm^{-2}$ and 0.52 $A.cm^{-2}$ for the uncoated and coated mesh, respectively, at 800°C. The ohmic polarisation and ASR at OCV were 0.26 $\Omega.cm^2$ and 0.79 $\Omega.cm^2$ for the coated Crofer and 0.34 $\Omega.cm^2$ and 0.81 $\Omega.cm^2$ for the uncoated. The authors measured the increase in ohmic resistance over 1000 hours of the bare vs coated Crofer mesh via impedance spectroscopy. Relative to a virgin sample, the degradation was reduced nearly 5 fold from $6.7x10^{-2}$ $\%.hr^{-1}$ to 1.4 $\%.hr^{-1}$.

In 2015, Laguna-Becero et al. [127] achieved the highest current density of a tubular cell with a nickel, bore side anode mesh. The design achieved a current density at 0.7 V of 0.6 $A.cm^{-2}$, 0.99 $A.cm^{-2}$ and 1.15 $A.cm^{-2}$ at 750°C, 800°C and 850°C, respectively. Platinum wire and paste were used on the cathode. The fuel and flow rate were not disclosed. At 750°C, the ohmic polarisation and ASR at OCV were 0.12 $\Omega.cm^2$ and 1.10 $\Omega.cm^2$, respectively.

A recent study where a nickel anode side mesh and a silver cathode mesh were used as current collectors was reported by Liu et al. [124] in 2020. Operating on H_2, the current density at 0.7 V was

0.52 A.cm^{-2} at 850°C. The ASR of the same cell at the aforementioned operating conditions was 0.1 Ω.cm^2.

In 2020 Khan et al. [128] used silver mesh on both the anode and cathode side for a flattened-tube cell design. On the anode side, silver mesh, silver wire and a silver-glass contact/sealing paste were used. On the cathode side, silver mesh, silver wire and LSC contact/sealing paste were used. At 800°C, the current density at 0.7 V was 0.65 A.cm^{-2} and the peak current density 1.55 A.cm^{-2}.

An anode side silver mesh for a tubular design was reported by Cui et al. [129] in 2020. The cell produced a current density at 0.7 V of 0.21 A.cm^{-2} and a peak current density of 0.29 A.cm^{-2} at 800°C. A silver mesh was used for cathode contacting.

A tubular cell using a silver-based mesh was reported by Chen et al. [130]. The current density at 0.7 V and 750°C was 0.21 A.cm^{-2} and peak power density 1.07 W.cm^{-2}. They used silver mesh and silver wire on both the anode and cathode side of their cell with a proton-conducting BZCYYb electrolyte.

2.2.5 Foams

Foam inserts, essentially a highly porous expanded 3D mesh, are a solution to avoid pressure drops and flow disturbances that anode side meshes can have while achieving a large cross-sectional contact patch for current collection. Loss of contact between foams and the cell wall from sagging has not been reported/studied in literature and is unlikely due to the ease in shaping allowing the foam to fully fill the tube bore, analogous to a filter inside a cigarette. The filling of the tube will reduce the conduction pathway within the current collector in the radial direction compared to a mesh, for example. Foams are characterised by high mechanical strength and low weight, favourable for a portable fuel cell device interconnect [131]. The foams are typically made of silver, nickel or steel alloys and have been shown in recent literature to exhibit excellent current collecting capabilities [132]. In 2017 Huang et al. [133] reported a current density at 0.7 V and 750°C in H_2 of 0.95 A.cm^{-2} with a peak power density of 1 W.cm^{-2}, achieving 24 W from a single cell. The cell had an outer diameter of 9 mm and was 100 mm in length. They performed a degradation study over 4000 hours, operating at 18.5 A with a fuel utilisation of 64.38% observing a degradation rate of 26 mV.kh^{-1}. The ASR estimated from the polarisation plot at 750°C was 0.27 Ω.cm^2.

The high surface area to volume ratio of foams positions them as an ideal candidate as a catalyst support, increasing the functionality of the current collector. The catalyst can either be alloyed into the base material during fabrication or added post-fabrication by doping. Typical dopants include metals such as copper, cobalt, nickel, manganese and tin. Recent studies into doping have shed light on the possibility to control anode side degradation from coke deposition and increase tolerance to sulphur derivatives [134]. The improved tolerance leads to improved fuel flexibility for operation on lower purity hydrocarbon fuels such as syngas and sour gas [135]. Yan et al. [136] developed a phosphorous doped nickel foam for current collection. When compared to a bare mesh, they observed an improved electrochemical performance and durability under operation under syngas for coatings with phosphorous contents above 6.4%. Weight loss was negligible for the plated mesh sample, compared to the approximately 250% weight gain observed for samples exposed (ex-situ) to syngas for 50 hours at 750°C.

2.2.6 Brush Type

Brush type interconnects are structured wire forms that are inserted into the bore of the inner electrode of a tubular cell. Patents published by AMI reveal an internal interconnect with the option for increased functionality when doped with a catalyst [137]. Nevertheless, no experimental results or analysis have been published in the literature. The design has an ordered, axially repeating floral-like cross-section. The brush loops are attached to a central core wire which emerges from the tube end for interconnection as seen in Figure 2.8. The electron flow path is in the radial direction and non-circumferential like in a mesh as the shortest path is from the electrode-interconnect joint of the loop tributary to the central core, which acts as a highway for the electrons. Increasing the number of loops in a given length will also reduce current conduction pathways in the axial dimension. Coiled wires are reported in the patent for cathode current collection and can be an extension of the anode wire from the interior or joined to a different wire of a different material.

Materials inside the tube bore such as brushes, coil meshes and foam types will certainly impact the fluid flow, causing flow instability, encouraging turbulence and better mixing at the expense of an increase in pressure drop [138]. The aforementioned will likely enhance heat transfer within the cell, primarily from convection but also conduction when contacted to the wall [139]. An increase in radial velocity is also likely, improving mass transport through the cell. A study by Rahimi et al. showed an increase of 41% in electrochemical performance from a PEM fuel cell with a coil insert

inside the fuel channels when compared to an empty channel [140]. They used a combined experimental and modelling approach and attributed the electrochemical improvement to an increase in tangential fluid velocity that resulted in better transport of reactant from the mainstream to the reaction zone.

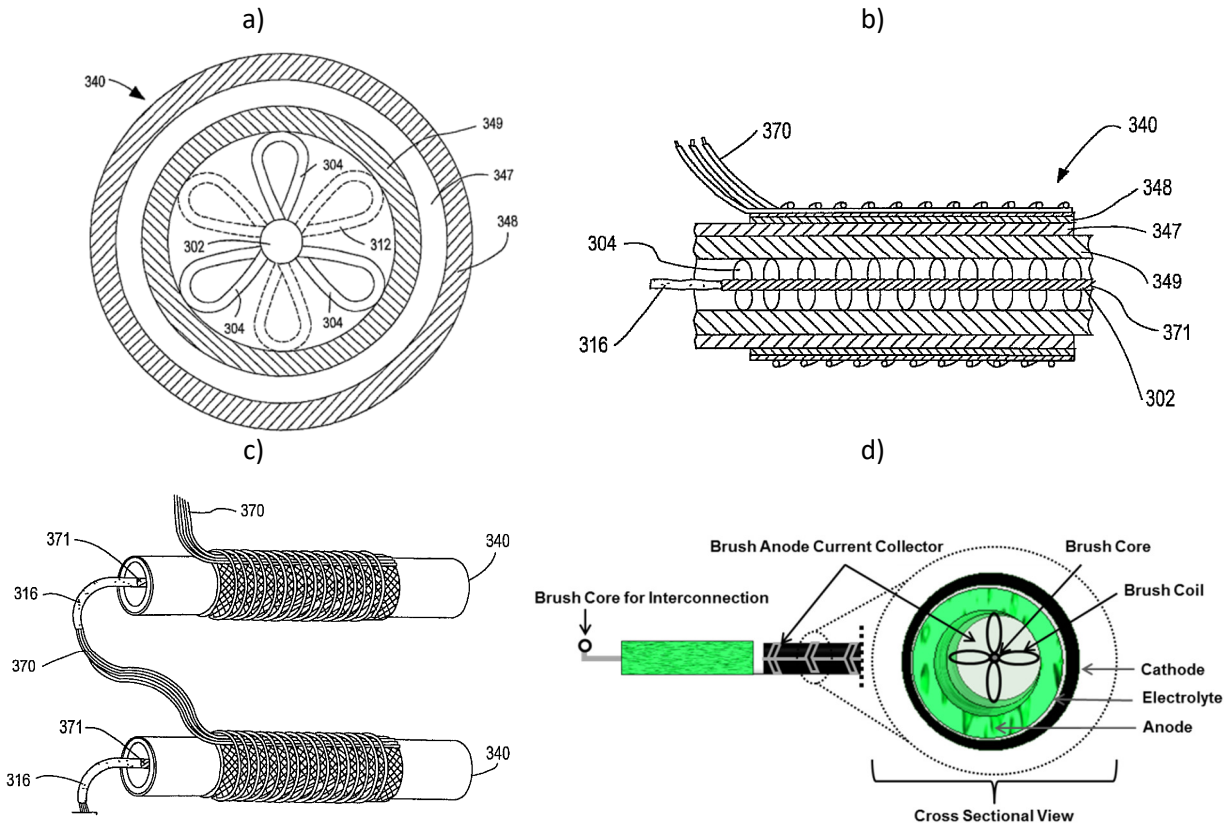

Figure 2.8- AMI brush collector with integrated catalyst functionality – a) front view, b) side view, c) cell-to-cell interconnection (series connection) [137] **d) schematic reproduced from** [137]**.**

2.2.7 Structurally Integrated/Embedded

A novel interconnection methodology was first reported by De la Torre et al. [141] in 2011 and later in 2013 [142]. The design involved the integration of current collector wires into the anode support during the manufacturing process as seen in Figure 2.9 b). The wire is coiled around a sacrificial central support pin (pencil led/carbon fibre) and then 'dip-coated' with layers of the anode. The wire passes through the entire length of the anode and protrudes from either end of the tube.

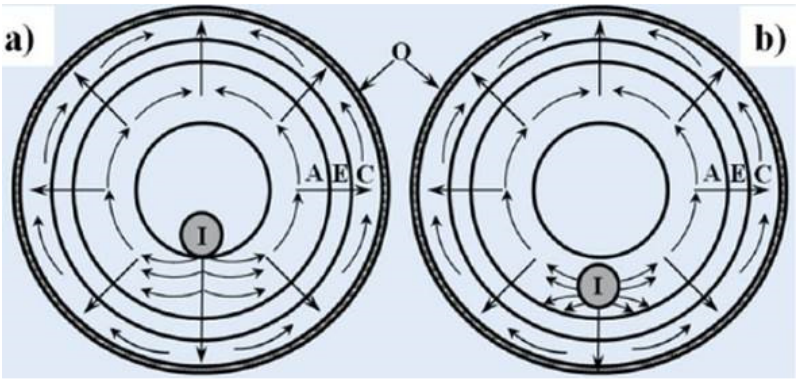

Figure 2.9 –a) Internal current collector, b) embedded current collector, where A, C, E and O refer to the anode, electrolyte, cathode and outer current collector, respectively [142]**.**

Electrochemical performance of two cells with the internal and embedded designs seen in Figure 2.9 a) and b), respectively, were reported. At 750°C and operating on dry H_2, the embedded wire achieved a current density of 0.15 A.cm^{-2} at 0.7 V. This was a 3.8 times increase in performance when compared to the internal current collector wire as seen in Figure 2.9 a), which achieved 0.04 A.cm^{-2}. At the same conditions, the peak power density was 0.035 W.cm^{-2} and 0.142 W.cm^{-2} for designs a) and b), respectively. The ASR of the embedded cell as estimated from the gradient of the polarisation curve was 1.74 Ω.cm^2. The configuration allowed for current collection along the entirety of the anode length, ensuring a well-distributed anode electron conduction profile. The option to collect the current from either end of the cell will approximately halve the lateral current conduction pathway of electrons in the wire compared to a single end connection, also reducing the axial path length. Integrating the wire into the anode ensured sound mechanical contacting and might have somewhat shielded the wire from the harsh gas stream environments. However, some concern surrounded the difference in CTE of the nickel wire and the Ni-YSZ anode which could lead to bending and cracking of the anode, the wire and the surrounding fuel cell components, leading to failure [143].

In 2015, Casarin et al. [144] looked into the effect of coiling anode-embedded, nickel (Figure 2.10) and palladium wires, versus an embedded straight wire. They changed the number of coil rotations (coil density) in a given length to increase the surface area and amount of wire available for collecting current. They found that increasing the nickel wire coil density (by 83%) from 6 turns.cm^{-1} to 11 turns.cm^{-1} significantly increased the performance. They observed a 3.5 times increase in current density at 0.7 V and 800°C from 0.055 A.cm^{-2} to 0.19 A.cm^{-2}, citing a more homogenous current distribution and an increased contact area resulting in lower ohmic polarisation as the root causes.

The ASR of the 11 turns.cm^{-1} nickel wire as estimated from the gradient of the polarisation curve was 1.6 Ω.cm^{-2} at 800°C.

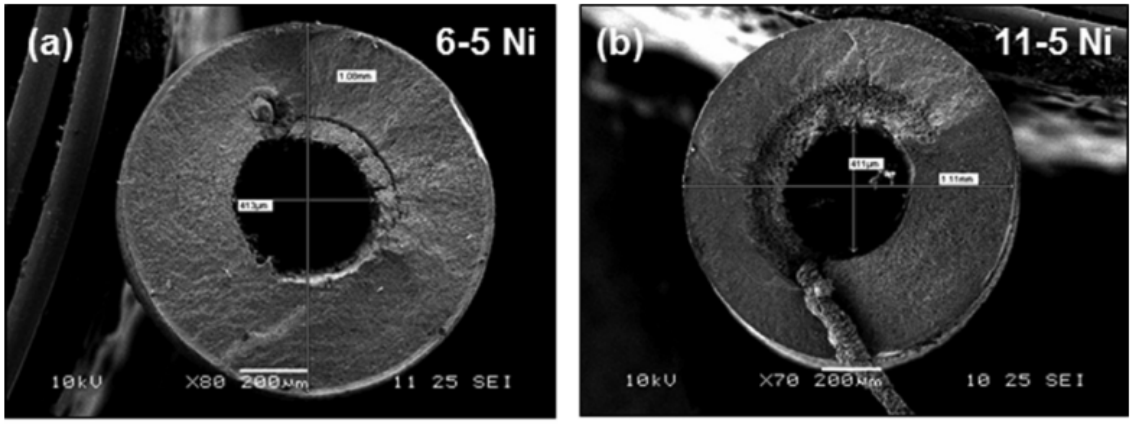

Figure 2.10 – Embedded nickel coils with a) 6 turns.cm^{-1}, b) 11 turns.cm^{-1} [144]**.**

The palladium wires broke, which did not allow a direct comparison between materials and number of coils. However, the authors tested a (non-embedded) palladium wire which achieved a similar current density of 0.2 A.cm^{-2} at 0.7 V and 800°C operating temperature when compared to the 11 turns.cm^{-1} nickel wire. The authors claimed that the palladium enhanced the catalytic activity of the anode, resulting in higher performance. They did not attribute any difference in performance to the different material conductivity even though palladium is 35% more conductive than nickel at 20°C and 6.8% more conductive at 750°C.

2.2.8 Current Collector Sizing, Spacing and Positioning

It is intuitive to expect that current collection from a larger area of the electrode will decrease the ohmic losses of a cell. Contacting the entirety of the electrode, however, is unfeasible concerning blocking gas transport through the electrode as well as increasing weight and cost. Depending on the configuration, maximising the current collecting area and thus minimising ohmic loss could lead to a loss of available active area which will reduce the total amount of current that can be produced. Therefore, there is a tradeoff in the current collector design concerning the sizing of the current collector node, positioning on the electrode and, if opting for multiple nodes, their spacing. Collecting current from either end of an anode has been common in literature for externally accessed anode current collectors. As can be seen from Figure 2.11, this has the effect of shortening the

distance that the electrons travel from where they are produced, as compared to a single collection node.

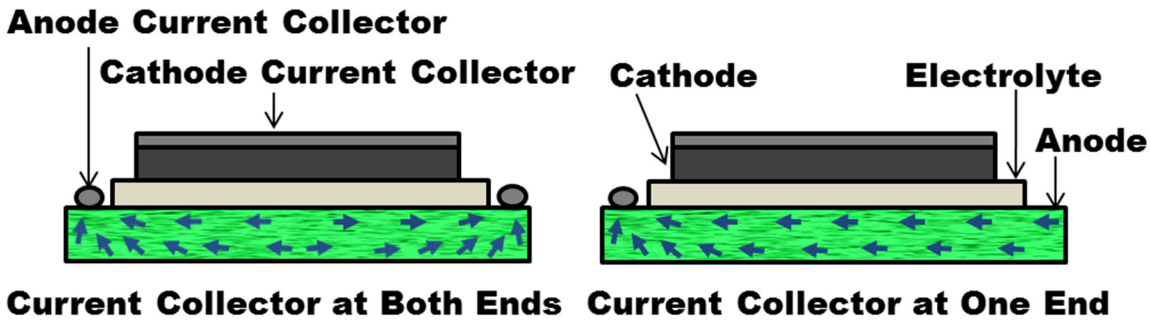

Figure 2.11- Current conduction pathway for current collection at both ends of the electrode reproduced from [143]**.**

As cells become longer, the distance between current collectors at each end of a cell increases and the need for additional current collectors can be justified. Some empirical research has been conducted to determine just how many current collectors are needed for a particular cell length. To do so, the cell is segmented, with multiple current collector nodes spaced along the electrode in question. Since cells are typically anode supported, electrons can travel further in the thicker anode and thus incur more loss in the anode. Although the anode is typically an order of magnitude more conductive than the cathode, nickel-based anodes cermets typically have an electronic conductivity of similar order of magnitude (and below) to the conductivity of pure nickel which is around 2.7×10^6 S.m^{-1} at 750°C. Values of the effective cermet electronic conductivity reported in the literature vary between 1×10^6 and 1×10^5 S.m^{-1} at typical SOFC operating conditions [145]. Traditional cathodes have relatively lower electronic conductivities compared to the anode at around 1×10^3 S.m^{-1} but more recent mixed ionic-electronic conductors such as LSCF are comparable and can display electronic conductivities up to 1×10^4 S.m^{-1}, depending on composition and microstructure [146,147].

Bai et al. [148] looked into determining the optimal number of anode current collectors of their 4.8 cm long and 7 mm OD segmented single-chamber fuel cell. They spaced five current collectors along the length of the cell, creating 4 active areas connected in series. The geometry and configuration of the current collectors are seen in Figure 2.12.

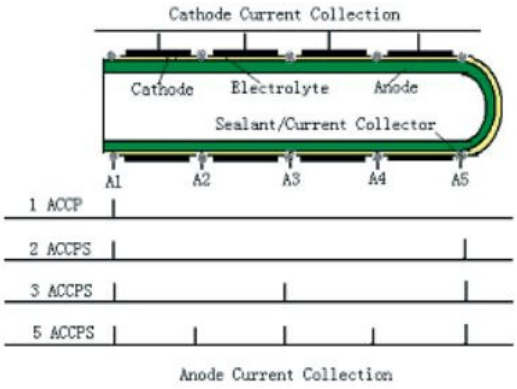

Figure 2.12 - Anode current collector configuration in a segmented tubular SOFC cell [148]**.**

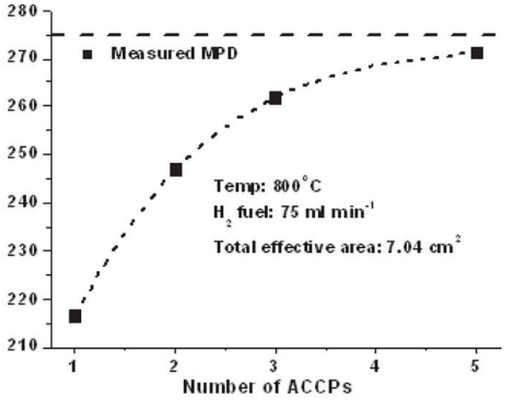

Figure 2.13 - Number of anode current collection position versus maximum power density [148]**.**

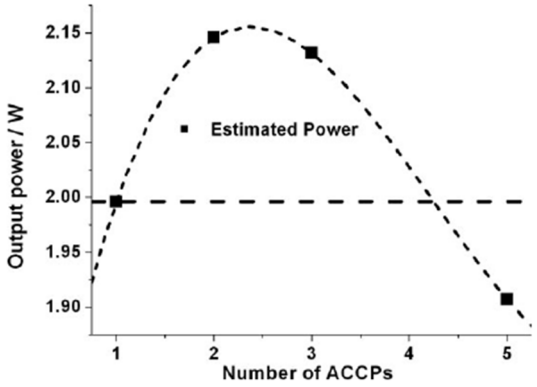

Figure 2.14 - Number of anode current collector positions versus total power available from the cell [148]**.**

They found that increasing the number of current collectors from the single inlet and the symmetrically spaced inlet and outlet, inlet and centre and outlet, and then all five, positions increased the power density from the cell setup as seen in Figure 2.13. They did not, however, look at the effect of the positioning of a single current collector node on performance, measuring only the current observed from a single current collector at the inlet. The authors only presented data from 5 of the 31 possible current collector combinations for this setup. They did, however, consider the resulting loss of active area from increasing the number of current collectors, each collector incurring a 5.6% loss of the total active area available. They used the power density data from their segmented cell to estimate the total power that could be derived from a cell of the same geometry but with a different number of current collectors. They found 2 current collectors, one at either end was the optimal configuration, incurring a penalty of loss of active area and increased ohmic resistance if they deviated, as seen in Figure 2.14

Contrary to this finding, Meadowcroft et al. [149] found that for their cell geometry, a single current collector node, at the centre of the cell specifically, was superior to that of a cell with multiple anode current collectors, notably two at either end of the active area. The single central current collector incurred a 6 to 9% (estimated) loss in active area, whereas the two current collectors did not. The geometry of the cell was around 3 times longer than that of Bai et al. at 152 mm in length but had a similar diameter of 6.7 mm. Evidently, the cell geometry has a considerable effect when it comes to finding the optimal current collector configuration to maximise the total power from a cell. The experimental data presented in the literature is limited on this subject and more research needs to be conducted to get a better understanding. The data produced must be representative of the typical cell geometries and materials used in tubular SOFC. Models built from this data could reliably predict the optimum sizing of current collectors for a wide range of cell designs and would be a cost and time-effective tool.

Shimizu et al. [150] conducted a similar experiment with an anode supported segmented tubular cell 48 mm in length and 8 mm OD. They positioned three 2.5 cm^2 cathode segments 2 mm apart on their in-house fabricated cell. They performed an initial comparison of the cell with all three cathodes connected in parallel to that of a cell of the same active area but with no segmentation and determined that the performance was the same and that the segmentation had no noticeable impact. They compared the performance from each cell segment with a 120, 80 and 40 $ml.min^{-1}$ total flow rate of equimolar H_2 and N_2 as seen in Figure 2.15.

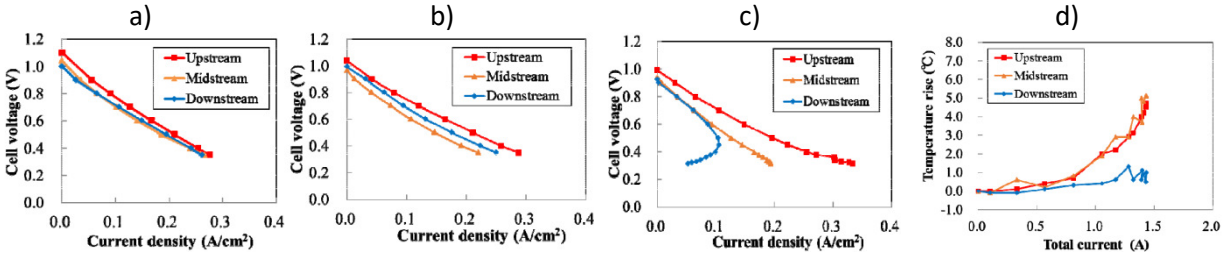

Figure 2.15 –a) Electrochemical performance of a segmented tubular cell at a total flow rate of a) 120 $ml.min^{-1}$, b) 80 $ml.min^{-1}$, c) 40 $ml.min^{-1}$ of equimolar H_2 and N_2 and d) temperature difference versus current measured at the upstream, midstream and downstream segments [150].

For the highest fuel flow rate, they observed a similar performance from all three cell configurations which indicated a homogenous current distribution in the cell and sufficient volumetric flow rate to minimise the effect of concentration polarisation. The current density at 0.7 V, in this case, was around 0.125 $A.cm^{-2}$ for the upstream, 0.105 $A.cm^{-2}$ for the midstream, and 0.1 $A.cm^{-2}$ for the

downstream segments, respectively, i.e values were within 23% (or less) of each other. Reducing the flow rate resulted in a larger difference of 50% (or less) between current density values at 0.7 V. The current density of the upstream cell remained at 0.125 A.cm^{-2} while the midstream and downstream segments dropped to 0.075 A.cm^{-2} and 0.095 A.cm^{-2}, respectively. The largest performance decrease of 29% occurred in the midstream segment. Shimizu et al. ascribed this to a relatively low activation potential at the downstream cell versus midstream cell, arising from improved anode kinetics due to increased partial pressure of water, the reaction product. For the lowest flow rate, the current distribution was highly inhomogeneous, with a difference of 58% in current density between segments at 0.7 V. The upstream cell was reduced to 0.11 A.cm^{-2} whilst the midstream and downstream segments were down to 0.06 A.cm^{-2}. Increasing the polarisation of the downstream beyond 0.7 V gave a somewhat unusual result, the peak current density was reached at 0.45 V. Increasing the polarisation beyond this did not increase the current density, in fact, the converse. Meanwhile, the current density of the upstream segment increased to a value higher than for higher flow rates. The starvation of the downstream segment came from the low inlet flow rate, compounded with the consumption of fuel and the increase in reaction product (water) from the upstream and midstream cell segments. The authors also measured the temperature at each segment for the lowest flow rate. The largest temperature rise was for the upstream and midstream segments which were both 5°C.

2.3 Effect of Cell geometry on Current Collection

An experimental study by Jin et al. [151] showed how the current density at 0.7 V of a single cell decreased by a third from 1.2 A.cm^{-2} (cell a) to 0.8 A.cm^{-2} (cell b) as the distance between the anode current collector and the active region/cathode current collector increased seven-fold. They spaced 4 electrically isolated 'cells' with a similar area along the 150 mm anode supported single-chamber cell as seen in Figure 2.16.

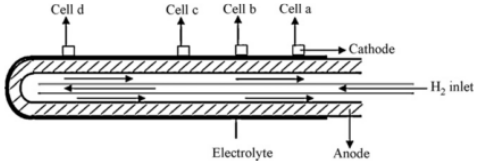

	d (cm)	Cathode area (cm^2)	OCVs (800 °C) (V)
Cell a	2	0.31	1.013
Cell b	5	0.33	1.038
Cell c	8	0.30	1.050
Cell d	14	0.31	1.045

Figure 2.16 - Current collector configurations and cell specifications [151]**.**

Through impedance spectroscopy, they attributed the difference in performance to an increasing ohmic resistance with length as seen in Figure 2.17. They observed that the ohmic and total cell resistance followed a similar linear trend whereas the interfacial polarisation did not change significantly between cells, determining that the electrode reaction was not affected by a varying fuel utilisation and therefore changes to the performance were dominated by the ohmic resistance of the anode for these fueling conditions.

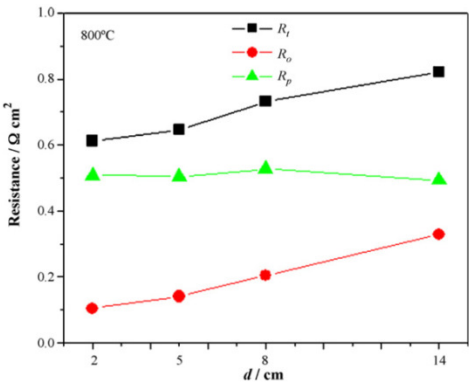

Figure 2.17 - Distribution of R_t, R_o and R_p of the four single cells. R_t, the total cell resistance; R_o, the ohmic resistance; R_p, the interfacial polarization resistance; d, the distance between the cathode of the cell and the anode current collecting point [151]**.**

In 2006 Suzuki et al. published two papers that estimated the effect of changing the anode wall thickness on cell resistance for the two geometries of µT-SOFC, 1.6 mm OD and 0.8 mm OD that were in development [63,64]. They based the estimates on impedance and conductivity data they had acquired empirically for each anode at various temperatures. They conducted the study to determine whether it was sufficient to use the anode as the sole current collector, i.e. collection at one end or both ends. They concluded that an anode length of a few centimetres was the limit for such a setup due to increasing ohmic resistance. They stated that careful stack design is of paramount importance to overcome this effect. It was concluded that the anode resistance did not change linearly with wall thickness. The data for wall thickness versus cell resistance is seen in Figure 2.18 for the 1.6 mm OD tube and in Figure 2.19 for the 0.8 mm OD tube.

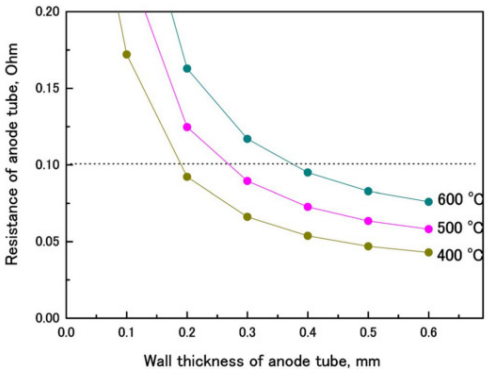

Figure 2.18 - Wall thickness versus resistance for 10 mm long 1.6 mm OD tube [63].

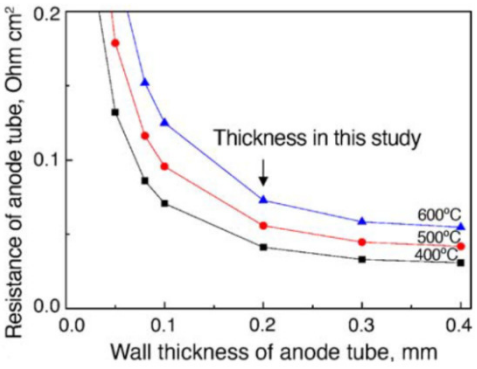

Figure 2.19 - Wall thickness versus area specific resistance for 12 mm long 0.8 mm OD tube [64].

2.4 Summary of Recently Reported µT-SOFC Cell Tests in Literature

Table 2.2 is a summary of tubular cells recently reported in academic literature. Research papers detailing the methods of current collection are of particular importance and salient designs are included in the table from literature dating back to the late 90s, around the time of the invention of tubular cells. Performance values have been reported at 750°C or as close to 750°C as reported. Values not reported explicitly in the text, for example, the current density at 0.7 V was estimated from the polarisation plots. Only the fuel contributing to electrochemical reactions is reported in the table and details of any inert/carrier gases are not included. Performance data of cell operating H_2 was reported where possible. Several papers were omitted from the table due to the poor quality of the results, namely low OCV.

Table 2.2 - Summary of recently reported µT-SOFC cell tests in literature, sorted by operating temperature first, then by year, descending.

Operating Temperature (°c)	Year	Author	Cell Support	Anode Material	Electrolyte Material	Barrier Material	Cathode Material	Diameter (mm)	Length (mm)	Active Area (cm^2)	OCV > 1 V [Y/N]	Current Density at 0.7 V ($A.cm^{-2}$)	Peak Current Density ($A.cm^{-2}$)	Peak Power Density ($W.cm^{-2}$)	Anode Current Collection Method (I/E/SI)	Cathode Current Collection Method (I/E)	Fuel	Fuel Flow Rate (ml/min)	Reference
900	2017	Jones	ASC	Ni-YSZ	YSZ	-	LSCF	10.2	100	32	Y	0.59	0.59	0.438	-	-	H_2	200	[152]
900	1999	Hatchwell	ESC	N-YSZ	YSZ	-	LSM	2	3.14	-	Y	0.04 [0.04] 0.015	0.065 [0.063] 0.022	0.013 [0.032] 0.032	Nickel wire, (I)	Silver wire, [Ducrolloy wire silver-LSC coated] Ducrolloy	Humidified H_2	25	[60]
900	1998	Hatchwell	ESC	N-YSZ	YSZ	-	LSM	2.5	3	-	Y	0.034 [0.049] 0.21 [0.20]]	0.051 [0.051] 0.033 [0.03]	0.26 [0.26] 0.16 [0.15]	Nickel wire, (I)	Nimonic 90 bare wire, [Nimonic 90 wire, LaCoO coated] Silver wire, [Silver strip, (E)]	Humidified H_2 (3 vol.%)	25	[59]
850	2020	Liu	CSC	Ni-YSZ	SSZ	-	LSM-SSZ /LSM	14	5	9.89	Y	0.52	0.85	0.38	Nickel mesh, (E)	Silver mesh, (I)	Humidified H_2 (3 vol.%)	40	[124]
850	2015	Paciejewska	ASC	Ni-YSZ	YSZ	GDC	LSCF	4	50	2.8	Y	-	1.1	0.77	Nickel wire, (I)	Silver wire, (E)	H_2	100	[153]
800	2020	Khan	ASC	Ni-SSZ	SSZ	GDC	GDC-LSCF /LSCF	-	230	12.5		0.65	1.55	0.6	Silver mesh/wire/paste, Silver-Glass paste, (E)	Silver mesh, Silver wire, LSCO paste, (E)	Humidified H_2 (3 vol.%)	1500	[128]
800	2020	Morales-Zapata	ASC	Ni-YSZ	YSZ	-	PNO /PNO-CGO	3.2	-	1	N	0.5	0.9	0.5	Gold wire, (I/E)	Gold wire, Gold paste, (E)	Humidified H_2 (50 vol.%)	100	[154]

800	2020	Cui	ASC	Ni-YSZ	YSZ	-	YSZ-LSM	3	52	0.94	Y	0.21	0.29	0.17	Silver mesh, Silver wire, (E)	Silver mesh, Silver wire, (E)	H_2	30	[129]
800	2020	Milcarek	ASC	Ni-YSZ	YSZ	SDC	LSCF-SDC	3.2	-	4.07	Y	0.5	0.78	0.42	Silver wire, Gold Paste, (E)	Silver wire, Silver paste, (E)	H_2	50	[155]
800	2019	Milcarek	ASC	Ni-YSZ	YSZ	SDC	LSCF-SDC	3.3	-	1.66	Y	0.55	1.6	0.46	-	Silver paste	Propane	6	[156]
800	2019	Soydan	ASC	Ni-YSZ	YSZ	-	LSM-YSZ	5.36	65	3.3	N	0 .23	0.69	0.26	Silver wire, Silver paste, (E)	Silver wire, Silver paste, (E)	H_2	40	[157]
800	2018	Ding	ASC	Ni-SDC	LDC/ LSGM -LDC	LDC	LSCF-LSGM /LSCF	-	-	1.16	Y	0.8	2.5	0.612	Silver wire, Silver paste, (E)	Silver wire, Silver paste, (E)	Humidified H_2 (3 vol.%)	75	[95]
800	2017	Park	ASC	Ni-YSZ	YSZ	-	LSM /LSCF	10	200	50	Y	0.5 [0.52]	0.12 [0.14]	0.4 [0.46]	Nickel mesh, Nickel paste, Platinum wire, (I)	Crofer Mesh, [LaMnO/CoO Coated Crofer Mesh], (E)	H_2	-	[126]
800	2016	Milcarek	ASC	Ni-YSZ	YSZ	-	LSM	3.2	-	1.67	Y	0.7	1.4	0.59	-	-	Methane	217	[158]
800	2016	Laguna-Bercero	ASC	NiO-YSZ	YSZ	CGO - PNO	PNO	3.4	50	1	Y	0.8	1.37	0.76	Silver wire, Gold wire, (I)	Gold paste, Gold wire coil, (E)	Humidified H_2 (3 vol.%)	-	[116]
800	2016	Monzon	ASC	Ni-YSZ	YSZ	-	LSM-YSZ	3.2	6	1	Y	0.44	0.69	0.66	-	LSM paste, (E)	Humidified H_2 (3 vol.%)	500	[159]
800	2015	Aydin	ASC	Ni-YSZ	YSZ	-	LSM	8	49	6.8	Y	0.13	0.29	0.12	Silver wire, (E)	Silver wire, Silver paste, (E)	H_2	-	[160]
800	2015	Casarin	ASC	Ni-YSZ	YSZ	-	LSM	1.08 [1.08] 1.04	30	0.7 [0.055] 0.65	Y	0.19 [0.08] 0.19	0.345 [0.20] 0.40	0.157 [0.040] 0.18	Coiled Nickel wire, (SI) [Coiled Nickel wire, (SI)] Palladium wire, (I)	Silver wire, Silver paste, (E)	Humidified H_2 (3 vol.%)	20	[144]

800	2015	Zhao	SSC	Ni-SDC	SDC /YSZ	-	LSCF	4.5	-	1	Y	0.63	2.5	536	Nickel layer (SI), Platinum mesh, Platinum wire, (I)	Platinum mesh, Platinum wire, (E)	H_2	200	[120]
800	2013	Shimizu	ASC	Ni-YSZ	YSZ	-	LSM	8	48	6.8	Y	0.8	2.45	0.72	Silver wire, Silver paste, (E)	Silver wire, Silver paste, (E)	Humidified H_2 (3 vol.%)	60	[150]
800	2009	Jin	ASC	Ni-YSZ	YSZ	-	LSM-YSZ/LSM	6	4 (In) [14](Out)	0.31	Y	1.2 [0.81]	-	-	Silver wire, Silver paste	Silver wire, Silver paste	Humidified H_2 (3 vol.%)	75	[151]
750	2020	Rabuni	ASC	Ni-YSZ	YSZ	-	YSZ-LSM /LSM	2.2	-	0.69	Y	1.25	4.5	1.2	Silver wire, Silver paste, (E)	Silver wire, Silver paste, (E)	H_2	30	[20]
750	2019	Milcarek	ASC	Ni-YSZ	YSZ	SDC	LSCF-SDC	3.3	15	1.66	Y	0.32	1.05	0.31	Silver wire, Gold Paste	Silver wire, Silver paste, (E)	Propane	617	[161]
750	2019	Vafaenezhad	SSC	Ni-YSZ /Ni-BZCYYb	BZCYYb	-	LCF-BZCYYb	6	40	1.6	Y	0.23	0.57	0.205	Nickel mesh, Platinum wire, (I)	Gold wire, Gold paste, (E)	Humidified H_2 (3 vol.%)	10	[162]
750	2019	Chen	ASC	Ni-BaZrCe YYb	BaZrCeYYb	-	LSCF-SDC	3	40	2	N	1.2	3.2	1.07	Silver mesh, Silver wire	Silver mesh, Silver wire	Humidified H_2 (3 vol.%)	30	[130]
750	2019	Chen	ASC	Ni-BaZrCeYYb	BaZrCeYYb	-	LSM-SDC	2.5-3	40	2	N	1.05	3	1.01	Silver mesh, Silver wire	Silver mesh, Silver wire	Humidified H_2 (3 vol.%)	30	[163]
750	2019	Dong	ASC	Ni-BaZrCeYYb	BaZrCeYYb	-	LSCF	2	30	1	N	1.15	2.8	1.04	Silver mesh, Silver wire	Silver mesh, Silver wire	Humidified H_2 (3 vol.%)	30	[164]
750	2019	Panthi	ASC	Ni-YSZ	YSZ	-	YSZ-LSM /LSM	5.5	110	1.19 (est)	Y	0.42	1.55	0.36	Silver wire, (E)	Silver wire, (E)	Humidified H_2	100	[165]

750	2018	Lopez-Robledo	ASC	Ni-YSZ	YSZ	GDC	LSCF-GDC	3.4	50	1	Y	0.7	1.27	0.74	Silver wire, (I)	LSCF, Gold wire, Gold paste, (E)	Humidified H_2 (3 vol.%)	80	[166]
750	2018	Liu	ESC	Ni-LDC	LDC-LSGM	-	LCNCO-LSGM	3.3	5.1	0.53	Y	0.21	0.59	0.18	Nickel foam, Silver paste, (I)	Silver wire, (E)	H_2	15	[167]
750	2017	Panthi	SSC	Ni–ScSZ	ScSZ	-	LSM–ScSZ	3.6	-	0.9	Y	0.8	2	0.724	Nickel layer, Silver wire, (I)	LSM, Silver wire, (E)	Humidified H_2 (3 vol.%)	20	[118]
750	2017	Huang	ASC	Ni-YSZ	YSZ	-	-	9	100	24	Y	0.95	1.56	1	Nickel foam, (I)	Silver wire, (E)	H_2	500	[133]
750	2017	Yoon	ASC	Ni-YSZ	YSZ	-	LSTM	11.4 (eqiv.)	150	4.5	Y	0.5	1.45	0.47	Platinum wire, Platinum paste, (E)	Platinum wire, Platinum paste, (E)	Humidified H_2	200	[168]
750	2016	Aydin	ASC	Ni-YSZ	YSZ	-	LSM	9	49	7.63	Y	0.2	0.6	0.22	Silver wire, (E)	Silver wire, Silver paste, (E)	H_2	80	[90]
750	2015	Panthi	SSC	Ni-ScSZ	ScSZ	-	LSM-ScSZ	-	-	-	Y	0.75	2	0.706	Nickel	LSM	Humidified H_2	20	[119]
750	2015	Lopez-Robledo	ASC	Ni-YSZ	YSZ	GDC	LSCF	3.5	120	1	Y	0.35	0.45	0.92	Nickel foam, Silver wire, (E)	Silver wire. Silver paste, (E)	Humidified H_2	80	[169]
750	2015	Laguna-Bercero	ASC	Ni-YSZ	YSZ	-	YSZ-LSM	3.2	100	-	Y	0.6	1.15	0.58	Nickel mesh, (I)	Platinum wire, Platinum paste, (E)	Humidified H_2	-	[127]
750	2015	Laguna-Bercero	ESC	Ni-GDC	GDC	-	NdNO	-	100	-	N	-	0.1	0.04	Platinum paste, (E)	Platinum wire, Nickel paste, (I)	Humidified H_2 (3 vol.%)	100	[117]
750	2014	Park	ASC	Ni-YSZ	YSZ	GDC	LSCF-GDC / LSCF	7.5	80	3.69	Y	1.2	1.6	0.9	Nickel felt, Nickel wire, (I)	Platinum gauze, Silver wire, (E)	Humidified H_2	300	[170]

750	2014	Panthi	SSC	Ni-YSZ	YSZ	-	YSZ-LSM	3.6	-	1.1	Y	0.4	1.05	0.36	Nickel Layer, Platinum, paste, Platinum wire, (E)	LSM layer. Platinum paste, Platinum wire, (E)	Humidified H_2 (3 vol.%)	20	[171]
750	2014	Hanifi	SSC	Ni-SDC-YSZ	YSZ	GDC	LSCF-GDC	6	50	2	Y	0.25	0.53	0.195	Nickel mesh, NiO paste, (I)	Gold wire, Gold paste, (E)	Humidified H_2 (3 vol.%)	50	[125]
750	2014	Laguna-Bercero	ASC	Ni-YSZ	YSZ	-	NdNO-YSZ	-	-	1.1	Y	0.1	0.1	0.7	Nickel foam, Platinum wire, (I)	Gold paste. Platinum wire, (E)	Humidified H_2	100	[172]
750	2013	De la Torre	ASC	NiO-YSZ	YSZ	-	YSZ-LSM / LSM	1.2	30	0.75	N Y	0.15 [0.04]	0.52 [0.12]	0.142 [0.035]	Nickel wire, (SI) [Nickel wire, (I)]	Silver paste, Platinum mesh, (E)	Humidified H_2 (3 vol.%)	25	[142]
725	2018	Slodczyk	ASC	Ni-YSZ	YSZ	SCO	LSCF	6.8	150	19.7	Y	0.45	0.45	0.33	Nickel mesh (I)	Silver paste, Silver mesh, (E)	Humidified H_2 (3 vol.%)	150	[173]
700	2020	Ren	ASC	Ni-SDC	SDC	-	PBCO			0.23	N	1.4	5.6	1.5	Silver wire, (E)	Silver wire, Silver paste, (E)	Humidified H_2	30	[53]
700	2019	Omar	ASC	Ni-CGO	CGO	-	LSCF-CGO	-	-	-	N	0.25	3.3	0.67	Silver wire	Silver wire	H_2	-	[174]
700	2017	Tan	ASC	Ni-YSZ	LSGM	CMF /Ti-LDC	SSC/ LSGM	9.8	5	1.53	Y	0.9	1.95	0.782	Platinum wires, (E)	Platinum mesh, Platinum wire, (E)	Humidified H_2 (3 vol.%)	100	[175]
700	2017	Tan	ASC	Ni-SLT	LSGM	CMF /Ti-LDC	SSC	8.5	5	2.67	Y	0.54	0.97	0.41	Platinum wires, (E)	Platinum mesh, Platinum wire, (E)	Humidified H_2 (3 vol.%)	100	[176]

700	2017	Soydan	ASC	Ni-YSZ	YSZ	-	LSM	2.85	60	2.50	Y	0.55	0.67	0.38	Silver wire, Silver paste, (E)	Silver wire, Silver paste, (E)	H_2	30	[177]
700	2015	Majewski	ASC	Ni-YSZ	YSZ	SDC	LSCF	6.6	152	16.3	Y	0.5	0.9	0.45	Silver wire, Silver paste, (E)	Silver paste, Silver wire spine & ties, (E)	H_2	145	[178]
700	2015	Torrell	ASC	Ni-YSZ	YSZ	SDC	LSCF	6.6	150	19.7	Y	0.3	0.3	0.21	Nickel mesh (I)	Silver paste, Silver mesh, (E)	H_2	200	[179]
650	2019	Huang	ASC	Ni-YSZ	YSZ	-	-	8.5	100	28	-	0.57	-	-	Nickel foam, (I)	Silver wire, (E)	Propane	27	[180]
650	2018	Morales	ASC	Ni-SDC	SDC	-	LSCF	2.5	90	1.50	N	0.36	1.4	0.52	Silver wire, Silver mesh, (I)	Silver wire, Silver mesh, (E)	H_2	80	[181]
650	2017	Sumi	ASC	Ni-GDC	YSZ	GDC	GDC-LSCF	2.8	-	2.6	Y	0.28	0.65	0.27	Silver wire, Silver paste, (E)	Silver wire, Silver paste, (E)	Humidified H_2	-	[182]
650	2015	Sumi	ASC	Ni-GDC	YSZ	GDC	LSCF	2.8	-	2.6	Y	0.27	0.62	0.25	-	-	Humidified H_2	10	[183]
615	2019	Sumi	ASC	Ni-YSZ-LDC	YSZ	-	-	-	-	-	Y	0.4	0.75	0.38	-	-	Humidified CH_4	-	[184]
600	2020	Durango-Petro	ASC	Ni-CGO	CGO	-	LSFC-CGO	4	-		N	0.375	1.8	0.595	Silver wire, Silver paste	Silver wire, Silver paste	H_2	25	[115]
600	2019	Tan	ASC	Ni-YSZ	LSGM	-	SSC	10	-	1.57	Y	0.75	2.45	0.75	Platinum wire	Platinum wire, Platinum mesh, (E)	Humidified H_2 (3 vol.%)	100	[185]
600	2018	Jamil	ASC	Ni-CGO	CGO	-	LSCF-CGO	0.2	-	0.23	N	-	2	0.2	Silver wire, (I)	Silver wire, Silver paste, (E)	H_2	20	[186]

600	2017	Sumi	ASC	Ni-GDC-YSZ	YSZ	GDC	LSCF	1.8	-	1.7	Y	0.23	0.5	0.2	Silver wire, Silver paste, (E)	Silver wire, Silver paste, (E)	Humidified CH_4	10	[187]
600	2016	Kikuta	ASC	Ni-GDC	GDC	-	GDC-LSCF	-	-	-	N	0.55	2.1	0.6	NiO paste, Steel wire	-	Humidified H_2	20	[121]
570	2007	Shimzu	ASC	Ni-GDC	GDC	-	LSCF-GDC	1.6	10	0.45	N	0.25	1.49	0.35	Silver wire, Silver paste, (E)	Silver wire, Silver paste, (E)	Humidified H_2 (3 vol.%)	5	[188]
570	2006	Suzuki	ASC	Ni-GDC	GDC	-	LSFCF-GDC	1.6	10	0.35	N	0.85	0.6	0.35	Silver wire, Silver paste, (E)	Silver wire, Silver paste, (E)	Humidified H_2	5	[63]
550	2011	Sin	ASC	Ni-GDC	GDC	-	LSCF	1.6	12	-	N	0.9	3.75	1.31	Silver wire, Nickel paste	Silver wire, Silver paste	Humidified H_2 (3 vol.%)	-	[52]
550	2006	Suzuki	ASC	Ni-GDC	GDC	-	LSFCF-GDC	0.8	12	0.2	Y	0.05	2.25	0.35	Silver wire, Silver paste, (E)	Silver wire, Silver paste, (E)	Humidified H_2	5	[64]
500	2019	Jamil	ASC	Ni-CGO	CGO	-	LSCF-CGO /LSCF	1.6	20	-	N	-	0.34	0.027	Silver wire, Silver wool, (I)	Silver wire, Platinum paste, (E)	H_2	20	[189]
500	2016	Jamil	ASC	Ni-CGO	CGO	-	LSCF-CGO	1.4	10	-	N	-	4.2	0.66	Silver wire, (I)	Silver wire, Silver paste, (E)	H_2	20	[190]
-	2015	Wang	ASC	Ni-YSZ	ScSZ	-	LSM	5	108	9.42	Y	0.42	1.4	0.32	Nickel foam, (E)	Silver mesh, (I)	CH_4	2700	[191]

2.5 Modelling µT-SOFC Current Collection

The overall goals of SOFC models are to be a cost and time-effective tool for R&D to reduce the cost of experimental fuel development and maximising performance and durability for commercialisation [192]. Models can be used as a tool for developing our understanding of physical phenomena occurring and support the insight necessary for improving fuel cell design [40]. Modelling is a powerful tool for understanding hard to observe phenomena such as ohmic loss as well as current and potential distribution in tubular cells. Models can aid current collector design and help minimise long electron conduction pathways that cause a large ohmic loss in tubular geometries [193,194].

The trends of SOFC model-based research have been dictated by modelling computer processing power and regularly modelling times for a given model will decrease with the latest computer technology. Also, the drive for low-carbon technology has pulled the modelling direction towards macro-scale modelling, taking the best of the materials currently available and optimising the design on a component, cell and stack level. This is indicative of the advance in technology readiness level and the rising demand for fuel cell products. Such macro models can be integrated into control systems for example in fuel cell vehicles [17]. Models are typically used for understanding the effects of altering geometrical design or operation parameters (such as fuel type, fuel/air flow, gas/furnace temperatures) on cell power and fuel utilisation [195]. To capture this level of detail, continuum level models are the most appropriate [40]. A representation of the real geometry or a region of interest is represented from 0D to 3D. Reducing the dimension reduces model size but also increases the number of assumptions made in a trade-off. SOFC continuum models for the component/cell level typically approximate solutions to the governing partial differential equations (PDE) describing the conservation of momentum, mass, energy and charge. Stack models often add solid mechanics to this to understand the thermomechanical deformation to analyse the stress between adjacent components [196]. To capture the most detail, SOFC models should include all of the phenomena, however, it is common for tubular SOFC models to opt to solve one or two of these and may consider those particular physics in more depth [197]. While 0D and 1D models can be solved numerically with software such as Excel or Matlab, commercially available computational fluid dynamics (CFD) packages are typically used, in particular, for higher dimension models. The model geometry is discretised in a technique known as meshing where splines connected to one or more nodes bound sub-domains [198]. In general, the smaller the mesh size (the smaller the distance between adjacent nodes), the more accurate the solution, but the higher the computational intensity. The upper and

lower limits of mesh size should be determined for the physical phenomena being solved and the domain being considered and an optimal size based on a convergence study found. Boundary conditions, known solutions to the equations at a node(s) in the geometry, are used as a reference point for interpolating to find solutions to the equations for adjacent nodes within a known degree of error. For first-order PDEs, one boundary condition is required, for second-order PDEs, two boundary conditions are required and so on. In this way, solutions can be found for the entire geometry. Equations can be solved at a steady-state which is most common, or be a function of time, a so-called transient model, which can capture the response times of a cell to a change in a parameter and model operation during start-up and shut-down [199,200].

The form of the equations and discretisation method is explicitly linked. CFD software can use the finite volume (integral method), finite difference (differential form) and finite element methods (integral), to name but a few. Commercially available CFD software typically used are COMSOL, Ansys and Fluent [201]. More recent iterations of the aforementioned packages include dedicated fuel cell packages that group the necessary physics in a user-friendly interface [202]. This has led to an increase in more complete models without omitting physics in recent literature as compared to oversimplified models of the past [203].

Early fuel cell models were mathematical models that gave exact analytical solutions [204]. They could be solved for all dimensions but are often labour intensive above 1D. Such closed form exact solutions are useful for determining the contribution of various parameters on performance with ease and allow for a predictive capability to the model [205]. Drawing analogies to electrical circuits, using equivalent circuits to represent fuel cell physics is a common tool in such mathematical models. This technique, known as transmission line analysis, or circuit analysis is particularly used in ohmic polarisation and current distribution studies where resistor elements, in series or parallel, are combined in an equivalent ‘ladder’ [206]. Current generating element and voltage generating elements can also be added to better adapt the circuit to represent a fuel cell. Elements can be grouped into segments which can have a physical representation in a real cell. For example for individual electrodes, current collectors, current collecting regions or current generating regions. The models are underpinned by Ohm’s law and Kirchhoff’s laws which enable the description of the current/voltage/resistance in each ‘branch’ of the electrical ladder network [207]. The range of validity is typically limited for such models as numerous assumptions must be made. Models of this type cannot account for diagonal current paths as they are typically restricted by the dimension of

the study. Ohmic models typically omit the effects of thermal gradients, species velocity/concentration profiles which affect the current and potential distribution. Nevertheless, within the range of validity, typically in the 'ohmic dominated' fuel cell potential region (0.9 V to 0.6 V), results can show a good agreement to experimental data. The model validity can be widened and improve accuracy by accounting for the aforementioned gradients in temperature, species concentration and electric potential distribution. Such gradients can be significant in tubular cells, particularly longer cells over a few centimetres in length. Electrical models are thus integrated with computational numerical models to account for the aforementioned gradients [193,194]. Numerical models don't provide explicit solutions for simple parameter analysis, nevertheless, parametric and sensitivity analysis can be performed to identify the effects of a parameter on model outputs. Numerical models can be rapidly solved, applied to infinite geometric designs and integrated easily into fuel cell control systems. Both mathematical and numerical models can and act as a simple tool at the design level to aid cell design and interconnect strategy.

2.5.1 Commonly Oversimplified Phenomena

To fully describe the operation of a SOFC, the equations of the underlying physics must be well described. Fuel cell operation is complex with high temperature reacting fluids in motion producing charge. Thus we must describe the conservation of momentum to describe the fluid motion, the conservation of energy to describe the heat transfer and generation, conservation of mass to describe the reactions occurring and the conservation of charge to describe the current and charge transfer. The physical phenomena are intimately linked and so omitting physics will result in error. To fully understand the effects that a change in a parameter or design will have on the overall performance, as much as the phenomena must be included. Not doing so may result in the failure to identify, mute or over overstate a change in a parameter or design. Models linking two or more phenomena are called multiphysics models.

Radiative Heat Transfer

Models typically fail to account for all heat transfer mechanisms: convection, diffusion and radiation. Radiative heat transfer, which is often omitted, is a line-of-sight phenomenon, meaning 3D modelling is favoured to account for view factors of complex geometries although lower-order models can be used with simplifying assumptions [208].

Radiative modelling is particularly relevant for tubular fuel cell bundles were outer layers are hotter than the central ones due to shielding effects [209]. Radiative heat transfer occurs through three routes during a µT-SOFC operation; surface-to-surface heat exchange in anode and cathode channels; thermal radiation of participating media in reactants and products; thermal radiation through translucent electrolyte and electrode layers. Radiation intensity at a given point in time is dependent on seven independent variables. Namely time, three position variables, two angular variables describing the direction of propagation of radiation rays, and the wavelength [210]. The review paper by Kakaç et al. [211] gives an outline of SOFC modelling results from 1994 to 2005, highlighting results that a lack of experimental data was an issue regarding model validation. Also, the review suggested that heat transfer from radiation was omitted in many studies and required further research.

In 2012, Hajimolana et al. [212] developed a numerical model to determine the effect of radiative heat transfer in a µT-SOFC. The cell design had the anode on the cell exterior with the cathode on the bore side. The model included the heat from endothermic internal reforming, shift reactions and heat produced from electrochemical reactions. They observed that a model considering radiation between fuel components and the electrode predicted a lower cell-tube temperature than one omitting the physics as the fuel absorbed heat. Increasing the inlet pressure increased the divergence between the predicted temperatures of the two models. They determined that the amount of energy absorbed by radiative heat transfer to the fuel increased with increasing cell length and should be included for cell lengths above 0.02 m. The fuel inlet was at 550°C and the air inlet was at 831°C. The plots of temperature for the model with and without radiative heat transfer versus fuel inlet pressure and cell length are shown in Figure 2.20 a) and b), respectively.

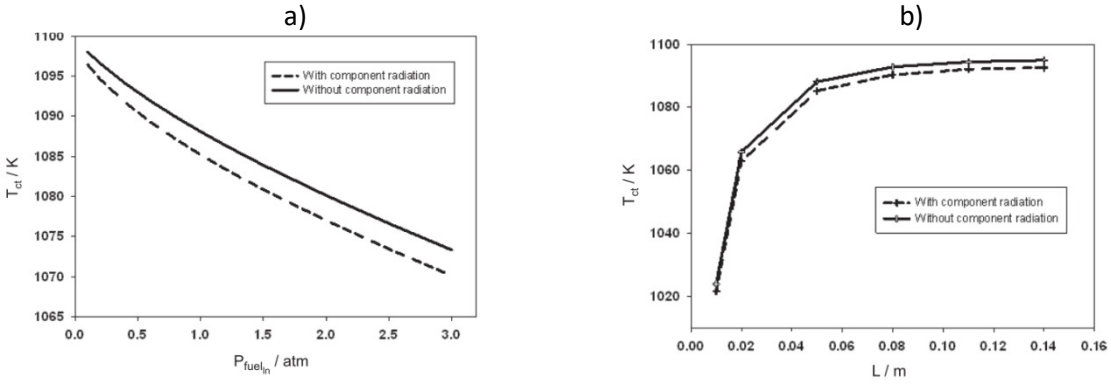

Figure 2.20 – Divergence in predicted cell temperature with the model including and not including component radiation a) versus fuel inlet pressure, b) versus cell length [151].

Mass Transfer

The study of mass transfer of a fuel cell model must describe mass transfer due to convection (momentum-driven) and diffusive Fickian mass transfer (concentration-driven) at the least. Gasses will be continually moving throughout the cell with some/all species partaking in electrochemical reactions and so the effects of the change in composition must be considered. Models must account for the movement of mass through the gas flow channels but also the tortuous electrodes. Depending on the pore size of the electrodes, Knudsen diffusion must also be considered, accounting for the interactions between gas molecules and the surrounding pore solid. Mass transport through the complex tortuous electrode structures is complex and often underdescribed, particularly compared to the detailed electrochemical models presented. Failure to use representative parameters of the microstructure can nullify the effort of detailed electrochemical models [213]. Several mass transport models have been adopted in SOFC modelling literature such as Fick's model (FM), Maxwell-Stefan model (MSM) and dusty-gas model (DGM) to name a few. Bertei et al. [214] highlighted the advantages and limitations of the five most commonly used gas transport models for SOFC electrodes, (including the aforementioned models) with common inconsistencies in their application. It was advised against assuming a uniform pressure in the DGM as this results in Graham's law of effusion, instead leave total pressure to be calculated. They also stated that the FM should be used exclusively for binary mixtures as the Bosanquet formula, which it uses, has a narrow validity range and so the sum of diffusive flux often does not sum to 0. Incompatible assumptions can also lead to fluxes inconsistent with molar balances and stoichiometry and molar fractions that do not sum to 1. The complex, inhomogeneous electrode microstructures coupled with incompatible assumptions, errors and inconsistencies often limit the validity of mass transfer models. As such electrochemical multiphysics models including mass transfer often poorly describe the 'mass transport' dominated regions of the polarisation plot at high current densities, high overpotential and low hydrogen concentration. To combat this, researchers have incorporated standalone mathematical mass transfer models that can be integrated into a numerical CFD model [213]. State of the art X-ray computed tomography (XRCT) images of the anode and cathode can be used to improve the mass transfer model. Modern CFD packages allow the detailed image in 2D or 3D to be used as the model geometry [215,216]. Modelling in this way avoids the use of bulk, generalised material parameters. Instead, local estimations of parameters such as particle size, pores size, porosity and tortuosity can be made. Such parameters can feed directly into the model physics, or be used to better estimate derived parameters such as effective diffusion coefficients. This technique

not only benefits mass transport models but extends to the intimately linked momentum, energy and electrochemical models for example estimation of local triple phase boundary density for electrochemical models, respectively [213]. Images from degraded cells can also be used to provide critical insight into microstructure degradation mechanisms [217].

Sawanwarangkul et al. [218] evaluated three mass transport models in their 1D steady-state model for predicting concentration overpotential in an SOFC anode. The model used a FM, a DGM and a SMM, finding that the DGM was the most appropriate for all operating conditions. The three key parameters for selecting the appropriate mass transport model were current density, reactant concentration and pore size. When operating at low current, high reactant concentration and with large pore size, the less computationally intensive SMM and FM are deemed an appropriate substitute. Only the DGM was suitable for multicomponent systems. The study assumed that the total pressure gradient inside the electrode was negligible which would differ from reality, especially if the device was operated with higher fuel pressures. Overpotential data from Yakabe et al. [219] was used for model validation.

Bhattacharyya et al. [220] developed a 2D dynamic model of an anode-supported tubular SOFC validated experimentally over a wide operating range using a commercial cell. Progressing from their steady-state model [221], the model's objective was to study the effect of Knudsen diffusion and the effect of increased electrochemically active area for the design of a system control unit. The transient model could only be validated when considering the Knudsen diffusion and extended active area. The diffusion inside the electrodes was the primary factor for the slow response of the cell to a step input of load. The electrochemical response, which depended on the double layer capacitance proceeded in the order of a few milliseconds which was faster than the simulated time step.

Pasaogullari and Wang [222] developed a comprehensive multi-dimension, multiphysics planar SOFC model as a stepping stone towards an internal reforming simulation. The model incorporated dual (diffusion/reaction) layer electrodes supported by a YSZ electrolyte. The commercial CFD package Fluent solved for the conservation of mass, conservation of momentum and energy, multi-component species transport, charge transfer and electrochemical kinetics. The model failed to consider the losses ascribed with interconnection when predicting polarisation curves, current and reactant concentrations. The model predicted polarisation curves, also giving information on internal processes, like flow field, specifies concentration, potential and current distribution at a 2D level. The

authors concluded that mass transport limitations 'play an important role in SOFC performance, especially under high current density operations'.

Kong et al. [223] developed a modified Fick's model for the approximation of the DGM. The purpose was to avoid uncoupled partial differential equations for species fluxes that caused complexities with the model conversion. Instead, the DGMFM gave explicit analytical expressions for species fluxes and proved to be accurate for reproducing results of the DGM for multicomponent mixtures. Compared to the convective and diffusive fluxes, the species flux was negligible.

2.5.2 Mathematical Modelling of µT-SOFC Current Collection

Zhu and Kee [194] developed a mathematical model to investigate axially distributed current collection. The model considered coupled momentum and heat transfer within the tube in the axial direction, reactive porous media flow within the electrodes in the radial direction, electrochemical charge transfer and thermal transport throughout the MEA (x-direction) and an electrical circuit to represent the current collection system. The electrical network was described by an electrical circuit model. The model accounted for axial electrical conduction in the electrodes by utilising an effective electrical conductivity coefficient to represent 2D effects. Four current collection configurations were used. Firstly, a 'base case' with fifty cathode and ten anode connection points, secondly a 'reduced case' with twenty-five cathode and ten anode connections. Thirdly, 'without anode collection' where the collection was by axial conduction through the cell and assumed the cathode electric potential was uniform, and finally 'uniform cell potential' which assumes perfect current collection. Their findings are summarised in Table 2.3.

Table 2.3 - Predicted overall performance for various current collection setups. Reproduced from Zhu et al (2007) [194]**.**

Case Name	Efficiency	Utilisation (%)	Power (W)
Base Case	52.5	95.3	32.4
Reduced Cathode Attachment	52.9	90.4	32.7
Without Anode Collection	14.6	23.1	9.0
Uniform Cell Potential	48.6	97.2	30.0

The 'without anode collection' exhibited significantly reduced performance, indicating the scale of the importance of anode connection to the overall collection strategy. Altering nickel content in the YSZ will alter the bulk electrical conductivity, current distribution, structural properties, degradation,

and catalytic activity. The remaining cases were relatively similar in performance, noting the reduced efficiency of the 'uniform cell potential' demonstrated 5% lower efficiency than the 'base' and 'reduced cathode' case but had a higher fuel utilisation. It is evident the study was thorough and revealing from a mathematical perspective; it would be interesting to see a fit profile to mirroring experimental data. It becomes explicitly clear that cell performance is intimately related to the current collection strategy.

Suzuki et al. [224] developed a circuit analysis to determine the current collection efficiency in their 1.6 mm OD microtubular cells. The model divided the anode length into N segments and each segment was assigned a representative equivalent circuit. Two sub-models were developed to determine the efficiency loss of a cell with a single anode current collector versus a cell with current collectors at both ends of the cell. They used the ASR measurement of their cell with a single current collector as the reference value for the efficiency loss. The authors only considered current collector positions at either end of the cell. They concluded that the dual connection with a current collector at each end of the cell was superior to a single current collector at one end. The performance gain from a dual connection was increased with increasing operating temperature and tube length. The associated loss of the double terminal was two to four-fold lower than that of the single terminal for their cell geometry, materials and operating conditions. They were unable to determine the exact analytical solution to the model although they established that a solution should exist. The single terminal model converged after approximately 50 divisions whereas the double terminal converged above 100 divisions.

Suzuki et al. [225] also applied the model to their 0.8 mm OD cell, fixing the current collector position at one end and increasing the cell length to determine the efficiency loss at a given length. They determined that there was a 7% loss in performance for cell lengths above 1 cm, indicating that cell length was a critical performance parameter for determining current collector spacing.

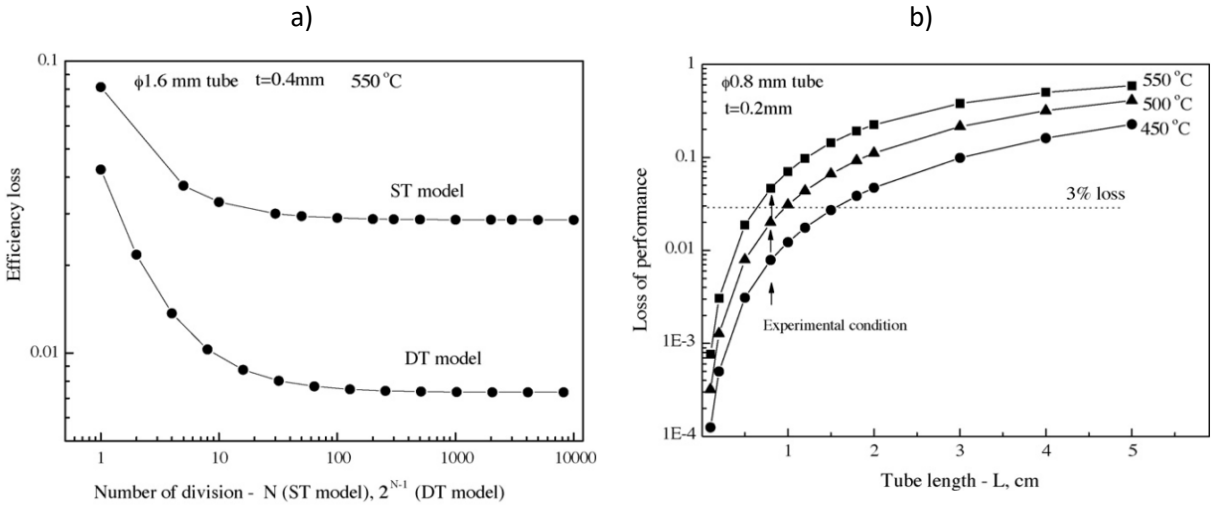

Figure 2.21 – a) Convergence of efficiency loss with N for single terminal and double terminal models [224]**, b) efficiency loss versus tube length for 0.8 mm OD cell** [225]**.**

Virkar et al. [205] conducted a transmission line analysis to determine the effect of current collection from single and double connection current collector configurations, concluding that a dual current collector setup was superior to the single setup having the added benefit of built-in redundancy and increased durability. The current paths for the interconnect configuration at the same end and opposing ends are seen in Figure 2.22.

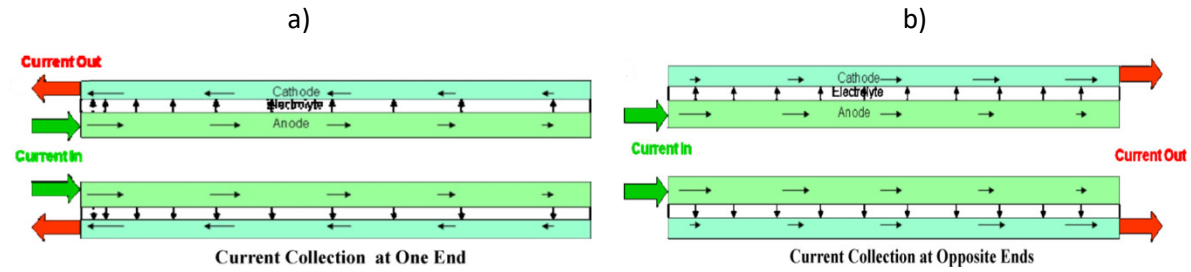

Figure 2.22 – Current direction for a) same end connection nodes and b) opposing end collection nodes [205]**.**

The authors suggested that reducing the conductivity along the cell length would greatly reduce the ohmic loss from current collection. They suggested applying strips of more conductive material along the length of each electrode to reduce the ‘sheet resistance’.

2.5.3 Numerical Modelling of µT-SOFC Current Collection

In 2007, Cui et al. [226] developed a 2D model of a micro-tubular fuel cell, considering momentum, mass and charge transport. Three different current collector configurations were studied, inlet only (IC), outlet only (OC), and both inlet and outlet connections (BC). They were compared to a baseline of the total anode connection (TC) whereby the entire anode was the current collector. The cathode current was collected from the entire length for all cases. The effects were determined on tubes of differing length. It was found that efficiency loss with the BC mode was 2 to 4 times lower than with the single IC or OC modes. The vector plots for the current density for the four current collecting modes can be seen in Figure 2.23.

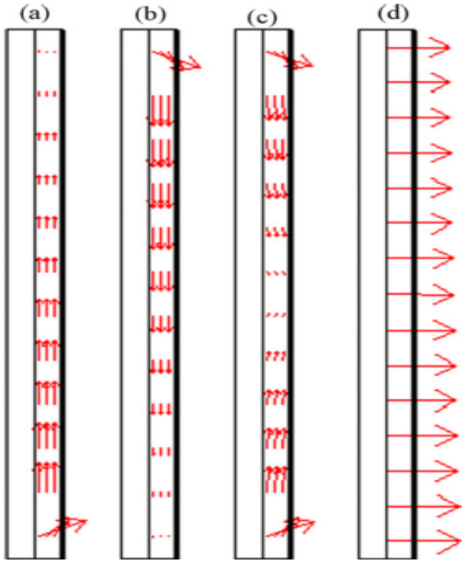

Figure 2.23 - Vector Plots of current density inside anode under (a) IC, (b) OC, (c) BC, (d) TC modes [226].

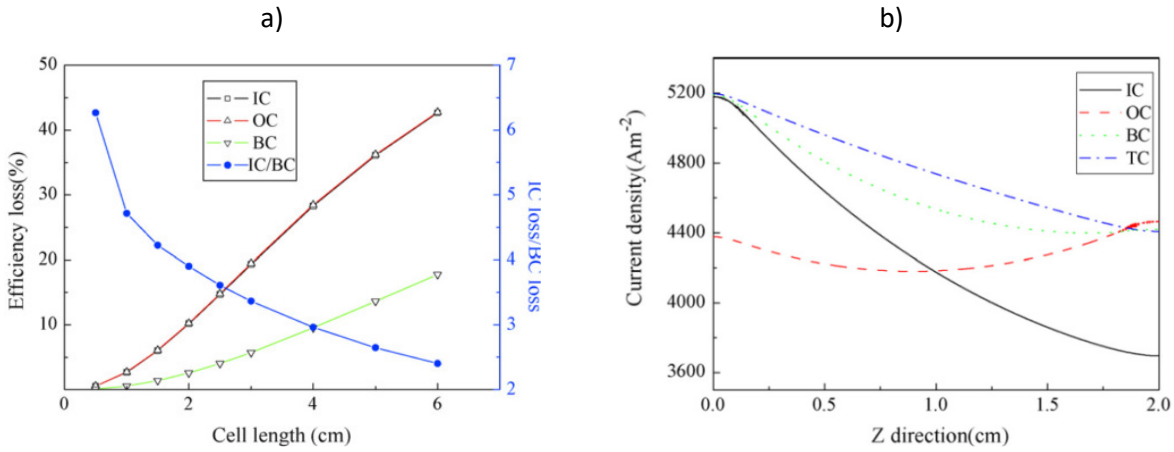

Figure 2.24 –a) Cell length versus efficiency loss, b) current density for multiple connection configurations [226].

As seen in Figure 2.24, the efficiency loss for the IC/BC case decreases with cell length whereas for OC the efficiency loss increases with cell length. Unfortunately, the IC plot is not shown in a). The OC mode gives a rather uniform hyperbolic $y = cosh(x)$ shaped current distribution along the Z direction with the inlet current density lower than the outlet, a minimum of 0.42 A.cm^{-2} in the centre of the cell and the smallest difference of 0.03 A.cm^{-2} between the maximum (0.45 A.cm^{-2}) and minimum current density. The current density distribution profiles in the IC, BC and TC modes were in the form $y = \frac{1}{1+\exp(x)}$, with inlet current density notably higher than the outlet. The IC, BC and TC all had a far higher peak current density of around 0.52 A.cm^{-2}. The difference between the maximum and minimum of the IC was the most at approximately 0.15 A.cm^{-2} with TC and BC similarly 0.075 Acm^{-2}.

Cui et al. [227] improved the model in 2009, including the conservation of energy in a validated model using polarisation curves. They found that the heat produced at the cathode-electrolyte interface is around five times greater than the heat consumed at the anode-electrolyte interface and state that a significant amount of heat expelled to the environment occurs at the cathode external surface. The cell surface temperature [K] for the inlet (IC), outlet (OC) and combined inlet and outlet (BC) current collection, from left to right, respectively is seen in Figure 2.25 a). In addition, they plotted the variation in temperature along the axial length of the anode/electrolyte interface as seen in Figure 2.25 b). They observed a different profile for each current collecting mode with the OC current collector giving the highest temperature at the outlet and the lowest temperature at the inlet. The BC and IC had very similar temperatures at the inlet side, with the outlet side temperature around 10 K higher for the BC compared to the IC. The thermal gradient was the lowest for the BC connection.

The streamline and arrow plots of anodic current density in the IC, OC and BC modes as seen in Figure 2.25 c). They observed that current flow is not parallel to the anode/electrolyte interface and that current streamlines converge to a point. The surface plots of current density distribution [A.m^{-2}] is seen for the IC, OC and BC from left to right, respectively, in Figure 2.25 d). The maximum current density value for the IC and BC where within 4 A.m^{-2} of each other while the OC value was 1728 A.m^{-2} lower. The minimum current density values were lowest for the IC, followed by the OC and then BC. The largest gradient of current density along the cell length (axial) was for the IC followed by the BC and then OC.

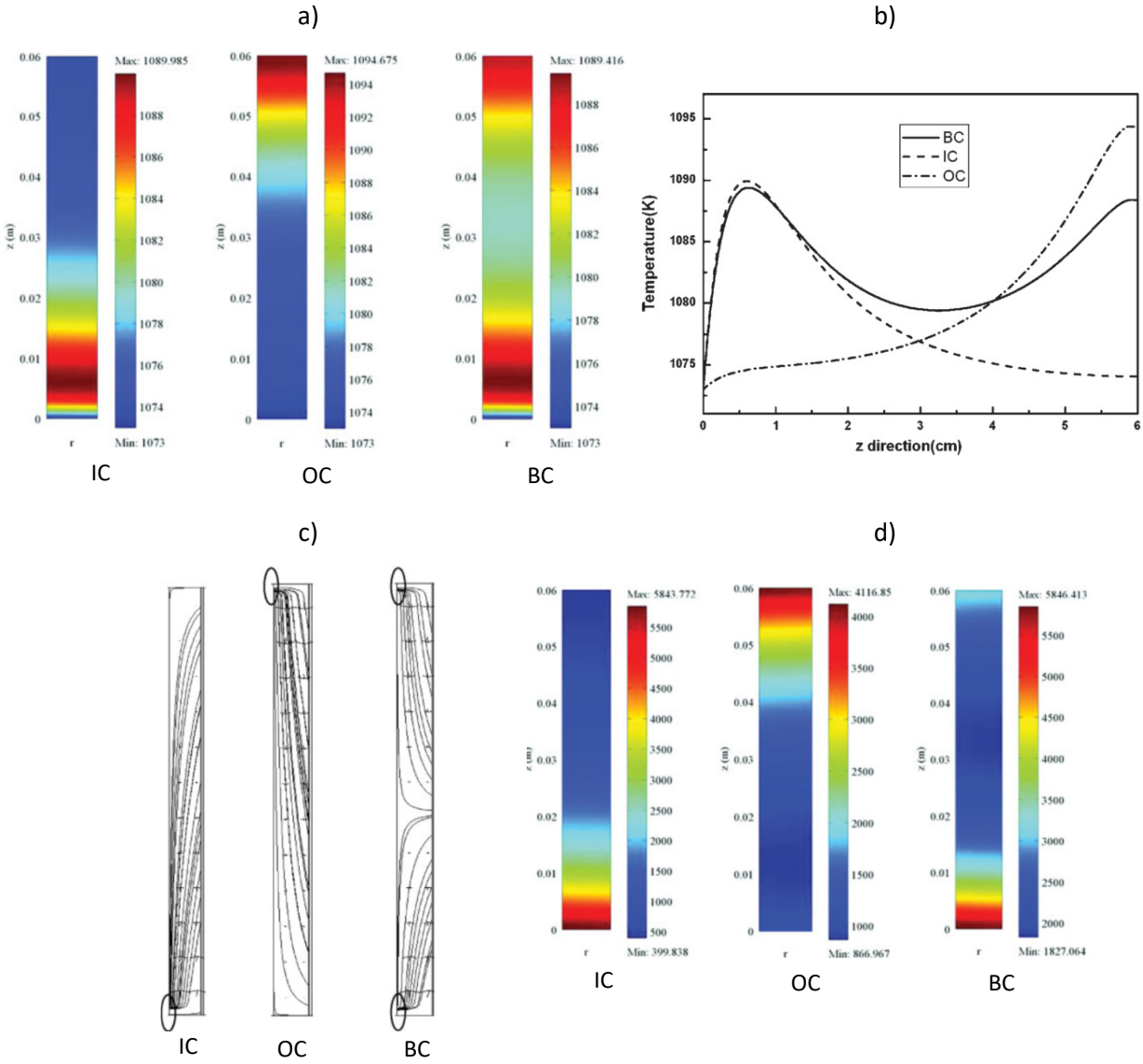

Figure 2.25 – a) Temperature surface plot [K], b) temperature along the anode/electrolyte interface, c) anodic current density streamline and arrow plot, d) surface plot of current density distribution [A.m^{-2}] [227]**. IC, OC and BC denote an inlet, outlet and both current collectors, respectively**

In 2020 Cui et al. [129] developed a multiphysics FEM model of a tubular SOFC MEA and current collector, solving the concentration of momentum, mass, energy and charge. They fitted their model to experimental data for three flow rates, 10, 20 and 30 ml.min^{-1} with the model showing good agreement, particularly between 0.9 V and 0.6 V where the standard deviation was 0.013, 0.007 and 0.007 A.cm^{-2}, respectively. For the lowest flow, there was a significant divergence between 0.8 V and 1 V. The current collectors were placed at each end of the electrode, at the fuel inlet and fuel outlet. The current density distribution was compared at high and low flow rates. The vector plots of current density are seen in Figure 2.26. A shift in the centerline of the current density distribution was

observed as indicated by the streamline current density plot. At the lower flow, the majority of the current passed to the inlet current collector while at the higher flow there was a more homogenous split. 16% more current passed through the inlet for the low-flow compared to the high-flow case, indicating that current density distribution and current collector efficiency had a strong dependency on fuel utilisation and flow rate.

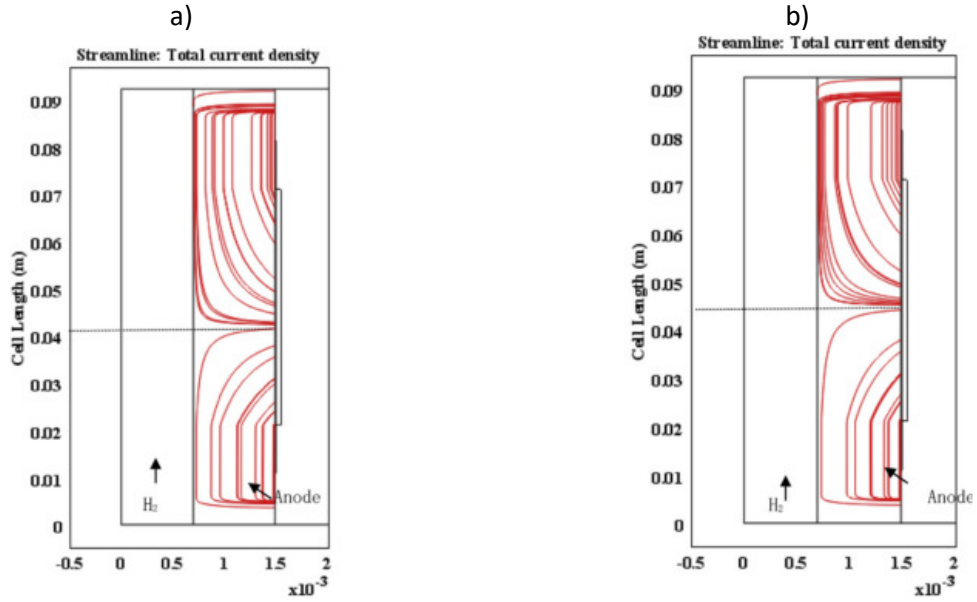

Figure 2.26 - Current density distribution at low flow a) and high flow b) [129]**.**

In 2016 Aydin et al. [90] presented a 2D multiphysics model of a segmented tubular cell for estimating current and temperature distribution. The model solved for the conservation of momentum, energy, mass and charge. All three types of heat transfer mechanisms were solved. Radiative heat transfer between the outer electrode and the furnace was considered but was omitted on the anode side (to the fuel), justifying this assumption by stating that the fuel was pre-heated. They compared the numerical results to a mirroring experimental setup and used both polarisation data and temperature measurements for fitting. They stated that including temperature data for fitting improved the model accuracy, particularly at low cell voltages. The model follows the experimental data trend of the upstream cell being the best followed by the midstream and downstream as seen in Figure 2.27. The temperature rise at each stream position from the experimental measurements and predicted numerically with and without temperature validating data is seen in Figure 2.28.

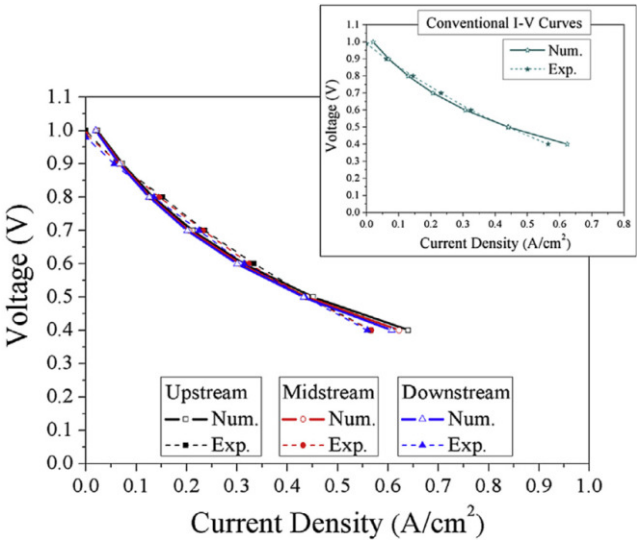

Figure 2.27 - Empirical and model polarisation curves for upstream, midstream and downstream cells [90].

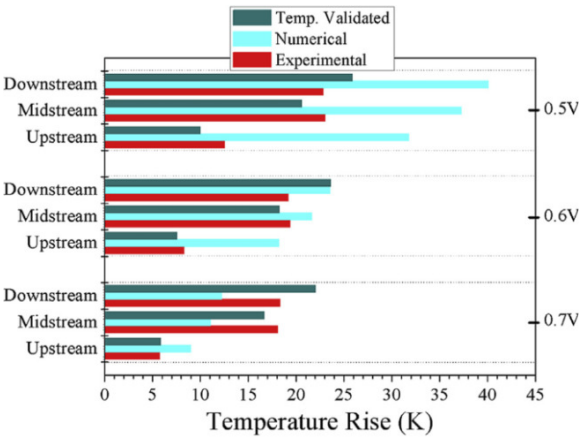

Figure 2.28 - Temperature rise over furnace temperature determined experimentally and numerically in an unfitted model versus a thermal data fitted model [90].

Otomo et al. [228] coupled a 2D FEM mass and charge transport multiphysics model of a segmented-in-series tubular cell to an economic model of a fuel cell system. The model covered a potential range of 0.9 V to 0.5 V for a single cell showing a good fit to experimental data from another author data over a voltage range of 0.8 V to 0.5 V. They determined the relative overpotential contribution from the anode and cathode as well as the ohmic loss at a current density of 0.28 A.cm^{-2} (approx. 0.66 V), finding that the ohmic contribution to overall cell polarisation losses was 65%. A good agreement from their derived ASR values to those in literature was shown with an approximately 2/3 share of ohmic contribution to the cell ASR as seen in Figure 2.29. They determined that increasing the power produced per cell reduced production cost, especially between 50 W and 100 W. Increasing the cell diameter increased production cost only marginally. The segmented design meant that multiple cells are stacked along the support. A parametric study was conducted to determine the optimal sizing of the effective generation part (EGP) and the interconnect part (ICP) length. They determined that the optimal ratio of EGP/ICP, i.e. the ratio of the active area to the current collector (L_c/L_{ic}) was between 1 and 2. Increasing the ratio to 1 improves power density due to an increased electrode area however increasing the ratio above 2 induces a high ohmic loss from the cell. The values were presented normalized to $Lc/Lic = 10$.

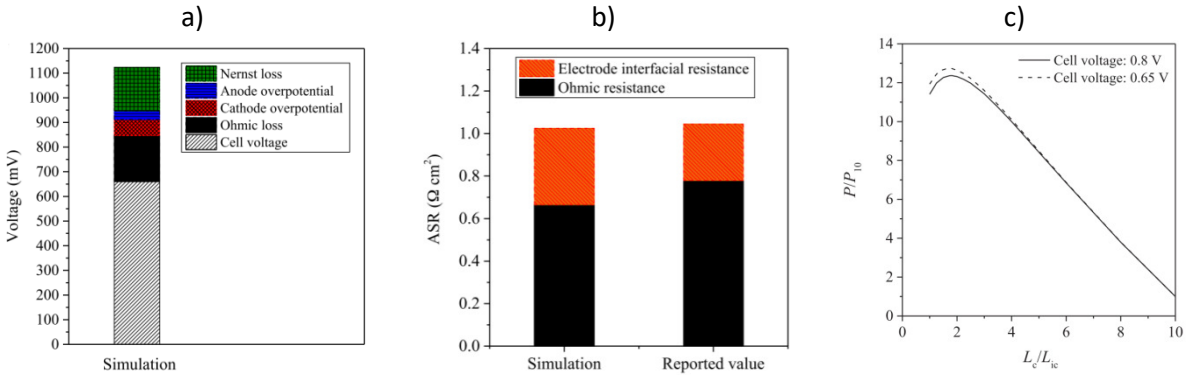

Figure 2.29 – a) Model predicted overpotential contribution, b) simulation versus experimental contribution to ASR, c) normalised cell power versus Lc/Lic [228]**.**

In 2019 Lu et al. [229] developed a 2D multiphysics model that incorporated mass transport data obtained from 3D tomography images of a real fuel cell. The conservation of mass throughout the anode was well described with a Knudsen mass transport model solved via a Direct Simulation Monte Carlo method applied to the 3D image where an estimation of apparent permeability was obtained for a range of porosities. It was determined that the Knudsen tortuosity factor was twice that of respective values determined by continuum flow. The study also focused on the optimised microstructure of micro-channelled anodes fabricated by phase-inversion. Channels penetrating more than 60% of the electrode eliminated fuel depletion to the reaction sites.

2.6 Summary of µT-SOFC Cell Level Models in Literature

The table below summarises the cell level tubular SOFC models which had a particular focus on current density distribution and/or the influence of current collection on cell performance. Detailed in the table are the model dimension and the discretisation method. Also, the momentum physics, whether Navier-Stokes (NS), Darcy's model (D), Brinkman model (Br) or a simple velocity input (V). The heat transfer mechanisms in the energy physics, convection (CV), conduction (CD) and radiation (R). Whether the model included electronic (E) and ionic (I) charge modelling. And also whether the model was fitted to experimental data and whether a parametric/sensitivity analysis was conducted.

Table 2.4 - Summary of µT-SOFC cell level models in literature.

	Cui et al. (2020)) [129]	Lu et al. (2019) [229]	Amiri et al. (2018) [230]	Otomo et al. (2017) [228]	Jin et al. (2017) [231]	Aydin et al. (2016) [232]	Cui et al. (2015) [233]	Cui et al. (2010) [234]	Serincan et al. 2009 ([235]	Cui et al. (2009) [227]	Cui et al. (2007) [226]	Kong et al. (2012) [223]	Hajimolana et al. (2012) [212]	Virkar et al. (2010) [205]	Suzuki et al. (2007) [224]	Zhu et al. (2007) [194]	Feng et al. (2015) [236]	Sumi et al. (2013) [237]
Dimension																		
0D/1D/2D/3D	2D	2D	2D	2D	2D	2D	2D	2D	2D	2D	2D	1D	1D	1D	1D	1D	0D	0D
Discretisation Method																		
FDM/FEM/FVM/N	FEM	FEM	FEM	FEM	FEM	FEM	FEM	FEM	FEM	FEM	FEM	FEM	N	N	N	-	N	N
Governing Physics																		
Momentum NS/D/Br/V	NS/Br	NS	NS/D	-	-	NS/Br	-	-	NS	NS	NS/Br	-	V	-	-	NS	-	-
Energy CV/CD/R	CV/CD	-	CV/CD	-	-	CV/CD/ R	-	-	CV/CD	CV/CD/ R	-	-	CV/CD/ R	-	-	CV/CD	CV/CD/ R	-
Mass D/C/K [MS/DGM/DGFM/F]	D/C/K	D/C/K [DGM]	D/C/K [DGM]	D/C	D/C/ K	D/K [MS]	D	D/K	D/C/K [MS/DGM]	D/C/K	D/C/K	D/C/K [DGFM]	D/K/C	-	-	D/C/K [DGM]	-	-
Charge E/I	E/I	E/I	E/I	E/I	E/I	E/I	E/I	E/I	E/I	E/I	E/I	-	E/I	E	E	E	E	E
Model Fitting to Experimental Data																		
Yes/No, Y/N	Y	Y	N	Y	Y	Y	N	N	N	Y	N	N	N	N	Y	N	N	Y
Parametric Analysis																		
Yes/No, Y/N	N	Y	Y	Y	N	N	N	N	Y	N	N	Y	N	N	N	N	N	N

2.7 µT-SOFC Stacks

The rapid start-up time, high thermo-mechanical integrity and high volumetric density of tubular stacks specifically lend them to use as portable power devices [238]. Power densities of up to 1.5 $W.cm^{-2}$ recently reported making them competitive with planar SOFC and PEM devices with fewer issues surrounding fuel availability [53]. Portable tubular stacks can be categorised by the range of power required for the application: sub 2W for micro-portable, 10 to 50 W for small portable and 100 W to 250 W for medium portable and sub kW for large portable units [112]. Units in the kW class can be used as auxiliary power units in vehicular applications, for example, recreational vehicles (RVs), delivery vehicles and trucks but are typically used for residential combined heat and power (CHP) units where system weight is less of an issue. Commercial CHP and backup power/power generation are typically reserved for planar units. Primarily because the larger stack/system footprint, higher mass and also the lesser mechanical durability of a planar stack versus a tubular counterpart is not important for such applications. A table classifying the typical applications of SOFC stack by power range is seen in Table 2.5.

Table 2.5 - SOFC Applications.

Power Range	Category	Typical Application	Stationary / Portable, (S) / (P)	Planar / Tubular, (P) / (T)
<2 W	Micro-portable	USB / Phone Charger	P	T
10-50 W	Small-portable	Laptop Charger	P	T
100-250 W	Medium-portable	UAV / Drone / Robot	P	T
250-1 kW	Large-portable	Military / Generator / RAPS	P	P / T
1-10 kW	APU / CHP	Automotive APU/ Residential CHP	P / S	P / T
10 kW-MW	CHP / Power Gen.	Commercial CHP / Power Gen. / UPS	S	P/T

The performance/efficiency of a stack can be measured similarly to a single cell, typically the current density and power density with respect to the active area. The cell or stack efficiency can also be measured by the fuel utilisation by using the current density and the inlet flow rate or by measuring the fuel consumption from the inlet and outlet flow rate and species concentration. The volumetric and mass-based current density and power density values are used exclusively for stacks. These values account for the space occupied, or the mass of the stack component of the system, typically

the cells and the manifold. The volumetric and mass density values are useful from a commercialisation perspective for system sizing and cost analysis.

As seen in Figure 2.30, 57% of single cells reported achieved a total power of less than 1 W and 28% between 1 W and 5 W. With 70% delivering less than 2 W. To achieve a useful power output of more than a few watts, cells must be combined into stacks. Fuel cells can either be connected in series, in parallel or a combination of both, depending on whether high voltage or high current is desired. Modular designs mean sub-modules can be easily combined for a desired stack power output and can be a configuration of series, parallel or hybrid. Modular designs allow for facile maintenance, rather than splitting/replacing the whole stack when a fault is detected, a module can be easily replaced and in some cases, the stack can continue to operate (at a reduced capacity) during the replacement of a sub-element. The same quantity of fuel must be supplied to each module and in turn, distributed equally into each cell and so the design of manifolds must be optimised, a problem not discussed on a single cell level. To ensure all the fuel provided is delivered to the cell, gas-tight, durable sealing must be in place. This is a non-trivial task given the number of joints in a tubular stack and the logistics of sealing complex interior and exterior joints, not to mention selecting the 'perfect' material from the few applicable high-temperature sealants that are available.

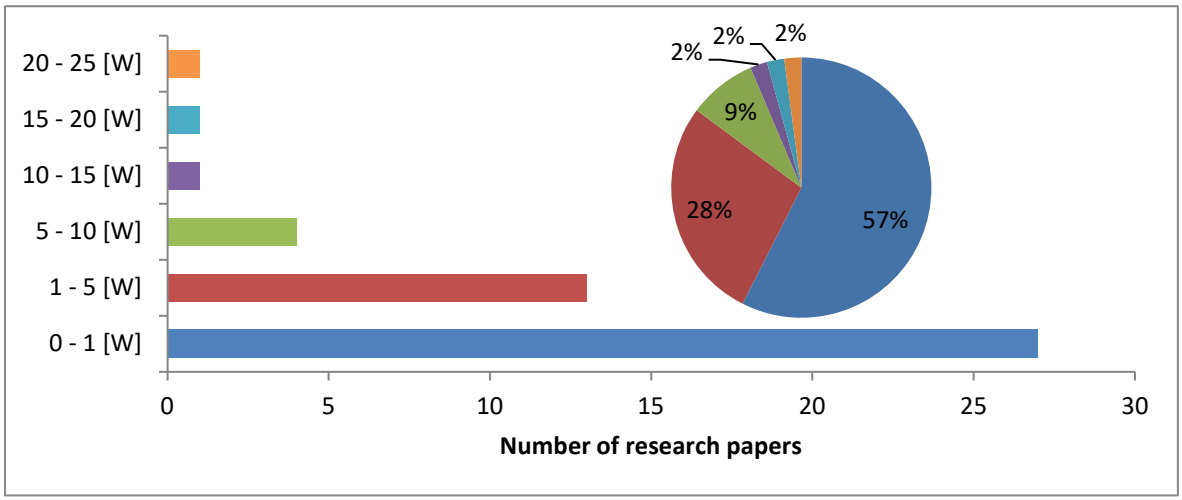

Figure 2.30 – Peak power of single cells in recent literature from Table 2.7 between 2015 and 2020.

2.8 Development Status and Objectives

Academic literature on SOFC stacks is scarcer in number and limited in detail compared to single cell papers. Stack level studies are typically linked with commercial stakeholders and so data is sensitive and often unpublished. Stack research objectives are focused on interconnection, sealing, manifold design, development of the balance of plant (i.e. heat exchangers, pumps, tank design, piping) and wider system integration/optimisation. Short stacks, typically two cells that are electrically connected, are the smallest configuration unit of cells that can be called a stack. Short stacks are a cost-effective way to prove concepts developed on a cell level can be scaled to a stack level. However, some details developed on the single cell and short stack level may not translate onto a sub-stack or stack level such as assembly and logistics, cell spacing, equal fuel supply, cooling and the homogenous supply of air/oxygen. The difficulty in translating performance on a single cell level can be seen when comparing Figure 2.31 and Figure 2.32. The peak power densities of a stack are always below 0.5 $W.cm^{-2}$ with the majority between 0.2 and 0.5 $W.cm^{-2}$. However, on a cell level, 46% of the cells reported have a peak power density of over 0.5 $W.cm^{-2}$.

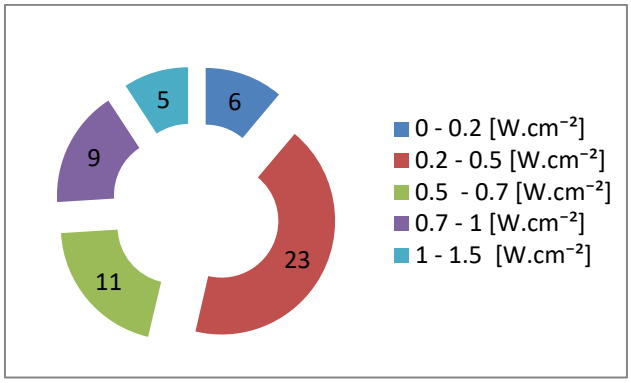

Figure 2.31 - Peak power densities of single cells reported in literature from Table 2.2 between 2015 and 2020.

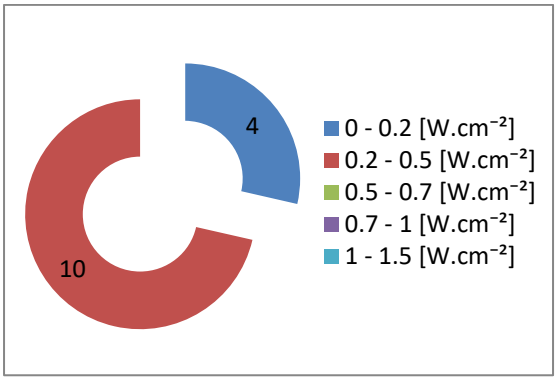

Figure 2.32 - Peak power densities of stacks reported in literature from Table 2.7 between 2015 and 2020.

The difference in performance is difficult to isolate to a single cause. Clearly, improvements at the cell level will benefit the stack levels, however, weaknesses will also be amplified. It is imperative that decisions made at the cell level consider stack level design. The same should be said at any design level, from micro to macro. A large portion of the loss will likely arise from the interconnecting between cells. The interconnecting is directly affected by the manifolding that governs cell spacing and hence the wiring of adjacent cells. The manifolding is, amongst other things governed by the optimisation of oxidant supply and heating/cooling requirements. Electrochemical measurement of a single cell or multiple cells within the stack is useful and often reported in the literature. In particular,

comparison of the impedance from a single cell test, to that of the same cell within the stack and also to the impedance of the whole stack can elucidate the relative contribution from different losses at the stack level. The power output of tubular SOFC stacks recorded in the academic literature between 2008 and 2020 is seen in Figure 2.33. In the 0 W to 10 W class, results on 6 stacks were reported between 2015 and 2020, whereas 11 stacks were reported in between 2008 and 2015, totalling 17 over the 2008 to 2020 period. This indicated a reduction in R&D activities, at least at the level of publications.

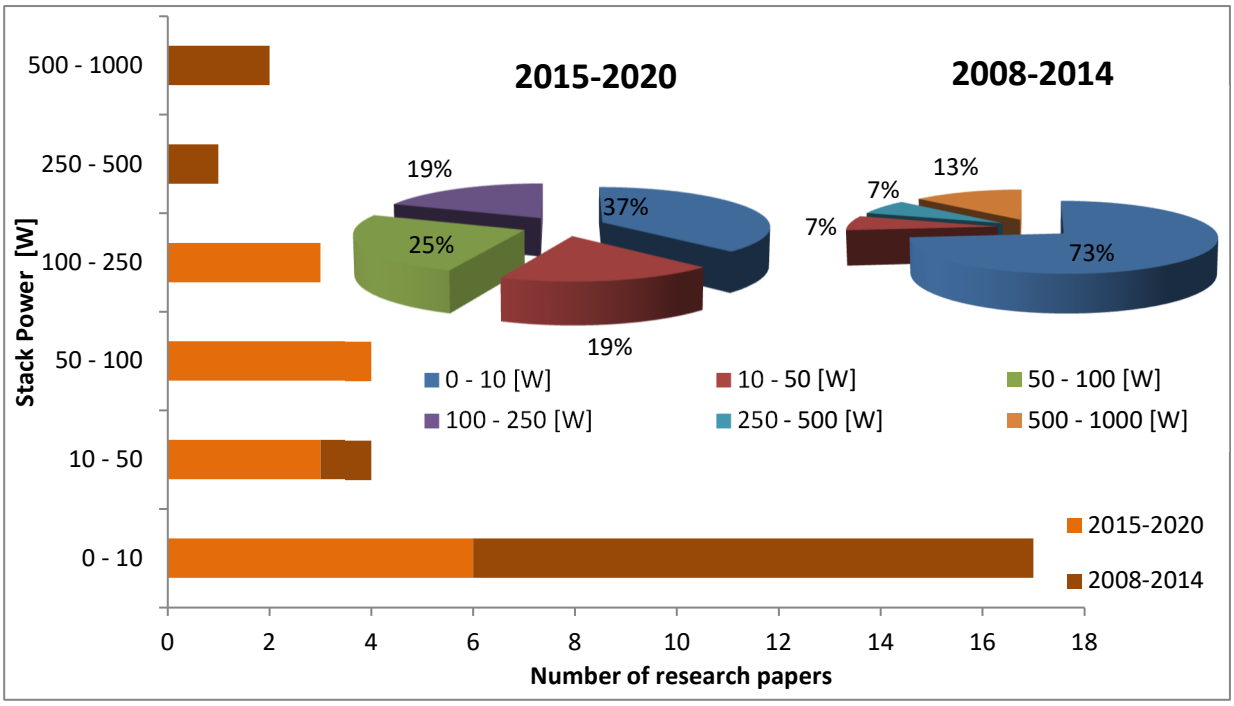

Figure 2.33 - Power output of stacks reported in literature from Table 2.7 between 2008 and 2014 and between 2015 and 2020.

2.8.1 Manifolding

To supply fuel to and remove reaction products from cells, a manifold must be used, simple for a single cell but non-trivial at the stack level. A stack manifold will provide fuel to multiple cells, with the task of supplying an equal amount to each cell. The manifolds should allow gas to pass freely, incurring a minimal pressure drop. A manifold must also securely position the cell and act to separate the fuel and oxidant streams. For tubular stacks, manifold design controls the spacing of each cell which in turn affects the volumetric power density of a stack. The lower limit of spacing is restricted by assembly/interconnection logistics as well as oxidant/coolant supply requirements. The

intimate contact between cells and the manifold lead to a material selection issue. High-temperature manifold materials are limited to ceramic which has a similar CTE to fuel cell components (and a limited selection of steels). Ceramic manifolds are difficult to shape and are typically machined from blocks. The brittle nature and hardness of ceramics increases manufacturing time/cost/difficulty and restricts designs. Intermediate temperature manifolds can be metallic which are easily machined, moulded, cut and formed into complex geometries. Metallic manifolds can have similar CTE to fuel cell components which reduces thermomechanically induced stress during operation, favouring durability. This, combined with facile machining means component compatibility can be incorporated at the design stage, for example using spring fittings. Metallic manifolds can also be joined to adjacent cell/stack components (to a greater extent if metallic interconnects are used) via standard joining techniques such as welding and brazing which lowers manufacturing time and cost. Metallic manifolds are typically lighter, lower in cost and have a higher thermal conductivity compared to ceramic components, which can drastically reduce start-up time and aid thermal management. The conductive nature of metallic manifolds means that they can also be incorporated into the interconnect design but must be electrically well insulated if the current flow is not desired. Plastic manifolds can be used as a so-called 'cold manifold' outside the SOFC hot zone. Plastic, metal and, more recently, ceramic manifolds can be made by additive manufacturing with 3D printers. This allows for rapid prototyping of complex and highly optimised designs to fine tolerances which simply cannot be achieved by traditional manufacturing methods. Table 2.6 highlights the key features of typical manifold material types.

Table 2.6 - Manifold material features.

	Ceramic	Metal	Plastic
Temperature Resistance	High	Med (High if coated)	Low
Manufacture	Difficult	Easy	Easy
Assembly	Difficult	Easy	Easy
Compatibility	Good	OK	OK
Weight	High	Med	Low
Cost	Med	Med	Low
Durability	Low	High	Med

2.8.2 Interconnection

Cells can be connected in series, parallel or a combination of both. In a parallel configuration, the total current is a summation of the current of each cell while the potential of the cells is fixed at the

potential of the weakest cell. For series connections, the total potential is a summation of each cell potential while current is fixed at the current of the weakest cell. Like old fashioned Christmas tree lights, if a cell fails in a series-connected stack, the whole stack will fail. However, for cells connected in parallel, if one cell fails the stack will continue to operate but at a reduced capacity. Connecting cells in series can be logistically difficult whereas parallel is often easier and allows connecting electrode terminals onto common rails, reducing wiring length/loss and can easily be integrated into metallic manifolds which can have dual functionality.

Cells can be bundled into sub-modules of cells in series or parallel. The bundles can then be combined to make a stack, with the best configuration chosen for the particular application. For a portable power supply that will likely encounter mechanical impact, the redundancy offered by a stack with a bias toward parallel connections will be favoured. For stationary CHP, mechanical damage is unlikely and the high current draw for a long duration will favour a stack with a bias towards series connection. For remote area power systems (RAPS), uninterrupted power supply (UPS) or a drone, a more equal split of series and parallel may be required so that efficiency is sufficiently high but in case of damage, which would be critical, the stack would remain online with sufficient power to operate at a reduced capacity while emergency measures can be taken before maintenance.

2.8.3 Sealing

A good sealant should be mechanically durable, have similar CTE to cell/stack components, maintain hermeticity, chemically compatible and inert, simple to apply and be low in cost [101]. The requirement for an electrically insulating or an electrically conductive seal depends on the stack/cell design. Seals can be categorised as a compressive seal or a rigid seal. Compressive seals deform slightly and become gas tight under load, akin to a gasket in an internal combustion engine. Compressive seals such as mica-based seals are typically suitable for planar devices where the whole stack is under a compressive load. Rigid seals are favoured in tubular stacks and make a bond with the materials to be joined [202]. Glass-ceramics are state-of-the-art rigid seal for SOFCs. They are electrically isolating and have a dual, amorphous and crystalline phase produced through a controlled crystallisation process. Glass ceramics are suitable for high-temperature and dual reductive and oxidative environments [101]. The elevated viscosity of glass-ceramics at high temperatures allow some variants to be mobile enough to spread and cover any nearby leaks,

securing hermetic seals, so-called ‘self-healing’. Sabato et al. [239] developed a barium-free glass for use with stainless steel interconnects. The gas tightness was tested over 1100 hours at 1073 K and showed no evidence of leaks. The authors concluded that coated stainless steels exhibited enhanced chemical compatibility with the glass seal compared to uncoated steels.

Precious metal pastes such as dense silver pastes have also been used as sealants [240]. While favoured for their ease of application and rapid curing times they are costly and electrically conductive. The most common, silver pastes, face the previously mentioned degradation issues that affect silver current collector wiring, namely porosification, which results in loss of mechanical integrity and hermeticity during medium to long term operation [92,241]. When used in conjunction with glass-ceramic sealants, migration of metals from the paste into the glass occurs leading to accelerated degradation and is a concern for long term operation [93].

Metallic brazing alloys are also used as an SOFC sealant [101]. Metallic braze materials align well with the increasingly used metallic interconnects and manifolds concerning material compatibility. Metallic brazes are conductive and so if current flow through the seal is not desired they must be electrically insulated. Metallic brazes are more ductile than glass-ceramic seals which favours them as a compliant, more thermomechanically durable seal [48,242]. Commonly used silver-based brazes adhere well to SOFC components but face issues surrounding hermeticity and mechanical integrity during medium to long term operation [86]. Alloying elements in the braze can be used to reduce such issues to an acceptable level. Alloying elements can also be used to tailor the braze seal to adjust CTE, improve thermomechanical durability and adjust chemical compatibility and inertness [243]. Low-cost, non-precious alternatives to the costly silver brazes are also in development. Nickel-based braze seals adhere well to both SOFC anodes and electrolytes and are a low-cost alternative braze material. Nickel-based braze materials have very low gas permeability in typical SOFC operating conditions and environments and have characteristically high joint strength and oxidation resistance [244].

Ceramic based slurries and pastes are also used as sealants [127,245]. They adhere well to ceramic and metal surfaces and can bridge large gaps. Ceramic sealants can withstand very high temperature but can often become brittle and porous after short to medium-term operation [246]. Ceramic sealants can be applied as the mechanical, filler component for sealing a gap, with a thin topcoat of a more dense and gas-tight sealant on top.

Certain cell and stack designs permit the use of low-temperature sealing. Such designs implement so-called ‘cold-side’ manifold regions where parts of the cell and stack are heavily shielded with insulation from the hot active region of the stack. In these designs, large thermal gradients will be present along the cell length, which tubular cells are inherently able to withstand [247]. This greatly improves the choice of sealing materials such as silicon, rubber and plastics and epoxy-based materials [248,249]. The aforementioned materials are somewhat pliant and can reduce thermomechanically induced stress and deformation across the cells and manifolds.

2.8.4 Stack Design

One of the earliest stacks in the literature that provided a detailed design was by Sammes et al. in the mid-2000s [109,250]. They discussed a 100 W ‘planar multi-cell array’ (PMA) 40-Cell stack with a novel Lego-like manifold that also functioned as a current collector. The fuel cells, 110 mm in length and 13 mm in OD were successfully brazed to the manifold using a silver-based braze material and showed a decent electrochemical performance without leakage on a single cell level. Unfortunately, no electrochemical stack testing was presented. The connection was available in parallel or series. The manifold design is seen in Figure 2.34.

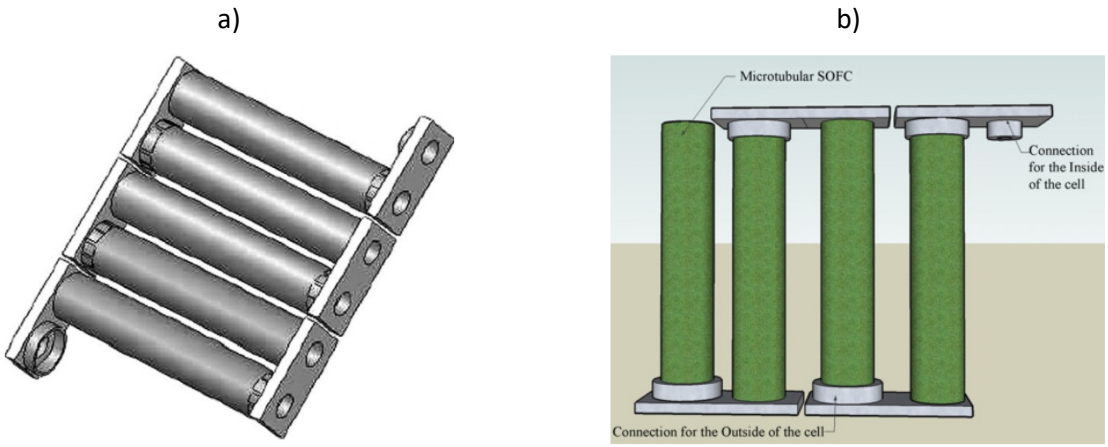

Figure 2.34 - Brazed 'Lego' PMA stack proposed by a) Sammes et al. [109], b) schematic by Lawlor et al [202]**.**

In 2007/08 Suzuki et al. developed a three-cell bundle with an interconnecting terminal (bar) that could be connected to other bundles in a so-called micro SOFC chip design for their 0.8 mm and 1.6 mm to 2 mm OD microtubular cells as seen in Figure 2.35 [238,251–253]. They extruded a porous cathode support matrix that could then be integrated with complete cells. They had flexibility in how

many cells could be incorporated in each bundle and showed bundle sizes of three, five and six cells as adjusted by the cathode matrix. Each bundle could be placed on top of one another in multiple-story designs as seen in the 6x6 'cube-type' stack below. The bundle, chip and cube type design are seen in Figure 2.35.

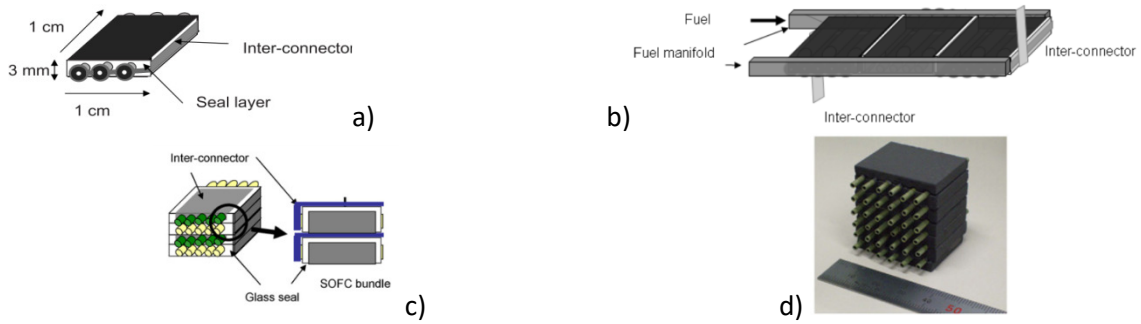

Figure 2.35 – a) 3-cell bundle [254]**, b) SOFC chip with manifold** [238]**, c) 3x5 cell bundle** [251]**, d) 6x6 cube-type stack** [252] **(all the aforementioned are affiliated to AIST and FRCA).**

For their 0.8 mm OD cell, a 5-cell-in-series bundle achieved around 0.4 W [253]. They then scaled this to make a four-story stack of the 5-cell bundle and achieved 2 W within a 0.8 cm^3 volume to achieve a volumetric power density of 2.5 $W.cm^{-3}$ [251]. For the 1.6 mm to 2 mm OD cells, they achieved 1.79 W for their 9 cell module consisting of three, 3-cell in-series bundles connected in parallel within a 1 cm^3 volume giving a volumetric power density of 1.79 $W.cm^{-3}$ [254].

In 2009, Yamaguchi et al. [240] developed a novel miniaturised honeycomb SOFC, a hexagonal cathode matrix 10 mm wide with 37 tubular channels. Each channel was then coated with the electrode and electrolyte layers. Each honeycomb unit was stacked in parallel to adjacent units with a metallic interconnect. Sealing was done via a dense silver paste and glass sealant. The single unit achieved 0.66 W while the two-unit stack achieved 1.17 W and a volumetric power density of 0.6 $W.cm^{-3}$ at 600°C. The OCV of the single unit and two-unit stacks were approximately 0.95 V and 1.9 V respectively. The ohmic resistances were 2.5 Ω and 6.3 Ω respectively.

In 2015 Sumi et al. [183] developed a 64-cell LPG powered stack with reformer for a 200 W generator. The cells which had a 2.8 mm OD and were fabricated via at-scale dip-coating and 3D printing for the electrolyte, cathode and current collectors. The wired cells in the manifold and the finished products are seen in Figure 2.36.

a) b)

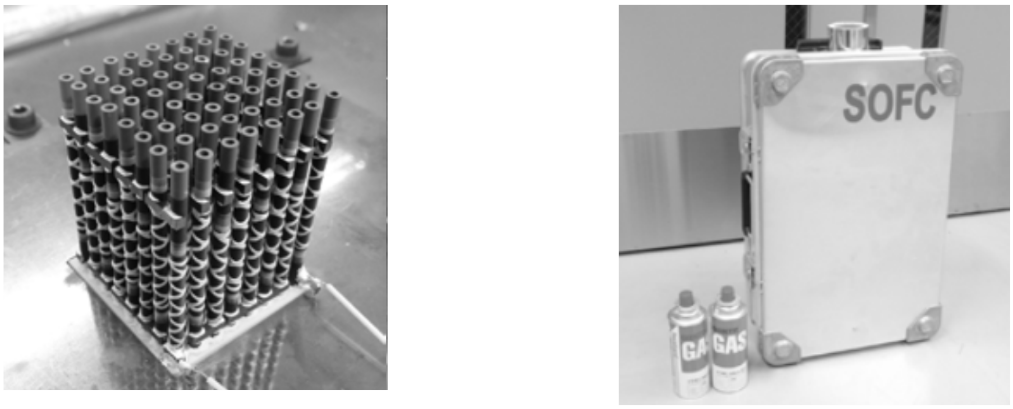

Figure 2.36 a) 64-cell bundle, b) stack unit (AIST) [183]**.**

In 2019, Mehran et al. [255] from NUST in collaboration with researchers from KIER developed a 150 W stack and reformer unit to run on propane. They presented electrochemical data of a 14-cell short stack and a 75-cell stack operating on H_2 and propane for a 100 mm long, 13 mm OD cell. Cells were available with a 15 cm^2 or 60 cm^2 active area. The 14-cell stack achieved an OCV of around 13 V and 12.4 V operating on H_2 and propane, respectively at 800°C. The high OCV was indicative of good manifold design and sealing with minimal leaks. Each cell had a 15 cm^2 active area corresponding to a total active area of 211 cm^2. The peak power on H_2 was 51.8 W, giving a peak power density of 0.245 $W.cm^{-2}$ on H_2, and a peak power density of 0.18 $W.cm^{-2}$ on propane.

The 75-cell unit had 15, five-cell bundles and had a total active area of 1125 cm^2. The cells in each bundle were connected in series while bundles were connected in parallel. Insulating sheets were placed between the adjacent metallic bundles to prevent short-circuiting. The stack was first tested without any balance of plant (BOP) in a furnace and then connected to a thermally self-sustaining BOP including CPOX reformer and heat exchanger. Tested without the BOP, the 75-cell unit achieved 201 W peak power and an OCV of 15.2 V under H_2 at 800°C, corresponding to a power density of 0.179 $W.cm^{-2}$ on H_2. The stack achieved 0.142 $W.cm^{-2}$ on propane at 800°C. The combined stack and BOP setup achieved a peak power of 140 W corresponding to a 0.124 $W.cm^{-2}$ peak current density. The stack performed well with stability on propane over 15 hours.

The authors also presented data for an optimised 30-cell stack and BOP unit with improved reforming and thermal integration. The stack had five, 6-cell bundles, with each cell within the bundle in series and each bundle connected in parallel. The total active area of the stack was

1413 cm^2. The OCV was measured between 5 V and 5.5 V at 700°C. The peak power was 156 W at 800°C corresponding to a 0.114 $W.cm^{-2}$ power density. Degradation, however, was high at 66.7 $mV.h^{-1}$ and a 50% drop in voltage was observed after 30 hours of operation at 30 A. The 30-cell stack is seen in Figure 2.37 c).

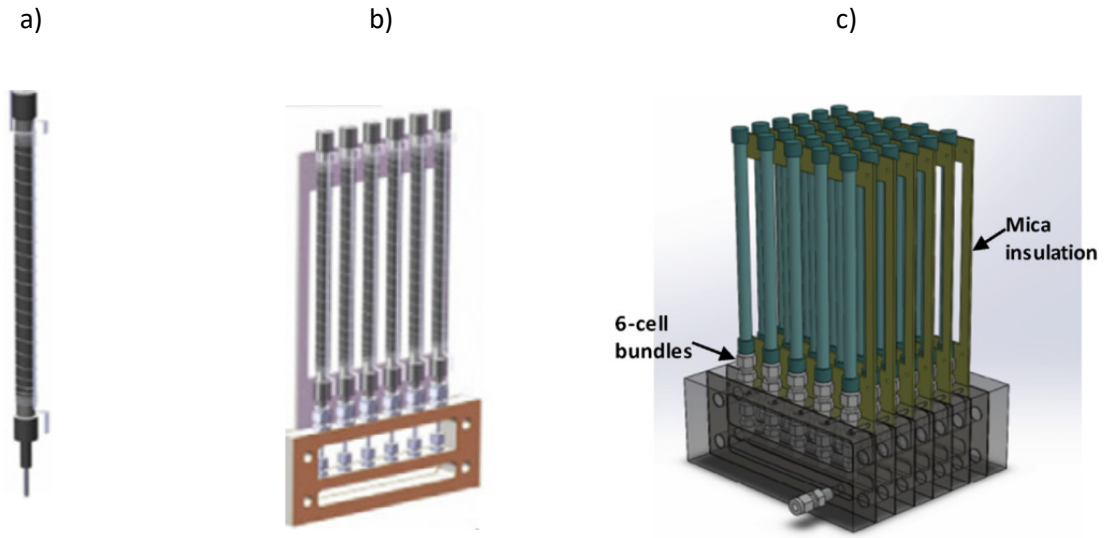

Figure 2.37 – Cell/stack design with current collectors and cap manifold a) Single cell (NUST,KIER) [256]**, b) 6-cell bundle** [256]**, c) 30–cell stack (NUST,KIER)** [255]**.**

The design used by Mehran et al. was earlier reported by Mushtaq et al. [256] again from KIER in 2017. A 100 W and 200 W class stack was presented. Manifolding was achieved using a metal cap at either end of the tube secured with glass sealant. The caps were then attached to the metal frame, each bundle being 6 cells connected in parallel. The single cell with manifold caps and a 6-cell bundle is seen in Figure 2.37 a) and b), respectively. Current collection on the anode side was done internally by a nickel felt spot welded to a nickel wire. Mica was used as an electrical insulator to prevent short-circuiting between bundles. Peak power of the smaller 30-cell stack at 750°C was 93.5 W, reaching an OCV of 4.91 V operating on 350 $ml.min^{-1}$ of CO_2. The larger stack achieved a peak power at 750°C of 224 W operating on 15000 $ml.min^{-1}$ of CO_2. A degradation rate of 0.55 $mV.h^{-1}$ was recorded for the 200 W class stack over 200 hours under a load of 25 $mA.cm^{-2}$. The high OCV was indicative of a good manifold and sealing design.

Hong et al. [257] from KIER published the system design for a stack using four 6 mm OD and 10 cm long cells with an active area of 15 cm^2 per cell. They used a rolled nickel mesh within the anode interior for anode current collection. The mesh was attached to the anode surface with nickel paste. Silver wire and an LSC contact paste were used for cathode current collection. The stack achieved an

OCV of 4.32 V and peak power of 24.78 W in 800 ml.min^{-1} of H_2 at 750°C. The authors also operated the stack in diluted H_2 in N_2 at 50% and 75% H_2 concentration. The stack fuel utilisation was 48.8% when operating on H_2. The total resistance of the stack as measured by impedance spectroscopy was approximately 0.80 Ω.cm^2, 0.55 Ω.cm^2 and 0.40 Ω.cm^2 at 650°C, 700°C and 750°C, respectively. It was determined that the electrode polarisation had a dominant effect on cell performance and highlighted as an area for improvement. The ohmic and electrode polarisation values and total impedance values extracted from the EIS plots of the stack in H_2 and diluted H_2 are seen in Figure 2.38 a) and b), respectively.

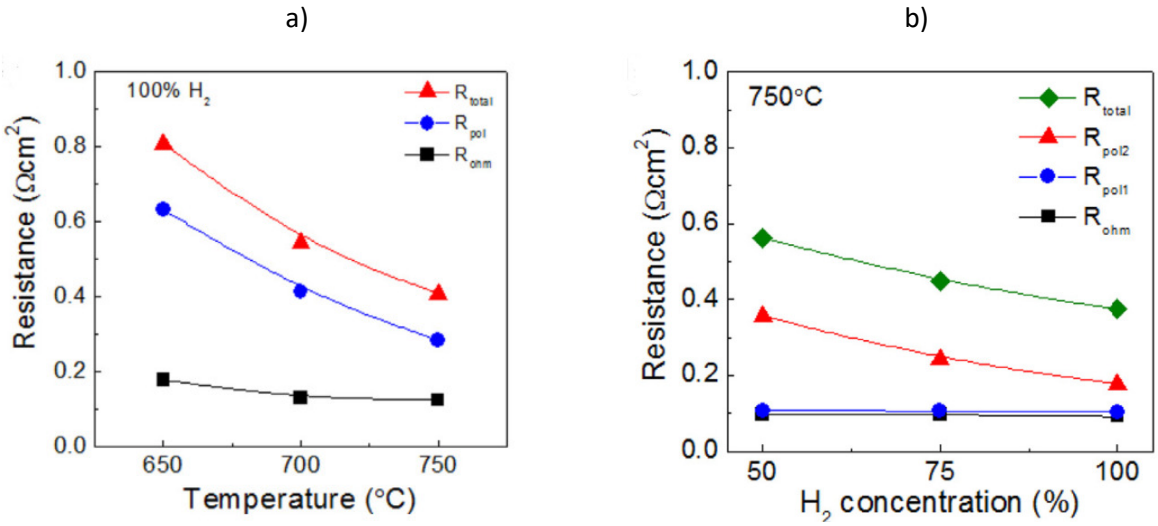

Figure 2.38 – Extracted impedance data from EIS operating on a) H_2, b) diluted H_2 in N_2 [257].

Research from Meadowcroft et al. (University of Birmingham) and Kendall et al. (Adelan) have shown multiple fuel cell stack modules in several designs from 20 W to 250 W for applications in drones, robotics and an automotive APU between 2013 and 2017 [247,258,259]. The designs featured a cold-side manifold at the fuel inlet region and a hot-side manifold at the outlet region. The inlet side manifold was kept outside of the heating zone, aided by the asymmetry of the active area positioning on the anode support. This design allowed for the use of low-temperature materials such as plastics which could be 3D printed, also, silicon-based seals could be used to interface the cells with the manifold which allowed for the thermo-mechanically induced expansion of the cells. This reduced stress build-up in the cell which could lead to failure when joined to two fixed manifolds. Their studies used a porous outlet manifold with a catalyst that burned any excess fuel. Interconnection occurred via silver wire for the anode and cathode side. Results for a 4-cell sub-stack were presented. The cells were connected in series and achieved 17 W although it was stated that 20 W was possible

at a 50% fuel utilisation on H_2. The 250 W stack was operated on propane with an electrical efficiency of 55%. This design limited the fuel inlet temperature which inhibits the cell performance and results in large axial temperature gradients. Nevertheless, a lightweight, compact and cost-effective stack could be achieved with simple manifolding and sealing with the issues of CTE mismatch alleviated with minimal cell-manifold stress. The 4-cell sub-module and 16-cell modules are seen in Figure 2.39.

a) b)

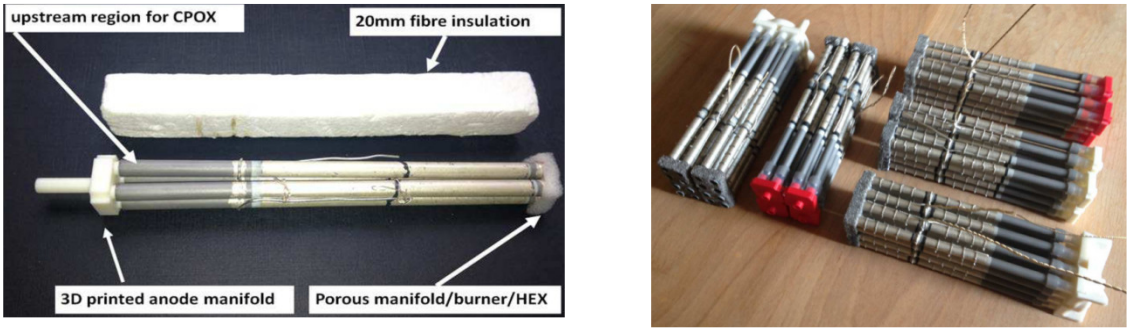

Figure 2.39 –a) 4-cell sub-module [247,258]**, b) 16-cell modules** [259]**.**

Watanabe et al. [260] developed a 700 W class tubular SOFC stack and achieved a peak power of 743 W with a fuel utilisation of 75%. A pre-reformer and desulphurising unit processed town gas fuel before entering the fuel cell. A 64.7% reforming rate was achieved with an energy conversion efficiency of 49.5% (LHV). The system design and finished product with BoP are seen in Figure 2.40. They conducted heat balances across the system and adjusted operating parameters and achieved thermally self-sustaining operation within a narrow temperature range. They defined a thermally self-supporting state as a temperature variation smaller than 0.5°C.h^{-1}.

a) b)

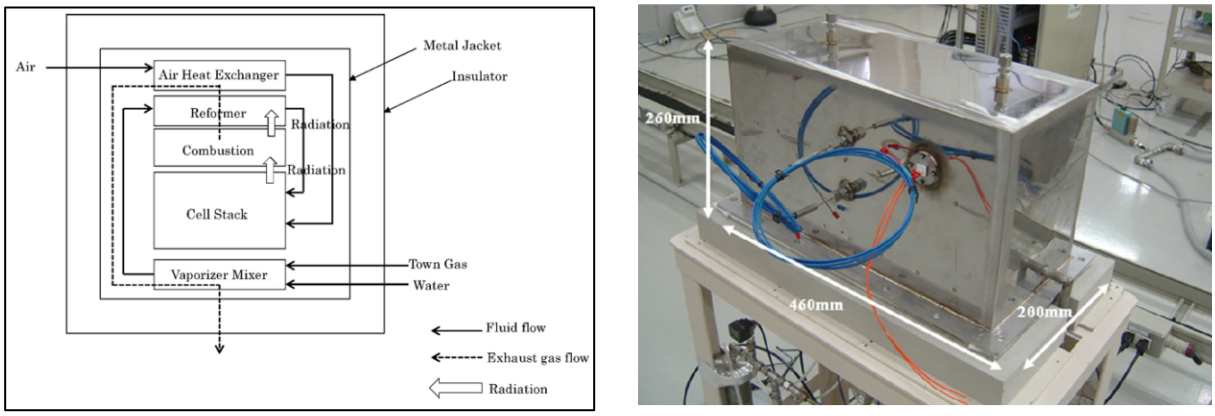

Figure 2.40 - System and BoP design a), fabricated stack and BoP [260]**.**

In 2008, Lee et al. [261] from KIER presented a 700 W stack for use as an automotive auxiliary power unit as seen in Figure 2.41 c). The cells had an OD of 10 mm and 200 mm in length with an active area of 50 cm^2. The authors incorporated a metallic fuel gas supply tube with nickel wire and nickel felt an internal anode current collector. The fuel supply tube passed unreacted fuel along the cell length through the centre of the tube where an outlet manifold at the end of the tube reversed the flow direction of the fuel bringing into contact with the anode for consumption with the exhaust leaving at the fuel inlet side. This design allowed pre-heating of unreacted fuel along the cell length and reduced manifold complexity. The authors state that the reduction in fuel chamber diameter as compared to feeding into the anode directly would lead to an enhancement of gas utilisation. The manifold designs were metallic caps, brazed to the cell with a nickel-based braze (Nicrobraz). At 800°C, a single cell in this design achieved 0.77 $A.cm^{-2}$ at 0.7 V in H_2 with a fuel utilisation of 45%. The peak power density was 0.56 $W.cm^{-2}$. A bundle of 6 cells were connected in series with each cell having a very similar OCV of 1.1 V indicating the bundle manifold design and sealing were functioning well.

Six, 6-cell bundles were connected in series to make a stack with an active area of 1800 cm^2. The 36-cell stack was operated at 750°C on 15000 $ml.min^{-1}$ of H_2 and achieved a peak power density of 0.38 $W.cm^{-2}$ with a 49% fuel utilisation. This corresponded to a peak power of 700 W. The stack OCV was 6.75 V. The peak power outputs of the bundles had a difference of more than 15.5%, ranging between 107 W and 125 W at 700°C. This indicated an area for improvement in the gas supply to each bundle. As measured by the gradient of the polarisation plot between 4.75 V and 5.50 V the ASR of the stack was estimated at 16.88 $\Omega.cm^2$.

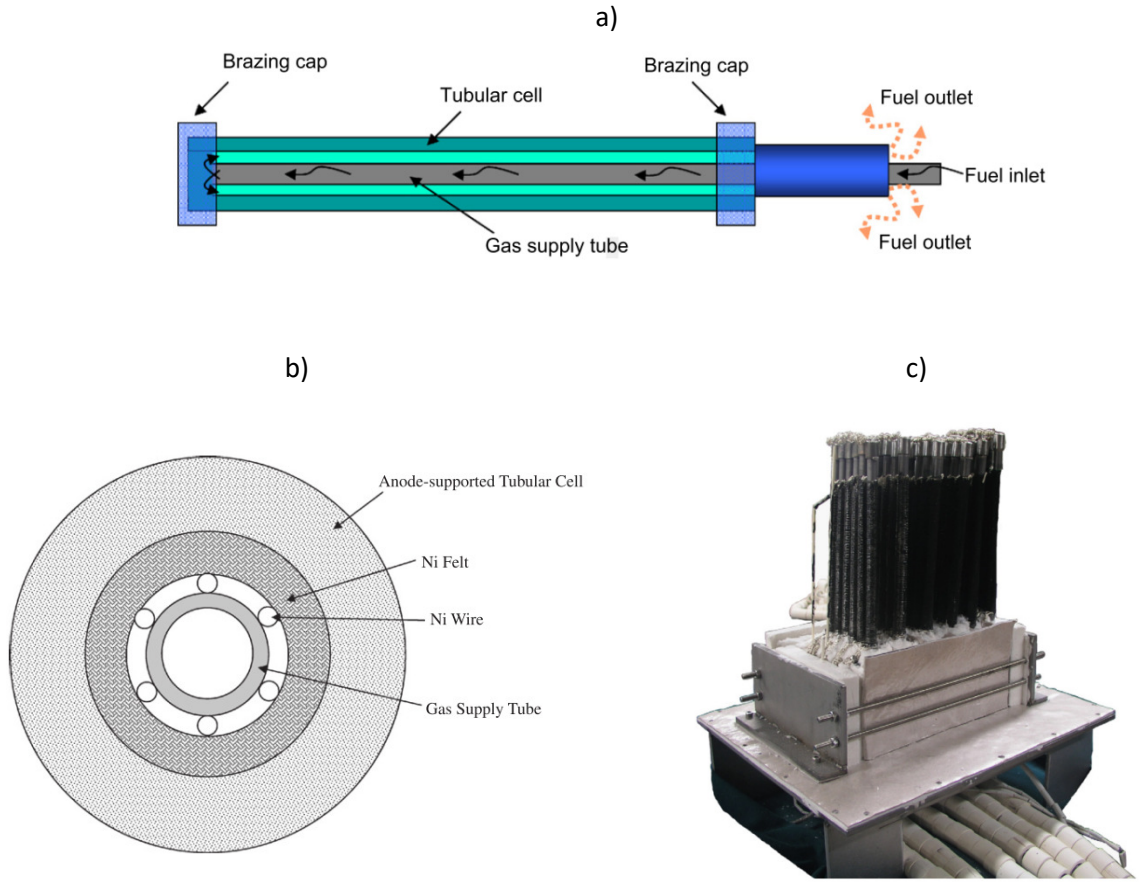

Figure 2.41 - Cell and manifold with brazed cap design schematic a), anode current collector and gas supply b), 700W stack c) [261]**.**

2.9 Summary of Recently Reported µT-SOFC Stack Tests in Literature

Table 2.7 is a summary of tubular stacks recently reported in academic literature. Research papers detailing the methods of current collection and manifold design are of particular importance and salient designs are included in the table from 2008. Performance values have been reported at 750°C or as close to 750°C as reported. Values not reported explicitly in the text, for example, peak power density was estimated from the polarisation plots. Only the fuel contributing to electrochemical reactions is reported in table and details of any inert/carrier gases are not included. Performance data of cell operating H_2 was reported where possible. Where fuel flow rate was not reported, fuel utilisation values were reported in the table instead.

Table 2.7 - Summary of recently reported µT-SOFC stack tests in literature.

Year	Author	Location	Institution	Technology	Cell Diameter (mm)	Cell Length (mm)	Cells	Total Active Area (cm^2)	Series (S) / Parallel (P)	Open Circuit Voltage (V)	Operating Voltage (V)	Power at Operating Voltage (W)	Peak Power (W)	Peak Power Density (W $.cm^{-2}$) / (W.cm^{-3})	Peak Current (A) / Peak Current Density (A $.cm^{-2}$)	Temperature (c)	Anode Current Collection	Cathode Current Collection	Manifold Type	Fuel	Fuel Flow rate ($ml.min^{-1}$), F.U	Reference
2020	**Milcarek**	USA	Arizona State University	Ni-YSZ /YSZ/SDC /SDC-BSCF	32	-	2	8.14	S	1.9	-	-	1.67	0.205	0.75	-	Silver wire, Gold paste, (E)	Silver wire, Silver paste, (E)	Metal	H_2	-	[262]
2019	**Mehran**	KOR	KIER	Ni-YSZ/YSZ/LSM-LSCF/LSCo	13	230	14 [75]	211 [1125]	S [S/P]	12.4 [15.9]	-	-	51.8 [190]	0.245 [0.169]	10.7 [33]	800	Nickel wire & Nickel felt (spot welded), (I)	Silver wire, Silver mesh	Metal cap, metal frame	H_2	1000 [4000]	[255]
2019	**Hong**	KOR	KIER	Ni-YSZ /YSZ/LSM-YSZ/LSM/LSCO	6	100	4	60	S	4.32	-	-	24.78	0.413	18	750	Nickel wire & Nickel felt (spot welded), Nickel paste, (I)	Silver wire, Silver mesh, LSCO paste, (E)	-	Humidified H_2 (3 vol.%)	750	[257]
2019	**Zeng**	CHN	Tsinghua University	Ni-YSZ /Ni-ScSZ/ScSZ /LSM-ScSZ	3.5	-	4	30.8	P	1.06	0.84	2.53	3.85 (est)	0.125 (est)	7.26 (est)	700	Nickel Felt	Silver mesh	Metal	H_2	200	[263]
2018	**Milcarek**	USA	Arizona State University	Ni-YSZ /YSZ/YSZ-LSM	3.2	-	9	24.3	S	7.5	-	-	6.32	0.260	19.44	700	Silver wire, Gold paste	Silver wire	-	CH_4	2400	[264]
2018	**Ding**	CHN	Zhongkai University of Agri. & Eng.	Ni-SDC/LSGM /LDC/LSCF-LSGM/LSCF	11	10	4	4.62	S	3.5	-	-	1.16	0.25	1.24	750	Silver wire, Silvear paste	Silver wire, Silver paste	Ceramic	Humidified H_2 (3 vol.%)	75	[95]
2017	**Jones**	USA	Worcester Polytechnic Institute	Ni-YSZ/ YSZ/LSCF	10.2	100	5	160	S	5	-	-	52	0.325	36	900	-	-	-	CH_4/CO	90/110, 31%	[152]

2017	**Mushtaq**	KOR	KIER	Ni-YSZ/ YSZ/LSM-YSZ/LSM/LSCO	13	100	30 [70]	1800 [4200]	S/P [S/P]	4.8 [12.99]	4.4	39.6	93.5 [222.4]	0.052 [0.053]	36 [40]	750	Nickel wire & Nickel felt (spot welded), (I)	Silver wire, Silver mesh	Metal cap, metal frame	CO_2	5000 [15000]	[256]
2016	**Milcarek**	USA	Syracuse University	Ni-YSZ/ YSZ/LSM	3.2	16.6	9	15.03	S	9.8	-	-	5	0.34	2.25	790	Silver wire, Gold paste, (E)	Silver wire, Silver paste, (E)	Metal	H_2	300	[265]
2015	**Jung**	KOR	Pohang University of Science & Tech.	Ni-ScSZ /ScSZ/LSCF	-	90	9	-	-	-	-	-	5	-	-	-	-	-	Ceramic	H_2	-	[266]
2015	**Sumi**	JPN	AIST	Ni-GDC/YSZ /GDC/LSCF	2.8	29.6	256 (est)	-	S	-	-	-	200	-	-	-	External bar	External bar	Metal plate	LPG	-	[183]
2015	**Meadowcroft**	GBR	University of Birmingham	Ni-YSZ/YSZ/ SDC/LSCF	6.7	150	4	79	S	4.5	-	-	30	0.38	13	734	Silver paste, Silver wire, (E)	Silver paint, Silver wire, (E)	3D printed plastic	H_2	600	[249]
2015	**Kendall**	GBR	Adelan	Ni-YSZ/YSZ /SDC/LSCF	6.7	150	4 [16]	79 [315]	S [S}	4.2 [17]	- [12]	- [64 (est)]	17 [68 (est)]	0.215 [“” (est)]	6.5 [6.5 (est)]	650	Silver paste, Silver wire, (E)	Silver paint, Silver wire, (E)	3D printed plastic	H_2	- 50% [-]	[258]
2014	**Sumi**	JPN	AIST	Ni-GDC/YSZ /GDC/LSCF	1.8	30	36	61	S,P, S/P		5-36	-	20-50	-	-		Silver wire, (E)	Silver wire, (E)	Ceramic block	LPG	-	[267]
2013	**Ye**	CHN	SICCAS	Ni-YSZ/Ni/ScSZ	5	50	2 [4]	15.7 [31.4]	S [P]	2 [4]	2.05	-	4.5 [7.5]	0.29 [0.24]	4.5 [15]	800	Nickel foam	Silver mesh	Metal box (inc catalyst)	Humidified H_2		[268]
2013	**Meadowcroft**	GBR	University of Birmingham	X	6.7	150	16	315	S/P	-	-	-	250	0.79 /0.27	-	750	Silver paint, Silver wire, (E)	Silver paint, Silver wire, (E)	3D printed plastic	Humidified H_2	55%	[247]
2012	**Ferriz**	ESP	University of Zaragoza	Ni-YSZ/YSZ /LSM-YSZ	-	-	2	8	S	2.02	-	-	0.9	0.113	0.8	800	Nickel foam, Platinum wire, (I)	Platinum mesh, Platinum Paste, Platinum wire, (E)	Ceramic	Humidified H_2 (3 vol.%)	200	[269]
2012	**Yamaguchi**	JPN	AIST	Ni-ScSZ/ScSZ/ GDC/LSCF-GDC	4	40-50	12	-	S	13	8.4	-	7.5	-	1.45	630	Metallic tubular	Current collection paste	Metal	Humidified H_2 (3 vol.%)	500 [26%]	[270]
2012	**Watanabe**	JPN	Kyushu	Ni-YSZ/Ni-GDC	10	105	c.100	-	S	c.100	-	-	743	0.17	-	600	Metal cap x2,	Metal wires, (E)	Metal cap,	City gas	75%	[260]

			University	/LSGM/LSCF												Silver braze, (E)		Metal pipe	13A		
2011	**Howe**	GBR	University of Birmingham	Ni-YSZ/ YSZ/LSM	2	50	6	11.76	S	6	-		2.95	0.25	1.62	750	Silver wire, (E)	Silver paint, Silver wire, (E)	Ceramic, Ceramic paste	Humidified H_2	100	[197]
2009	**Suzuki**	JPN	AIST	Ni-GDC/ GDC/LSCF-GDC	0.8	10	15	3.77	S/P	2.53	-	-	1.39	0.37 /2	1.4	550	Silver wire, Silver sheet, Silver paste, (E)	LSCF matrix, Silver wire, Silver sheet, Silver paste, (E)	Metal (fuel)	Humidified H_2	40	[271]
2009	**Funahashi**	JPN	AIST	Ni-GDC/ GDC/LSCF-GDC	2	15	9	2.8	P/S	2.5	-	-	0.61	0.22	0.84	500	Silver wire, Silver paste, Silver foil, (E)	Silver wire, Silver paste, Silver foil, (E)	MgO Matrix	Humidified H_2	200	[272]
2009	**Yamaguchi**	JPN	AIST	Ni-GDC/ScSZ/ GDC-LSM	-	10	36 (1) 72 (2)	-	P/S	0.9 [1.8]	-	-	0.6 [1.17]	/ 0.6	0.138	600	Platinum mesh, Silver paste, (E)	Platinum mesh, Silver Paste, (E)	Ceramic Honeycomb Matrix (LSM), Metal	Humidified H_2 (3 vol.%)	-	[240]
2008	**Suzuki**	JPN	AIST	Ni-GDC/GDC/ LSCF-GDC/GDC	2	10	9	5.65	P/S	2.6	-	-	1.79	0.32	1.7	550	Silver wire, Silver sheet, Silver paste, (E)	LSCF matrix, Silver wire, Silver sheet, Silver paste, (E)	Ceramic (LSCF)	Humidified H_2	50 [80%]	[254]
2008	**Suzuki**	JPN	AIST	Ni-GDC/ GDC/LSCF-GDC	0.8	10	20	5	P/S	3.6	0.7	1.25	2	0.4	2	490	Silver wire, Silver sheet, Silver paste, (E)	LSCF matrix, Silver wire, Silver sheet, Silver paste, (E)	Ceramic (LSCF)	Humidified H_2	100	[251]
2008	**Lee**	KOR	KIER	Ni-YSZ/YSZ/ LSM/LSCF	10	160	36	1808	P/S	6.75	-	-	700	0.38	160/0.09	750	Nickel wire & Nickel felt (spot welded), (I)	-	Metal cap, Metallic	H_2	49%	[261]

2.10 Stack Level µT-SOFC Models

SOFC stack models are typically macroscopic continuum models that use CFD to predict the flow distribution and temperature distribution. Stack models typically incorporate less physics than single cell models but geometries are far more complex. Models often omit charge and mass transport in favour of a more detailed description of the conservation of momentum and energy. Thermal 'hot spots' and flow dead zones can be identified and fed back to the CAD design for optimisation surrounding cell spacing, canister design and baffling. Stack model data is then fed into system design surrounding flow configuration and fed into models for control strategy on a system level such as the blower and heat exchanger to control the stack temperature.

FEM is used to analyse solid mechanics of a stack design. Models analyse the thermo-mechanical properties of a stack and identify potential weaknesses in design and highlight high-stress areas where mechanical failure is likely to occur. FEM models aid in stack sealing design, identifying thermo-mechanically induced displacement which can result in a loss in hermeticity. Combined CFD and FEM solid mechanics models can be used to aid in material selection and the material and component designs can be rapidly interchanged which would take considerable time and effort to achieve empirically. While single cell models are typically steady-state, it is very useful for stack models to capture operation during start-up and shut-down where failure is most likely to occur.

An early stack model was presented by Lockett et al. in 2004 [273]. The CFD model was built with Ansys Fluent to characterise heat transfer in a 20-cell stack and identify an optimal geometric design and operating conditions. The stack model was built to aid the development of a 20-cell experimental stack also presented in the paper. Each cell, 55 mm in length and with 2 mm OD produced between 0.4 W and 0.6 W. No mass transfer was included in the model. It was concluded that an optimal operating temperature should be sufficiently high to increase performance but low enough to reduce degradation.

In 2019 Hari et al. [274] published a cylindrical 3D tubular stack CFD and FEA model, a development from an earlier model presented in 2015 [275]. The model described one half of a symmetric 48 cell stack, for integration with a compact BoP to be positioned within the fuselage of a UAV. The model objectives were to describe the fluid distribution inside the stack, heat dissipation from the stack to the environment, and the thermo-mechanical stresses and deformation. The CFD package COMSOL

was used to describe the conservation of momentum and energy. Flow within the porous electrodes was omitted and the heat produced by the cell was considered as a heat source. Radiative heat transfer was also omitted from the model. It was found that a 150°C gradient between the innermost and outermost cells, the cells being positioned near the air inlet and the air outlet, respectively. The study analysed the effect of changing the inlet temperature from 650°C to 750°C. Figure 2.42 a) shows the half-stack geometry and the temperature distribution and von Mises stress with the air inlet at 750°C in b). The peak stack temperature was 927°C which is above the annealing point and near the melting point of the silver interconnect material proposed for the stack. The peak von Mises stress was $1x10^9$ $N.m^{-2}$ ($1x10^3$ MPa) around the cell-manifold joint. The maximum displacement was 1.8 mm at the outlet region.

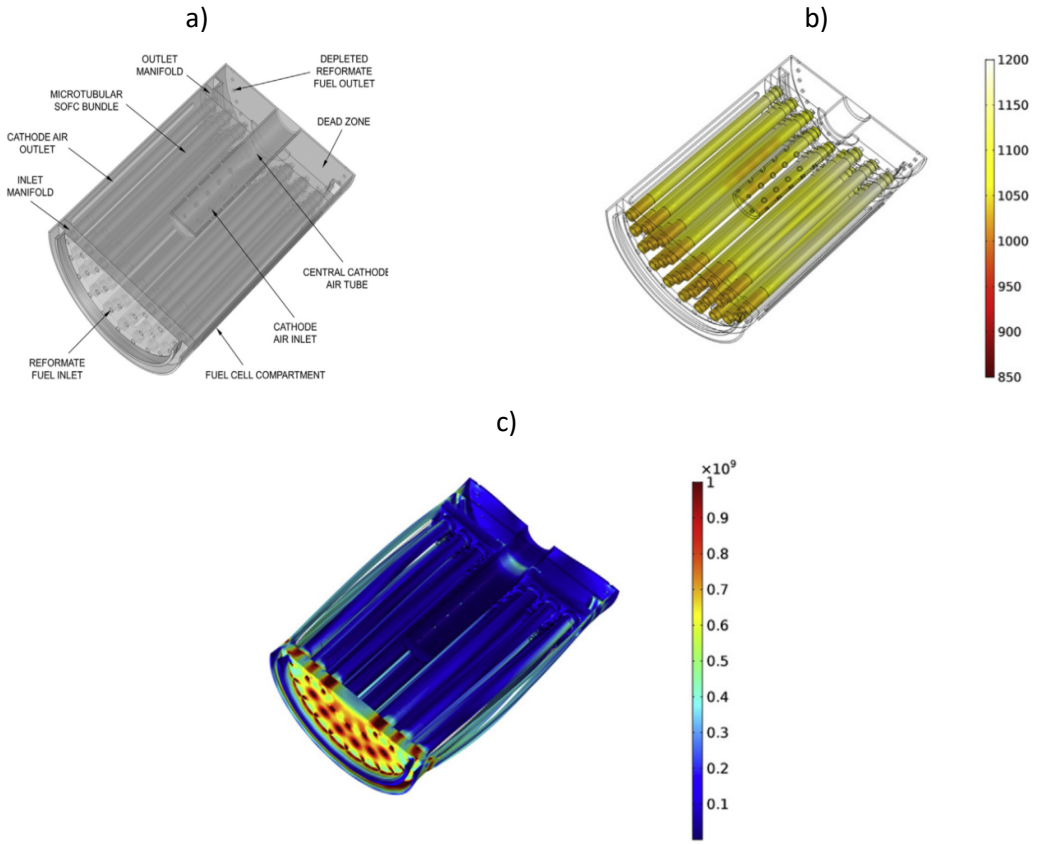

Figure 2.42 – a) Half-stack geometry, b, surface temperature distribution [K], c) von Mises stress [$N.m^{-2}$] of stack with 750°C cathode air inlet [276].

Pianko-Oprych et al. [277] published computational work in the same project as [274,275] for the UAV power unit. In 2015 they published a coupled CFD and FEA model for the same half-stack geometry [276]. The model included conservation of momentum, energy, mass and charge and the model polarisation curve showed a good fit to experimental results. The model included radiative

heat transfer which is known to be a significant heat transfer mechanism in tubular SOFC stacks. The stack canister in this design was not circular as in the Hari design but hexagonal. Temperature profiles were imported from the CFD model into the FEA model in contrast to the constant power heat source data as used by Hari. The maximum axial displacement of the stack under thermal stress was observed as 1.11 mm at the outlet region of the stack and 1.24 mm at the cell tip and exhaust manifold, respectively. The peak radial displacement of 0.79 mm was observed at the outer circumference of the canister, near the outer ring of cells where most heat was being rejected. The maximum stress was 746.74 MPa, also at the outer circumference of the canister, around 23% lower than in the Hari design. The peak stress on the cells were much lower at 464.43 MPa, at a small section at the cell-manifold joint but the average was a lot lower, well below 250 MPa. The operating conditions and the boundary conditions of the Hari and Pianko-Oprych models differ and so a direct comparison is difficult. Hari's model uses a reformate fuel, and the volumetric flow was given, whereas Pianko-Oprych used hydrogen with the fuel velocity given. The data for the operating temperature of 750°C has been presented here and the plots for air velocity profile, cell temperature and von Mises stress distribution of the stack are seen in Figure 2.43.

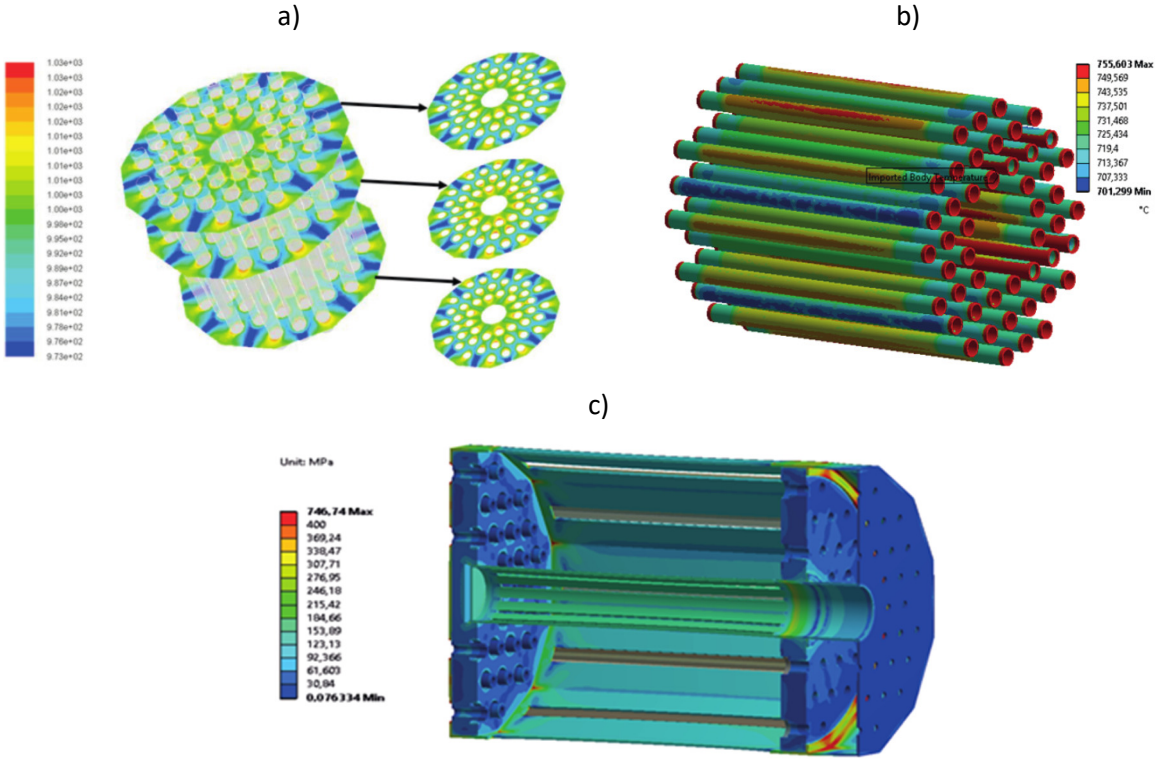

Figure 2.43 – a) Air temperature distribution [K], b) cell temperature distribution [°C]), c) von Mises stress of stack (exc. cells) [276]**.**

In 2018 Chen et al. [195] developed a 3D CFD model for a 49-cell (7x7) stack to investigate the flow distribution on the air side. The proposed one-in-one-out air flow feed system geometry was analysed and an inhomogeneous flow distribution was observed with the cells nearer the inlet experiencing a higher mass flow of the air than near the outlet as seen in Figure 2.44 a) and b). This led to thermal gradients and it was proposed that this design would lead to greater degradation and risk of damage. To combat this, a new manifold design was proposed with sub-branches and multiple inlet and outlet feeds and from c) it can be seen there was a significant improvement. The manifold also tapered in the z-plane which acts to increase velocity from the first inlet to the last.

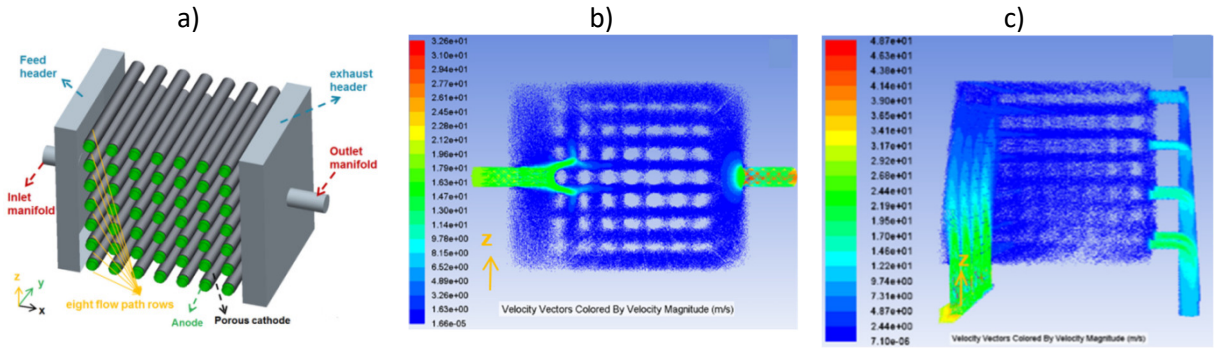

Figure 2.44 – a) Stack geometry, b) flow distribution for stack geometry, c) optimised manifold flow distribution [195]**.**

In 2017 Hering et al. [278] proposed a quasi-3D dynamic model of a tubular stack with integrated cooling. The model drew upon tubular heat exchanger concepts and adapted it to a tubular fuel cell stack. The model described convective, conductive and radiative heat transfer of the complex geometry accounting for a range of view factors between the cells and the cooling tube. The model accounted for the heat produced by the electrochemical reactions and different operating conditions which could be fed into a thermal management control system. The manifold design had a metallic cone, ferrule like fittings which allowed for facile sealing and cell orientation, and reduced joint stress. Cascading cells could be connected in both series and parallel configurations. It was proposed that designs with integrated cooling systems could use the heat produced to drive BoP units such as reformers and pre-heaters or as an external heat sink to drive heat-engines. The stack produced a power output of 1.1 kW and when operated at a power density of 0.3 $W.cm^{-2}$ achieved an electrical efficiency of 63%. At a high power density of 0.5 $W.cm^{-2}$, the air side pressure drop for the cross-flow blower configuration was deemed to be sufficiently low at 1.5 kPa. The manifold, interconnector, cooling tube and radiative heat view-factors are seen in Figure 2.45.

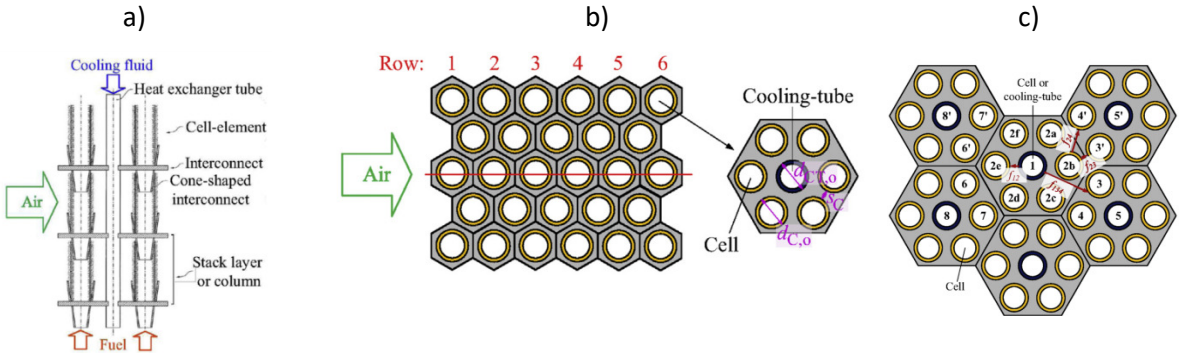

Figure 2.45 – a) Manifold and interconnect design, b) stack and sub-manifold design with integrated cooling, c) radiative heat transfer view-factors [278]**.**

The authors had earlier proposed a design for geometrical optimisation of the stacked sub-module units [279]. The base case was for 81 cells in 9 rows and 9 columns for a total of 3294 cells with 61 cooling tubes. They improved on this design by making a shorter and wider stack, reducing the cell diameter, length and spacing while increasing the cell length to interconnect height ratio. Both designs achieved the same power output of 1.1 kW, the best case delivering a 6% increase in electrical efficiency with lower parasitic losses from the blower. However, the stack required 864 more cells and 77 cooling tubes. The volumetric power density was not improved from the base case, decreasing from 1.73 $W.cm^{-2}$ to 0.98 $W.cm^{-2}$. Nevertheless, the maximum temperature gradient per cell was decreased by 49% to 45.3°C and the more uniform temperature distribution resulted in a more homogenous distribution of power density. For most layers of the stack, this also resulted in a more uniform fuel utilisation but the best case observed a lower fuel utilisation overall. Critically, the peak temperature occurring in the cell for the base case was 1096°C which was deemed unacceptable. This was reduced to 995°C.

In 2008 Lee et al. [261] developed a CFD model for their 6-cell bundle of cells as part of their 36-cell 700 W stack reported in Table 2.7 and described previously in the Stack Design section. Ansys Fluent was used to describe the distribution of velocity, temperature, current density and species concentration. The size of the slit within the fuel supply chamber and the angle of the inclined wall at the fuel exhaust chamber was modified to ensure an equal distribution of fuel to each fuel cell within the bundle. From Figure 2.46 a) and b), the velocity vector and H_2 mass fraction distribution plots it is clear that this was achieved. This was confirmed in the fabricated module as the OCV of each 6 cells were nearly identical at 1.1 V.

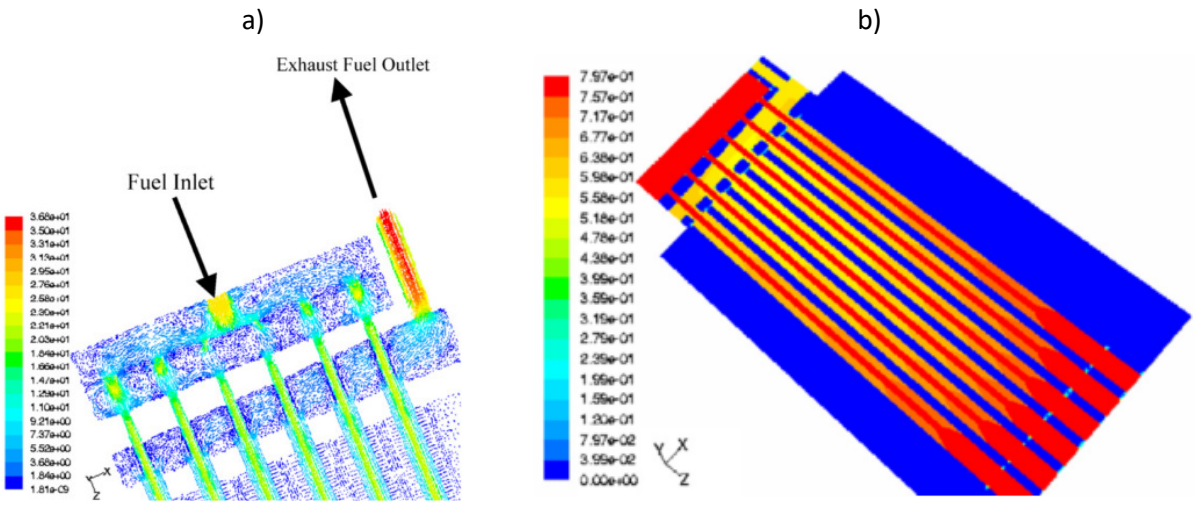

Figure 2.46 – a) 6-cell bundle velocity vector, b) H_2 mass fraction [261]**.**

2.11 Thesis Outline

From a thorough study of µT-SOFC literature, current collection, interconnection and stacking were highlighted as key bottlenecks for a high-efficiency design to boost competitiveness and widespread adoption of the technology. Very little research into current collector design and optimisation was found and techniques to reduce contact resistance and ASR was underdeveloped. Research into stack design was even more limited. Modelling was identified as a promising tool to explore both current collector design and stacking. The approach to address the aforementioned bottlenecks of µT-SOFC development are as follows:

Chapter 3: In this chapter, the strategy, apparatus, procedure and analysis tools for electrochemical testing and characterisation of µT-SOFCs are discussed. A method for mechanical testing of the contact between the anode and current collector is also detailed.

Chapter 4: This chapter details the numerical modelling strategy, apparatus and procedure for modelling the conservation of momentum, energy, mass and charge of a µT-SOFC. The 2D model geometry is constructed to allow the effects of varying current collector position on the cell performance to be studied. The CFD tools used to solve for the conservation of momentum and energy phenomena described here for 2D modelling are later applied to a 3D stack level model.

Chapter 5: In this chapter, empirically and numerically derived electrochemical data used to determine the effect of current collector position and number on µT-SOFC performance are presented. The numerical data presented from two models, a mathematical resistance path based model and a fitted, predictive multiphysics CFD model is used to provide insight into the empirical data on µT-SOFC current collection. A set of standard operating conditions to isolate the effects of varying current collector design performance are defined. The results of the state-of-the-art current collector design at the standard operating conditions are presented and used a baseline dataset. The shortcomings of the design are detailed and requirements of an improved current collector design are specified.

Chapter 6: This chapter details the design and implementation of a novel, internal brush-like anode current collector, adopted from heat exchanger turbuliser technology. The optimisation of the design for use as a current collector and the results from characterisation, thermo-fluid analysis, mechanical testing and electrochemical testing are presented. The final design is presented and the results of a further optimisation study into reducing the current collector-anode contact resistance through coatings are detailed. The results are compared to the state-of-the-art cell testing data throughout.

Chapter 7: In this chapter, the theory, strategy, apparatus, materials, methodology and results of brazing for current collector-anode contacting to minimise contact resistance is presented. A novel braze and braze application method is detailed. The electrochemical performance, mechanical testing and imaging of the brazed current collectors are presented and compared to the un-brazed design.

Chapter 8: The final results chapter is a stack level study, presenting the design and 3D CFD optimisation of µT-SOFC manifolds, and stack operating parameters which are underpinned with parameters obtained from empirical data of cells with the novel internal brazed current collector. The performance and durability data of two 4-cell stacks designs is presented and analysed.

Chapter 3 Experimental Methodology

This chapter discusses the strategy, apparatus and procedure for electrochemical testing and characterisation of Adaptive Materials Inc. (AMI) microtubular fuel cells. The preparation for electrochemical testing details the manifold assembly, electrode preparation, current collection, sealing and cutting. The apparatus for SOFC testing is partitioned into the gas supply/removal setup, heating system, electrical analysis hardware and software and a current collector control system. The chapter discusses the start-up sequence of the fuel cell, an overview of fuel cell current-voltage analysis and operating regions of interest. The use of electrochemical impedance spectroscopy is justified along with a brief overview of theory and the plots of the obtained data. Analysis of the impedance data is supplemented with equivalent circuit modelling, detailing the theory, the power and relevance in impedance analysis and the limitations of the technique. The chapter continues to detail techniques used for microstructural analysis, reasoning for their use and derived results, namely SEM, XRCT and optical microscopy. Compositional analysis of the solid phase via EDX is also discussed. Interconnection related issues will be developed from Chapter 6 onwards.

3.1 Cell Specification - AMI 152

Complete, anode-supported cells were supplied by AMI having an internal diameter of 5.5 mm, an external diameter of 6.8 mm and a total length of 152 mm seen in Figure 3.1 [280]. The inner-most layer, the anode, is a nickel oxide/yttria stabilised zirconia (YSZ) tube 152 mm in length and 0.56 mm wall thickness. According to the manufacturer, a thin electrolyte coating (10±2 μm) of yttria stabilised zirconia (YSZ) electrolyte is atop the entire anode surface. A thin samarium doped ceria (SDC) barrier layer (8±2 μm) covers 100.7 mm of the electrolyte, starting 45 mm from the ‘inlet side’ and ending 6.6 mm short of the ‘outlet side’. Atop of the barrier layer is a lanthanum strontium cobalt ferrite (LSCF) cathode (55±2 μm), 95.5 mm in length and starting 47.5 mm from the ‘inlet side’. All cells were measured and weighed once received to check for consistency. The cells were received fully reduced and the majority of the anode’s appearance was dull and grey, some surface oxidation of the nickel was observed, indicated by its green hue. A visual inspection was carried out to check for cracks, delamination and other anomalies.

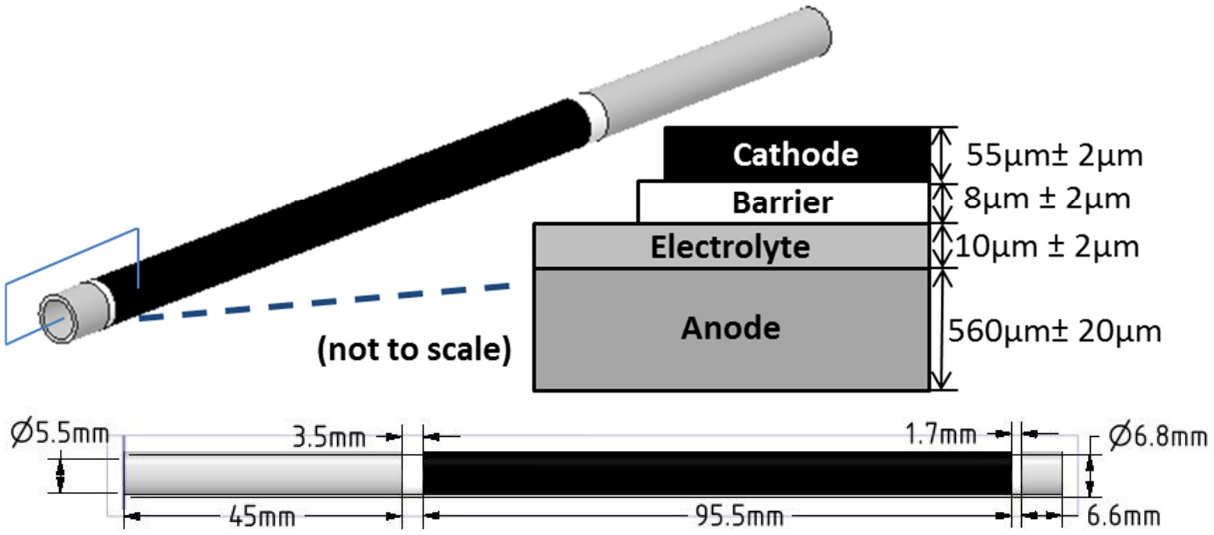

Figure 3.1 - Cell Geometry.

3.2 Testing Preparation

To prepare the cell as received for electrochemical testing, anode and cathode current collectors must be applied, as well as the gas supply and removal manifolds, which also act as mechanical supports for the cell in the furnace. Gas-tight sealing of all joints was paramount to minimise any loss of fuel which would result in a loss of performance.

3.2.1 Manifold Assembly

To safely and effectively supply reactants and remove products, gas-tight inlet and outlet manifolds must be attached to the cell. Correct material selection is paramount here as a mismatch in thermal coefficient between the cell and manifold materials can lead to cell damage and require a system shutdown to minimise hazard. Alumina (Al_2O_3) tubes are mechanically sound at the fuel cell operating temperatures, have a similar expansion coefficient to the anode cermet leading to their use for all AMI 152 single cell tests. For minimisation of fuel leakage, an injector style fuel inlet was developed using a large-bore 'support tube' and a narrow bore 'supply tube' seen in Figure 3.2. The fuel cell slots 10 mm into the 'support tube' with the 'supply tube' protruding from the 'support tube', emerging 15 mm into the fuel cell, past the joint between the fuel cell-manifold joint. Fuel was supplied to the alumina tube through a pre-drilled metal reducer fitting with rubber O-rings. The reducer was sized to allow the 'supply tube' to pass through the reducer into a plastic push-fit tube

where a metal ferrule clamped to seal and ensure no fuel passed through the outer tube. The inlet manifold was leak tested before attaching the fuel cell by a feeding 10 $ml.min^{-1}$ of N_2 while, submerging the end in water to ensure bubbles emerge solely from the 'supply tube', tightening the ferrule clamp till any leakage ceased.

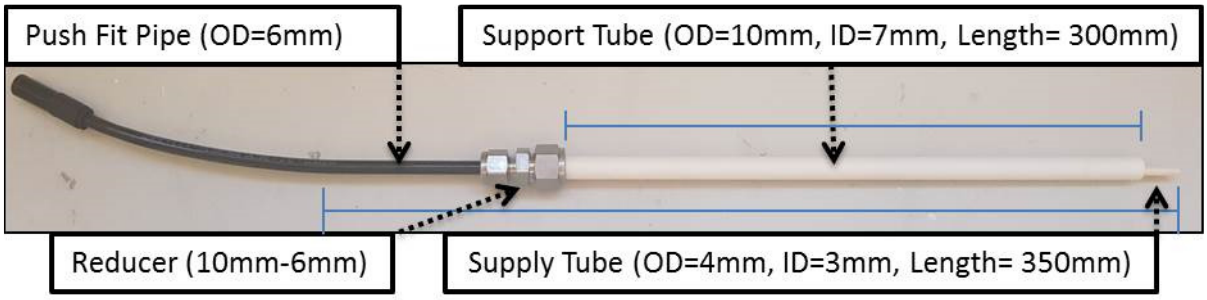

Figure 3.2 - Fuel Inlet Manifold.

Only the larger 'support tube' was used as an outlet manifold, the fuel cell was slotted 7 mm inside the cell leaving the entire cathode exposed to the air. The outlet support tube was joined to a 10 mm-6 mm reducer mated to a 6 mm push-fit plastic tube. To minimise leakage, and the potential for combustion induced local hot-spots, a physical barrier was formed between the 'support tube' on both the inlet side and outlet side using Ceramabond ceramic sealant supplied by Aremco [281]. The sealant was applied on each end of the cell, shaped using a plastic spatula and slotted into the respective manifolds simultaneously. A further layer of Ceramabond was then applied to create a neat joint, finished by a brush painted top coat of Cermabond thinner which gave a smooth, less porous top coating (as per supplier instructions). The setup was allowed to dry in air for 1 hour at room temperature and then cured in a vacuum oven in a two-stage process, first held at 93°C for 2 hours and then at 260°C for 2 hours with a 10°C.min^{-1} ramp for each heating step. Once the Ceramabond had been cured, a leak test was conducted by passing 100 $ml.min^{-1}$ of N_2 through the inlet manifold, blocking the exhaust manifold to induce a pressure build-up and spraying leak detector at each joint. Any bubbles observed indicated a leak which was marked and then touched up with another layer of Ceramabond and cured again, a crucial step for minimising degradation onset in testing.

3.2.2 Anode Preparation

The anode must be prepared for extracting current using current collectors. In this study, the anode current collection was generally split into internal current collection techniques and external current collection techniques. For the external anode current collection there were 3 different cell setups:

1. Central Current Collector (base line),
2. Inlet/Centre/Outlet Current Collector,
3. Segmented Cell - multi-connect.

All external anode current collection positions required removing of outer component layers to expose the innermost anode layer. Depending on the contact position, this may include solely the electrolyte or the cathode, barrier layer and electrolyte. Using a razor blade, two guide lines were scored around the cell circumference spaced 8 mm apart for connections within the cathode area. The width was determined to be the minimum width for the wiring to be located without the risk of short-circuiting.

A layer by layer shaving technique gradually removed the black cathode and white barrier layer, exposing the shiny clear/greyish electrolyte. Using a fine file, a 6 mm wide band of the electrolyte was then removed, exposing the dull grey anode surface. Care was taken to space the band with a 1 mm gap between surrounding barrier/cathode surfaces to avoid short-circuiting. Removing too much of the anode material could leave areas of thinned material in the anode (acting as a support) leading to mechanical weak spots and the formation of ringlets in the anode structure upon heating.

Silver ink supplied by the Shanghai Research Institute of Synthetic Resins [282] was used to cover the exposed anode band. This dense paste acted as a physical barrier preventing fuel/air crossover in addition to providing a highly conductive contact region. The ink was applied sparingly using a fine paintbrush, left to air dry for 30 minutes, followed by furnace drying at 120°C for 1 hour. The anode was then ready for wiring.

3.2.3 Cathode Preparation

The entire cathode was painted using an artist's fine paintbrush with a porous silver ink supplied by SPI [283] to maximise lateral conductivity along the cathode and ensure a continuous, low contact resistance connection between current collector wiring. Care was taken to avoid any short-circuiting between electrodes. The cell was left to air dry for 30 minutes, followed by furnace drying at 120°C for 1 hour.

3.2.4 Cell Wiring

Braided wires were formed by twisting together 0.375 mm thick wire. In baseline tests, wires were made from silver, however, in some cell tests, nickel wire was used. For single cell testing a four-probe testing technique was used which required two separate wires for each electrode, one for measuring voltage and one for measuring current. The anode and cathode current measuring wires used 8 cores of wire twisted together. To prepare, wire was passed 4 times around two 'L shape' 7.5 mm diameter rods spaced 1 metre apart. One rod was fixed, while the other end was mounted in a pillar drill whereby the drill rotation braided the wires together. Wires used for measuring voltage and for securing cathode spine wires were made similarly, except only 4 cores (2 passes) are used. Care had to be taken not to over-tighten as this would snap the wires and make them harder to work.

A 300 mm length of the 8-core wire was wrapped twice around the anode connection point/s, the leads were then twisted together by hand to make a single anode lead. A 300 mm length of the 4-core wire was then attached as close to the base of the 8-core anode wire by wrapping and then tying. A dab of dense silver paste was applied at the joint. This was repeated for the 3 and 5 anode connections in the inlet/central/outlet and segmented cell cases, respectively.

For the cathode wiring, a 300 mm length of the 8-core wire was used, the end was then unpicked to form two strands of 4 wires each around 50 mm long. The strands were then attached to the cathode using tie wires wrapped twice around the cathode, cut, with the ends twisted together to tighten. However, the tie wire nearest the cell centre was not cut and was kept at around 30 mm length and used for voltage measurements. In the case of the segmented cell, four cathode regions would be created, each cathode current wire connected to a 0.71 mm diameter cathode rail, thus connecting

all of the cells in parallel. All wires were insulated using Ecosil silica braided sleeving which is temperature resistant up to 1200°C [284]. A cell with 4-probe wiring of a single central anode current collector with silver conductive paste on the anode and cathode is seen in Figure 3.3.

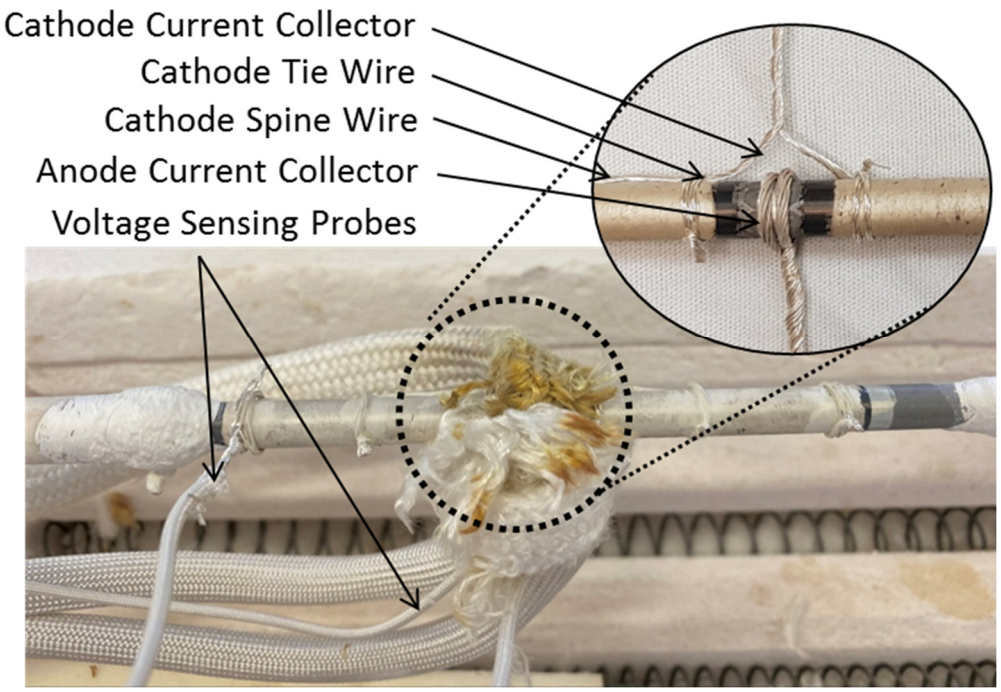

Figure 3.3 - Single cell in the furnace with manifolds and zoom, 4-probe wiring with a single central anode current collector, cathode spine and tie wiring, with silver conductive paste on the anode and cathode and cell wiring insulation.

3.2.5 Cell Sealing

The removal of the electrolyte for the formation of external current collector/s left the anode exposed to oxidation and had to be covered. Schott sealing glass was prepared by adding powder sealing glass to acrylic binder in a 4:1 ratio, then mixing on a magnetic sealing plate for 2 hours [285]. A thin layer was painted onto the anode wiring surrounding the joint and any exposed anode surface. The glass sealant was air-dried at room temperature for 10 minutes followed by a binder burn-off stage where the joint was heated to 360°C for 1 hour with a 10°C.min^{-1} ramp and then left to cool to room temperature. The final sintering at 750°C happened in situ with cell testing. A thin layer of sealing glass was also applied to the manifold joints at this point to further improve sealing.

3.2.6 Sawing and Laser Cutting

Conventional drilling and cutting techniques were tried on fuel cell samples but led to undesired cracking and shattering of the brittle cermet from the vibration of the rotating blade. A diamond saw and diamond-tipped files were used to cut and smooth the fuel cell from the ends and to cut the manifold tubes to size. A Lasea Multi-Axis Laser was used to make slots in the fuel cell. The feed holes allowed wires accessing the anode interior to protrude out to the cathode side for interconnection to adjacent cells. The laser machine included a stack of 5 mechanical stages, 3 linear and 2 rotary axes, and a 3D scan head with 3 optical axes. A 5W, Yb-doped Satsuma femtosecond laser from Amplitude Systems operate at a central wavelength of 1030 nm and maximum repetition rates of 500 KHz. The laser micromachining (LMM) system also had a 100 mm telecentric focusing lens with a machining field of view (FOV) of 35 mm x 35 mm. Its optical beamline configuration provides a beam spot diameter of 30 µm at the focal plane. The laser had a cold beam which prevented damage to fuel cell components from localised thermal hot spots. The laser featured a controllable cutting depth. This allowed a single window to be made on one side of the cell, leaving less area to seal.

3.3 Testing Apparatus

The testing apparatus can be split into the gas supply/measurement system, the heat supply/measurement system and the electrical control/measurement system. The synchronisation of the manual and automated systems was important to ensure the measurements were made at the intended operating parameters. A process and instrumentation diagram (PID) of the testing apparatus is given in Figure 3.4.

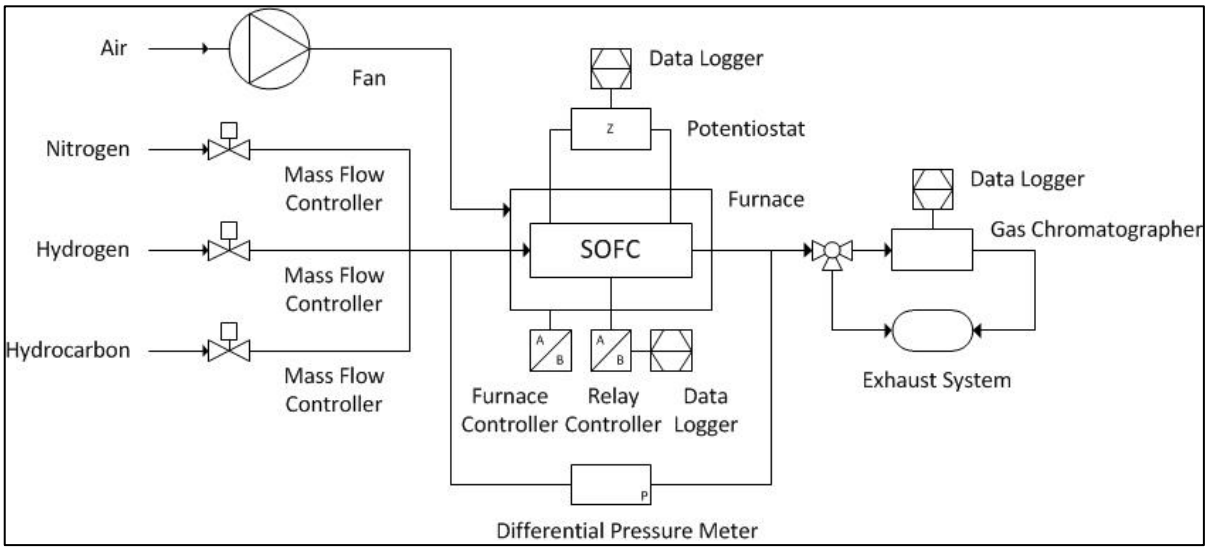

Figure 3.4 - Testing Apparatus PID.

3.3.1 Heating and Temperature Measurement

To raise, hold and cool the fuel cell to its operating temperature for the desired operation an Elite THH12 horizontal tubular furnace was used. An external K-Type thermocouple was in conjunction with the furnace thermocouple to validate the furnace temperature. Temperature measurements of components within the furnace were made using three different techniques, K-Type thermocouples, a laser thermometer, in addition to a Micro-Epsilon TIM 160 thermal imaging camera with 160 x 120 pixel optical resolution was used with a temperature range set between 150°C and 900°C.

3.3.2 Gas Supply

Fuel and nitrogen were supplied using three Aalborg 0-500 $ml.min^{-1}$ mass flow controllers (including a hydrocarbon option) which led to the inlet manifold. Fuel preheating was achieved in the first section of the inlet manifold within the furnace. Often µT-SOFC researchers will supply humidified hydrogen, steam must be present on the anode for there to be an electrical potential as per the Nernst equation. The humidifying of the fuel is done to protect the anode from cracking, particularly under startup/redox when there is a volume change in the microstructure when NiO changes to Ni [286]. Once the cell was operational, steam was generated regardless and given the cells are received reduced the decision was made to operate with dry hydrogen which simplified the fueling system and would favour cost and compactness when considering commercialisation in a portable

device. The addition of steam is highly recommended when using hydrocarbon fuel to facilitate internal reforming. Atmospheric air was allowed to flow in and out of the furnace apertures via natural convection and was sufficient not to starve a single cell of oxygen. Additional air supply was available as an option if/when natural convection was not sufficient using a 3-speed fan placed at the mouth of the furnace inlet. Air could also be supplied from a 2 bar airline connected to a flow controlling needle valve before entering an alumina 'support tube' which was placed in the furnace to supply preheated air.

3.3.3 Pressure Measurement

The pressure drop across the fuel cell was measured using a Digitron digital differential pressure meter with a 0 Pa to 250 Pa measurement range. The pressure drop was calculated across anode inlet and outlet manifold, giving insight on flow characteristics and residence time within the cell. Pressure measurement was in parallel with the flow and had a negligible effect on the flow. A quartz tube with similar internal diameter to the fuel cell was also used for pressure measurement using the same differential pressure meter. The quartz tube was used as a simple way to measure the flow effects of internal current collectors. The quartz tube setup was simple and quick to assemble, avoided the lengthy setup of a real fuel cell while also mitigating the risk of potential leakage from fuel cell-manifold/current collector joints.

3.3.4 Electrical Analysis

Electrical data acquisition of cell current, voltage and impedance with time was obtained via a Solartron™ Analytical 1470E Cell Test System (Solartron) coupled to a Solartron™ Electrochemical Impedance Spectroscopy unit and data logger with Cell Test ™ software. The predicted current of the AMI 152 superseded the maximum allowed current for a single input channel on the Solartron and so a Solartron 50 V/25 A booster system had to be used in series between the fuel cell and the Solartron. Measurement of resistance of cell components and cell setup while offline was done using a TTi BS407 Precision Milliohmmeter. Electrical continuity tests were done with a Clarke CDM 45 multi-meter on 'beep test function' and to ensure no short-circuiting was present between electrodes.

3.3.5 Current Collector Relay Controller

For the segmented cell setup, a current collector relay controller was used for non-intrusive switching between interconnect positions, ensuring no wires were broken and that control of the wiring sequence was simple. The switching system comprised six 6 A relays mounted on an aluminium din rail. A Velleman K8055 interface board was then screw mounted, alongside the din rail in a pre-drilled plastic control box. Six signal outputs from the control board were wired to communication input terminals. The current collector wires were fed into the input relay terminal. The 6 relay output wires were connected to a common rail of 3 core 0.71 mm diameter braided wire and then connected to the booster and Solartron in turn. The control board was controlled by the data logger using LabView 2011 software.

3.4 Fuel Cell Testing

A standard testing procedure was developed for fuel cell testing, with a primary focus of obtaining maximum cell power. Small modifications were made to the standard procedure when durability was a primary focus. The baseline conditions for testing was a blend of dry H_2, supplied at 200 $ml.min^{-1}$, with 10 $ml.min^{-1}$ of N_2 as a reference gas for GC purposes (which was never eventually used). Care had to be taken not to starve the fuel cell of fuel, especially at the high current densities as this would lead to anode oxidation. The 200 $ml.min^{-1}$ flow was deemed to be a conservative excess of fuel at the maximum current draw, estimated by preliminary calculations of fuel utilisation by the Nernst equation using the cathode area and estimated current density. This was validated experimentally in flow rate calibration measurements. The fuel cell operating temperature was 750°C. For a cell to be deemed worthy of testing, the open circuit potential should be stabilised at 1.1 V ±0.1 V at baseline conditions. Failure to meet the criteria led to test termination and typically indicated a cracked electrolyte, an incomplete electrolyte, short-circuiting or in extreme cases severe inlet manifold leakages. The external central current collector served as a baseline setup for comparison to other current collector configurations.

3.4.1 SOFC Start-Up

To bring the fuel cell to its operating conditions a start-up profile was determined. To avoid re-oxidation of the anode upon heating, a blend of ‘safe gas’, 4% H_2 in N_2 with a total flow of 210

ml.min^{-1} was introduced to the fuel cell at temperatures above 400°C. Once the furnace had ramped to 650°C, the amount of H_2 was gradually increased and the amount of N_2 gradually decreased (simultaneously), ensuring a total flow of 210 ml.min^{-1} was always maintained. A 10°C.min^{-1} ramp rate was used for ramping between all temperature intervals and is typical for µT-SOFC testing. Reduction of the cell would start once the fuel was introduced, but to ensure the anode was fully reduced before testing, a reduction step was included once the furnace had ramped to 750°C; the fuel cell is held at OCV for 1 hour at the operating conditions before any current is drawn.

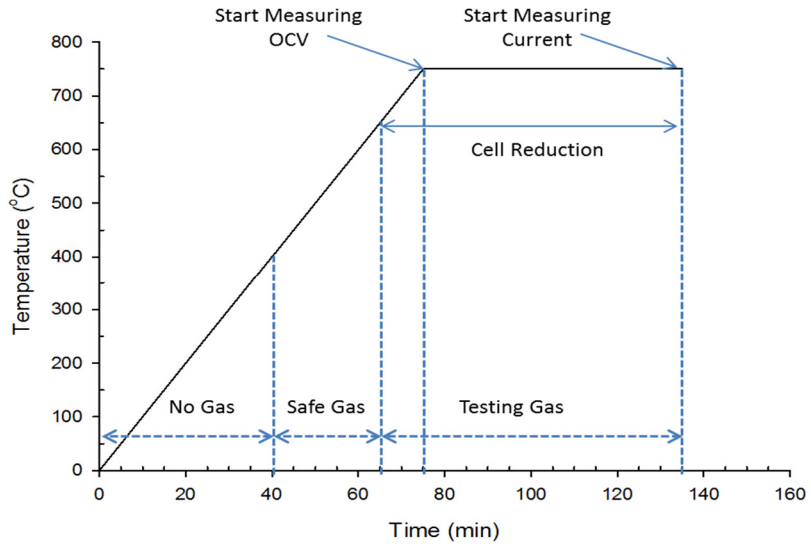

Figure 3.5 - Fuel cell testing start-up profile.

3.4.2 Current-Voltage Analysis

The most typical characterisation of fuel cells is a plot of voltage against current density (i-V), and the subsequently derived power against voltage plot. To obtain i-V plots in this study, a potential stair-step function was used to control the voltage and observing the current, sweeping downwards and then upwards between two voltage intervals. Increasing the potential difference from the OCV (towards 0 V) increases the driving force of the reaction, increasing the current density until the maximum current density is reached. Fuel cells are more efficient at part load than full load and so fuel cells are often run in the mid-upper voltage range (0.9 V to 0.7 V). However, the peak cell power is not achieved at the maximum current density and is typically approximately half the OCV (0.5 V to 0.55 V). Fuel cells are seldom run at peak power for efficiency and durability reasons, besides, operation at such point does not give the device the flexibility to increase power with demand. Nevertheless, the peak power is a common metric for comparison. Instead, the fuel cell is 'oversized'

for the average power demand and typically operates at 0.7 V which is also a common metric for comparison. A maximum voltage range between OCV and 0.4 V is used in this study. Given the constant flow rate, the fuel utilisation will vary with the operating potential and resulting current draw for each step in the i-V plot.

The fuel cell i-V curve can be characterised by three distinct regions, the activation energy loss dominated region at low current densities where there is a sharp voltage drop-off, the mass transport loss dominated region at high current densities with sharp voltage drop-off and an approximately linear region in between (med current density) controlled by ohmic losses. Potentiostatic measurements are also of use to observe the current drop of the fuel cell with time and can be held at regions of interest in different loss dominated regions of the i-V curve. In this study, constant potential measurements were taken at OCV, 0.9 V, 0.7 V and 0.5 V with a H_2 flow of 200 $ml.min^{-1}$. It can also be useful to perform galvanostatic measurements and observe the resulting potential or driving force required to deliver that current as an indication as to how hard a cell is working.

While the relative shape of the curve and current/power figures are useful for comparison, the i-V curve can be used to derive information about the fuel cell performance such as fuel utilisation but also exchange current density which can be used for model fitting. The region of interest for deriving the exchange current density is in the low overpotential regions where cell voltage is between OCV and 0.9 V and so in some i-V curves a small voltage step size of 1 mV was used to improve the resolution. For i-V plots where such data is not being derived, a larger step size of 50 mV was used for a reduced data acquisition time.

3.4.3 Electrochemical Impedance Spectroscopy Analysis

Electrochemical Impedance Spectroscopy (EIS) is a non-destructive in-situ performance and degradation characterisation technique for electrochemical devices, utilising the variables voltage, current and time. EIS gives an insight into the individual contribution of major sources of loss in a fuel cell device such as anode activation loss, cathode activation loss and ohmic losses. Analogies can be drawn between resistance and impedance; this more common concept can assist in the understanding of SOFC loss processes. Both are a measure of the ability to resist the flow of current. However, impedance is a more complex terminology capable of dealing with time or frequency-

dependent phenomena of single or multiple circuit elements. The basic formula for impedance is given by:

$$Z = \frac{V(t)}{i(t)} \tag{45}$$

Measurements are made by applying a small sinusoidal voltage in the form $V(t) = V_0 \cos(\omega t)$, where V_0 is the voltage magnitude and ω is the frequency, to an electrochemical cell at steady-state. The current response is recorded and is in the form $i(t) = i_0 \cos(\omega t - \varphi)$, shifted in phase by φ from the incident voltage, however, still possessing the same frequency. SOFC operation is complex, containing multiple mass transfer, electrochemical and chemical processes and as a result, exhibits nonlinear behaviour. Interpretation of nonlinear systems is problematic and so the perturbation amplitude of the applied AC potential should be sufficiently small so that the cells response can be considered to be pseudo-linear, in this study a 10 mV perturbation amplitude is used. The impedance can, therefore, be calculated by substitution of the incident and response signals into the basic impedance equation:

$$Z = \frac{V_0 cos(\omega t)}{i_0 cos(\omega t - \varphi)} = Z_0 \frac{\cos(\omega t)}{\cos(\omega t - \varphi)} \tag{46}$$

in this form, impedance is expressed in terms of magnitude Z_0 and phase φ. With some mathematical manipulation using Euler's relationship:

$$\exp(j\varphi) = cos\varphi + jsin\varphi, \qquad j = \sqrt{-1} \tag{47}$$

it is possible to write the impedance response as a complex function with real and imaginary components. The voltage can then be described as $V = V_0 \exp(j\omega t)$ and the current as $I = I_0 \exp(j\omega t - \varphi)$, therefore substituting into equation (46) we get:

$$Z = \frac{V_0 exp^{j\omega t}}{i_0 exp^{(j\omega t - j\varphi)}} = Z_0 exp^{j\varphi} = Z_0(cos\varphi + jsin\varphi) \tag{48}$$

where the real component is $Z_{real} = Z_0 cos\varphi$ and the imaginary component is $Z_{imag} = Z_0 sin\varphi j$. The purpose of the mathematical manipulation is for ease of data presentation. A plot of the real part on the x-axis and imaginary part on y-axis is known as a Nyquist plot.

Several data interpretation methods exist, namely the equivalent circuit model (ECM) technique and more modern state-space model, local operation model, nonlinear impedance model, finite element model and noncharge transfer approach. The most common method is the Equivalent Circuit Model used in this study using Z-View software. The ECM is easily understood and a close relation exists between the electric properties of an equivalent circuit and the SOFC physiochemical process. Circuit elements, which the model uses, must be selected in combinations which not only fit the data accurately but also have a physical representation of the phenomena occurring. Consequently, the total number of elements used should be minimised. Table 3.1 lists the most commonly used circuit elements.

Table 3.1 - ECM circuit elements.

Circuit Element	Impedance
Resistor	R
Capacitor	$1/j\omega c$
Inductor	$j\omega L$
Constant-Phase Element	$1/[Q(j\omega)^{\alpha}]$
Infinite Warburg	$(\sigma_i/\sqrt{\omega})(1-j)$
Finite Warburg	$(\sigma_i/\sqrt{\omega})(1-j)\tanh(\delta\sqrt{j\omega/D_i})$

A single element seldom describes an electrochemical cell. Instead, elements are connected in a network and can be connected in series, parallel or a combination. The total impedance of elements connected in series and parallel configurations are different. For linear elements in series, impedance is given by equation (49), whereas for linear elements in parallel is given by equation (50).

$$Z_{eq} = Z_1 + Z_2 + Z_3 \quad \textbf{(49)}$$

$$\frac{1}{Z_{eq}} = \frac{1}{Z_1} + \frac{1}{Z_2} + \frac{1}{Z_3} \quad \textbf{(50)}$$

The parallel combination of a capacitor and resistor can be used by ECM software to adequately fit the impedance arc produced by the anode or cathode polarisation. This combination has a justifiable

physical representation. The resistor describes the kinetic resistance to electrochemical processes and the capacitor describes the charge separation (double-layer capacitance) between ions and electrons at the electrode-electrolyte interface. The resulting Nyquist plot, in conjunction with the frequency information, can be used to derive the value of the resistance and capacitance as shown in Figure 3.6. The frequency decreases from left to right, the highest frequency being at spatial coordinate (0,0). The high-frequency arc represents the contribution from mainly the anode, whereas the lower frequency arc represents the contribution from mainly the cathode although there can be some overlap in contribution. The resistor-capacitor parallel combination can be placed in series with a resistor to describe the ohmic resistance from the electrolyte and another resistor to describe resistance from interconnection.

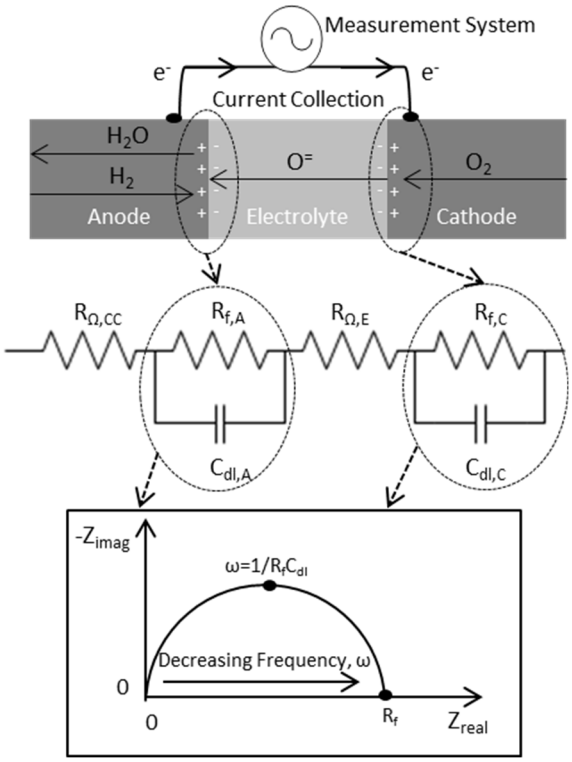

Figure 3.6 - Typical fuel cell ECM and Nyquist interpretation.

The circuit used in this study is shown in Figure 3.7. The addition of an inductor element at the start of the circuit accounts for noise arising from the acquisition equipment, namely the Solartron, the booster and its wiring. The x-axis intercept at $R_{\Sigma\Omega}$ is the combined resistance of the ohmic and current collection and is a useful metric in this study for comparing the development of current collectors. Given the electrolyte resistance will be the same for all cells at a given temperature, variations in this value will be an indication of current collector performance.

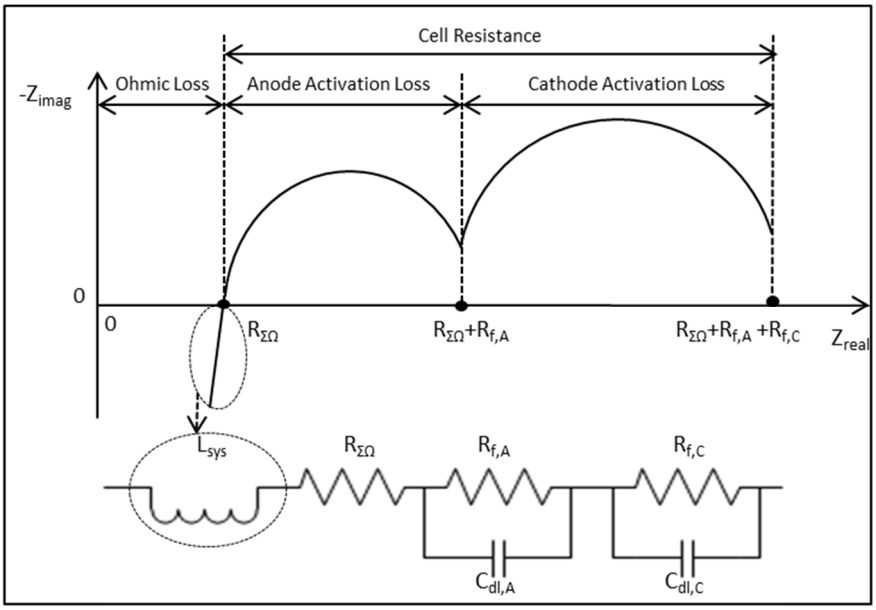

Figure 3.7 - ECM used and Nyquist interpretation.

Taking impedance values at different voltages on the i-V curve will give different results and so impedance was taken at multiple points. The constant current parameter was used for values near OCV, taking measurement at a 0.1 A draw. This was done so oscillations of voltage and current did not reverse into the electrolysis region which might have damaged the fuel cell. Impedance was also recorded at a constant potential of 0.9 V, 0.7 V and 0.5 V. Frequency of oscillation was between $1x10^6$ Hz and 1 Hz.

3.5 Microstructural Characterisation

Microstructural characterisation was conducted on the µT-SOFC and current collectors before testing and post-testing. Pre-test images of fuel cell and current collectors were used for feeding the fuel cell model with parameters and served as a baseline for comparison to post tested images, giving insight on the extent of microstructural damages development and degradation mechanisms.

3.5.1 Scanning Electron Microscopy Analysis (SEM)

A scanning electron microscope was used to examine the surface morphology and cross-section of µT-SOFCs and current collector samples. The µT-SOFC samples were fragments, polished lightly with fine grade wet and dry sandpaper to achieve a flat finish. A Hitachi Tabletop Microscope TM3030

Plus was used, employing secondary electron (SE) functionality to obtain topographic information and backscattered electron (BSE) functionality for compositional distribution. From the images of the anode, image processing software was used to receive estimates of pore size, pore size distribution and porosity of fresh and tested samples.

3.5.2 Energy-Dispersive X-Ray Spectroscopy Analysis (EDX)

The Hitachi TM3030Plus had Energy-Dispersive X-ray spectroscopy (EDX) functionality, a powerful technique used for elemental mapping, used in conjunction with SEM analysis. This was used to determine any compositional change in samples after testing or pre-treatment and identify any element migration in the fuel cell during operation.

3.5.3 X-ray Computed Tomography (XRCT)

XRCT is a non-destructive imaging tool which produces a series of 2D X-ray images which can then be mathematically reconstructed to form a 3D image. The filtered back-projection procedure is the most common algorithm for 3D reconstruction [287]. Images were taken and collected from multiple angles using a tomograph. These images were then spatially corrected and reconstructed into a dataset known as a tomogram. The images produced gave a great level of detail about the internal structure of the subject such as porosity, tortuosity, percolation, and particle diameter as well as component layer thicknesses. A 520 Versa X-ray micro-CT (Zeiss Xradia 520 Versa, Carl Zeiss., CA, USA) was used in this work with a tungsten anode that produced characteristic X-ray emission peaks at 59.3 keV. The Versa had a power supply that could be varied by voltage up to 160 kV, had a polychromatic cone beam and four imaging modes with a 0.4, 4, 20 and 40 times optical lens magnification. Doubling the magnification from 20 to 40 times halved the pixel length from 400 nm to 200 nm. The field of view (FOV) for 20 times magnification was 768 µm by 768 µm, while for 40 times magnification the FOV was halved at 384 µm by 384 µm.

3.5.4 Optical Microscopy

Optical microscopy was used to characterise the effect of anode-electrode contacting using a filler material in a brazing technique. The parent materials, contacting materials and anode-current

collector joint were inspected. The optical microscope was a Zeiss AX10 Lab A1 and allowed up to 20x magnification; it was combined with Image-Pro Insight software for 3D analysis, ideal for looking for joint 'witness', detail on the anode structure that a joint had been made.

3.5.5 Archimedes Method

The Archimedes method can be used to estimate the porosity of objects, in our case of the fuel cell electrodes. The porosity is defined as the fraction of the bulk material volume that is not occupied by solid matter seen in (51).

$$\emptyset = \frac{V - V_S}{V} = \frac{V_P}{V_B} = \frac{Pore\ Volume}{Total\ Bulk\ Volume} \quad \textbf{(51)}$$

Where V_S is the solid volume [m^3] and V_P [m^3] is the pore volume. The Archimedes method uses a reference fluid (such as water in this study) with known density ρ_f [$kg.m^{-3}$] to saturate the porous structure. The material is first submerged in water, removed, surface water is dried and then the object is weighed to obtain a saturated weight, W_{sat}[kg]. The material was then once again submerged, this time weighed while suspended in the reference fluid to get a submerged weight W_{sub} [kg]. We took the dry weight W_{dry}[kg] and substituted into (52) and (53) to calculate an estimate for the pore volume and the total bulk volume V_b[kg], respectively, to be used in (51) to calculate the porosity [288].

$$V_P = \frac{W_{sat} - W_{dry}}{\rho_f} \quad \textbf{(52)} \qquad V_b = \frac{W_{sat} - W_{sub}}{\rho_f} \quad \textbf{(53)}$$

The most significant source of error here was making sure no fluid drained from the sample while trying to measure the saturated weight and also determining how much excess fluid to remove from the surface. This method also cannot account for closed pores and does not give any information on pore size, pore distribution and pore connectivity.

3.6 Mechanical Testing

To determine the strength of the joints between the anode and current collector, an Instron 5848 Environmental Mechanical Tester (Instron) was used for tensile tests. The Instron had a fixed vice grip at its base with an upper vice grip attached to a load cell. The load cell could be changed depending on the force required; here a 100 N load cell was used. To avoid any damage to the fuel cell when securing in the vice grip, the fuel cell was loaded into an in-house fabricated metal cell holder which would then be held in the vice. The tubular cell holder was 180mm in length, had an 8mm outer diameter with a flat stop at the end which only the current collector wire could pass through to be held in the vice grip of the upper load cell. Bluehill software was used to control the Instron, setting the extension rate at 2 mm per minute with a maximum extension of 20 mm.

Chapter 4 Modelling Methodology

The previous chapter outlined the experimental approach used to determine fuel cell performance. This chapter aims to outline a respective modelling approach, using commercially available computational fluid dynamics (CFD) software to describe the underlying physical phenomena. The computations were performed on a custom-built Windows Server machine with a dual Intel(R) Xeon(R) CPU E5-2660 v2 @ 2.2 GHz processor with 128 GB of memory.

COMSOL Multiphysics 5.4 was chosen to model the fuel channel, electrodes, electrolyte, current collectors and furnace of a µT-SOFC. COMSOL uses the Finite Element Method (FEM) to evaluate the approximations to partial differential equations, solving for the conservation of momentum, heat, mass and charge. The interrelated conservation equations were solved at steady-state reflecting the fuel cell at fixed operating conditions, thus time-dependent terms were neglected. The axial symmetry of the tubular cell led to a 2D axisymmetric model geometry, offering a reduction in model complexity and computational intensity over a 3D setup.

4.1 Model Assumptions

In order to mathematically describe real-world phenomena, simplifications based on some assumptions of the physics are often made. These assumptions reduce model complexity, and if realistic, will give a reasonable approximation. The following assumptions were made:

- Flow is steady and isothermal,
- Fully developed laminar flow in the anode gas channel and furnace gas channel,
- Hydrogen and oxygen are the only electrochemically active species,
- Electrodes are selective for respective electrochemical reactions; oxidation of the fuel occurs, at the anode and reduction of oxygen occurs at the cathode,
- Electrochemical reactions occur in the entirety of the electrode layers,
- The electrolyte is non-porous, gastight and dense,
- The outer surfaces of the anode and cathode layers act as current collectors (therefore the effect of interconnects are neglected),
- Radiative heat transfer is ignored.

The last assumption on radiative heat transfer must be analysed further as at temperatures above 550°C, and certainly, at typical SOFC operating temperatures, there will be a significant amount of radiative heat. Including radiative heat transfer, physics complicates modelling significantly and causes problems. However, one can estimate what the error from excluding it was and make some comments on how temperature profiles estimated may differ from those expected.

4.2 Geometry

A cell geometry mirroring the experimental setup was used. A simplification was made to mitigate the fuel inlet region and outlet regions which do not contribute to the electrochemical performance. This new fuel inlet/outlet domain as modelled was to the anode gas channel cell section under the active area, so-called 'model fuel inlet and outlet', respectively. The length of the anode and the electrolyte were therefore restricted to a maximum length of the cathode of 95.5 mm. An 8 mm length of the cathode and electrolyte was removed to represent the current collection node which was accessed from the cell exterior as in the experimental setup. The furnace was restricted to a dimension four times the thickness of the fuel channel thickness, large in comparison, but not at full scale to avoid unnecessary meshing and computational intensity. The cell geometry used is given in Table 4.1.

Table 4.1 - Model geometry.

µT-SOFC Model Dimensions	Thickness [µm]	Length [mm]
Fuel Channel	2750	95.5
Anode Support Layer	550	95.5
Anode Functional Layer	10	95.5
Electrolyte	152	87.5
Cathode	95.5	87.5
Furnace	11,000	95.5

The single current collector node could be moved to be at the inlet, centre and outlet section of the electrochemical region. This node was defined in the model as the cell ground, at which the potential was held at zero, a boundary probe is applied here and was where the cell performance was observed. The central anode connection geometry was used for model development and fitting, displayed in Figure 4.1 and Figure 4.2.

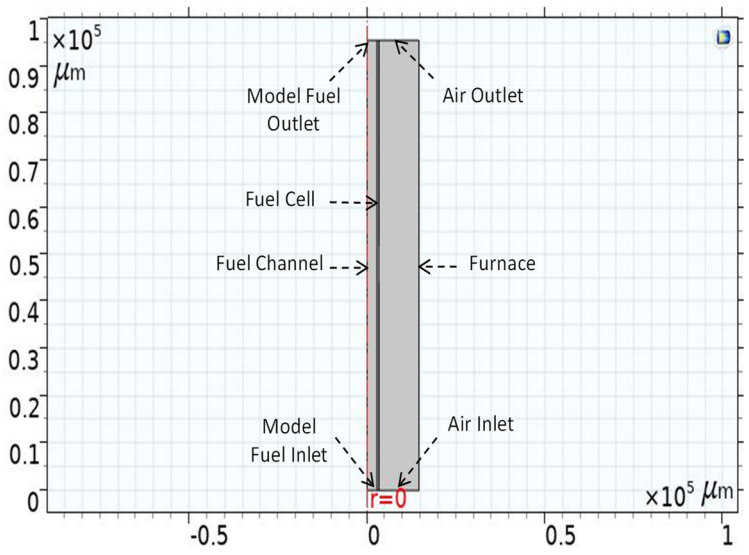

Figure 4.1 - COMSOL model geometry.

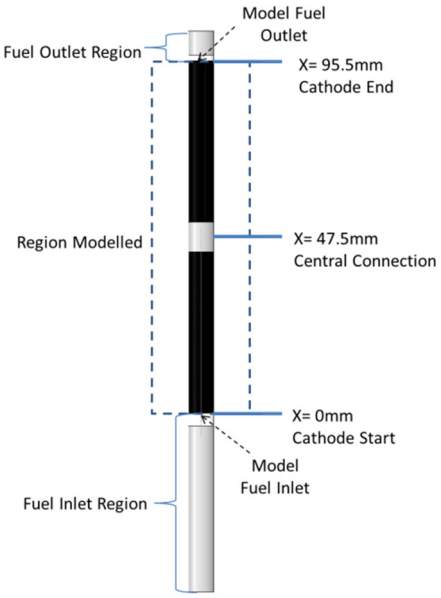

Figure 4.2 - Region modelled.

A zoom of the COMSOL model geometry around the central current collection geometry is shown in Figure 4.3. The removed cathode and electrolyte section left the anode exposed to the furnace, given that no combustion physics have been included and the electrodes are selective for their respective electrochemical reactions, it was assumed that no hydrogen passed through to the furnace and so no loss occurred here.

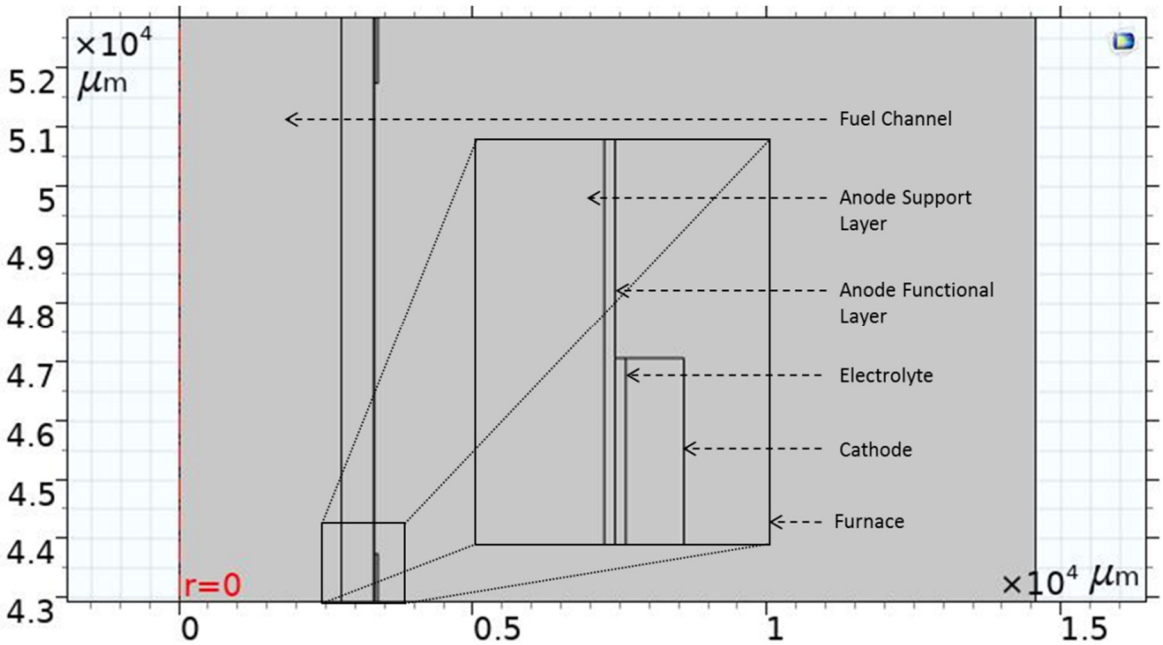

Figure 4.3 - COMSOL model geometry with a magnification of the central connection region.

4.3 Mesh

The 2D geometry was discretised with a custom computational mesh with a total of 53,432 elements and had a mesh quality measured in skewness of 0.90, which was sufficient for solving the momentum and energy equations [198]. The high element number arose from the difficulty in generating mesh suitable for very thin fuel cell layers. A mapped mesh was used for the fuel channel, anode support and functional layer, electrolyte and cathode while a free triangular mesh was used for the rest of the geometry as seen in Figure 4.4. The most refined mesh was used in the electrochemically active region where a higher resolution is required to capture the expected large gradients. The minimum element size in the anode support layer, anode functional layer, electrolyte and cathode were set at 20 µm, 1.5 µm, 2 µm and 2 µm, respectively.

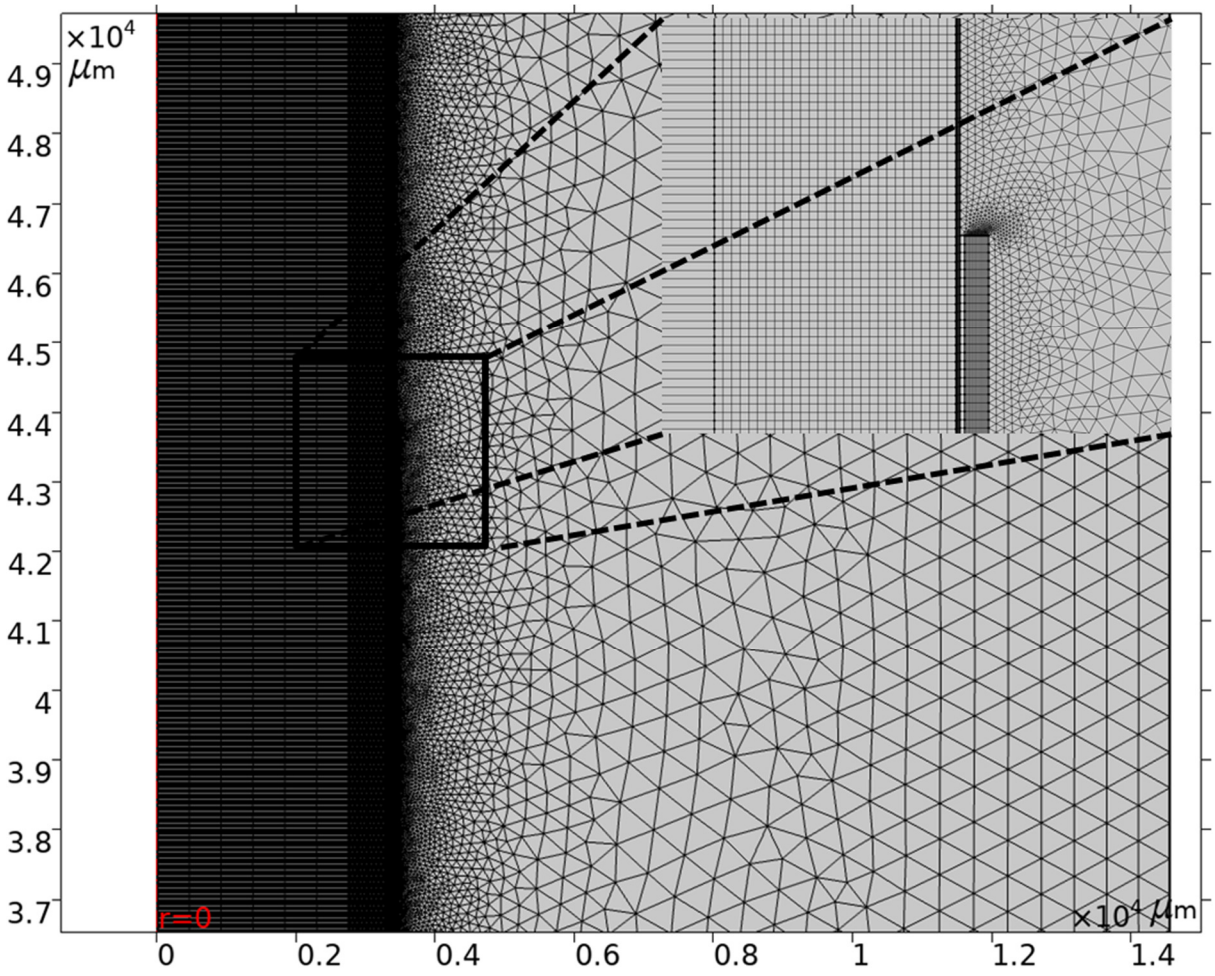

Figure 4.4 - COMSOL model mesh.

4.4 Materials

The region of the modelled µT-SOFC was subdivided into its constituent layers and equations were solved within each domain and then linked together. The dual-layered anode was fed with a pre-heated 3% humidified hydrogen mixture. A nickel-YSZ gas diffusion layer provided the support for a nickel-YSZ anode catalyst layer, a YSZ electrolyte, a GDC barrier layer and an LSCF cathode. In an attempt to simplify the model, the GDC barrier layer, which prevents electron flow from the LSCF towards the electrolyte, was omitted. The furnace was represented by a body of continually replenished hot air that supplied the oxygen to the cathode.

4.5 Modelling Strategy

COMSOL 5.4 has a modular approach to solving physical phenomena. The physio-chemical sets of equations are grouped into modules most suited to their application. The Batteries and Fuel Cells, CFD, and Chemical Reaction Engineering modules were required for this study. Table 4.2 lists the equations and domains the modules were applied to. The equations presented in this section are reproduced from the COMSOL database unless stated otherwise [289].

Table 4.2 - COMSOL modules, equations and domains.

COMSOL 5.4 Multiphysics Module	Equations	Domains
Free & Porous Media Flow	• Momentum balances	• Fuel and furnace gas channel • Anode and cathode
Heat Transfer in Porous Media	• Energy balance • Convective heat transfer Coefficient	• Fuel and furnace gas channel • Anode and cathode Electrolyte
Transport of Concentrated Species	• Mass balances • Diffusion and convection • Density of gases	• Fuel and furnace gas channel Anode and cathode
Secondary Current Distribution	• Electrochemical reactions • Ionic and electric charge balances • Heat generation - power dissipation • Heat generation -reaction	• Fuel and furnace gas channel • Electrolyte

4.5.1 Conservation of Momentum

The Free and Porous Media flow module in COMSOL Multiphysics uses the Navier-Stokes equation for describing the momentum balance of gases in the anode and furnace gas channels:

$$\rho(u\nabla)u = \nabla\left[-PI + \mu\left(\nabla u + (\nabla u)^T - \frac{2}{3}\mu(\nabla u)I\right)\right] + F_b \quad \textbf{(54)}$$

where ∇ is the del operator, ρ is the fluid density [kg.m^{-3}], u is the velocity vector [m.s^{-1}], P is the pressure of the fluid [Pa], I is the identity matrix [dimensionless], μ is the dynamic viscosity and F_b is the volume force vector [N.m^{-3}]. The gases are assumed to be compressible given that the Mach number (Ma) was less than 0.3, and so the steady-state continuity equation was used in conjunction:

$$\nabla(\rho u) = 0 \quad \textbf{(55)}$$

To describe the conservation of momentum in the electrodes, the module used an extended Navier-Stokes equation which accounted for the porosity and permeability of the electrodes:

$$\frac{\rho}{\epsilon}(u\nabla)\frac{u}{\varepsilon} = \nabla\left[-PI + \frac{\mu}{\varepsilon}\left(\nabla u + (\nabla u)^T - \frac{2\mu}{3\varepsilon}(\nabla u)I\right)\right] - \left(\frac{\mu}{\kappa} + \beta_F|u| + \frac{Q_{br}}{\varepsilon^2}\right) + F_b \quad \textbf{(56)}$$

where κ is the permeability [m^2], ε is the porosity [dimensionless] and T is the transpose matrix [dimensionless]. A new Brinkman effective viscosity (β_F) term, [Pa·s], was introduced and is assumed to be the dynamic viscosity of the gaseous mixtures in the fuel cell. The second term in the square brackets is the viscous stress tensor, τ [N.m^{-2}]. An additional species source term (Q_{br}) [kg.m^{-2}.s^{-1}], was also introduced and resulted in a varying gas composition in the anode and furnace streams, implying that density and velocity were no longer constant:

$$\nabla(\rho u) = Q_{br} \quad \textbf{(57)}$$

The species source term Q_{br} was given by:

$$Q_{br} = \sum_x \sum_A R_{A.x} \quad \textbf{(58)}$$

which for the consumption/production of species A in reaction x is given by:

$$R_{A.x} = \frac{\nu_{Ax} i_{vx}}{n_x} \quad (59)$$

where ν_A is the stoichiometric coefficient of species A for reaction x, i_{vx} [A.m^{-3}] is the local volumetric exchange current density for species x and n_x is the number of electrons transferred in reaction x. Equation (60) is a form of the well-established Faraday's equation which links the flow rate of the fuel and the current generated:

$$n_A = \frac{iA}{n_A F} \quad (60)$$

where i is the current density [A.cm^{-2}], A is the electrochemically active cell surface area [m^2], n_A is the number of electrons equivalent per mole of species A and F is Faraday's constant [C.mol^{-1}]. To solve the first-order density equation the density of the gases needed to be defined, calculated using the ideal gas law:

$$\rho = \frac{PM_n}{RT} \quad (61)$$

where the molecular of the gas species is given by (62):

$$M_n = \left(\sum_A \frac{\omega_A}{M_A} \right)^{-1} \quad (62)$$

The flow regime can be determined at the operating conditions in both the anode and furnace gas channel by the dimensionless Reynolds number to test the assumption that the flow was laminar. The Reynolds number is the ratio of inertial to viscous forces within a fluid in motion:

$$Re = \frac{\rho u d}{\mu} \quad (63)$$

Laminar conditions occur at low Reynolds number Re<2300 where viscous forces are dominant, typical for fuel cell gas channels [290]. The calculated Reynolds number was used to get an understanding of the development of the velocity boundary layer. Using engineering correlations, the hydrodynamic entry length, L_h[m] could be estimated, which was required for fully developed flow to occur from the entrance region of the fuel cell. For laminar flow in a pipe, this is given by:

$$L_h \approx 0.05ReD \quad (64)$$

where D is the internal diameter [m]. The typically low Reynolds numbers for fuel cells, combined with a typically low internal diameter of µT-SOFCs, indicates that the entrance length will be short and flow will become rapidly fully developed. Table 4.3 gives the Reynolds number and hydrodynamic entry lengths for several inlet velocities at 298 K and atmospheric pressure using the cell internal diameter of 5.5 mm.

Table 4.3 - Reynolds number and hydrodynamic entry length for typical fuel flow rates.

Inlet Velocity [m/s] (Volumetric flow rate [ml/min])	Reynolds Number [-]	Hydrodynamic Entry Length [m]
0.112 (160)	5.76	1.59×10^{-3}
0.126 (180)	6.48	1.78×10^{-3}
0.14 (200)	7.20	1.98×10^{-3}
0.15 (220)	7.93	2.18×10^{-3}

4.5.2 Conservation of Energy

The overall energy balance of the µT-SOFC model is:

$$\rho C_p \boldsymbol{u} \cdot \nabla T = \nabla \cdot \boldsymbol{q} + Q_{conv} + Q \quad (65)$$

where u is the velocity vector [$m.s^{-1}$] and C_p is the specific heat capacity at constant pressure [$J.kg^{-1}.K^{-1}$]. The first term on the right-hand side represents the heat transfer from conduction and is given by Fourier's Law:

$$q = -\lambda \nabla T \quad (66)$$

the conductive heat transfer coefficient being denoted by λ [$W.m^{-2}.K^{-1}$)]. Within the porous electrode media, an adjusted conductive heat transfer has to be considered:

$$\boldsymbol{q} = -k_{eff} \nabla T \quad (67)$$

where the effective conductive heat transfer coefficient, k_{eff} is:

$$k_{eff} = \theta_p k_p + \left(1 - \theta_p\right)k \quad \textbf{(68)}$$

using the volume fraction θ to consider the pore and void. The convective heat transfer between the anode and anode gas channel and the cathode to the furnace gas channels is given by equation (69) and equation (70), respectively:

$$q_{a.conv} = h_a(T_{aw} - T_{ac}) \quad \textbf{(69)} \qquad q_{c.conv} = h_c\left(T_{cw} - T_{fc}\right) \quad \textbf{(70)}$$

where $h_{a/c}$ is the anode/cathode convective heat transfer coefficient [$W.m^{-2}K^{-1}$]. Within the porous electrode layers, exothermic electrochemical reactions produce heat. Heat generation is from irreversible and reversible loss and power dissipation, arising from the resistance of ion and electron movement within the solid and porous media. The overall equation is:

$$q_g = q_{irrev} + q_{oh} + q_{pd} \quad \textbf{(71)}$$

The irreversible heat flux q_{irrev} is, given by the product of voltage overpotential η [V], and the local current I_v, [A]:

$$q_{irrev} = I_v \eta \quad \textbf{(72)}$$

Ohmic heat is generated by power dissipation when drawing the electric current:

$$q_{oh} = \nabla(I_s \phi_s) \quad \textbf{(73)}$$

where Φ is the electric/ionic potential [V]. The model assumes that there is no ion flow through the electrolyte and therefore no consumption/generation, meaning no power is dissipated in the electrolyte:

$$q_{pd} = \nabla(I_I \phi_I) \quad \textbf{(74)}$$

Table 4.4 - Energy balance equations.

Model Component	Energy Balance Equation	Equation
Anode and furnace gas channels	$\rho C_p u \nabla T_{gc} = \nabla(k \nabla T_{gc}) + h_{gc}(T_{gcw} - T_{gc})$	**(75)**
Electrode diffusion layers	$C_p u \nabla T_{gcw} = \nabla(k \nabla T_{gcw}) + h_{gc}(T_{gc} - T_{gcw}) + I_v \eta + \nabla(I_s \phi_s) + \nabla(I_I \phi_I)$	**(76)**
Electrode reaction layers	$C_p u \nabla T = \nabla(k \nabla T) + h_{gc}(T_{gc} - T) + I_v \eta + \nabla(I_s \phi_s) + \nabla(I_I \phi_I)$	**(77)**
Electrolyte	$\nabla(k \nabla T) + \nabla(I_I \phi_I) = 0$	**(78)**

Table 4.4 gives the energy balance for each of the domains in the modelling geometry. The dimensionless Prandtl number shown in (79) can be used to describe the ratio of the momentum diffusivity to thermal diffusivity and thought of as the relative ease of momentum and energy transport of a flow system:

$$Pr = \frac{C_p \mu}{k} \quad \textbf{(79)}$$

Values of Pr<<1 indicate thermal diffusivity dominates whereas Pr>>1 indicates momentum diffusivity dominates. The engineering correlation for the estimation of the thermal entry length L_T[m] for laminar flow is:

$$L_T \approx 0.05 ReDPr \quad \textbf{(80)}$$

which is the length required for fully developed thermal boundary layer to occur from the thermal entrance region. For gases $Pr \approx 1$, therefore looking at the relationship between equation (64) and equation (80) we can see that the thermal boundary layer and velocity boundary layer become fully developed at a similar length. At 298 K the Prandtl number is 0.69. The thermal entrance length for hydrogen at 298K with a cell internal diameter of 5.5 mm for typical fuel flow rates is seen in Table 4.5.

Table 4.5 - Thermal entry length for typical fuel flow rates.

Inlet Velocity [m/s] (Volumetric flow rate [ml/min])	Thermal Entry Length [m]
0.112 (160)	1.10×10^{-3}
0.126 (180)	1.23×10^{-3}
0.14 (200)	1.37×10^{-3}
0.15 (220)	1.50×10^{-3}

The dimensionless Nusselt number is the ratio of convective (advective and diffusive) to conductive heat transfer at a boundary in a fluid:

$$Nu = \frac{hD}{k} \tag{81}$$

where h is the convective heat transfer coefficient [W.m^{-2}K^{-1}] and k is the conductive heat transfer coefficient [W.m^{-1}K^{-1}]. The Nusselt number is calculated by correlations depending on the flow regime. Within the thermal entrance region (which is approximately 1.4 mm for a 200 ml.min^{-1} H_2 flow), the Nusselt number is calculated by [290]:

$$Nu = 3.66 + \frac{0.0668\left(\frac{d}{L}\right) Re \cdot Pr}{1 + \left(0.04\left(\frac{d}{L}\right) Re \cdot Pr\right)^{2/3}} \tag{82}$$

Outside of the thermal entrance region where the flow is fully developed the Nusselt number is constant, assuming a uniform surface temperature it is estimated at 3.66 and 4.36 for a uniform surface heat flux.

4.5.3 Conservation of Mass

The law of mass conservation states that mass cannot be created nor destroyed and is the governing equation for mass transfer throughout the µT-SOFC. The diffusion and convection model applies the law to gases in the anode and anode gas channel separately to the cathode and furnace chamber. The model accounts for free molecular diffusion and Knudsen diffusion. The latter accounts for interactions between the gas molecules and pore walls within the tortuous electrodes. The addition of Knudsen terms is therefore only applied to the electrode domains. Knudsen effects become significant when the mean free path of the species is larger than the pore size. Oxygen ion diffusion is neglected in this model meaning hydrogen reduction is not proportional to oxide ion concentration. The mass balance is therefore given by:

$$\nabla J_A + \rho(u \cdot \nabla)\omega_A = R_A \tag{83}$$

where J is the mass flux [$kg.m^{-2}s^{-1}$)], ρ is the density [$kg.m^{-3}$], and ω is the mass fraction [dimensionless]. Three mass transport models, the Fick's model (FM), Stefan-Maxwell Model (SMM), and dusty-gas model (DGM) are reasonable approximations for simulating mass transfer within the μT-SOFC. The DGM is the best approximation for all operating conditions and accounts for Knudsen diffusion, which describes interactions between the pore wall and the fluid. The mass flux is given by:

$$J_A = -\left(\rho D_A^{eff} \nabla \omega_A + \rho \omega_A D_A^{eff} \frac{\nabla M_n}{M_n} - \rho \omega_A \sum_k \frac{M_A}{M_n} {D_k}^m x_k + {D_A}^T \frac{\nabla T}{T}\right) \quad \textbf{(84)}$$

where D is the diffusion coefficient [m^2s^{-1}], M is the molar mass [$kg.kmol^{-1}$], and the molecular diffusion coefficient is given by:

$$D_A^m = \frac{1 - \omega_A}{\sum_{k \neq A} \frac{x_A}{D_{AB}}} \quad \textbf{(85)}$$

M_n , the average molecular mass, is defined by:

$$M_n = (\sum_i \frac{\omega_A}{M_A})^{-1} \quad \textbf{(86)}$$

For gas pressures up to 10 atmospheres at moderate to high temperatures, the binary diffusion coefficients of a binary gas mixture A and B can be estimated from the empirical Fuller, Schettler and Giddings relation in the anode and cathode furnace gas channel [291]:

$$D_{AB} = \frac{1\text{x}10^{-7} T^{1.75} \left(\frac{1}{M_A} + \frac{1}{M_B}\right)}{P \left(V_A^{1/3} + V_B^{1/3}\right)^2} \quad \textbf{(87)}$$

where V is the diffusion volume of a given molecule [m^3], P is the pressure [Pa], T is the operating temperature [K], M is the molecular mass [$g.mol^{-1}$] and τ is the tortuosity [dimensionless]. The values for V_A of the molecules of interest are given in Table 4.6.

Table 4.6 - Fuller diffusion volumes.

Molecule	Diffusion Volume [$m^3.mol^{-1}$]
H_2	$6.12x10^{-6}$
H_20	$1.31x10^{-5}$
O_2	$1.63x10^{-5}$
N_2	$1.85x10^{-5}$

The values of the binary diffusion coefficients of molecular pairs given in Table 4.7 are calculated at the standard operating temperature and pressure of 1023 K and 101.325 kPa.

Table 4.7 - Binary diffusion coefficient.

Molecular Pair	D_{AB} [$m^2.s^{-1}$]
H_2:H_2O	$7.83x10^{-5}$
H_2:N_2	$6.72x10^{-5}$
H_2:O_2	$2.23x10^{-5}$
O_2:H_2O	$2.27x10^{-5}$
N_2:H_2O	$2.23x10^{-5}$
O_2:N_2	$1.78x10^{-5}$

The DGM uses an effective diffusivity, using the Knudsen diffusion coefficient:

$$D_A{}^K = \frac{97}{2} d_{pore} \sqrt{\frac{T}{M_i}} \tag{88}$$

where d_{pore} is the electrode pore diameter [m], T is the temperature [K] and ε is the porosity. The Knudsen coefficient was combined with the binary diffusion coefficients seen in (87), in a weighting equation to get an effective diffusion coefficient for mass transport within the pores:

$$D_A^{eff} = \frac{\varepsilon}{\tau} \left(\frac{1}{D_{AB}} + \frac{1}{D_A{}^K}\right)^{-1} \tag{89}$$

4.5.4 Conservation of Charge

The charge balances are conducted in the electrochemical model. For the porous electrode layers, a current is generated due to the consumption and production of the electrons at the cathode and anode, respectively. Therefore, the change in the electric current density is given by:

$$\nabla I_s = \sum_x i_{v.x} = \nabla(\sigma_s \nabla \phi_s) \quad \textbf{(90)}$$

The change in ionic current density has the same form as the change in electron current density and is given by:

$$\nabla I_I = \sum_x i_{v.x} = -\nabla(\sigma_I \nabla \phi_I) \quad \textbf{(91)}$$

where σ is the electric/ionic conductivity [S.m^{-1}], Φ is the electric/ionic potential [V], and I is the current [A]. Although the anode and cathode areas of the SOFC are modelled separately, an ionic charge balance can be done for the electrolyte:

$$\nabla I_I = -\nabla(\sigma_I \nabla \phi_I) \quad \textbf{(92)}$$

A modified version of the Butler-Volmer equation is used involving the concentration kinetics of the gas species to calculate the local current density in the anode and cathode:

$$I_{loc} = I_o \left(\frac{C_R}{C_{Ri}} exp\left(\frac{\alpha_a F \eta}{RT}\right) - \frac{C_O}{C_{Oi}} exp\left(\frac{-\alpha_c F \eta}{RT}\right) \right) \quad \textbf{(93)}$$

where C is the concentration of a given species [mol.m^{-3}], α is the electron transfer coefficient [dimensionless], F is Faraday's constant [C.mol^{-1}], η is the overpotential [V], R is the Avogadro constant [mol^{-1}], and T is the temperature [K]. The local current density must then be multiplied by the active specific surface area of the electrode A_s[m^{-1}] to get:

$$I_{v.x} = A_s I_{loc} \quad \textbf{(94)}$$

The overpotential for the anode and cathode is given by:

$$\eta = \phi_s - \phi_l - V_{eq} \quad \textbf{(95)}$$

The voltage of the cell is calculated based on the equilibrium voltages of the anode and cathode as well as the voltage polarisation:

$$V_{cell} = V_{eq.c} - V_{eq.a} - V_{pol} \quad (96)$$

4.6 Boundary Conditions

To solve the partial differential equations (PDE), initial conditions and/or boundary conditions had to be defined, constraints to which the solutions to the equations had to adhere. For a 1st order PDE, one boundary condition had to be defined and for a 2nd order PDE, two.

- **Boundary conditions at the inlet**

At the model fuel inlet of the anode gas channel and furnace gas channel inlet, the inlet volumetric flow rate at room temperature and pressure (R.T.P) was defined:

$$Q = Q_{in} \quad (97)$$

The inflow temperature and pressure of the fluid at the model fuel inlet of the anode gas channel and furnace gas channel inlet were defined at the upstream location seen in equation (98) and equation (99), respectively.

$$T_{ustr} = T_{in} \quad (98) \qquad P_{ustr} = P_{in} \quad (99)$$

The inlet mass fraction at the anode and furnace gas channels was defined by:

$$\omega_A = w_{in} \quad (100)$$

- **Boundary conditions at the walls**

The no-slip boundary condition was applied at the walls. The walls are defined here as the boundary between the electrolyte and adjacent electrode, and between the anode functional layer-furnace gas channel interface at the current collector location. This no-slip condition meant that at the boundaries defined, the fluid velocity was equal to that of the boundary velocity, which for a fixed wall is zero defined as:

$$u = 0 \quad \textbf{(101)}$$

A thermal insulation was applied at the surfaces of the inlet of the anode and electrolyte and the outlet region of all but the model anode fuel channel outlet:

$$-n \cdot \boldsymbol{q} = 0 \quad \textbf{(102)}$$

At the same boundaries applied with the no-slip condition, a mass insulation condition was applied, meaning no mass flux occurred across the boundary:

$$-n \cdot J_A = 0 \quad \textbf{(103)}$$

An insulation boundary condition was also applied to the flow of ions and electrons to define the conservation of charge equations, as seen in equation (104) and equation (105), respectively.

$$-n \cdot \mathrm{i}_I = 0 \quad \textbf{(104)} \qquad -n \cdot \mathrm{i}_s = 0 \quad \textbf{(105)}$$

- **Boundary conditions at the outlet**

The outlet momentum boundary condition at the model anode fuel channel outlet and furnace gas channel outlet was prescribed by the pressure:

$$p = p_0 = p_{atm} \quad \textbf{(106)}$$

where the pressure was the ambient atmospheric pressure. The thermal outflow temperature condition was applied to the model anode fuel channel outlet and the furnace gas channel outlet and was defined by:

$$-n \cdot \boldsymbol{q} = 0 \quad \textbf{(107)}$$

The temperature of the outer wall of the furnace gas channel was defined as the furnace temperature:

$$T_0 = T_F \tag{108}$$

The outflow mass boundary condition was defined at the outlet of the model anode fuel gas channel inlet and furnace gas channel outlet:

$$-n \cdot \rho D_A^{eff} \nabla \omega_A = 0 \tag{109}$$

To further define the electrochemical model, the electric boundary conditions had to be prescribed to the electrodes. The anode current collector had the electric ground boundary condition, which meant the electric potential was held at zero along the boundary:

$$\phi_s = 0 \tag{110}$$

The cathode electric potential shown in (111) was held at the cell potential, V_{cell}:

$$\phi_{\mathbf{s}} = V_{cell} \tag{111}$$

4.7 Solver

Four stationary study steps were used, the first solved the conservation of charge, the second and third solved the conservation of momentum on the anode side and cathode side, respectively. The fourth solved for all physics, using multiphysics coupling features, reacting flow and temperature coupling. These features coupled the expressions for temperature, pressure, density, concentration and velocity between modules. Each study step used a direct stationary solver. COMSOL Multiphysics has several direct solvers to choose from, ranging from fastest to slowest: MUMPS, PARDISO and SPOOLES. The PARDISO solver was used for the model due to being more robust than the MUMPS solver at the expense of a slower computational time. Regardless of the direct solver used, the model results should not be affected by the choice of the solver. The physical phenomena were fully coupled, meaning that the physical equations were solved simultaneously by the PARDISO solver, using Gaussian elimination. The tolerance of the model was set to 0.001 meaning that the maximum error of the model results would be no greater than 0.1%.

Chapter 5 Single Cell Modelling and Experimental Validation[1]

This chapter details the effect of anode current collector position, number and material on µT-SOFC performance. Calibration is performed to identify a set of operating conditions that isolates the ohmic effects of varying current collector configuration on cell performance. The state-of-the-art central silver current collector is defined as a baseline for comparison. Electrochemical performance testing of cells with 3 and 5 anode current collectors is conducted to give insight on the effects of current collector position and the number of current collectors. CFD and mathematical models are developed to give insight into the physics behind the observed change in cell performance with varying current collector designs.

5.1 Baseline & Calibration

The tubular fuel cell as received was set up in the state-of-the-art style with a central anode connection as described in Chapter 3. To determine the effects of varying the fuel flow rate on performance, a calibration was made, decreasing fuel flow rate in 10 $ml.min^{-1}$ increments between 230 $ml.min^{-1}$ and 170 $ml.min^{-1}$ as seen in Figure 5.1. Given that the aim of the study was to determine the effects of current collector position and number of current collectors on performance, it was important to operate the fuel cell in such a way that any changes in setup could be ascribed to a change in ohmic effects, rather than mass transport effects. The booster unit (described in Section 3.3.4) used for cell testing had a maximum rating of 25 A, thus determining the maximum current density that the fuel cell could operate at which for the active area available with a single current collector position was 1.27 $A.cm^{-2}$. At this maximum, the fuel consumption rate at 100% fuel utilisation would be 176 $ml.min^{-1}$ as seen in Table 5.1.

[1] This chapter uses model parameters determined as part of a collaborative work published in a co-written paper detailed in the text. The parameters were estimated by fitting (which I did not conduct) to empirical data which I produced. Any work not conducted by myself has been referenced appropriately in the text.

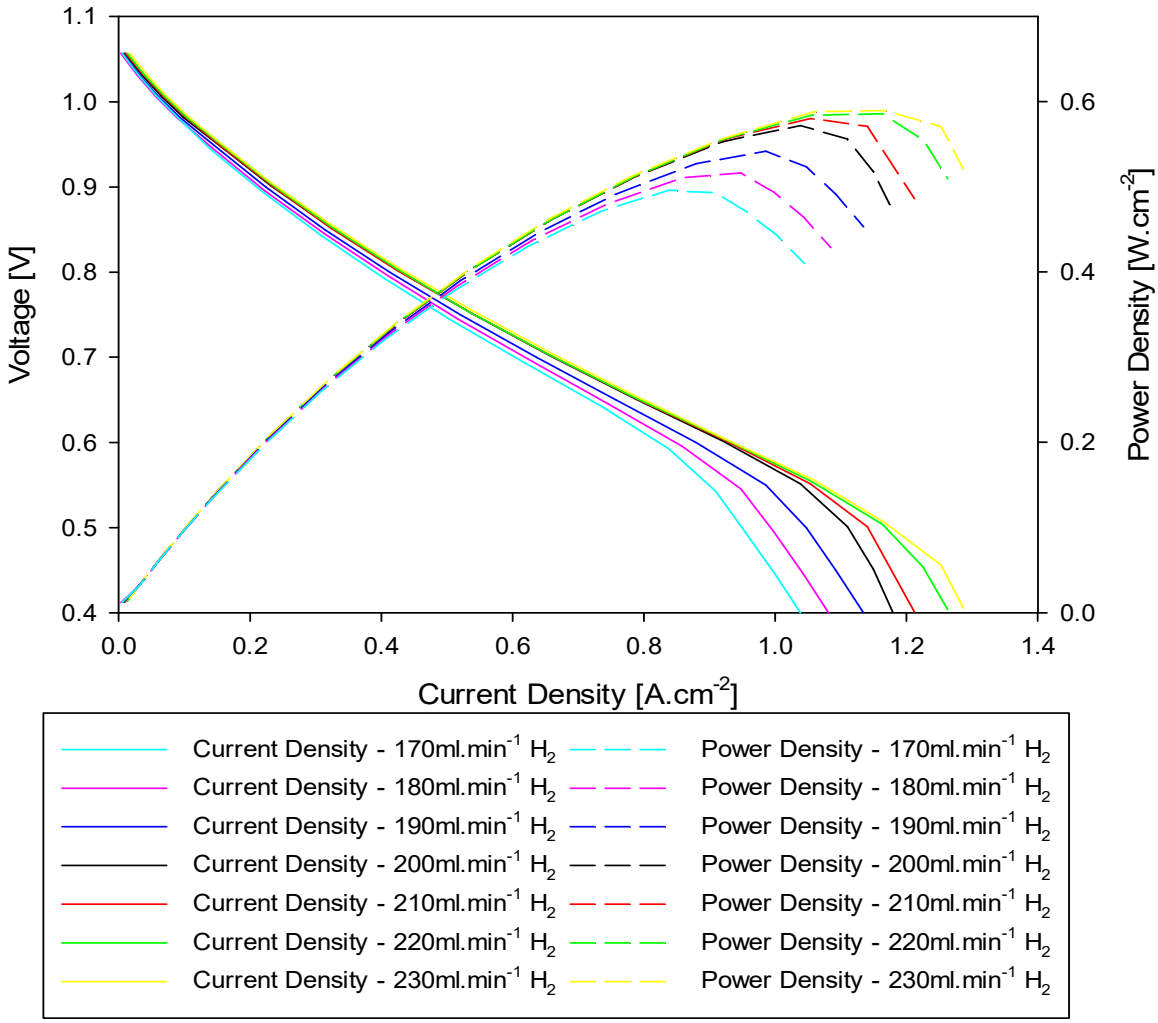

Figure 5.1 - Hydrogen flow rate calibration polarisation plots between 170 ml.min^{-1} and 230 ml.min^{-1}.

Table 5.1 - Fuel utilisation for typical operating current density.

Current Density [A.cm^{-2}]	Total Current [A]	Fuel Flow Rate for 100% F.U [ml.min^{-1}]	F.U at 200ml.min^{-1} H_2 [%]
1	19.6	138	69
1.05	20.6	145	72.45
1.1	21.6	152	75.9
1.15	22.5	159	79.35
1.2	23.5	166	82.8
1.25	24.49	172	86.25
1.27	25	176	88

The polarisation data acquisition began at the higher flow rate first, so that any degradation from fuel starvation that may occur during the low flow rate of 170 ml.min^{-1} would not affect the performance of subsequent potential sweeps, assuming that the maximum current density could be achieved. The current density and power density values at 0.7 V did not vary significantly and were within 5.6% of each other across the whole range of flow rates as seen in Figure 5.2. The fuel utilisation at 0.7 V differed by 10.98% from the highest fuel utilisation of 50.3% occurring at the lowest flow rate. If the fuel cell was operated at this potential there would be little reason to operate at the higher range of flow rates. When operated at the peak cell power at an operating potential of 0.55 V, the divergence of current density values increased to 15.2% with a 10.29% difference in the fuel utilisation across the range of flow rates. The highest value of fuel utilisation was 73.8%. At 0.4 V, corresponding to peak current density, the divergence in current density across the flow rate range increased to 20.7%, with the peak value increasing by 22.9% from 1.05 A.cm^{-2} at 170 ml.min^{-1} to 1.29 A.cm^{-2} at 230 ml.min^{-1}. A 7.6% difference in fuel utilisation was observed across the fuel flow rate range. At the lowest flow rate of 170 ml.min^{-1} the fuel utilisation was 84.8% while at 230 ml.min^{-1} the fuel utilisation was 77.19%.

The increasing divergence of the polarisation plots at a current density of around 0.85 A.cm^{-2} indicated the onset of starvation. Past this point, the current produced would not be independent of fuel flow rate, for example, operating at peak power density and peak current density. At 0.7 V the current density reached a plateau at 200 ml.min^{-1} of H_2, therefore, this flowrate would be the minimum flow rate for studying ohmic effects at this potential. While the fuel utilisation was low, these are the requirements for R&D in this case and would not be flow rate for a technically optimised cell study.

The increase in peak current density (observed at an operating potential of 0.4 V in this study) with an increase in fuel flow rate beyond 230 ml.min^{-1} would begin to diminish and finally plateau as the fuel cell tends towards the limit at which the electrodes can consume the fuel. Increasing the fuel flow rate beyond that point would result in lower fuel utilisation (<77.2% at 0.4 V) and would no longer improve the instantaneous cell performance. However, the increase in fuel could be useful to minimise degradation, providing momentum to push reaction products (steam) out of the cell. Fuel recycling could be implemented to further improve overall fuel conversion. Lowering the fuel flow below 170 ml.min^{-1} would result in an increased fuel utilisation (>84.4% at 0.4 V) and starvation beyond that. While operating at high fuel utilisation gives a high fuel conversion efficiency, the

reaction products will not be removed effectively, particularly in the latter parts of the cell and might promote degradation of the anode through mechanisms such as nickel volatisation, re-oxidation and even cell fatal failure. That is unless additional gasses are fed (such as inert gasses) to aid removal of the reaction products (steam). The latter parts of the cell will have a lower concentration of fuel and so will not perform as well as if a lower fuel utilisation was used. This results in a more inhomogeneous current distribution along the cell length.

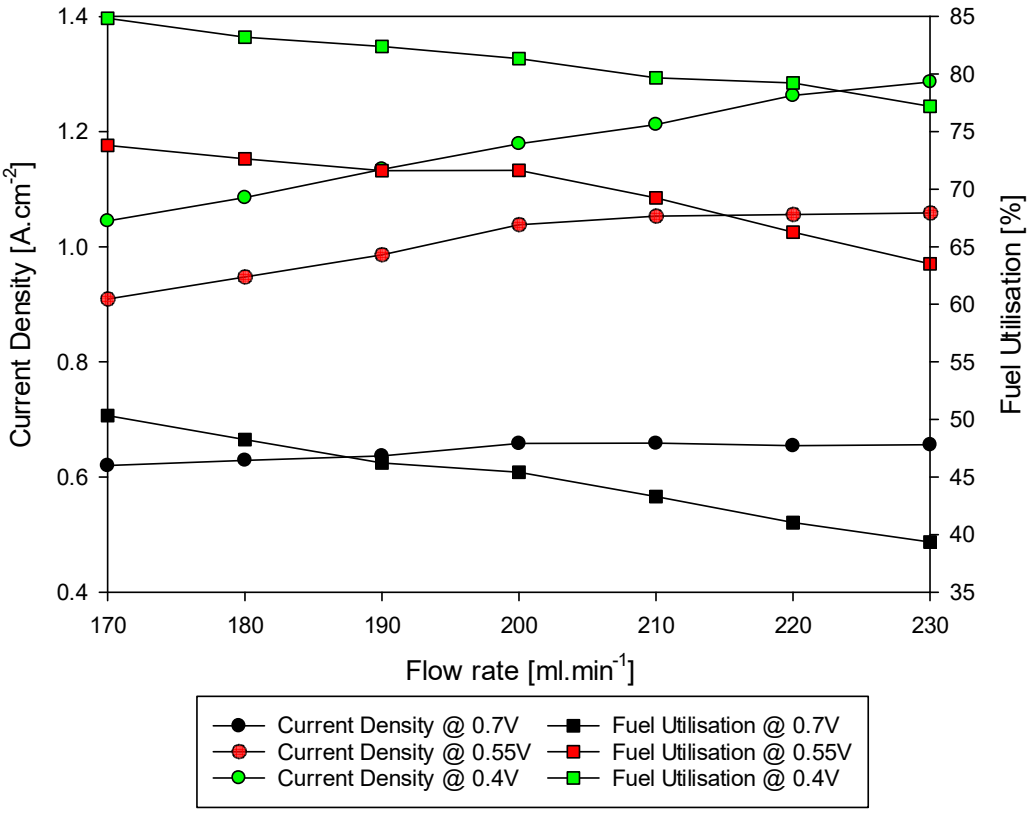

Figure 5.2 - Hydrogen flow rate versus current density and derived fuel utilisation.

Torrell and Slodczyk et al. [173,179] conducted performance and degradation studies on cells very similar to the ones used in this study. The authors operated the µT-SOFC on 200 ml.min^{-1} of H_2 with a fuel utilisation of 40, 60 and 80%, observing degradation rates of 0.07, 0.25 and 0.89 mV.h^{-1}, respectively. They suggested operating at low fuel utilisation but high total flow rate. To achieve this they used the inert carrier gas Argon to test at 80% fuel utilisation, but with a total flow rate of 300 ml.min^{-1} observing a degradation rate of 0.21 mV.h^{-1}, over four times lower than with H_2 alone. To maximise the cell performance, minimise fuel usage, while protecting the cell at operating potential in the range OCV to O.4 V, it was decided to operate the cell at 200 ml.min^{-1} of H_2. At the

peak current density at 0.4 V, the fuel utilisation was 81% and at the typical operating potential of 0.7 V would be approximately 66%.

Setting up and testing of fuel cells in a research environment is typically a multi-stage process that requires skilled manual labour. This combined with the variance of the cells as received can lead to difficulties in reproducibility. To obtain a reliable baseline for interconnect optimisation, multiple cells were tested to receive a robust result, giving the average polarisation and power density plots seen in Figure 5.3. A 10 ml.min^{-1} flow of nitrogen was added to the fuel as a reference gas for GC analysis (which was never eventually conducted). The average current density at 0.7 V was 0.83 A.cm^{-2} and the average peak power density was 0.65 A.cm^{-2}. The largest error term was ±88 mΩ.cm^2 at 0.7 V, 11% of the average value. The ASR estimated from the gradient of the polarisation plot was 0.78 Ω.cm^2 calculated within the linear ohmic region [22]:

$$\frac{dV}{di} = ASR = 0.78\ [\Omega.cm^2] \quad \textbf{(112)}$$

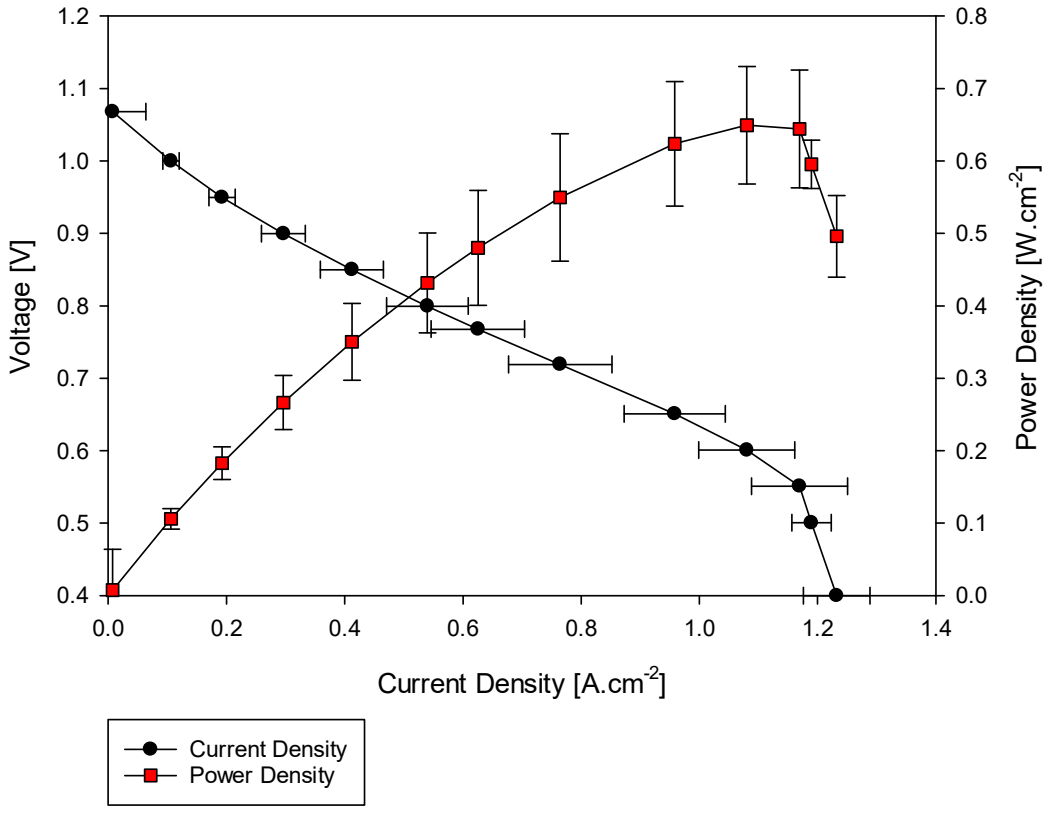

Figure 5.3 - Average IV and power curve at 750°C and flow of 200ml.min^{-1} H_2 and 10ml.min^{-1} N_2.

A cell test was then conducted to determine whether the addition of 10 ml.min^{-1} nitrogen reference gas had any effect on cell performance. The test results are shown in Figure 5.4. The current density with 200 ml.min^{-1} H_2 was 0.745 A.cm^{-2} at 0.7 V and 1.147 A.cm^{-2} at 0.5 V. The maximum current density recorded was 1.21 A.cm^{-2} at 0.4 V. The current density at a flow rate of 200 ml.min^{-1} H_2 and 10ml.min^{-1} of N_2 was 0.742 A.cm^{-2} at 0.7 V and 1.152 A.cm^{-2} at 0.5 V, the highest recorded at 1.219 A.cm^{-2}. The current densities at 0.7 V and 0.5 V were within 0.5% of each other with the difference between the measured values being greater at 0.5 V than at 0.7 V. The power density of the 200 ml.min^{-1} H_2 was 0.517 W.cm^{-2} at 0.7 V and 0.569 W.cm^{-2} at 0.5 V, the highest recorded at 0.607 W.cm^{-2}. The power density of the 200 ml.min^{-1} H_2 and 10 ml.min^{-1} of N_2 was 0.515 W.cm^{-2} at 0.7 V and 0.569 W.cm^{-2} at 0.5 V, the highest measured at 0.650 W.cm^{-2}. The power densities at 0.7 V and 0.5 V were within 0.4% of each other. The negligible difference in performance meant that the conditions used for GC (which was never eventually used) could be assumed to be a good representation of the cell performance under pure H_2.

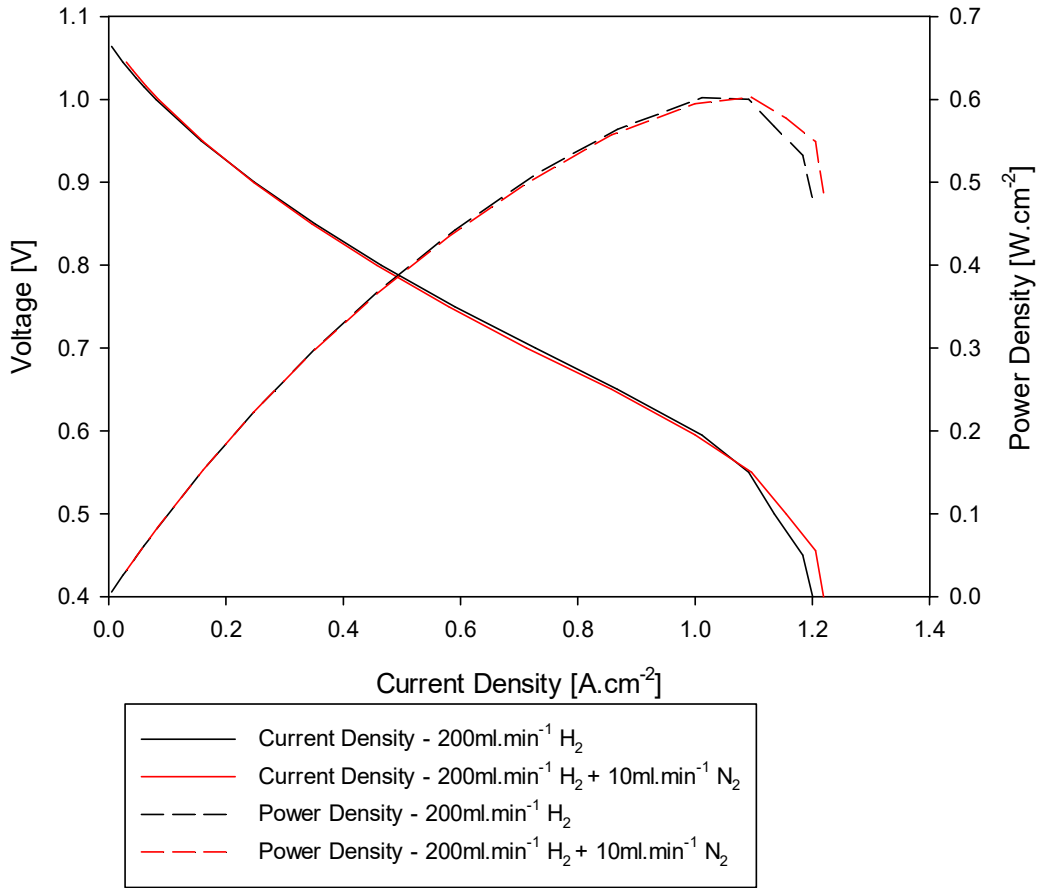

Figure 5.4 – Polarisation and power density plot at 750°C with test flow conditions and GC test flow conditions.

A further study was then conducted to determine the effect of using different flows of an inert carrier gas on cell performance. Nitrogen was favoured for its low cost and availability over Argon and its function for measurement as a reference gas for GC (which was never eventually used). An equal volumetric flow rate and thus an equimolar concentration of hydrogen and nitrogen was supplied to the cell, increasing from 170 ml.min^{-1} of H_2 and 170 ml.min^{-1} of N_2 (total flow of 340 ml.min^{-1}) to 180, 200 and 220 ml.min^{-1} of each gas. In this way, more fuel was being supplied to the cell as the flow rate increased, but respective to the carrier gas, was not becoming increasingly diluted. Similar fuel flow rates and thus fuel utilisation presented in Figure 5.5 were used for the cell in Figure 1.2 and Figure 5.2. At a given potential and flow rate of fuel, it was possible to observe the current density to determine the effects of the carrier gas. Care must be taken when comparing the results as they are from different cells and thus a relative analysis can back up the findings of a direct comparison.

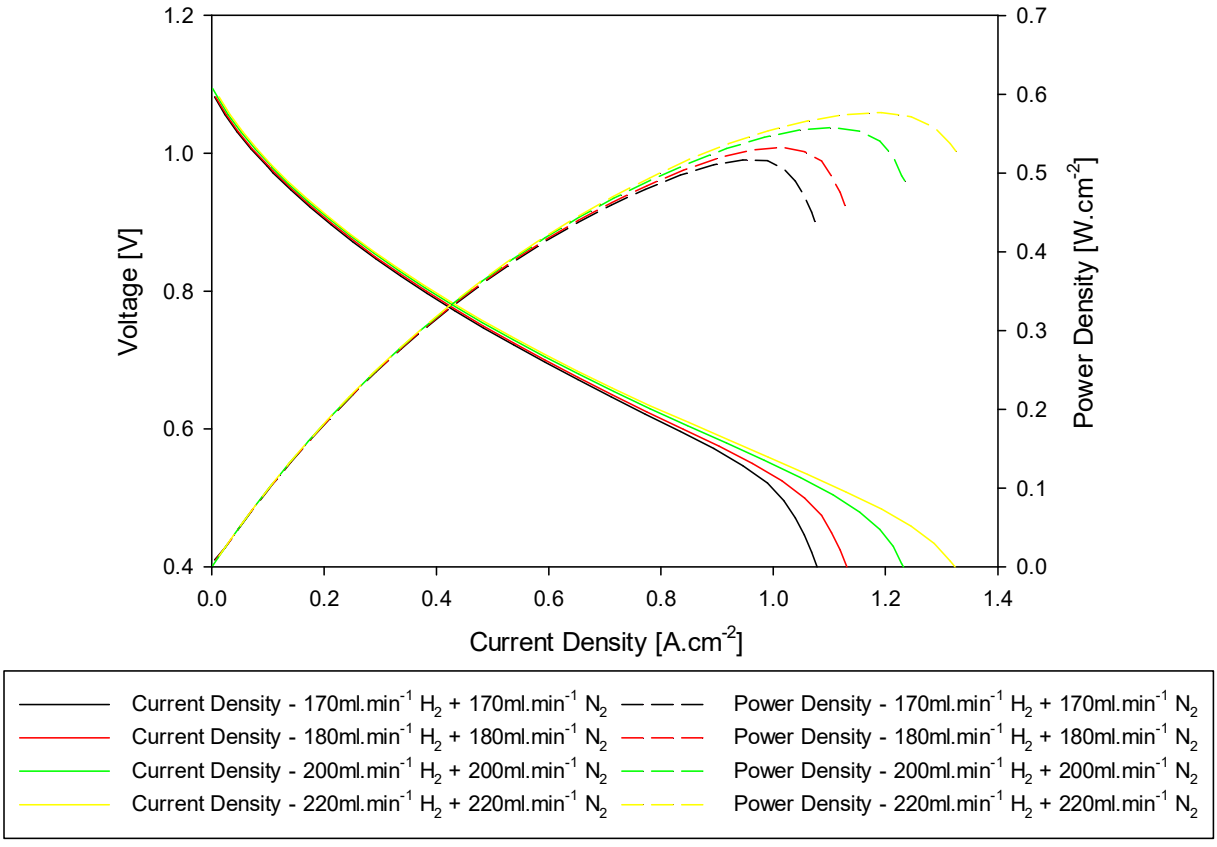

Figure 5.5 - Polarisation and power density plot with an increasing equimolar H_2 and N_2 flow rate.

The current density at 0.7 V, 0.55 V (peak power density) and 0.4 V (peak current density) were extracted at each flow rate from Figure 5.5 and presented along with the calculated fuel utilisation in

Figure 5.6. The plot indicated that increasing the total flow rate of hydrogen and nitrogen increased the cell performance at high current densities as expected.

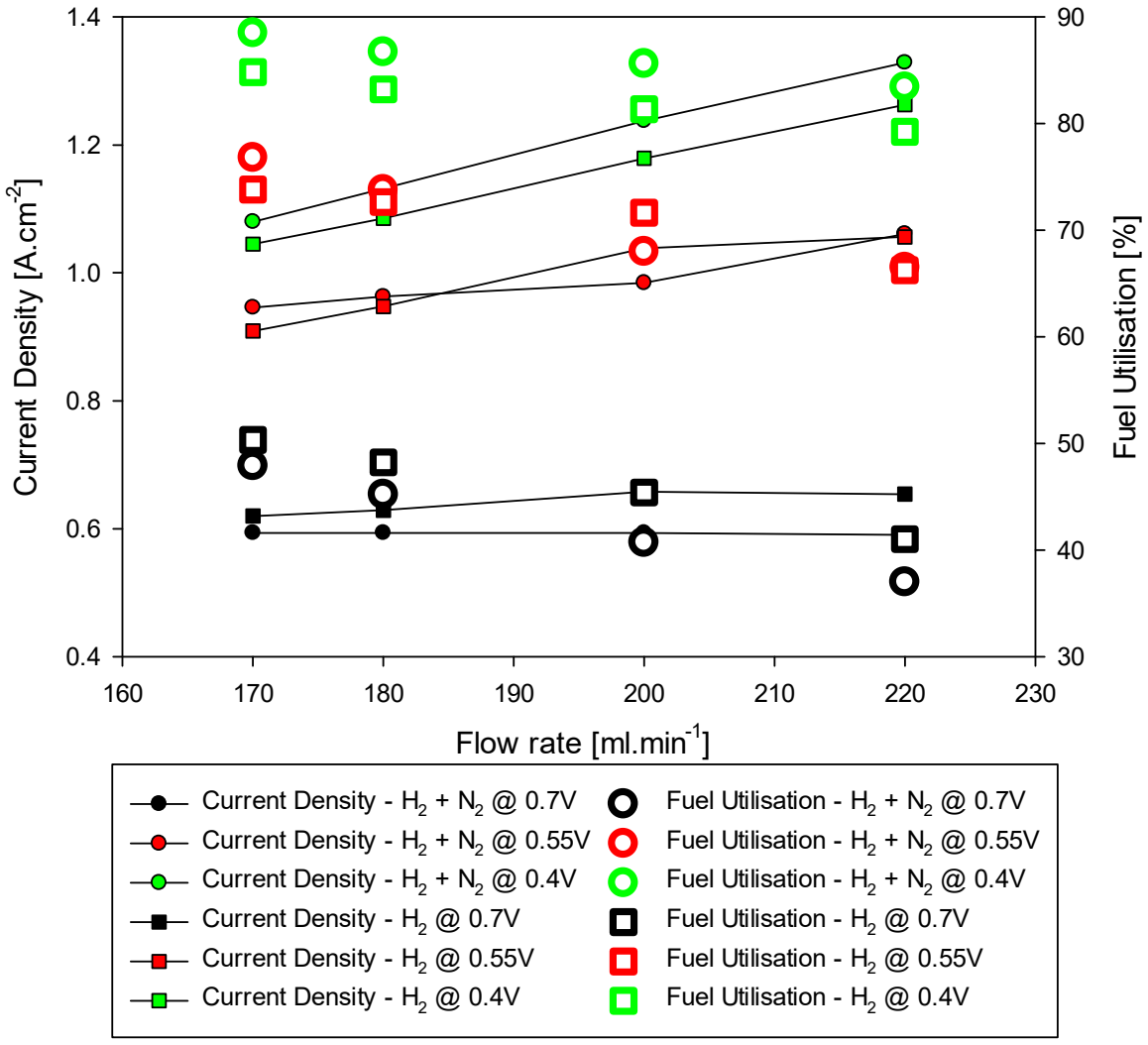

Figure 5.6 - Current density and fuel utilisation at 0.7 V, 0.5 V and 0.4 V versus hydrogen flow rate and equimolar hydrogen and nitrogen flow rate at 750°C.

At 0.7 V, within the ohmic loss dominated region, the cell fueled by solely hydrogen outperformed the cell with additional nitrogen across the flow range. Little divergence between current density values was observed and the value for all flows was 0.59 $A.cm^{-2}$ to 2d.p. In this region, the addition of nitrogen was not beneficial with respect to performance. Fuel utilisation was low, meaning fuel was in excess and little/no starvation occurs. The addition of nitrogen would likely have an effect of cooling the cell which may lead to a decrease in performance. At 0.55 V, which corresponds to the peak power, a change in trend was observed, for the 170 and 180 $ml.min^{-1}$ flows the cell with

nitrogen outperformed the H_2 only cell, whereas the inverse occurred at 200 ml.min^{-1}, converging at the highest flow rate. At an operating potential of 0.4 V, within the mass transport dominated region, the cell with the nitrogen carrier gas consistently outperformed the cell fed solely with hydrogen. The increase in pressure and turbulence from the additional mass flow of gas within the cell enhances mass transport of hydrogen to the triple phase boundaries. The increase in pressure will increase the Nernst potential which will increase the current produced at a given operating potential:

$$\Delta V = \frac{RT}{4F} \ln \left(\frac{P_2}{P_1}\right) \tag{113}$$

The current density at 0.4 V increased by 23% for the nitrogen and hydrogen mixture across the flow rate range while a 20.8% increase was observed for the cell operated on hydrogen. The polarisation and power curve for the same cell operated solely on hydrogen is seen in Figure 5.7. As can be seen, fed with solely hydrogen the OCV is lower than with the inert nitrogen flow owing to the Nernst related pressure effect aforementioned.

The hydrogen flow rate was then fixed at 200 ml.min^{-1} and increasing amounts of nitrogen were added until an equimolar mixture was achieved with 200 ml.min^{-1}, giving a combined flow of 400 ml.min^{-1}. The values of current density and power density at 0.7 V and 0.5 V for each mole fraction recorded were extracted from polarisation plots. As seen in Figure 5.8, the current density and power density at 0.7 V decreased with increasing dilution of the fuel with nitrogen. The current density decreased by 5.8% from 0.745 A.cm^{-2} at a hydrogen mole fraction of 1, to 0.704 A.cm^{-2} at a hydrogen mole fraction of 0.5 while power density decreased from 0.517 W.cm^{-2} to 0.489 W.cm^{-2}, respectively. At 0.5 V, as seen in Figure 5.9, the current density and power density increased with increasing dilution of the fuel with nitrogen, inversely to the relationship at 0.7 V. The current density increased by 2.5% from 1.147 A.cm^{-2} at a hydrogen mole fraction of 1 to 1.176 A.cm^{-2} at a mole fraction of 0.5. Power density increased by 2.1% from 0.569 W.cm^{-2} 0.581 W.cm^{-2}, respectively. This opposing trend at 0.7 V versus 0.5 V confirms that the most significant mechanism (at typical operating potentials) from adding the carrier gas was from the increased turbulence and mixing. Nernst effects described in equation (113) are observed in the low overpotential region and have little effect below 0.95 V.

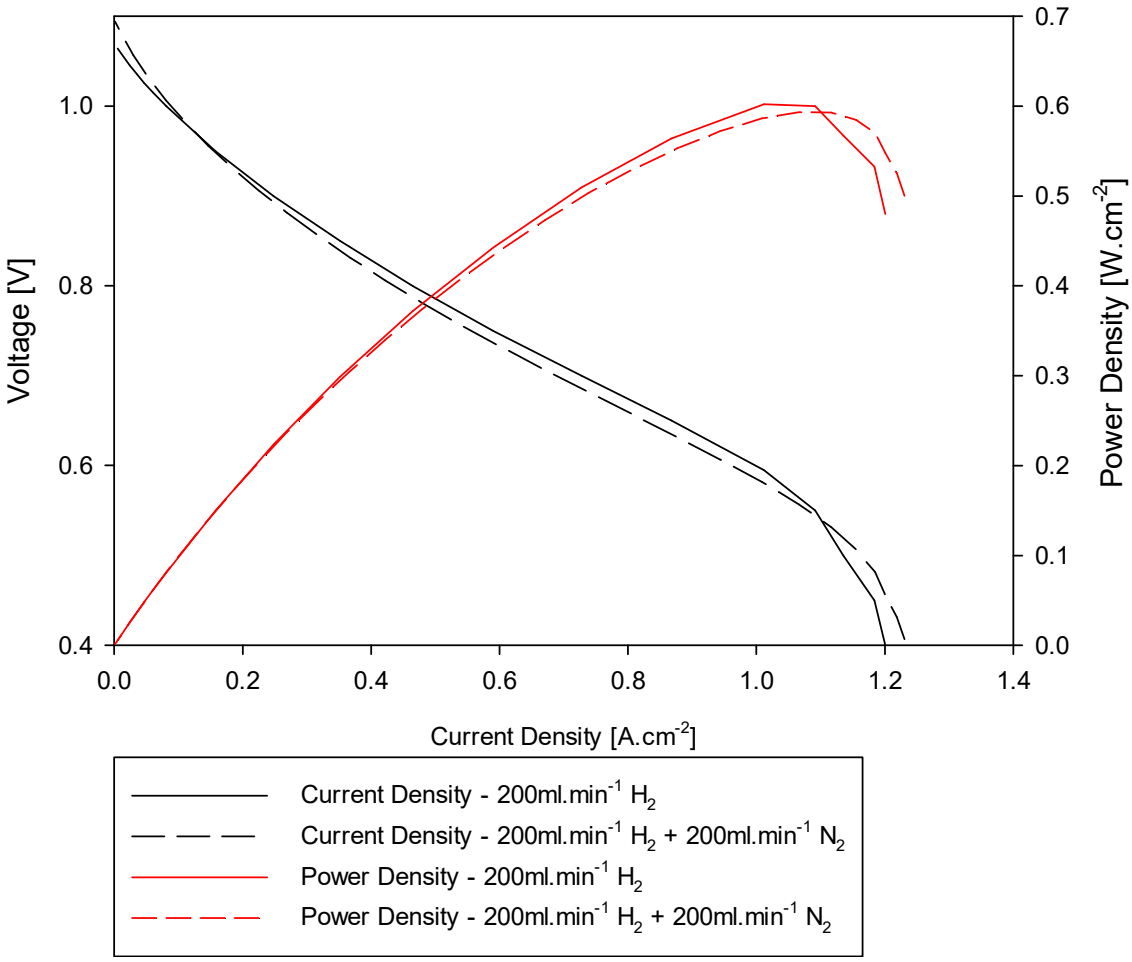

Figure 5.7 – Polarisation and power density plot of mole fraction 1 and 0.5 of H_2 in N_2.

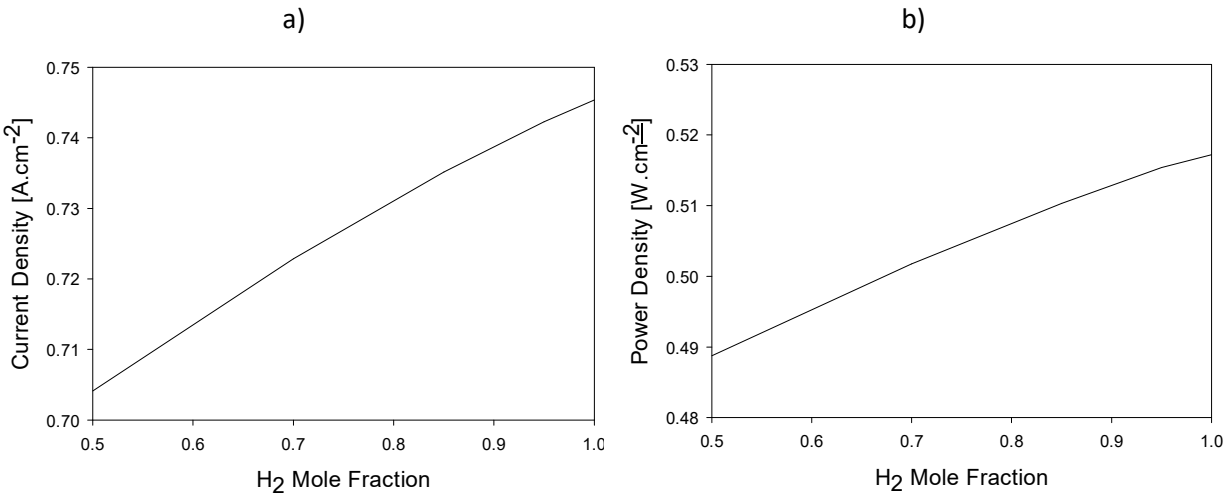

Figure 5.8 - Hydrogen mole fraction (H_2 in N_2) at 0.7 V a) versus current density, b) power density.

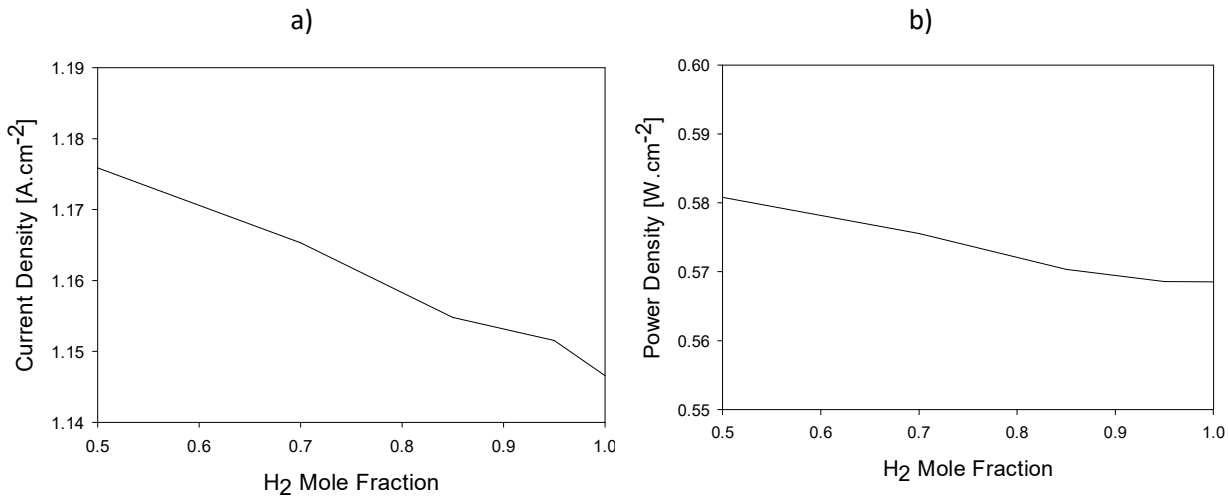

Figure 5.9 - Hydrogen mole fraction (H_2 in N_2) at 0.5 V versus a) current density, b) power density.

The Nyquist plot for the baseline central silver cell setup described in Chapter 4, operating on 200 ml.min^{-1} H_2 and 10 ml.min^{-1} N_2 with a 750°C furnace temperature is seen in Figure 5.10. Values for the ohmic polarisation, $R_{\Sigma\Omega}$, combined polarisation from the anode and cathode electrodes, R_P, and the total polarisation, R_T, are extracted and displayed in Figure 5.11. Ohmic polarisation follows a linear decrease when moving from OCV to 0.7 V and 0.5 V with the value dropping by 62.5% over the operating range. At lower operating potentials, more current is being produced and as a result, the cell temperature will increase which will lead to an increase in conductivity of the electrolyte which will cause a drop in $R_{\Sigma\Omega}$. It can be seen that the total polarisation does not follow a linear trend and shows a strong correlation to the electrode polarisation. This is due to the relative size of the ohmic versus electrode polarisation with the latter being around 2.8 times larger than the former at OCV. The total polarisation value at 0.7 V was 0.019 Ω which corresponds to an ASR of 0.38 Ω.cm^2, which is 2.2 times lower than the R_T value of 0.041 Ω at 0.5 V, indicating that the cell will operate more efficiently at 0.7 V than 0.5 V. This is due to the exponential relationship of concentration polarisation with increasing current density/cell polarisation [17]. The focus of this research is centralised around the enhancement of the ohmic polarisation and so frequency and capacitance related data was omitted.

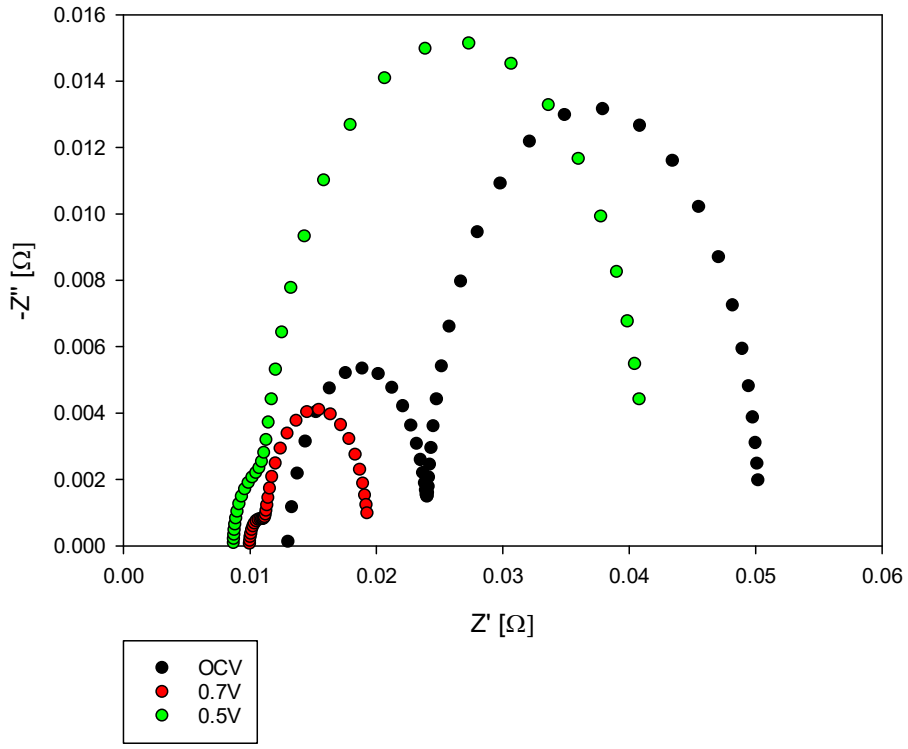

Figure 5.10 - Nyquist plot of baseline cell setup at 750°C operating at OCV, 0.7 V and 0.5 V.

The calibration study thus far has given key insights into the operating parameters, specifically the fuel, fuel flow rate and operating potential required to conduct a study on ohmic polarisation in µT-SOFCs. At 0.7 V, operating on an equimolar nitrogen and hydrogen mixture would enable a 170 ml.min^{-1} hydrogen flow for current density values independent of flow rate whereas a 200 ml.min^{-1} flow rate of hydrogen would be required for an undiluted fuel stream. Given that fuel utilisation was not a priority in this study operating on pure hydrogen was favoured over a mixture. This would also more closely replicate the real-world operation of a portable device which would require significant cost and weight to include a separate N_2 tank. The thermal gradients from using solely hydrogen stream would be more extreme given the lower flow rate of relatively cooler fuel, meaning any floors in the cell setup and interconnect design could be more easily identified. Nevertheless, a small 10ml.min^{-1} of N_2 was included as a reference gas for GC analysis (which was never eventually used and) which was already deemed to have a negligible effect on performance. Therefore the standard operating conditions used throughout the following study (unless stated otherwise) are defined as an operating temperature of 750°C with a fuel flow rate of 200 ml.min^{-1} of H_2 with 10 ml.min^{-1} of N_2.

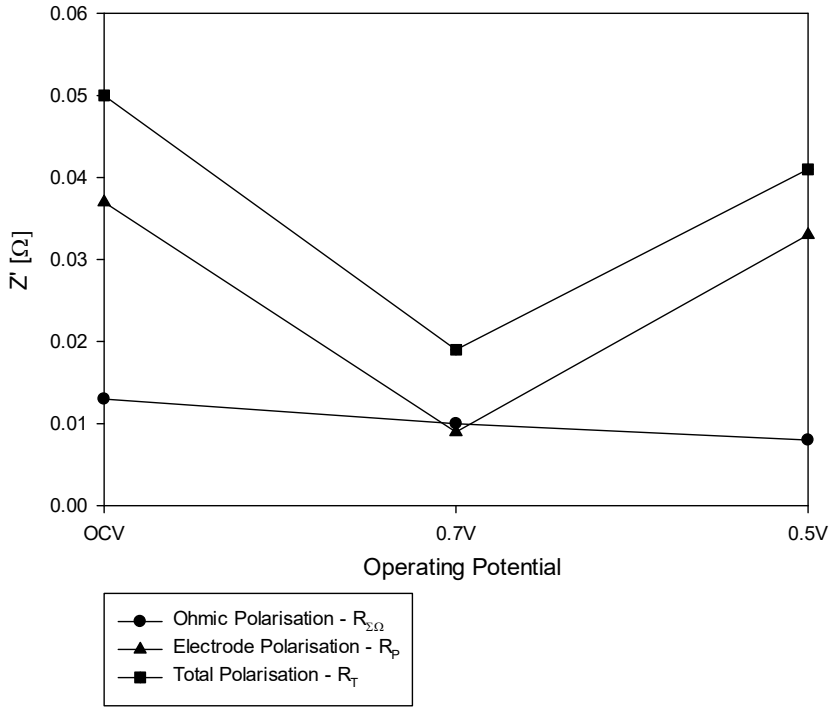

Figure 5.11 - Distribution of $R_{\Sigma\Omega}$, R_P, R_T at OCV, 0.7 V and 0.5 V derived from Figure 5.10.

5.2 Influence of Interconnect Position on Performance

To determine the effect of current collection position on performance, cells were prepared with three equidistant external anode current collectors (nodes) centred around the middle of the cathode. The schematic of the cell setup is seen in Figure 5.12. The performance of the current collector nearest the fuel inlet, cathode centre and nearest the outlet are seen in Figure 5.13 at the standard testing conditions. The OCV recorded from each connection position was near identical at 1.06 V (to 2 d.p) indicating that there were no leakages at the current collector nodes. Below 1 V a divergence began, increasing through the ohmic loss region into the mass transport region. At 0.7 V the current density of the inlet, centre and outlet were 0.45 A.cm^{-2}, 0.56 A.cm^{-2} and 0.37 A.cm^{-2}, respectively with the maximum difference between the values of 38.8%. At 0.4 V the divergence decreased slightly to 30.6%, with the current density for the inlet, centre and outlet at 0.98 A.cm^{-2}, 1.15 A.cm^{-2} and 0.84 A.cm^{-2}, respectively. Below 0.5 V the inlet and outlet curves showed a linear relationship, seemingly not incurring mass transport limitations as observed with the tailing off of the central curve. The ASR estimated by a gradient method between 0.8 V and 0.6 V from Figure 5.13 gave 0.56 Ω.cm^2, 0.44 Ω.cm^2 and 0.65 Ω.cm^2 for the cell with an inlet, centre and outlet current collector position, respectively.

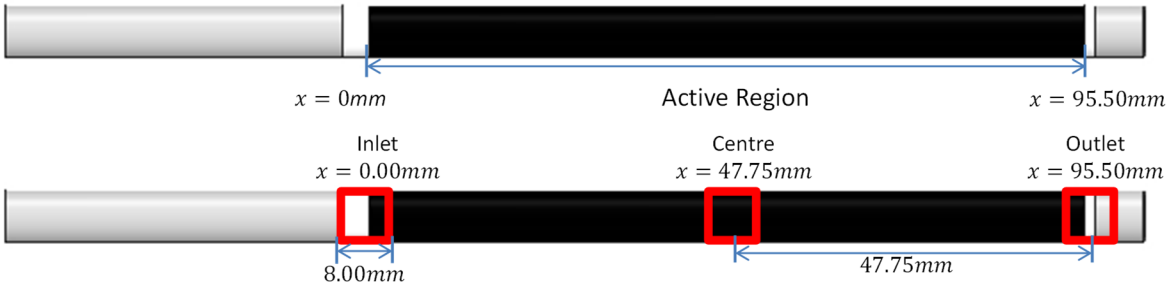

Figure 5.12 - Schematic of 3 current collector node cell at the inlet, centre and outlet of the active region.

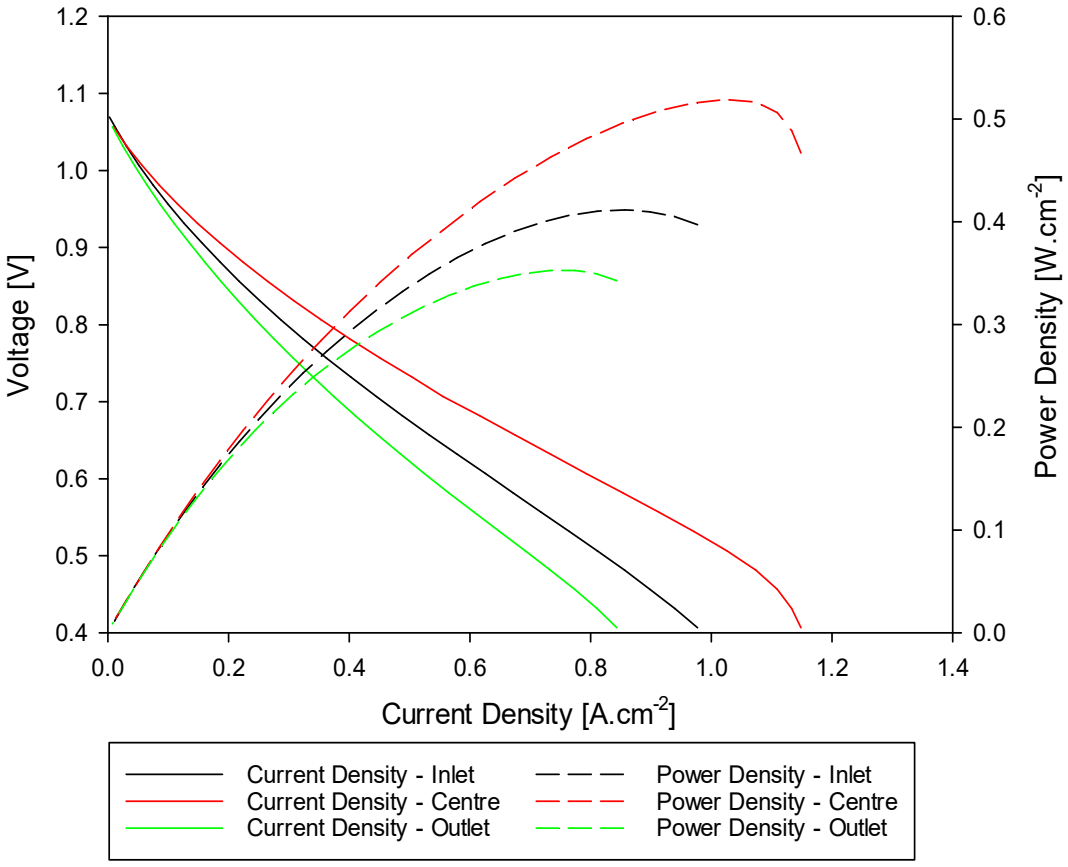

Figure 5.13 - Polarisation and power density plot for a cell with inlet, central and outlet current collection at the standard conditions of 750°C and a flow of 200 ml.min^{-1} of H_2 and 10 ml.min^{-1} N_2.

At this point, we can also observe the effect of increasing the number of current collections and the resulting loss of active area by comparing the central current collector values to those for the baseline test in Figure 5.3. The peak current density for a single central connection was 1.22 A.cm^{-2} whereas in Figure 5.13 the central current collector achieved 1.15 A.cm^{-2}, down by 5.8%. It should be noted that in the two cell setups, there were different active areas and values have been scaled accordingly. The difference was likely due to the increased probability of fuel leakage incurred as the

number of current collectors was increased. Nevertheless, making three current collector nodes to only use one would be futile, but in this instance was useful as a tool for experimental analysis.

The Nyquist plot at OCV obtained via impedance spectroscopy of the cell at each current collector position was overlaid with the fitted ECM plots seen in Figure 5.14. A good fit was observed between the model and the experimental data. Filtering was performed on the raw data to remove noise. Unless stated otherwise, the impedance data presented henceforth will be from ECM fitting of the raw data from the model developed.

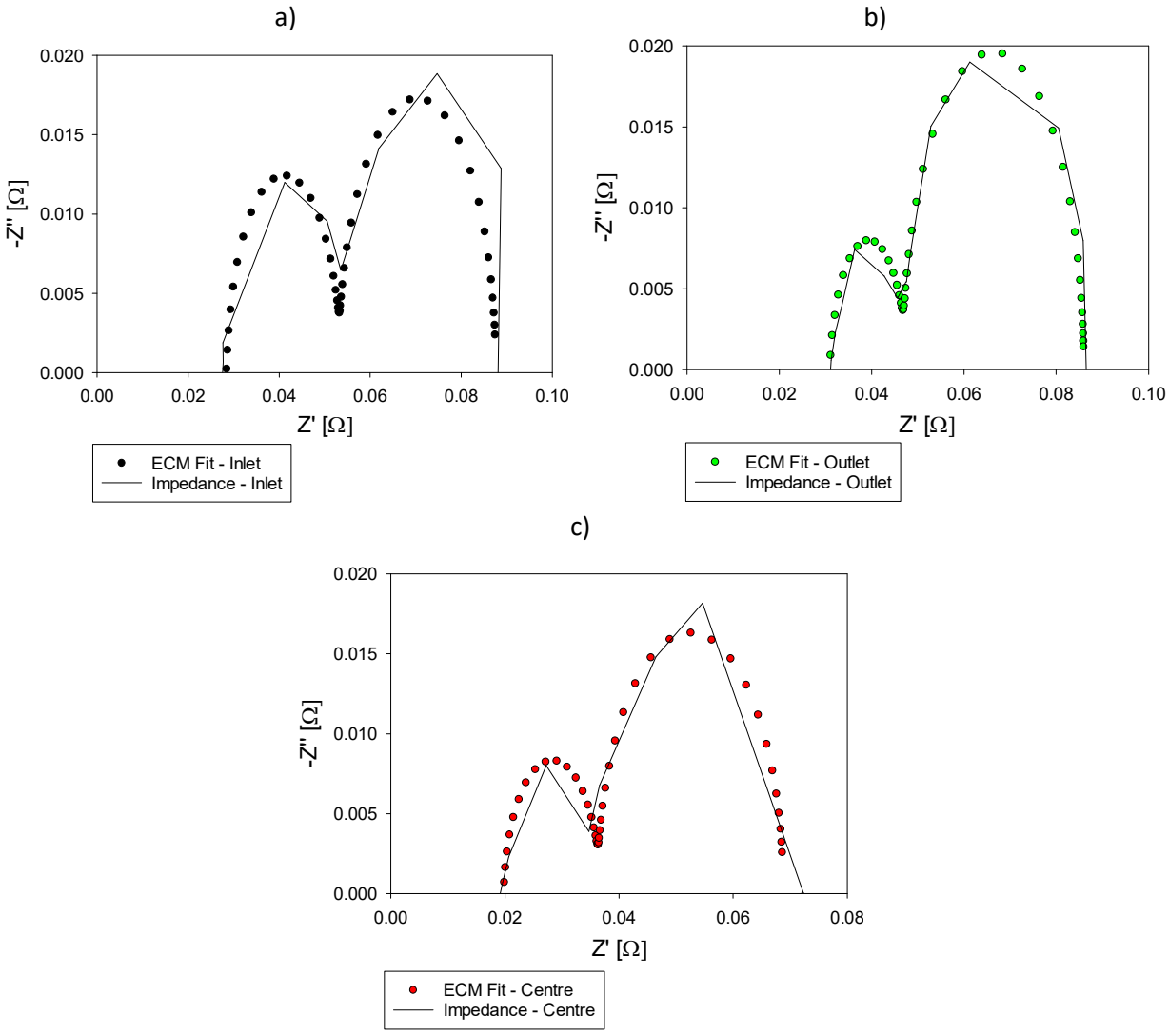

Figure 5.14 - Nyquist plot and fitted ECM plot at OCV for the current collector at the a) inlet, b) centre, c) outlet.

Figure 5.15 is a comparison of the fitted ECM Nyquist plots for the inlet/centre/outlet current collectors at OCV, 0.7 V and 0.5 V. The plots show that the central current collector consistently

outperforms the inlet and outlet current collection positions across the operating potential range given the relative position nearest to the origin (0,0).

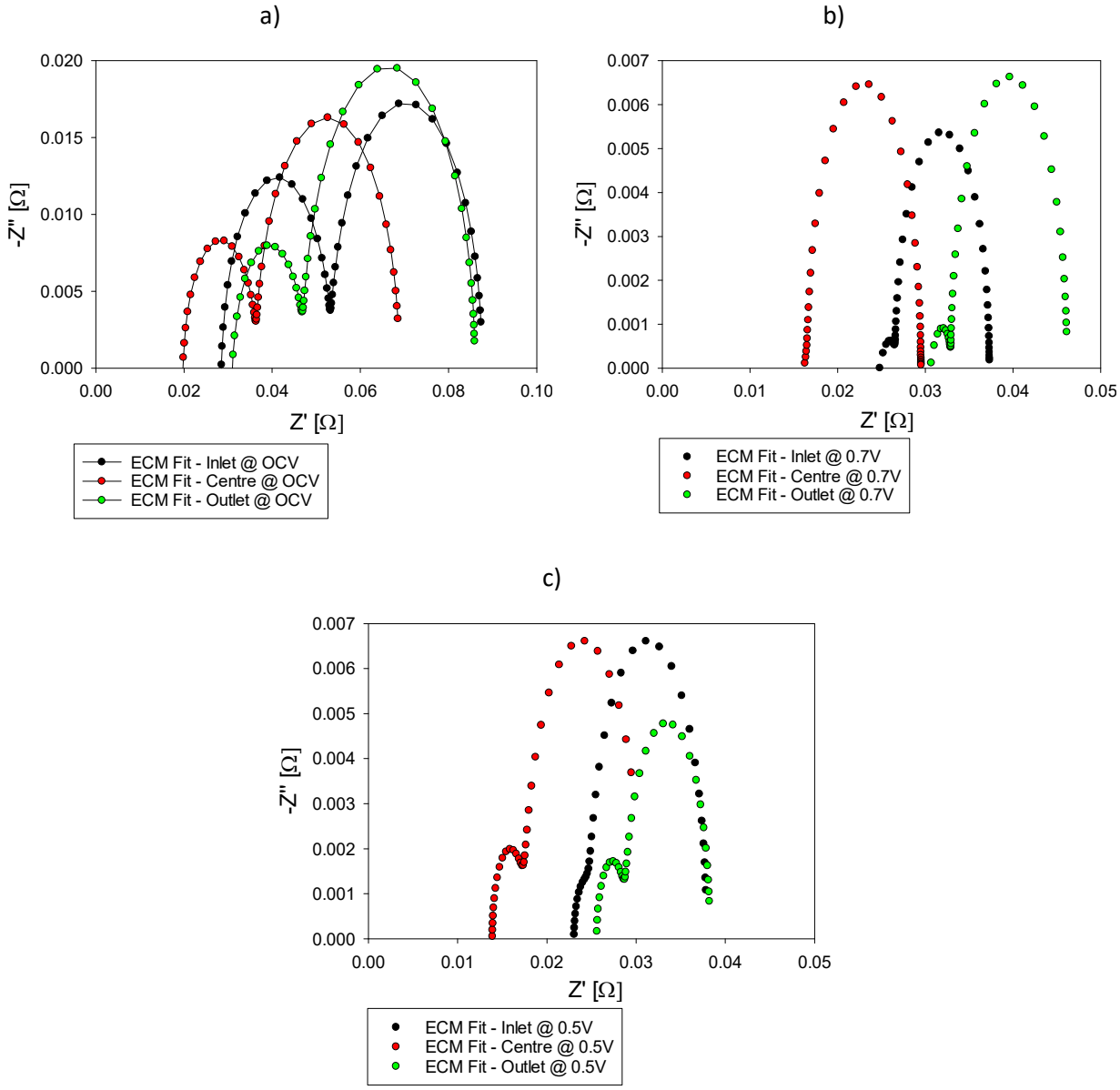

Figure 5.15 - ECM plots for a current collector at the inlet, centre and outlet at a) OCV, b) 0.7 V, c) 0.5 V.

The values for ohmic polarisation, electrode polarisation and the total resistance were extracted from Figure 5.15 and are presented at each operating potential in separate plots in Figure 5.16. As seen in a), at OCV, the total polarisation followed the trend of both the ohmic and electrode polarisation indicating a relation to the electronic and electrochemical phenomena. It should be noted that the measurements for the OCV data set were made using an applied perturbating current,

a trickle current close to zero and so the cell was not truly at OCV whereby the net current was zero. In the case of 0.7 V, b), the electrode polarisation observed a linear relationship along the cell length and the total resistance showed a correlation to the ohmic polarisation. At 0.5 V, c), the total resistance showed a strong correlation to the ohmic polarisation and a small correlation to the electrode polarisation. In both the OCV and 0.7 V cases the electrode polarisation was the lowest at the centre, whereas at 0.5 V the polarisation for the central connection was the highest.

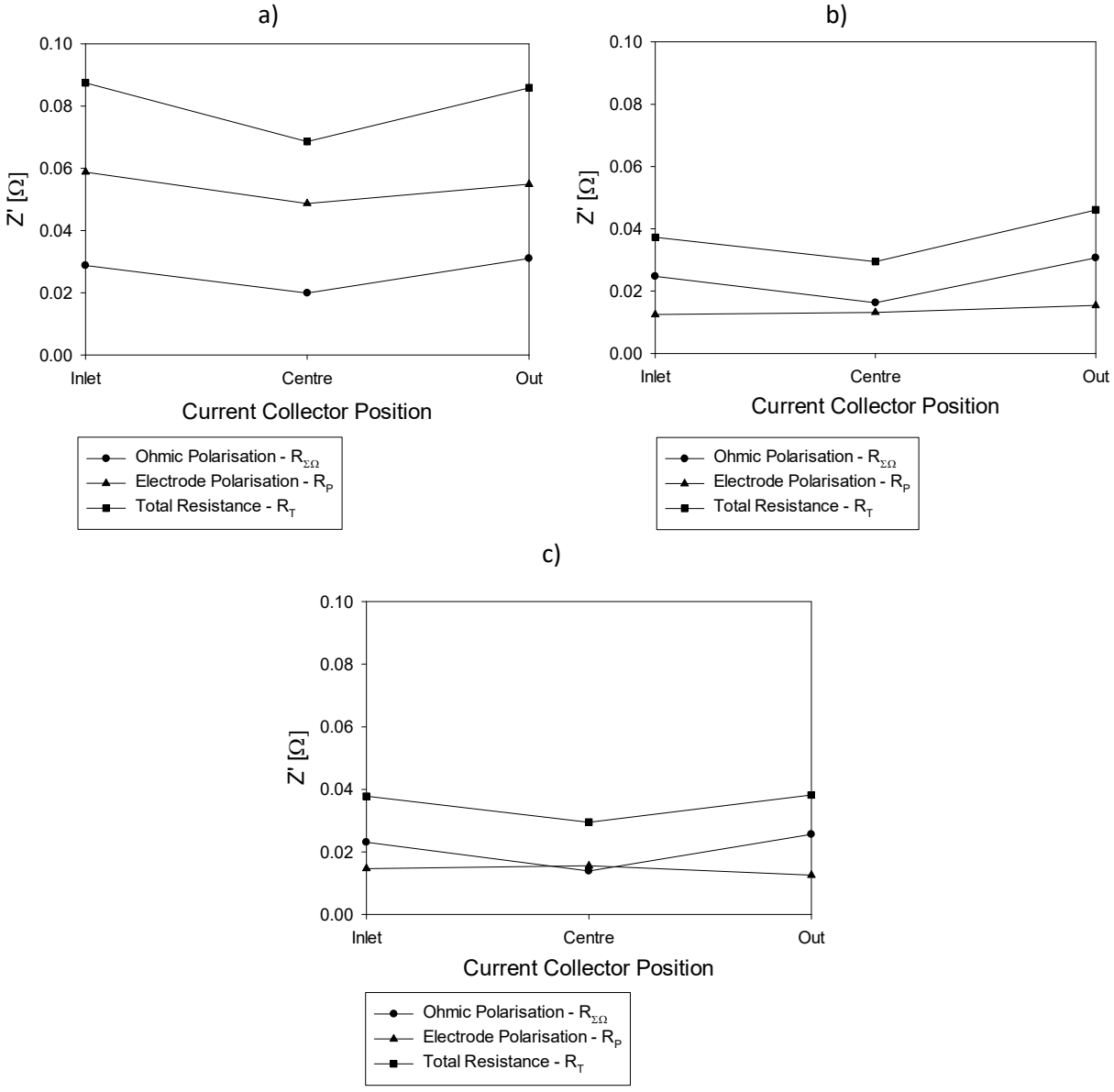

Figure 5.16 - Distribution of $R_{\Sigma\Omega}$, R_P and R_T versus current collector position at a) OCV, b) 0.7 V, c) 0.5 V.

The data extracted from Figure 5.15 is presented in another way in Figure 5.17, splitting the polarisation/resistance into separate plots, each plot comparing the effect of the operating potential

at a given current collector position. The ohmic polarisation for each current collector at all operating potentials is shown in a). At all potentials the ohmic polarisation was the lowest at the centre, followed by the inlet and then the outlet. The electrode polarisation at OCV was higher than at 0.7 V and 0.5 V for at all positions. At the inlet and central connection, the electrode polarisation was higher at 0.5 V than 0.7 V, the converse was observed at the outlet.

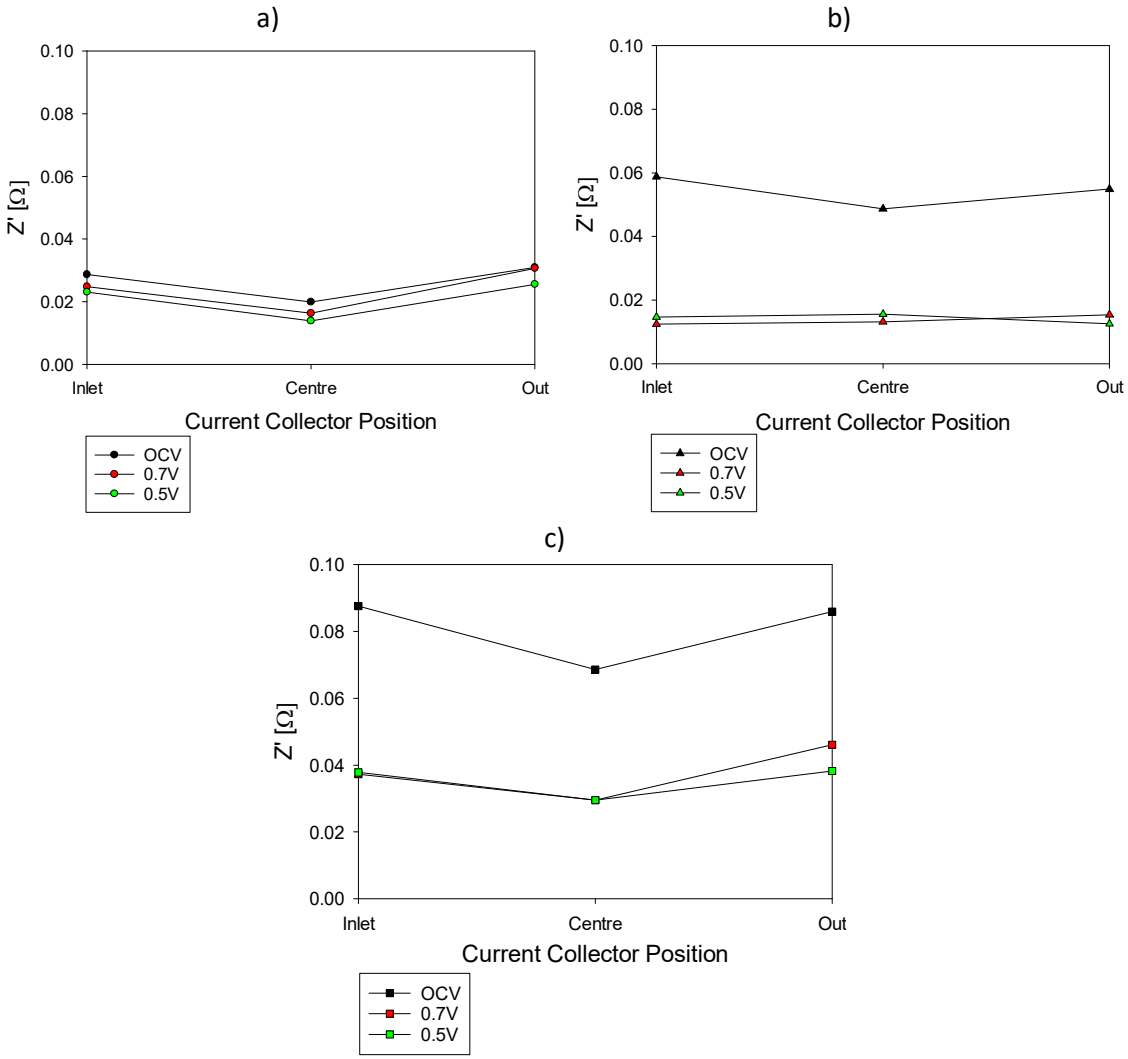

Figure 5.17 - Distribution of a) $R_{\Sigma\Omega}$, b) R_P and c) R_T versus current collector position at OCV, 0.7 V and 0.5 V.

The flow direction was reversed and the current collector position names adjusted accordingly so that the inlet current collector in the previous setup was now the outlet current collector in the flow reversed setup. This was to determine whether the quality of the individual electrode-current collector connection affected the results and to eliminate any thermal effects resulting from temperature gradients along the cell due to positioning in the furnace and from fuel preheating. As

can be seen in Figure 5.18, the trend in the performance was the same as in the original flow case seen in Figure 5.13. The difference in performance may be ascribed to the differing fuel manifolds. The original case used the injector pipe manifold at the inlet; whereas the flow reversed case used a standard 'support pipe' for the inlet which may have led to minor leakages. The small time interval (in the order of seconds) that was required for the switching of the gas supply to the manifolds may have also resulted in a loss in performance.

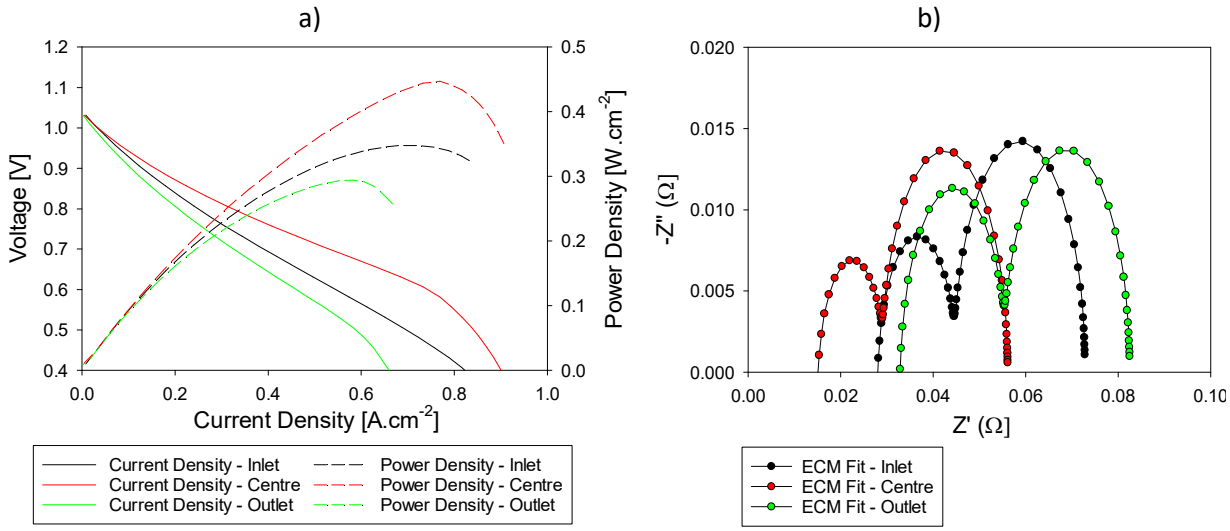

Figure 5.18 – a) Reversed flow direction polarisation and power density plot, b) ECM fit at OCV, for current collectors at the inlet, centre and outlet, at the standard conditions of 750°C and a flow of 200 ml.min^{-1} of H_2 and 10 ml.min^{-1} N_2.

To determine an optimum for the number of interconnect positions, a segmented cell setup was used as seen in Figure 5.19. Five equidistant anode nodes were created 23.875 mm apart (23.88 mm to 2 d.p), A1 being at the inlet to the active region, A3 being at the centre of the active region and A5 being at the outlet of the active region. As seen in Figure 5.20 the four cathode regions formed as a result of the segmentation were connected to a common rail. Lateral conduction paths in the cathode were minimised by using silver paste across the entire surface and by using horizontal spines of silver wire which were secured with circumferential bands of silver wire which also acted to increase hoop conductivity.

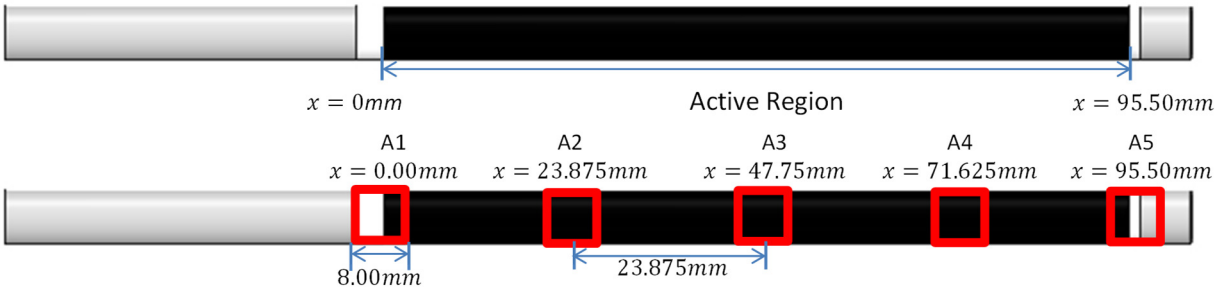

Figure 5.19 - Segmented cell schematic.

Figure 5.20 - Segmented cell.

Figure 5.21 is a plot of the current density recorded at each of the five interconnect positions during a potentiostatic hold at 0.7 V and 0.5 V at the standard conditions of 750°C and a flow of 200 ml.min^{-1} of H_2 and 10 ml.min^{-1} N_2. The current was drawn through a single node for each measurement. The data is an average of 5 cells tested at the same testing conditions. Anomalous data points that did not fit with the general trend observed from the 5 cells tested were omitted. The few anomalous results were attributed to poor electrode-current collector contacting and/or insufficient sealing of the porous joint. A non-hermetic seal was undesirable for any of the joints along the cell, however, a leak from a current collector near the inlet side of the cell had severe repercussions for the current collector and indeed anode of the latter parts of the cell which could be subjected to fuel starvation and oxidation. Oxidation on the anode side would be exacerbated by the inflow of air from the anode side due to the less positive pressure gradient radially outwards from the anode gas channel. This would cause a degradation profile along the cell with the outlet region degrading at a higher rate than the fuel-rich inlet region.

A degradation profile was observed in early cell tests when solely an inlet fuel manifold was used and the outlet region of the cell was left open to spontaneously combust exhaust gases in the furnace. In this case, the degradation rate was further increased by the larger thermal gradient induced by the

flame at the fuel cell tip. Nevertheless, the degradation was so severe as to completely deactivate current collectors A4 and A5 within hours of testing. The flow rate of fuel was increased until such effects were minimised but this led to poor fuel utilisation with at least 50% more fuel required. This undesired degradation profile, while insightful, was not useful for the study of outright performance of current collector position on cell performance and so the use of an exhaust manifold as detailed in the experimental methodology was mandatory.

The central A3 node was the best performing. The current density was 0.169 $A.cm^{-2}$ at 0. 7 V and 0.295 $A.cm^{-2}$ at 0.5 V. The adjacent position on the inlet side, A2, was the next best performing. The current density was 0.159 $A.cm^{-2}$ at 0.7 V and 0.288 $A.cm^{-2}$ at 0.5 V, a decrease of 5.9% and 2.4%, respectively, versus A3. The next best performing was A4, the node adjacent to A3 but on the outlet side. The current density at 0.7 V was 0.156 $A.cm^{-2}$ and 0.286 $A.cm^{-2}$ at 0.5 V, which was 7.7% and 3.1% lower than A3, respectively. The current density at 0.7 V and 0.5 V was 1.9% and 0.7% lower, respectively, at A4 versus A2. The current density at 0.7 V was 0.150 $A.cm^{-2}$ at A1 and 0.135 $A.cm^{-2}$ at A5, 11.2% and 20.1% lower than A3, respectively.

The current density at 0.5 V was 0.271 $A.cm^{-2}$ at A1 and 0.241 $A.cm^{-2}$ at A5, 8.1% and 18.3% lower than A3, respectively. The difference between A1 and A5 at 0.7 V was 10.5% and was 11.7% at 0.5 V. The difference between A2 and A4 at 0.7 V was 1.9% and was 0.7% at 0.5 V. The two largest error terms at 0.7 V are for the A4 and A5 connection at ±0.016 $A.cm^{-2}$, an error of less than 10%. The two largest sources of error at 0.5V were at A3 and A2 at ±0.033 $A.cm^{-2}$ and ±0.026 $A.cm^{-2}$, respectively. This corresponded to an error of less than 9% and 11% at 0.5V for A3 and A2. This study agreed with the findings of the 3 node cell setup in that a current collector at the centre of the cell was the optimal positon. Indeed, the current collector should be placed as close to the centre of the active region as possible, favouring positioning in the inlet portion of the cell.

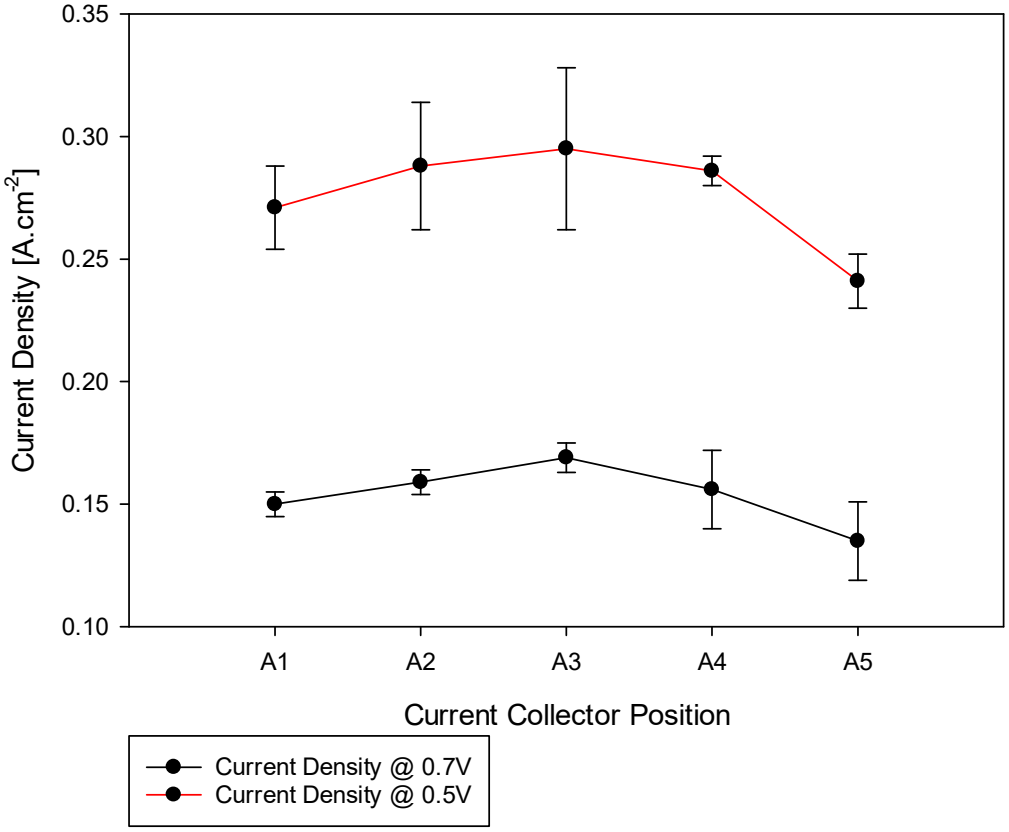

Figure 5.21 - Current density at potentiostatic conditions versus current collector position at the standard conditions of 750°C and a flow of 200 ml.min^{-1} of H_2 and 10 ml.min^{-1} of N_2.

5.3 Influence of Number of Interconnect Positions on Performance

The main purpose of the segmented cell setup was to determine the number and position of interconnect positions for optimised performance. The five nodes resulted in 2^5 combinations of connection combinations, having single terminal, double terminal, triple terminal, quadruple terminal and a five terminal setup. A 2^5 full factorial design of experiment (DOE) was used to generate a testing sequence as seen in Table 5.2 to avoid bias during testing. A zero was ascribed to the terminal in the off position whereby the switching system had electrically isolated the current collector. A one was ascribed to a live connector through which current was passing to the measurement system. The 32 combinations led to 31 sets of tests, excluding the case where all connections were off (00000). There were five single terminal configurations as previously seen, 10 double terminal configurations, 10 triple terminal configurations, 5 quadruple terminals and 1 five terminal configuration. While the switching time of the interconnecting control system was in the order of milliseconds and the response of the cell in the order of seconds, the cell was held at OCV

for 2 minutes to stabilise and for thermal equilibrium to be reached for each run before polarisation curves or potentiostatic measurements were made.

Table 5.2 - Full factorial DOE run sequence for the segmented cell setup.

StdOrder	RunOrder	A1	A2	A3	A4	A5	Combination	Number of Positions
17	1	0	0	0	0	1	A5	1
13	2	0	0	1	1	0	A3 & A4	2
32	3	1	1	1	1	1	A1 & A2 & A3 & A4 & A5	5
18	4	1	0	0	0	1	A1 & A5	2
4	5	1	1	0	0	0	A1 & A2	2
29	6	0	0	1	1	1	A3 & A4 &A5	3
2	7	1	0	0	0	0	A1	1
16	8	1	1	1	1	0	A1 & A2 & A3 & A4	4
10	9	1	0	0	1	0	A1 & A4	2
27	10	0	1	0	1	1	A2 & A4 & A5	3
7	11	0	1	1	0	0	A2 & A3	2
1	12	0	0	0	0	0	Off	0
20	13	1	1	0	0	1	A1 & A2 & A5	3
12	14	1	1	0	1	0	A1 & A2 & A4	3
26	15	1	0	0	1	1	A1 & A4 & A5	3
14	16	1	0	1	1	0	A1 & A3 & A4	3
21	17	0	0	1	0	1	A3 & A5	2
3	18	0	1	0	0	0	A2	1
25	19	0	0	0	1	1	A4 & A5	2
5	20	0	0	1	0	0	A3	1
15	21	0	1	1	1	0	A2 & A3 & A4	3
30	22	1	0	1	1	1	A1 & A3 & A4 & A5	4
24	23	1	1	1	0	1	A1 & A2 & A3 & A5	4
9	24	0	0	0	1	0	A4	1
28	25	1	1	0	1	1	A1 & A2 & A4 & A5	4
19	26	0	1	0	0	1	A2 & A5	2
8	27	1	1	1	0	0	A1 & A2 & A3	3
6	28	1	0	1	0	0	A1 & A3	2
31	29	0	1	1	1	1	A2 & A3 & A4 & A5	4
23	30	0	1	1	0	1	A2 & A3 & A5	3
11	31	0	1	0	1	0	A2 & A4	2
22	32	1	0	1	0	1	A1 & A3 & A5	3

The values of the current density at 0.7 V and 0.5 V were averaged over the data sets, for example, the single (1) connection was an average of 5 data point and, the double (2) connection was an average of 10 data points, and so on. The data presented in Figure 5.22 is an average of the data sets of multiple cell tests with the same cell setup tested at the standard conditions of 750°C and a flow of 200 ml.min^{-1} of H_2 and 10 ml.min^{-1} N_2. The largest error terms at both 0.7 V and 0.5 V are for the five terminal connections. This relatively large error is due to these being the smallest data set to average over. At 0.7 V the error for the single connection was ±0.020 A.cm^{-2} and for the five terminal connections was ±0.017 A.cm^{-2}. At 0.5 V the error for the single connection was ±0.030 A.cm^{-2}, for

the four terminal connections was ±0.045 A.cm^{-2} and for the five terminal connections was 0.069 A.cm^{-2}.

At both cell potentials, the current density increased as the number of connections increased. The largest increase occurred when the connection was increased from one to two connections. At 0.7 V the average current density for a single terminal was 0.114 A.cm^{-2}, doubling the number of connections (+100%) to two terminals increased the current density by 28.2% to 0.159 A.cm^{-2}. The corresponding increase at 0.5V was 25.7%, from 0.193 A.cm^{-2} to 0.260 A.cm^{-2}. At 0.7 V the current density increase from 2 to 3 connections (+50%) was 8.6% and at 0.5V the increase was 9.6%, which was nearly 20% and 16% less, respectively, compared to the increase from 1 to 2 terminals. This trend of diminishing returns continued as the number of connections increase to the maximum of 5.

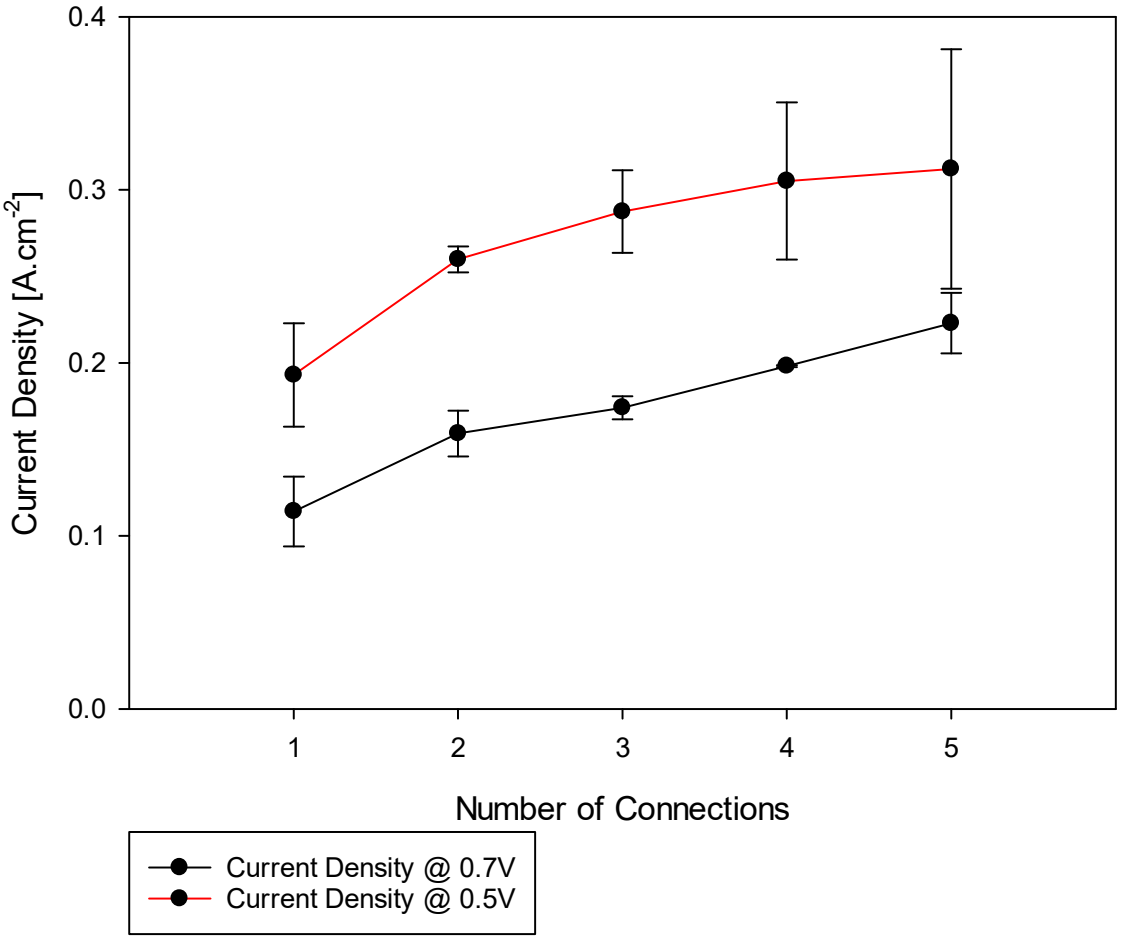

Figure 5.22 - Number of current collector positions versus current density at 0.7 V and 0.5 V at the standard conditions of 750°C and a flow of 200 ml.min^{-1} of H_2 and 10 ml.min^{-1} N_2.

5.4 Mathematical Model

To gain insight into the reasons behind the experimentally observed change in cell performance when varying the current position and the number of current collectors, a modelling approach was required. The model insight could then be used to improve the current collector design and as a rapid development tool at the design stage. A mathematical model was built using known laws and equations. Using Ohm's law as a starting point, we can define the potential of a fuel cell:

$$V = V_0 - IR \tag{114}$$

where V is the open circuit potential difference of the cell, V_0 is the potential difference (operating potential) of the cell, I is current and R is the resistance. It is useful to define the cell with respect to current density to get a better picture of both the local and global performance of a cell. To do so, it must be assumed that the cell performance is symmetrical and has no variation in performance along the cell length. This assumption can be somewhat be replicated in real-world cell tests, where the fuel flow rate is high, fuel utilisation is low and the cell has a homogenous temperature distribution.

The total current is defined with respect to the local current density, i (dimensions of [A/L^2]) over the length of the cell:

$$I = \pi D \int_0^L i dx \tag{115}$$

where D is the diameter of the fuel cell, noting that L is the length of the active region. We now expand our definitions to describe an average current density, $\hat{\imath}$, which is defined by:

$$\hat{\imath} = \frac{I}{A} = \frac{I}{\pi D L} \tag{116}$$

that is the total current produced by the cell divided by the active area of the cell, a commonly defined parameter in fuel cell literature, used as a metric for cell performance comparison, where A is the active area of the cell. The current generated in an infinitesimal ring element is defined as $\tilde{\imath}$ (dimensions of [A/L]). The total current produced by the cell can be defined by:

$$I = \int_0^L \tilde{\imath} dx = \hat{\imath} \pi D L \tag{117}$$

here expressed in terms of $\tilde{\imath}$, the current generated by the entire circumference of the ring element (dimensions of [A/L] integrated over the length, and in terms of the global $\hat{\imath}$ term easily obtainable from empirical measurements. Rearranging, $\tilde{\imath}$ can be defined:

$$\hat{\imath} = \frac{\int_0^L \tilde{\imath} dx}{\pi D L} \tag{118}$$

For a constant current density, we can now present our more useful definition of equation (114):

$$V = V_0 - \hat{\imath} A R \tag{119}$$

noting here that the gradient is not the resistance but the resistance multiplied by the active area of the cell.

5.4.1 Resistance Path Model

To address the commonly stated problem long conduction pathways limiting cell performance in the µT-SOFC literate a resistance path model was developed. All of the average resistance paths are analysed to identify the shortest path. The model assumes that the electrical path within a SOFC consists of a path radially through the cell and a path along the cell that depends on the positioning of the current collector terminals. The resistance of the average path is given by:

$$R_b = r \ < l > \tag{120}$$

where R_b is the average of the path-dependent resistance, r is the resistance per unit length and $< l >$ is the average path length. That is the average path length of all direct paths to the current collector. The definition of the average path length was described in a way to account for the change in distance between a current collector and the current producing region of the cell. For a single current collector, $< l >$ is defined by:

$$< l >= \frac{1}{L}\int_0^{x_0} x_0 - x dx + \frac{1}{L}\int_{x_0}^{L} x - x_0 dx = \frac{1}{L}({x_0}^2 - Lx_0 + \frac{L^2}{2}) \quad \textbf{(121)}$$

where x_0 is the location of the current collector defined with reference to the inlet of the active area. Note here that at this stage of the model, the current collector is of infinitesimal width. The average resistance of a SOFC with the current collector positioned at x, is given by:

$$R = R_{cell} + r < l > \quad \textbf{(122)}$$

where the radial resistance across the cell is defined as R_{cell}. Dividing the position of the current collector and the average path length by the active area, a dimensionless plot of the current path length per unit cell length as a function of the current collector position is obtained, seen in Figure 5.23. Provided the length of the SOFC active area does not change, it is sufficient to minimise the resistance to optimise the SOFC performance. For an infinitesimal current collector, there is no loss of active area and so it is sufficient to consider the minimum of equation (121) as the optimum position. Taking the derivative of equation (121) with respect to the current collector position, we get:

$$\frac{d < l >}{dx_0} = \frac{1}{L}(2x_0 - L) \quad \textbf{(123)}$$

Setting the derivative of (123) to zero to find the minimum, we get the optimal placement at $x_0 = \frac{L}{2}$. Thus the position of a current collector should be in the centre of an active region to minimise the ohmic resistance of the cell.

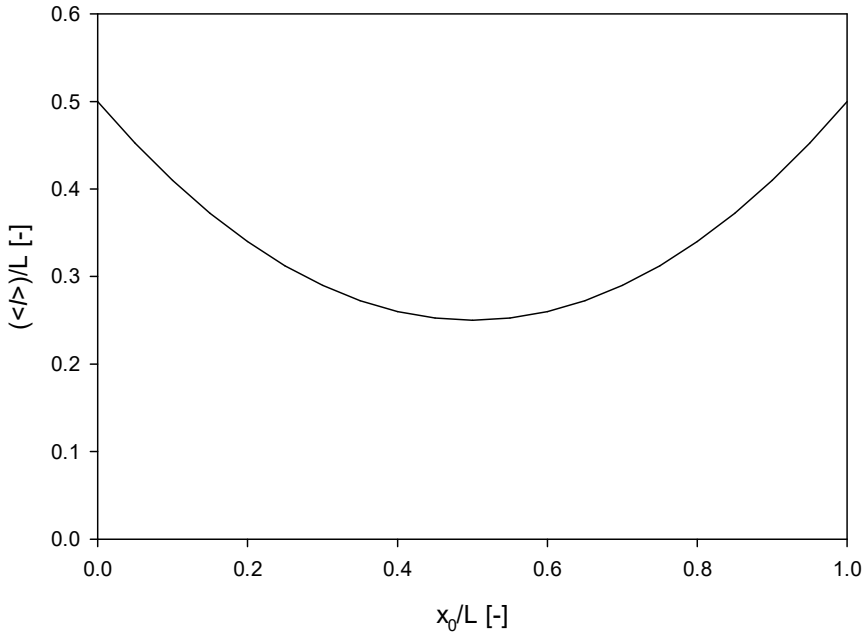

Figure 5.23 - Dimensionless average path length as a function of infinitesimal current collector position.

5.4.2 Current Generating Ring Model

It is more relevant for this study to extend the resistance path model to provide insight into how the resistance affects current production and how the current varies along a cell length. Ignoring the resistance of the current collector itself, this is done by describing the total current production from the cell as the sum of the current produced by a series of infinitesimal rings. We can study the current produced by a ring as its position is increased from a current collector. The current generated by each ring is given by:

$$\lim_{\varepsilon \to 0} \int_{x}^{x+\varepsilon} \tilde{\imath} dx = \frac{V_0 - V}{R_{cell} + rx} \tag{124}$$

The fundamental theorem of calculus yields:

$$\tilde{\imath} = -\frac{(V_0 - V)r}{(R_{cell} + rx)^2} \tag{125}$$

which represents the current generated per unit length, where x is the distance from the current collector to the nearest ring. The sign is controlled by the direction of the current, for a single current collector at either the beginning or at the end can be ignored. For a single infinitesimal current collector, we can study the effect on the current produced per unit length. An active area with a length of 100 mm is described here for simplicity, 0.5 mm longer than the cells used in cell tests. When x_0 is varied from 0 mm to 50 mm and 100 mm, the study represents current collectors positioned at the inlet, centre and outlet region of the active area, respectively. Substituting x_0 values and using $L = 100\,mm$, $R_{cell} = 0.0771\,\Omega$, $r = 0.0006356\,\Omega.mm.^{-1}$, $V_0 = 1$ with the cell operating potential $V = 0.7\,V$ we get Figure 5.24. The values used for R_{cell} and r were obtained from analysis and processing of data derived from electrochemical testing of the 3 node and 5 node current collector setup detailed in Chapter 3 and Chapter 5. The derived values of r and R_{cell} were part of a collaborative effort. The collaborative work is detailed in a co-written paper 'in preparation' entitled: Analysis of current collection in a tubular solid oxide fuel cell: An empirical and mathematical approach for minimised ohmic polarisation. Authors, O. Hodjati-Pugh, J. Andrews, A. Dhir, R. Steinberger-Wilckens.

Figure 5.24 showed that the current produced by the cell is highest at locations nearest the current collector, with the peak at the current collector location itself. The current produced decreased as the distance/path length between the current generating ring and the current collector increased. The area under the curves in Figure 5.24 represent the current produced. The sum of the orange and grey area represent the increase in the current production of the central current collector versus the inlet current collector. Likewise, the sum of the orange and blue shaded area represent the increase in current production versus the outlet current collector. The model agrees with the finding that the current produced be a central current collector is higher than an inlet or outlet current collector. Due to the symmetrical assumptions and construction of the model, the area of the black and blue shaded area is the same as the green and grey shaded area. Thus this model predicted that the performance of an inlet and outlet current collector to be the same. Which from empirically attained data was not supported, with a deviation of up to 22% observed at 0.7 V in Figure 5.13. Nevertheless, we extend the model to further our knowledge.

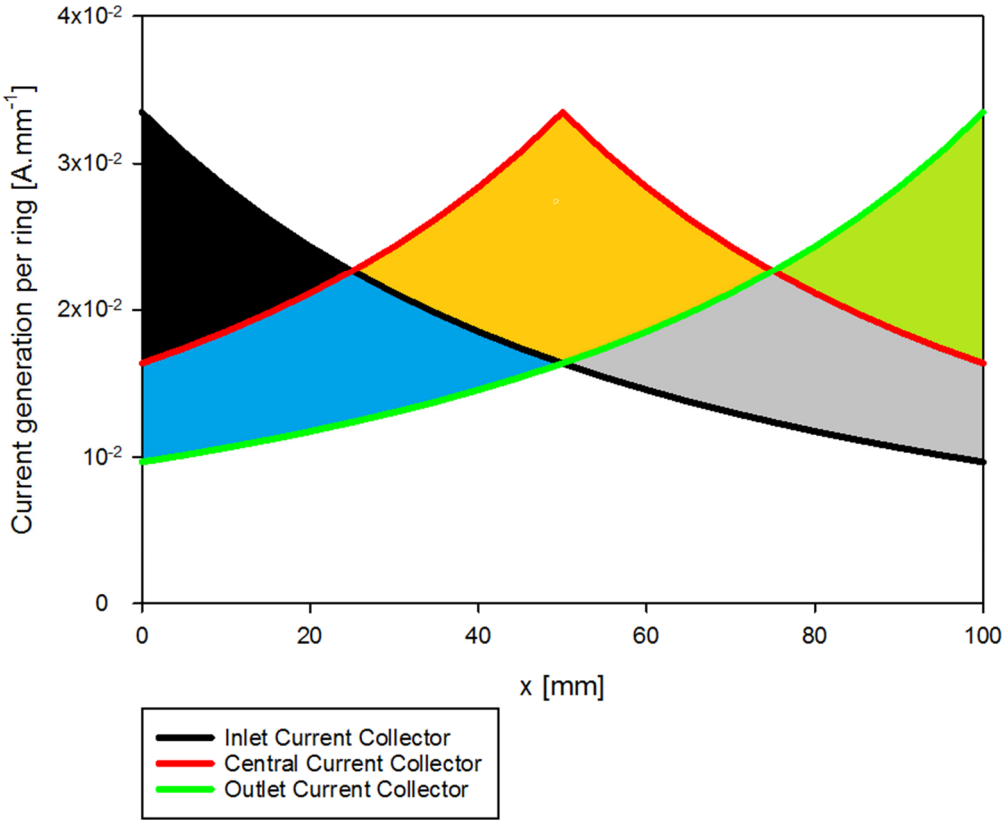

Figure 5.24 - Current generation at 0.7 V as a function of current collector position along the cell length, shown for current collection at the inlet, centre and outlet of the active area.

The total current produced can also be found by evaluating the integral of equation (125). For a current collector at the start of the active area:

$$I = (V_0 - V)r \int_0^L \frac{1}{(R_{cell} + rx)^2} dx = \frac{V_0 - V}{R_{cell}} \frac{rL}{R_{cell} + rL} \quad \textbf{(126)}$$

here noticing the sign change from equation (125), given the convention of a positive current in the start to end direction, with the current being in the opposite direction in this instance.The heat lost per unit ring q is given by:

$$\frac{dQ}{dx} = q = \tilde{\imath}^2 L(rx + R_{cell}) \quad \textbf{(127)}$$

giving a total heat produced by the cell as a function of cell length and current collector position as:

$$Q = \frac{(V_0 - V)^2 r^2 L^3 (2R_{cell} + rL)}{2(2R_{cell} + rL)^2 {R_{cell}}^2} \quad \textbf{(128)}$$

The heat produced by the cell along the cell length for a current collector at the inlet, centre or outlet of the active area of the cell is seen in Figure 5.25. A similar trend is observed to that in Figure 5.24, here the square relationship of $\tilde{\imath}$ causing a change in shape of the curves. Again, the sum of the orange and grey area represents the increase in the current production of the central current collector versus the inlet current collector. Likewise, the sum of the orange and blue shaded area represents the increase in current production versus the outlet current collector. Noting again that due to the symmetrical assumptions and construction of the model, the area of the black and blue shaded area is the same as the green and grey shaded area.

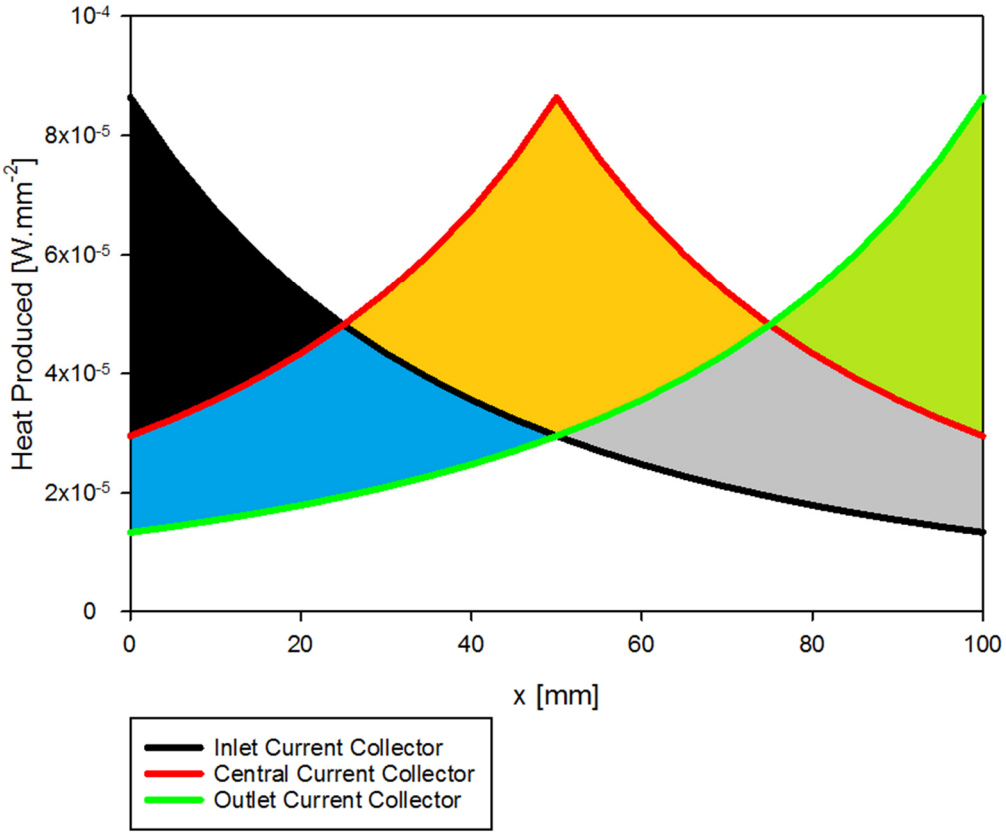

Figure 5.25 - Heat production as a function of current collector position along the cell length, shown for current collection at the inlet, centre and outlet of the active area.

5.4.3 Number of Current Collectors

The current produced by a cell with an inlet current collector is seen as a function of cell length in Figure 5.26. Up to a 100 mm cell length, the current produced from the cell rapidly increases with increasing length. Up to 200 mm the gain decreases and above 200 mm the current produced flattens significantly with the long resistance path inhibiting cell performance. Cells above 200 mm with an inlet current collector would suffer from a low power density and would benefit from an additional current collector.

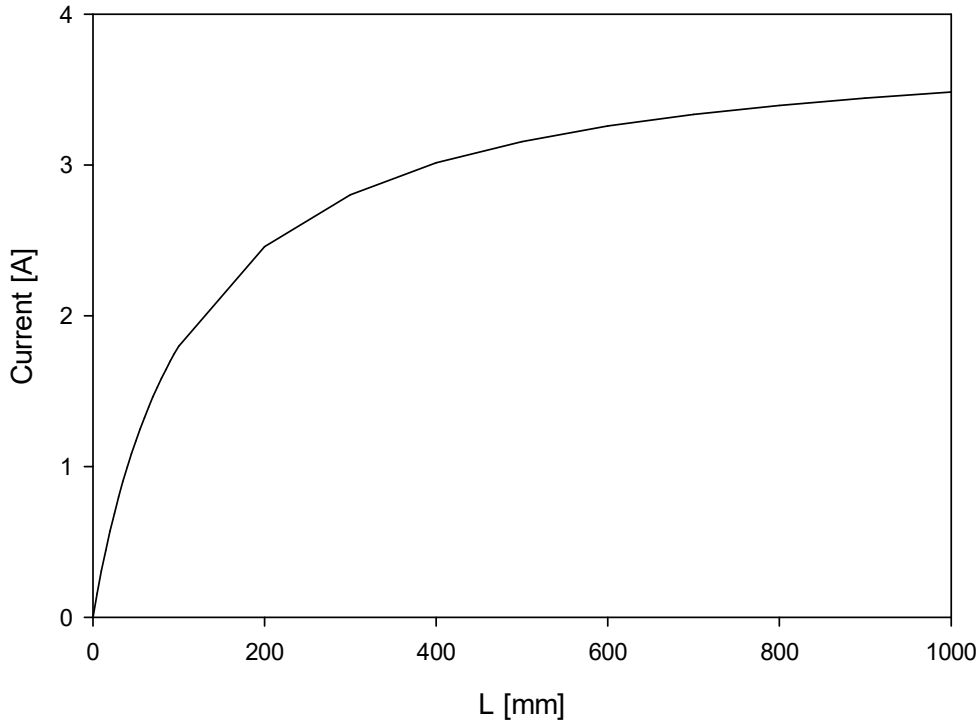

Figure 5.26 - Current produced by a cell with an inlet current collector as a function of cell length.

Here we apply the model to find the ideal positioning of 2 current collectors. Allowing the position of the current collectors to be represented by x_0 and x_1, respectively. Assuming $x_0 < x_1$ the average path length is given by:

$$< l >= \frac{1}{L}\left(\int_0^{x_0} x_0 - x dx + \int_{x_0}^{\frac{x_0+x_1}{2}} x - x_0 dx + \int_{\frac{x_0+x_1}{2}}^{x_1} x_1 - x dx + \int_{x_1}^{L} x - x_1 dx\right) \quad \textbf{(129)}$$

$$= \frac{1}{4L}(3{x_1}^2 - (4L - 2x_0)x_1 + 2L^2 + 3{x_0}^2)$$

Taking the partial derivatives of equation (129) with respect to x_0 and x_1 and setting them both to zero, the critical points can be found. These were determined to be at $x_0 = \frac{L}{4}$ and $x_1 = \frac{3L}{4}$. Substituting these values into equation (129), as well as the values of $x_0 = 0$ and $x_1 = 100$ to represent a current collector at the start and end of the active region, respectively, we get Figure 5.27. The dark red shaded area represents the increased current generated by the electrodes at the optimal location versus the inlet and outlet whereas the blue shading represents the increased current generated by the inlet and outlet current collectors compared to the optimal location. The dark red shaded area is larger than the blue area, a clear visual representation to show that the current collectors placed at the optimal location outperform ones at sub-optimal locations.

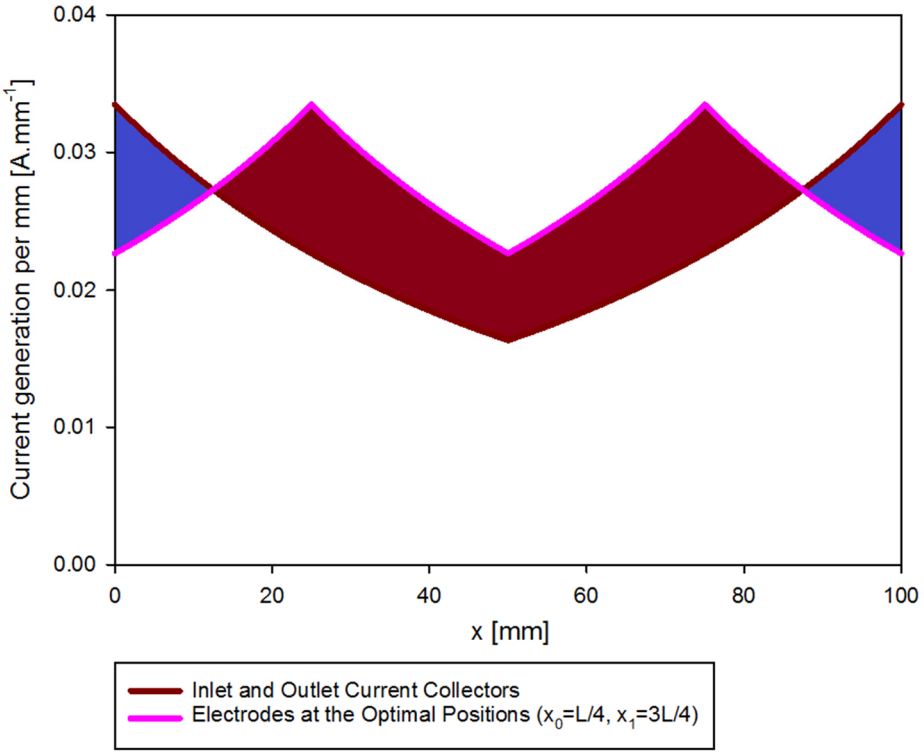

Figure 5.27 - Current generation per cell length over the cell length for two, two node current collector setups, at the inlet and outlet (black) and the optimal positions (blue).

The power lost by the cell was also plotted using:

$$P = I^2 R \tag{130}$$

and equation (125), and the resistance at a given cell length to get Figure 5.28, presented for the same current collector configuration as in Figure 5.27 with inlet and outlet current collection and

with two current collectors at the optimal positions. A similar trend is observed as in Figure 5.27 whereby the dark red shaded area is larger than the blue area, indicating that current collectors placed at the optimal location result in a reduced path length and thus higher performance/power than current collectors at sub-optimal locations (in this case at the inlet and outlet).

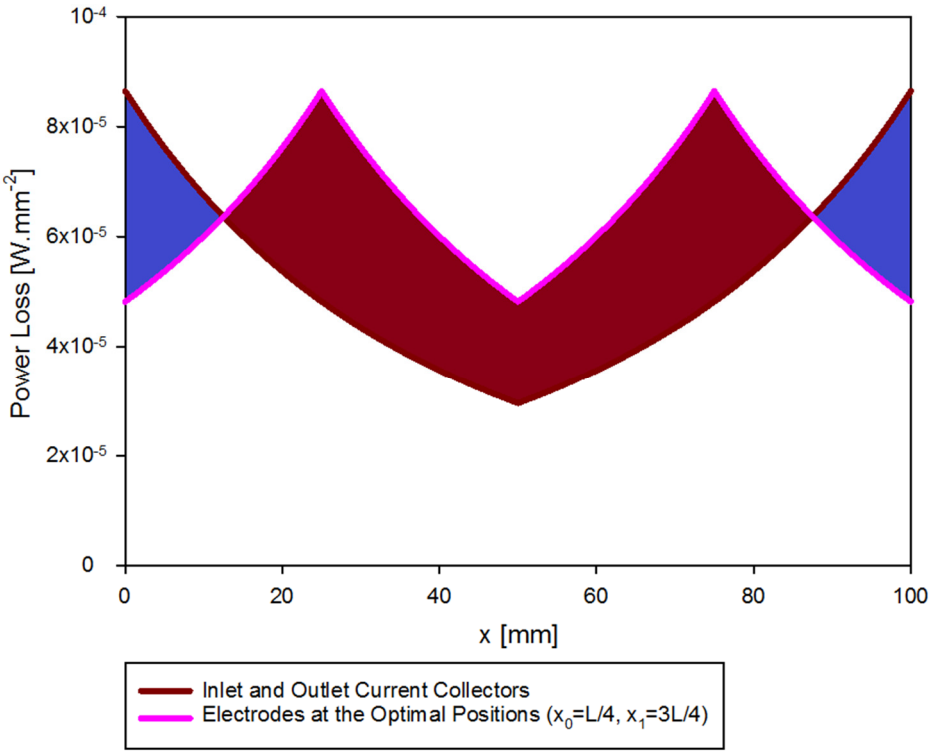

Figure 5.28 - Power lost per cell length over the cell length for two, two node current collector setups, at the inlet and outlet (black) and at the optimal positions (blue).

It was noticed that the optimal position will occur when the distances between current collectors are split into equal sections. In the case of 2 current collectors at the optimal locations, numerically speaking, the active area is split into four segments as indicated by the number of integrals in equation (129). The first segment of length, *m*, from the start of the SOFC active area to the first current collector location, two of length, *m*, between the two current collectors and the final segment of length, *m*, from the second current collector to the end of the µT-SOFC active area. For clarity, in reality, when preparing a cell with two optimally placed current collectors, three active regions would be produced, with the central section twice the length of the others.

The optimal location and average path length were extended in the same way as previously shown for the single and dual current collector, to three current collectors. From observation, a trend was

identified as the number of current collector positions increased. As a result, the generalised average path length and optimal location for n number of current collectors was found, as seen in Table.5.3.

Table.5.3 - Optimal location and average path length for one, two, three and n number of current collectors of infinite size.

Number of current collectors	Optimal locations	Average path length
1	$L/2$	$L/4$
2	$L/4, 3L/4$	L/8
3	$L/6, 3L/6, 5L/6$	$L/12$
n	$L/(2n)$, $(L+2L)/(2n)$, $(L+4L)/(2n)$,..., (2nL−L)/(2n)	$L/4n$

The current generation of a cell with a single infinitesimal current collector positioned at the centre of the active region versus a cell with a current collector at both the inlet and outlet is present for the 100 mm cell length in Figure 5.29. The blue shaded area is the increased current generation of the cell with a central current collector versus a cell with the inlet and outlet current collector while the brown shaded areas are the increased current of an inlet and outlet current collector setup over the single central current collector. The sum of the brown shaded areas is equal to the sum of the blue shaded area.

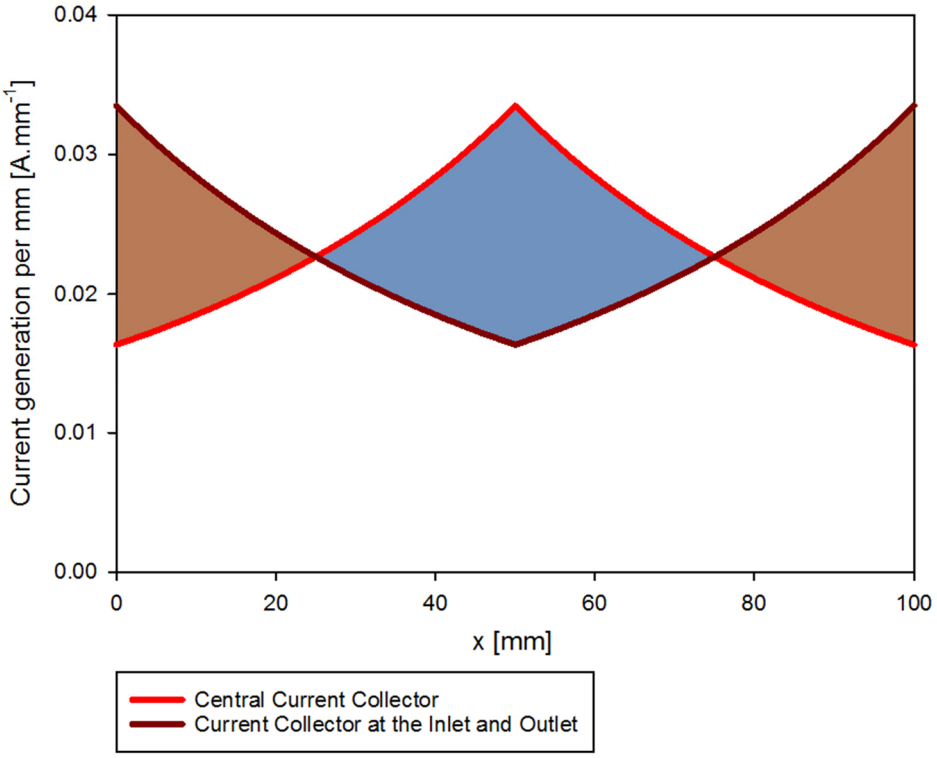

Figure 5.29 - Current generation per mm along the cell length for a single central current collector versus a current collector at the inlet and outlet.

5.4.4 Current Collector Size

The model progressed from current collectors of infinitesimal width to consider current collectors with a finite width. Current collectors of finite width are required for placement of the wiring on the electrode. In the case of an external anode current collector of an anode supported cell, placement of the current collector typically comes at the expense of active area. Thus a trade-off occurs between a reduced conduction pathway and the loss of active area. The same methodology previously used for average path length was followed. However, in this instance, the length of the active area is allowed to vary:

$$< l >= \frac{1}{L}\left(\int_0^{x_0-w/2}(x_0-\frac{w}{2})-x dx+\int_{x_0-w/2}^{x_0+w/2}0 dx+\int_{x_0+w/2}^{L}x-\left(x_0+\frac{w}{2}\right)dx\right) \quad (131)$$

$$= \frac{1}{4L}(2L^2-(2w-4x_0)L+w^2+4{x_0}^2)$$

therefore enabling the ascertainment of the optimal width of the current collector and the effect of the loss of active area as a result of current collector size on the current produced:

$$I = (V_0 - V)r\left(\int_0^{x_0-\frac{w}{2}} \frac{1}{(R_{cell} + r(x_0 - {}^{w}/_{2} - x))^2}dx + \int_{x_0-w/2}^{x_0+w/2} 0dx + \int_{x_0+w/2}^{L} \frac{1}{(R_{cell} + r(L - x_0 - w/2 - x))^2}dx\right)$$
$$= \frac{(V_0 - V)r}{R_{cell}}\left(\frac{x_0 - w/2}{R_{cell} + r(x_0 - w/2)} + \frac{L - x_0 - w/2}{R_{cell} + r(L - x_0 - w/2}\right) \quad \textbf{(132)}$$

The optimal solution to equation (131) is again at $L/2$, while the optimal width is $w = 0$, i.e. when the width of the current collector is zero as expected. The total current produced for a given cell length with an infinite current collector is compared for a finite inlet current collector with a 4 mm and 8 mm width in Figure 5.30. For the 100 mm active area, the current was 5% and 11% lower for the 4 mm and 8 mm current collector width, respectively, versus the infinitesimal width current collector.

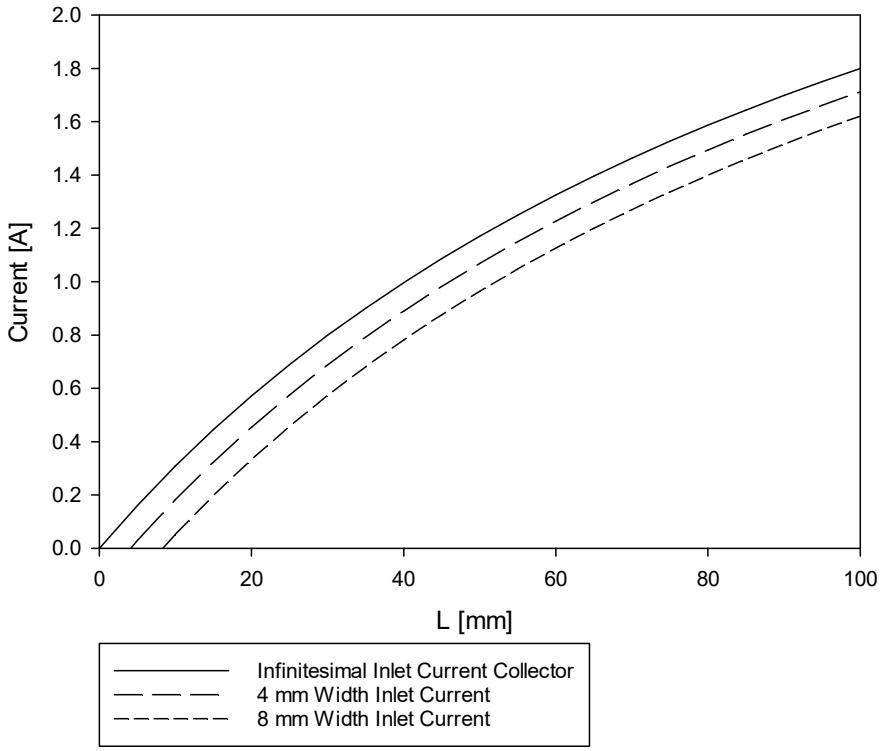

Figure 5.30 - Current produced versus cell length for a cell with an infinitesimal width current collector and a cell with a finite current collector width of 4 mm and 8 mm.

The numerical model showed that a cell with a single central current collector node has the same performance as a cell with current collectors at the inlet and outlet. Also, increasing the current

collector width decreased the amount of current a cell can produce given the loss of active area of cathode required to locate the current collector. In a real-world µT-SOFC cell setup, increasing the number of current collectors also requires additional manufacturing steps/time, sealing and the potential to cause weak spots on the cell if cutting of electrode layers is required to make the contact. However, increasing the number from a single node adds built-in redundancy to the cell and in the event of the failure of one of the current collectors, the cell could still function on the remaining current collector (at a lower efficiency). Multiple current collectors can be used to provide information about the local performance of the cell and a wide range of derived parameters. This information can be useful for integration into a fuel cell management system with real-time feedback and monitoring for optimised cell operation. In addition, the longitudinal degradation profile that develops during SOFC operation can cause poor performance at the outlet region of the cell over time [173]. A cell with both an inlet and outlet current collector would compensate somewhat from this phenomenon versus a cell with, for example only an outlet current collector or a central connector.

5.5 CFD Model Development and Parameter Estimation

To build on the knowledge gained by the numerical model and address its asymmetry related shortcomings in describing the phenomena observed in the empirical study on µT-SOFC current collector position and number, a CFD model was developed. The fuel cell model was set up to reflect the state-of-the-art central silver connection at the standard operating conditions with a furnace temperature of 750°C with a H_2 flow rate of 200 ml.min^{-1} and a N_2 flow rate of 10 ml.min^{-1}. The experimental data at these conditions was used to fit the model. The fitted model was used as a predictive tool to de-convolute the effects of varying the anode current collection configuration. Particularly with respect to fuel concentration profile, temperature profile and current density distribution, which were hard to observe experimentally. To fully describe the cell operation, conservation of momentum, energy, mass and charge physics, and their representative parameters and boundary conditions were required. While many of the parameter values that are somewhat standardised for SOFCs can be found in the literature, an effort was made to approximate the values of the exact cells used in this study. This ensured unknown values which are then used for fine-tuning/fitting the model can also be representative. The parameters were determined from the characterisation of the cell before and during electrochemical testing.

5.5.1 SEM & EDX

SEM was used to confirm the layer thickness of the fuel cell components provided by the manufacturer. Using ImageJ software for image analysis, the thickness of the ASL was estimated at 498.1 µm ± 4.4 µm, the AFL was determined to be 13.4 µm ± 0.9 µm, the electrolyte was 13.1 µm ± 0.8 µm, the barrier layer was 9.1 µm ± 0.4 µm and the cathode was 17.6 µm ± 0.8 µm. The images are seen in Figure 5.31. All of the layers were well defined with relatively uniform thickness, were in intimate contact with each other, and had a homogenous microstructure. A clear step change in the microstructure was observed between the two anode layers with the AFL having a much smaller pore diameter than the ASL to favour triple phase boundary density over low resistance to mass transport. The electrolyte was complete and fully dense, with only a few pinhole defects observed.

a)

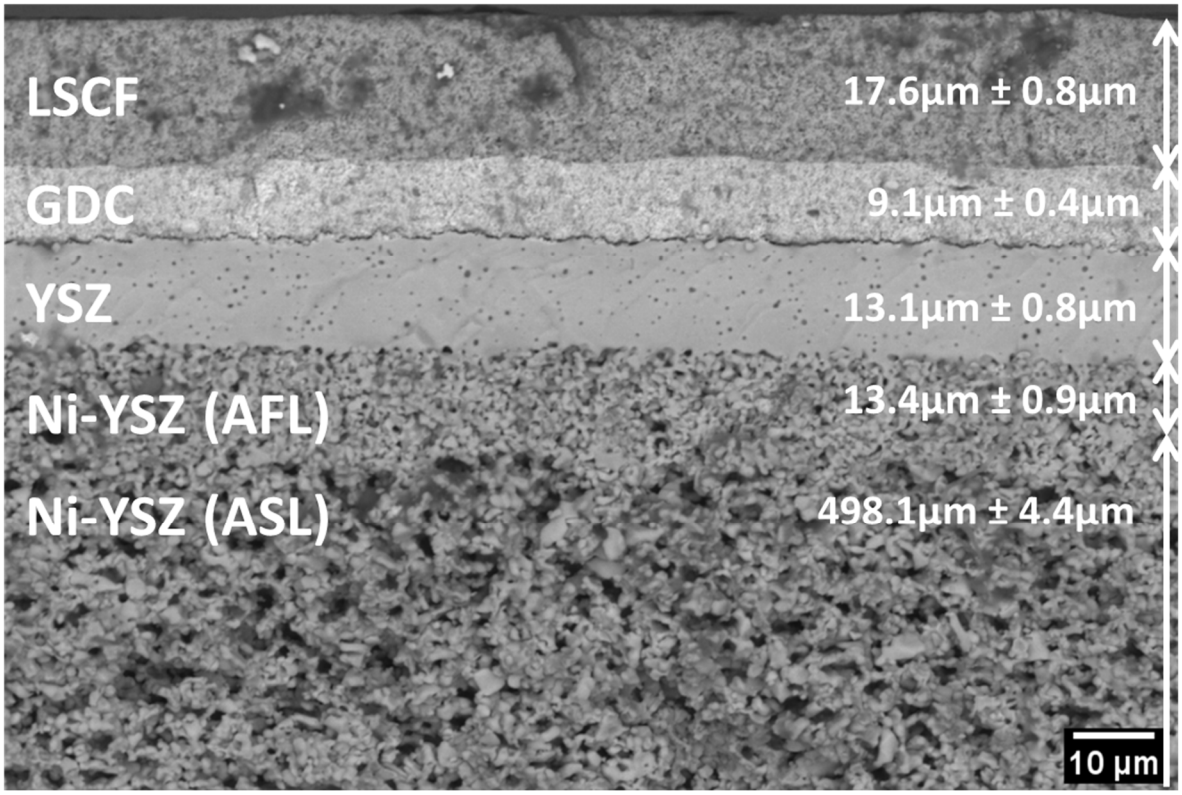

b) c)

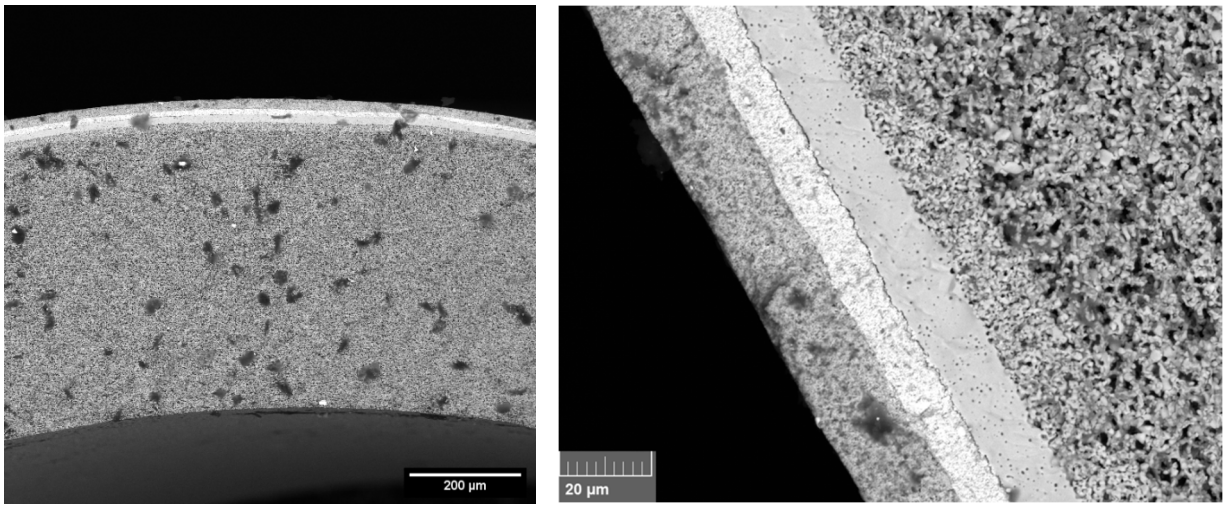

Figure 5.31 - SEM image of a) fuel cell cross-section with annotations, b) cross-section, c) zoomed cross-section.

EDX analysis was performed on the cross-sectional image in Figure 5.31 a). The elemental analysis is seen in Figure 5.32 with the original image included for reference. The quantity of each element was not determined as the purpose of the analysis was to simply understand which materials were being used for parameter estimation.

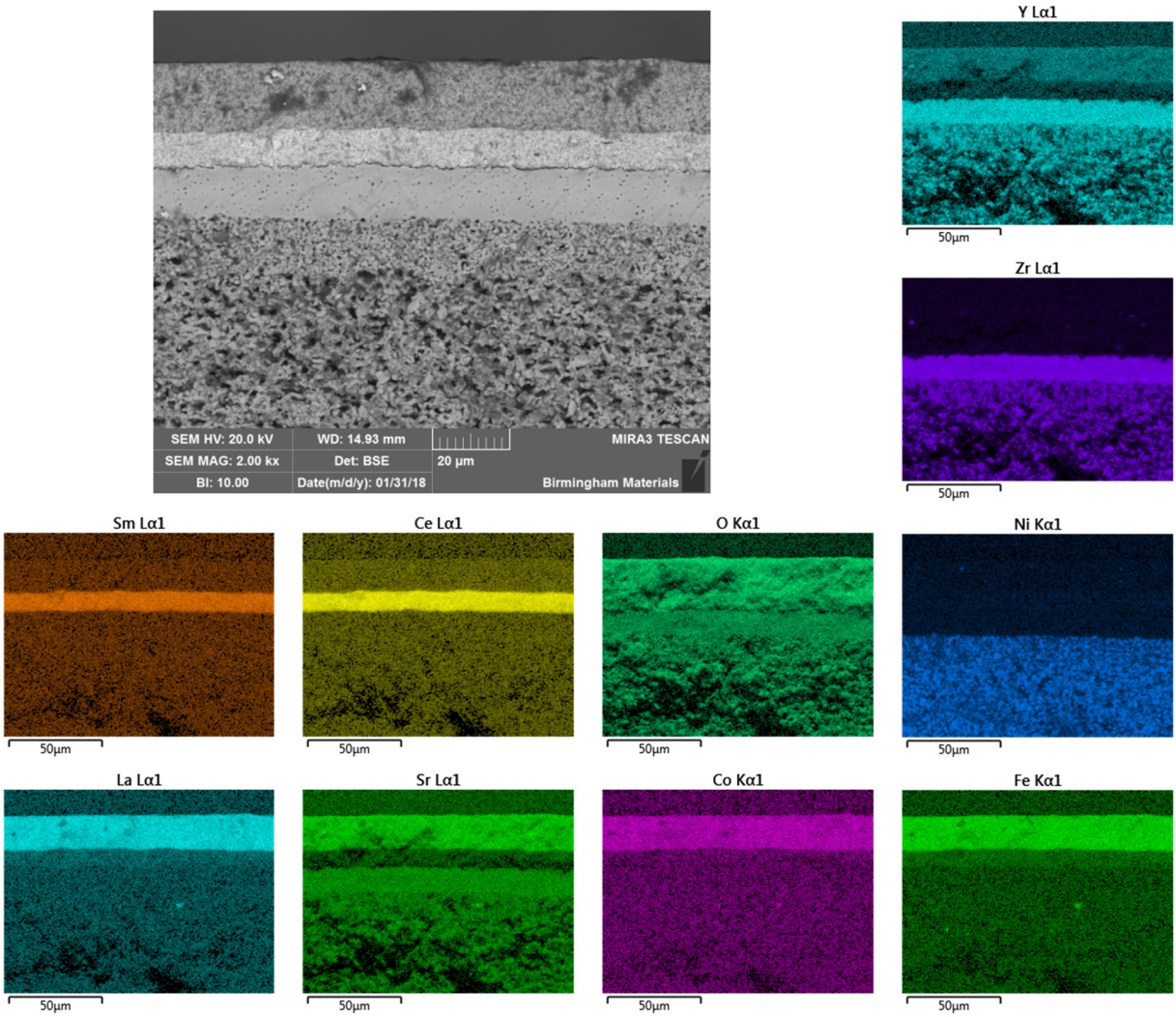

Figure 5.32 – SEM and EDX elemental analysis of fuel cell cross-section.

Further image analysis was performed on a close-up of the anode support layer as seen in Figure 5.33. The thick support layer would have the largest contribution to mass transport effects through the anode and therefore was the focus of the analysis. The average pore diameter was estimated at 1.97 µm. The spread of the data was quite large with the average having an error of 1.60 µm.

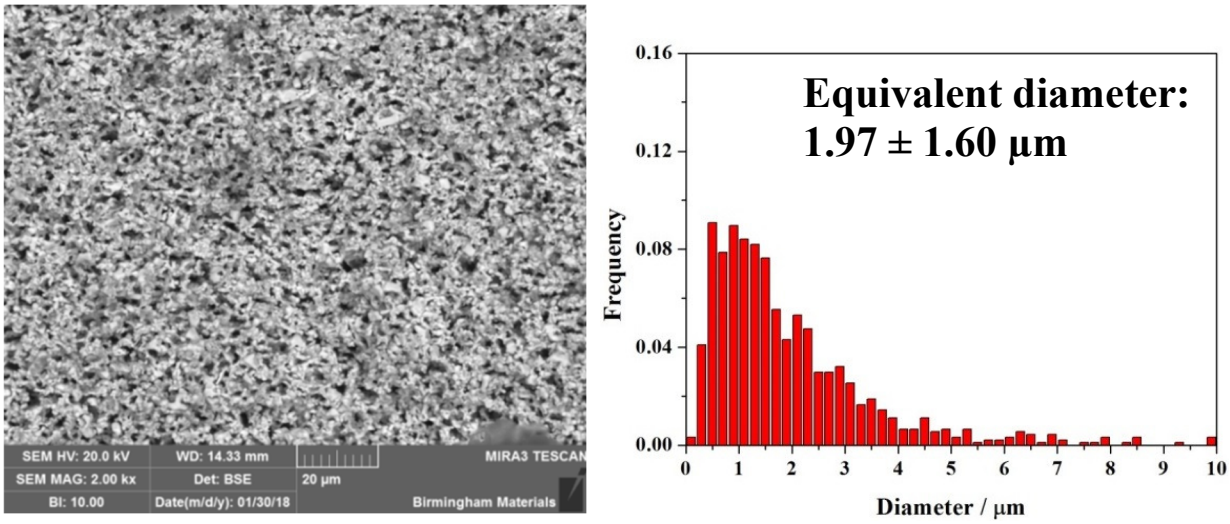

Figure 5.33 - SEM of anode and pore size distribution.

5.5.2 XRCT

XRCT was performed on a section of the complete fuel cell. This powerful technique was used to gain insight into the microstructural properties of the ASL, AFL, barrier layer and cathode. The post-processed images are seen in Figure 5.34. The ASL is seen in green, the AFL in blue, the barrier layer in yellow and the cathode in red. The non-porous electrolyte was not analysed as parameters are well defined in literature.

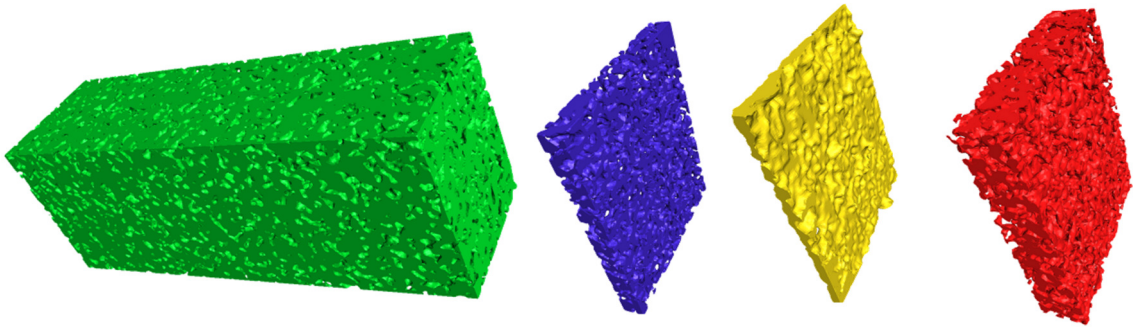

Figure 5.34 - XRCT of ASL (green), AFL (blue), barrier layer (yellow) and cathode (red).

Analysis of the post-processed image enabled the determination of the porosity, tortuosity of the solid and pore and pore diameter, the values are seen in Table 5.4. With this data, we could extract a vast amount of information with respect to momentum, energy, mass and charge transport within the cell.

Table 5.4 - Derived parameters from XRCT image analysis.

	Porosity [%]	Tortuosity-factor Tau pore [-]	Diameter of Pore [µm]	Tortuosity-factor Tau Solid [-]	Diameter of Solid [µm]
Anode Support Layer	32	5.90	2.54	1.61	4.53
Anode Functional Layer	44	1.90	2.01	2.83	1.90
Cathode	33	2.75	1.96	2.76	1.80

For the electrochemical model, the active specific surface area of each electrode was required. This is defined as the reactive surface area per unit volume, A_V:

$$A_V = \pi Sin^2\theta {r_{el}}^2 n_t n_{el} n_{io} \frac{Z_{el}Z_{io}}{Z} p_{el}p_{io} \quad \textbf{(133)}$$

The concept was well described by Costamagna et al. in their theoretical percolation model of SOFC electrodes in 1998 which was based on the particle coordination number in a binary random packing of spheres [292], where θ is the contact angle between the electron and ion conducting particles in the electrode, r_{el} is the radius of the electron-conducting particle, n_t is the total number of particles per unit volume and is a function of the porosity, ε:

$$n_t = \frac{1-\varepsilon}{(4/3)\pi {r_{el}}^3[n_{el} + (1-n_{el})(r_{io}/r_{el})^3]} \quad \textbf{(134)}$$

where the terms n_{el} and n_{io} are the number of electron and ion conducting particles, respectively, and Z_{el} and Z_{io} are the coordination numbers of the electron and ion conducting particles. The terms p_{el} and p_{io} are the probabilities of electron and ion conducting particles. Equation (133) and (134) along with the equations for all of the aforementioned parameters can be found in [293]. The values applied in this are seen in Table 5.5.

Table 5.5 - Active specific area parameters.

Parameter	Value	Units	Ref.
$\boldsymbol{\theta}$	15	°	[294]
$\boldsymbol{r_{el,a}}$	4.85x10^{-7}	m	[213]
$\boldsymbol{r_{io,a}}$	5.28x10^{-7}	m	[213]
$\boldsymbol{n_{el,a}}$	0.63	-	[213]
$\boldsymbol{n_{io,a}}$	0.37	-	[213]
$\boldsymbol{Z_{el,a}}$	5.58	-	[213]
$\boldsymbol{Z_{io,a}}$	6.72	-	[213]
$\boldsymbol{Z}$	6	-	[213]
$\boldsymbol{p_{el,a}}$	0.97	-	[213]
$\boldsymbol{p_{io,a}}$	0.87	-	[213]
$\boldsymbol{n_{t,ASL}}$	1.12x10^{18}	-	This study
$\boldsymbol{n_{t,AFL}}$	9.25x10^{17}	-	This study
$\boldsymbol{A_{V,ASL}}$	**4.28x10^{5}**	m^{-1}	This study
$\boldsymbol{A_{V,AFL}}$	**3.52x10^{5}**	m^{-1}	This study
$\boldsymbol{r_{el,c}}$	2.6x10^{-7}	m	[213]
$\boldsymbol{r_{io,c}}$	1.7x10^{-7}	m	[213]
$\boldsymbol{n_{el,c}}$	0.22	-	[213]
$\boldsymbol{n_{io,c}}$	0.78	-	[213]
$\boldsymbol{Z_{el,c}}$	8.42	-	[213]
$\boldsymbol{Z_{io,c}}$	5.32	-	[213]
$\boldsymbol{p_{el,c}}$	0.80	-	[213]
$\boldsymbol{p_{io,c}}$	0.99	-	[213]
$\boldsymbol{n_{t,c}}$	2.08x10^{9}	-	This study
$\boldsymbol{A_{V,c}}$	**1.91x10^{6}**	-	This study

The porosity along with the active specific area of each electrode can be substituted into the Carman-Kozeny correlation to determine the flow permeability which is given by [295]:

$$K = \frac{\varepsilon^3}{k_K(1-\varepsilon)^2 {A_V}^2} \quad \textbf{(135)}$$

The Kozeny constant, k_K, is 5 for porous media of spherical particles. The values in each electrode are seen in Table 5.5.

Table 5.6 - Flow permeability.

Parameter	Value	Units	Ref.
$\boldsymbol{K_{ASL}}$	3.10x10^{-13}	m^2	This study
$\boldsymbol{K_{AFL}}$	1.9x10-^{12}	m^2	This study
$\boldsymbol{K_c}$	2.01x10^{-14}	m^2	This study

The porosity and tortuosity were also used to define the effective binary diffusivities and effective Knudsen diffusivities for each electrode as previously defined in Chapter 4. The binary diffusivities are given for each binary pair, along with the respective effective binary diffusivity values for each electrode in Table 5.7. The Knudsen diffusivities and effective diffusivities at the operating conditions are seen in Table 5.8.

Table 5.7 - Binary diffusivities and effective binary diffusivities.

Binary Pair	Binary Diffusivity	Ref.	Electrode	Effective Binary Diffusivity	Units
H_2:H_2O	7.82×10^{-5}	[213]	ASL	4.24×10^{-6}	$m^2.s^{-1}$
			AFL	1.81×10^{-5}	
H_2:N_2	6.726×10^{-5}	[213]	ASL	3.65×10^{-6}	$m^2.s^{-1}$
			AFL	1.56×10^{-5}	
H_2O:N_2	2.23×10^{-5}	[213]	ASL	1.21×10^{-6}	$m^2.s^{-1}$
			AFL	5.16×10^{-6}	
O_2:H_2O	2.27×10^{-5}	[213]	Cathode	2.26×10^{-5}	$m^2.s^{-1}$
N_2:H_2O	2.23×10^{-5}	[213]	Cathode	2.68×10^{-6}	$m^2.s^{-1}$
O_2:N_2	1.78×10^{-5}	[213]	Cathode	2.14×10^{-6}	$m^2.s^{-1}$

Table 5.8 - Knudsen diffusivities and effective Knudsen diffusivities.

Molecule	Electrode	Knudsen Diffusivity	Ref.	Effective Knudsen Diffusivity	Units
H_2	ASL	2.77×10^{-3}	[295]	1.50×10^{-4}	$m^2.s^{-1}$
	AFL	2.19×10^{-3}		5.08×10^{-4}	
H_2O	ASL	9.29×10^{-4}	[295]	5.04×10^{-5}	$m^2.s^{-1}$
	AFL	7.35×10^{-4}		1.70×10^{-4}	
N_2	ASL	7.45×10^{-4}	[295]	4.04×10^{-5}	$m^2.s^{-1}$
	AFL	5.89×10^{-4}		1.36×10^{-4}	
O_2	Cathode	5.37×10^{-4}	[295]	6.45×10^{-5}	$m^2.s^{-1}$
N_2	Cathode	5.75×10^{-4}	[295]	6.90×10^{-5}	$m^2.s^{-1}$

5.5.3 Archimedes Method

The submerged and dry fuel cell sample weight was 7.28 g and 6.71 g, respectively. The submerged sample weight was 5.64 g. This resulted in anode bulk porosity value of 35%:

$$\emptyset = \frac{V_P}{V_B} = \frac{Pore\ Volume}{Total\ Bulk\ Volume} = \frac{0.57}{1.63} = 0.35 \quad \textbf{(136)}$$

This value estimated by the Archimedes method is in between the porosity values of 32% and 44% of the ASL and AFL estimated by XRCT. The value is closer to the ASL value, which is sensible given the relative thickness of the ASL versus the AFL.

5.5.4 Tafel Analysis – Exchange Current Density

In order to receive an estimate for the exchange current density of the cell, Tafel analysis, typically reserved for PEM fuel cell analysis was performed. A small voltage step size of 1 mV was used for the polarisation plot to capture as much detail at a high resolution. The region of interest and region of validity for Tafel analysis is the low overpotential region. The average plot of multiple polarisation plots of the same cell at the standard conditions is seen in Figure 5.35.

The impedance analysis of the same cell was used to adjust the internal cell resistance by using a voltage loss correction to calculate what the polarisation loss would be without the ohmic contribution. Impedance was measured at 0.2 V intervals from OCV (approx. 1.1 V) to 0.5 V. The polarisation data could then be adjusted in segments by the appropriate ohmic impedance value, Z'_{Ω} [Ω], seen in Table 5.9. The ohmic free potential, E_{iRfree} was plotted against the effective current density, i_{eff} on a logarithmic scale, known as a Tafel plot as seen in Figure 5.36.

Table 5.9 - Ohmic polarisation data extracted from EIS.

Potential	OCV	0.9 V	0.7 V	0.5 V
Impedance Z'_{Ω} [Ω]	0.017	0.0168	0.0139	0.0122

The curve was then extrapolated to the equilibrium potential (theoretical OCV) at 750°C operating with hydrogen as a fuel and air as the oxidant which was calculated by the temperature and pressure

dependent Nernst equation to be 1.105 V. The extrapolation resulted in a value of exchange current density of 0.01 A.cm^{-2} or 100 A.m^{-2}. This value was for the most sluggish electrode, which for SOFCs is the cathode. Therefore this was taken to be the exchange current density of the cathode. The anode exchange current density would likely be 1 to 5 orders of magnitude larger [17].

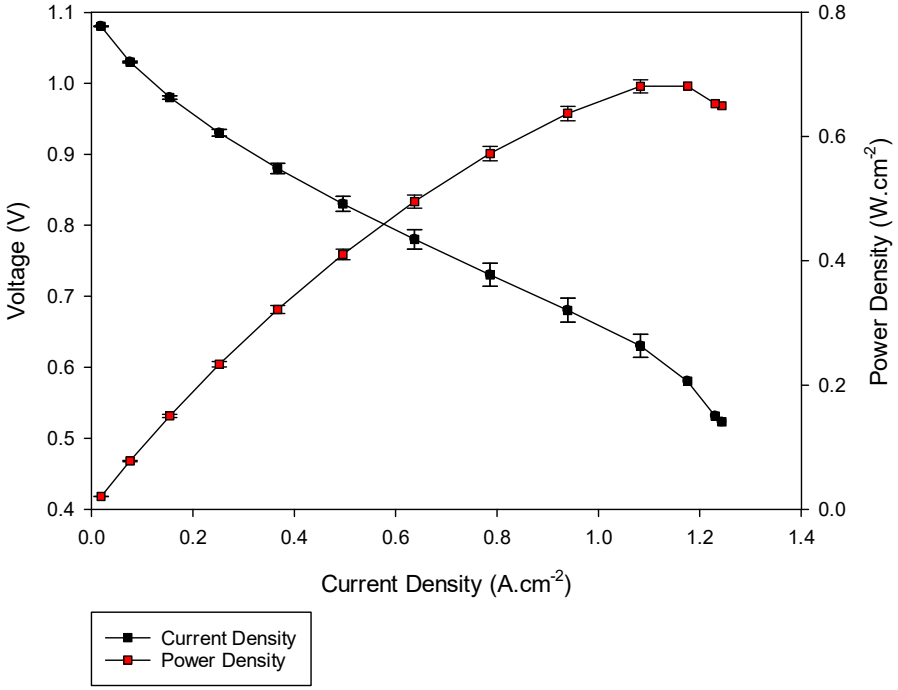

Figure 5.35 - Polarisation and power density plot average data.

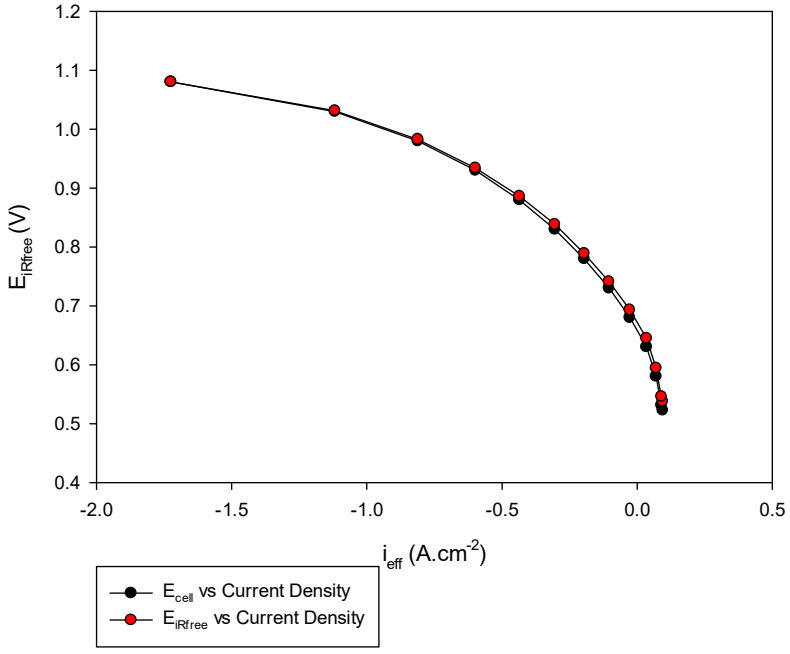

Figure 5.36 - Tafel plot.

5.5.5 CFD Model Parameters from Literature

Widely accepted formulas and values for properties of fuel cell components exist in the literature which are typically derived from experimental observation. Some properties are a function of temperature, pressure and species concentration, to name a few. The properties must therefore be calculated for the specific operating conditions of the study. Several models can exist in the literature to estimate the same parameter and so care must be taken to select the most appropriate version.

Exchange Current Density

Many empirically based models exist for predicting the exchange current density of the anode and cathode. The two most widely accepted are by Mogensen et al. [296,297] which does not respect the electrochemical reaction stoichiometry and by Costamagna et al. [292,294] which does. The models are generally a function of the Arrhenius law and of the composition of the reacting gasses. Equation (137) and equation (138) are commonly accepted forms of the anode exchange current density, $i_{0,a}$ and $i_{0,c}$, respectively, and were used in this study, the latter solely for a credibility check of the empirically estimated parameter from Tafel analysis [298]. γ_a and γ_a are the pre-exponential factor and $E_{act,a}$ and $E_{act,c}$ are the activation energies for the anode and cathode, respectively. The indices A, B and C are parameters to adjust the exchange current density to the partial pressure dependence of the relevant species. In this study, A and B were selected to be both 1 in the style of Mogensen et al. [296,297]. The choice of model for the cathode was less critical than the anode because the cathodic side utilisation of oxygen is usually low. Using a C value of 0.25 gives an cathode exchange current density of 0.1 A.cm^{-2} which is an order of magnitude higher than estimated from the Tafel analysis [294]. A C value of 1.78 was required to fit the model to the value recorded by the Tafel analysis. Estimates for exchange current density vary greatly in literature and a value out by an order of magnitude is still deemed sensible [298]. Costamagna et al. reported that an anode exchange current density value of 0.1 A.cm^{-2} was sensible for Ni-YSZ anodes (at 1000°C) [292].

$$i_{0,a} = \gamma_a \left(\frac{p_{H_2}}{p_{H_{2,ref}}}\right)^A \left(\frac{p_{H_2O}}{p_{H_2O_{ref}}}\right)^B exp\left(\frac{-E_{act,a}}{RT}\right) \quad \textbf{(137)}$$

$$i_{0,c} = \gamma_c \left(\frac{p_{O_2}}{p_{O_{2,ref}}}\right)^C exp\left(\frac{-E_{act,c}}{RT}\right) \quad \textbf{(138)}$$

Table 5.10 - Exchange current density parameters and exchange current density at the standard operating conditions.

Parameter	Value	Units	Ref.
γ_a	$5.5\text{x}10^{10}$	A.cm^{-2}	[294]
γ_c	$7\text{x}10^{9}$	A.cm^{-2}	[294]
$E_{act,a}$	$1.2\text{x}10^{5}$	J.mol^{-1}	[294]
$E_{act,c}$	$1.3\text{x}10^{5}$	J.mol^{-1}	[294]
$i_{0,a}$	0.12	A.cm^{-2}	[294]
$i_{0,c}$	0.1	A.cm^{-2}	[294]

Electrical Conductivity

The electronic conductivity of the anode and cathode and the ionic conductivity of the electrolyte are key parameters for describing the ohmic loss within the electrochemical model. Equation (139) and (140) are the temperature dependent estimate for a Ni-YSZ anode and LSM cathode electronic conductivity while equation (141) is for the ionic conductivity of the YSZ electrolyte [299]. The conductivity values at 750°C are seen in Table 5.11. The anode support layer and anode functional layer were assumed to have the same electronic conductivity. Temperature dependent expressions for the electronic conductivity of the LSCF cathode used in this study were not currently available in literature. Research published by Navasa et al. [147] estimated the electronic conductivity of LSCF to be $2\text{x}10^{3}$ S.m^{-1} at 750°C although a reference was not provided. The electronic conductivity of LSCF is known to be higher than for LSM so it seemed that a value between $1.27\text{x}10^{3}$ and $2\text{x}10^{3}$ S.m^{-1} was appropriate. The conductivity of pure nickel, the electronic conductor in the Ni-YSZ cermet, is two orders of magnitude higher (approx. 10^{6}) at 750°C than the estimated value from equation (139). The value estimated from equation (139) accounts for the porous nature of the cermet and the tortuous pathway the electrons must follow, an effective conductivity which will always be lower than the conductivity of pure nickel.

$$\sigma_a = \left(\frac{9.5\text{x}10^{7}}{T}\right)\exp\left(-\frac{1150}{T}\right) \quad \textbf{(139)}$$

$$\sigma_c = \left(\frac{4.2\text{x}10^{7}}{T}\right)\exp\left(-\frac{1200}{T}\right) \quad \textbf{(140)}$$

$$\sigma_e = \left(\frac{3.3\text{x}10^{4}}{T}\right)\exp\left(-\frac{10300}{T}\right) \quad \textbf{(141)}$$

Table 5.11 - Electronic conductivity of the electrodes and ionic conductivity of the YSZ electrolyte at 750°C.

Parameter	Value	Units	Ref.
σ_a	$3.02X10^4$	$S.m^{-1}$	[299]
σ_c	$1.27X10^3$	$S.m^{-1}$	[299]
σ_e	1.41	$S.m^{-1}$	[299]

Table 5.12 - Thermal properties of electrodes and electrolyte.

Parameter	Value	Units	Ref.
ρ_a	3310	$kg.m^{-3}$	[300]
ρ_c	3030	$kg.m^{-3}$	[300]
ρ_e	5160	$kg.m^{-3}$	[300]
C_{p_a}	450	$J.mol^{-1}.K^{-1}$	[300]
C_{p_c}	470	$J.mol^{-1}.K^{-1}$	[300]
C_{p_e}	430	$J.mol^{-1}.K^{-1}$	[300]
λ_a	1.86	$W.m^{-1}.K^{-1}$	[300]
λ_c	5.84	$W.m^{-1}.K^{-1}$	[300]
λ_e	2.16	$W.m^{-1}.K^{-1}$	[300]

5.6 Mesh Independency

A mesh independence study was conducted to determine the minimum acceptable mesh resolution required for the simulation results to be independent of the meshing. Values below this minimum would result in a deviation in the solution due to a mesh resolution too coarse to adequately embrace the problem, however, an increase in the value would merely result in excessive computing time. It is useful to determine this minimum value to reduce model solving time and memory usage while still providing an accurate solution. The metric used for mesh independency was degrees of freedom (DOF) which is a function of the number of different mesh elements used and the number of variables the model is solving for. The metric used for mesh quality was skewness (dimensionless).

5.6.1 Current Density

The current density was chosen as the primary parameter for the mesh independence study. This was firstly due to the stringent requirements on maximum mesh size in the electrodes and electrolyte required to capture sufficient detail to describe the phenomenon as detailed in Chapter 4. Secondly, the current density was the key fitting parameter to experimental data and so it was critical to predict the current density as accurately as possible. The plot of degrees of freedom versus

current density at 0.7 V is seen in Figure 5.37. The COMOSL default mesh had $1.25x10^6$ degrees of freedom with $3.25x10^5$ elements and had a skewness of 0.82. The custom mesh chosen, indicated by the red dot had $2.43x10^6$ degrees of freedom with $4.14x10^5$ elements and skewness of 0.94. This was chosen as it was the mesh with the lowest degrees of freedom at which the results were independent of mesh size and within the ±1% deviation in current density compared to the COMSOL mesh. The custom mesh required slightly less time to solve than the COMSOL mesh and the flexibility to customise the mesh led it to its use in the study.

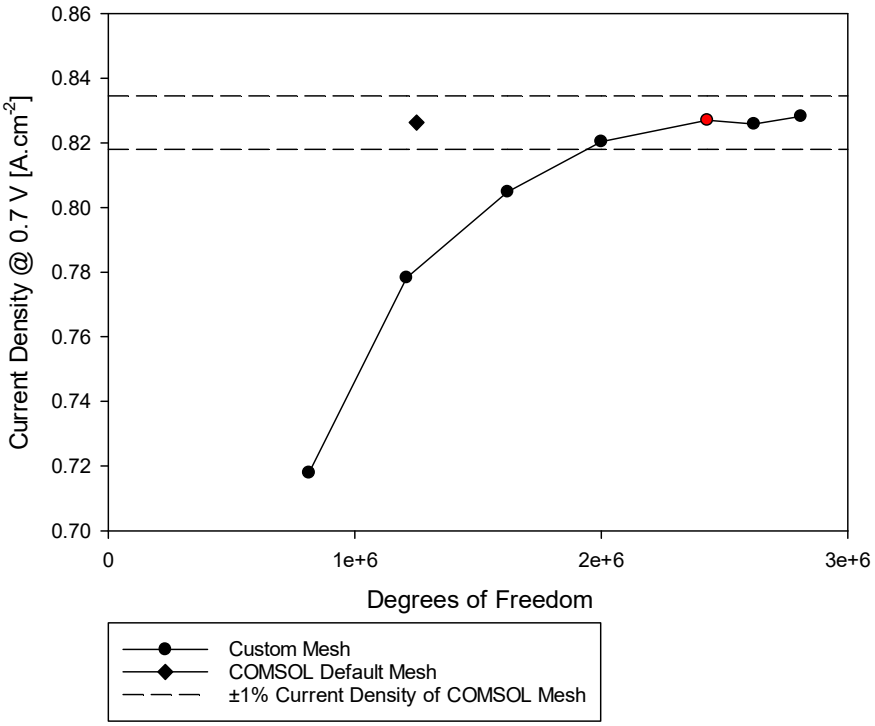

Figure 5.37 - Mesh independency test; current density at 0.7 V versus degrees of freedom for custom and default COMSOL mesh.

5.6.2 Velocity

Now that the minimum DOF threshold for prediction of current density independent of mesh size had been determined, the mesh independency was checked for the velocity. A cut line across the 2750 µm anode gas channel from the exterior wall towards the anode wall was chosen to determine the velocity profile. The cut line positioned 10 mm above the inlet was chosen to be in the region of fully developed flow determined in Table 4.3, avoiding the transitional entrance region effects nearer the inlet. The same DOF used in the current density study was used for the velocity. The velocity profile along the cut line at DOF an order of magnitude apart is seen in Figure 5.38. As can be seen,

the data points overlap and the values are the same to 3d.p across the whole range indicating the velocity had converged far below $1x10^6$ as expected. The $2.43x10^6$ DOF mesh determined from the current density study was then used to inspect the velocity profile at the cut line at OCV and 0.7 V as seen in Figure 5.39. As the potential was decreased from OCV to 0.7 V, the velocity at 2750 µm increases from 0.214 $m.s^{-1}$ to 0.216 $m.s^{-1}$. The values were within 1% of each other.

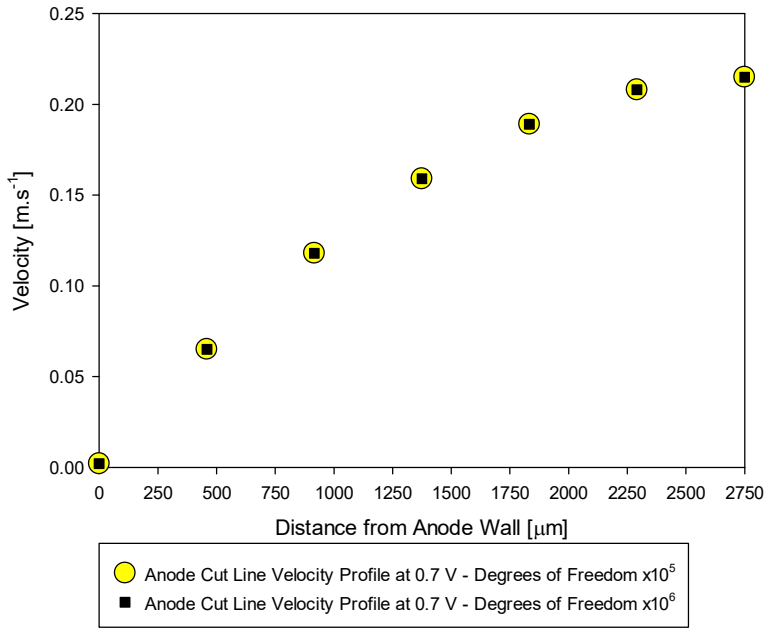

Figure 5.38 - Mesh independency test, velocity versus distance from the anode wall at $x10^5$ and $x10^6$ degrees of freedom.

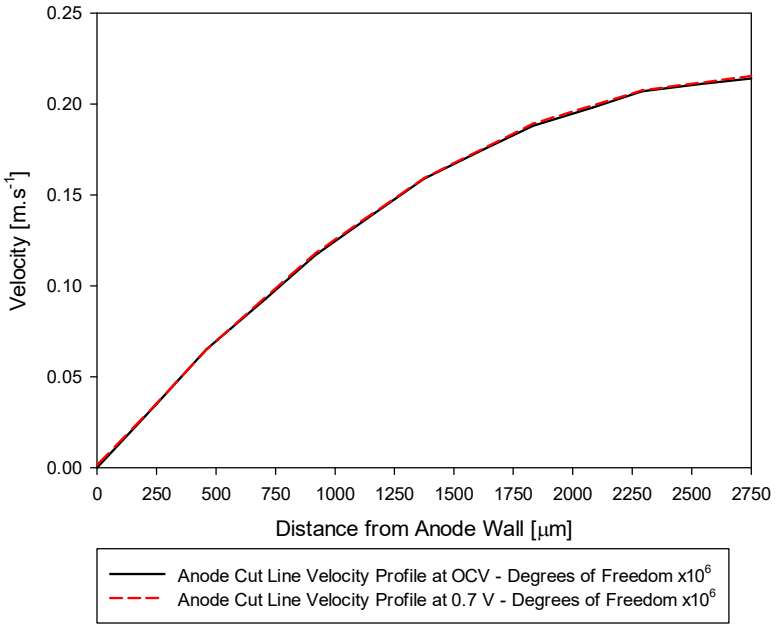

Figure 5.39 - Velocity profile versus operating potential at the $2.43x10^6$ DOF custom mesh.

5.7 Modelling Results – Central Current Collector

Once the central silver model was fitted to the experimental data using the fitting parameters, it served as a predictive tool to understand the effect of changing the current collector geometry on the performance. The key output for comparison to experimental data is the polarisation and power density plot. However, as a tool for understanding, plots of temperature distribution, species concentration, heat sources and localised current density will be used to support the following analysis. The 2D COMSOL model geometry previously described in Chapter 4 is shown again in Figure 5.40 as a reference.

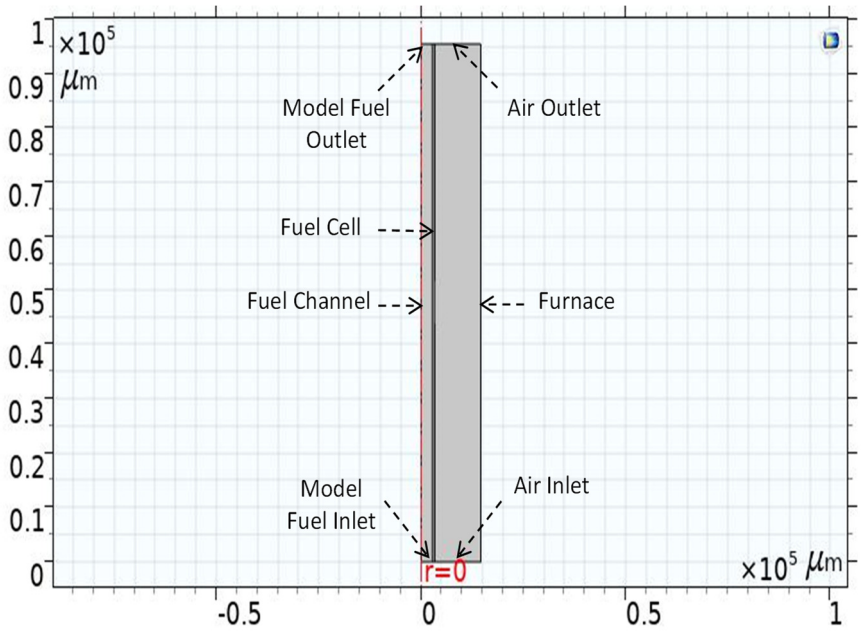

Figure 5.40 - COMSOL model geometry (repeated from Chapter 4).

5.7.1 Polarisation and Power Plots

The fitted i-V curve and resulting power density plot from cell tests and the CFD model are seen in Figure 5.41. The empirical plots are an average over multiple cells tested at 750°C operating on 200 ml.min^{-1} of H_2 and 10 ml.min^{-1} of N_2. The fitted model showed a good fit within the range of operating potential between OCV and 0.55 V, covering the activation, ohmic and the beginning of the mass transport dominated regions. Of particular importance was the good fit in the ohmic loss dominated region between 0.6 V to 0.9 V. The current density at 0.7 V predicted by the model was 0.82 A.cm^{-2} and the experimental value was 0.83 A.cm^{-2} (to 2 s.f), within 1.2% of each other.

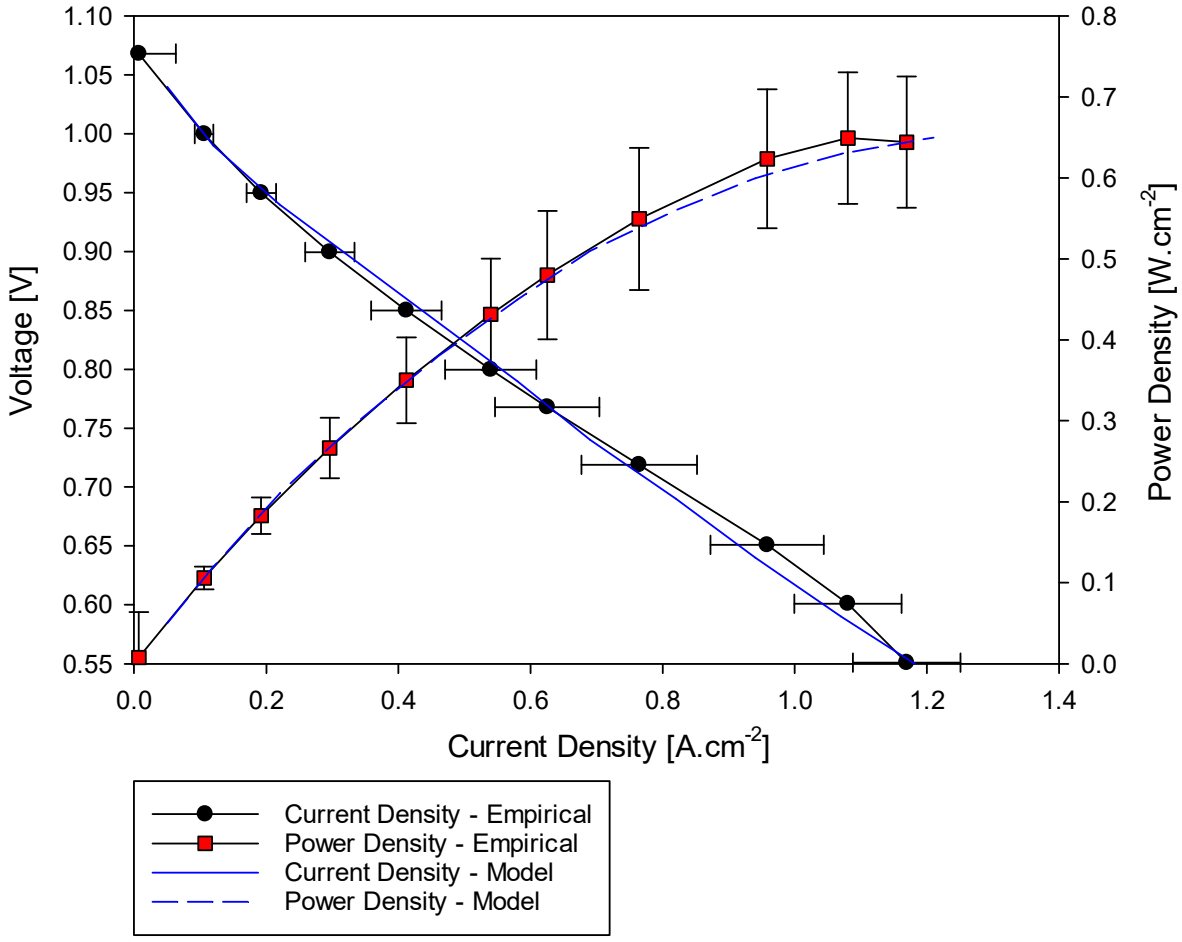

Figure 5.41 - Polarisation and power density plots from averaged empirical data from cells with a central silver current collector and the CFD model of a µT-SOFC with a central current collector at a furnace temperature of 750°C and flow of 200 ml.min^{-1} of H_2 and 10 ml.min^{-1} N_2.

5.7.2 Electrolyte Current Density Distribution

2D plots of the electrolyte current density magnitude, overlaid with the arrow plot of electrolyte current density vector at 1 V, 0.7 V and 0.55 V are seen in Figure 5.42 a), b) and c), respectively, for the central current collector. The axes are the geometric distance measured in µm with coordinate (0,0) being at the centre of the anode fuel channel at the inlet region of the cell. The colour scale is the current density measured in A.m^{-2}. The peak current density magnitude was 0.02 A.cm^{-2}, 0.24 A.cm^{-2}, 0.35 A.cm^{-2} at 1 V, 0.7 V and 0.55 V, respectively. At the central current collector, no current producing electrochemical reactions occur given the lack of active area/cathode. The current density generally decreased from the inlet to the outlet region. However, electrolyte current density spikes are seen at the electrolyte/cathode boundary with the current collector where the ground

boundary condition is applied as defined in Section 4.6, setting the potential to zero. These spikes do not represent the real-world phenomena and are a weakness of this model. The spikes occur due to the sharp corners at the interface of the electrode layer which lead to field singularities, similar to a Blasius boundary layer issue. The issue can be viewed as a meshing problem or a geometry problem. In this model, we have understood this limitation of the model and decided to ignore these spikes which do not significantly affect the model results and the trends observed, and will be relatively consistent for all current collector configurations. In later plots, the peak values arising from the singularities are omitted to capture more detail in the plot for analysis.

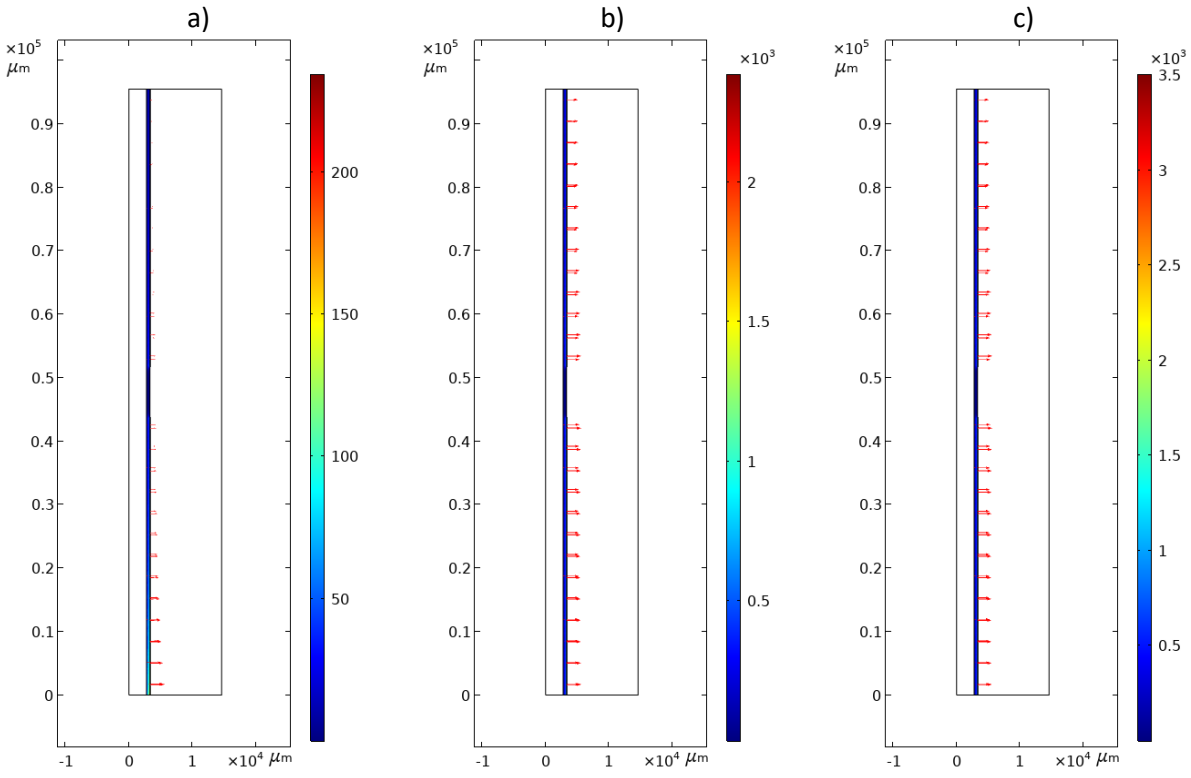

Figure 5.42 - Magnitude and arrow plot of electrolyte current density [A.m^{-2}] at a) 1 V, b) 0.7 V, c) 0.55 V.

5.7.3 Velocity Profile in the Fuel Channel, Fuel Cell and Furnace

Due to the model being designed in a 2D axisymmetric configuration, the geometry can be rotated to form a 3D plot which makes for an easier visual analysis of the results. The 3D velocity profile plot in the fuel channel, fuel cell and furnace is seen in Figure 5.43 at a) 1 V, b) 0.7 V and c) 0.55 V. The axes are the geometric distance measured in µm. The fuel and air inlet are at $z = 0$ at the bottom of the plot. The colour scale is the fluid velocity measure in m.s^{-1}. The left-hand scale in the purple

dominated colour scheme ranging between 0 and approximately 1.5 $m.s^{-1}$ is for the cathode and furnace (air) gas flow. The rainbow colour scheme of the right-hand scale is for the gas velocity in the anode gas channel and within the fuel cell with a range between 0 and approximately 0.23 $m.s^{-1}$. The velocity in the cell is largest at the centre of the fuel channel in the free stream, decreasing until the velocity becomes zero at the anode-electrolyte interface. On the air side, the velocity is stationary at both the outer furnace wall and cathode electrolyte interface and so the velocity profile for the cathode/furnace air stream has two minima in the radial direction. The maximum flow rate is in the centre of the furnace chamber at the inlet region.

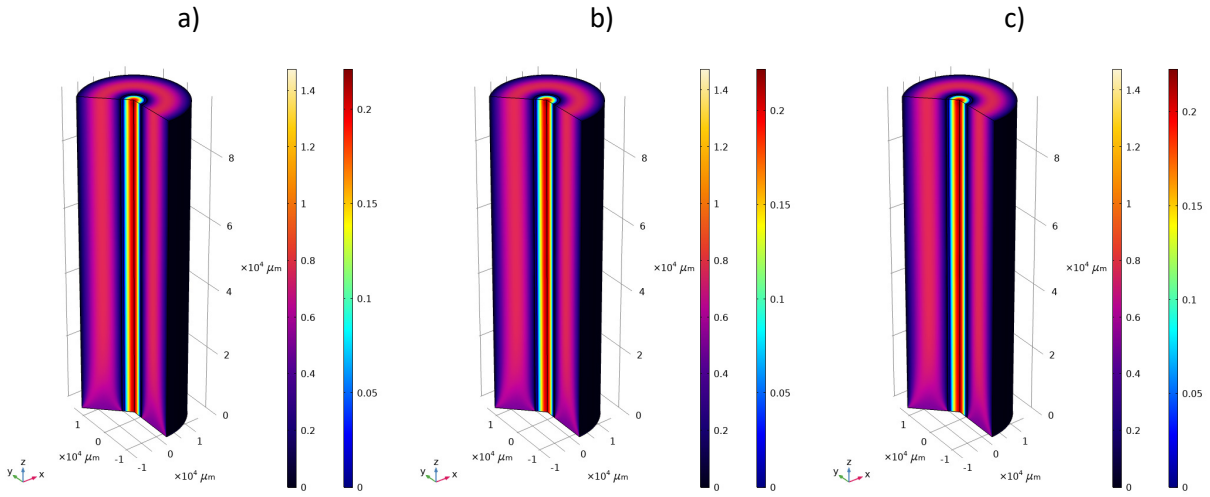

Figure 5.43 - Velocity profile in the fuel cell and furnace [$m.s^{-1}$] at a) 1 V, b) 0.7 V, c) 0.55 V.

5.7.4 Temperature Profile

The 3D temperature profile in the fuel channel, fuel cell and furnace is seen in Figure 5.43 at a) 1 V, b) 0.7 V and c) 0.55 V. The axis is geometric distance measure in µm. The scale is temperature measured in °C. The relatively cooler fuel entering the active region is heated by the air at the furnace temperature. There is also a contribution to the temperature profile from the heat generated by the electrochemical reactions and the ohmic heating from the resistance to electron flow within the electrodes. This is evident from the increasing peak temperature with decreasing operating potential (increasing load) recorded throughout the geometry.

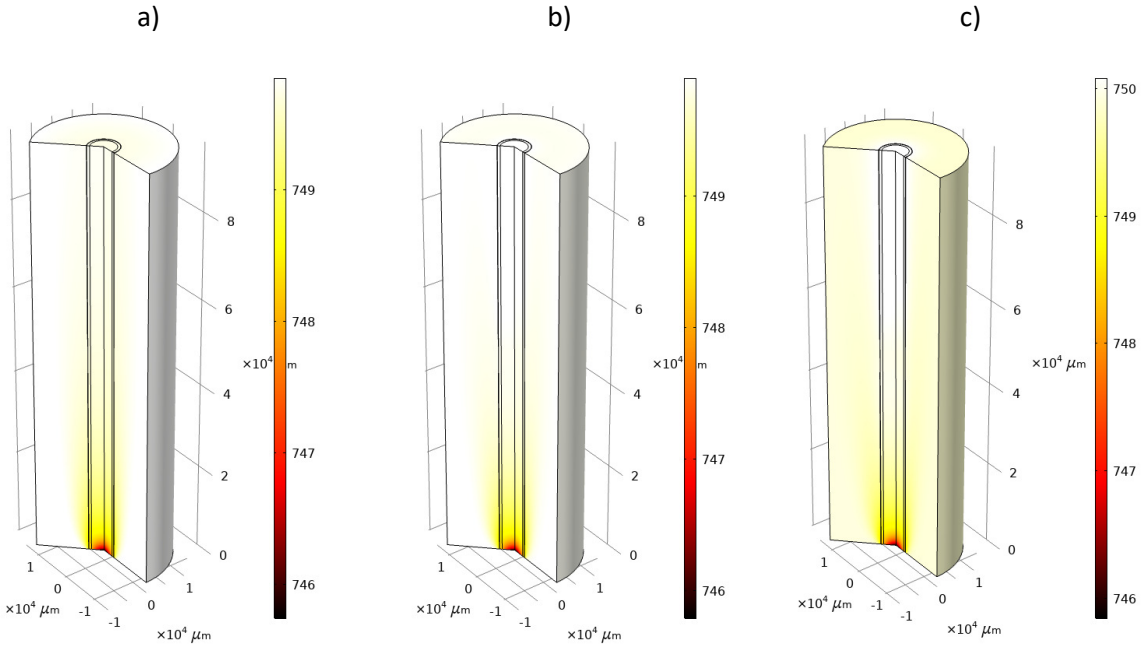

Figure 5.44 - Temperature distribution in the fuel channel, fuel cell and furnace at a) 1 V, b) 0.7 V, c) 0.55 V.

5.7.5 Concentration Profile

The 2D plots of hydrogen mole fraction throughout the anode fuel channel, anode support layer and anode functional layer at 1 V, 0.7 V and 0.55 V are shown in Figure 5.45 a), b) and c), respectively. The high flow rate and low fuel utilisation that was chosen to avoid mass transport limitations when changing current collector positions resulted in a similar hydrogen mole fraction at the outlet regardless of operating potential.

The 2D plots of oxygen mole fraction throughout the furnace and cathode at 1 V, 0.7 V and 0.55 V are shown in Figure 5.46 a), b) and c), respectively. The axes are the geometric distance measured in µm. The scale is the oxygen mole fraction. The oxygen mole fraction in air is 0.21 at atmospheric conditions, which is the inlet concentration boundary condition. Oxygen is consumed at the cathode in the reduction reaction and hence the mole fraction of oxygen is lower at the cathode-electrolyte interface. The air flow rate is sufficient to avoid any oxygen starvation as is indicated by the high mole fraction above 0.2 just a few hundred microns from the active region.

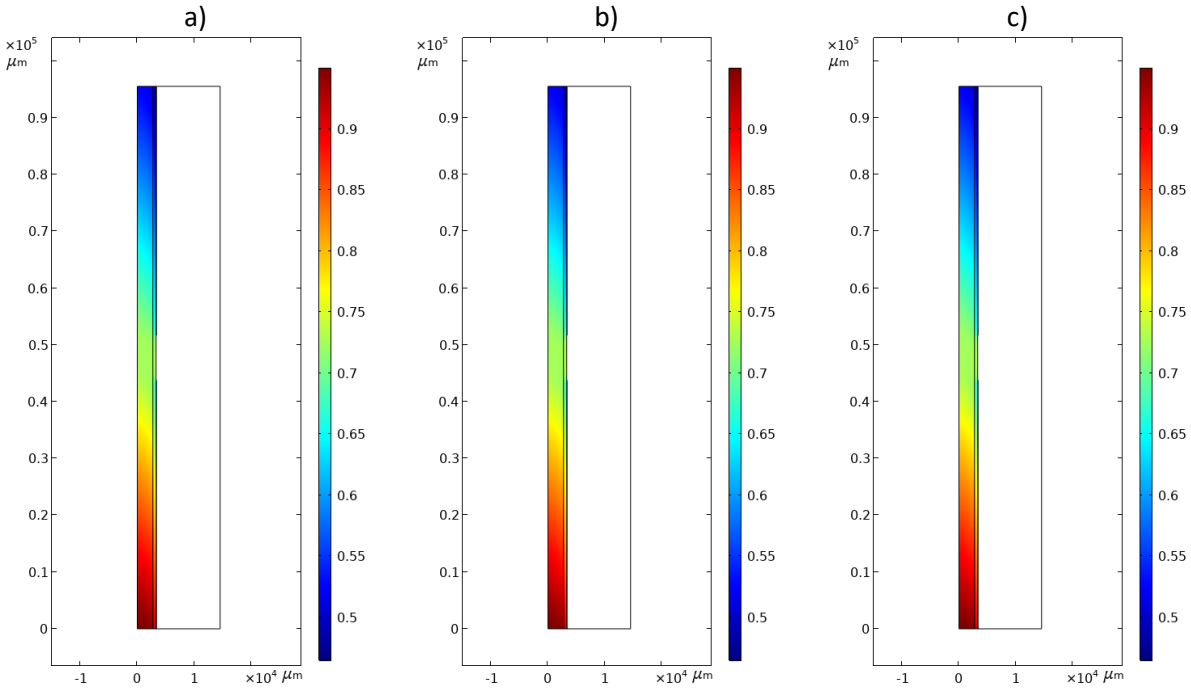

Figure 5.45 - 2D plot of hydrogen mole fraction at a) 1 V or b) 0.7 V, c) 0.55 V.

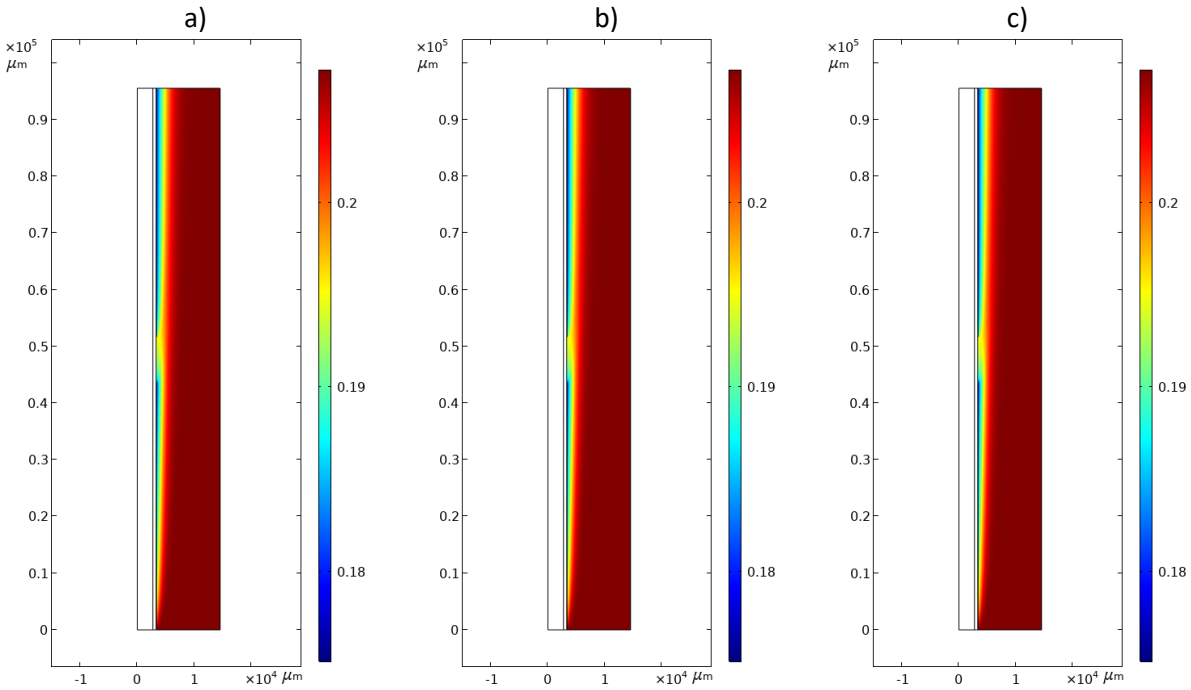

Figure 5.46 - 2D plot of oxygen mole fraction at a) 1 V, b) 0.7 V, c) 0.55 V.

5.8 Effect of Current Collector Position – CFD Analysis

The polarisation and power density plots predicted by the CFD model with a single current collector positioned at either the inlet, centre or outlet of the active region are seen in Figure 5.47. For this analysis, the model mesh used for each geometry was the standard COMSOL optimised mesh with a minimum skewness of 0.85. This was to ensure there was consistency when switching between model geometries. The operating temperature was set to 750°C and the fuel was 200 $ml.min^{-1}$ of H_2 and 10 $ml.min^{-1}$ of N_2, replicating the standard conditions defined in the empirical study (Section 5.1). The current density at 0.7 V was 0.637 $A.cm^{-2}$, 0.800 $A.cm^{-2}$ and 0.630 $A.cm^{-2}$ for the inlet, central and outlet current collector, respectively. This corresponded to a current density ay 0.7 V around 25.6% and 27.0% higher when utilising a central current collector compared to an inlet and outlet current collector, respectively. The peak power density was 0.502 $W.cm^{-2}$, 0.616 $W.cm^{-2}$ and 0.493 $W.cm^{-2}$ for the inlet, central and outlet current collector, respectively. The central current collector had a peak power density of 22.7% and 24.9% higher than the inlet and outlet current collector, respectively. The divergence between the inlet and outlet current collector performance increased with increasing current density. At the peak power density, corresponding to a 0.55 V operating potential, the difference between the power density values at the inlet and outlet was 1.8%. The ASR estimated from the gradient of the polarisation plot was 0.55 $\Omega.cm^2$, 0.45 $\Omega.cm^2$ and 0.57 $\Omega.cm^2$ for the inlet, central and outlet current collector configuration, respectively.

The plot of hydrogen mole fraction along the anode-electrolyte interface for the inlet, central and outlet current collector geometry is seen in Figure 5.48. The y-axis is hydrogen mole fraction. The x-axis is given by axial position along the anode-electrolyte interface. An axial position of zero is the anode-electrolyte interface at the fuel inlet region of the cell. The axial length of the model geometry is $9.55x10^5$ µm (95.5 mm) which is the cathode length and hence an axial position of $9.55x10^5$ µm is located at the anode-electrolyte at the outlet region of the cell. The 'hump', seen in each plot corresponds to the position of the current collector where no fuel is consumed. For the inlet current collector plot (black), the hydrogen enters at a mole fraction of 0.95 and is not consumed until past the 8000 µm current collector length where the active region begins. The current collector length was mirroring the length used in the experimental setup defined in Section 3.2.2. The length was chosen for current collector preparation logistics, leaving space for the wiring and to avoid short circuits between adjacent fuel cell layers. The gradient of each plot excluding the hump was estimated. For the inlet current collector, the gradient was $-1.699x10^6$ μm^{-1}. The central plot was split

into the upper and lower portion. The gradients were -2.685x10^{6} µm^{-1} and -2.116x10^{6} µm^{-1}, respectively with the average being -2.401x10^{6} µm^{-1}. The outlet current collector had a gradient of -2.317x10^{6} µm^{-1}. The steeper average gradient of the central current collector versus the inlet and outlet indicated that more fuel was being consumed with the central geometry. The central current collector had a steeper gradient at the upper region nearer the fuel inlet versus the lower outlet region of the cell with a central current collector. Indicating that more fuel was being consumed in the upper region where the concentration of the fuel was at its highest. For the inlet current collector, the gradient was steeper at the inlet region and then decreases slightly towards the outlet. The converse can be said for the outlet current collector which had a shallower gradient at the inlet region, becoming steeper towards the outlet region. Evidently, the fuel cell converts more hydrogen into electrons near the current collectors. The fuel concentration for at the inlet current collector was higher than at the outlet current collector and so there was more fuel to be converted into electrons, leading to higher conversion efficiency.

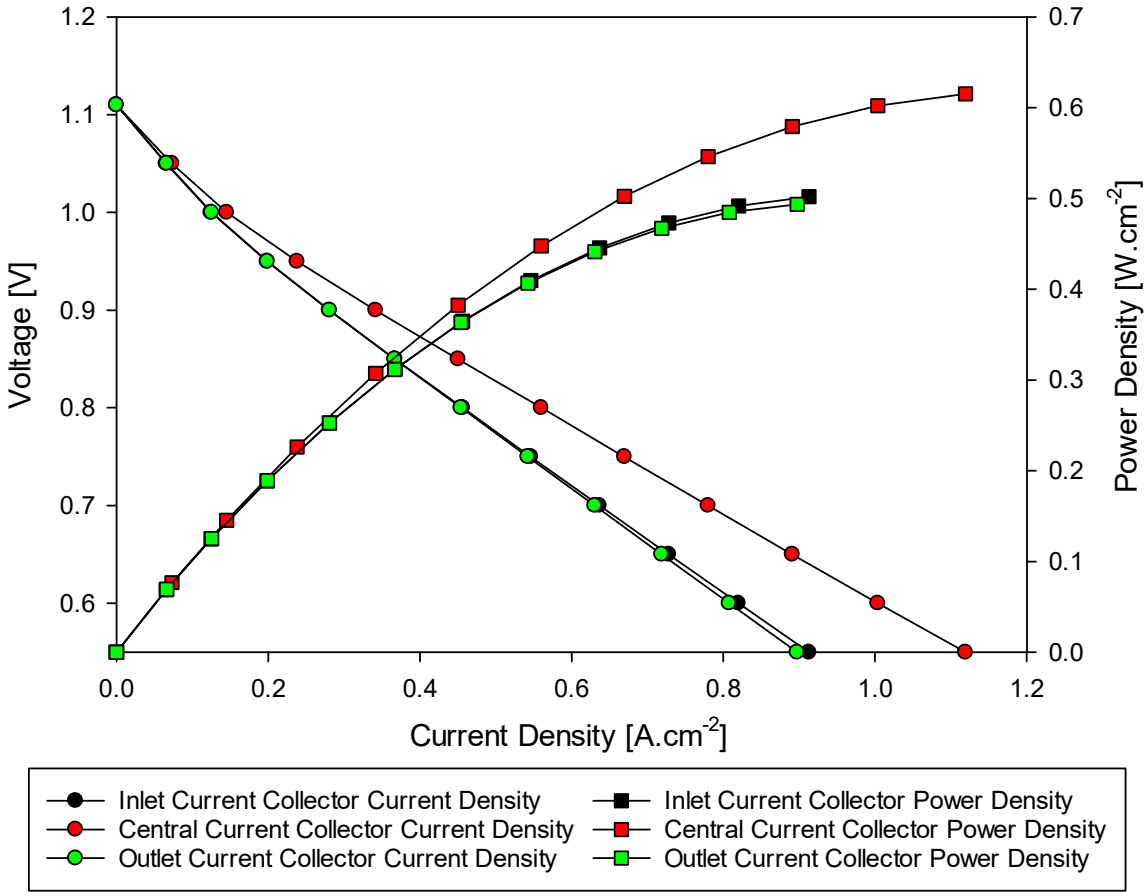

Figure 5.47 - Polarisation and power density plots as predicted by CFD modelling for an inlet, central and outlet current collector.

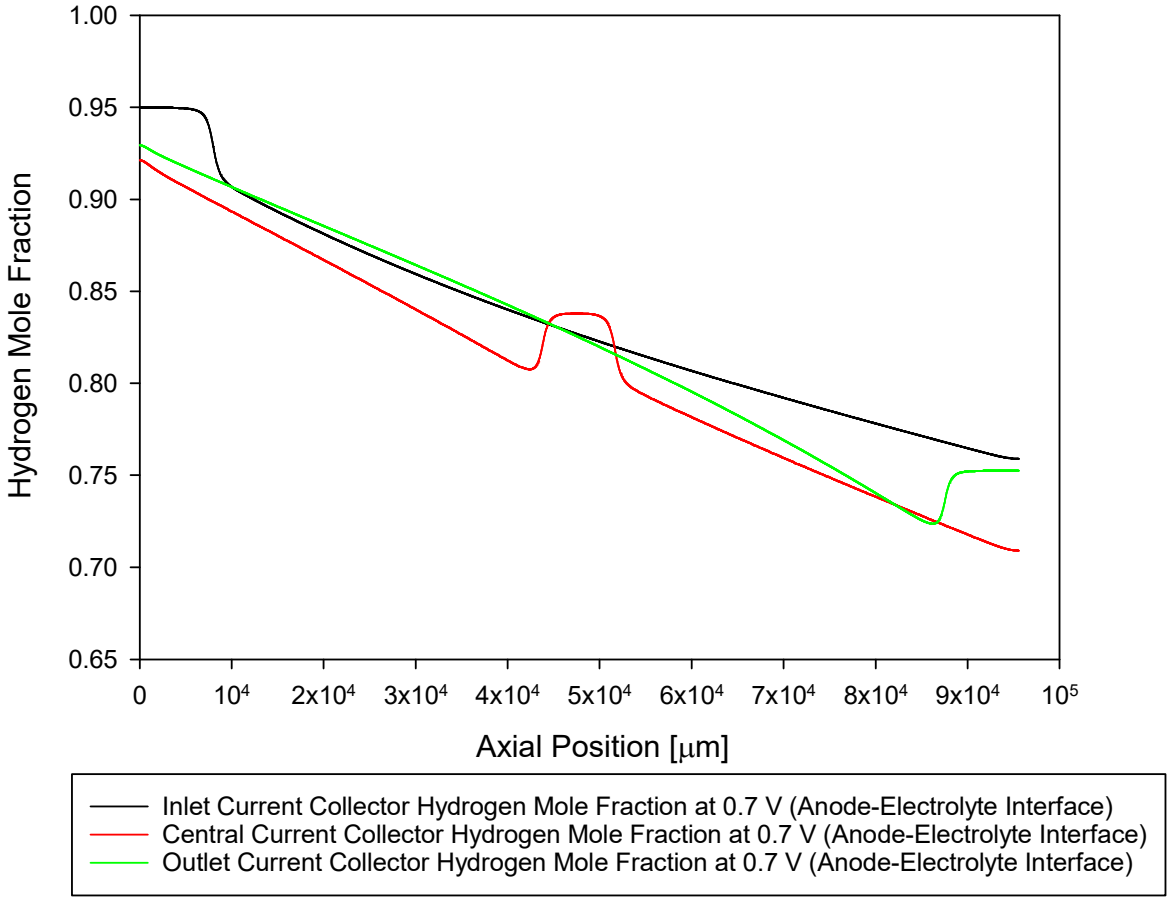

Figure 5.48 - Hydrogen mole fraction along the anode-electrolyte interface in the axial direction for the inlet, central and outlet current collector configurations.

Increasing the load on the cell from 1 V to 0.55 V increased the rate of reaction and thus the consumption of fuel along the anode-electrode interface as can be seen in Figure 5.49. The y-axis is the hydrogen mole fraction. The x-axis is the axial position, zero being at the inlet region of the cell and a position of $9.5x10^5$ μm being at the outlet region of the cell. At 1 V there was a very small current density and the conditions were very close to replicating OCV. The gradient was shallow and the 'hump' was very small. Increasing the load clearly increased the gradient and the size of the 'hump'.

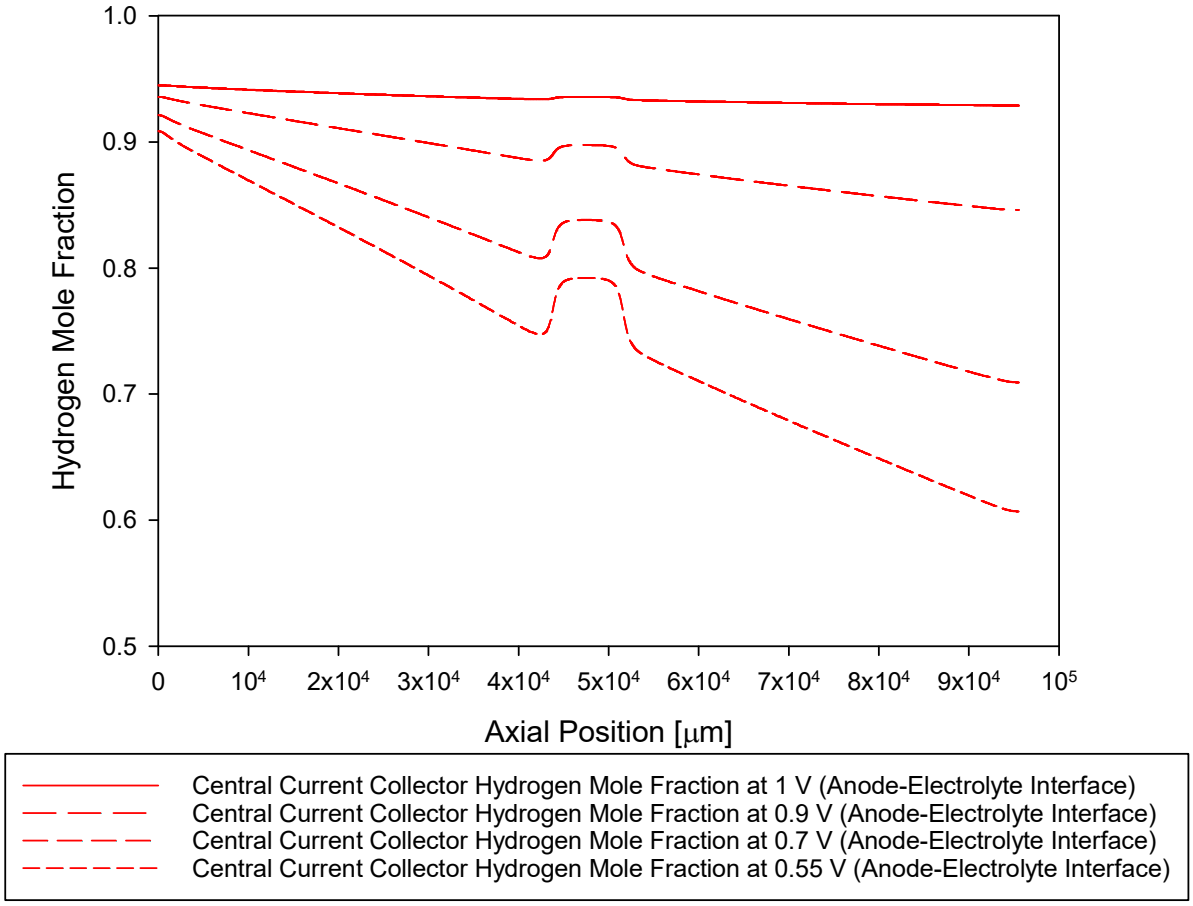

Figure 5.49 - Hydrogen mole fraction along the anode-electrolyte interface at 1 V, 0.9 V, 0.7 V and 0.55 V.

The irreversible heat loss at 0.7 V for an inlet, central and outlet current collector measured along a cut line at the anode-electrolyte interface is seen in Figure 5.30. The production of irreversible heat is as a result of the heat due to ohmic polarisation in the process known as Joule heating. In macroscopic form, this is given by:

$$P = I^2 R \tag{142}$$

where *P* [W] is the power loss, *I* [A] is the current and *R* [Ω] is the electrical resistance of the anode. The more current produced, the more power lost due to Joule heating. The difference in heat source for the inlet, central and outlet current collection positions was attributed to the different ohmic polarisation of current collector positons which is dependent on the resistance/electron path length. Q_{irrev} is the irreversible heat production, the product of the heat flux q_{irrev} over the cell volume. q_{irrev} was previously defined equation (72) in Chapter 4 as the product of voltage overpotential η [V], and the local current I_v, [A].

$$q_{irrev} = I_v \eta \quad (72)$$

At a given operating voltage, in this case 0.7 V, the overpotential η for each configuration are the same. The current density at 0.7 V predicted by the CFD model for the central current collector was 22% and 24% higher than the inlet and outlet current collector, respectively. Therefore, the Joule heating/irreversible heat loss for a central current collector was predicted to be higher than both the inlet and outlet current collector configurations.

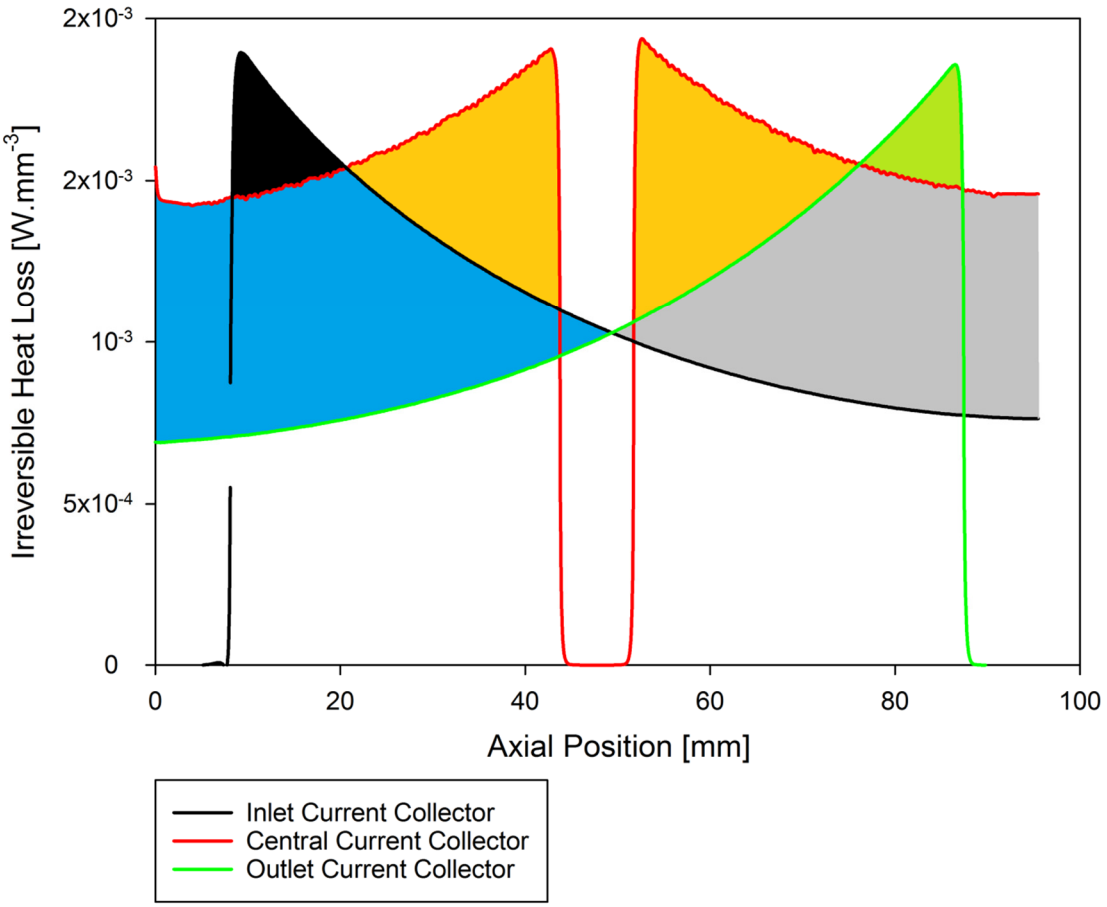

Figure 5.50 - Irreversible heat loss [W.mm^{-3}] of the cell measured along a cut line of the anode-electrolyte interface [mm] at 0.7 V for inlet, central and outlet current collection.

The irreversible heat loss was displayed in W.mm^{-3} and the length in mm for comparative purposes at the same length scale to the similar plot Figure 5.25, obtained from the mathematical model. The mathematical model and CFD model differ dimensionally, in that the mathematical model displays the irreversible heat produced over the cell area while the CFD model presents over the cell volume,

nevertheless, a comparison of relative values is valid. The CFD model showed good agreement to the mathematical model, predicting that the irreversible heat loss of the cell was higher for the central current collector than the inlet and outlet current collector. The CFD model geometry had a current collector of finite width (8 mm) whereas the numerical model was for an infinitesimal current collector. As a result, the irreversible heat loss profile differs between the plots given that the current and heat production at the current collector in the CFD model is zero, as defined by the ground conditions defined in Section 4.6. The orange and grey shaded area represent the additional irreversible heat loss from the central current collector compared to the inlet current collector. Similarly, the orange and blue shaded area represent the additional irreversible heat loss from the central current collector compared to the outlet current collector.

The temperature profile measured along a cut line at the anode-electrolyte interface at 1 V (dark blue), 0.9 V (green), 0.7 V (red) and 0.55 V (light blue) for the inlet, outlet and central current collector geometries are seen in Figure 5.51 a), b) and c), respectively. The x-axis in the plot is the z coordinate measured in μm, with the axial cell position of zero being at the inlet region and 95000 at the outlet region. For each plot, increasing the load (decreasing the potential), increased the cell temperature at the outlet region. The divergence in the values at each operating potential occurs nearer the inlet region than for the central current collector than the inlet and outlet. The temperatures at the outlet region are very similar for each current collector mode. At 0.7 V, the temperature was 750°C to 1d.p for the inlet, central and outlet current collector geometry.

The cell temperature profile measured along the anode-electrolyte interface at 0.7 V for the inlet, central and outlet current collector is seen in Figure 5.52. At the current collector, zero current was produced given the ground boundary condition. Therefore at the current collector zero heat from electrochemical reactions was produced which led to a local drop in cell temperature at that location. At all positions along the cell length the temperature of the cell with a central current was higher than the temperature of the inlet or outlet current collector. The inlet current collector had the lowest temperature at the inlet and outlet region of the cell. However, it should be noted that the temperature difference between current collector configurations at all positions along the cut line are very similar at the present operating conditions. The largest difference between values at the outlet region was less than 0.01%. Such a small temperature difference would have a negligible effect on the local current production and it was concluded that the CFD model did not attribute the difference in cell performance to thermal effects.

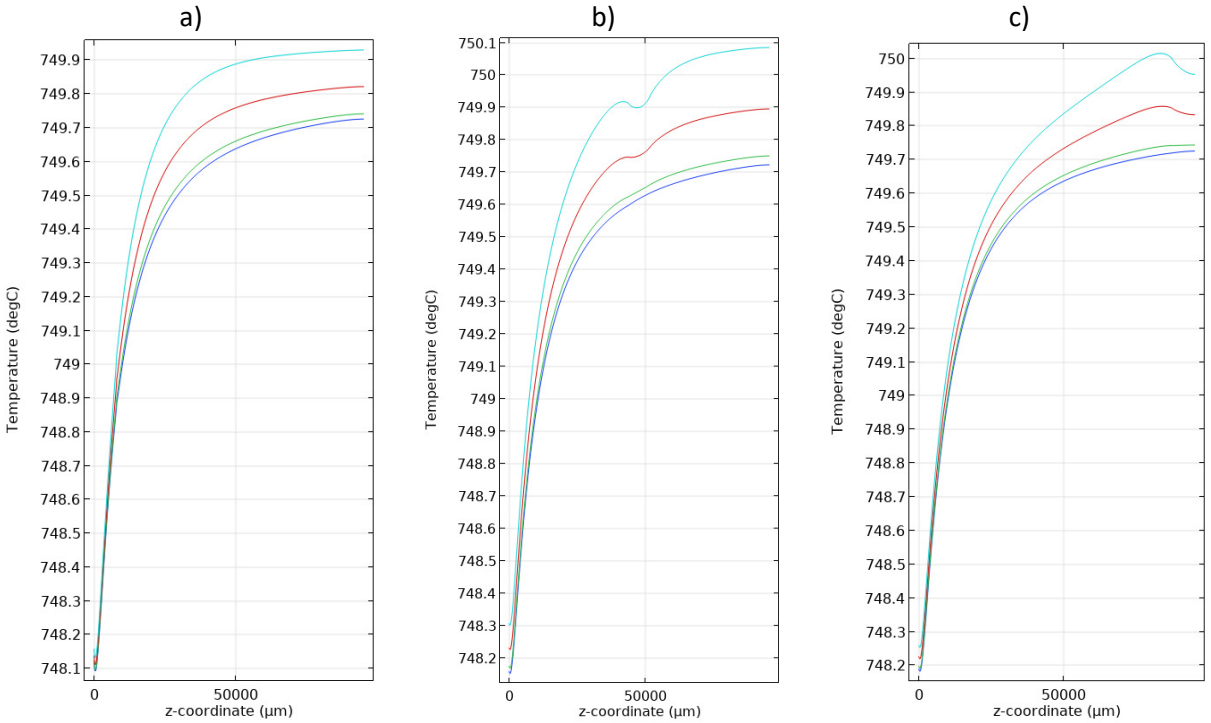

Figure 5.51 - Temperature profile of the cell measured along an anode-electrolyte interface at 1 V, 0.9 V, 0.7 V and 0.55 V for a) inlet, b) central and c) outlet current collector geometry.

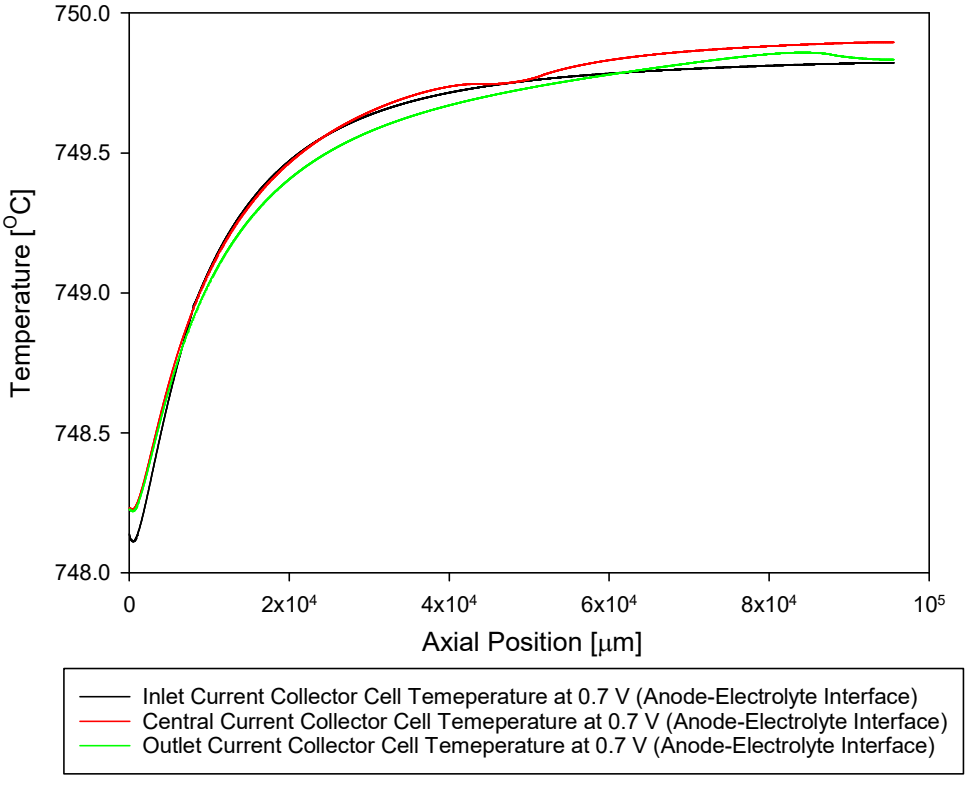

Figure 5.52 - Cell temperature measured along a cut line of the anode-electrolyte interface at 0.7 V for inlet, central and outlet current collection.

The electrolyte current density magnitude and vector plot of electrolyte current density [A.m^{-2}] are seen in Figure 5.53 for a) inlet, b) central, c) outlet current collector geometries. The axes are the geometric distance measured in µm. The scale represents the electrolyte current density magnitude. The peak electrolyte current density in each geometry occurred adjacent to the current collector. Ignoring the singularity associated spikes previously discussed in Section 5.7.2, the peak values are still adjacent to the current collector nodes. The peak electrolyte current density value was highest for the inlet current collector followed by the central and outlet current collector geometries.

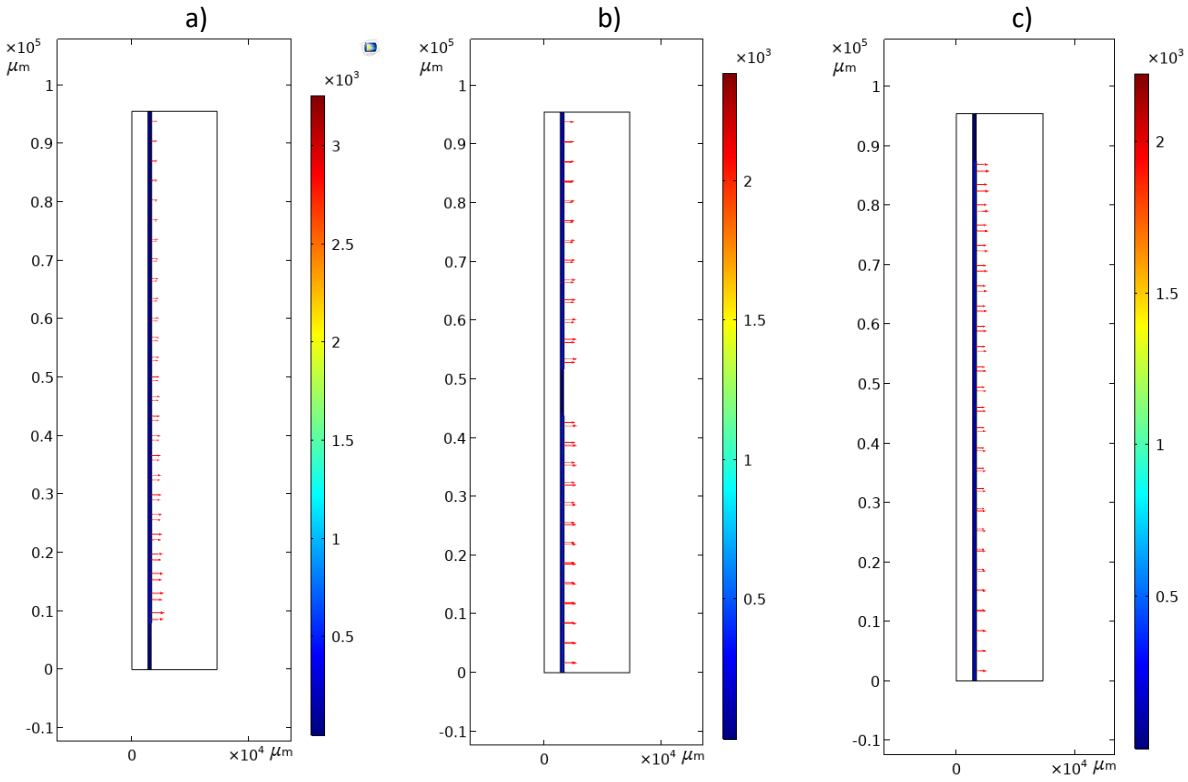

Figure 5.53 - Electrolyte current density magnitude and vector arrow plots of current density [A.m^{-2}] with a) inlet, b) central, c) outlet current collector geometries.

The electrode current density [A.cm^{-2}] at 0.7 V measured along a cut line at the anode-electrolyte interface is seen in Figure 5.54 for a single inlet, central and outlet current collector. The x-axis is the axial position, zero being at the inlet region of the cell and 9.55x10^4 µm being at the outlet region of the cell. The current density values seen for the outlet current collector and first half of the central current collector are indicative of the current direction which is positive (by convention) in the outlet to inlet direction (opposite to the fuel flow direction). For each case, the peak current production is directly adjacent to the current collector with the value decreasing with the distance away from the current collector to a value of zero at the end of the active area. The current density values were

around an order of magnitude higher than expected and observed in literature [226,227]. This was attributed to the singularity pulling up the peak values. The peak current density was 10 A.cm^{-2}, 6.8 A.cm^{-2} and 9.9 A.cm^{-2} for the inlet, central and outlet current collector geometry, respectively. The peak current density value of the central current collector was directly adjacent to the current collector on the inlet side; the second peak value adjacent to the collector at the outlet side was 90% of the inlet side peak value, owing to decreasing fuel concentration along the axial position/fuel flow direction.

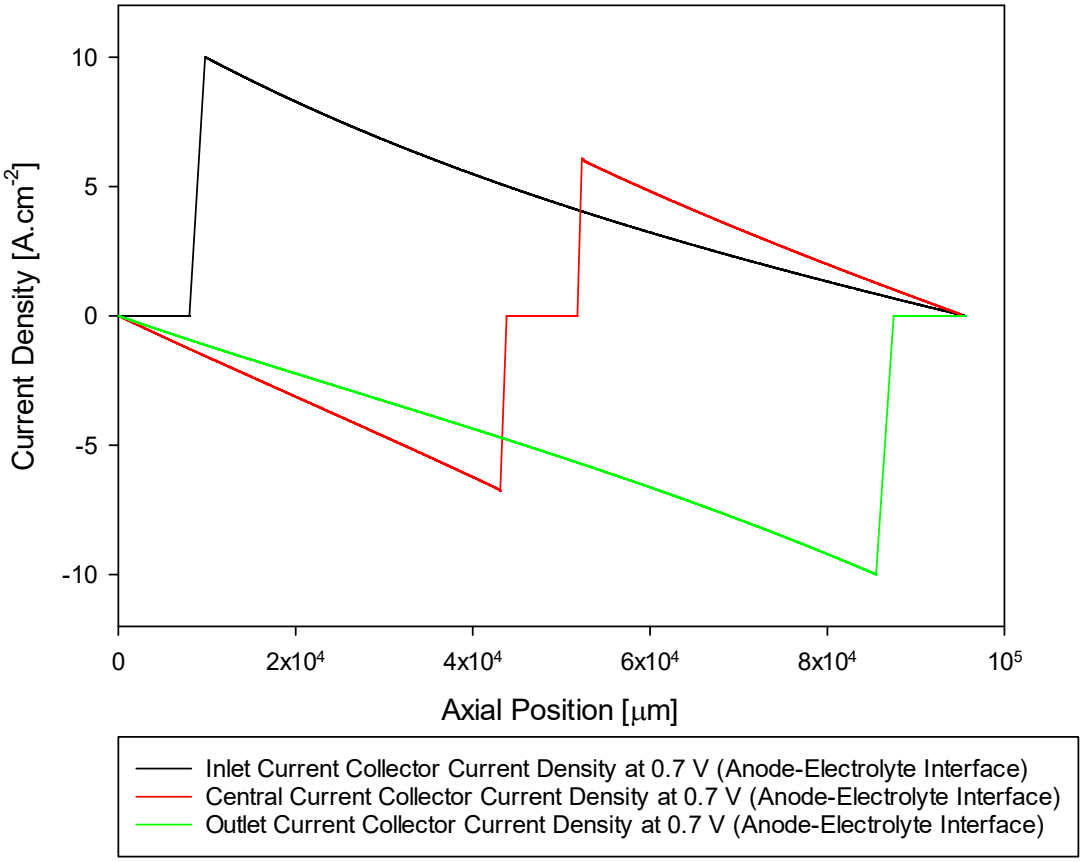

Figure 5.54 - Current density along of the cell measured at a cut line along anode-electrolyte interface for inlet, central and outlet current collector.

To allow for a direct comparison between the current density estimated from the mathematical model seen in Figure 5.24, the current density data [A.cm^{-2}] presented in Figure 5.54 was divided by the cell circumference. This was to give a somewhat crude approximation to the current density per unit length [A.mm^{-1}] as a function of the position along the cell length in mm. The peak current density values were an order of magnitude higher than those estimated from the mathematical model, again as a result of the singularity in the model pulling up the peak values.

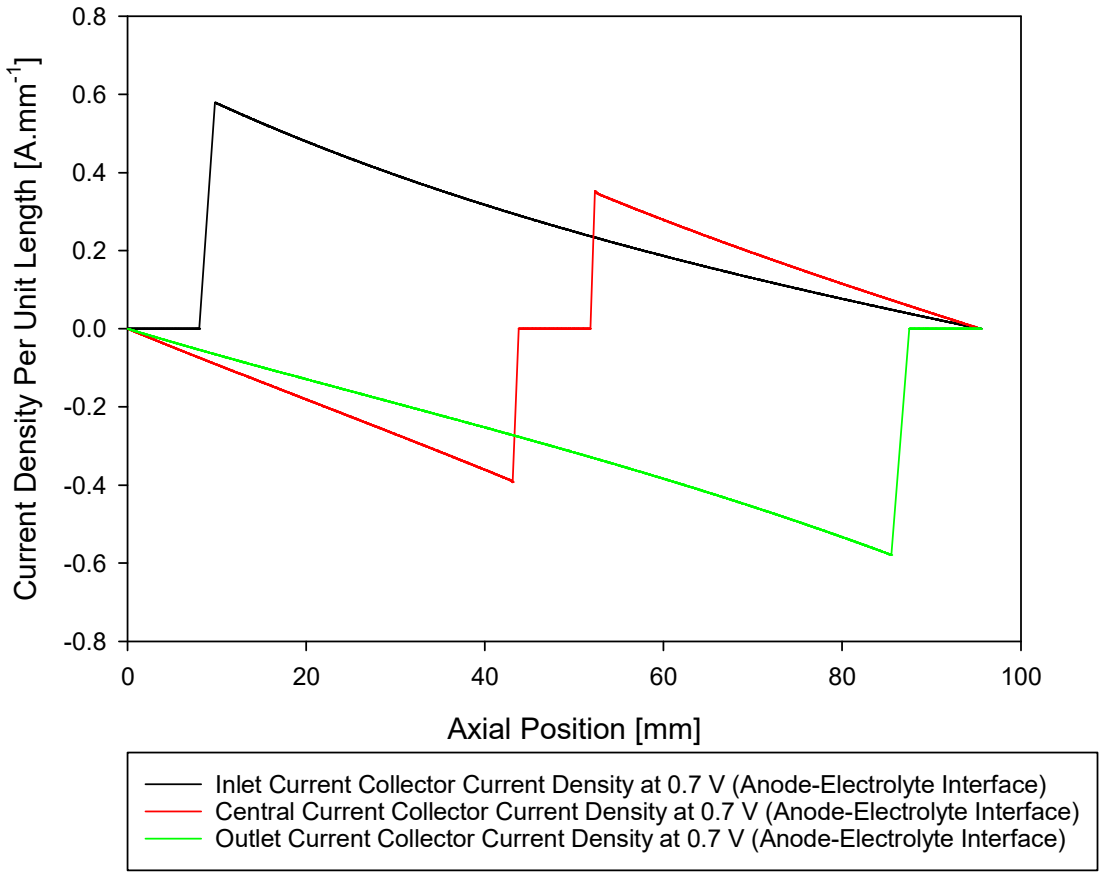

Figure 5.55 - Current density per unit length along of the cell measured at a cut line along anode-electrolyte interface for inlet, central and outlet current collector.

The electrode current density magnitude, electrode current density streamline and arrow line plot [$A.m^{-2}$] and zoom at the current collector electrolyte/cathode interface for the inlet current collector is seen in Figure 5.56. The direction of the vector represents the direction of the electron flow and the length of the arrows is proportional to the magnitude. As seen in the magnified image, the peak current density occurred at a fictional singularity related concentrated point within the anode reaction layer, at the interface between the current collector, anode and the electrolyte. The magnitude of current density decreased away from this point. The current direction was away from the current collector towards the outlet region and was not parallel to the anode/electrolyte interface.

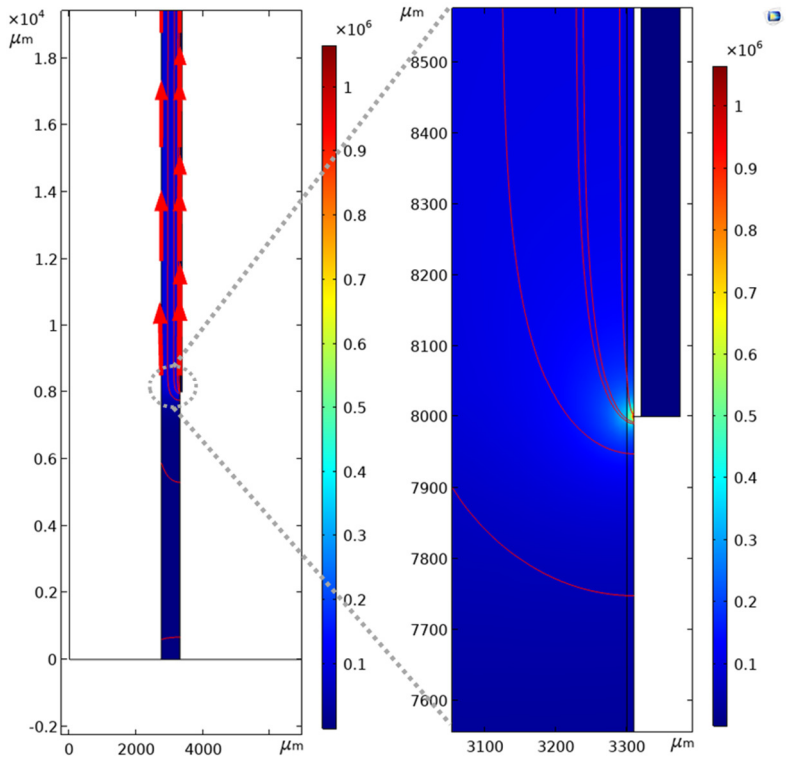

Figure 5.56 - Electrode current density magnitude, electrode current density vector and streamline and arrow plot [A.m^{-2}] with inlet current collection at 0.7 V

The electrode current density magnitude, electrode current density streamline and vector plot [A.m^{-2}] and zoom at the current collector electrolyte/cathode interfaces for the central current collector are seen in Figure 5.57. The direction of the vectors represent the direction of electron flow. As can be seen, the direction of travel is away from the current collector node. From the magnified image, the peak current density at the two fictional singularity regions are seen. Located within the anode reaction layer, at either side of the current collector, at the current collector, anode and electrolyte interface. The magnitude of current density decreased away from those peaks towards the inlet and outlet of the cell.

The electrode current density magnitude, electrode current density streamline and vector plot [A.m^{-2}] and zoom at the current collector electrolyte/cathode interfaces for the outlet current collector is seen in Figure 5.58. The direction of the arrow plots represent the direction of electron flow. The direction of travel is away from the outlet current collector node towards the inlet region. As seen in the magnified image, the peak current density occurred at a concentrated point within the anode reaction layer, at the interface between the current collector and the electrolyte. The magnitude of current density decreased away from the concentrated peak.

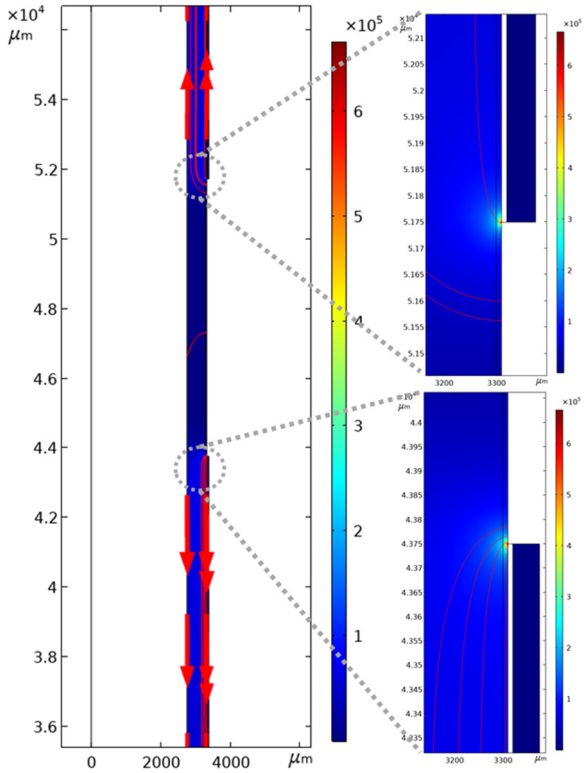

Figure 5.57 - Electrode current density magnitude, electrode current density vector and streamline and arrow plot [A.m^{-2}] with central current collection at 0.7 V

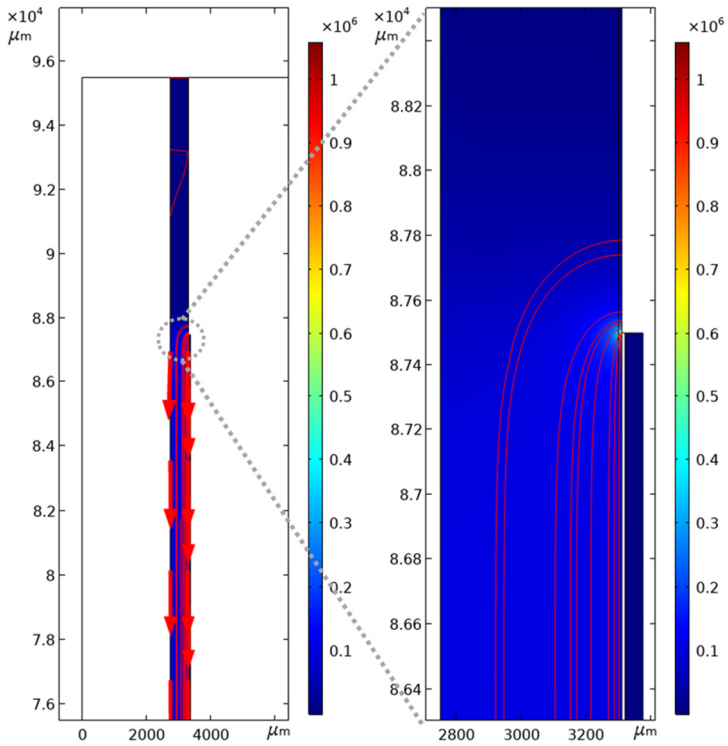

Figure 5.58 - Electrode current density magnitude, electrode current density vector and streamline and arrow plot [A.m^{-2}] with outlet current collection at 0.7 V

5.9 Summary

A fuel flow calibration study of cells setup with the state-of-the-art central silver anode current collector and spine and tie cathode current collector was conducted to find the optimal flow rate for studying varying current collector configuration on cell performance, isolating the ohmic contribution. The effects of using N_2 as a carrier gas was explored, determining that the carrier gas acts to increase turbulence and mixing of the fuel, also increasing the Nernst due to increased fuel pressure, with the effects more significant at higher current densities. A standard operating condition of 200 $ml.min^{-1}$ of H_2 and 10 $ml.min^{-1}$ of N_2 at 750°C was defined. An average baseline polarisation and power density plot were obtained from multiple cells with the state-of-the-art current collection at the standard testing conditions.

Cells were prepared with 3 equidistant anode current collectors to study the effect of current collector position on cell performance. Plots of polarisation, power density and Nyquist plots from EIS were obtained for the current collector positions at the inlet, centre and outlet of the cell. Results from both techniques confirmed that the central current collector was the best performing followed by the inlet and outlet current collectors. The impedance analysis confirmed that the ohmic polarisation of the different current collector positions had a strong influence on the performance. Cells set up with 5 equidistant anode current collectors were used for studying the effect of again varying anode current collector position, as well the effect of increasing the number of anode current collectors. It was found that increasing the number of anode current collector positions increased cell performance, however, following a trend of diminishing returns.

A mathematical resistance path model was developed giving insight into the reasons behind the empirically observed effects of varying current collector position and number on the resistance to electron flow within a µT-SOFC. The model was extended to account for the current, heat loss and power produced for a given current collector configuration. The model determined that the optimal location of a current collector of finite width is at the centre of the active region where the current conduction path is at its minimum. The model found the performance of the inlet and outlet current collectors to be the same given the model symmetry and assumptions. From experiments, it was found that this is not the case, and the numerical model failed here as it could not account for the variation of the cell potential, temperature profile and species concentration profile. In addition, the model found the performance of a current collector at the inlet and outlet to give the same cell

performance as a single current collector at the centre. Again, from experiments we know this not to be true, primarily due to the loss of active area from the location of the additional current collector, but also from fuel loss due to improper sealing. The model found that a cell with two current collectors at their optimal location outperformed a cell with a single current collector at optimal locations which was also observed from experiments.

To account for the effects of variation in cell potential, temperature profile and species profile on current collector configuration within a μT-SOFC, a 2D axisymmetric CFD model mirroring the μT-SOFC cell setup with a central silver anode current collector was constructed. The model geometry was limited to the electrochemically active region of the cell and described the conservation of momentum, energy, mass and charge. Characterisation via XRCT, SEM, EDX, the Archimedes method and Tafel analysis was used to obtain a wide range of cell parameters for use in CFD analysis. The model was fitted to the experimentally derived average polarisation and power density plots. The fitted, predictive model was then used to provide insight into the effects of varying current collector position on performance. The model geometry was modified to have a current collector at the inlet, centre or outlet of the active region. The CFD predicted polarisation plots agreed with the experimentally derived data and the numerical model in finding that a central current collector was the optimal location for the best cell performance. The model also agreed with the empirical research (which the numerical model did not) in establishing that an inlet current collector outperformed an outlet current collector due to the highest concentration of fuel available at a location nearer to where the fuel is being consumed.

While the central external current collector performed the best due to a reduced electron path length versus an inlet and outlet connection, it required cutting of the external cell layers and loss of active area. Increasing the number of external current collectors would further reduce the electron conduction pathway, reducing the cell ASR, but at the cost of sacrificing active area. A current collector with a high surface area for contacting the anode that reduced the current path within the anode, without the need to sacrifice active area was required.

Chapter 6 Interconnect Development

This chapter details the development of a novel internal current collector to address the shortcomings of the state-of-the-art central external configuration. A low-cost, durable, and simple solution is proposed that does not require the cutting of the fuel cell layers and the sacrifice of active area. The chapter explores the use of an internal current collector, a brush-like, high surface area device named hiTRAN which is produced by CalGavin Ltd based in Warwickshire, UK. The device, typically used in heat exchangers is adapted for use as a current collector. The chapter details the effectiveness of hiTRAN as a µT-SOFC current collector and characterises the thermo-fluidic effects on the cell.

6.1 CalGavin hiTRAN

The flow turbuliser technology designed by CalGavin, typically used in tubular heat exchangers has been used in this study for primary use as an internal current collector for µT-SOFC. The hiTRAN protruding from a heat exchanger tube is seen in Figure 6.1.

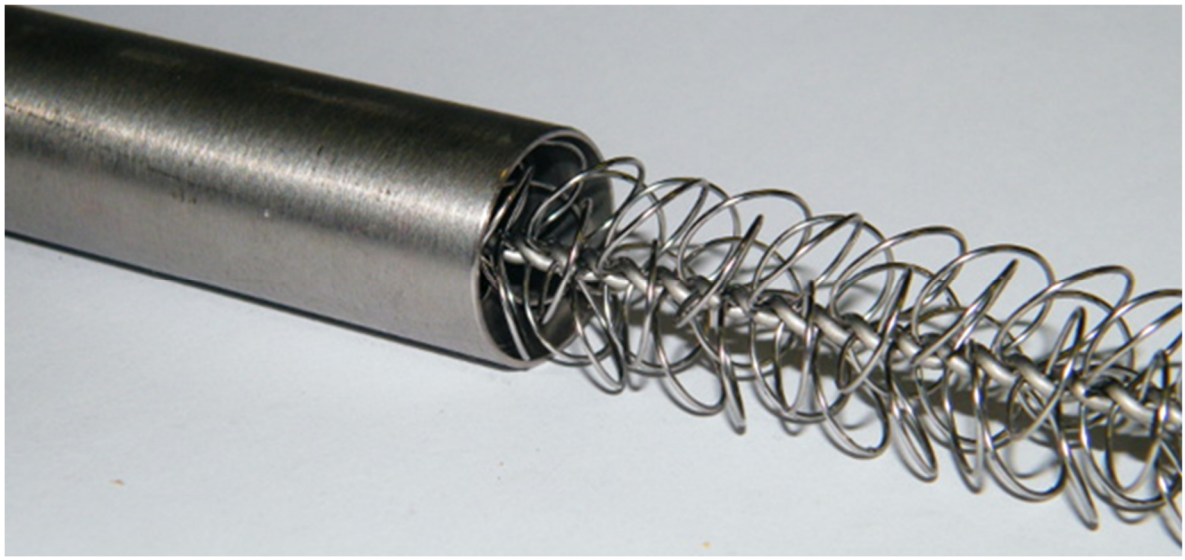

Figure 6.1 - CalGavin hiTRAN promotional picture.

When used in heat exchangers, the hiTRAN turbuliser (hiTRAN) removes the laminar boundary layer by inducing turbulence in the tube side fluid, affecting the velocity and temperature distribution in order to reduce the resistance to heat transfer [301]. This is particularly useful for low Reynolds

number (Re) flows which are well within the laminar region. These are typical in fuel cell applications where the flow rate is determined by the fuel utilisation of the electrochemical device. As seen in Figure 6.2, two velocity maxima occur since the centre of the tube is occupied by the hiTRAN core and hence the maxima either side of the core are shifted nearer the wall [302]. A much steeper velocity gradient is present at the wall and thus higher wall shear forces occur. The larger velocity gradient will promote better mixing of the fluid which is characteristically poor in the laminar regime. The enhanced mixing and higher radial velocity will enhance the heat and mass transfer, the latter ensuring fresh fuel is moved from the free steam to the wall and into the electrode, improving the electrochemical reactions by reducing mass transport limitations and increasing local fuel partial pressure.

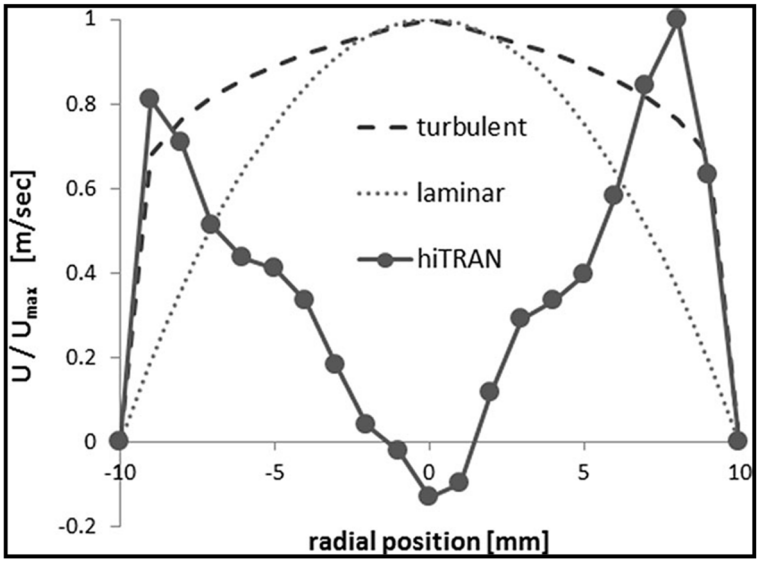

Figure 6.2 - Normalised velocity profile in turbulent (Re=20000), Laminar and hiTRAN (Re=500) [302]**.**

The estimated Reynolds numbers at 20°C are presented in Table 6.1 for tubular cells with an active area of 20 cm^2, a wall thickness of 0.5 mm, at a current density of 1 $A.cm^{-2}$ and an internal diameter between 1 and 9 mm for fuel utilisation values of 100%, 75%, 50% and 25%. At the smallest internal diameter and lowest fuel utilisation, the Reynolds number is 116.73. The transitional Reynolds number for flow within a circular pipe is 2300 and so in this case flow is well in the laminar region [290].

Table 6.1 - Reynolds number for various cell dimensions with a fixed active area of 20 cm^2 wall thickness of 0.5 mm at a current density of 1 $A.cm^{-2}$ for 100% F.U, 75% F.U, 50% F.U and 25% F.U.

ID [mm]	OD [mm]	Length [mm]	Velocity at 100% F.U [m/s]	Re [-]	Velocity at 75% F.U [m/s]	Re [-]	Velocity at 50% F.U [m/s]	Re [-]	Velocity at 25% F.U [m/s]	Re [-]
1	2	318.47	3.04	29.03	4.06	38.78	6.09	58.27	12.21	116.73
2	3	212.31	0.76	14.52	1.01	19.39	1.52	29.13	3.05	58.37
3	4	159.24	0.34	9.68	0.45	12.93	0.68	19.42	1.36	38.91
4	5	127.39	0.19	7.26	0.25	9.69	0.38	14.57	0.76	29.18
5	6	106.16	0.12	5.81	0.16	7.76	0.24	11.65	0.49	23.35
6	7	90.99	0.08	4.84	0.11	6.46	0.17	9.71	0.34	19.46
7	8	79.62	0.06	4.15	0.08	5.54	0.12	8.32	0.25	16.68
8	9	70.77	0.05	3.63	0.06	4.85	0.10	7.28	0.19	14.59
9	10	63.69	0.04	3.23	0.05	4.31	0.08	6.47	0.15	12.97

6.1.1 hiTRAN Specifications

The hiTRAN turbuliser has a central core wire providing a backbone of support which is then threaded with a coil wire to create a repeating loop structure. Wire thickness, material, core length, coil length, outer diameter, loop section length and loop packing density (PD) was varied in this study to achieve an optimal design for the specific application. The hiTRAN had to be designed considering its primary electrical function for current collection, and its secondary function for flow and thermal distribution. As a current collector, the metallic hiTRAN acts as a highly conductive conductor with high surface area along the cell at multiple contact points along the anode wall. The current collected from the anode is extracted out of the cell and through the hiTRAN into the external circuit. As a flow/thermal distributor the hiTRAN works by the same mechanisms as used in heat exchangers, that is removal of the laminar boundary layer. The hiTRAN also acts as a conductor of heat within the cell and gas channel given its high thermal conductivity and intimate contact with the gas and anode. As a current collector, minimisation of ohmic resistance was the key optimising parameter by reducing bulk resistance and contact resistance. As a flow/thermal distributor, maximising (pseudo) turbulence and heat transfer coefficient and minimising pressure drop were key optimising parameters. Multiple design configurations were trialled varying the material and core thickness, but mainly the packing density from a low packing density (LPD), to a medium packing density (MPD), and finally a high packing density (HPD).

Increasing the packing density increased the number of coils and hence length of coil wire in a defined coil section length, thus increasing the number of contact points between the hiTRAN and the tube wall. Increasing the packing density in a typical hiTRAN heat exchanger would increase the turbulence and improve heat transfer. In this instance more contact points would allow more current to be extracted to the circuit. A packing section length of 100 mm was selected to collect current from the entirety of the 95.5 mm cathode length where current is produced, also determining the positioning of the hiTRAN within the tubular cell. From a flow/thermal enhancement perspective, the low Reynolds flow meant that disturbances to the flow caused by the hiTRAN quickly decayed and did not propagate, thus the coil section had to be present throughout the region where flow affected performance and where heat was produced [302].

The outer diameter of the packing section was chosen to be oversized with respect to the 5.5 mm tube bore, ensuring the hiTRAN was fixed firmly in position during assembly. The coil was fixed at a thickness of 0.375 mm. Three core thicknesses were studied, 0.71 mm, 0.5 mm, 0.375 mm. The core acted as a 'highway' for all of the current extracted in the coils and thus was a key parameter. A core thickness of 0.71 mm was chosen as a final design to give a total core diameter of approximately 1.42 mm (slightly less when braided). This gave a structurally sound support with some flexibility, sufficient cross-sectional area for a minimised resistance while not occupying too much of the anode gas channel. The total core length was 250 mm, 115 mm of which sat inside the cell acting as a support for the loop section with the remaining 'tail' used for interconnection to the cathode of an adjacent cell. Two materials were selected for fabricating the hiTRAN elements, nickel and silver. Nickel for its material similarity and hence compatibility with the Ni-YSZ cermet anode material w.r.t CTE, low cost and inertness in the anode gas environment. Silver was trialled for its favourably high conductivity. The materials selected for electrochemical testing are seen in Table 6.2.

Table 6.2 - hiTRAN material choices.

Core thickness [mm]	Low Packing Density [LPD]	Medium Packing Density [MPD]	High Packing Density [HPD]
0.71	N	N, S	N

*N refers to nickel; S refers to silver

6.1.2 hiTRAN Fabrication

The hiTRAN were fabricated by hand, firstly the coil wire was fed through a wire straightener, then through a roller which fed the wire through a slot in an adjacent mandrel. A mandrel was attached to a motor which rotated to create a coil. The diameter of the mandrel was a key factor in determining the outer diameter of the hiTRAN. A 40 mm length of loop was then cut, 30 mm of which would make up the desired 100 mm loop section length with 5 mm each side of the coil for mounting to the core-coil assembly rig and for maintaining the structural integrity of the hiTRAN when mounting in the fuel cell. The core section was then loaded onto one pass of a 2 pass wire with each pass being 300 mm in total. One end of the pass was attached to a rotating head fixing point, the other end of the pass was attached to a stationary clamp fixing point at the desired loop section length with the rest of the 'tail section' free. The coil was then stretched along the core wire pass and secured to either fixing point. The rotating head then wound the coil wire and core wire together, adjusting the number of rotations to achieve the desired packing density for the specified loop section length. The three nickel hiTRAN designs of HPD, MPD and LPD are seen in Figure 6.3. Achieving a regular repeating structure with the LPD hiTRAN was difficult as the coil wire had fewer contact points to the central coil wires. The coils were not secured well to the central core and began to unwind near the ends. This weak contacting force led to concerns about an increased contact resistance between the coil wire to core wire joints along the hiTRAN length. The MPD and HPD were easily produced and reproduced and hence were favoured over the LPD from a fabrication point of view.

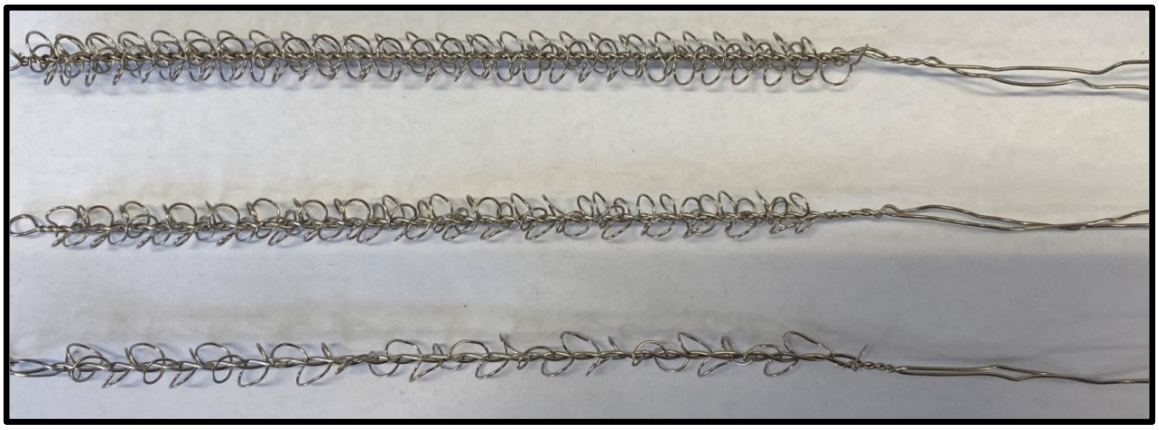

Figure 6.3 – Nickel hiTRAN a) HPD, b) MPD, c) LPD.

6.1.3 hiTRAN Installation

Fitting direction was from right to left (opposite to the fuel flow direction) in Figure 6.4, loading the tail through the outlet region of the cell, feeding the tail through the laser cut hole/s and pulling through until the loop section was seated in the desired location. Once 70 mm of the 100 mm loop section was inside the cell the spring force of the coils of the oversized hiTRAN against the cell wall provided a strong resistance to motion. It was found that a steady and continuous feed speed was the key to minimising damage to the hiTRAN and the cell.

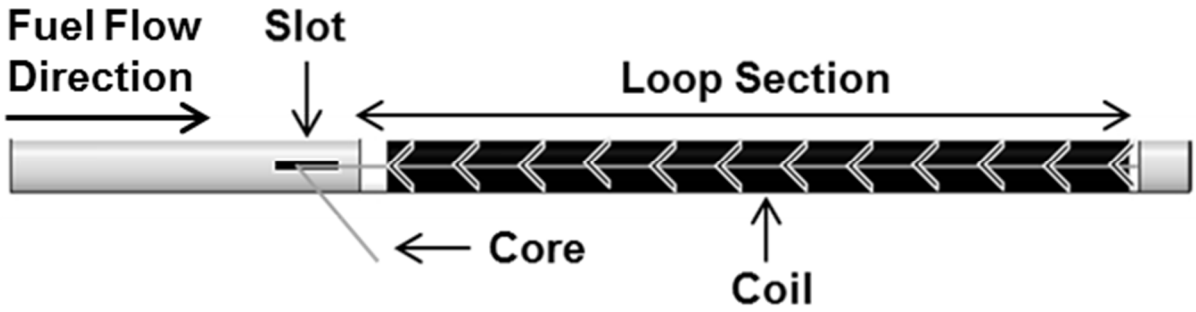

Figure 6.4 – Installing a hiTRAN inside a µT-SOFC.

A slot was required to allow the core wire of the hiTRAN to exit the cell for connection to the external circuit and/or for interconnection. Several laser cut designs were trialled. The optimal design favoured installation simplicity while minimising size to maintain the mechanical integrity of the anode and require less sealing. The design progression is seen in Figure 6.5, from early development on anode stubs in a) to the final single small slot in e). The final design had a width of 2.3 mm and a length of 6.5 mm and was positioned 9 mm from the nearest edge of the barrier layer which is seen in white in Figure 6.5 b) to e).

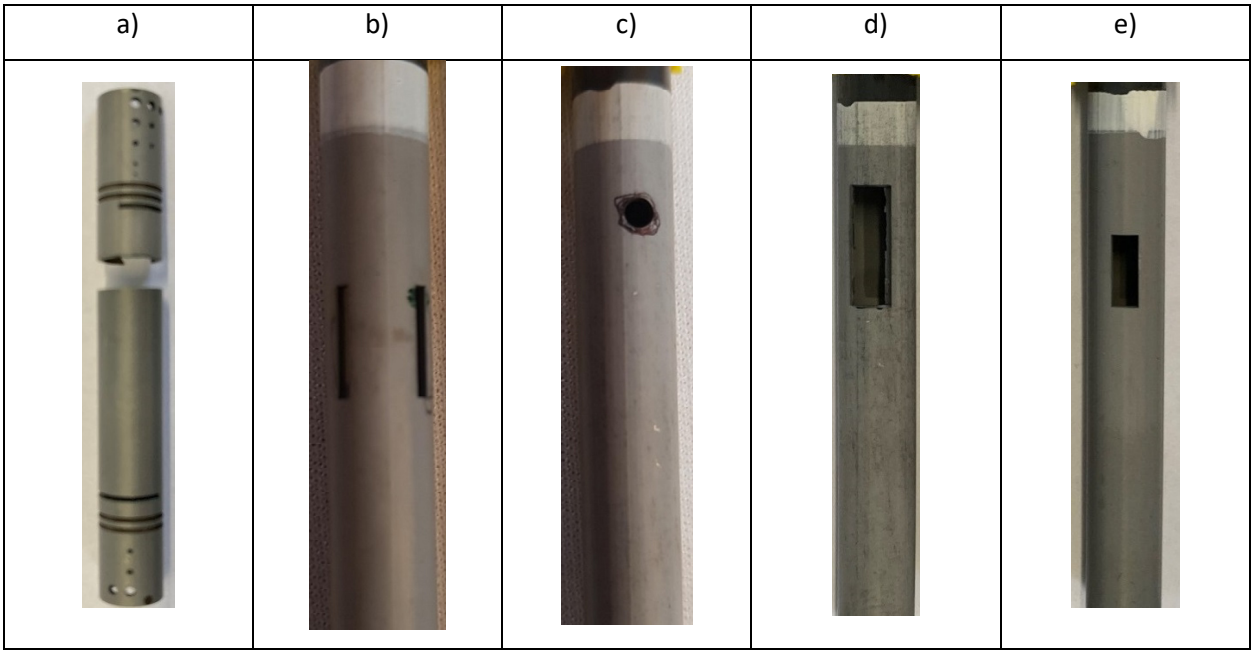

Figure 6.5 - Laser slot development, a) early calibration, b) double slit, c) hole, d) single large slot, e) single small slot.

6.1.4 hiTRAN and Cell Electrochemical Testing Preparation

The testing preparation for the hiTRAN remained largely similar to the central current collector preparation detailed in Section 3.2. A redundant central current collection node was prepared as a means for comparison to the hiTRAN as a sole current collector in addition to allowing the option to have a combination of both the hiTRAN and central current collection. The combined wiring setup as seen from the cell exterior is seen in Figure 6.6.

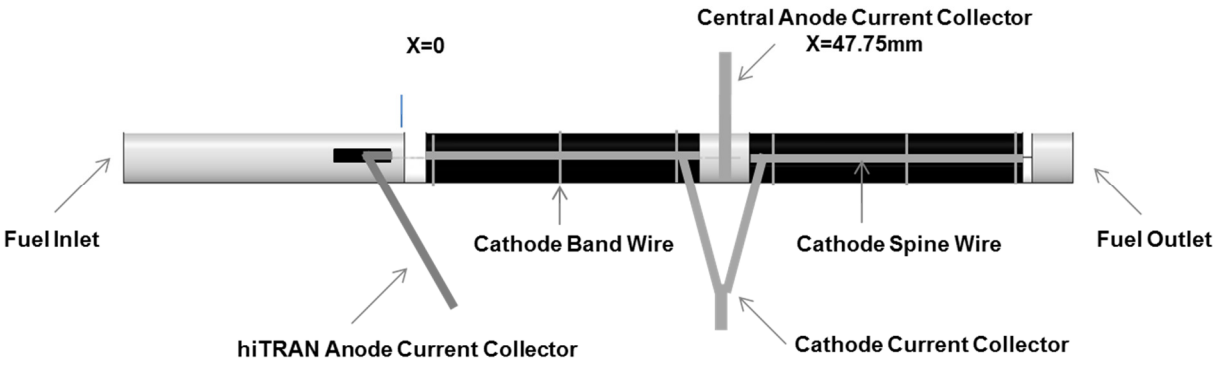

Figure 6.6 - hiTRAN testing setup.

The manifold assembly differed from the central connection setup, the ceramic fuel inlet manifold support tube detailed in Section 3.2.1 covered the laser slot, while still allowing the interconnect tail section to be free. The inlet manifold supply tube was then adjusted to feed fuel just past the slot, protruding past the inlet manifold support tube to minimise leakage. The inlet support tube was then sealed to the fuel cell with a Cermabond and glass sealant, as previously described in Chapter 3. The inlet region of the cell with a zoom of the cross-section of the anode, electrolyte and manifold setup and a zoom of the cell interior (hiTRAN and anode only) within the active region of the cell with hiTRAN coils is seen in Figure 6.7.

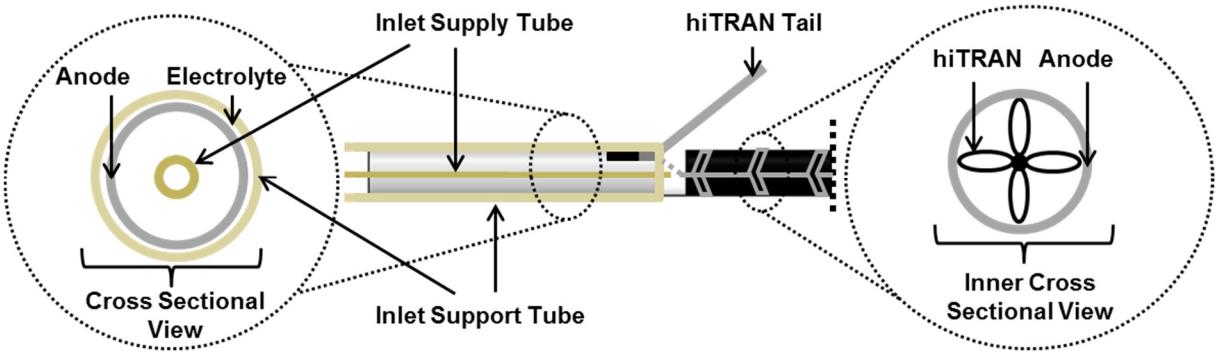

Figure 6.7 - Inlet µT-SOFC cross-section with hiTRAN, zoom at inlet manifold and zoom of cell interior with hiTRAN.

6.2 hiTRAN Electrical Performance

The hiTRAN designs were weighed and their resistance measured at room temperature once assembled. Increasing the loop density increased both the mass and electrical resistance as can be seen from Figure 6.8. The mass increased by 5.7% from LPD to MPD and by 28.6% from MPD to HPD. The electrical resistance increased by 7.1% from LPD to MPD and by 12.1% from MPD to HPD. From an electrical resistance point of view, the LPD and MPD designs were favoured over the HPD hiTRAN.

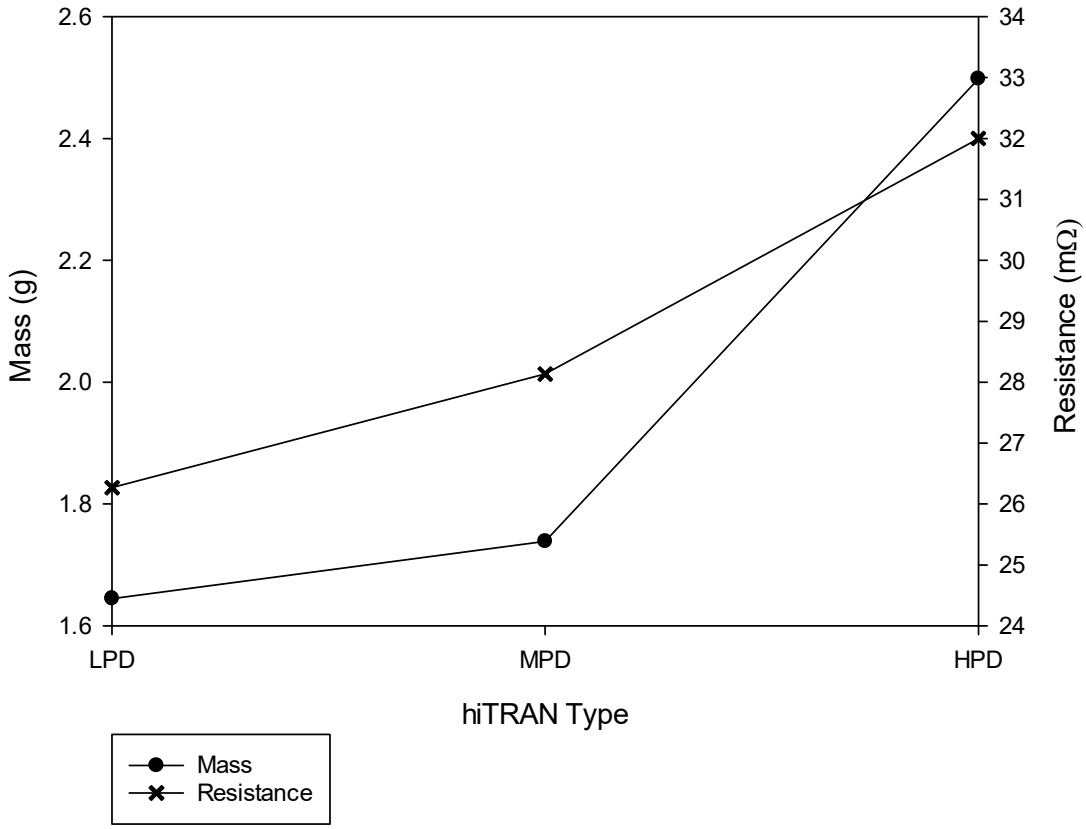

Figure 6.8 - hiTRAN mass and ohmic resistance versus packing density.

6.3 hiTRAN - Fluid Dynamics Enhancement

The pressure drop across a quartz tube with the same internal diameter of the fuel cell and a similar length was used to measure the pressure drop across the hiTRAN as detailed in Section 3.3.3. Measurements were made at 25°C instead of at SOFC operating conditions to avoid the rapid volume change of the gas, and thus the acceleration that would occur from heating. Measurements were then compared to an estimated pressure drop, ΔP [Pa] using the Darcy-Weisbach equation [303]:

$$\Delta P = f_D * \frac{L}{D} * \frac{\rho V^2}{2} \quad \textbf{(143)}$$

where L [m] is tube length, D [m] is the tube diameter, ρ [kg.m^{-3}] is the fluid viscosity and V is the fluid velocity [m.s^{-1}]. The Darcy friction factor, f [-], for laminar flow in a pipe (empty tube) is given by:

$$f_D = \frac{64}{Re} \quad \textbf{(144)}$$

Friction factor correlations as seen in equation (145) were provided by CALGAVIN Ltd as a function of packing density, Reynolds number and design parameters (α,β) which were estimated for each hiTRAN design and substituted into equation (143).

$$hiTRAN\ f_D = f(PD, \alpha, Re^{-\beta}) \quad \textbf{(145)}$$

The baseline, empty tube measurement was used to show improvement, in an analogy to the tubular SOFC with external current collection only. Measurements were made at the fuel cell testing fuel flow conditions of 200 ml.min^{-1} of H_2. The estimated friction factor, estimated pressure drop and percentage increase in pressure drop versus an empty tube are seen in Table 6.3. For these conditions, the Reynolds number was very low at 7.2, indicating laminar flow conditions, far from any transition to turbulent conditions (Re = 2300) [290].

Table 6.3 - Varying hiTRAN PD vs friction factor and pressure drop.

	Empty tube	LPD	MPD	HPD
Friction Factor [-]	30.3	41.9	61.6	121.3
Pressure Drop [Pa]	0.7	1.0	1.4	2.8
Increase from Base [%]	-	42	100	300

The estimated pressure drop and measured pressure drop is plotted in Figure 6.9 for the empty tube and the LPD, MPD and HPD hiTRAN. The empty tube and LPD hiTRAN pressure drop as recorded was under-predicted in comparison to the estimated, while the MPD and HPD configurations over-predicted the pressure drop, with the MPD showing the best fit. It was seen that increasing the packing density increased the pressure drop as expected. It should be noted that the correlations for friction factor provided by CalGavin Ltd were from experimental data using 10 mm ID and above. Using extrapolation of the data, the correlations were provided for the 5.5 mm ID of the fuel cell. The standard deviation for all measurements was below ±0.06 Pa. A 42%, 100% and 300% increase over the base case empty tube was recorded for the LPD, MPD and HPD hiTRAN, respectively. The difference in pressure drop from LPD to HPD was 61%. A 40% increase in pressure drop was measured between the LPD and MPD hiTRAN and a 100% increase in pressure drop was measured between the MPD and HPD hiTRAN. A lower pressure drop is favourable for reducing parasitic pumping loss of fuel pumps which would be multiplied per amount of cells across a stack; hence the

LPD and MPD would be favoured. However, operating the cell with a higher back pressure will act to increase the Nernst potential and increase fuel cell efficiency at a given current density which would favour the HPD hiTRAN as described previously in (113).

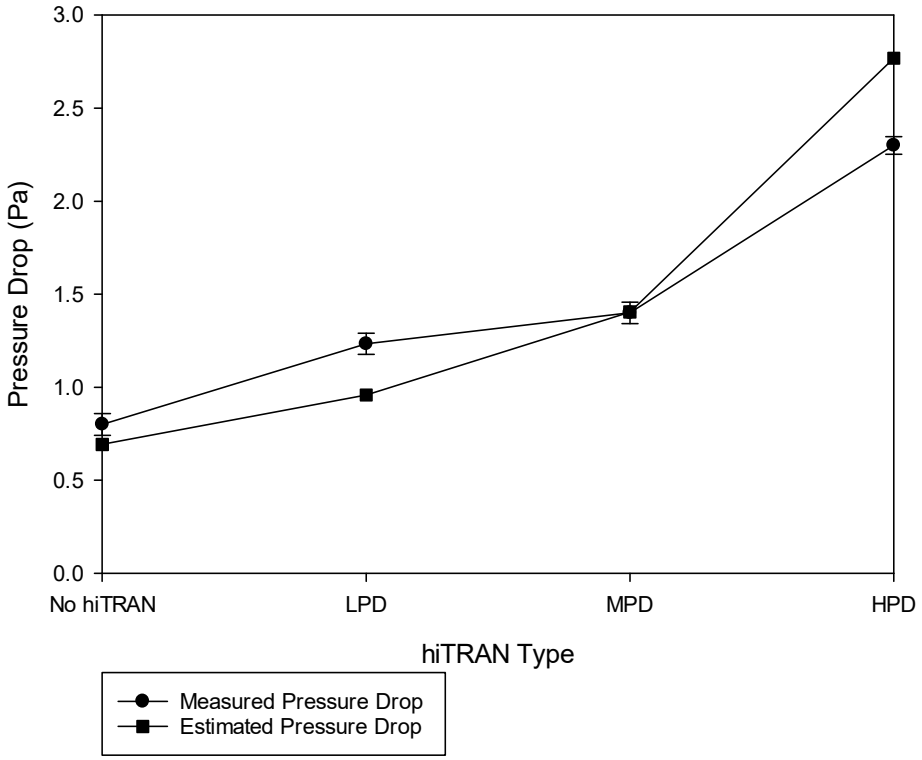

Figure 6.9 – Measured and estimated pressure drop of empty tube versus LPD, MPD and HPD hiTRAN.

6.4 hiTRAN Heat transfer Impact

To investigate the heat transfer impact of the hiTRAN, the temperature of the fuel and fuel cell were measured with and without the hiTRAN installed using the cells setup for electrochemical testing and using the quartz tube setup as a simulated fuel cell operation as detailed in Chapter 3. CalGavin Ltd state that broadly speaking, the hiTRAN will give a 2 to 4 fold improvement in the heat transfer coefficient. While this was not a primary objective of the study, understanding the thermal effects of the hiTRAN was important for insight into the cell performance.

Accurate measurement of temperature at typical SOFC operating conditions is non-trivial. Three temperature measurement techniques were used in this study to get as complete an understanding as possible, namely thermal imaging, infra-red thermometry and thermocouples. Thermal imaging

and the infra-red thermometry can be done from outside the hot zone of the furnace and are non-invasive techniques to measure surface temperatures. They operate by detecting radiation absorbed/emitted by a body and require knowledge of the emissivity of the sample being analysed. Thermocouples use the thermoelectric effect and thus must be placed inside the furnace. Placement of the thermocouple is crucial to ensure the correct body is being measured. Thermocouples can be used to measure surface temperature and fluid temperature. Contacting of the fuel cell components would be invasive and could lead to short-circuiting given the metallic surface of the thermocouple. Consideration had also to be taken to account for the lag in measurement from a thermocouple. The thermocouple tip was insulated with a white ceramic insulator tip to maintain a steady probe temperature, shielded from radiation.

The thermal image of the inlet region of the tubular cell with a central current collector and MPD hiTRAN overlaid with a labelled schematic is seen in Figure 6.10. The reference bar is in °C and the scale has increments of 60°C. The fuel cell was tested at the standard operating conditions of 750°C and a 200 $ml.min^{-1}$ fuel flow. The image gives information on the surface temperature of the cell setup. It was seen that the fuel entering at 25°C was rapidly heated in the inlet manifold as per the transition from purple to a dark orange but did not reach the peak temperature of 748°C at the beginning of the active area. The white, hottest region was at the active region of the cell at the cell centre. The wire and insulation leaving the central current collector are blocking some of the image.

The infra-red thermometer was used on the same cell to confirm the surface temperature measured by the thermal imaging camera. Values were recorded at start, centre and end of the active region and are seen in Figure 6.11. The average temperature at the inlet region was 742°C, at the central current collector was 748°C and at the outlet region was 747°C. The error values were ±1.7°C, ±2.6°C and ±2°C, respectively. This confirmed that there was a temperature profile along the active region. The inlet region was cooled by the fuel entering at room temperature. At the operating potential of 0.7 V, the cell produced heat through exothermic electrochemical reactions and through ohmic heating. The central node through which current was drawn was the hottest region and the temperature tended towards the furnace temperature. At the outlet region, the fuel that had travelled further in the hot zone was heated, becoming hotter than at the inlet region. At the outlet region, there was less fuel to provide cooling and hence the temperature is on average 1°C below the central node and around 5°C hotter than at the inlet. As the fuel becomes hotter and tends towards

the furnace temperature, the driving force for heat transfer is reduced making thermal equilibrium harder to achieve.

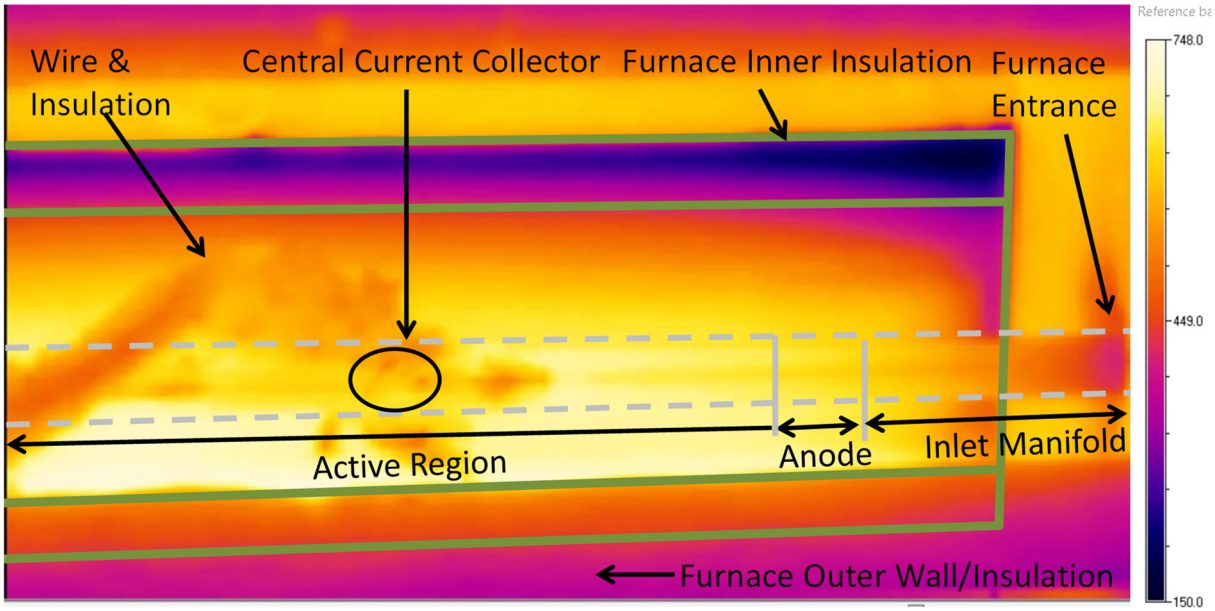

Figure 6.10 - Thermal image of a cell with central current collection and MPD hiTRAN in the furnace at 0.7 V at the standard operating conditions of 750°C and a flow of 200 ml.min^{-1} H_2 and 10 ml.min^{-1} N_2.

To remove any temperature effects from fuel combustion (arising from leakages associated with real-world testing of a cell) and to get a measurement of the fuel temperature rather than fuel cell surface temperature, the quartz tube setup used previously to measure pressure drop with and without hiTRAN was used. The thermocouples were placed 2 mm before and 2 mm after the hiTRAN loop section in the free stream within the quartz tube. This was to simulate the fluid temperatures that would be observed just prior and just after the active region of the cell where the hiTRAN loop sections would sit. The values would represent the fuel cell at OCV when there is no heat generation. The temperatures were measured at the same location for the empty tube and for the LPD, MPD and HPD hiTRAN. Care was taken to ensure the thermocouple tip did not touch the wall of the tube or the hiTRAN. The inlet and outlet temperatures and the temperature difference are seen in Figure 6.12. The average temperature difference was 2.4°C for the empty tube, increasing marginally to 2.43°C for the LPD hiTRAN. The average MPD and HPD temperature difference were 3.0°C and 4.3°C. The temperature difference error was ±0.1°C for the empty tube and less than ±0.06°C for the hiTRAN. Increasing the packing density of the hiTRAN acted to increase the fluid temperature difference along the cell. The hiTRAN was effective at mixing the fluid and removing the laminar boundary layer, ensuring cooler fuel from the free stream, typically at the tube centre, was brought into contact with

the relatively hotter tube wall which in turn absorbs heat from the furnace. The direction of the heat transfer was from the furnace air to the fuel stream. The outlet temperature increased for all hiTRAN compared to the empty tube, increasing by 5.5°C to 748°C for the HPD hiTRAN. Inlet temperatures also increased with the MPD and HPD hiTRAN. This was somewhat unexpected but can be seen as a result of two effects. Firstly, the flow rate of the fluid was lower as the packing density was increased. This was due to the momentum loss caused by the fluid being disturbed by the hiTRAN which resulted in a pressure drop. The slower fluid velocity resulted in the fluid before the hiTRAN spending longer in the pre-heating section and thus absorbing more heat, resulting in a higher temperature. Secondly, the intimate contact with the hiTRAN and the wall results in better conductive heat transfer along the tube. This could result in an elevated wall temperature prior to the hiTRAN region which would, in turn, mean a higher heat transfer rate to the fluid.

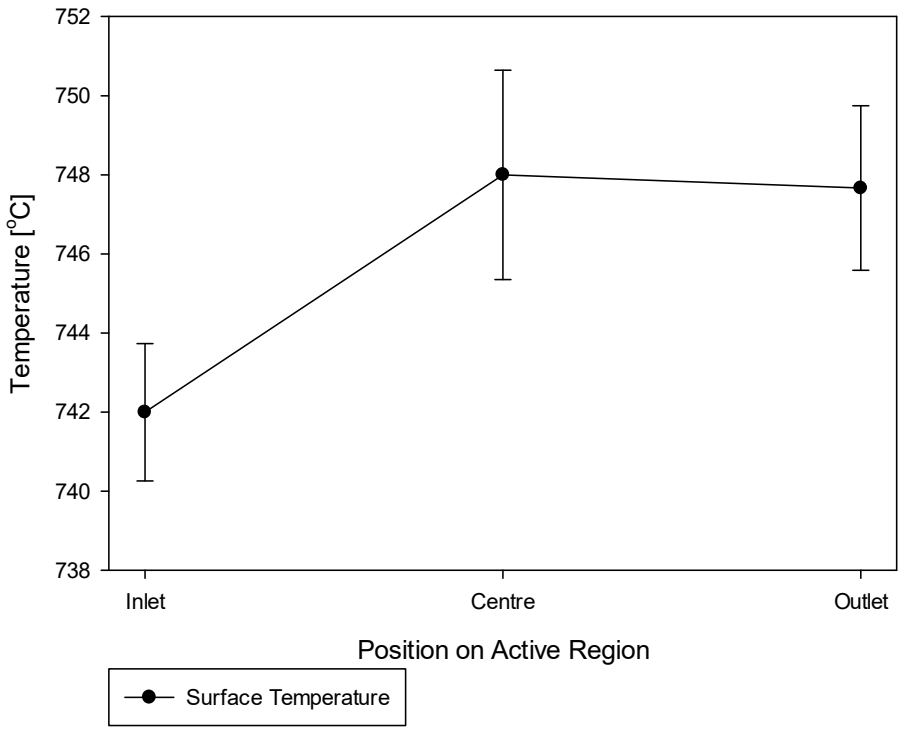

Figure 6.11 - Surface temperature of the fuel cell with hiTRAN MPD and central connection at 0.7 V at the standard operating conditions of 750°C and a flow of 200 ml.min^{-1} H_2 and 10 ml.min^{-1} N_2.

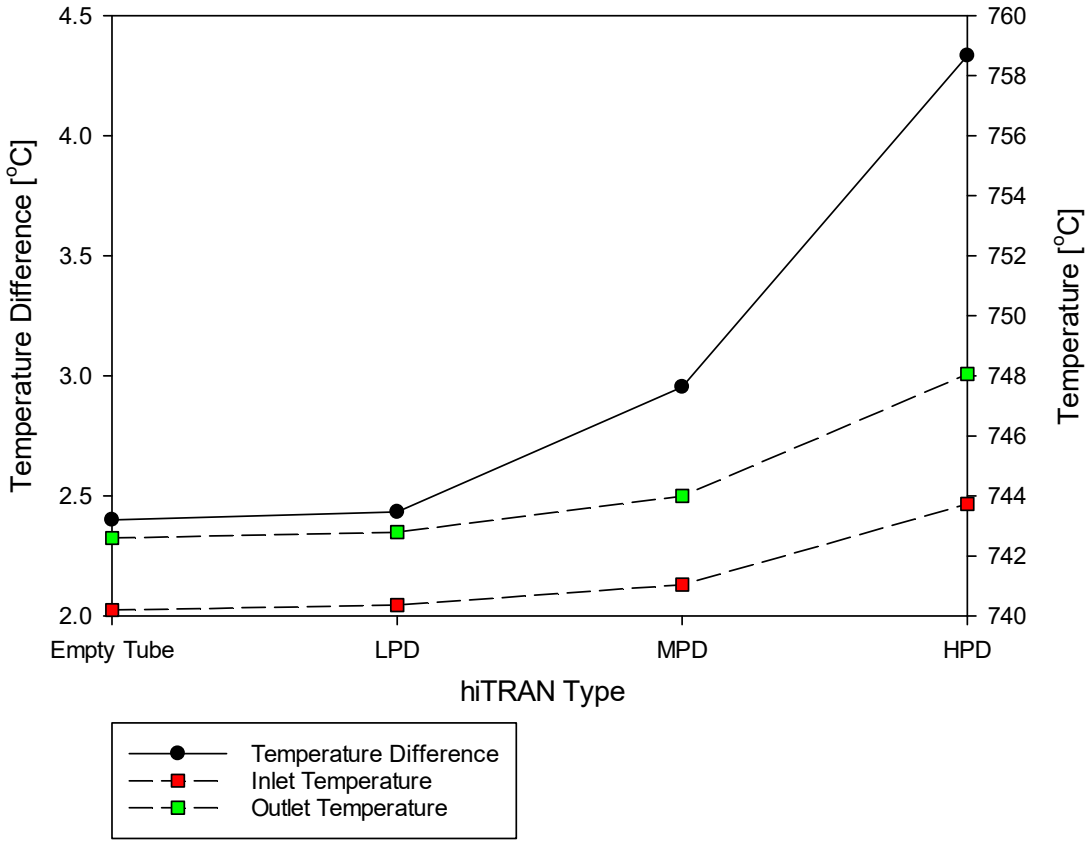

Figure 6.12 - Inlet temperature, outlet temperature and temperature gradient across the hiTRAN loop section position in a quartz tube at a furnace temperature of 750°C and a 200 ml.min^{-1} H_2 flow.

Both the conductive and convective effect of the hiTRAN heat transfer enhancement can be seen from Figure 6.13 whereby the inlet flow rate of hydrogen to the quartz tube was increased from zero to 400 ml.min^{-1} for the empty tube, MPD and HPD hiTRAN. At a flow rate of zero, the temperature difference along the cell was higher when hiTRAN was used and increases with packing density. Explained by the increased heat conduction effects (in the axial direction) arising from the metallic and highly thermally conductive hiTRAN contacting the tube wall. For the no-flow case, the inlet temperatures for the empty tube and MPD hiTRAN were similar while an increase of 4°C was observed for the HPD hiTRAN. As flow was introduced and increased, the inlet temperature was reduced slightly, given the larger volume, and thus larger thermal mass of cold air entering the tube. Outlet temperature remained similar. In laminar flow, doubling the flow rate will typically achieve a 10 to 20% increase in the heat transfer rate [302].

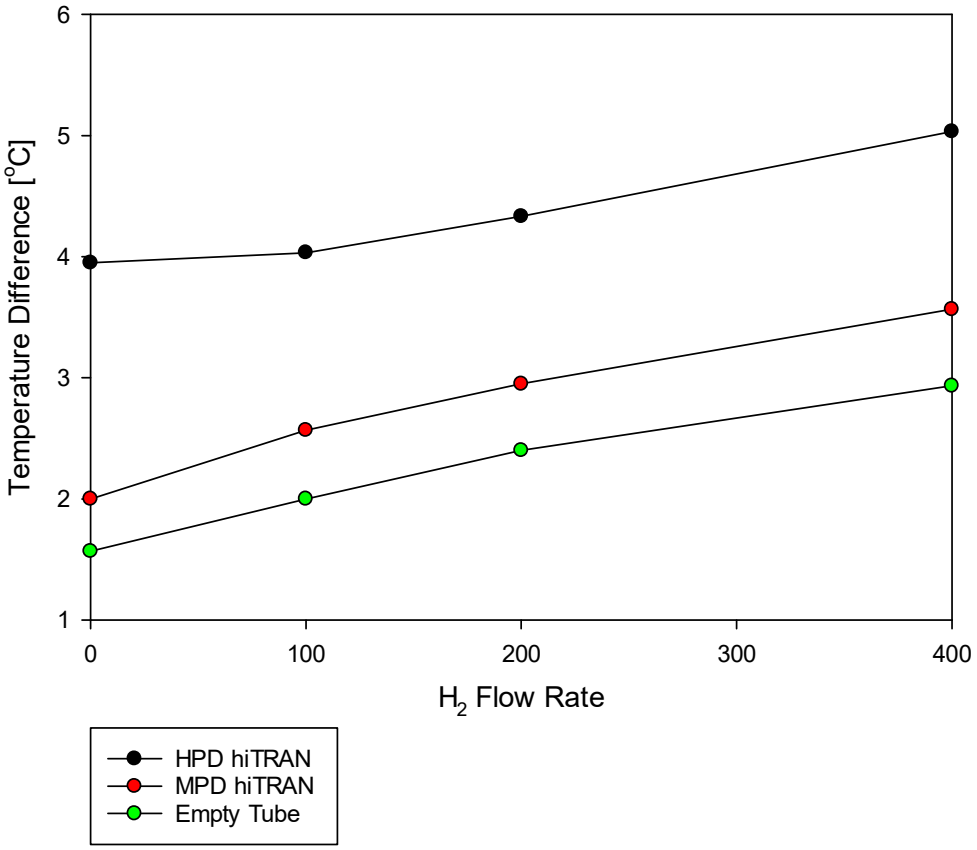

Figure 6.13 - Temperature difference across the hiTRAN loop section position in a quartz tube for an empty tube, MPD and HPD hiTRAN versus flow rate.

The effect of operating potential on the fuel outlet temperature was studied using a single thermocouple. It was not possible to locate a probe at the inlet without a high risk of leakage due to the manifold configuration. The outlet temperature at OCV, 0.7 V and 0.5 V for the fuel cell with a MPD hiTRAN, extracting current solely using the central current collector along with the percentage increase in outlet temperature versus OCV is seen in Figure 6.14. As the operating potential increased, more current was produced, resulting in more heat produced from electrochemical reactions and through ohmic loss. This caused the cell temperature to increase, which in turn heated the reactants and products exiting the cell. The outlet temperature increased from the temperature at OCV by around 0.7% and 1.8% at 0.7 V and 0.5 V. The outlet temperature of the fuel cell with MPD hiTRAN and 200 ml.min^{-1} of H_2 at OCV was just below 742°C, 2°C lower than the outlet temperature from the quartz tube experiment set up at the same conditions. This small difference can be attributed to the difference of thermal conductivity of the quartz versus the ceramic manifolds and fuel cell components (primarily the Ni-YSZ), the difference in emissivity of the materials and the

resulting different radiative heat transfer, and the slight difference in pressure drop between the quartz tube fittings and the more complex fuel cell setup.

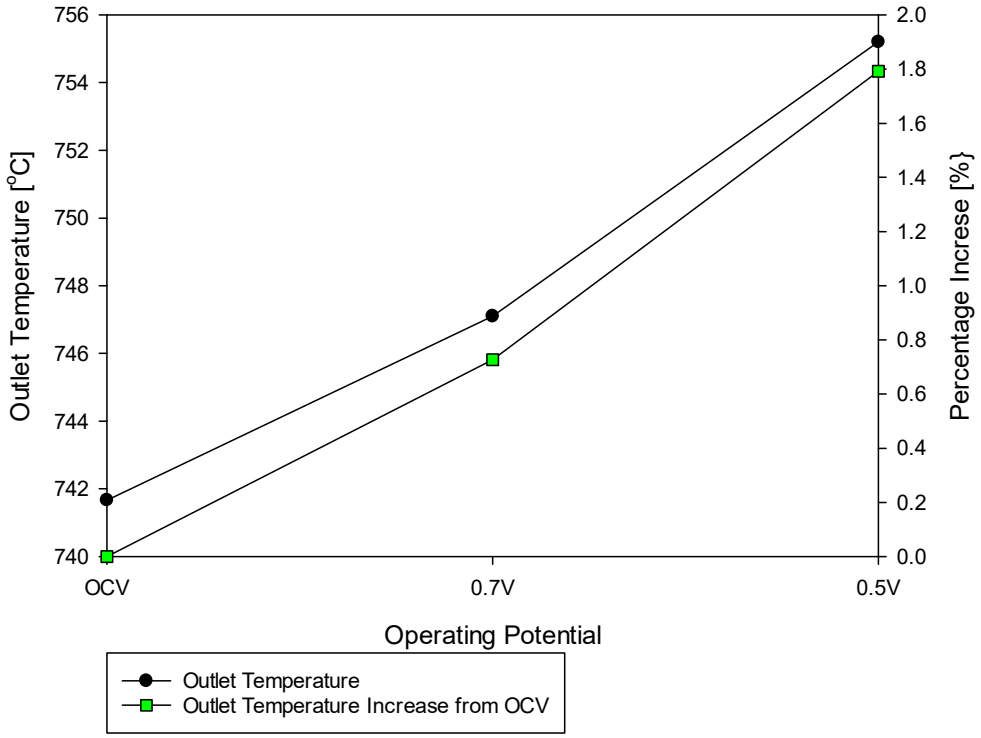

Figure 6.14 - Outlet temperature from the fuel cell with MPD hiTRAN at OCV, 0.7 V, 0.5 V and percentage increase in outlet temperature versus OCV.

From a thermomechanical perspective, the LPD hiTRAN would be favoured due to the relatively lower temperature gradient along the cell, 21% and 75% lower than the MPD and HPD, respectively. Lower temperature gradients along the cell would result in a smaller cell displacement in both the axial and radial direction, resulting in minimal stress on the manifolds, joints and sealing. From a mass transfer perspective, the HPD would be favoured as higher heat transfer also relates to a higher mass transfer rate from the free stream into the anode, reducing mass transport losses. However, if the cell is at a higher temperature the Nernst potential will be reduced. Nevertheless, cell efficiency increases with increasing temperature. From a pumping and pressure drop perspective, the LPD design was favoured, with the pressure drop of the LPD being 1.4 and 2.8 times lower than the MPD and HPD, respectively. From a system weight and cost perspective, the LPD hiTRAN design was favoured. Using less material resulted in a LPD mass 5.7% and 51% lower than the MPD and HPD hiTRAN, respectively. From a resistance perspective, the LPD hiTRAN was favoured, with a resistance 7.1% and 13.7% lower than the MPD and HPD designs, respectively. However, the lower loop density would result in fewer contact points between the hiTRAN and cell wall and thus a lower contact area,

contact force and higher ASR. From a manufacturing perspective, the poor reproducibility and the poor structural integrity favoured the MPD and HPD designs and was a strong factor against the LPD design. The tradeoff in the aforementioned factors made selection difficult and so all designs were put forwards for initial testing to determine the effectiveness of the hiTRAN designs as a current collector in a real cell. The final design could be chosen for optimisation.

6.5 hiTRAN Electrochemical Testing

The LPD, MPD and HPD hiTRAN designs were tested in three cells at the standard operating condition of 750°C and a flow of 200 ml.min^{-1} H_2 and 10 ml.min^{-1} N_2. The ohmic, high frequency intercept value was extracted from the raw EIS data at 0.7 V and is shown in Figure 6.15. As can be seen, the LPD hiTRAN had the highest value at 0.27 Ω. The corresponding value for the MPD and HPD hiTRAN were both 0.23 Ω to 2d.p. The relatively lower loop density of the LPD hiTRAN meant that there were fewer contact points between the hiTRAN and the cell wall compared to the MPD and HPD hiTRAN. The lower contact area meant there was an increase in contact resistance of the hiTRAN functioning as a current collector. A lower number of contact points also meant that there was a weaker contact pressure between the hiTRAN and the cell wall. This was evident during the installation of the MPD and HPD hiTRAN which required greater force to install (deduced by feel rather than measurement). The higher contact force between the hiTRAN and the wall acted to decrease the contact resistance. The higher bulk resistance of the HPD hiTRAN versus the MPD hiTRAN acted against its benefit and the effect of greater contact area and contact force were counteracted to bring them to the same value. The ASR of the cell with the MPD and HPD hiTRAN as the sole current collector was 5.3 Ω.cm^2 which was far too high.

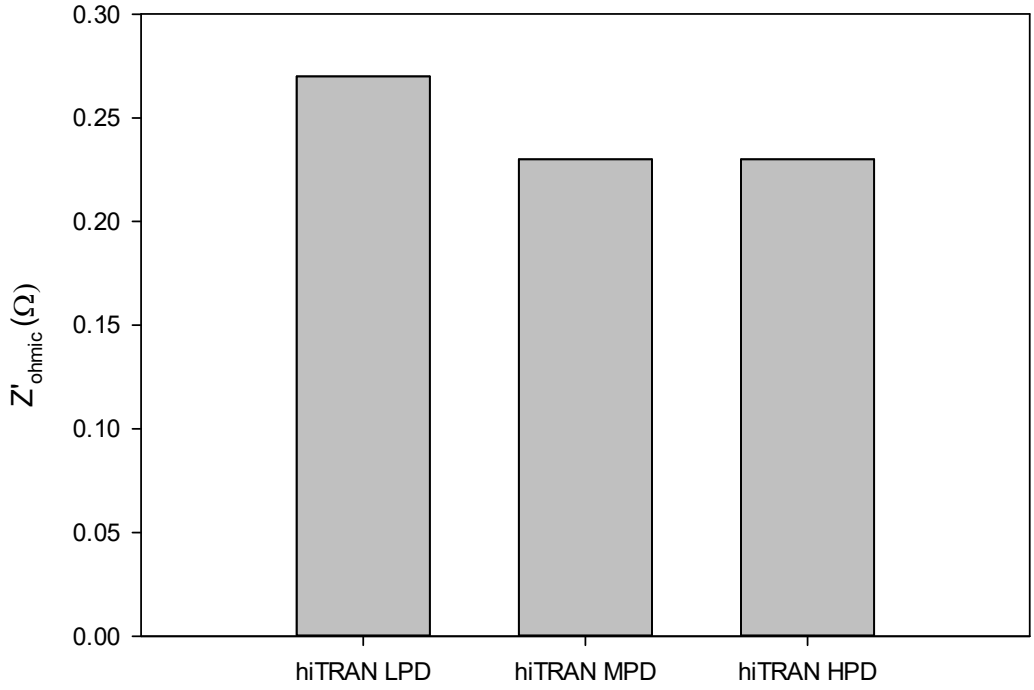

Figure 6.15 - Ohmic resistance of hiTRAN LPD, MPD and HPD used as the sole fuel cell current collector extracted from EIS at the standard operating conditions at 0.7 V.

The typical polarisation and power density plots of the three cells from Figure 6.15 can be seen in Figure 6.16. The current density of the LPD hiTRAN at 0.7 V was 0.075 A.cm^{-2} and was 0.081 A.cm^{-2} for both the MPD and HPD variants. The peak power density of the LPD, MPD and HPD hiTRAN was 0.056 A.cm^{-2} 0.061 A.cm^{-2} and 0.062 A.cm^{-2}, respectively. As also indicated by the impedance analysis, the performance of the MPD and HPD hiTRAN were very similar. The LPD hiTRAN performed relatively poorly with the peak power density around 10% lower than the MPD and HPD hiTRAN. The ASRs were estimated from the gradient of the i-V curve between 0.9 and 0.65 V were 5.6 Ω.cm^2, 5.0 Ω.cm^2, 4.9 Ω.cm^2 for the LPD, MPD and HPD hiTRAN, respectively. The estimate for the ASR from EIS and by the gradient of the IV curve differed by 0.3 Ω.cm^2 for both the MPD and HPD hiTRAN.

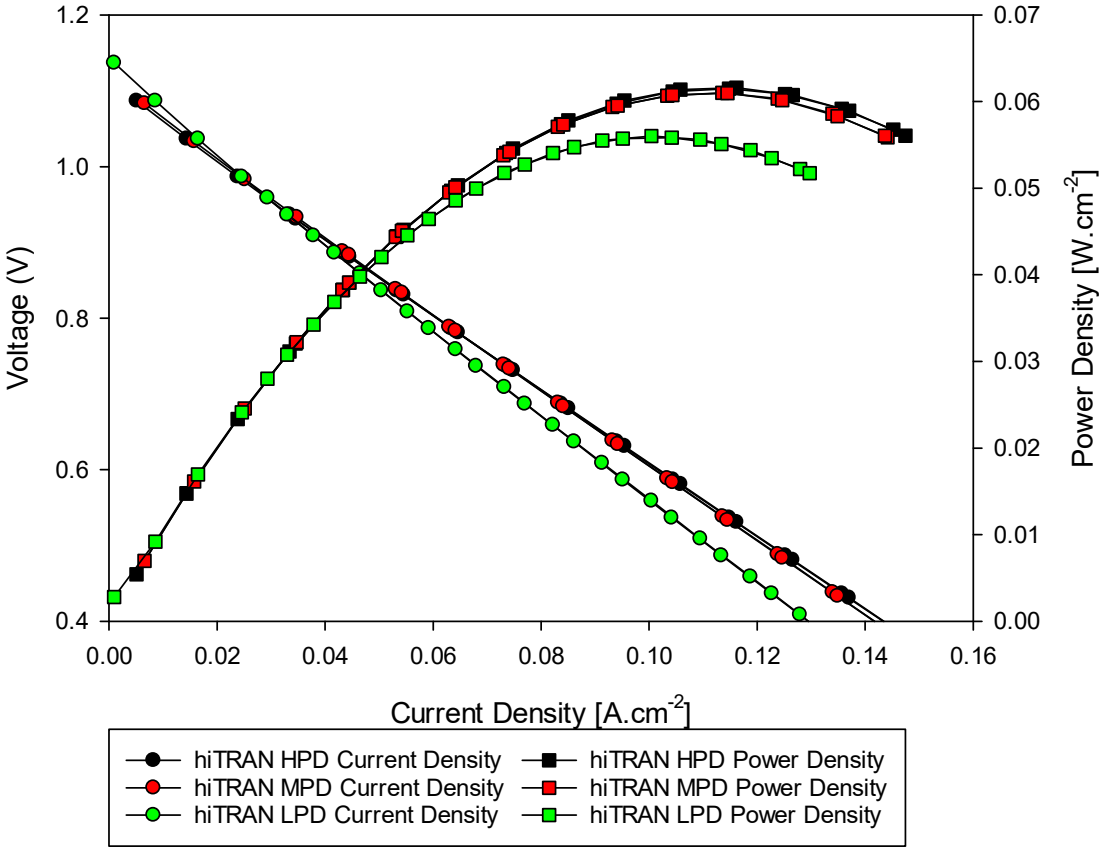

Figure 6.16 - Polarisation and power density plot as a function of hiTRAN packing density.

After the design, fabrication, characterisation and initial electrochemical testing had been conducted it was decided to choose the MPD hiTRAN for further optimisation. This decision was based on the following conclusions:

1. From a fabrication viewpoint, the LPD proved hard to manufacture consistently and the loop patterns were irregular and not secured well to the central core favouring the MPD and HPD designs.
2. From an installation viewpoint, the LPD design did not sit firmly in the cell compared to the MPD and HPD design. While a firm fit was desired, the HPD design required excessive force to install and in some instances damaged the anode when pulling through the laser slot. The MPD had a snug fit and became tight when all of the loop section was positioned.
3. From a mass perspective, the relatively lighter LPD and MPD designs would result in a cell with a higher power density by mass which would multiply on a stack level.

4. From a bulk resistance viewpoint, the LPD and MPD designs were favoured over the HPD design which had a higher resistance.
5. From a fluid dynamics viewpoint, the lower pressure drop of the LPD hiTRAN would favour lower parasitic fuel pumping losses of a stack balance of plant, however, the higher fuel back pressure of the HPD would lead to a higher Nernst potential and thus higher efficiency. The approximately doubling of loops in a given length from the LPD to MPD design, and thus doubling of electrical contact points, on the other hand, resulted in a 12.9% increase in pressure drop
6. From a heat transfer viewpoint, increasing the packing density acted to increase the temperature gradient along the cell, leading to thermomechanically induced dilation of the cell which would induce stress on the manifolds and sealing. The temperature difference in the HPD design was increased by 44% over the empty quartz tube, whereas with the MPD it was increased by 20%.
7. From initial EIS and polarisation data it was determined that the MPD and HPD performed similarly. The ASR of the LPD design was 11% higher than that of the MPD design.

The trade-off of the aforementioned conclusions led to the selection of the MPD hiTRAN design for further study and optimisation. The chosen hiTRAN design was now compared against the state-of-the-art current collector design, namely the central current collector. To compare like for like, a nickel central current collector wire was used to avoid any difference in performance due to the bulk conductivity and contact resistance changes with material properties. Figure 6.17 shows the typical polarisation and power density plots for a cell with the hiTRAN MPD as the sole current collector, with a sole nickel central current collector and then for the hiTRAN and central nickel current collector collected in parallel. The current density at 0.7 V for the MPD hiTRAN was 0.08 $A.cm^{-2}$, for the central nickel connection was 0.14 $A.cm^{-2}$, and was 0.15 $A.cm^{-2}$ for the combined connection. The peak power density of the MPD hiTRAN was 0.06 $W.cm^{-2}$, the central nickel was 0.08 $W.cm^{-2}$, and 0.11 $W.cm^{-2}$ for the combined connection. The ASR estimated from the gradient for the cell using solely the MPD hiTRAN was 5.0 $\Omega.cm^2$, using solely the central nickel connection was 3.9 $\Omega.cm^2$ and for the combined connection was 2.8 $\Omega.cm^2$. Calculating the combined resistance of the two current collectors in parallel gave 2.2 $\Omega.cm^2$, 21.4% lower than the recorded value. This was attributed to the increased contact resistance from the joint between the central nickel current collector and the hiTRAN that in turn led to the measurement system.

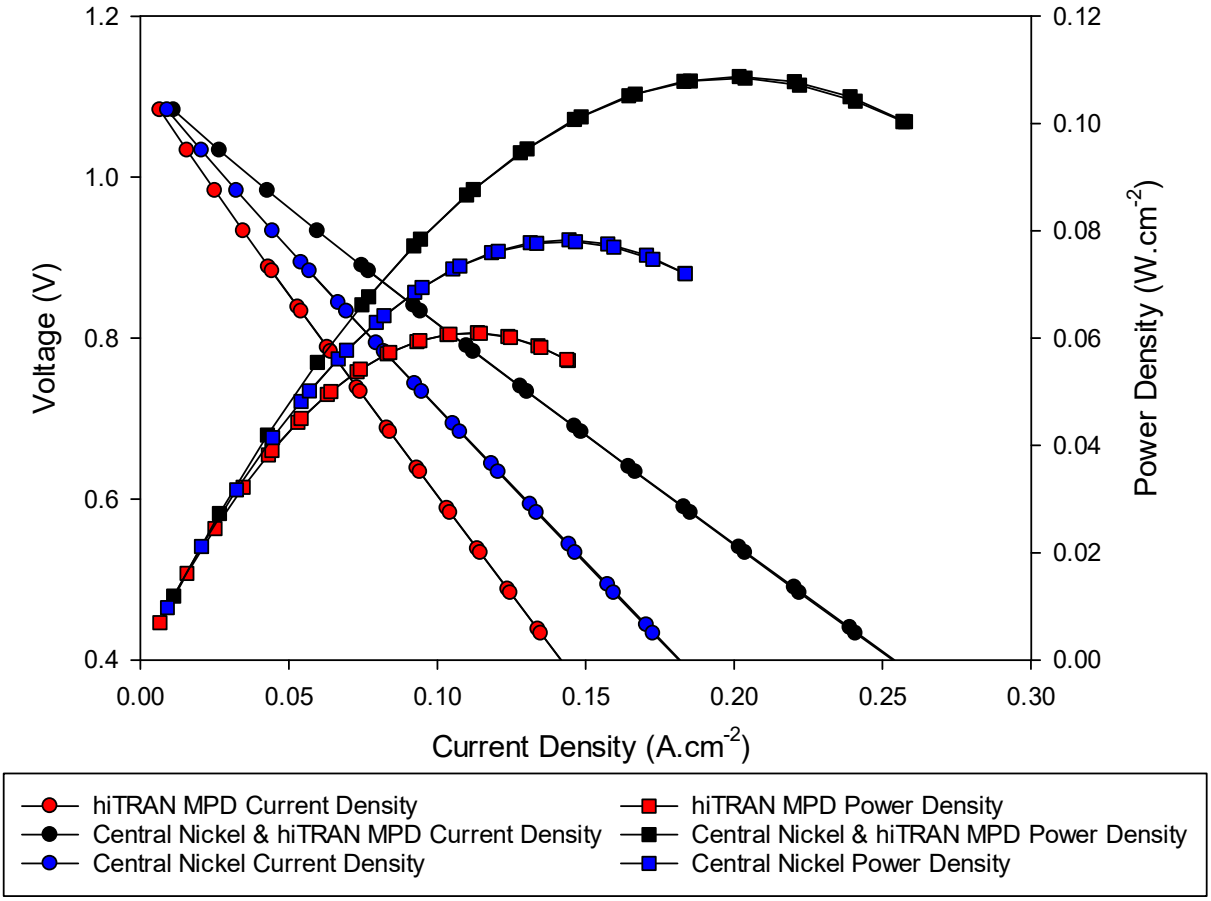

Figure 6.17 - Polarisation and power density plots for central nickel current collector, hiTRAN MPD and combined central nickel and hiTRAN MPD.

In order to determine any negative impact of the hiTRAN on the flow pressure drop along the anode, tests with and without the hiTRAN were conducted as follows. The polarisation and power plots of the central nickel connection with hiTRAN in place but not electrically connected were compared to the same cell without the hiTRAN. The hiTRAN was carefully removed (at temperature) from the cell and extracted through the outlet manifold. The central nickel current collector was then tested again. As seen in Figure 6.18, the difference in performance was negligible, indicating that at these fuel conditions and operating temperature, the hiTRAN had negligible flow effects on the cell.

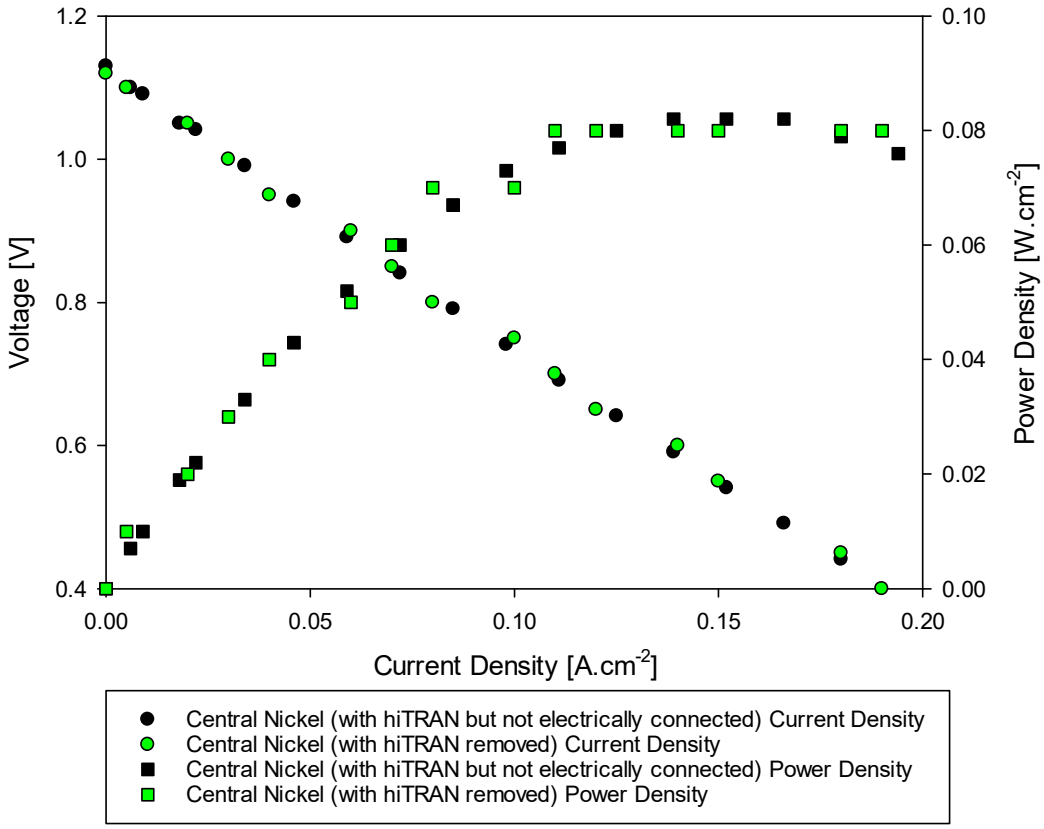

Figure 6.18 - Polarisation and power density plot of a central nickel connection with hiTRAN in but not electrically connected versus central nickel connection with the hiTRAN removed.

To compare the effect of material type, the results of the cell with a central connection made with silver wires were tested. The polarisation data was compared to the nickel central connection and hiTRAN MPD in Figure 6.19. The current density at 0.7 V of the central silver current collector was 0.22 A.cm^{-2}, the peak power density was 0.17 A.cm^{-2} and the ASR was 1.7 Ω.cm^{2}. Comparing the central node connection in both silver and nickel it is evident that the effect of current collector material has a significant effect on cell performance.

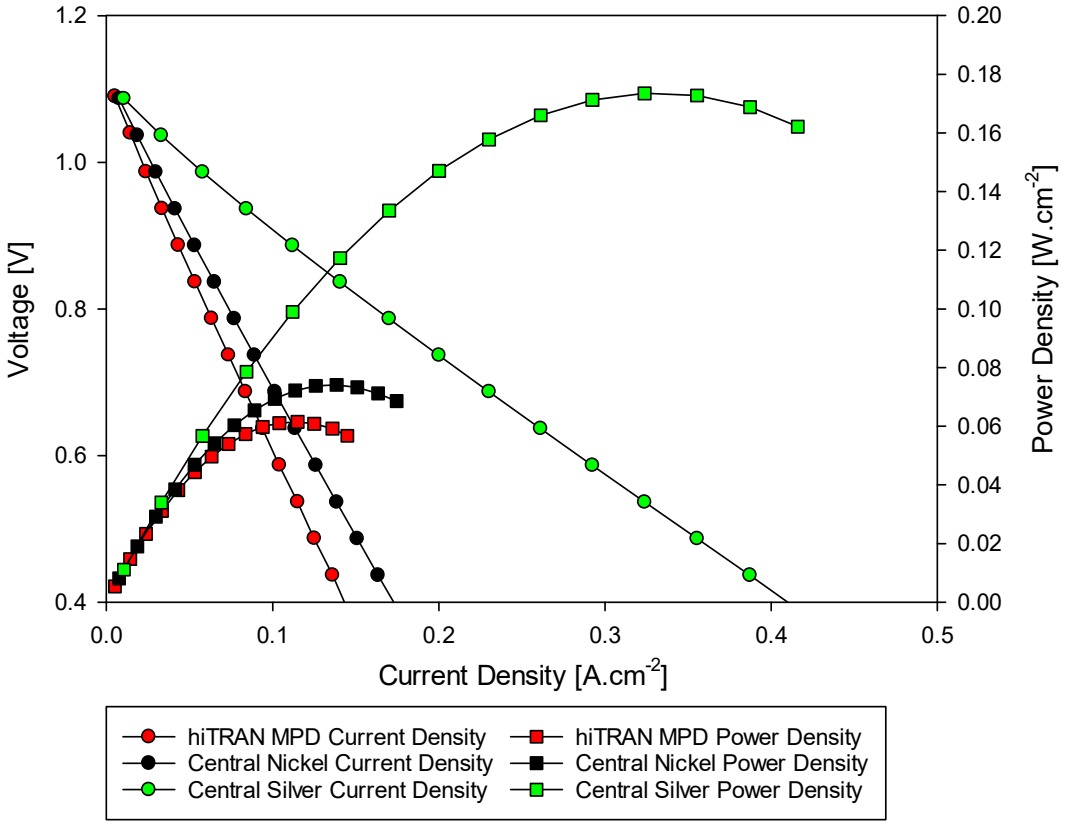

Figure 6.19 – Polarisation and power density plots of hiTRAN MPD, central nickel and central silver current collector.

From Figure 6.20, the ohmic resistance of the MPD hiTRAN, central nickel, combined hiTRAN MPD and the central silver current collector was 0.234 Ω, 0.180 Ω, 0.127 Ω and 0.073 Ω, respectively. Using an active area of 19.6 mm^2 and the total resistance values, the ASR of the MPD hiTRAN was 4.7 $\Omega.cm^2$ and 3.9 $\Omega.cm^2$ for the central nickel connection. For the combined MPD hiTRAN and central nickel current collection, the ASR was 2.78 $\Omega.cm^2$, and for the central silver was 1.78 $\Omega.cm^2$. It was expected that the increased number of contact points of the hiTRAN, that were spaced along the region of the cell where current was being produced, would lead it to outperform the single central current collector. The hiTRAN had an ohmic resistance 24% higher and a current density at 0.7 V 43% lower than the central nickel current collector.

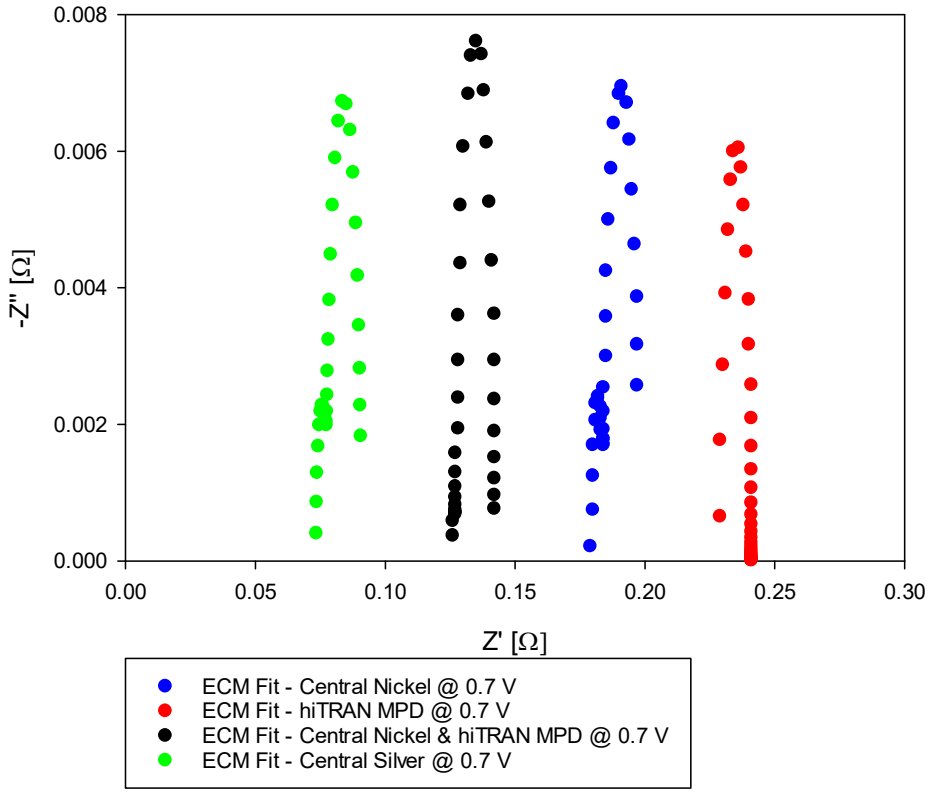

Figure 6.20 - ECM impedance fit of central nickel, hiTRAN MPD and central silver current collection at 0.7 V.

The hiTRAN MPD was then fabricated in silver to compare the effects of the material on the cell performance when compared to the nickel design. The polarisation and power plots are seen in Figure 6.21 with the hiTRAN as the sole current collector, operating at 750°C and 200 ml.min^{-1} flow of H_2 and 10 ml.min^{-1} N_2. The current density at 0.7 V of the hiTRAN MPD in nickel and silver was 0.082 A.cm^{-2} and 0.090 A.cm^{-2}, respectively, with the peak power density 0.057 W.cm^{-2} and 0.096 W.cm^{-2}, respectively. The ASR as estimated from the polarisation plot was 5.09 Ω.cm^2 and 3.93 Ω.cm^2, respectively. The shape of the polarisation plot of the silver MPD hiTRAN was atypical. Below 0.7 V the gradient of the polarisation plot became shallower, suggesting a lower polarisation resistance in this region. While this change in gradient started in the ohmic polarisation region, the non-linear plot continued into the mass transport dominated region. The increasing temperature of the cell and wires at higher current density led to an expansion of the silver hiTRAN. Given the relatively higher CTE of silver compared to the anode, the contact force between the wire and the anode apparently increased and resulted in lower contact resistance.

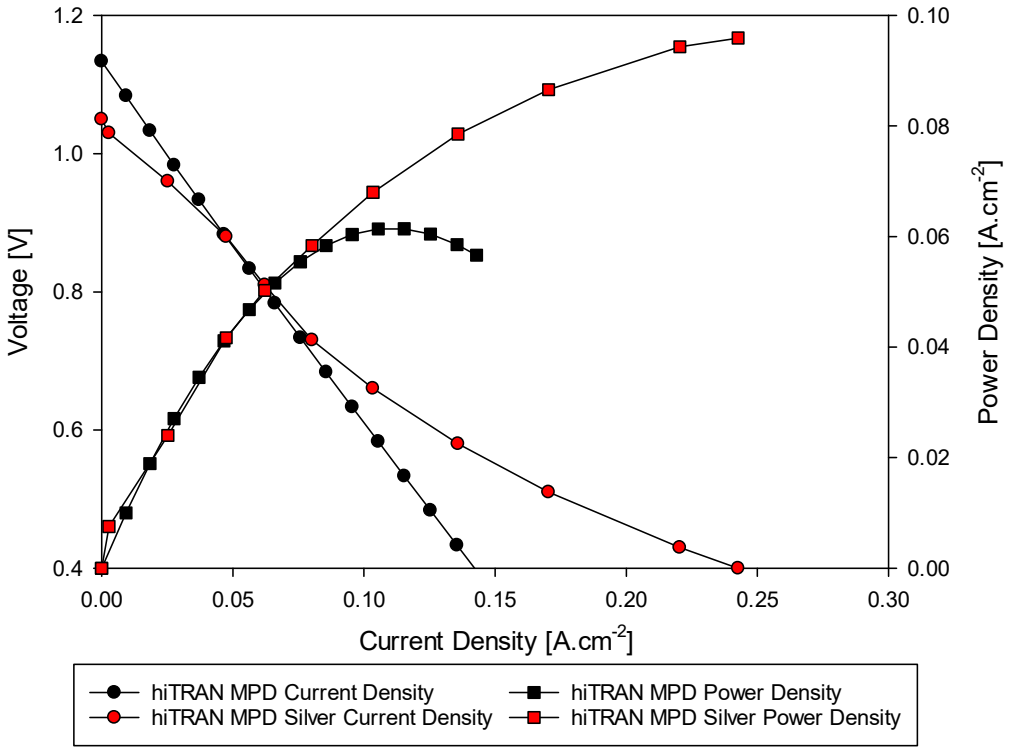

Figure 6.21 - Polarisation and power density plots of hiTRAN MPD fabricated in silver and in nickel.

While the initial performance of the silver hiTRAN MPD with respect to peak power density was superior to that of the nickel, over the first hour of testing the cell performance fluctuated and the degradation was far greater than that of the hiTRAN made from nickel. This was due to the softening of the silver given the proximity of the annealing and melting temperature of silver to the SOFC operating temperature. The brush-like design of the hiTRAN necessitated a mechanical spring force from the coils to maintain in contact with the anode wall. During the startup and operation of the cell, the structure of the silver hiTRAN became compromised, resulting in a loss of contact, primarily at the upper wall surface, where sagging originated. The loss of contact points/area and contact force led to an increase in contact resistance and thus an increased ohmic polarisation of the internal current collector. While some current could still be drawn in its compromised geometric form, the current collector could easily be dislodged in a portable device, particularly if the cell/stack was operated in a vertical orientation. In addition, the fluctuating power could damage system components if not managed properly.

The data from impedance and polarisation plots of cells with the same current collection design but different materials from this study were consistent with those found in literature. Figure 6.22 shows the average current density at 0.7 V of tubular cells reported in academic literature at 750°C using

either silver or nickel as the primary anode current collector material. The average current density when using nickel was 0.5 A.cm^{-2} which was increased by 55% to 0.77 A.cm^{-2} when using silver. Peak power density at the same conditions was increased by 32% when using silver versus nickel.

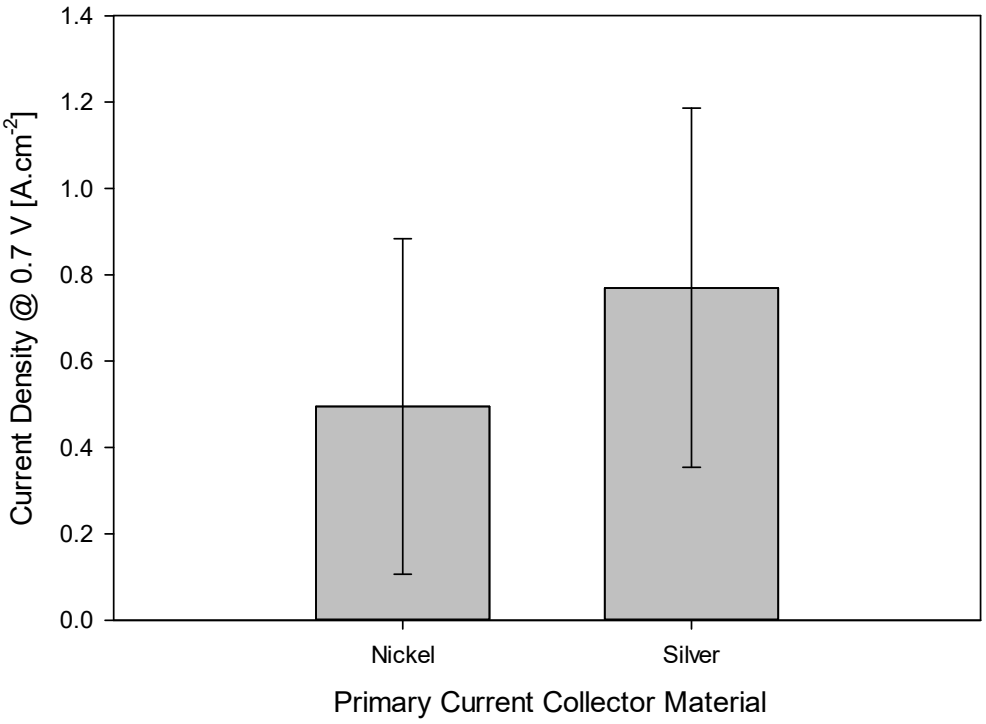

Figure 6.22 - Average current density of tubular cells reported at 0.7 V in literature at 750°C using nickel or silver anode current collection.

Figure 6.23 a) shows the resistivity and resistivity increase of typical µT-SOFC current collector materials observed in the literature review and presented in Table 2.4. At 750°C nickel has a resistivity 6 times that of silver. Silver is less sensitive to an increase in cell temperature than nickel, with the gradient of the plot being 6.05x10-^{11} and 4.2x10^{-10} [Ω.m.°C^{-1}], respectively, over the temperature range presented. From a current collector ohmic loss perspective, decreasing the operating µT-SOFC operating temperature with a nickel current collector would be more beneficial than a silver counterpart. The lower resistivity of a silver current collector compared to nickel at a given temperature would contribute strongly to the effects seen in Figure 6.19 (this study) and Figure 6.22 (literature). The relatively lower conductivity acts to reduce the electrode-current collector contact resistance and the bulk conductivity of the current collector itself.

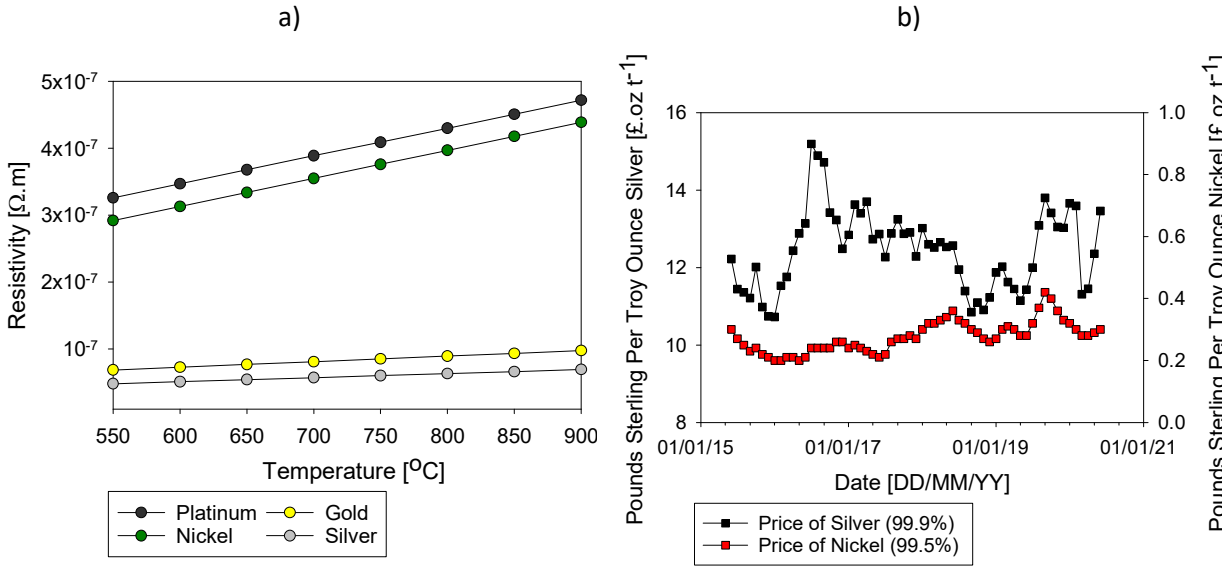

Figure 6.23 - a) Resistivity of typical µT-SOFC current collector materials over typical SOFC operating temperatures [71], b) market price [£.ozt^{-1}] of silver and nickel between June 2015 and June 2020 reproduced with data from [304]**.**

Figure 6.23 b) shows the fluctuation in market price of silver and nickel measured in £.ozt^{-1} between the period June 2015 to June 2020. The LHS y-axis is the price of silver and the RHS axis is the price of nickel. The market price of silver is significantly higher than that of the nickel over the entire period. The price of silver and nickel changed by 10.14% and -0.76%, respectively, over the period presented, indicating that a stack manufacturing process (at scale) would be more stable and less subject to market fluctuations with a design heavily reliant on nickel than silver.

The cost and mass for the central anode current collector design used in this study and the hiTRAN MPD design when constructed from silver versus nickel are seen in Figure 6.24. The cost was based on the price of wire per 10 metres of the supplier used in this study per 100 g [305]. The central current collector wires were the same diameter and total length regardless of the material used. The cost and mass of the voltage sensing wires were not included. The mass of the central current collector and hiTRAN MPD was increased by 17% when using the more dense silver compared to nickel. The cost was 4 times higher when using silver in comparison to nickel as the current collector material for either the central current collector or hiTRAN MPD.

The relatively higher cost and price fluctuation of silver versus nickel, combined with the poor mechanical properties of silver outweighed its lower resistivity and so nickel was chosen as the primary material for further optimisation of the hiTRAN internal current collector.

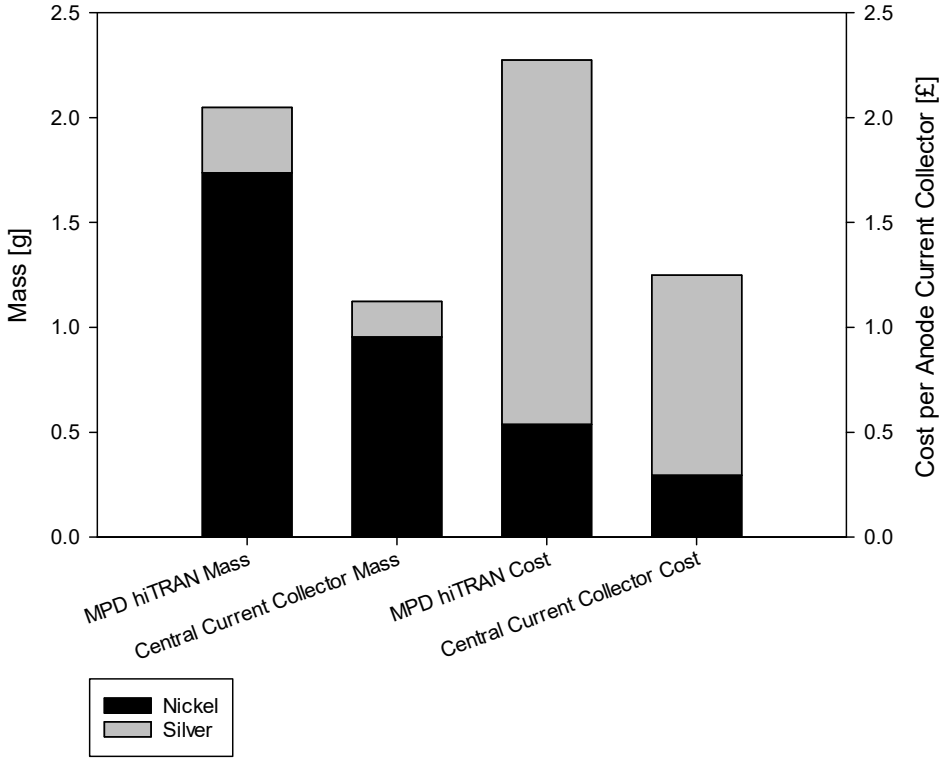

Figure 6.24 - Cost and mass of the central anode current collector and hiTRAN MPD made from silver versus nickel.

6.6 hiTRAN Coating Development

In order to reduce the ohmic resistance of the nickel hiTRAN current collector, the objective was to increase the bulk conductivity of the hiTRAN and/or reduce the contact resistance between the hiTRAN and the electrode. To do so, coating of the nickel hiTRAN in a more conductive material was trialled. Given the success of the central silver current collector, silver was identified as the primary conductive material to be used. Gold was also identified as a suitable candidate given its inertness in redox environments, high melting temperature and high electrical conductivity/low resistivity as seen in Figure 6.23 a).

Electroplating was a low-cost option to apply the coating and could be done at scale in a time-effective way. The typically thin coatings of plated material had a greater impact on the contact resistance than the bulk conductivity. Two coating thicknesses were selected, the thinner plating thickness was 15 µm and the thicker coating was 30 µm with a variance of ±5 µm. Once the coatings were applied, the coated hiTRAN were heated in N_2 for 1 hour at 750°C. This was to sinter the silver and gold particles to the support and improve the adherence in order to prevent the coatings being

removed during the installation of the hiTRAN in the cell. Silver nanoparticles have been used in the past to join SOFC interconnects to a Ni-YSZ anode but this technique was not explored in this study [306]. The image of the thick silver and gold plated designs are seen below in Figure 6.25 a) and b), respectively.

a)

b)

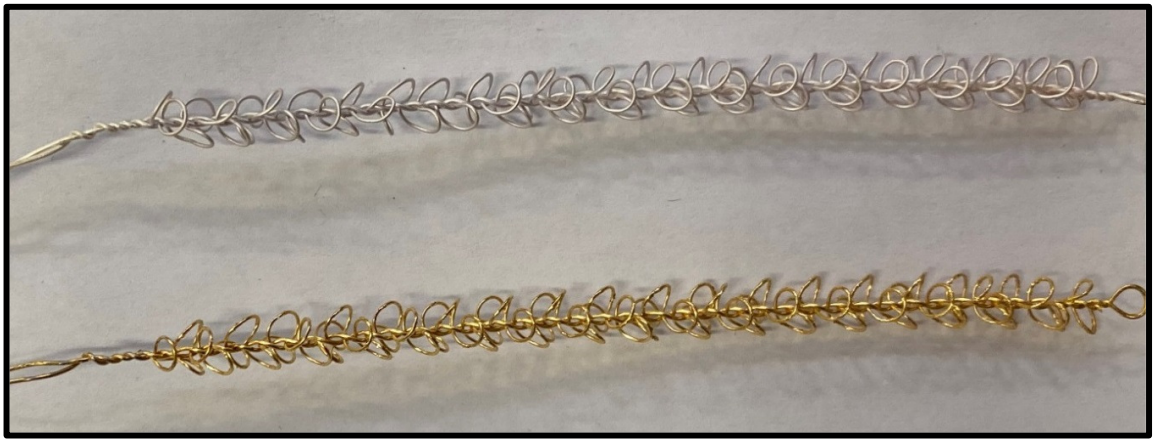

Figure 6.25 - hiTRAN MPD electroplated in a) silver, b) gold.

The ex-situ resistance at room temperature of the standard nickel MPD hiTRAN was compared to the coated hiTRAN designs and the silver base hiTRAN MPD as seen in Figure 6.26. The measurement probes of the milliohmmeter (described in Section 3.3.4) used to measure the resistance were clamped on the core wire just before and after the coil section. The resistance decreased by 35.8% and 58.5% for the thin and thick silver coating, respectively, compared to the standard nickel hiTRAN MPD. The resistance decreased by 16.8% and 20.7% for the thin and thick gold coatings, respectively compared to the standard nickel hiTRAN. The resistance of the silver hiTRAN MPD decreased by 90.4% over the nickel MPD hiTRAN. By sintering the thinly silver plated hiTRAN the resistance decreased by 5.3% and decreased by 7% for the thicker coating. The resistance of the silver hiTRAN was 4 times lower than the thick silver plated hiTRAN. The sintered thick silver coating and silver based hiTRAN designs were chosen for further testing.

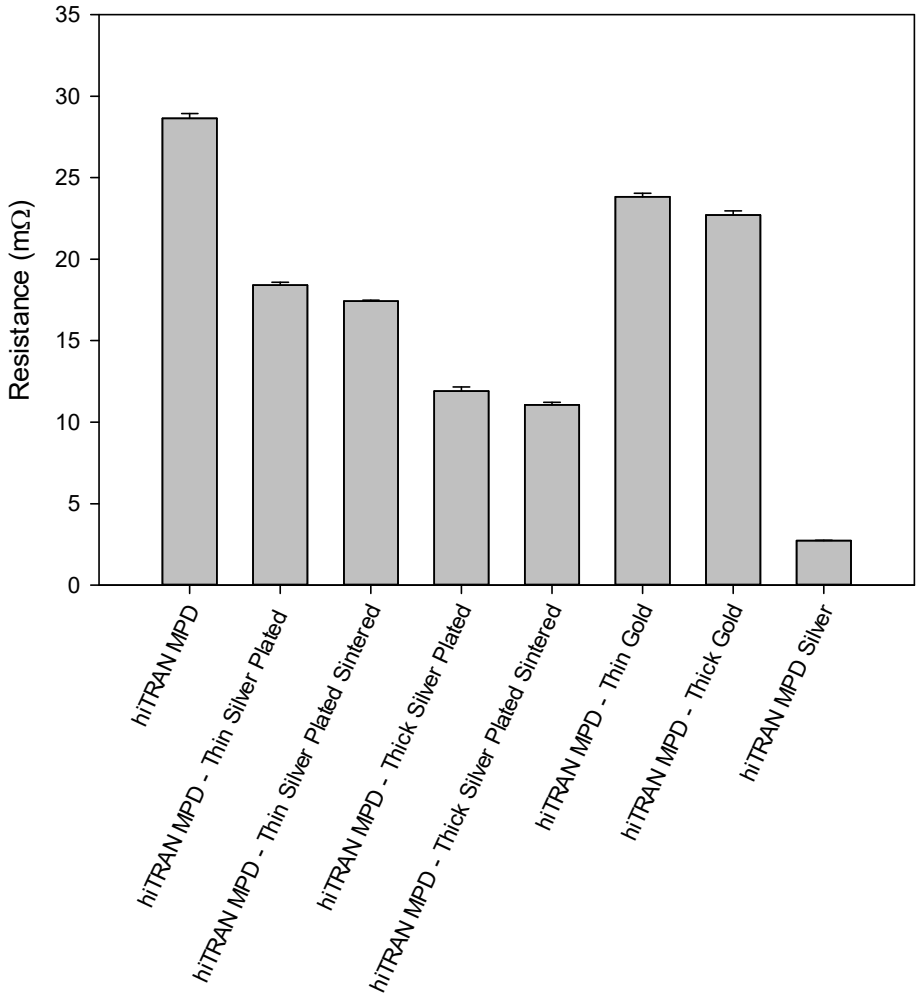

Figure 6.26 - Resistance of hiTRAN, silver plated hiTRAN, gold plated hiTRAN and silver hiTRAN.

The polarisation and power density plots of the thick silver plated hiTRAN MPD, and the previously presented nickel hiTRAN MPD and silver hiTRAN MPD (for reference) is seen in Figure 6.27. All of the cell data presented was measured at the standard operating conditions of 750°C operating on a flow of 200 $ml.min^{-1}$ of H_2 and 10 $ml.min^{-1}$ N_2. The current density at 0.7 V was 0.379 $A.cm^{-2}$ for the silver plated hiTRAN and the peak power density was 0.267 $W.cm^{-2}$. The ASR as estimated from the gradient of the polarisation plot was 0.83 $\Omega.cm^2$. The peak power density of the silver plated hiTRAN MPD was around 4.3 times and 2.8 times higher than the nickel hiTRAN MPD and silver hiTRAN MPD, respectively. The ASR of the silver plated hiTRAN MPD was reduced to 16% and 21% of the nickel hiTRAN MPD and silver hiTRAN MPD values, respectively.

The relatively lower resistance of the silver hiTRAN MPD with respect to the nickel hiTRAN MPD and silver plated hiTRAN did not translate into a superior performance. This was due to the

aforementioned thermomechanically induced deformation of the silver hiTRAN at the SOFC operating temperature. The coating of the nickel hiTRAN in silver dramatically improved the performance of the nickel hiTRAN current collector. The superior mechanical performance of the nickel versus silver at high temperature lent itself as current collector with superior contact and contact force. The nickel hiTRAN lent itself well as a support for a more conductive coating material. It was clear then that the contact force, acting to lower the contact resistance, was an important factor in current collector design. The bulk conductivity of the silver hiTRAN MPD was far higher than that of both the nickel and silver coated hiTRAN MPD. However, the contact resistance of the silver hiTRAN MPD and silver coated hiTRAN MPD, given the same contact force, would be very similar. The high OCV of the hiTRAN MPD was due to the data being obtained at the very start of the test with dry hydrogen.

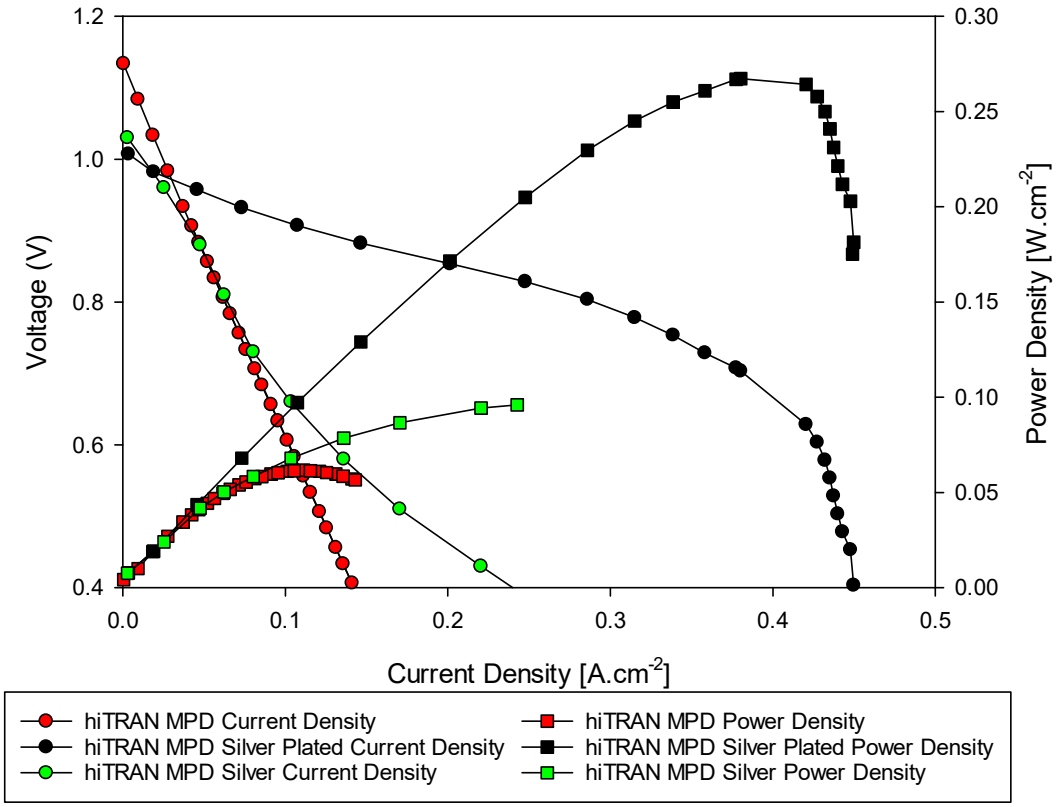

Figure 6.27 - Polarisation and power density plot of nickel hiTRAN MPD, silver plated (nickel) hiTRAN MPD and hiTRAN MPD in silver at 750°C with a flow of 200 ml.min^{-1} of H_2 and 10 ml.min^{-1} N_2.

The thick gold plated hiTRAN was then tested and the polarisation density power plot operating on a flow of 200 ml.min^{-1} of H_2 and 10 ml.min^{-1} of N_2 at 750°C was compared to that of the thick nickel plated hiTRAN MPD at the same conditions in Figure 6.28. The gold plating improved the

performance of the nickel hiTRAN MPD, but not as much as the silver plating. The gold plated hiTRAN achieved a current density at 0.7 V of 0.11 A.cm^{-2} and a peak power density of 0.087 W.cm^{-2}. The ASR of the cell as estimated from the polarisation plot was 3.23 Ω.cm^{-2}. The peak power density of the gold plated hiTRAN MPD was 45% higher than the nickel hiTRAN MPD but 33% of the silver plated hiTRAN MPD value. The ASR of the gold plated hiTRAN MPD was 57% of the nickel hiTRAN MPD and 3.9 times larger than the silver plated hiTRAN MPD.

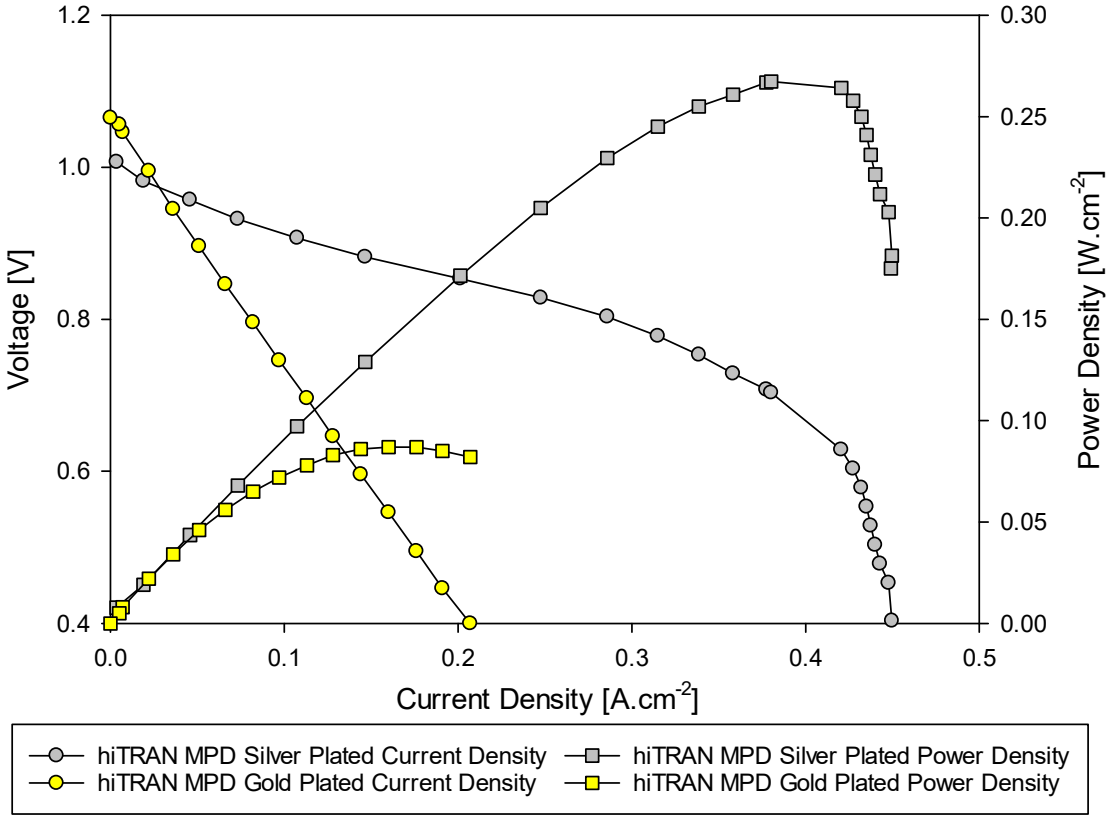

Figure 6.28 - Polarisation and power density plots of silver and gold plated hiTRAN.

In addition to the improvement in electrochemical performance of the coated hiTRAN current collectors, improved durability could be expected given, that silver and gold are more oxidation resistant than bare nickel [48]. While this is not so important for internal anode current collection in tubular cells, the inert coating will protect any wiring that will be used for interconnection to the cathode side, for example, the hiTRAN tail wire leaving through the laser cut slot. While silver coating has a higher electrical conductivity than the gold coating, which results in a higher performance, gold has a higher melting point than silver and is more inert. However, gold is significantly more expensive than silver [304].

6.7 hiTRAN-Anode Mechanical Testing

While the contacting of nickel based hiTRAN MPD designs was good upon installation, after heating to the SOFC operating temperature the difference in CTE between the nickel and the Ni-YSZ anode led to a decrease in contact force leading to an increased contact resistance, thereby negating any improvement in performance that was achieved by plating of the hiTRAN in silver or gold.

The force required to extract the hiTRAN as installed and after electrochemical testing is seen in Figure 6.29. The peak load required to remove the pre-tested hiTRAN MPD as installed was 80.2 N. The peak load post-testing was around 10 times lower at 7.39 N, a 90.3% decrease of the pre-test value. A load of this value meant that the hiTRAN would fall out of the cell if held vertically and would certainly become dislodged if the cell/stack was being moved, which would occur if powering a portable device. The dislodging of the hiTRAN could lead to short-circuiting and cause physical damage to cell and stack components. The gain in performance as a result of plating the nickel hiTRAN would be lost over the operation of the cell, exaggerated by thermal cycling. The loss of contact would contribute to an increase in the typical degradation rate of the cell. The loss of contact leading to unstable performance under load could damage stack and system components if not controlled. A solution was required to securely attach the hiTRAN. This would improve the hiTRAN as a current collector through a lower contact resistance and reduce the conductive heat transfer resistance from a heat transfer perspective.

6.8 Summary

A novel internal, brush-like structure called hiTRAN used as a flow turbuliser in heat exchanger technology was adopted and adapted for use as a µT-SOFC current collector. Three hiTRAN designs were fabricated in nickel with varying loop packing density. All of the designs were characterised with respect to mass, electrical resistance and thermo-fluid enhancement. Each design was electrochemically tested as a µT-SOFC current collector with the polarisation and impedance data favouring the medium packing density hiTRAN. The performance of the MPD hiTRAN as a current collector compared against the state-of-art central current collector, also made from nickel for consistency. The hiTRAN did not perform as well as expected given the large current collecting span of the hiTRAN across the active region of the cell. The performance of a cell with the hiTRAN and central current collector connected in series outperformed the sole hiTRAN or sole central current

collector. From impedance analysis, it was determined that the ohmic polarisation and ASR when using the hiTRAN as a current collector was too high. To improve the performance of the hiTRAN, methods to reduce the contact resistance between the hiTRAN and anode were explored. The MPD was fabricated in silver, increasing the bulk conductivity and contact resistance of the hiTRAN. However, at the operating temperature, the relatively poor mechanical integrity of silver (w.r.t nickel) and structural requirements of the brush like hiTRAN design led to a loss of contact of the internal current collector with the anode. As such the outright performance was not as high as expected and the design would not be suitable for even short term operation of a stationary or portable device. Coating of the nickel hiTRAN with highly conductive precious metals was then explored to reduce nickel hiTRAN-anode contact resistance. Gold and silver were trailed at two different thicknesses with the thicker silver coating being the best performer. However, separation of the nickel hiTRAN due to thermal mismatch of the hiTRAN and fuel cell led to separation of the spring fitted hiTRAN during steady-state operation which was further exasperated by thermal cycling. A technique was therefore required to form a physical joint between the hiTRAN and anode.

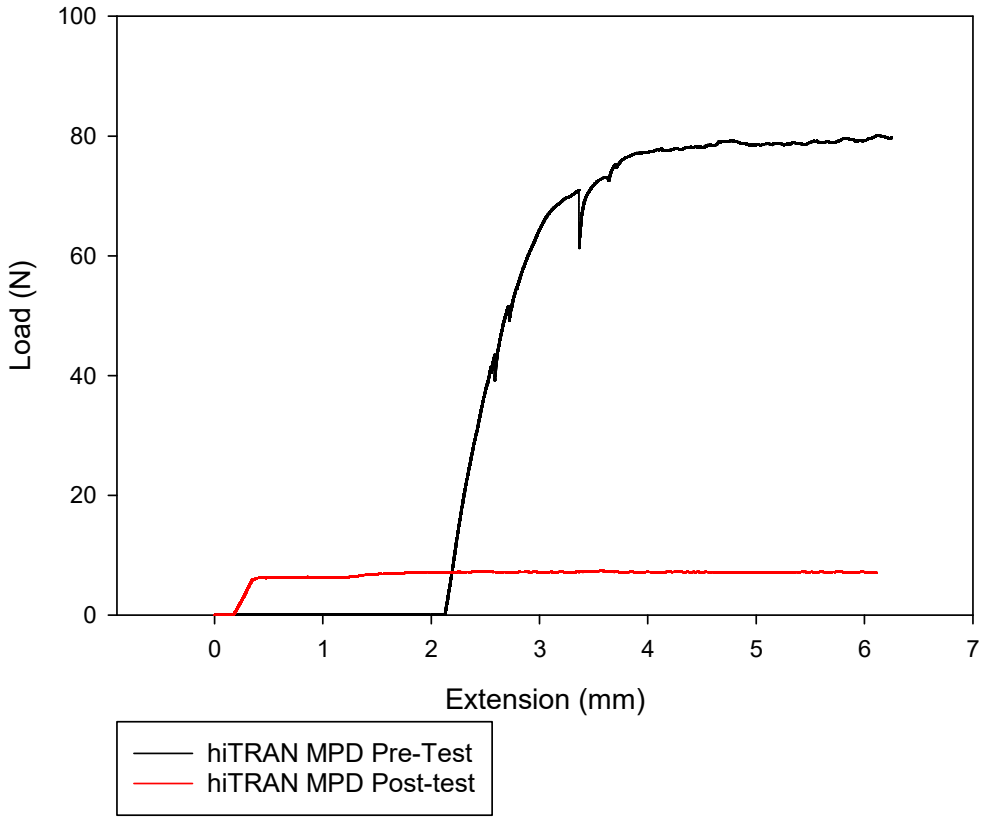

Figure 6.29 - Mechanical load-extension test of hiTRAN MPD pre-testing and post-testing in a fuel cell.

Chapter 7 Brazing hiTRAN

To create a reliable physical joint between the anode current collector, namely the hiTRAN MPD and the anode, in particular the anode interior, a joining technique was required. Joints at the anode-current collector contact points ensure the wires do not loosen, reducing functionality. Loss of contact typically arises during thermal expansion from operation/heating/cooling or when the fuel cell is moved. Typical joining techniques such as flame brazing, welding and spot welding were all attempted on the anode but were either not suitable for ceramics, resulting in no joint being made, or resulted in anode mechanical failure due to the thermal shock from large thermal gradients arising from the concentrated heating (flame or current induced) required for the process. The aforementioned techniques also posed access issues given the narrow bore of the tubular fuel cell. Therefore joints would only be able to be made near the tube ends. Vacuum/Inert brazing was proposed as a solution.

7.1 Brazing Fundamentals

Brazing is a technique that is used to bond two substrate materials, similar or not, by the addition of another filler material which can be applied to exterior or interior joints. The materials, specifically the joint, would be subject to heat (<450˚C) to induce a phase change in the filler without impacting the substrate materials [307]. A brazing schematic is seen in Figure 7.1.

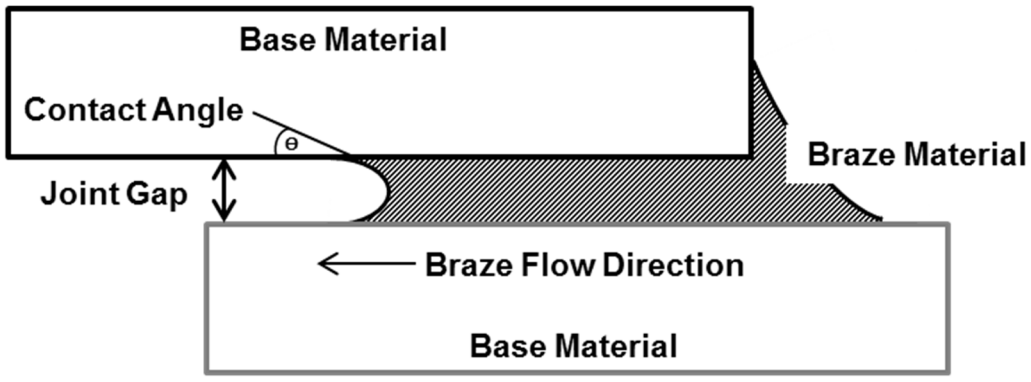

Figure 7.1 - Brazing schematic reproduced from [307]**.**

Heat is typically applied using an electrically heated furnace and so all components are brought to the same (brazing) temperature in a controllable heating profile. By using furnace heating, in contrast

to that by flame, allows all of the brazing components, which will heat at different rates, to be brought to thermal equilibrium. The homogenous temperature distribution of base and braze material reduces thermally induced stresses in the base and braze materials, which have different CTE's, allowing the formation of a durable joint with minimal damage to the base material components and minimal strain. This is of particular importance considering the relatively brittle nature of ceramic compared to metallic components.

Joining by brazing is possible if the liquid filler/braze material will firstly spread and fill the joint gap and secondly adhere to the solids to be joined when cooled. The ability of the liquid braze to maintain contact with a solid surface is known as wetting. Braze materials are metal alloys and are selected/developed to ensure wetting can be achieved. Braze materials can be categorised as a reactive and non-reactive braze. Brazing materials can be further categorised into base metal alloys and precious metal alloys. Precious metal alloys are often based on palladium, platinum, gold and silver. Base metal alloys are typically based on copper, nickel, aluminium and titanium and are a low cost brazing material option. Non-reactive brazes are described by the well understood Young-Dupre equation:

$$cos\theta = \frac{\sigma_{SV} - \sigma_{SL}}{\sigma_{LV}} \quad \textbf{(146)}$$

The contact angle θ describes the relative contributions from two competing forces, (i) adhesion forces between solid and liquid phases and (ii) cohesion forces of the liquid, where σ_{SV} is the solid surface free energy, σ_{SL} is the solid/liquid interfacial free energy and σ_{LV} is the liquid surface free energy. The most common criteria to define whether brazing is applicable is whether a solid-liquid contact angle of less than 90° can be achieved as seen in Figure 7.2. This is indeed the case for ceramics with a partially metallic character such as an anode cermet.

Alloying elements such as boron, silicon and phosphorous are used as braze melting point depressants. These alloying elements decrease the melting point of the base alloy of the braze material and their quantity can adjust the brazing temperature range to suit the application. Alloying elements are also used to adjust the CTE of the braze material, in this case with respect to the electrodes and/or the electrolyte. This is essential to reduce the stress between the joined components which could lead to crack formation and propagation, and ultimate failure of the joint.

The ductile nature of metals lends them to a somewhat forgiving joint when joined to the relatively brittle ceramic/cermet fuel cell components [48].

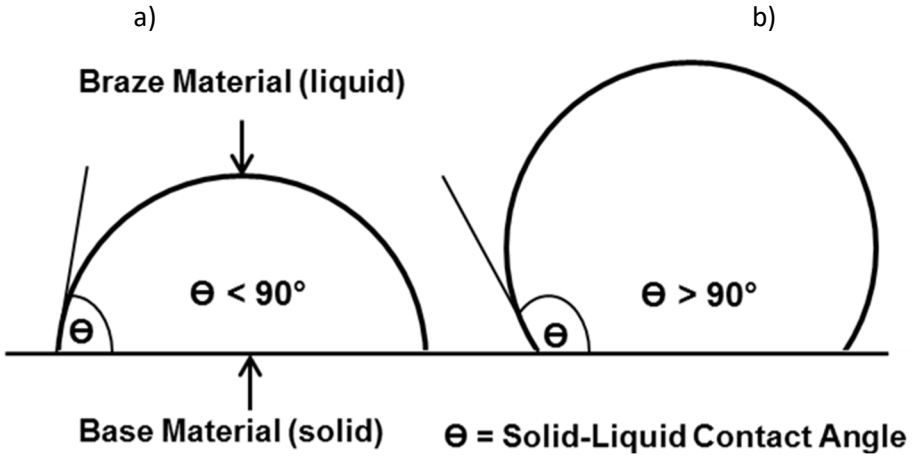

Figure 7.2 - Solid-liquid contact angle a) less than 90°, b) greater than 90° reproduced from [308]**.**

'Active' elements may be added to a braze material to promote wetting. Typical 'active' elements include chromium, zirconium and indium. Active/reactive brazes are often used for ceramic components where wetting can be problematic. They avoid the need for costly pre-treatment of a surface which is often through metallising. Active braze alloys are often alloys based on silver, copper and titanium.

Non-reactive silver and gold based brazing alloys are typically favoured for SOFC applications due to their ability to wet to cermets and their inertness in reducing environments. However, these alloys are very costly and are subject to market price fluctuation of the precious elements. In addition, similar problems, that plague silver interconnects affect silver brazes such as porosification in dual oxidising/reducing environments that can affect the mechanical properties of the joint over time [309]. That said, silver alloys exhibit a higher tolerance to the aforementioned effects compared to pure silver [310]. Silver/copper braze alloys with moderate joint strengths were developed for use with perovskite ceramics by Erskine et al. [311]. Indicating that brazing of the cathode to the cathode current collector is feasible. Chao et al. conducted a study to investigate the joint strength of brazed stainless steel interconnects to an SOFC anode [243]. They used vacuum brazing to successfully join SS430, Crofer22 APU and Crofer22 H to the Ni-YSZ anode with a silver based Ag-9Pd-9Ga braze. Sammes et al. used a silver based braze to join a nickel based current collector to the Ni-YSZ anode in a 40 cell stack [109]. The authors brazed in a slightly reducing/inert atmosphere of 98% argon and 2%

hydrogen. A brazing temperature of 1100°C was used with a 6 minute dwell time at the braze temperature. The ramp rate between room temperature to 900°C was 3°C.min^{-1} and was increased to 10°C.min^{-1} between 900°C and 1100°C. They used optical microscopy and conductivity tests to analyse the joint.

Kim et al. used induction brazing to join the Ni-YSZ anode and YSZ electrolyte of an anode supported tubular cell to a ferritic stainless steel, SUS430, metallic cap [244]. The steel cap is used as a manifold, joined to the YSZ electrolyte, and as an anode current collector joined to the Ni-YSZ support. The braze joint between the cell and the manifold meant that the braze acted as a sealant, necessitating hermeticity. The induction brazing process uses current to locally heat the joint and mobilise the filler. This process does not require a furnace and is a low cost and rapid process. Kim et al. brazed in a mildly reducing environment of 96% argon and 4% hydrogen. They trialled four braze materials, two nickel based brazes, namely BNi-2 and BNi-5, and two silver-copper based brazes, namely Nicusil 8 and Palcusil 10. When the braze was used as a sealant to the cap, the nickel based braze materials outperformed the silver-copper based braze materials with respect to the permeability of helium as seen in Figure 7.3. The BNi-2 was the best performing and had a permeability of 1x10^{-6} l.cm^{-2}.s^{-1} at a differential pressure of 3 atm. From a microstructural analysis, this was determined to be as a result of superior wetting and flow of the BNi-2 around a round surface, even compared to the BNi-5. This was attributed to the content of the melting point depressants, silicon and boron. The BNi-2 and BNi-5 were then selected for further testing as a current collector braze material for contacting the anode.

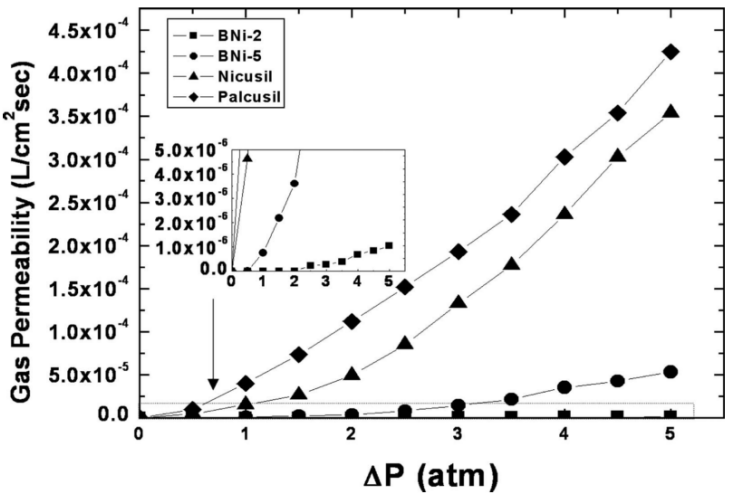

Figure 7.3 - Gas permeability of nickel and silver-copper based braze materials versus differential pressure in helium [244].

Kim et al. used a four-probe electrical conductivity test on tubular fuel cells with the BNi-2 and BNi-5 braze as a current collector. The cells had a Ni-YSZ anode, a YSZ electrolyte and a dual LSM and LSCF cathode and had an active area of 11.2 cm^2. Hydrogen was fed to the anode at 50 $ml.min^{-1}$ and air was supplied to the cathode. The electrical conductivity of the cell with BNi-2 braze was higher than with the BNi-5 braze as can be seen from Figure 7.4 a). The conductivity of the cell at 750°C with BNi-2 was 450 $S.cm^{-1}$, 80% higher than the BNi-5 cell at 250 $S.cm^{-1}$. The durability of the fuel cell with a BNi-2 braze in both oxidising and reducing atmosphere was indicated by its stable conductivity values over the 6 days of testing as seen in Figure 7.4 b). The electrical conductivity measured by a 4-probe technique versus thermal cycling of the cell with a BNi-2 brazed current collector is seen in Figure 7.4 c). A ramp rate of 3.33°C.min^{-1} was used between the dwell temperatures of 150°C and 750°C. The brazed joint was stated to have remained unchanged during thermal cycling. The cell had a current density at 0.7 V of 0.2 $A.cm^{-2}$, a peak power density of 0.21 $W.cm^{-2}$ and an estimated ASR from the polarisation curve of 1.1 $\Omega.cm^2$ at 750°C. The OCV was greater than 1 V, again indicating no fuel leakage meaning the BNi-2 worked well as a manifold sealant.

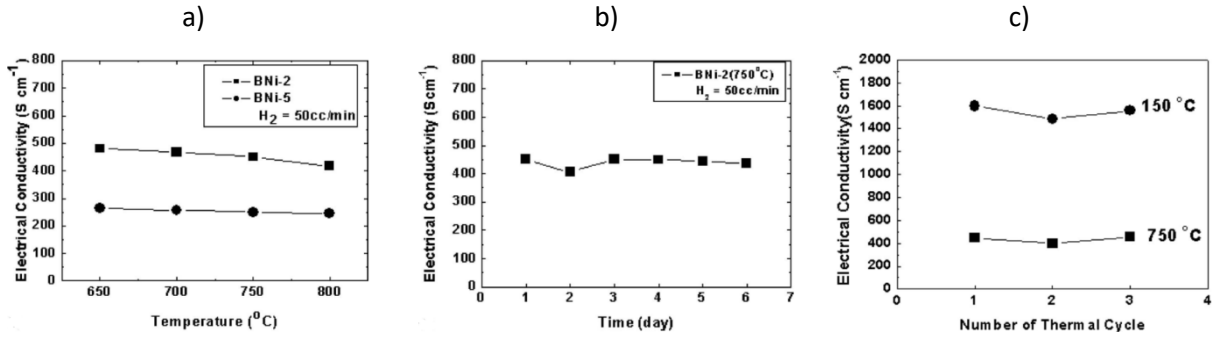

Figure 7.4 - Electrical conductivity of fuel cells with BNi-2 and BNi-5 braze versus a) operating temperature, b) operating time, c) electrical conductivity of BNi2 versus thermal cycling to 150°C and 750°C [244]**.**

From a review of the very few literature articles of brazing in the µT-SOFC, it was evident that brazing is a successful technique for contacting metallic current collectors and the anode. In addition, it was determined that there are cost-effective, non-reactive, non-precious brazing alloys that are able to wet to and attach the anode and current collector.

7.2 Brazing Apparatus

Brazing was conducted both in-house and at Kepston Limited, a company based in the West-Midlands with a speciality in vacuum furnace brazing and mesh belt brazing. In-house brazing was done using an Elite tubular furnace, brazing chamber and gas supply. The quartz tube brazing chamber was designed and manufactured in-house, tapering at each end to gas-tight screw valves which were connected to an argon mass flow controller (0 to 500 $ml.min^{-1}$) at the inlet side and exhaust system at the outlet side. The rig process and instrumentation diagram are seen in Figure 7.5. Vacuum brazing was also attempted in-house with the modification of the rig to include a vacuum pump, however, the sealing and pump capacity was not sufficient to achieve a strong enough vacuum to eliminate oxidation of the cell during heating. An additional hydrogen mass flow controller option was also available to expand the environment options to include mildly reducing conditions.

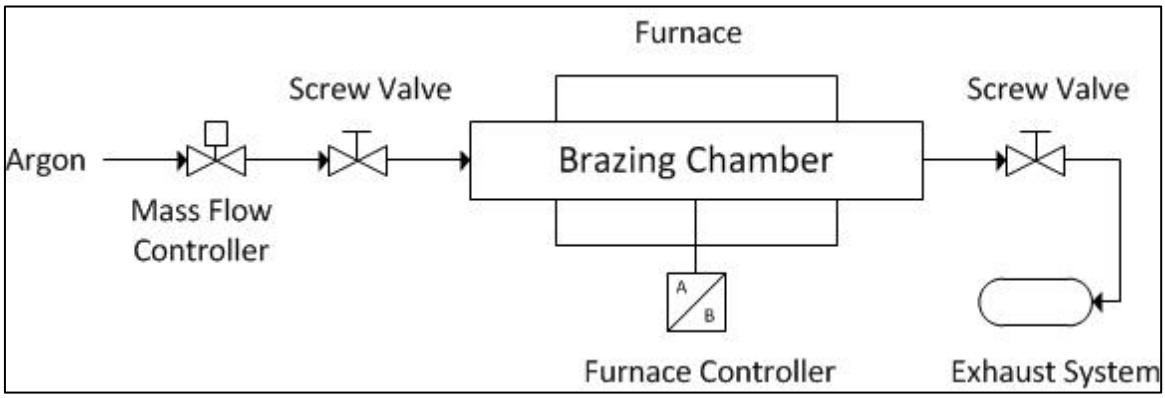

Figure 7.5 - In-house brazing rig PID.

Brazing at Keptson Limited was first attempted using a Mahler mesh belt furnace in a process commonly referred to as continuous brazing. Parts are loaded onto a conveyer belt which passes parts through a series of heating chambers. The heating chambers are sealed to the outside air using a flame curtain at the inlet and outlet, hydrogen and other inert gases can then be pumped into the furnace to achieve an inert or reducing environment. A reducing environment cleans/reduces the oxides that are usually present on the parent materials to be joined and aids the wetting/bonding which again promotes joint strength. This technique is suitable for mass production and can achieve a high throughput and is particularly useful for feasibility studies and material development/selection trials. However, control over the temperature rate and brazing time was rudimentary and achieved by controlling the belt speed, trialling a 275 $mm.min^{-1}$ and 400 $mm.min^{-1}$ rate. The flame curtain

caused scorching of the fuel cell surface even when shielded and proved this technique was unsuitable for this application. Nevertheless, valuable insight was gained from this rapid development process, the key outcome being the successful wetting of the braze material to the anode surface which will be discussed further in Section 7.3.

Once the proof of concept had been achieved in the mesh belt trails, finer control over temperature profiles and brazing environment necessitated the use of an R&D scale HTS Vacuum furnace. The furnace can achieve a hard vacuum, referring in this study to the conditions at which sufficient air is removed to eliminate the chance of oxidation of brazing components at elevated temperatures. A strong vacuum condition is also used to promote homogenous temperature distribution and lower the melting temperature of brazing materials. The vacuum furnace was used for multiple vacuum brazing trials and was capable of achieving vacuum conditions in the order of $1x10^{-5}$ Pa with a fine control ($1°C.min^{-1}$) over the heating profile and pressure profile. The hard vacuum was achieved in a three-stage pumping process, the first using a mechanical pump to evacuate the heating chamber from $1x10^{5}$ Pa (atmospheric pressure) to $5x10^{-1}$ Pa, then a roughing pump to achieve $5x10^{-2}$ Pa and then a diffusion pump to evacuate down to $5x10^{-5}$ Pa. Annotated images of the furnace front and rear are seen in Figure 7.6. The rig used multiple thermocouples to differentiate between the wall temperature of the furnace, the air temperature and sample temperature. Insulating the sample thermocouple was important for measuring the real temperature of the sample, shielding the tip from radiation and controlling temperature lag with respect to the furnace thermocouple.

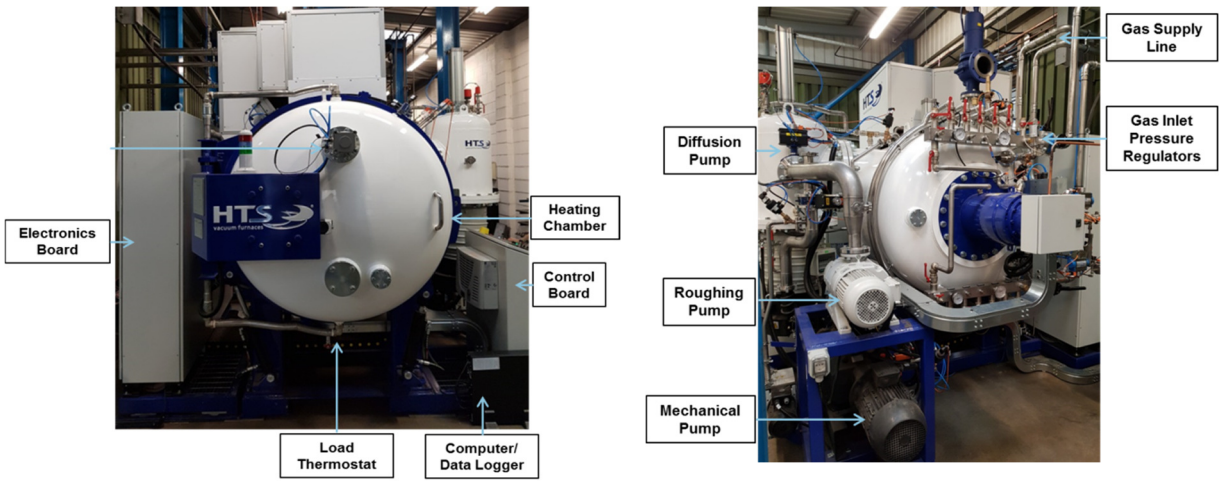

Figure 7.6 - R&D vacuum brazing rig.

7.3 Braze Selection

The choice of braze material was based on the following:

1. wettability to the parent materials,
2. chemical compatibility to the parent materials,
3. compatibility of brazing range operating temperature of the fuel cell,
4. compatibility with maximum allowable component temperature,
5. CTE match to the fuel cell components.

Given that the current collector material was nickel and the anode cermet was nickel based (Ni-YSZ), a nickel based braze was chosen. This combination favours CTE match, material similarity, and chemical compatibility, with the added benefit of being low-cost as compared to precious metal brazes. The nickel based braze materials were also suitable with respect to brazing temperature range as braze materials are typically chosen to have a brazing temperature a minimum of 100°C (ideally 200°C) higher than the joint will be exposed to in service (750°C) to avoid softening during operation. A maximum braze temperature of 1150°C was chosen based on the highest temperature that the fuel cell would be exposed to in its manufacturing process, which was the sintering temperature of the cathode. A supplier, VBC Group Ltd was chosen to provide the material and four braze alloys where identified. Braze material was available in paste, powder or pre-formed foil/ringlets.

Table 7.1 - Proposed braze materials.

Product Name AWS A58	Ni (wt%)	Cr (wt%)	Fe (wt%)	B (wt%)	Si (wt%)	P (wt%)	Melting Range (°C)	Suggested Brazing Temperature (°C)
BNi-1a	73.9	14.0	4.5	3.1	4.5	-	980-1070	1120
BNi-2	82.4	7.0	3.0	3.1	4.5	-	970-1000	1060
BNi-7	75.9	14.0	-	-	-	10.1	960-1127	1065
BNi-9	79.9	15.0	1.5	3.6	-	-	1055-1205	1055

BNi-1a is typically used for brazing stainless steel alloys at high temperature [312]. BNi-2 is ideal for low temperature brazing of thick stainless steel, nickel and cobalt based alloys [313]. BNi-7 is a eutectic nickel brazing alloy ideal for honeycomb and thin walled structures [314]. BNi-9 is a eutectic nickel brazing alloy with a high melting point, suitable for brazing stainless steel, nickel and superalloys [315]. The braze material BNi-2 was seen as the most promising option of the materials in question with respect to the favourably lower Cr content, which upon volatilisation would cause cathode poisoning. In addition, the relatively small 30°C melting range promotes mobilisation of the braze considering the limitation of ramp rate for protecting fuel cell components which are typically around 10°C.min^{-1} compared to the approximately 100°C.min^{-1} ramp rate typical to brazing. BNi-2 was also reported in literature to wet stainless steels to Ni-YSZ [244], as described in Section 7.1.

In the continuous brazing materials development process at Kepston Ltd, BNi-2, BNi-7 and BNi-9 were selected for wetting trials on anode and electrolyte stubs, some of which had been cut in half to allow easy access to the anode support. Figure 7.7 shows the successfully brazed nickel wire to the anode stubs using BNi-2.

Figure 7.7 - Continuous brazed anode stubs using BNi-2 braze to join nickel wire to the anode.

BNi-1a was omitted due to the higher suggested brazing temperature which was within 30°C of the maximum braze temperature. Strips of 0.375 mm nickel wire were positioned on the length of the anode wall of the stub and braze paste applied with a syringe either side of the wire strip. All of the three braze materials tested wetted to the Ni-YSZ anode surface to create a successful joint. Upon visual inspection, the BNi-2 created a superior joint to the BNi-7 and BNi-9. The BNi-7 and BNi-9 braze pooled into balls at the interface between the current collector wire and the anode surface as seen with the sample anode stub and nickel wire using BNi-9 in Figure 7.8. While the wire and anode were joined, the wire could be prized from the anode with reasonable force.

Figure 7.8 - Anode stub and nickel wire brazed with BNi-9 showing braze pooling.

In contrast, the BNi-2 had flowed along the joint length and created a strong joint that could not be removed with reasonable force. The BNi-2 was selected for further testing and optimisation on complete cells. According to the manufacturer, BNi-2 braze material is suitable to high temperature, high-stress components, heavy non-moving parts as well as honeycomb and thin materials, exhibiting very high joint strength and fluidity. The joint can withstand oxidation resistance up to 1060°C and has good corrosion resistance in a wide range of corrosive media [316].

7.4 Braze Application

Applying the braze material between the nickel hiTRAN and the inner wall of the complete tubular cell was non-trivial. The narrow tube bore, long tube length, high volume/complex structure of the hiTRAN and intimate fit (oversized hiTRAN OD) all posed problems. Ideally, the braze material would be applied to every surface in contact with the tube wall, however not covering too much of the anode surface which would impede the mass flow of reactants/products across the anode. To optimise the braze application for the hiTRAN, 5 cm long fuel cells stubs similar to those seen in Figure 7.7 were again cut, however, this time the sample was taken this time from within the active region of a cell. The knowledge gained on the trial pieces could then transfer for use on complete cells.

The most common way of braze application at Kepston Ltd was via syringing of braze paste. Syringes were loaded with material and then plungers were attached to air lines with a variable pressure controller to control deposition rate, a foot pedal acted as an on/off switch to free up hands for a controlled application. Syringe tips were typically 5, 10, and 15 cm in length and came in diameters of 10 gauge (G), 16 G, 18 G, 20 G. For working with stubs, a short, 16 G bore tip was identified to give the best control and deposition of the braze. A longer 15 cm version with the same 16 G bore was optimal for use on the complete cells. Braze was applied in two strips along the length of the tube,

spaced 180° apart. The braze strips only weakly adhered to the material surface and often sections became dislodged. The hiTRAN was pulled through the tube until in position. Seating of the hiTRAN often resulted in braze material agglomerating and being dragged out of position, leaving an uneven distribution of braze material along the tube length. Images of brazed hiTRAN stubs using syringed BNi-2 braze in continuous brazing trials are seen in Figure 7.9.

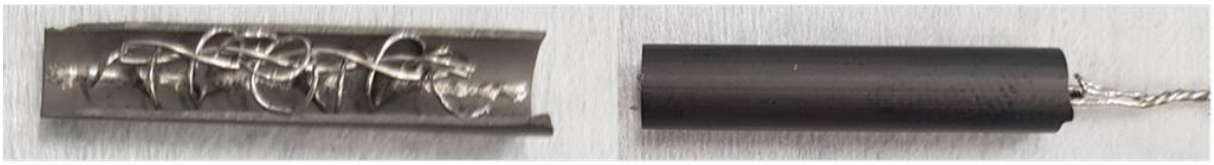

Figure 7.9 - Continuous brazed fuel cell stubs using BNi-2 braze to join hiTRAN to the anode.

The difficulties experienced when syringing strips along the anode wall lead to the idea of pre-loading braze material on the hiTRAN before loading. Two strips of braze were applied along the brush length, pressed gently to improve adherence and then the brush was seated. However, this still led to an uneven distribution of braze material along the tube length.

The problems with the braze paste application were avoided by using braze in a powdered form. The entire loop surface of the hiTRAN including the core wire was first sprayed with an aerosol-based acrylic adhesive. Powdered braze material was then dusted over the entire loop section length of the hiTRAN loop section to give a fine coating of braze material. The coated hiTRAN were then visually inspected under a microscope. The excess braze powder from the initial dusting was collected and formed into a bed for dipping any of the outer edges of the loops that did not have a sufficient coating of the braze material. The excess powder was shaken off and the hiTRAN was left to air dry for 5 minutes before installation into the cell as per the technique used for the standard hiTRAN detailed in Section 6.1.3. The hiTRAN were weighed before and after coating, the combined mass of the braze and adhesive was 0.2 g ±0.05 g. This braze application process was simple, quick and cost-effective and excess braze material could be retrieved and re-used. This technique had the added advantage of brazing the interior coil-core joints of the hiTRAN when compared to a syringe applied paste. This resulted in a stronger and more conductive joint between the coil and the core which acts to reduce the contact resistance of the joint, thus reducing the overall ohmic resistance of the hiTRAN itself. Some of the braze material was dislodged at the wire-electrode interface upon installation. The coated hiTRAN was pulled completely through a cell and upon inspection sufficient braze was still at the interface and the interior anode surface did not have agglomerated braze. The

good wetting of the BNi-2 meant that braze near, but not at the interface upon assembly, would flow to the interface and form/add to the joint upon heating.

7.5 Electroless Nickel-Alloy Braze

To achieve a homogeneous distribution of braze material that would not become dislodged upon assembly, electroless plating was explored. Electroless plating is common in the automotive and electronics sectors for electrical contacts/switches and printed circuit boards. Nickel plating is typically used for wear resistance, hardness and for corrosion resistance. Electroless deposition is a chemical reduction process that does not require a current as is used in electroplating processes. Fine control of deposition thickness can be achieved as well as superior uniformity, regardless of geometry, with respect to electrolytic processes. Parts are dipped into a bath with the nickel based plating solution and a reducing agent, adjusting the exposure time to control the deposition thickness [97]. Phosphorus is added between 2 and 14% to provide wear resistance, improve hardness, provide corrosion protection and enhance electrical properties. Parts are dipped into a bath with the nickel based plating solution and a reducing agent, adjusting the exposure time to control the deposition thickness [97]. The plating chemistry is available with phosphorous levels in a low (2-5 wt%), medium (5-11 wt%) and high (11-14 wt%) quantity. The coating density and wear resistance increase with increasing phosphorous content while hardness reduces. Noting the compositional similarity of the medium content electroless nickel (EN) coating to the BNi-7 braze material as seen in Table 7.2, the EN coating was identified as a candidate for brazing.

Table 7.2 - Electroless braze material vs BNi-7 properties.

Product Name AWS A58	Ni (wt%)	Cr (wt%)	Fe (wt%)	B (wt%)	Si (wt%)	P (wt%)	Brazing Range (°C)	Suggested Brazing Temperature (°C)
BNi-7	75.9	14.0	-	-	-	10.1	960-1127	1065
Electroless Ni-P Braze	Bal	-	-	-	-	6.0-9.0	900-1100	1060

For use as a braze material, the primary function of the phosphorous was for its use as a melting point depressant as used in typical braze materials. The correct content being crucial to enable the

nickel based EN braze deposited on the hiTRAN to surpass its liquidus temperature and become mobile before reaching the melting point of the nickel hiTRAN support. Increasing the phosphorous content decreases the melting point from around 1200°C for low phosphorous alloys to 800°C for high phosphorous content alloys seen in Figure 7.10 a). Given the application in interconnection, consideration had to be made to the conductivity of the joint as increasing phosphorous content also increased material resistivity as seen in Figure 7.10 b) [317].

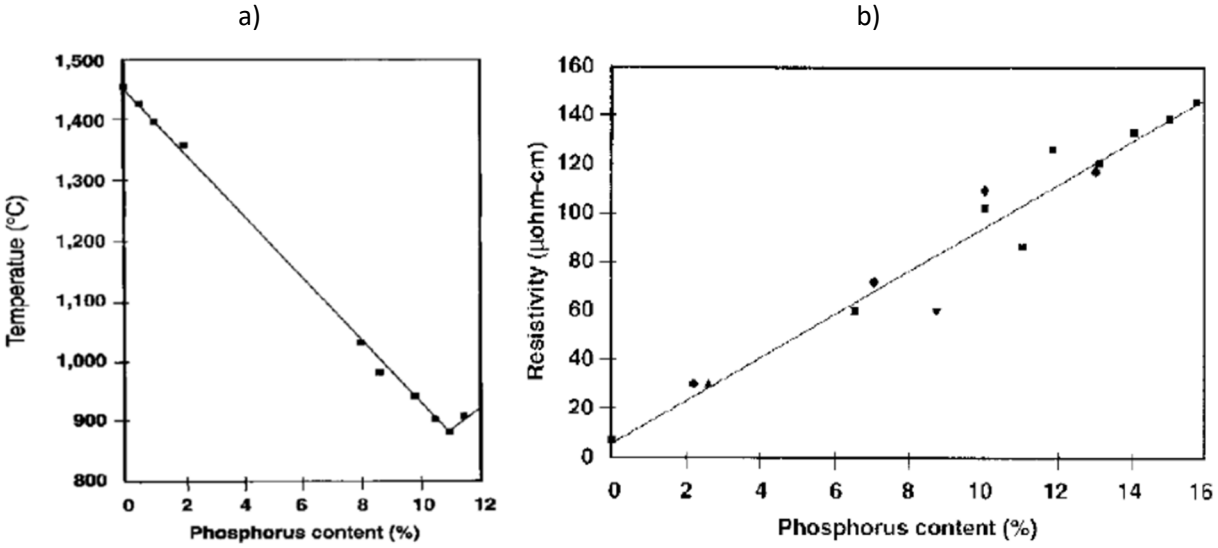

Figure 7.10 - Phosphorous content versus a) melting point of the EN alloy, b) versus resistivity of the EN alloy [317]**.**

The content of the phosphorous was chosen to be similar to that of BNi-2. The solution was estimated at 6 to 9 wt% phosphorous content which brought the melting range to between 900°C and 1100°C. Two coating thicknesses of 10 µm and 20 µm were trialled. Plating was provided by Frost Electroplating at £100 per batch per 10 µm. The hiTRAN was weighed before and after the 20 µm EN braze was applied and the braze mass was 0.18 g ± 0.02 g. The lower error term was indicative of the fine control over braze loading of EN versus the powder BNi-2 approach.

7.6 Brazing Profiles

Two brazing profiles were developed, the first optimised for the brazing conducted at Kepston Ltd using the BNi-2 in the vacuum brazing rig. The second brazing profile was developed for in-house atmospheric inert/reducing brazing for use with the EN braze and BNi-2. The brazing temperature was chosen as 1065°C for both brazing profiles. A fast ramp of 10°C.min^{-1} was chosen between room

temperature to 800°C, while a slow ramp of 2°C.min^{-1} was chosen between 800°C and the brazing temperature in order to minimise stress in the fuel cell, hiTRAN and braze material. An adhesive/binder burn-off stage was required for the BNi-2 at 450°C, adding 5 minutes to the brazing time versus the EN braze. For the vacuum braze cycle, strong vacuum conditions were required before any heating and cooling, adding a N_2 fan quench at 50°C to increase the cooling rate and allow the large thermal mass of the furnace to equilibrate. For inert/reducing brazing in-house, a high gas flow of 500 ml.min^{-1} was introduced for 5 minutes before heating commenced with backpressure purges, ensuring the removal of air from the chamber. A lower 300 ml.min^{-1} gas flow was used during the brazing process. The vacuum brazing profile is shown in Figure 7.11.

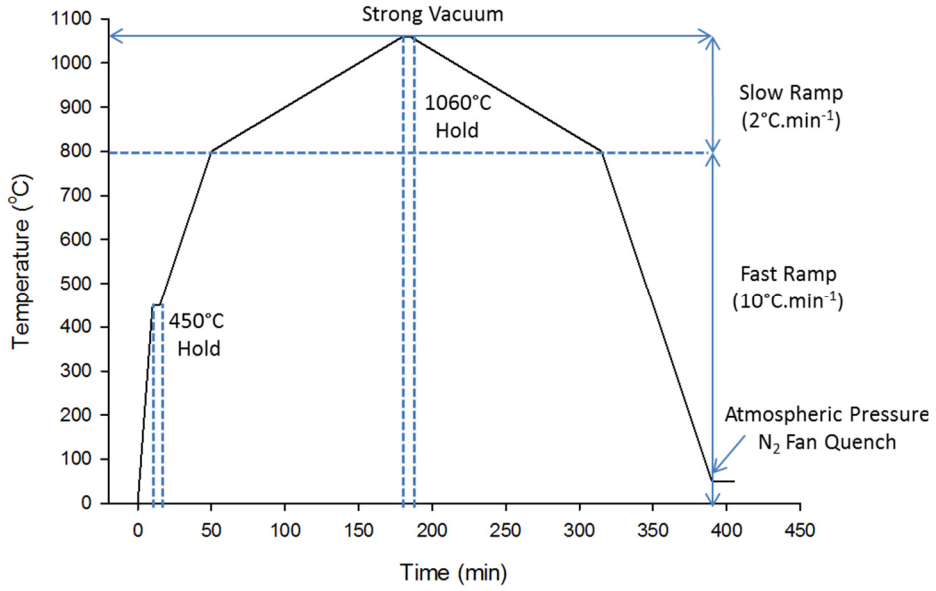

Figure 7.11 - Vacuum brazing profile for VBC braze materials.

7.7 Results

The BNi-2 braze was successful in forming a joint between the hiTRAN and the complete fuel cell using vacuum brazing and inert brazing. This indicated that the braze material and brazing conditions were suitable for brazing of the hiTRAN and N-YSZ anode. However, the cost and logistics of running off-site vacuum brazing favoured in-house brazing. All cells were analysed by mechanical testing and imaging. However, only in-house brazed cells with an inert and reducing environment using BNi-2 and EN braze were tested electrochemically.

7.7.1 Mechanical Testing

The results of the mechanical testing of the BNi-2 vacuum brazed hiTRAN-anode joints is seen in the load versus extension plot, Figure 7.12. The maximum load was 68.0 N. The staggered plot indicated that the hiTRAN was deforming in the cell, with loops breaking contact nearer the load head first. The maximum load of the BNi-2 vacuum brazed hiTRAN was around 85% of the value of the un-brazed hiTRAN pre-testing (80.2 N) and was around 9 times (an 820% increase) that of the un-brazed cell post-testing (7.4 N). The maximum load was deemed suitable in securing the hiTRAN to the cell to withstand any impact that would occur during operation in a portable device. The benchmark value was set at 50 N, approximately the force of a 5 kg stack being dropped, accelerating due to gravity.

However, upon visual inspection of multiple runs of vacuum brazed cells, brazing was not possible without damaging both the anode and/or cathode. The anode surface changed colour from grey to green. The cathode remained well adhered to the cell, however, became blotchy and discoloured. A fine green surface coating was observed on the YSZ and it was suspected to be volatile components from the braze, also causing the colour change on the anode. This coating was suspected to be Cr^{3+} which is green in colour. This surface coating could be removed with a fine file to expose the greyish surface of the anode. The high vacuum was suspected to have not been sufficient to completely remove all of the air and that the little oxygen remaining was able to oxidise the sensitive braze components and the anode at the 1060°C braze temperature. The high vacuum may have led to structural instabilities in the cathode, particularly given the elevated temperature. It is possible oxygen could have migrated from the cathode to the air and caused the oxidation of the nickel. Further characterisation was required to identify the exact reason behind the degradation. However, given the cost and logistics of running off-site vacuum brazing tests, and given the success in on-site atmospheric brazing, no further research into vacuum brazing was conducted. The furnace at Kepston Ltd did have the option to function with inert and reducing conditions. The large furnace chamber size with respect to the in-house rig meant that operating costs with respect to heating and gas supply would make in-house brazing far more cost-effective. As such brazing was shifted in house.

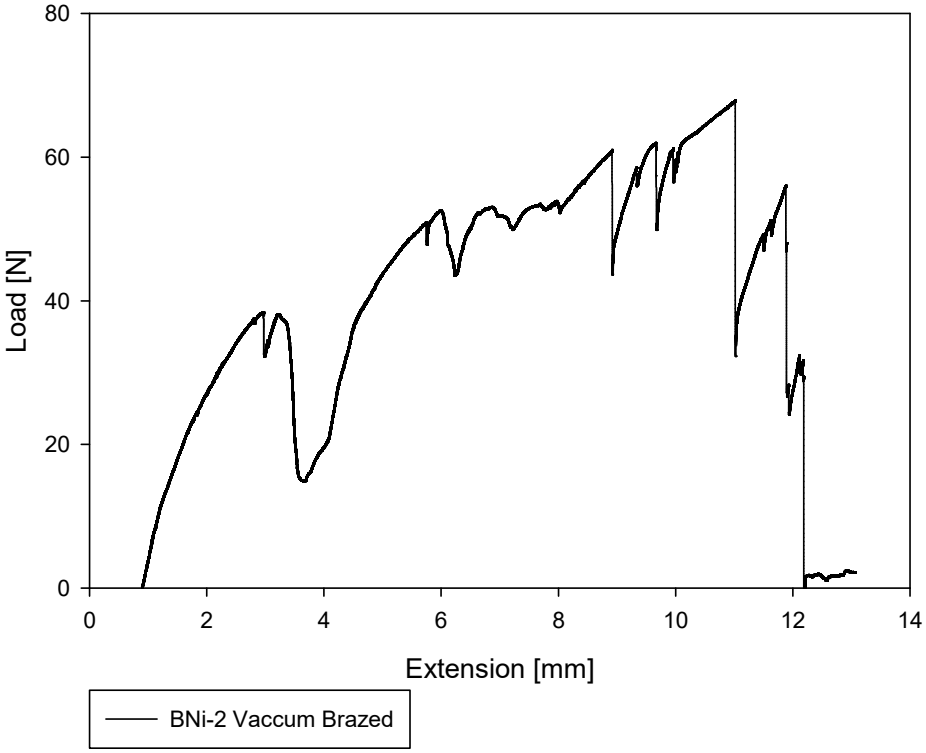

Figure 7.12 - Load vs extension plot of a cell with BNi-2 vacuum brazed hiTRAN.

The results of the mechanical testing of the BNi-2 inert brazed hiTRAN-anode joints are seen in the load versus extension plot Figure 7.13. The maximum load was 58.8 N, indicating that brazing with BNi-2 had been successful in an inert environment. The maximum load for the inert brazed cell was 86% of the vacuum brazed cell. The lower maximum load of the brazing under an inert environment compared to that of a reducing environment was expected. Joint strength is typically at a maximum in a vacuum environment, followed by a reducing environment and then an inert environment. The relatively smooth plot of the inertly brazed BNi-2 versus the vacuum brazed was attributed to more braze material at the coil-core joints which resulted in less deformation of the hiTRAN during the extension. Again, the maximum load was deemed suitable in securing the hiTRAN to the cell to withstand any impact that would occur during operation in a portable device. After electrochemical testing of the inert brazed BNi-2 cell, the hiTRAN was still firmly in place and could not be pulled out by hand. When using the mechanical testing rig, the anode, which became more brittle during testing, shattered before the hiTRAN was separated. This further confirmed that the joint strength was sufficient. This essentially meant that the hiTRAN acted as a metal support for the cell and so the setup could technically be called a metal-supported µT-SOFC.

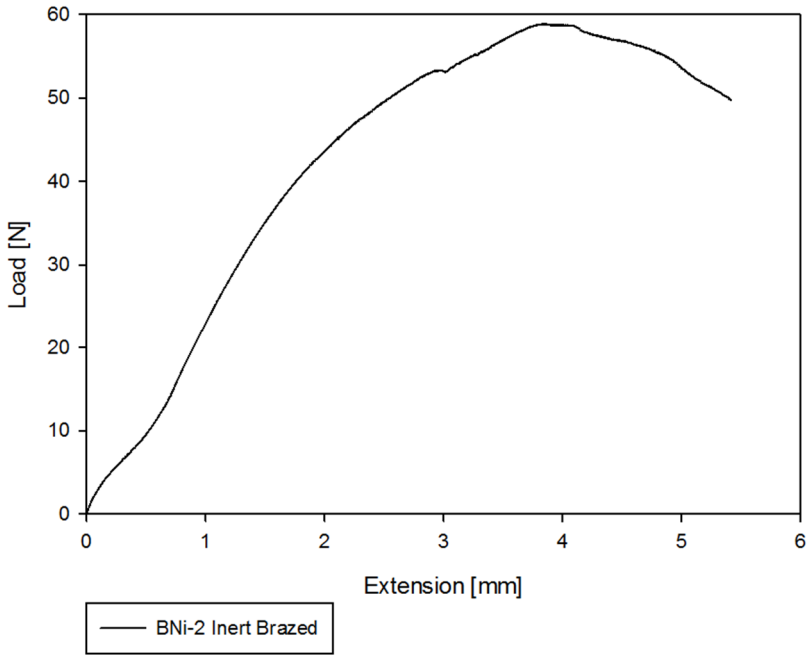

Figure 7.13 – Mechanical load vs extension curve of BNi-2 brazed hiTRAN.

7.7.2 Joint Imaging

Optical microscopy was performed on the interior anode wall of a cell that had the vacuum brazed BNi-2 hiTRAN extracted and the image along with a 3D render of the image is seen in Figure 7.14. The images show the 'witness' of the joint between the hiTRAN and the interior anode wall. The depressions occurred when the hiTRAN was removed from the cell, removing a section of material to which it was joined. Witness of this type was observed at multiple points along the cell wall of the fuel cell. The removal of the brazed hiTRAN and some of the anode to which it was attached indicated that the brazed joint was indeed stronger than the anode itself post-brazing. The shiny region near the deep recess is braze material.

SEM was performed on the interior anode wall of a cell that had the inert brazed BNi-2 hiTRAN extracted and the image is seen in Figure 7.15. The depressions are from the scoring of the anode surface by the hiTRAN during installation and the brazing process. The shiny regions in some of the recesses are the braze material that has been left on the surface. At these points, the joint between the electrode and the braze was stronger than that between the hiTRAN and the braze.

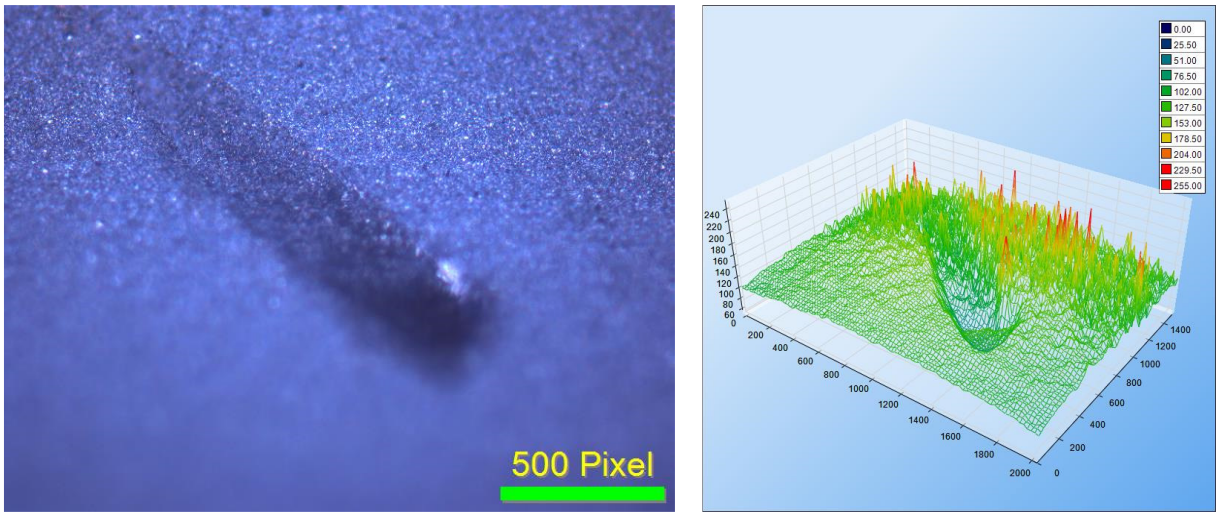

Figure 7.14 - Optical microscope image & 3D render of the interior anode wall joint witness post brazing with BNi-2 under vacuum.

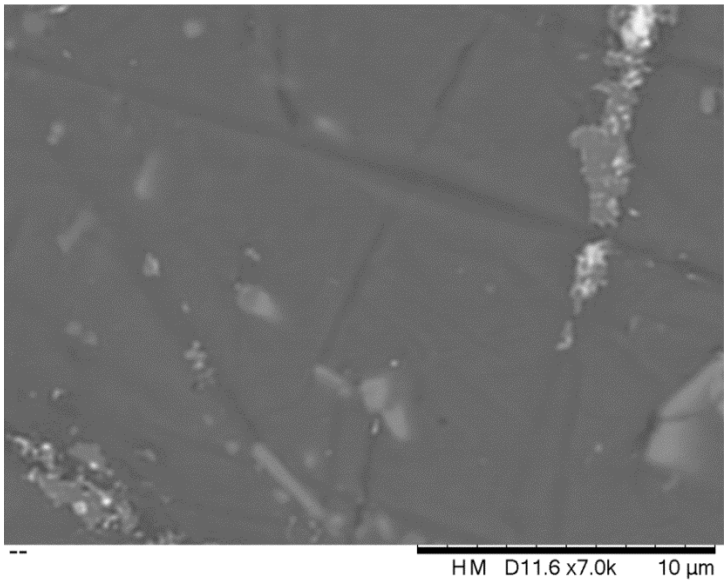

Figure 7.15 - SEM of the anode and braze post-testing.

7.7.3 Electrochemical Testing

The contribution of the ohmic polarisation and electrode polarisation to the total cell polarisation (the summation of the ohmic and electrode polarisation/resistance) for the hiTRAN as a current collector un-brazed, 10 µm and 20 µm EN reducing brazed, 20µm EN inert brazed, and with the BNi-2 inert brazed is seen in Figure 7.16. The impedance was measured at 0.7 V in the ohmic loss dominated region. The ohmic polarisation of the 10 µm EN reducing braze increased by 19% of the

un-brazed value indicating that brazing was not successful due to an insufficient content of braze material to form a joint. The ohmic polarisation value increased as the hiTRAN became separated from the wall, decreasing the number of contact points and the contact force of the remaining contact points. This separation was a result of the softening of the nickel and the mismatch in CTE between the nickel hiTRAN and the fuel cell over the brazing temperature profile. The resulting decrease in contact force and contact area caused an increase in contact resistance and thus polarisation resistance of the hiTRAN current collector.

The ohmic polarisation was reduced from 0.231 Ω for the un-brazed hiTRAN to 0.079 Ω, 0.090 Ω and 0.080 Ω for the thicker 20 µm EN reducing, 20 µm EN inert brazed and BNi-2 inert brazed hiTRAN, respectively. This corresponds to ohmic polarisation values 34%, 39% and 35% of the un-brazed value, respectively. This indicated that these brazing materials and techniques were successful. A comparison of ohmic polarisation values of the 20 µm EN brazed cells indicated that the brazing favoured a reducing environment. A reducing environment promoted the formation of an oxide-free joint which increased joint strength and durability [307].

The electrode polarisation of all of the brazed cells increased versus the un-brazed cell. The electrode polarisation of the un-brazed hiTRAN was 0.011 Ω, increasing to 0.067 Ω, 0.061 Ω, 0.019 Ω and 0.023 Ω for the 10µm EN reducing brazed, 20µm EN reducing, 20µm EN inert brazed and BNi-2 inert brazed hiTRAN cells, respectively. This was an increase by 510%, 455%, 73% and 110% of the un-brazed value, respectively. Upon visual inspection of the cells brazed in a reducing environment, the anode colour had remained unchanged throughout the brazing process indicating re-oxidation had not occurred. However, some delamination of the cathode was evident although the majority of the material had remained intact. The delamination was not evident in the cells brazed in an inert environment. This indicated the cathode delamination was a result of the environment rather than the furnace heating profile given the ramp rates and braze temperatures were the same in the inert and reducing brazing profiles. In the reducing brazed cells, some minor colour change from grey to green was observed around the tips of the anode indicating some re-oxidation had occurred. The electrode polarisation values indicated that overall, the electrodes favoured an inert environment. Indeed the cells with the lowest total resistance were the inert brazed cells. The ASR values with hiTRAN as the current collector were 4.77 $\Omega.cm^2$, 6.19 $\Omega.cm^2$, 2.76 $\Omega.cm^2$, 2.15 $\Omega.cm^2$, 2.04 $\Omega.cm^2$ for the un-brazed hiTRAN, the 10 µm EN reducing brazed, 20 µm EN reducing, 20 µm EN inert brazed and BNi-2 inert brazed hiTRAN cells, respectively.

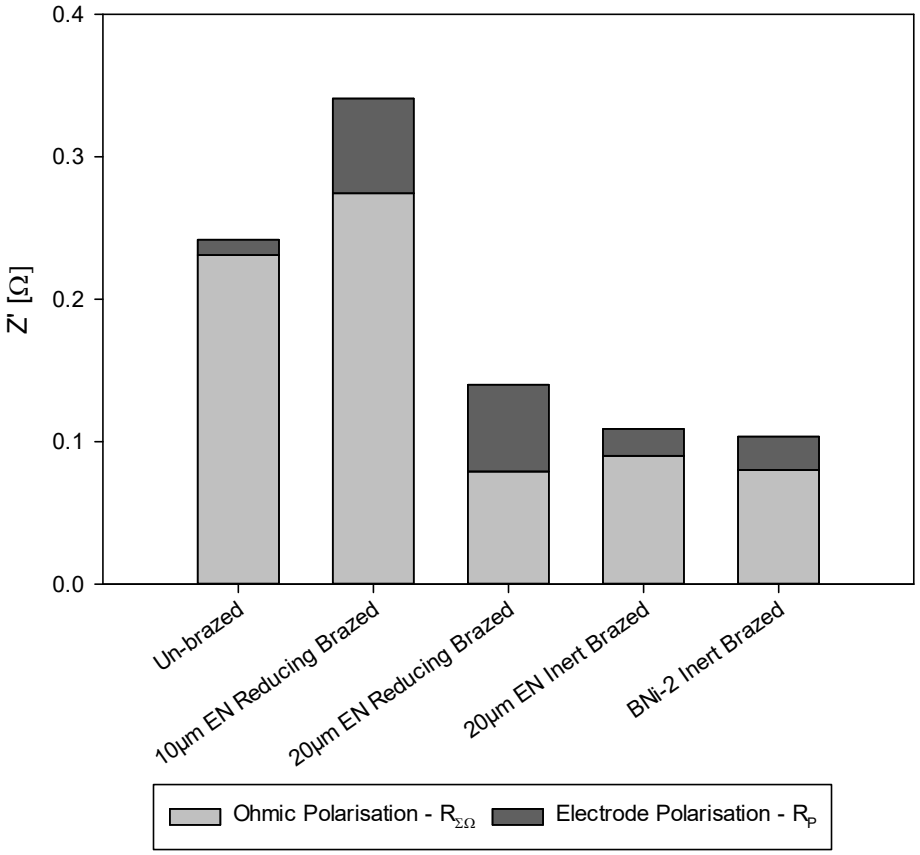

Figure 7.16 - Ohmic resistance at 0.7 V of hiTRAN un-brazed versus brazed in inert and reducing conditions.

If brazing with half cells (anode and electrolyte) it would be preferential to braze in a reducing environment. The cathode could then be prepared in a later process, taking care to select the sintering environment appropriately. Ideally with a reducing environment again on the anode side and in an oxidising air environment on the cathode side which is typical in the cathode sintering process.

The polarisation and power plot of the cells with hiTRAN as the current collector un-brazed, 10 µm EN reducing brazed and 20 µm EN reducing brazed are seen in Figure 7.17. The ASR estimated by the gradient of the polarisation plots is 5.00 Ω.cm^2, 7.34 Ω.cm^2 and 1.94 Ω.cm^2, respectively. The current density at 0.7 V was 0.079 A.cm^{-2}, 0.048 A.cm^{-2}, 0.176 A.cm^{-2}, respectively. The peak power density was 0.061 W.cm^{-2}, 0.038 W.cm^{-2} and 0.143 W.cm^{-2}, respectively. The lower current density at 0.7 V, lower peak power and higher estimated ASR of the 10 µm EN reducing brazed cell as compared to the un-brazed cell confirmed the findings from impedance spectroscopy. The loss of performance was attributed to an increase in both the ohmic polarisation and electrode polarisation, the former from the increased contact resistance between the hiTRAN and the anode and the latter from the

degradation of the cathode. The increase in coating thickness of the EN braze to 20 µm meant that there was sufficient braze loading to successfully join the hiTRAN and the anode at all points of contact. The physical joints resulted in relatively lower contact resistance between the hiTRAN and the wall. This led to an ASR value lower and a peak power density higher than with the un-brazed cell even though the electrode polarisation had increased.

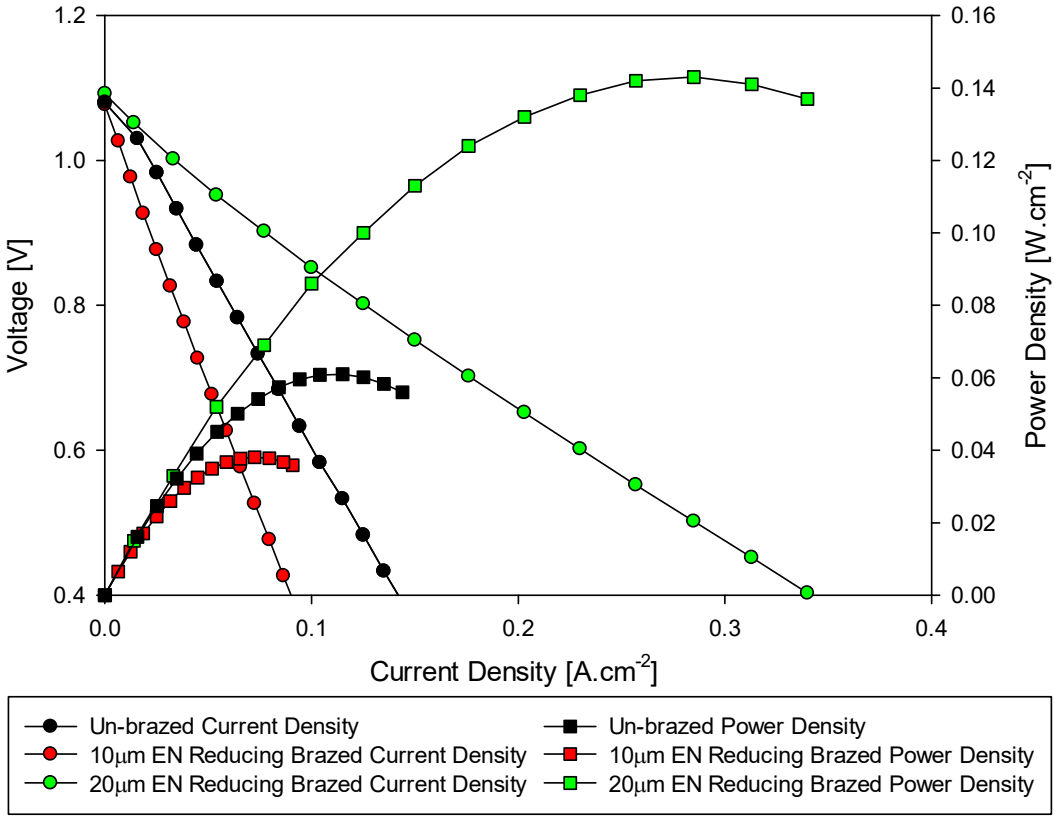

Figure 7.17 - Polarisation and power density plot with hiTRAN MPD as a current collector un-brazed, 10 µm EN reducing brazed and 20 µm EN reducing brazed at 750°C and 200 ml.min^{-1} H_2 and 10 ml.min^{-1} N_2 gas flow rate.

The polarisation and power density plot of the cells with hiTRAN as the current collector with a 20 µm EN reducing, 20 µm EN inert, and BNi-2 inert braze is seen in Figure 7.18. The ASR estimated by the gradient of the polarisation plots was 1.94 Ω.cm^2, 2.22 Ω.cm^2 and 1.53 Ω.cm^2, respectively. The current density at 0.7 V was 0.176 A.cm^{-2}, 0.162 A.cm^{-2} and 0.189 A.cm^{-2}, respectively. The peak power density was 0.143 W.cm^{-2}, 0.132 W.cm^{-2} and 0.151 W.cm^{-2}, respectively. Even though the electrode polarisation and total cell resistance (measured by EIS) was higher for the cell with the 20 µm EN reducing braze compared to the 20 µm EN inert braze, the lower ohmic polarisation of the former led to superior polarisation performance. The cell brazed with the BNi-2 in an inert environment had the lowest total cell resistance and was the best performing. A summary of the

electrochemical performance of the un-brazed hiTRAN and all of the brazed variants are seen in Table 7.3.

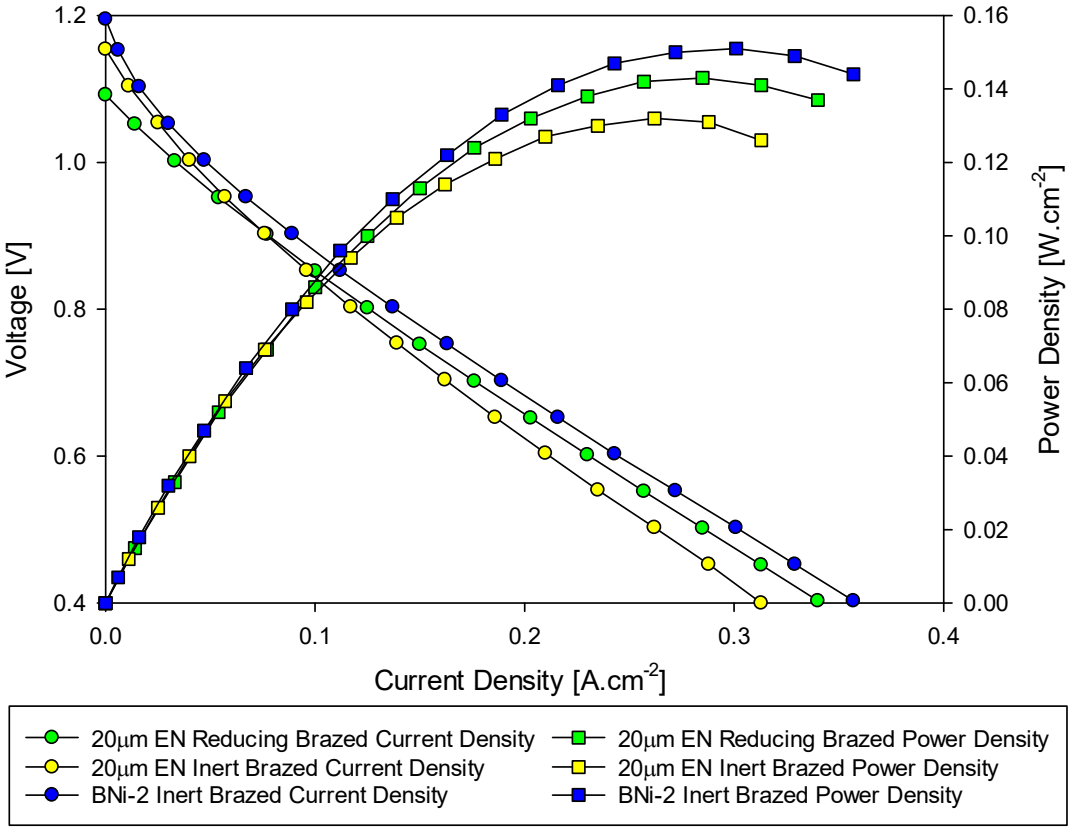

Figure 7.18 - Polarisation and power density plot of cells with hiTRAN MPD as a current collector 20 µm EN reducing brazed, 20 µm EN inert brazed and BNi-2 inert brazed at 750°C and 200 ml.min^{-1} H_2 and 10 ml.min^{-1} N_2 gas flow rate.

Table 7.3 - Summary of electrochemical data from cell tests with un-brazed versus brazed hiTRAN.

	Electrode Polarisation [Ω]	ASR (EIS) [Ω.cm^2]	ASR (IV) [Ω.cm^2]	Current Density at 0.7 V [A.cm^{-2}]	Peak Power Density [W.cm^{-2}]
Un-brazed hiTRAN	0.011	4.77	5.00	0.079	0.061
10 µm EN Reducing	0.067	6.19	7.34	0.048	0.038
20 µm EN Reducing	0.061	2.76	1.94	0.176	0.143
20 µm EN Inert	0.019	2.15	2.22	0.162	0.132
BNi-2 Inert	0.023	2.04	1.53	0.189	0.151

The average polarisation and power plots of different cells with a BNi-2 inert brazed hiTRAN as the current collector at the standard operating conditions with a furnace temperature of 750°C and fueled by 200 ml.min^{-1} of H_2 and 10 ml.min^{-1} of N_2 is seen in Figure 7.19. The average current density

at 0.7 V was 0.19 A.cm^{-2} and the peak power density is 0.15 W.cm^{-2}. The ASR as estimated by the gradient of the polarisation plot was 1.82 Ω.cm^2. The largest error term ±0.011 A.cm^{-2} was at low overpotential. This is explained by the polarisation data from one of the cells being an initial measurement at the start of the test after a brief hold at OCV. As the cell was being fed with dry hydrogen, there was little water content in the cell which drove the Nernst potential and OCV higher than for the other cells. Below 1.0 V the error terms are below ±0.003 A.cm^{-2}.

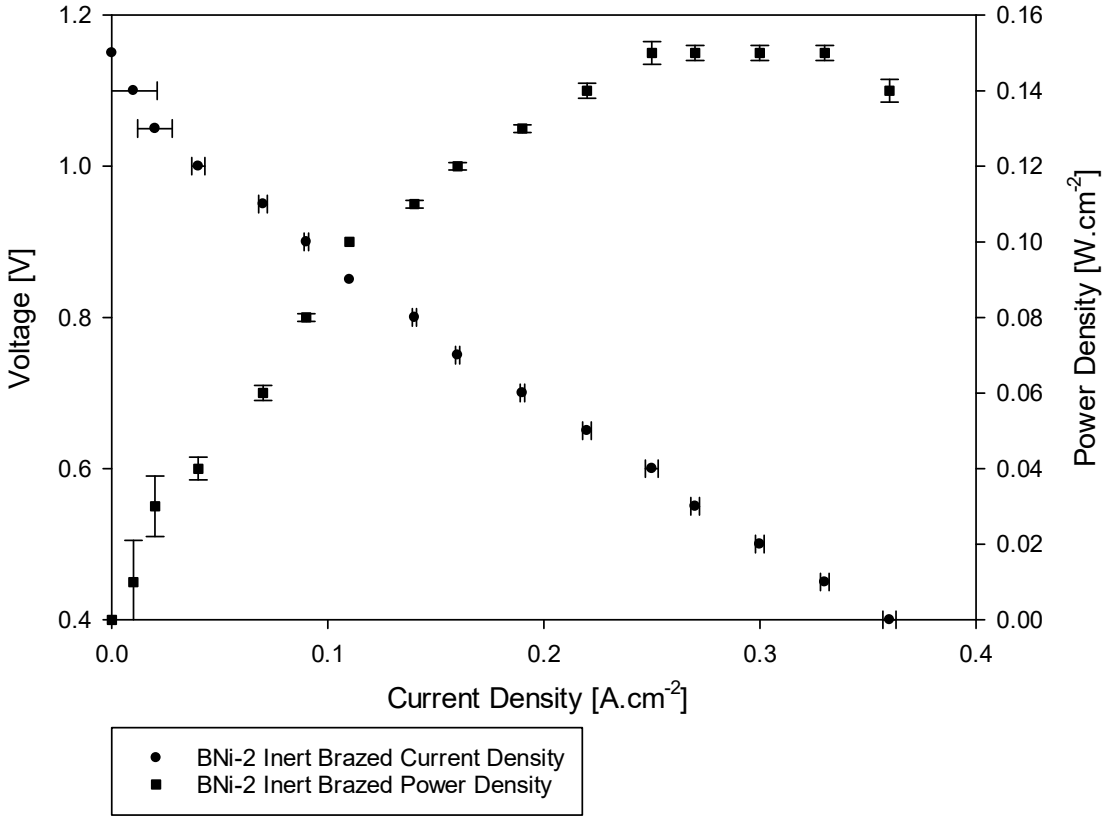

Figure 7.19 - Average polarisation and power density plot of cells with BNi-2 inert brazed hiTRAN as the current collector, tested at the standard operating conditions of 750°C and 200 ml.min^{-1} H_2 and 10 ml.min^{-1} N_2 gas flow.

7.8 Summary

Brazing was identified as a suitable joining technique for joining the hiTRAN to the SOFC anode. Brazing allowed the fuel cell, hiTRAN and the braze to be heated in an electrically heated furnace in a controlled manner to the braze temperature, avoiding damage to the fragile ceramic components. A range of cost-effective, nickel based brazes were identified as suitable candidates to wet to, and join the hiTRAN and anode together. Initial continuous brazing trials indicated BNi-2 as the ideal braze material. Vacuum brazing at Kepston Ltd led to the development of a brazing temperature profile

and a successful hiTRAN-anode braze, but the vacuum environment led to damage of the cathode. An in-house brazing rig was developed as a low-cost solution for inert and reducing brazing. The high surface area and intricate hiTRAN structure combined with the tight-fitting within the cell and narrow tube bore led to difficult braze loading for ensuring multiple contacts along the anode wall. A powder application of the BNi-2 braze was successful. A novel electroless plated nickel-phosphorous braze was developed as a simple solution to braze loading at an industrial scale. Two braze coating thicknesses were trialled with a 20 µm coating identified as the minimum thickness required for forming a joint at every contact point. The 20 µm braze loading of EN braze brazed in both an inert and reducing environment, as well as the inert BNi-2 brazed cells all outperformed the non-brazed hiTRAN as a current collector. From EIS it was determined that an inert brazing environment led to lower electrode polarisation values while a reducing brazing environment favoured a lower ohmic polarisation and a higher quality anode-electrode joint. The inert BNi-2 brazed hiTRAN with powder braze loading was the best performing electrochemically and with respect to stack durability. The design was chosen for incorporation into a stack.

Chapter 8 Stack Design & Fabrication

This chapter details the design and fabrication of two 4-cell µT-SOFC stacks using brazed hiTRAN current collection. Fuel inlet and outlet manifolds were designed and optimised using CAD and 3D CFD modelling. The manifolds were incorporated into a 3D stack model solving for the conservation of momentum and energy. The findings of the model were taken as a baseline for a CFD optimisation study. Two 4-cell stacks are fabricated using the optimised manifold design. The stacks were electrochemically tested and the performance and durability evaluated.

8.1 Overall Stack Design

Now that the novel brazed current collector design had been proven on a single cell, the design was to be up-scaled to a stack level. In tubular stacks, the manifold is a key element of the design as it determines the cell spacing, which is significant in determining the stack volume and hence volumetric energy density. A good cell manifold must:

- Supply an equal amount of fuel to each cell,
- Have a low fuel side pressure drop,
- Minimise spacing and thus current conduction pathways,
- Hold cells securely without leakage/crossover,
- Be compact, light and durable,
- Allow a good flow of oxidant to the cells.

The simplest 2-cell short-stack and 3-cell designs were set aside in favour of a 4-cell design, giving a theoretical stack approximately four times the power output of a single cell. A large deviation from this value would indicate a fault with the manifold or a poor interconnect design. Each cell within the stack was connected in parallel, increasing stack voltage to four times that of the voltage per cell (approximately summing to 4.4 V) while keeping wiring ohmic loss to a minimum. 4-cell sub-stacks could then be connected to form a larger stack, in series, parallel or a combination. Modularisation in this way would allow stack output to range from a few watts to kilowatts. The power can be tailored to suit the application, whether high voltage, high current or an intermediate. Modularisation also allows for easy maintenance, permitting the replacement of an individual module if one were to fail,

avoiding stack shutdown and reducing downtime. A modular design also improves stack operation resilience. The gas flow rate to each module would be a fraction of the total supply and so smaller bore piping could be used which pose a lower safety risk in the event of fuel leakage [318].

8.2 4-Cell Stack CAD

The primary manifold design specification was cell spacing, which was governed by a trade-off between the minimal spacing required for current collector wiring and logistics, the requirement for stack compactness and allowing sufficient spacing for a homogenous oxidant supply. Based on wiring experience, it was deemed that the minimum distance between the outer cell wall of adjacent cells was 6 mm. The spacing gave clearance between the wires of adjacent cells to avoid short circuiting. A two-piece manifold design consisting of a gas pipe side piece and a fuel cell side piece is seen in Figure 8.1. This two-piece design was chosen to allow for a mesh insert to be placed inside the manifold which could be used to mix the fuel before entering the cell to promote a homogenous distribution, but also for use as a support for a catalyst for pre-reforming on the inlet side and for combustion on the outlet side. Given that each cell in a 4-cell module had good oxidant access to the majority of its surface and was not surrounded by other cells, the spacing was set at 6 mm to keep the stack volume low. The two manifold pieces were threaded to allow them to be screwed together. The manifolds for the inlet side and outlet side were identical for manufacturing and assembly simplicity. To secure the cells in place and ensure minimal gas leakage, a 'cap' design, highlighted as a successful design from the literature was utilised [255,256,261]. Each cell would be positioned into a seat which would hold the cells in place. The seat was designed to have a low tolerance to the outer diameter of the cell, leaving a small sub-millimetre gap for glass sealant, which would provide hermeticity as well as securing the cell mechanically. To further minimise the potential for leakage, an injector protrusion was used to flow reactants and products past the cell-manifold joint in the inlet and outlet designs, respectively. A sub-millimetre recess was made in the fuel cell side piece to allow for the mesh distribution/catalyst support insert. The gas pipe piece featured a venturi design to promote mixing, arising from a velocity change resulting from an increased area from the fuel inlet injector pipe into the gas pipe piece. The fuel was then constricted in another venturi, accelerating the fuel into the injector hole. The annotated design including the geometry measurements is seen in Figure 8.1. The inlet and outlet manifold and the fuel cells for the 4-cell stack design are seen in Figure 8.2.

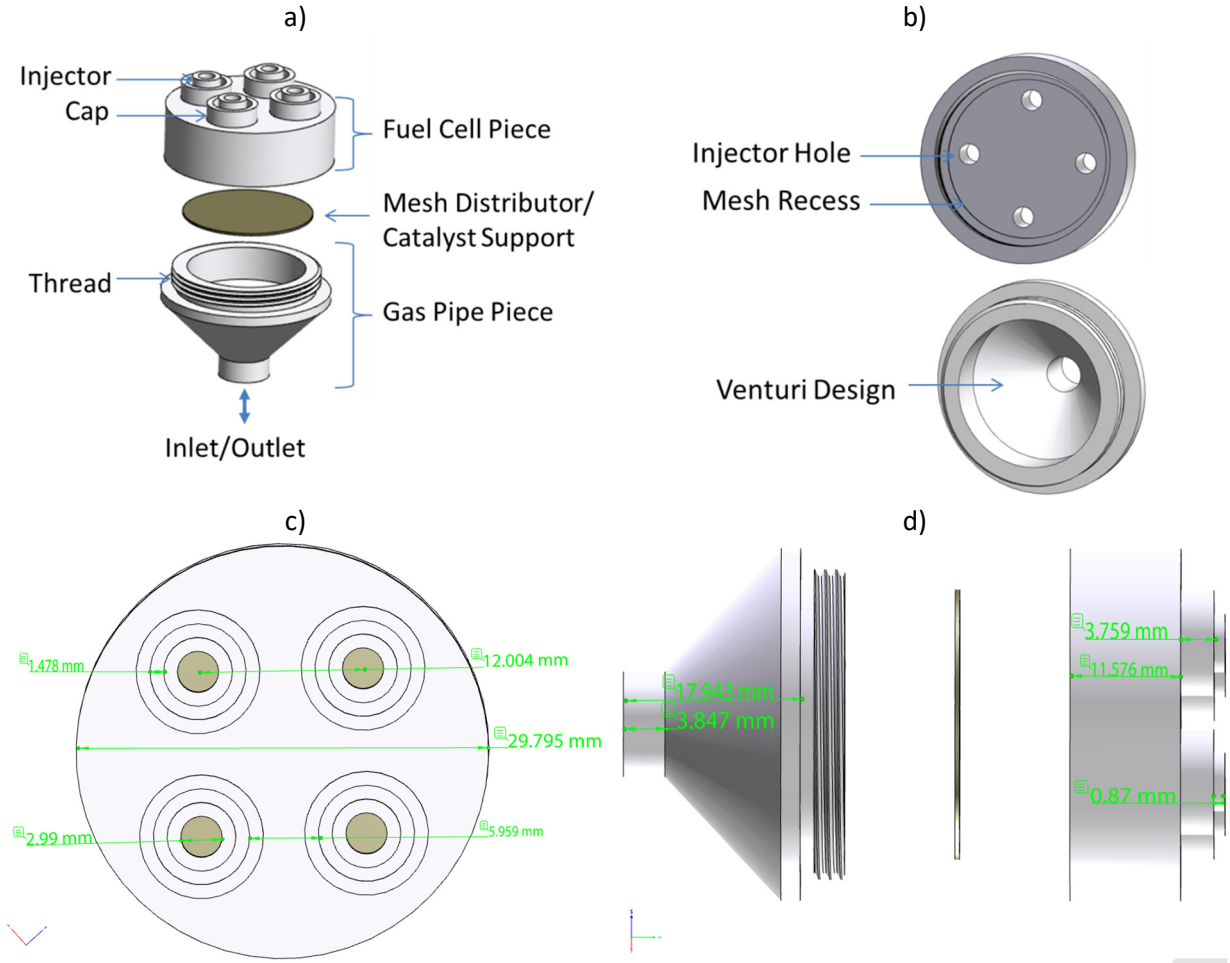

Figure 8.1 - 4-cell manifold CAD view in a) annotated exploded view, b) annotated inside view, c) fuel cell piece top view with measurement, d) exploded side view with measurement.

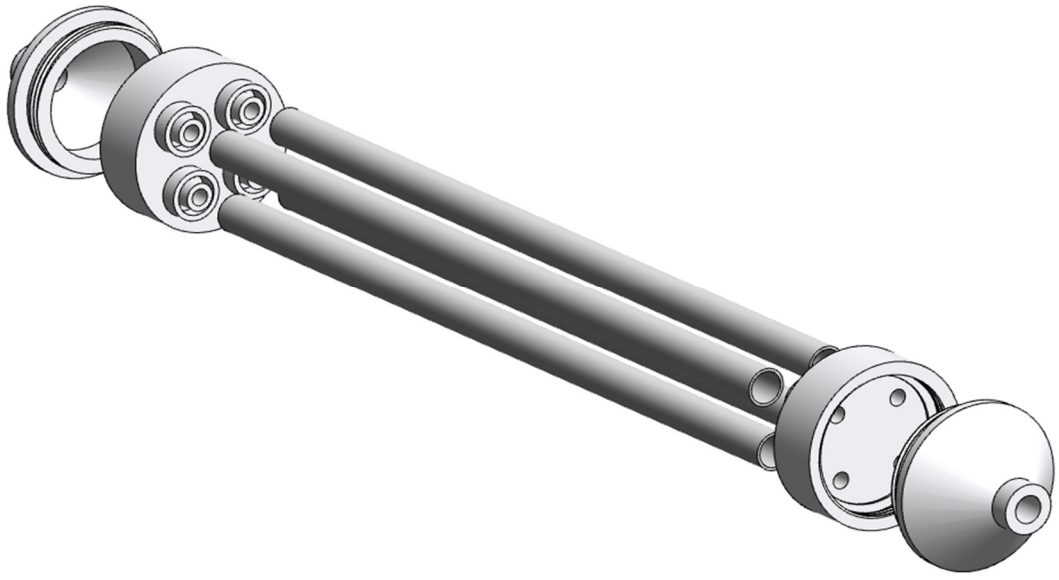

Figure 8.2 – 4-cell module CAD design in exploded view.

8.3 COMSOL CFD Model

The CAD design was then imported into COMSOL. The threads were omitted to avoid complexity with mesh generation. The mesh distributor was omitted from the design to determine the characteristics of the manifold design before any modification. The two-piece manifold was modelled as a single piece. The CFD model solved for the conservation of momentum within the manifolds and fuel cells. No heat transfer, mass transfer or electrochemistry was considered in this model iteration meaning that no fuel would be consumed or reactants produced. Therefore, the model has as limited validity and simply represents the distribution of fluid through the manifolds and fuel cells at room temperature.

8.3.1 4-Cell Stack Model Geometry and Mesh

The imported geometry was then meshed using the standard optimised COMSOL generated mesh. The geometry and the meshed geometry with the mesh quality measured by skewness are seen in Figure 8.3 a) and b), respectively. The mesh had 2.14×10^6 elements with mesh quality measured by skewness of 0.80, sufficient for a mesh independent description of the conservation of momentum and energy [198].

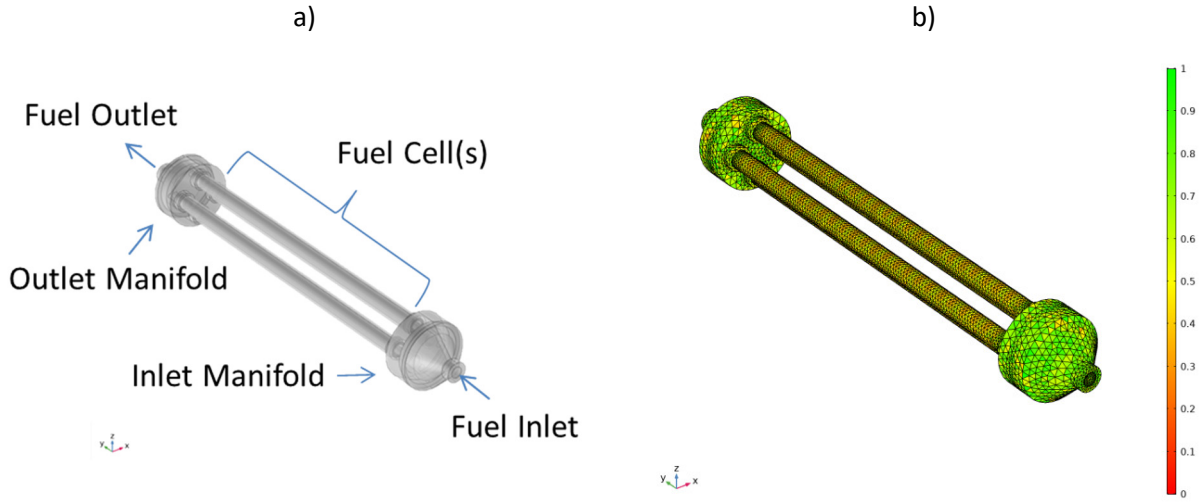

Figure 8.3 – 4-Cell COMSOL stack a) annotated geometry, b) mesh quality.

8.3.2 Model Parameters

Hydrogen was supplied to the stack inlet manifold at four times the standard flow rate at 800 ml.min^{-1}. If the manifold was successful in delivering an equal amount of fuel to each cell, this would closely represent the cell tests at the standard flow of 200 ml.min^{-1} H_2 (defined in Section 5.1) permitting a direct comparison and a feedback loop between the model and the empirical study data. Nitrogen was not supplied to the stack. This flow rate was used in the following electrochemical stack testing seen in Section 8.6. The fuel was supplied at 25°C and atmospheric pressure.

8.3.3 Boundary Conditions

To solve the partial differential equations (PDE), initial conditions and/or boundary conditions had to be defined, constraints to which the solutions to the equations had to adhere, for a 1st order PDE, one boundary condition had to be defined and for a 2nd order PDE two had to be defined.

- **Boundary condition at the inlet**

At the inlet to the inlet manifold, the inlet volumetric flow rate at room temperature and pressure (R.T.P) was defined:

$$Q = Q_{in} \quad \textbf{(147)}$$

- **Boundary condition at the walls**

The no-slip boundary condition was applied at the walls. This no-slip condition meant that at the boundaries defined, the fluid velocity was equal to that of the boundary velocity, which for a fixed wall is zero:

$$u = 0 \quad \textbf{(148)}$$

- **Boundary condition at the outlet**

The outlet momentum boundary condition at the outlet of the outlet manifold was prescribed by pressure:

$$p = p_0 = p_{atm} \quad \textbf{(149)}$$

where the pressure was the ambient atmospheric pressure.

8.3.4 Velocity and Pressure

The fuel velocity distribution within the inlet manifold, cells and outlet manifold is seen in Figure 8.4 a). The axes on the plot are the geometric distance measured in metres. The colour scale is the velocity measured in $m.s^{-1}$. A zoomed 2D slice within the inlet manifold is seen in b) and a zoomed 2D slice of the injector pipe is seen in c). As seen in a), the peak stack velocity is at the inlet to the inlet manifold and the outlet of the outlet manifold given that the entire flow is constricted into a single small inlet and outlet with a small cross-sectional area. As seen in b), the fuel decelerates from the inlet to the inlet manifold as a result of the manifold venturi where the cross-sectional area increases, reaching a homogenous velocity in the x-z plane near the injector inlet at approximately 0.25 $m.s^{-1}$. The fuel is then accelerated in another venturi within the injector pipe of the fuel piece of the manifold given the decrease in cross-sectional area, as seen in c). The peak velocity within the injector is approximately 0.7 $m.s^{-1}$.

As can be seen from Figure 8.5, the manifold design successfully distributed the single fuel inlet equally into each fuel cell injector. The velocity was highest in the centre of the free stream at the centre of the tube, decreasing radially outwards until the no-slip condition of zero velocity at the wall was met.

The findings from the velocity distribution were confirmed when looking at the pressure distribution, which is intimately linked, seen in Figure 8.6. The scale is the fluid pressure in Pa. The fluid pressure within each cell was the same at around 1.8 Pa. The differential pressure across the stack was very low at just over 2 Pa.

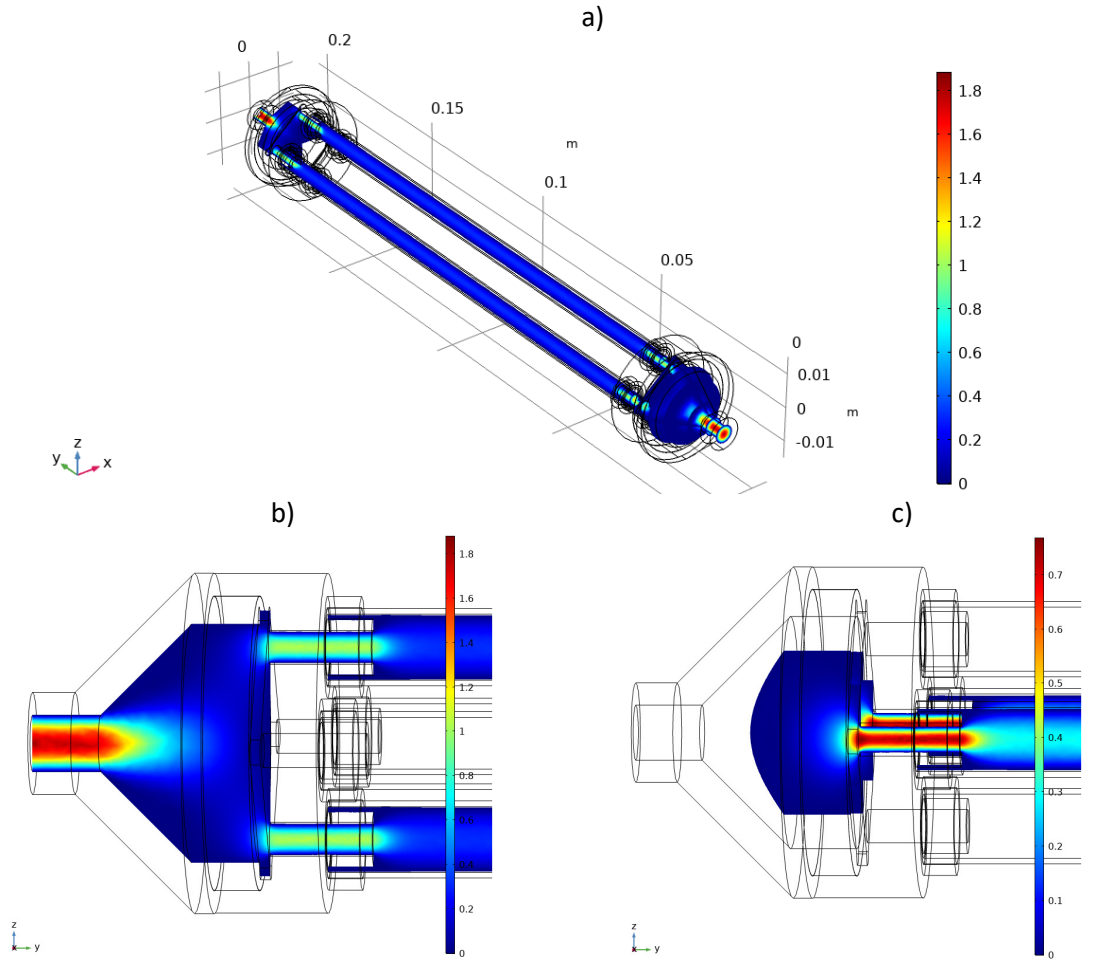

Figure 8.4 - Velocity distribution in the 4-Cell stack a) entire geometry, b) y-z slice at the inlet manifold venturi, c) y-z slice at the injector pipe.

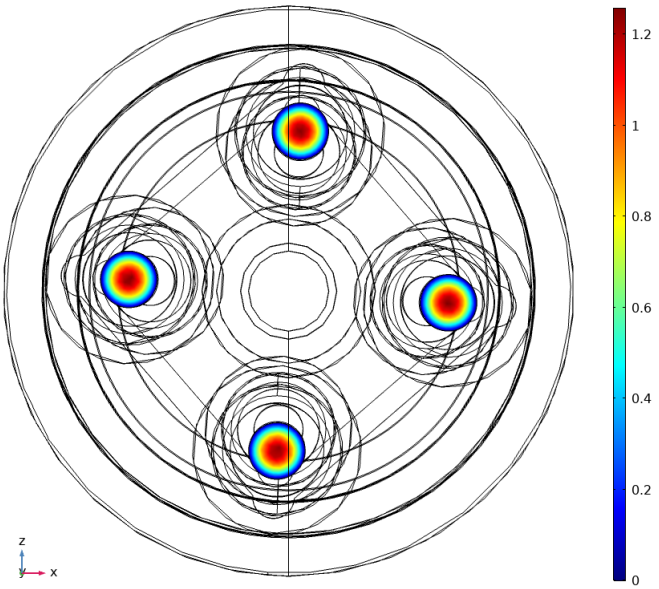

Figure 8.5 - Velocity distribution in the injector, x-z slice.

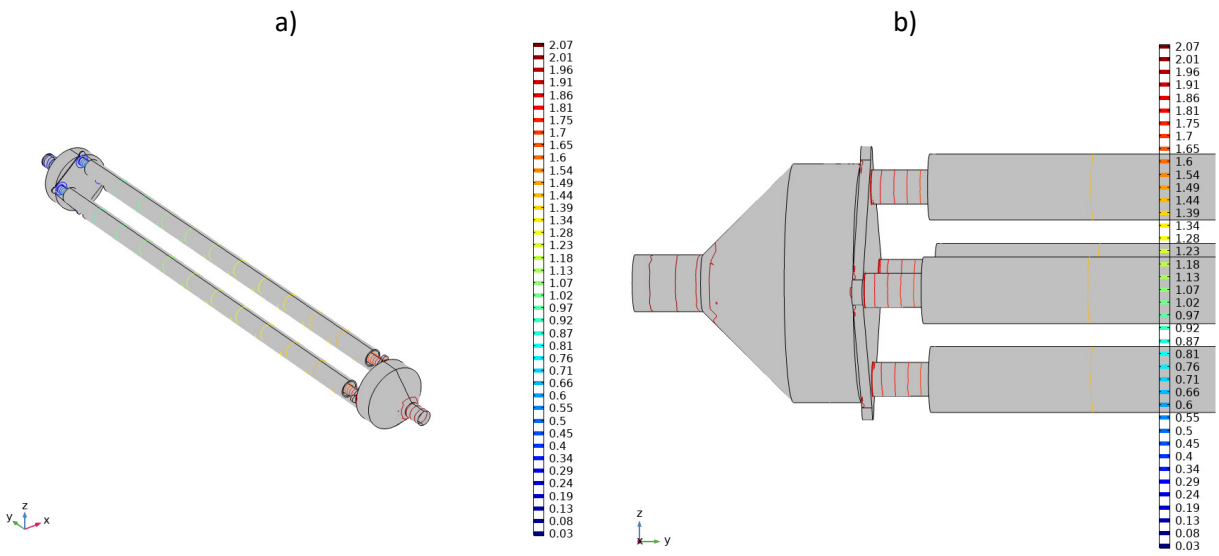

Figure 8.6 - Pressure distribution in a) the 4-cell stack, b) zoom on the inlet manifold.

8.4 4-Cell Stack and Canister CFD

To model the gas flow around the cells and receive a better representation of the real temperature profiles throughout the stack, a canister was added. The canister was required in the model as a domain for the air flow. Pre-heated air, flowing inside the canister closely represented the operation of a typical portable SOFC stack design [274]. Some insight was later to be gained for the operation of the stack in the furnace tested in this study. The CFD models were solved for the conservation of momentum as in the previous iteration, here extended to also solve for the conservation of energy. The model omitted radiative heat transfer physics for simplicity. This was further justified given that the cells were not shielded by other cells in an outer layer for example. A large portion of the exterior of the cells was covered in silver which has very low emissivity, meaning a significant rejection of radiation from the furnace to the cells [319]. The cells had good access to airflow and would see a significant contribution from convective heat transfer to the overall heat transfer mechanism. The fuel cells were modelled as a constant heat source meaning that no fuel was consumed or products. As a result, the model fuel stream would differ from a real stack with respect to composition, species concentration, and fluid properties such as density and viscosity. This limits the validity of the model somewhat. If no heat source were to be considered, the model would closely represent the fuel cell stack operating at OCV where no fuel was being consumed. However, this condition is not useful for capturing the peak stack temperatures that would occur during operation and the subsequent ascertaining of cooling requirements.

8.4.1 Model Geometry and Mesh

The tubular canister was 40 mm in diameter and 200 mm in length giving a total volume of 251 cm^2. The canister was sized encapsulate the entire stack, to provide a sufficient volume of air for electrochemical reactions and cooling, while minimising the stack volume and thus increasing the volumetric power density of the design. Depending on the boundary conditions, the design allowed for co-flow or counter-flow configurations of the air and fuel. The schematic of a co-flow orientation seen in Figure 8.7 a) has a single inlet and a single outlet at the front and rear of the canister. The mesh and mesh quality is seen in b) with the axes being geometric distance measured in metres and the colour scale measuring skewness (dimensionless). The mesh had 4.7x10^6 elements and skewness of 0.75.

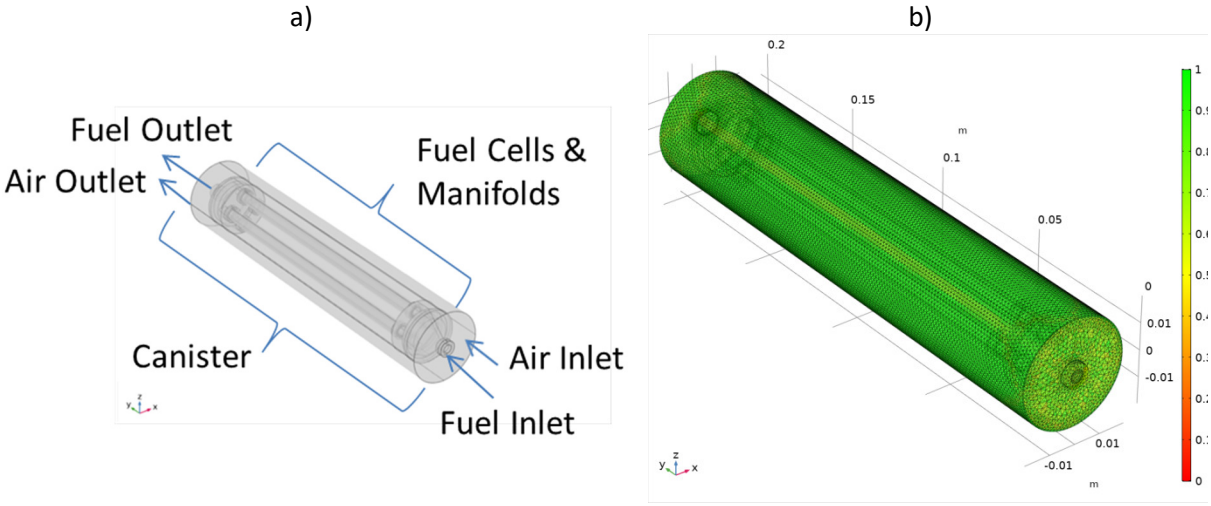

Figure 8.7 – 4-cell stack with canister co-flow configuration a) schematic, b) mesh quality measured in skewness.

8.4.2 Model Parameters

The heat source was estimated from the polarisation plot of the single cell with BNi-2 brazed hiTRAN seen in Figure 7.19. Therefore, the peak current density recorded at the lowest voltage vertex of 0.4 V was chosen for the estimation of the heat produced. The thermal management could be 'sized' around the most extreme operating condition. The heat was estimated by multiplying the overpotential (0.7 V) by the peak current density (0.36 $A.cm^{-2}$) and by the active area (20 cm^2) to obtain 5 W of heat per cell and 20 W per stack.

The air requirement for the stack at 100% utilisation was determined using Faraday's equation applied to oxygen where n=4:

$$n_{O_2} = \frac{i * A}{nF} = \frac{0.36 * 20}{4 * 96485} = 1.9x10^{-5}[mol.s^{-1}] \quad \textbf{(150)}$$

An oxygen molar flow rate value of $1.9x10^{-5}$ mol.s^{-1} corresponding to a mass flow rate of $5.97x10^{-4}$ g.s^{-1} and a volumetric flow rate at room temperature and pressure of 25 ml.min^{-1}. In typical stack operation, air was fed to the cathode rather than pure oxygen and it was estimated that the air flow rate required was 120 ml.min^{-1}. In addition, for typical stack operation, the air not only provides oxidant but also acts as a heat transfer fluid for thermal management and therefore air is typically supplied in excess with cathode stoichiometry values, (λ_c), between 2 and 8 [22]. A λ_c value of 5 was chosen in this design resulting in an air flow rate of 360 ml.min^{-1} per cell and 2400 ml.min^{-1} for the stack. This was a sufficient flow of oxidant for current densities of up to 1.5 A.cm^{-2}.

8.4.3 Boundary Conditions

We must describe further boundary conditions to the new model configuration accounting for the additional fluid stream within the canister. Thermal boundary conditions were provided to solve for the conservation of energy.

- **Boundary conditions at the inlet**

At the entrance of the inlet manifold and the canister, the inlet volumetric flow rate at R.T.P was defined as:

$$Q = Q_{in} \quad \textbf{(151)}$$

The inlet temperature and pressure of the fluids at the inlet to the inlet manifold and canister were defined by equation (152) and (153), respectively.

$$T = T_{in} \quad \textbf{(152)} \qquad P = P_{in} \quad \textbf{(153)}$$

- **Boundary conditions at the walls**

The no-slip boundary condition was applied at the walls. This no-slip condition meant that at the boundaries defined, the fluid velocity was equal to that of the boundary velocity, which for a fixed wall is zero:

$$u = 0 \tag{154}$$

A thermal insulation was applied at the outer wall of the stack and to domains where the heat source or inlet and outlet boundary conditions had not been applied:

$$-n \cdot \boldsymbol{q} = 0 \tag{155}$$

- **Boundary conditions at the outlet**

The outlet momentum boundary condition at the model outlet manifold was prescribed by the pressure:

$$p = p_0 = p_{atm} \tag{156}$$

where the pressure is the ambient atmospheric pressure. The thermal outflow boundary condition was chosen as the outlet boundary condition for the conservation of energy:

$$-n \cdot \boldsymbol{q} = 0 \tag{157}$$

8.4.4 Velocity

The fuel inlet conditions were set to the same 800 ml.min^{-1} flow rate of H_2 as in the previous model iteration in Section 8.3.2. In this iteration, the fuel inlet temperature is at 650°C, replicating the stack at operating conditions utilising fuel pre-heating. The air at the air inlet entered at 2400 ml.min^{-1} at a temperature of 750°C, replicating the furnace set point in the previous empirical study of the single cells at the standard conditions. The air and hydrogen velocity volume plot with streamlines and x-z slice with streamlines at the inlet manifold is seen in Figure 8.8 a) and b), respectively. The axes are

the geometric distance measured in metres and the scale is the velocity in m.s^{-1}. The air can be seen in b) to be circulating around the outer wall of the fuel cells indicating that air was reaching the entire cathode surface of each cell. The relatively high difference in velocity between the air stream and fuel stream led to a difficult analysis from the colour scale.

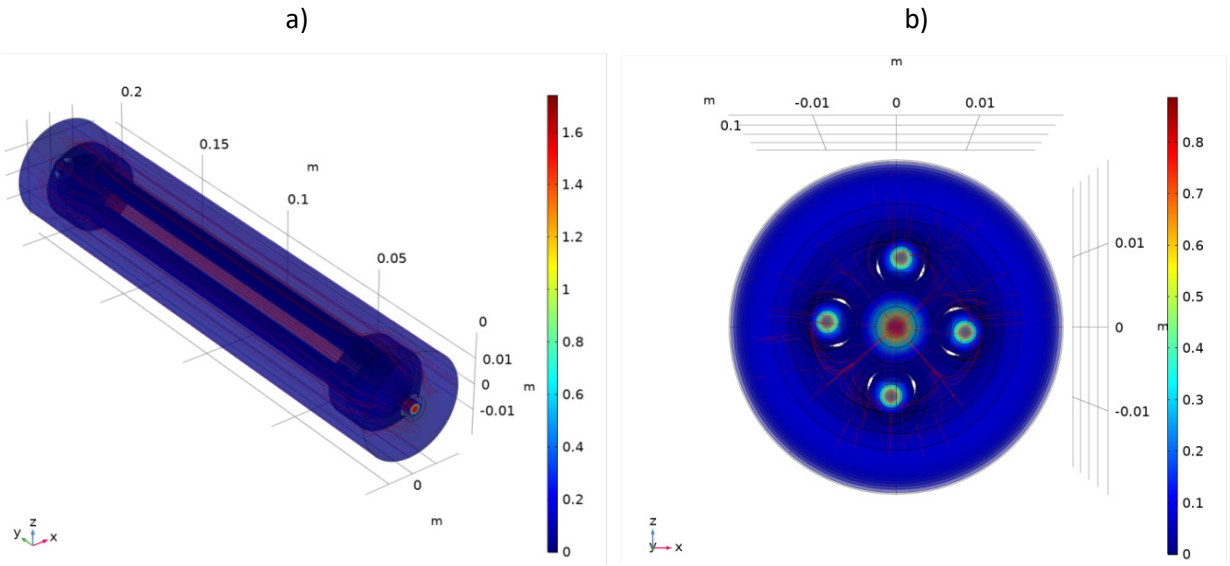

Figure 8.8 – 4-Cell stack with canister velocity a) volume plot with streamline, b) x-z slice with streamlines at the inlet canister and manifold inlet.

To deconstruct the scale, a velocity profile in the x-z plane at the inlet to the canister and inlet manifold was plotted as seen in Figure 8.9. The x-axis is the geometric distance along the centreline of the x-z plane, a horizontal line through 0,0 in Figure 8.8 b). The y-axis is the velocity magnitude in m.s^{-1}. The air within the canister had a peak air velocity of 0.06 m.s^{-1} at the inlet. The no-slip condition resulted in a zero velocity at the outer canister wall and the interface of the fluid and outer manifold wall. The low value in the laminar region would result in poor heat transfer. The hydrogen velocity which is the peak in Figure 8.9 was similar to that seen in Figure 8.4 and Figure 8.5 with a peak value of 1.6 m.s^{-1}.

A plot of stack velocity was then constructed with a velocity limit of 0.1 m.s^{-1} to better capture the air velocity within the canister and around the stack. The velocity within the stack and velocity streamline plot is seen in Figure 8.10 a) and b), respectively. The axes in a) are the geometric distance measured in metres and the colour scale is the velocity in m.s^{-1}. The air is pushed around the outer wall of the inlet manifold, causing an increase in radial velocity in the x-z plane. The streamlines straighten and become parallel indicating a constant velocity around the fuel cells between 0.06 m.s^{-1}

and 0.08 m.s^{-1}. To improve mixing around the cell which would improve heat and mass transfer, baffles could be placed at several intervals along the cell length to disrupt the flow, however, this design was never eventually trialled.

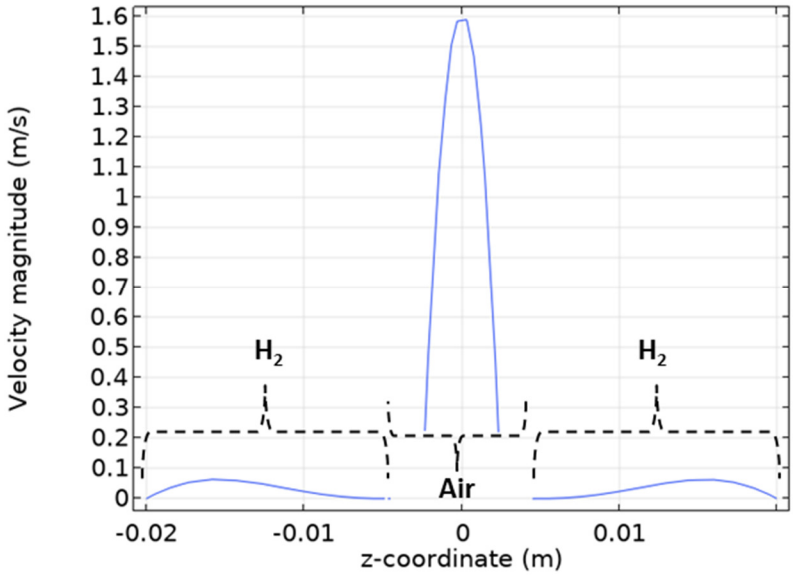

Figure 8.9 - 4-Cell stack including canister velocity profile in the x-z plane at the canister and manifold inlet.

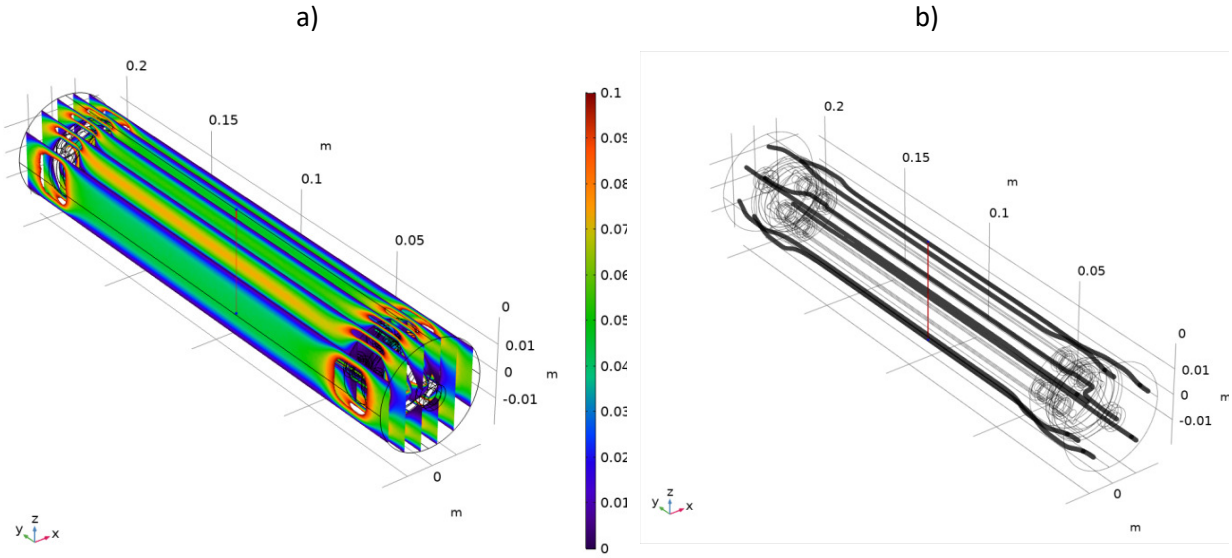

Figure 8.10 - 4-Cell stack canister a) velocity (values < 0.1 m.s^{-1}), b) velocity streamlines.

8.4.5 Temperature Distribution

The 4-cell stack and canister temperature in the co-flow configuration is seen for the entire stack and the cells in Figure 8.11 a) and b), respectively. The axes are the geometric distance measured in

metres and the scale is the temperature measured in °C. The peak temperature within the stack was 1007°C, resulting in a 350°C temperature across the stack. The peak temperature stack was located at the outlet region of the cells. The heat generated by the cells in addition to the influx of hot air at 750°C entering the canister heated the fuel and the stack. The stack temperature increased along the stack length in the y-direction as the heat generated by the cells heated the furnace air and the fuel. The minimum cell temperature was 751°C giving a temperature gradient across the cells of 256°C.

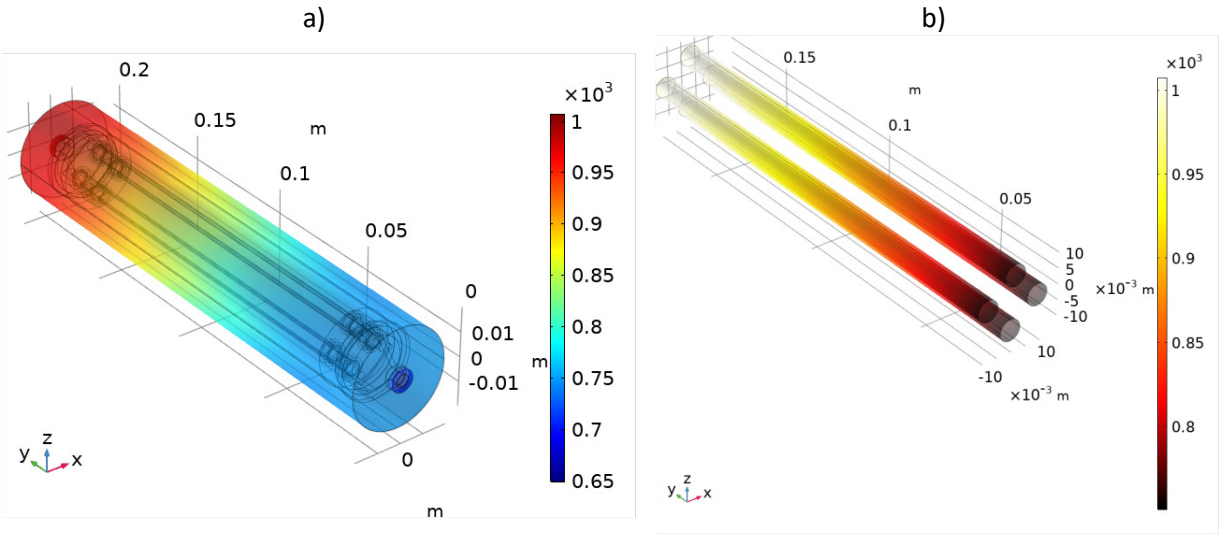

Figure 8.11 - 4-cell stack temperature co-flow a) entire stack, b) cells only.

The inlet and outlet manifold temperature can be seen in Figure 8.12. The fuel inlet manifold is seen at $y = 0$ on the LHS and the fuel outlet manifold on the RHS. The fuel inlet manifold is around 760°C while the fuel outlet manifold temperature is approximately 1003°C.

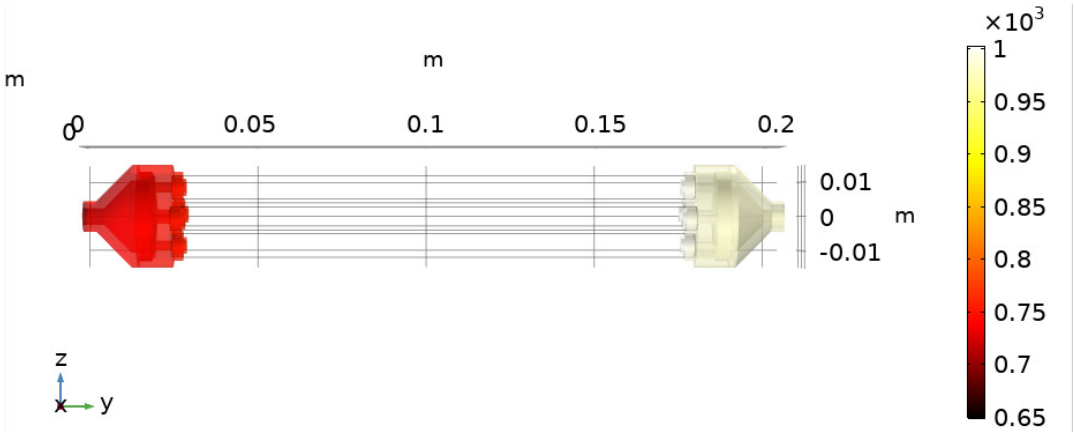

Figure 8.12 - 4-cell stack co-flow configuration manifold temperature (LHS inlet manifold, RHS outlet manifold).

The peak temperature of 1007°C was 46°C higher than the melting point of silver. This peak stack temperature would have led to the melting of the silver cathode current collector wires. This would cause short-circuiting and electrical failure of the stack leading to an emergency shutdown. If nickel was the sole current collector material then the current peak temperature would have been acceptable. The peak stack temperature was also within 53°C of the brazing temperature. This was too high given that the suggested operating temperature should be a minimum of 100°C (ideally 200°C) below the 1060°C brazing temperature. Melting of the BNi-2 braze would lead to separation of the nickel hiTRAN current collector from the anode, resulting in loss of contact and an increased cell ASR during operation. A parametric optimisation was required in order to reduce the peak stack temperature to a value suitable for safe operation. The aforementioned results are used as a baseline for comparison.

8.4.6 Parameter Optimisation

To lower the peak stack temperature to protect the silver wiring and brazed hiTRAN-anode joints, a parametric optimisation was required. The air inlet position, air inlet temperature and fuel inlet temperature were chosen as the key variables as these were parameters that could be easily controlled in real-world operation. Only one of these variables were changed at a time from the base case which had a co-flow arrangement, an air flow rate of 2400 $ml.min^{-1}$ and inlet temperature of 750°C, with a hydrogen flow rate of 800 $ml.min^{-1}$ and inlet temperature of 650°C. The cell power remained the same at 5 W per cell for each case.

For a stack with only nickel as the current collector material, the peak stack temperature was 960°C, set by the brazing requirement. However, for a stack that implements silver current collection, as used in this study at the cathode, the peak stack temperature was defined as 910°C. Set at a value 50°C below the melting point as a minimum safety limit. In an ideal case, the peak stack temperature would be nearer 800°C to avoid the loss of mechanical integrity of the silver being used as a wire. Sagging of the silver wire could lead to short-circuiting and an emergency stack shutdown. It was also important that the stack was not cooled so much that the cell temperatures were too low, resulting in poor electrochemical performance. The lowest cell temperature deemed acceptable was 650°C. Below this, direct internal reforming would not be possible narrowing the fuel selection to hydrogen only, unless a pre-reformer was used. A summary of the optimisation study results are tabulated in Table 8.1, found in Section 8.4.8.

Counter-flow Configuration

The position of the air inlet and air outlet was reversed to study the effects of a counter-flow configuration. All other parameters remained the same as the base case. The peak stack temperature was 16% higher than the co-flow case at 1163°C, 253°C above the maximum stack temperature. In contrast to the co-flow configuration, the peak stack and cell temperature occurred at the centre of the stack. The minimum cell temperature was 800°C and the peak cell temperature was 961°C, giving a 161°C temperature gradient across the cells. The global stack temperature difference was 513°C.

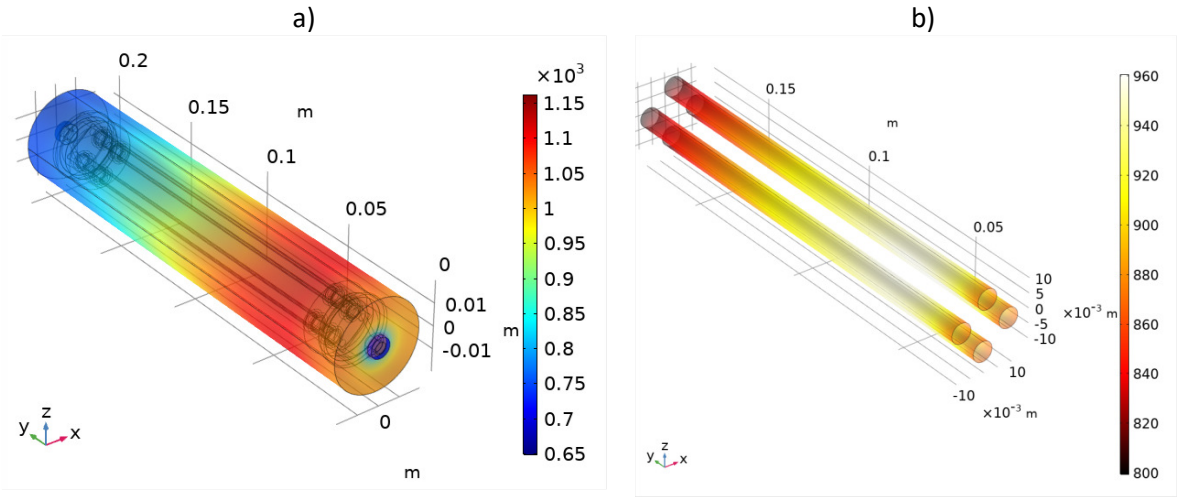

Figure 8.13 - 4-cell stack temperature with counter-flow configuration a) entire stack, b) cells only.

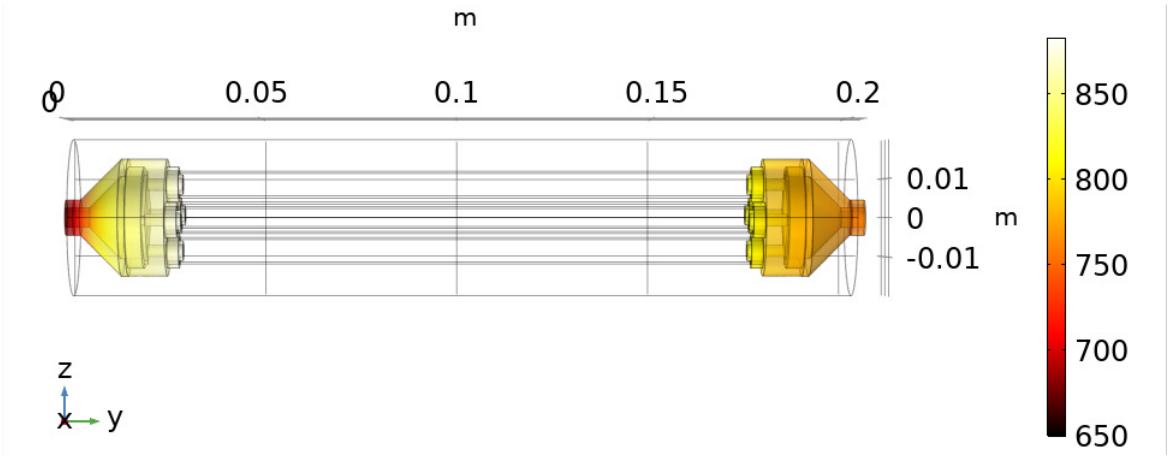

Figure 8.14 - 4-cell stack counter-flow configuration manifold temperature (LHS fuel inlet manifold, RHS fuel outlet manifold).

The fuel inlet and fuel outlet manifold temperature are seen in Figure 8.14. The fuel inlet manifold is seen at $y = 0$ on the LHS and the fuel outlet manifold on the RHS. The fuel inlet manifold temperature was at 880°C. Now with the air inlet now entering at the fuel outlet manifold side, the

fuel outlet manifold was at 760°C. Some 120°C cooler than the fuel inlet manifold, and 243°C cooler than the fuel outlet manifold in the co-flow case.

Fuel Inlet Temperature

The fuel inlet temperature was adjusted to accommodate for a system design without fuel pre-heating. The fuel inlet flow rate was kept the same as the base case but the temperature reduced from 650°C to 25°C. All other parameters remained the same as the base case. The stack temperature and cell temperature with a co-flow configuration and cold fuel inlet are seen in Figure 8.15 a) and b), respectively. The peak stack temperature was 925°C, located at the outlet region of the fuel cells, giving a total stack temperature gradient of 900°C. The inlet regions of the cells were at 630°C and the outlet region at 925°C giving a temperature gradient across the cell of 295°C. The peak stack temperature was reduced by 82°C compared to the base case and was 15°C above the peak stack temperature design specification. A peak stack temperature of within 36°C of the silver melting point could be deemed acceptable given that the heat estimation was for a worst-case-scenario at peak current density and the stack would rarely operate at these conditions for an extended period, if at all. A fuel cell stack is sized accordingly to allow for the typical power demand to be satisfied with the cells operating at 0.7 V and above where fuel cell efficiency is higher.

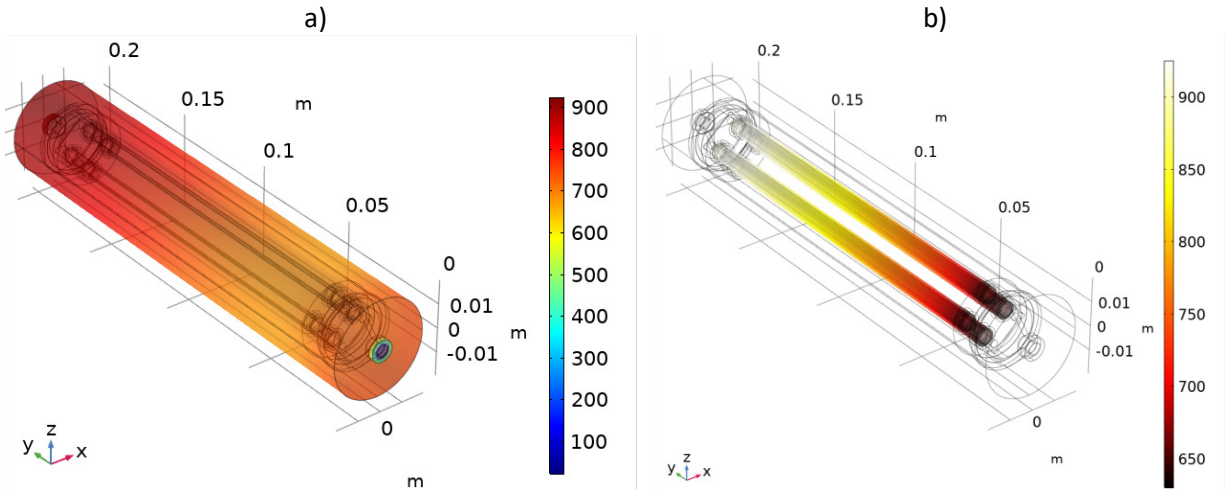

Figure 8.15 - 4-cell stack temperature with a cold fuel inlet a) entire stack, b) cells only.

The fuel inlet and fuel outlet manifold temperature are seen in Figure 8.16. The fuel inlet manifold is seen at $y = 0$ on the LHS and the fuel outlet manifold on the RHS. The fuel inlet manifold was at approximately 720°C while the fuel outlet manifold was at 910°C. The fuel outlet manifold

temperature was reduced by 93°C compared to the base co-flow case. This design was a cost-effective way to reduce the stack temperature that also reduced system complexity. However, if the stack design featured an external fuel pre-reformer, the fuel would need to be cooled.

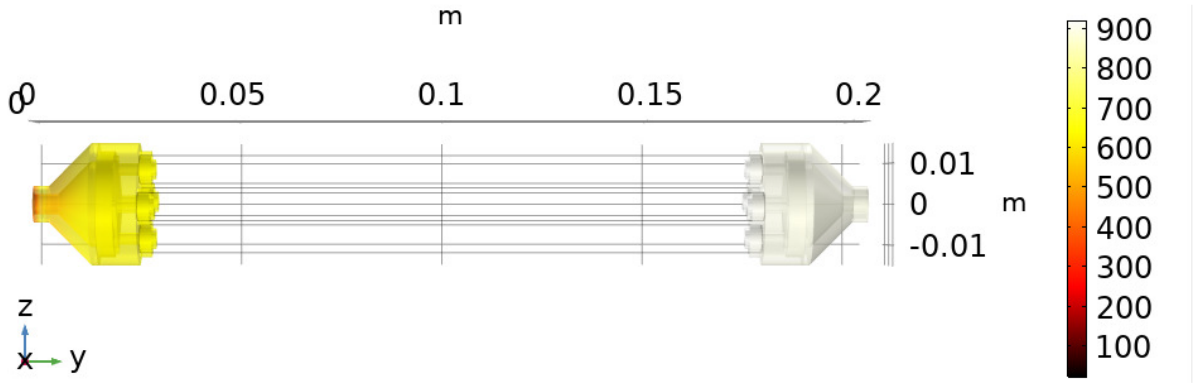

Figure 8.16 - 4-cell stack manifold temperature with a cold fuel inlet.

Air Inlet Temperature

The air inlet temperature was reduced by 50°C versus the base case to 700°C in the co-flow configuration. All other parameters remained the same as the base case. The stack temperature and cell temperature are seen in Figure 8.17 a) and b), respectively. The peak stack temperature was 967°C, located at the outlet region of the cells. The cell temperature at the inlet of the fuel cells was 709°C giving a cell temperature difference of 258°C. The global stack temperature difference was 317°C.

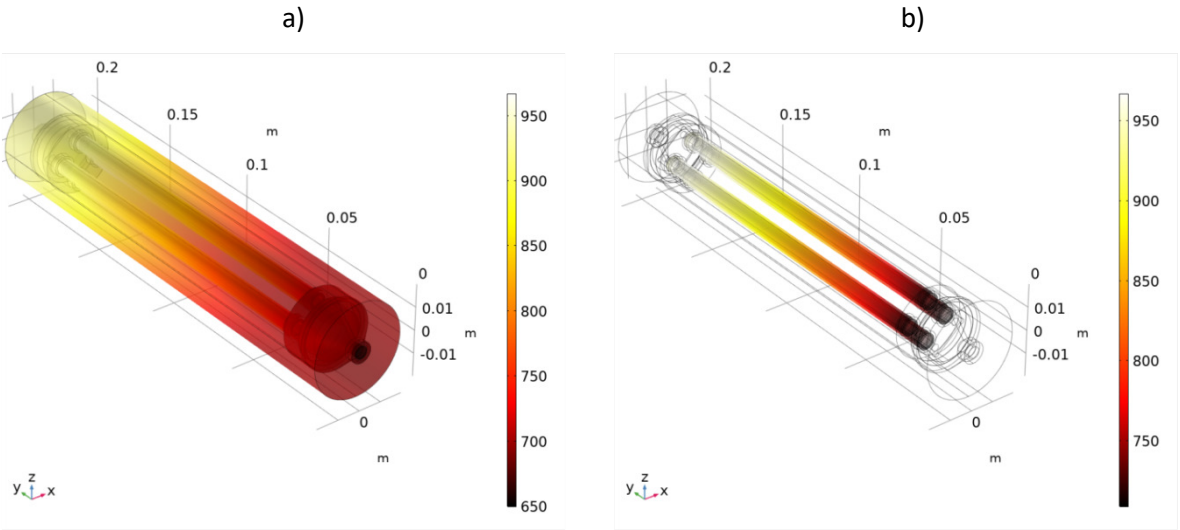

Figure 8.17 - 4-cell stack temperature with an air inlet temperature of 700°C a) entire stack, b) cells only.

The fuel inlet and fuel outlet manifold temperature are seen in Figure 8.18. The fuel inlet manifold is seen at $y = 0$ on the LHS and the fuel outlet manifold on the RHS. The fuel inlet manifold was at approximately 700°C while the fuel outlet manifold was at 950°C. The fuel inlet and outlet manifold temperatures were reduced by 60°C and 53°C, respectively, compared to the base co-flow case. The peak stack temperature was reduced by 40°C versus the base case but was still 7°C higher than the lower temperature limit set with respect to the braze (960°C) limit and 57°C above the defined peak stack temperature of 910°C.

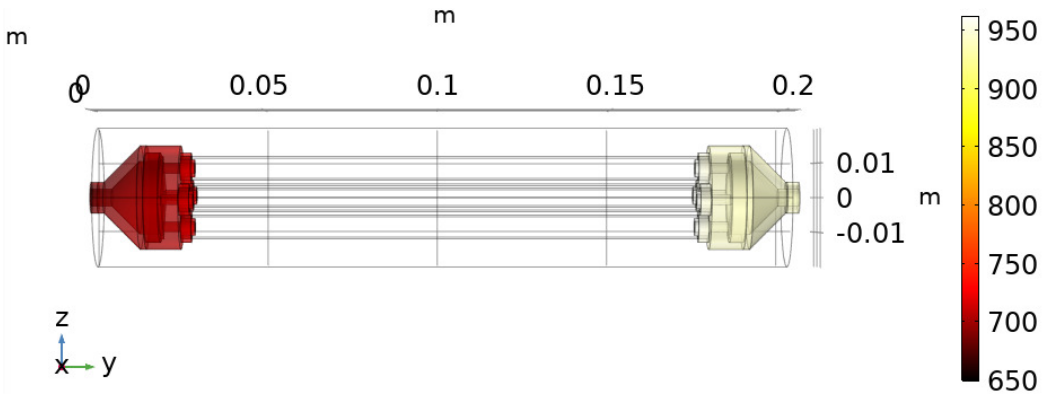

Figure 8.18 - 4-cell stack manifold temperature an air inlet temperature of 700°C.

The air inlet temperature was reduced by a further 50°C, 100°C lower than the base case now at 650°C with the co-flow configuration. The stack temperature and cell temperature are seen in Figure 8.19 a) and b), respectively. The peak stack temperature was 926°C, located at the outlet region of the cell. The cell temperature at the inlet was 668°C giving a cell temperature difference of 258°C. The global stack temperature difference was 276°C. The peak stack temperature was reduced by 81°C versus the base case and was 926°C. This was 34°C lower than the less stringent brazing temperature limit but 16°C above the defined allowable peak temperature, given that it was only 35°C lower than the melting point of silver. This design could be used for a stack using nickel as the sole current collector material. This stack design could also be considered to be successful for a stack with silver if operation at peak current density was limited.

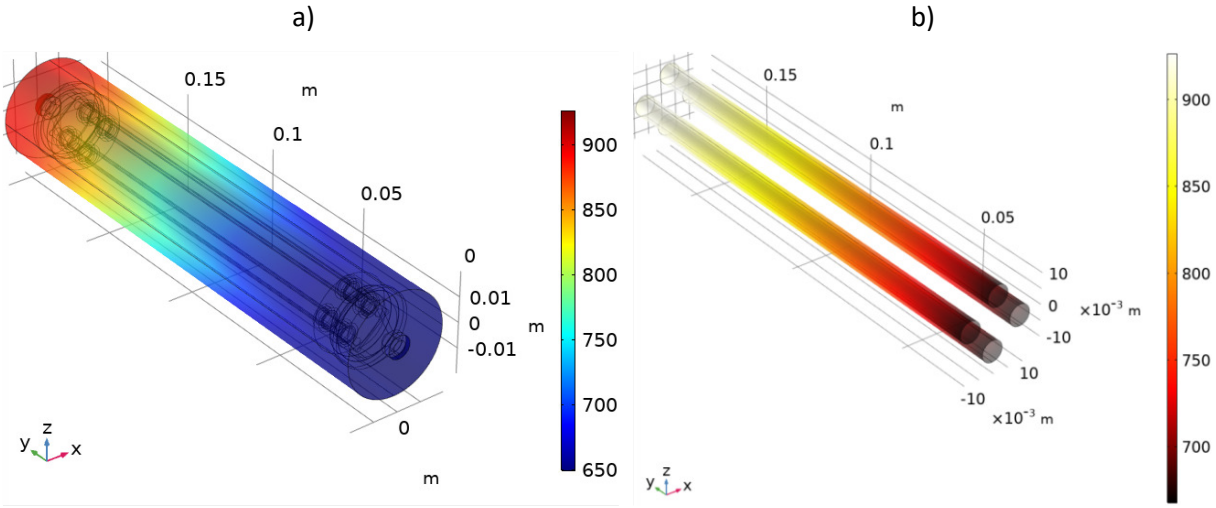

Figure 8.19 - 4-cell stack temperature with an air inlet temperature of 650°C a) entire stack, b) cells only.

The inlet and outlet fuel manifold temperature are seen in Figure 8.20. The fuel inlet manifold was at a temperature of approximately 660°C and the fuel outlet manifold was at approximately 920°C. The fuel inlet and outlet manifold temperatures were reduced by 100°C and 83°C, respectively, compared to the base co-flow case.

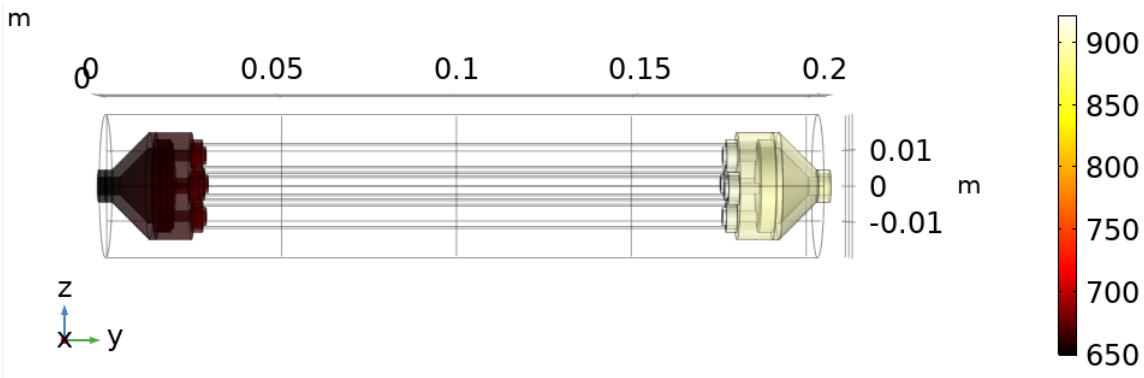

Figure 8.20 - 4-cell stack manifold temperature with an air inlet temperature of 650°C.

The air inlet temperature dropped by a further 50°C, 150°C lower than the base case now at a temperature of 600°C. The stack temperature and cell temperature is seen in Figure 8.21 a) and b), respectively. The peak stack temperature was 886°C located at the outlet of the cells. The minimum stack temperature of 600°C resulted in a global stack temperature difference of 286°C. The minimum cell temperature was 627°C giving a cell temperature gradient of 259°C. The peak stack temperature was 74°C below the brazing controlled temperature limit and 24°C below the defined maximum allowable peak temperature. While the lowest cell temperature was 627°C, the average fuel cell temperate was well above the 650°C lower limit and this design was deemed successful. Internal

reforming would only be possible after the 20 mm of the cell when cell temperatures surpass 650°C. The manifold temperatures are seen in Figure 8.22. The fuel inlet manifold was at 630°C and the fuel outlet manifold was at 881°C.

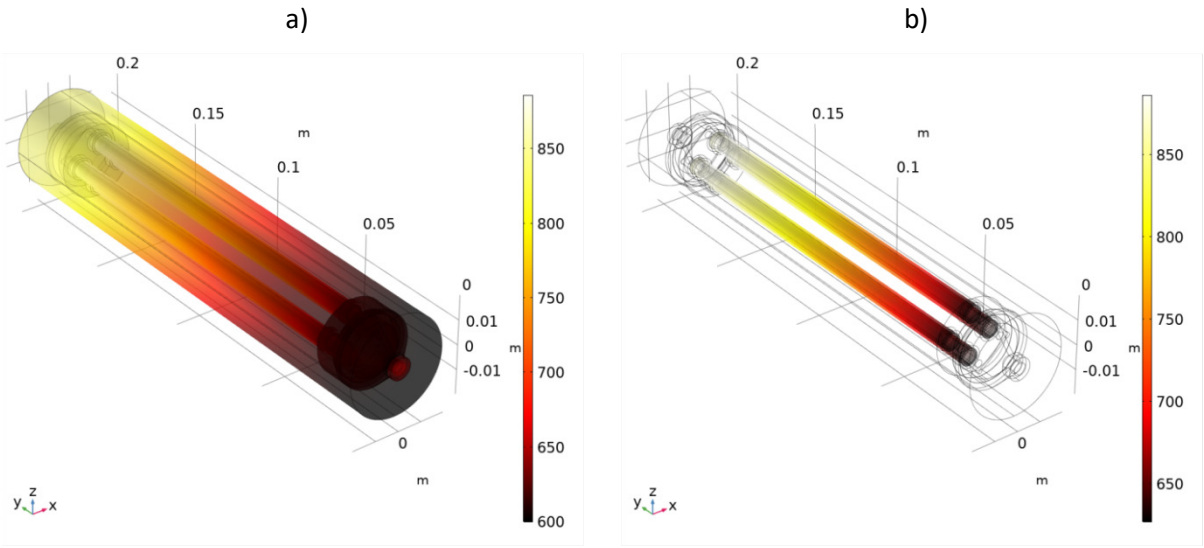

Figure 8.21 - 4-cell stack temperature with an air inlet temperature of 600°C a) entire stack, b) cells only.

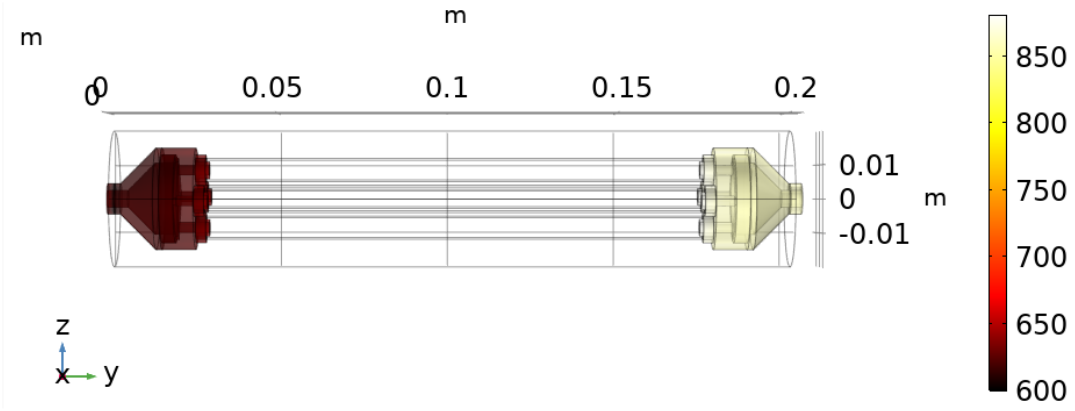

Figure 8.22 - 4-cell stack manifold temperature with an air inlet temperature of 600°C.

The air inlet temperature dropped by a further 50°C, 200°C lower than the base case now at 550°C. The stack temperature and cell temperature are seen in Figure 8.23 a) and b), respectively. The peak stack temperature was 846°C located at the outlet of the fuel cells. The minimum stack temperature of 550°C resulted in a global stack temperature difference of 296°C. The minimum cell temperature was 586°C giving a cell temperature gradient of 259°C. At this temperature, the inlet region of the cell would remain operational but performance significantly reduced. Internal reforming would be

unviable for these operating parameters. The peak stack temperature was 64°C below the maximum allowable temperature.

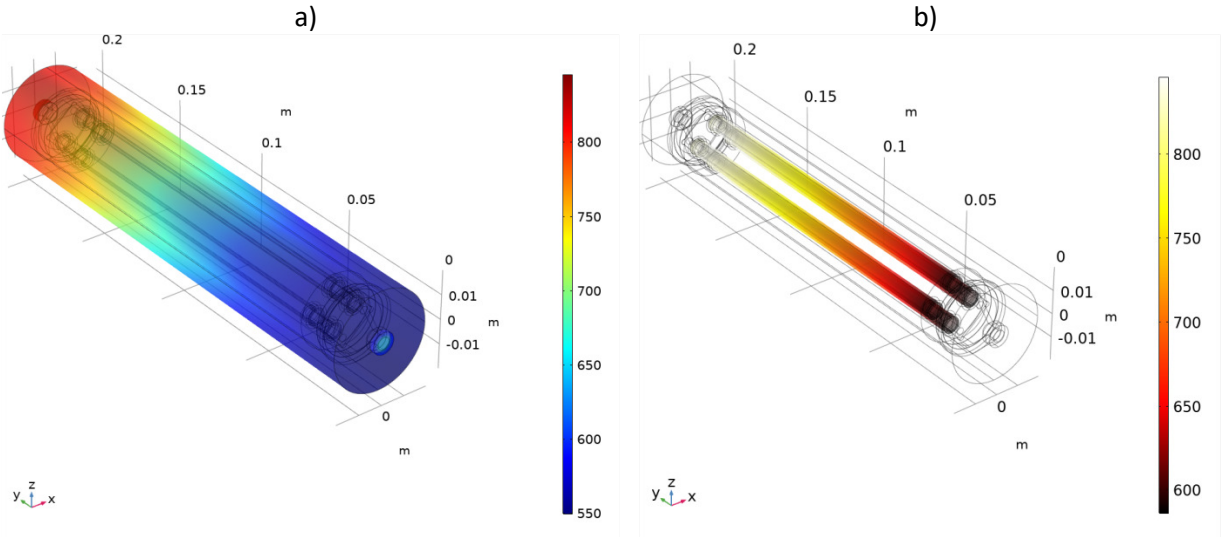

Figure 8.23 - 4-cell stack temperature with an air inlet temperature of 550°C a) entire stack, b) cells only.

The manifold temperatures are seen in Figure 8.24. The fuel inlet manifold was at 570°C and the fuel outlet manifold was at 841°C. This design was deemed as just acceptable and seen as the lower limit for the air inlet temperature for this configuration.

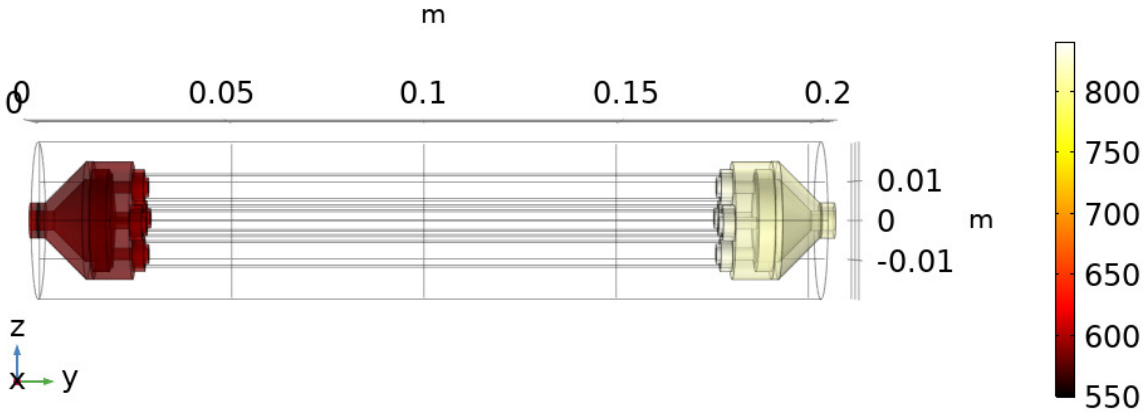

Figure 8.24 - 4-cell stack manifold temperature with an air inlet temperature of 550°C.

Air Utilisation λ_c

The air utilisation in the base case was determined by cathode oxygen utilisation. A λ_c value of 5 was used. While this value was towards the upper end of the typical excess flow used, the value was increased to study the effects on the temperature within the stack.

λ_c was increased to 6, giving a total air inlet volumetric flow rate of 2880 ml.min^{-1}. All other parameters remained the same as the base case. The temperature distribution in the entire stack and only in the cells is seen in Figure 8.25 a) and b), respectively. The peak stack temperature was 989°C, located at the outlet of the cells, 76°C above the maximum allowable temperature. The minimum cell temperature was 751°C giving a cell temperature gradient of 230°C. The global stack temperature gradient was 388°C. The manifold temperatures are seen in Figure 8.26. The inlet manifold had a temperature of 740°C and the outlet manifold had a temperature of 970°C.

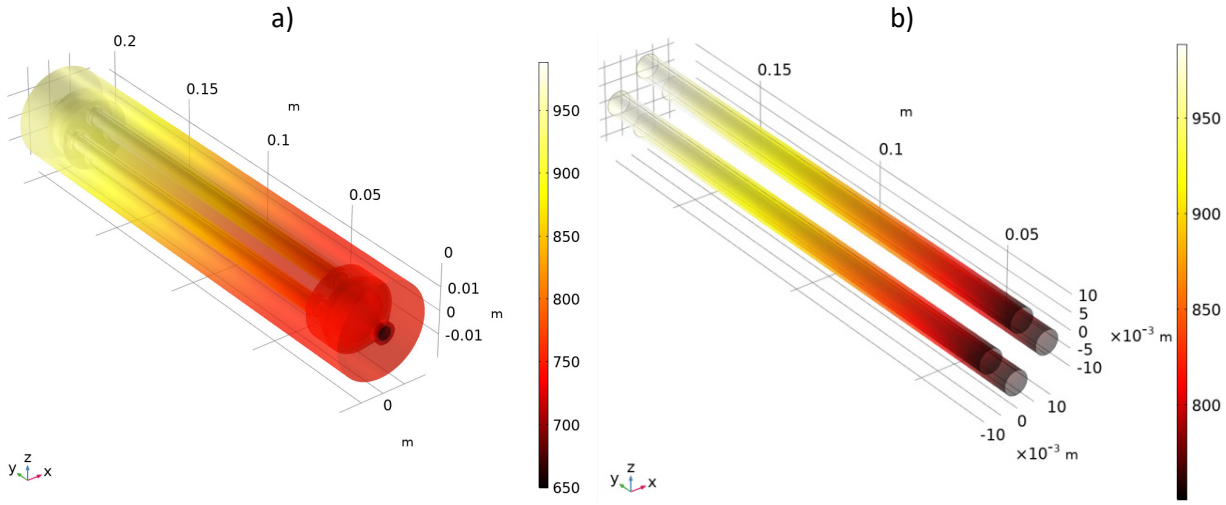

Figure 8.25 - 4-cell stack temperature with co-flow configuration and a λ_c value of 6 in the a) entire stack, b) cells only.

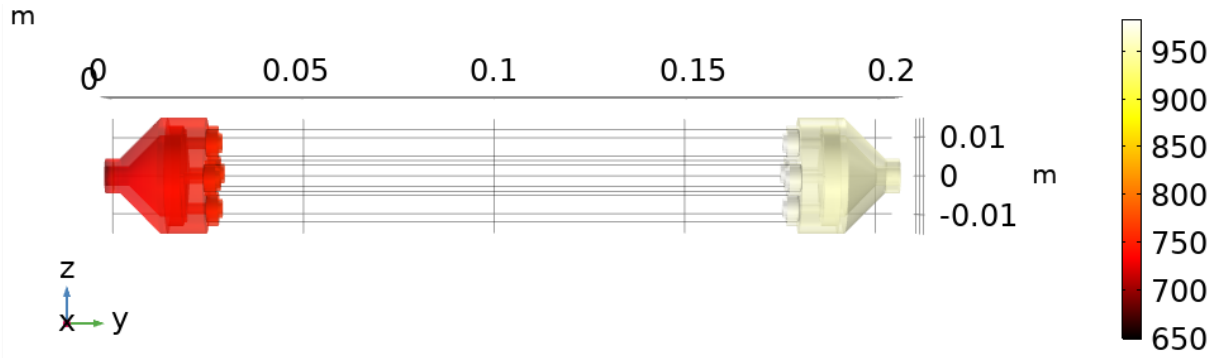

Figure 8.26 - 4-cell stack manifold temperature with co-flow configuration and a λc value of 6.

λ_c was increased to 7, giving a total air inlet volumetric flow rate of 3360 ml.min^{-1}. The temperature distribution in the entire stack and only in the cells is seen in Figure 8.27 a) and b), respectively. The peak stack temperature was 970°C, located at the outlet of the cells, 60°C above the limit for safe operation. The minimum cell temperature was 751°C giving a cell temperature gradient of 220°C. The

global stack temperature gradient was 320°C. The manifold temperatures are seen in Figure 8.28. The inlet manifold had a temperature of 761°C and the outlet manifold had a temperature of 964°C.

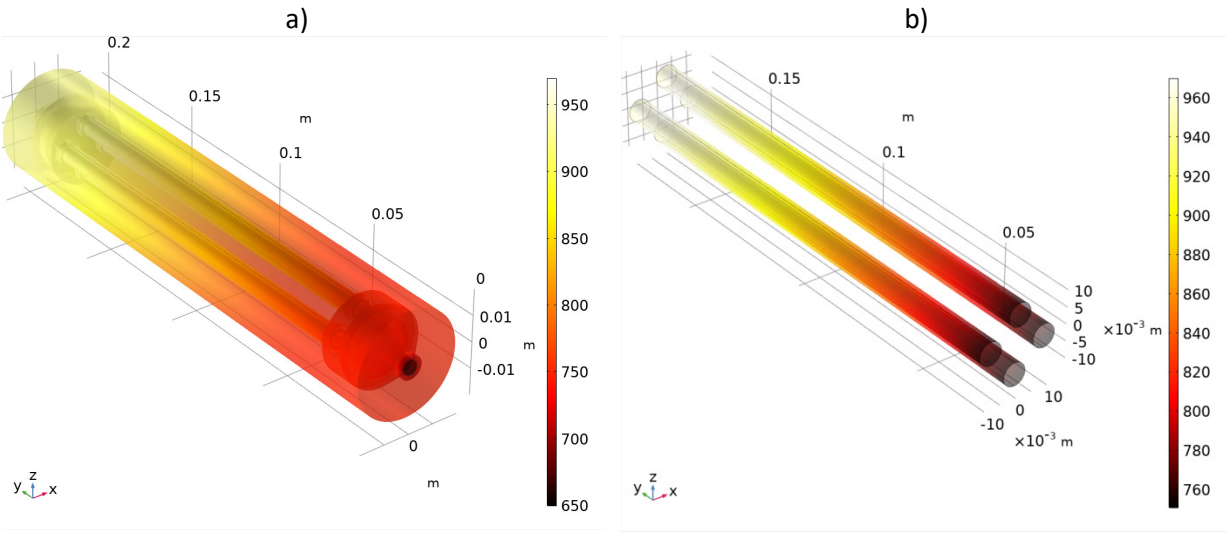

Figure 8.27 - 4-cell stack temperature with co-flow configuration and a λc value of 7 in the a) entire stack, b) cells only.

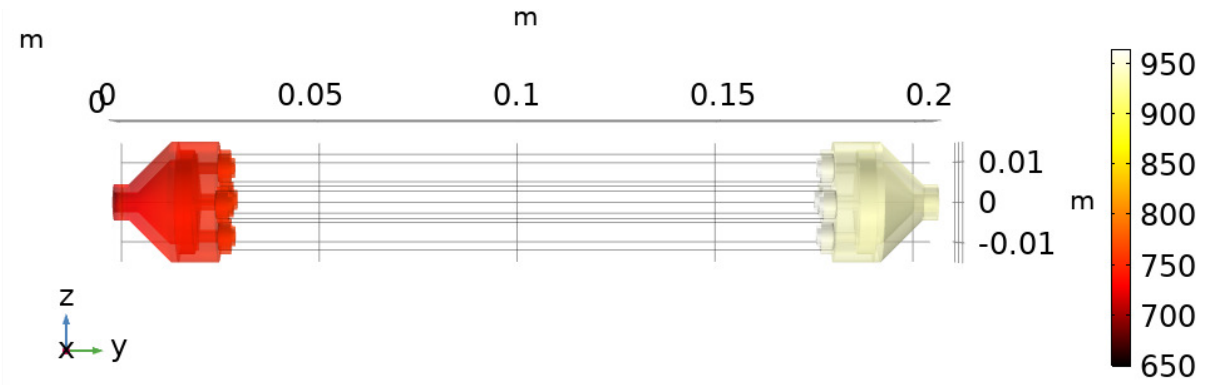

Figure 8.28- 4-cell stack manifold temperature with co-flow configuration and a λc value of 7.

8.4.7 Geometry Optimisation

The canister geometry was modified with canister slits to allow for different air flow configurations, including cross-flow. The slits were centred at the middle of the fuel cell tube and positioned every 60°, giving 6 equally spaced slots around the canister circumference. Each slot was 2 mm by 50 mm. The slits could be used as an air inlet or outlet domain with the boundary condition prescribed accordingly. The annotated canister geometry and mesh with mesh quality are seen in Figure 8.29 a) and b), respectively. The axes in b) are the geometric distance measured in metres and the scale is

the mesh quality measured in skewness (dimensionless). The mesh and had 4.8x10^6 elements with a skewness of 0.73.

a) b)

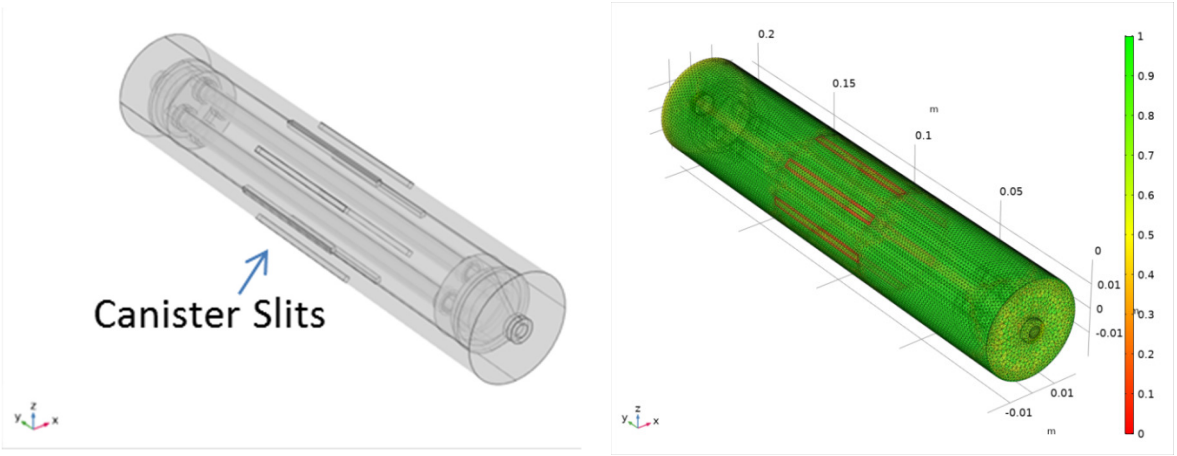

Figure 8.29 - 4-cell stack with canister and canister slits a) annotated geometry, b) mesh quality measured in skewness.

Canister Slits as Air Outlet

The air outlet domains and temperature outflow domains were changed from the canister outlet at the outlet fuel manifold to the slits. All other parameters remained the same as the base case. The stack velocity volume plot, y-z plane velocity slice plot and velocity streamlines are seen in Figure 8.30 a) and b) and c), respectively. The air velocity was increased at the inlet region of the stack and was highest at the slits. The air decelerated after the slits and velocity dropped drastically at the outlet region of the cells. Backflow occurred at the outlet region as the air is redirected by the canister wall (that was previously the air outlet domain) as indicated by the velocity streamlines seen in c).

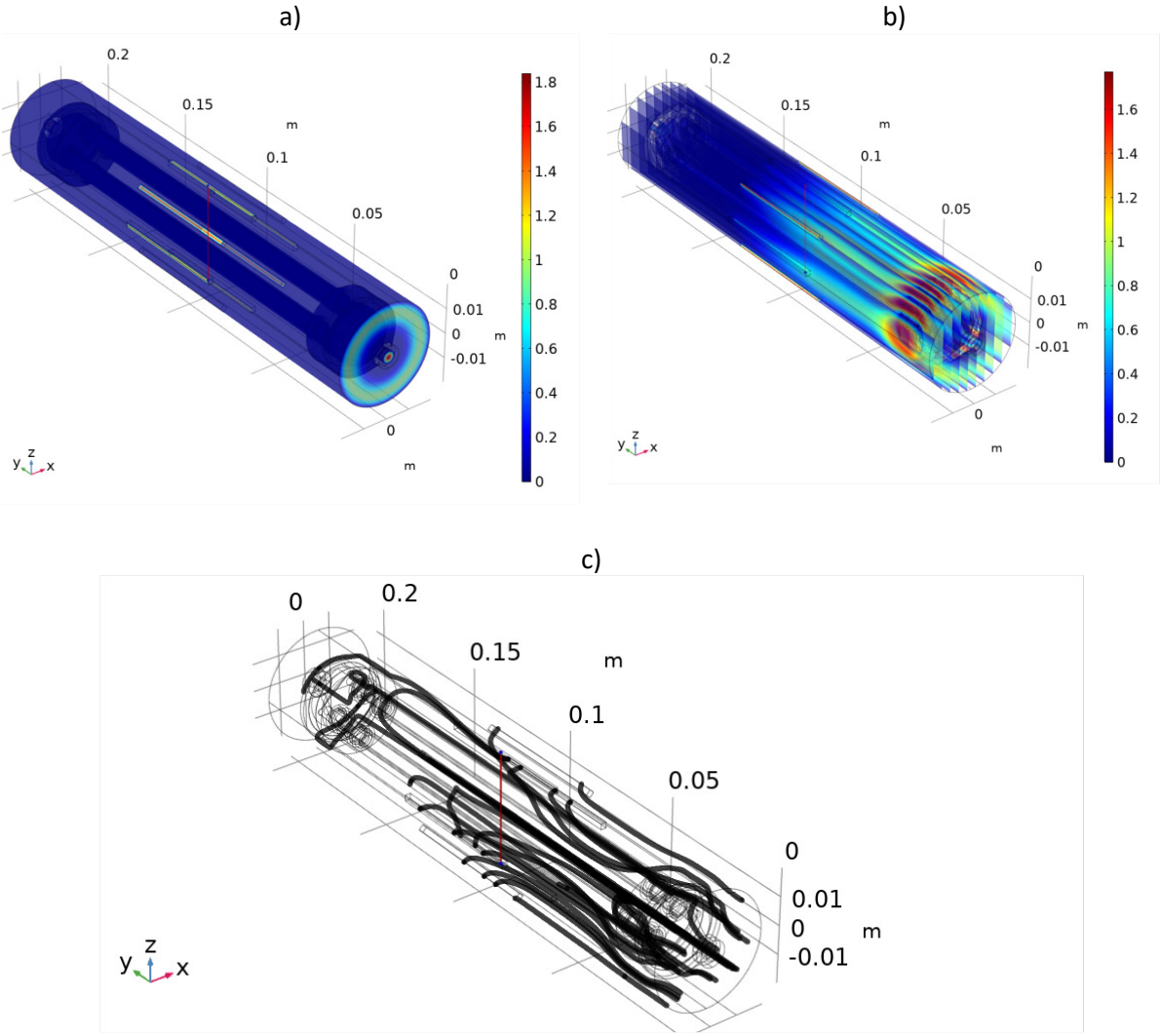

Figure 8.30 - 4-cell stack with canister slits as air outlet a) stack velocity volume plot, b) y-z slice velocity plot, c) velocity streamlines.

The stack temperature and cell temperature are seen in Figure 8.31 a) and b), respectively. The peak stack temperature was 1003°C, located in the outlet region of the cell. The minimum cell temperature was 752°C giving a cell temperature gradient of 251°C. The global stack temperature gradient was 353°C. The peak stack temperature was 4°C lower than the base case and 160°C lower than the counter-flow case. The peak stack temperature was still 93°C higher than the maximum allowable temperature. The manifold temperatures are seen in Figure 8.32. The inlet manifold had a temperature of 750°C and the outlet manifold had a temperature of 1000°C.

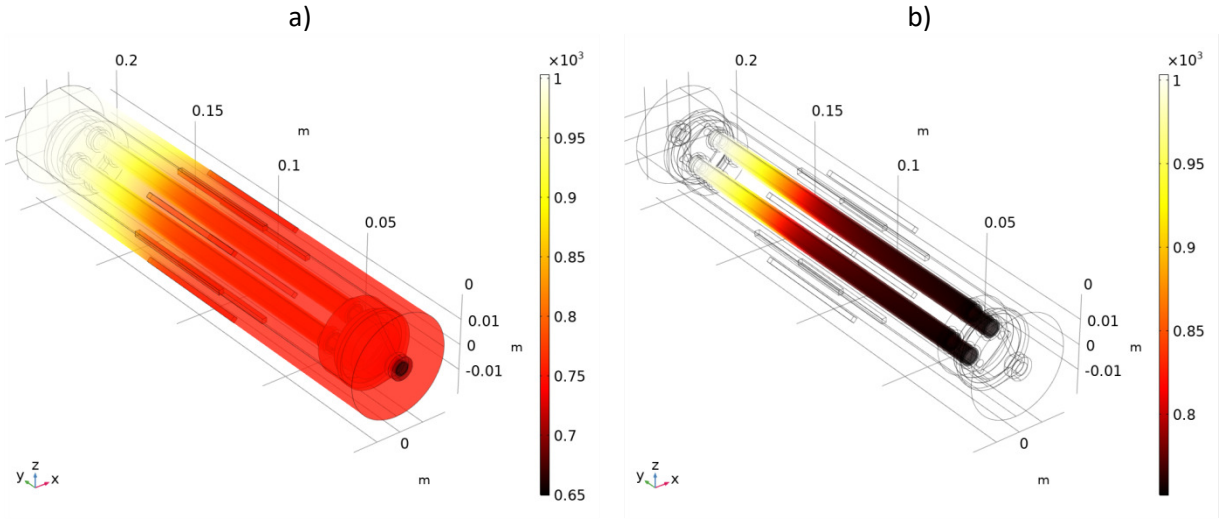

Figure 8.31 - 4-cell stack temperature with canister slits as the air outlet a) entire stack, b) cells only.

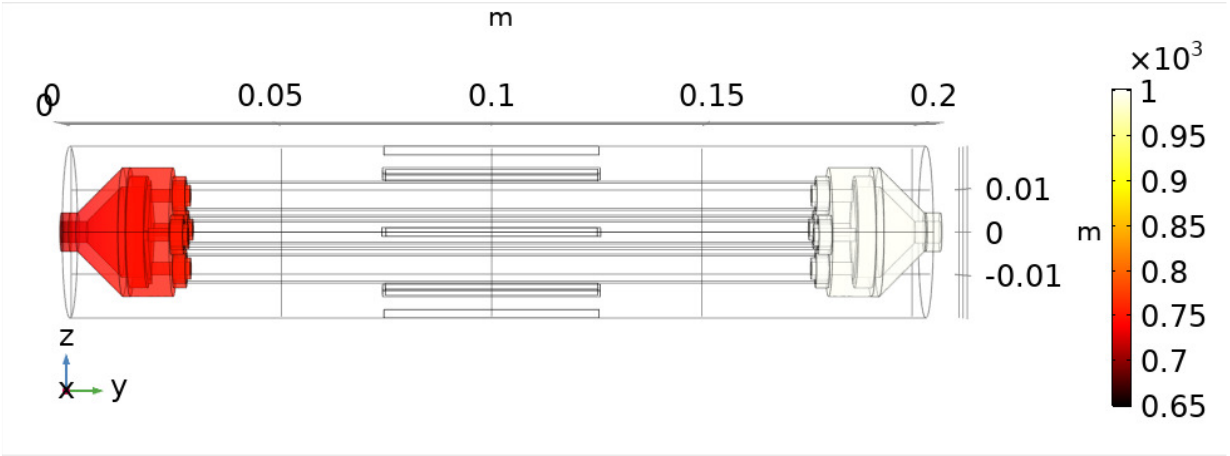

Figure 8.32 - 4-cell stack manifold temperature with canister slits as the air outlet.

Canister Slits as Air Inlet

The air inlet velocity and temperature domains were changed from the canister air inlet to the slits. The air outlet velocity and temperature outflow domains were changed to both canister faces (the air inlet and air outlet domains seen in Figure 8.7 a). This gave a cross-flow configuration. All other parameters remained the same as the base case. The stack velocity volume plot, y-z slice velocity plot and air streamlines are seen in Figure 8.33 a), b) and c), respectively. The narrow width of the slit resulted in a high air inlet velocity compared to the base case, improving the heat transfer ability of the fluid. The air outlets at each end of the canister improved the air distribution within the stack, and heat rejection surface area, further improving the cooling.

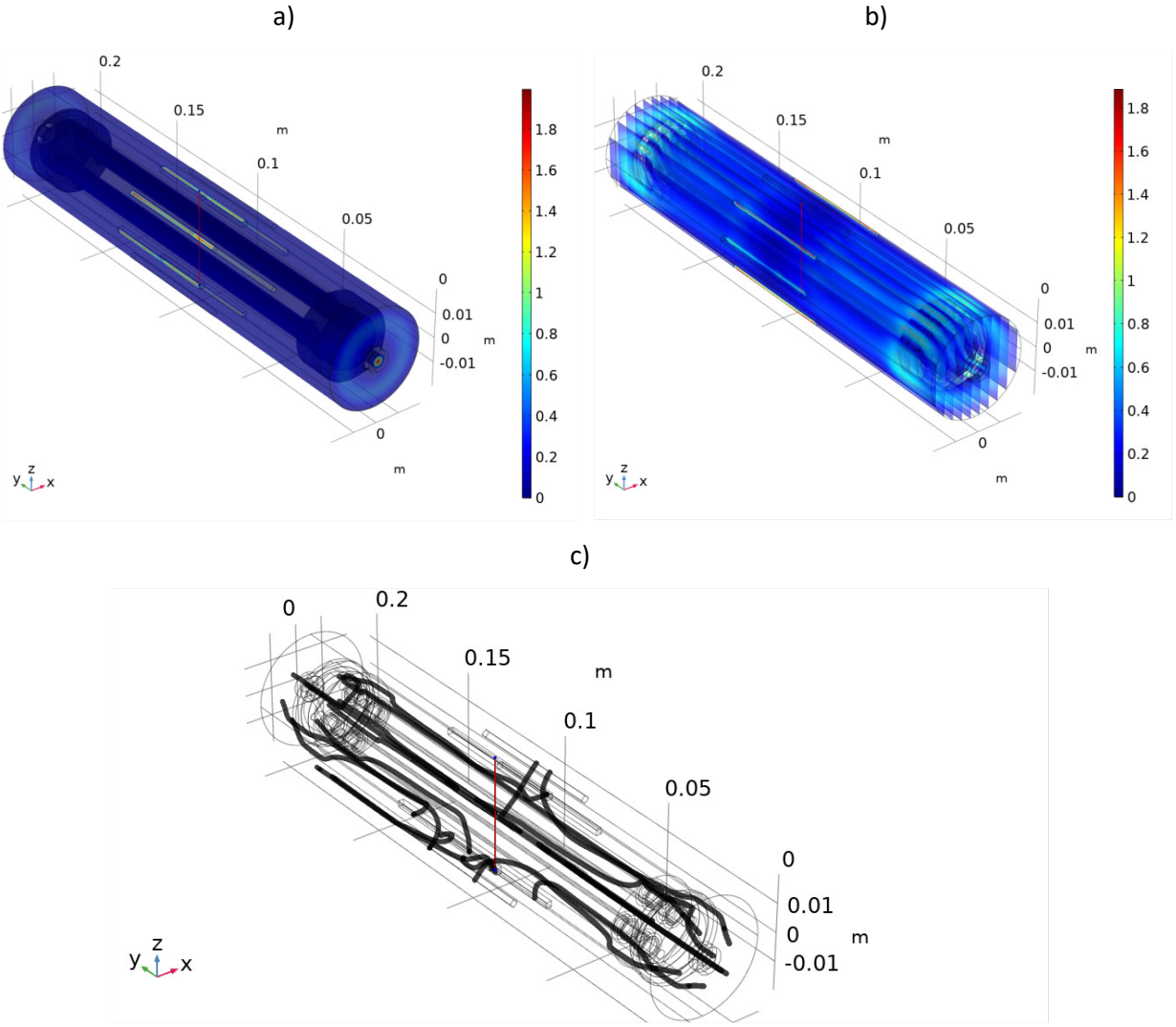

Figure 8.33 - 4-cell stack with canister slits as the air inlet a) stack velocity volume plot, b) y-z slice velocity plot, c) velocity streamlines.

The stack temperature and cell temperature are seen in Figure 8.34 a) and b), respectively. The peak stack temperature was 789°C, located at the outlet region of the cells and at the centre-inlet region of the cells by which point the cold fuel has been heated. The minimum cell temperature was 765°C giving a cell temperature gradient of 24°C. The global stack temperature gradient was 139°C. The peak stack temperature was 218°C lower than the base case and 374°C lower than in the counter-flow case. The peak stack temperature was 171°C lower than the maximum permitted temperature of 960°C. The manifold temperatures are seen in Figure 8.35. The inlet manifold had a temperature of 760°C and the outlet manifold has a temperature of 785°C. Coated steel could be used for both manifolds.

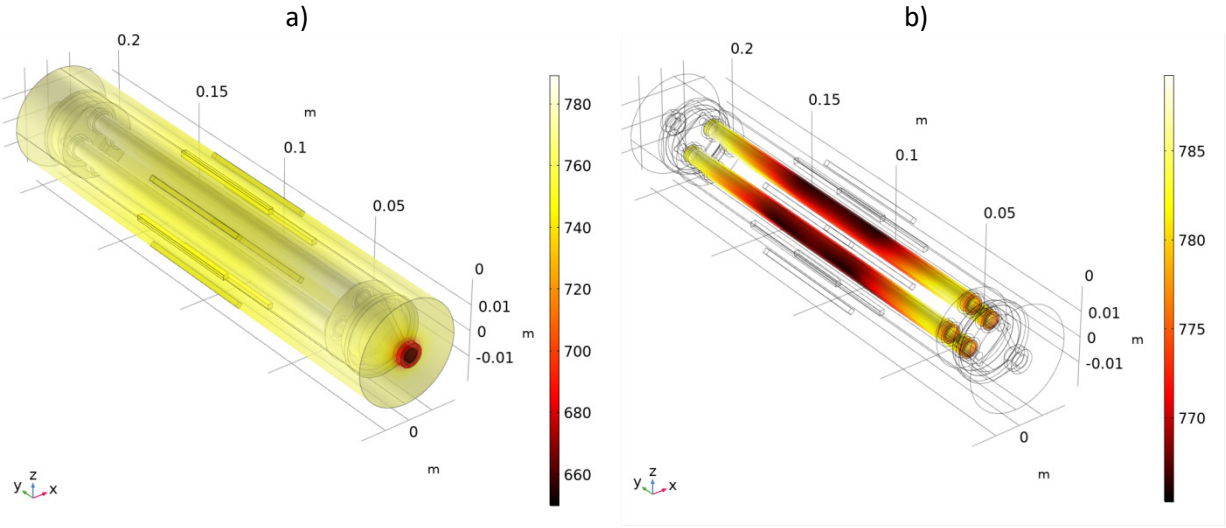

Figure 8.34 - 4-cell stack temperature with canister slits as the air inlet a) entire stack, b) cells only.

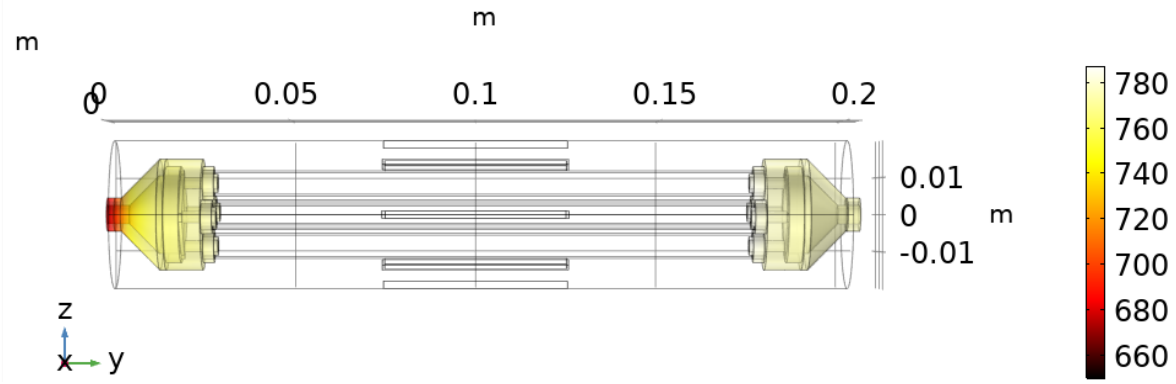

Figure 8.35 - 4-cell stack manifold temperature with canister slits as the air inlet.

8.4.8 Optimisation Summary

The key findings from the CFD optimisation are presented along with the base case data set in Table 8.1. The key optimising parameter was the peak stack temperature, requiring a value lower than 910°C to protect the silver wiring from melting and the BNi-2 brazed anode-hiTRAN joints from failing. Three designs met the criteria, those being the modified geometry with the slits as the air inlet and the modified air inlet design with temperatures of 550°C and 600°C. The air inlet design with an inlet temperature of 650°C was a viable option.

Table 8.1 - Summary of CFD optimisation results.

Optimisation Parameter	Peak Stack Temperature	ΔT Stack	ΔT Cell	Minimum Cell Temperature	Metal Manifold [I/O]
Base Case	1007°C	350°C	256°C	751°C	[I]
Flow Orientation					
Counter-flow	1163°C	513°C	161°C	800°C	[O]
Cross-flow with:					
Slits as Air Outlet	1007°C	353°C	251°C	752°C	[I/O]
Slits as Air Inlet	789°C	139°C	24°C	765°C	[I]
Fuel Inlet Temperature					
25°C	925°C	900°C	295°C	630°C	[I]
Air Inlet Temperature					
700°C	967°C	317°C	258°C	709°C	[I]
650°C	926°C	276°C	258°C	668°C	[I]
600°C	886°C	258°C	259°C	627°C	[I]
550°C	845°C	296°C	259°C	586°C	[I]
Air Utilisation λ_c					
6	989°C	388°C	230°C	751°C	[I]
7	970°C	320°C	220°C	751°C	[I]

A minimum cell temperature was defined as 650°C to avoid performance loss associated with low temperature operation, given that SOFC performance increases considerably with operating temperature [41]. In addition, internal reforming ability, a key advantage of the SOFC over low temperature counterparts, occurs at 650°C and above. All of the designs except ones with the air inlet temperature at 550°C and 600°C met this criterion with the latter considered as a possibility given only the first 20 mm of the cell was below the required reforming temperature.

An optimised stack was set to have a low global temperature gradient and a low temperature gradient across the cells. This was to avoid cell damage and cracking of stack components due to thermo-mechanically induced expansion, leading to accelerated degradation. The best performing in this regard was the modified geometry cross-flow design using the slits as the air inlet. The design resulted in a stack temperature gradient of 139°C and a cell temperature gradient of 24°C.

The inlet and manifold temperatures were analysed to determine whether low-temperature manifolds such as steel, coated or uncoated, could be used. The maximum temperature for a steel manifold was 800°C [72]. Only the modified geometry using the slits as the air outlet permitted the use of low-temperature manifold materials at both the inlet and outlet. All of the other designs permitted the use of single manifold, either at the inlet or outlet. In addition, the design with an air

temperature inlet of 650°C and below had an inlet manifold temperature of 700°C and below. Given that the oxidation rate of steels decreased with decreasing temperature, below 700°C the rate would be sufficiently low to use some uncoated steel variants for the entire stack lifetime. Oxidation of the steels results in increased electrical resistance. Therefore minimising the process is crucial if the manifold is used as part of the current collection strategy. However, oxidation of the steel negatively affects the mechanical properties of the material and could lead to embrittlement and a higher risk of mechanical failure.

The best design overall, meeting all of the criteria was the modified geometry with the slits as the air inlet. The optimised design had a peak stack temperature 28% below the base case and a minimum cell temperature of 765°C.

Performing a hand-based energy balance calculation seen in equation (158) and (159), an estimation of the expected temperature gradient can be performed to determine whether the values predicted by the CFD model are sensible. The heat generation of the stack is approximately 13 W based on a 50% electrical efficiency.

$$Q_{Cell} = Q_{Gen} + Q_{Fuel} + Q_{Air} \tag{158}$$

$$m_{cell} C_{p,cell} \frac{dT}{dt} = 13\ W + m_f C_{p,f}\left(T_{f,o} - T_{f,i}\right) + m_a C_{p,a}\left(T_{a,o} - T_{a,i}\right) \tag{159}$$

Substituting values for the base case on a per-cell basis we get:

$$\begin{aligned} 0.01[kg] * 570 \left[\frac{J}{kg.K}\right] * \frac{dT}{dt}\left[\frac{K}{s}\right] &= \frac{13}{4}\left[\frac{J}{s}\right] + 2.75x10^{-7}\left[\frac{kg}{s}\right] * 15060\left[\frac{J}{kg.K}\right] * (750-650)[K] + 2.07x10^{-6}\left[\frac{kg}{s}\right] \\ &* 1087\left[\frac{J}{kg.K}\right] * (750-749)[K] \end{aligned} \tag{160}$$

Assuming that the temperature in the fuel cell is uniform at any given time, the body is considered as a lumped capacitance heat reservoir and so the temperature gradient is estimated by:

$$\frac{dT}{dt} \rightarrow \Delta T_{cell} = 75°C \tag{161}$$

resulting in a value of 75°C for a fuel inlet temperature of 650°C, an air inlet temperature of 749°C and a fuel and air outlet temperature of 750°C. This is around 3 times lower than that predicted by the CFD indicating that in future work more effort must be placed in refining the thermal model, in particular, describing the heat produced by the cell.

8.5 3D Printing & Ceramic Machining of Manifolds

Once the manifold designs had been validated by CFD the 4-cell manifolds were 3D printed. This allowed for mock assembly of the stacks to identify any flaws that may have been missed at the design stage. This primarily concerned assembly and wiring logistics. Each manifold was made from two pieces, the tube side and the gas pipe side. The cell spacing was set at the minimum of 6 mm, pre-determined by the wiring logistics. The 3D designs had threads to connect the two manifold pieces as described in the CAD design in Section 8.2. Once the dry assembly was completed for each stack, the designs were machined from a solid Macor ceramic block. Macor is a machinable glass-ceramic with a high use temperature of 800°C in continuous operation and 1000°C peak operating temperature [320]. Macor is strong, rigid and has a similar CTE to the ceramic µT-SOFC components as well as the glass sealant, lowering the risk of mechanical failure of the stack during start-up/shut-down and thermal cycling. The electrically insulating properties of Macor were the prime reason for selection over stainless steel, thus avoiding complexities surrounding short-circuiting and electrical isolation of the cells and the manifold, which would be required for any configuration other than a parallel connection. Macor is also radiation resistant and has low emissivity. The threads were omitted for the Macor as permanent sealing would be used and it was suspected that the threads would either snap or seize during testing. The plastic cold side/mock-up and Macor manifold pieces are seen in Figure 8.36.

Figure 8.36 - 3D printed (plastic) and machined Macor 4-cell stack manifolds.

8.6 Stack Testing

Following the mock assembly of the stack for establishing wiring logistics, the cells were wired for testing. Two interconnect designs were proposed for the 4-cell stack testing. The first with cells having a combined central nickel anode current collector and BNi-2 inert brazed hiTRAN. The second a BNi-2 inert brazed hiTRAN-only stack. The current collector wires were applied to each cell; the cells were then preliminarily placed into the plastic manifold. Once the cells were in the manifold, the cells were interconnected with each other. Wiring in this way minimised interconnect distance and thus ohmic resistance of the interconnects in the stack. Once the cells had been wired accordingly the wired cells were then removed from the plastic manifolds. Sealant was syringed into each of the cell holding 'caps' on the tube side half of the inlet and outlet ceramic manifolds. The cells were then seated in the inlet and outlet ceramic manifold caps before a top coat of sealant was applied to each joint. The inlet manifold gas supply was then attached to the inlet manifold, taking care to position the supply feed pipe to protrude into the main manifold chamber to allow for an even distribution of gas to each cell. The outlet manifold gas supply section of the manifold was then attached to the cell, followed by the outlet manifold pipes. All of the manifold joints, the current collectors and the current collector joints were sealed with glass sealant. The sealant was sintered in-situ as stack testing began. The stack was heated at a ramp rate of 10°C.min^{-1}. Forming gas (4% H_2 in N_2) was supplied to the stacks from 400°C upwards at a total flow rate of 800 ml.min^{-1}. Once the stack had

reached 600°C the gas composition was slowly adjusted to the composition of 800 ml.min^{-1} H_2. The stack was heated to 650°C and held for 1 hour before measurements were made. The stack was then heated to 700°C and 750°C, again holding at OCV for 1 hour before any current was drawn for electrochemical testing.

8.6.1 4-Cell Stack – Central Nickel and hiTRAN MPD

Four cells were prepared for current collection in the standard procedure for a cell with both a central current collector and hiTRAN. The hiTRAN anode slots were sealed around the hiTRAN tail with Ceramabond and dried in air before curing in the furnace as per the standard method. Once cooled down, glass sealant was then applied to the covered slot with a fine brush, sealing the relatively more porous Ceramabond for hermeticity. The hiTRAN tails exiting the anode slot were electrically connected to the central anode connector in parallel. Each cell was then connected to the adjacent cell in series. The hiTRAN-central anode wire joint was then coated in the dense silver paste to reduce any contact resistance from loose wiring. The joint was made near the inlet region to allow for a minimum distance of the interconnection to the cathode. Voltage sensing wires were also integrated onto the 'first' and 'last' cells to allow four-probe measurements to give a four-probe measurement across the stack. The 'first' and 'last' cell being the cells with the main stack anode and cathode current wire, respectively, leading to the Solartron measurement system defined Section 3.3.4. An additional voltage wire was also added on the 'first' cell to allow for performance measurement of a single cell within the stack. The assembled stack was then positioned in the centre of the furnace on a ceramic support. The stack was spaced above the support with ceramic tiles to ensure there was sufficient supply to the cells nearest the support. All of the wires were then insulated. The wires were connected to the Solartron and the manifolds attached to the gas supply. The 4-cell stack with central nickel and BNi-2 inert brazed hiTRAN is seen in Figure 8.37.

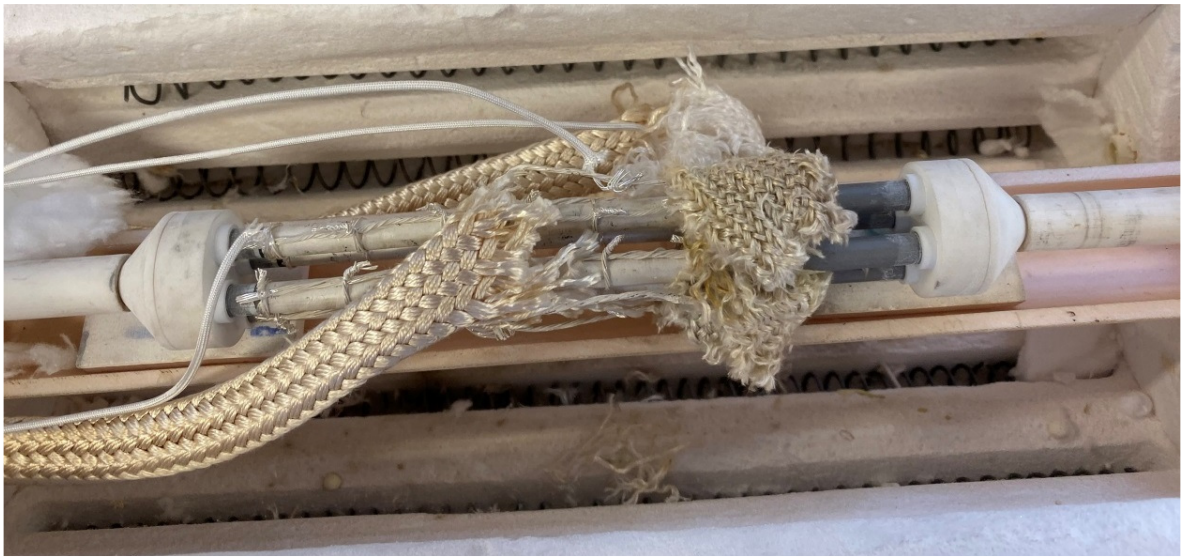

Figure 8.37 – 4-cell stack with central nickel and hiTRAN MPD current collection.

The polarisation and power density plots for the 4-cell-stack are seen in Figure 8.38. The stack current density at 2.8 V, corresponding to a nominal cell voltage of 0.7 V was 0.032 A.cm^{-2}, 0.043 A.cm^{-2} and 0.051 A.cm^{-2} at 650°C, 700°C and 750°C, respectively. The peak power density was 0.113 W.cm^{-2}, 0.146 W.cm^{-2} and 0.169 W.cm^{-2} at 650°C, 700°C and 750°C, respectively. This corresponded to a stack power of 8.9 W, 11.5 W and 13.3 W, respectively. The ASR estimated from the gradient between 2.4 V and 3.2 V was 37.56 Ω.cm^2, 29.09 Ω.cm^2 and 24.24 Ω.cm^2 at 650°C, 700°C and 750°C, respectively. The OCV of the stack was above 4 V at each temperature indicating that the electrolytes of each cell were intact with minimal to no fuel leakage. The value above 4 V was also indicative of homogenous fuel supply to all of the cells, implying that the manifold was distributing gas equally as indicated by the CFD in Section 8.3.4. The OCV decreased as temperature increased as per the temperature dependent Nernst equation, changing from 4.33 V at 650°C, to 4.28 V at 700°C and to 4.23 V at 750°C. The data is summarised in Table 8.2.

.

Table 8.2 - Performance data at 750°C and a total flow of 800 ml.min^{-1} H_2 for the 4-cell stack with hiTRAN and central nickel current collector at 650°C,700°C and 800°C.

Operating Temperature [°C]	OCV [V]	Current Density at 2.8 V [A.cm^{-2}]	Peak Power Density [W.cm^{-2}]	Stack Power Output [W]	ASR (IV) [Ω.cm^2]
650	4.33	0.032	0.113	8.9	37.56
700	4.28	0.043	0.146	11.5	29.09
750	4.23	0.051	0.169	13.3	24.24

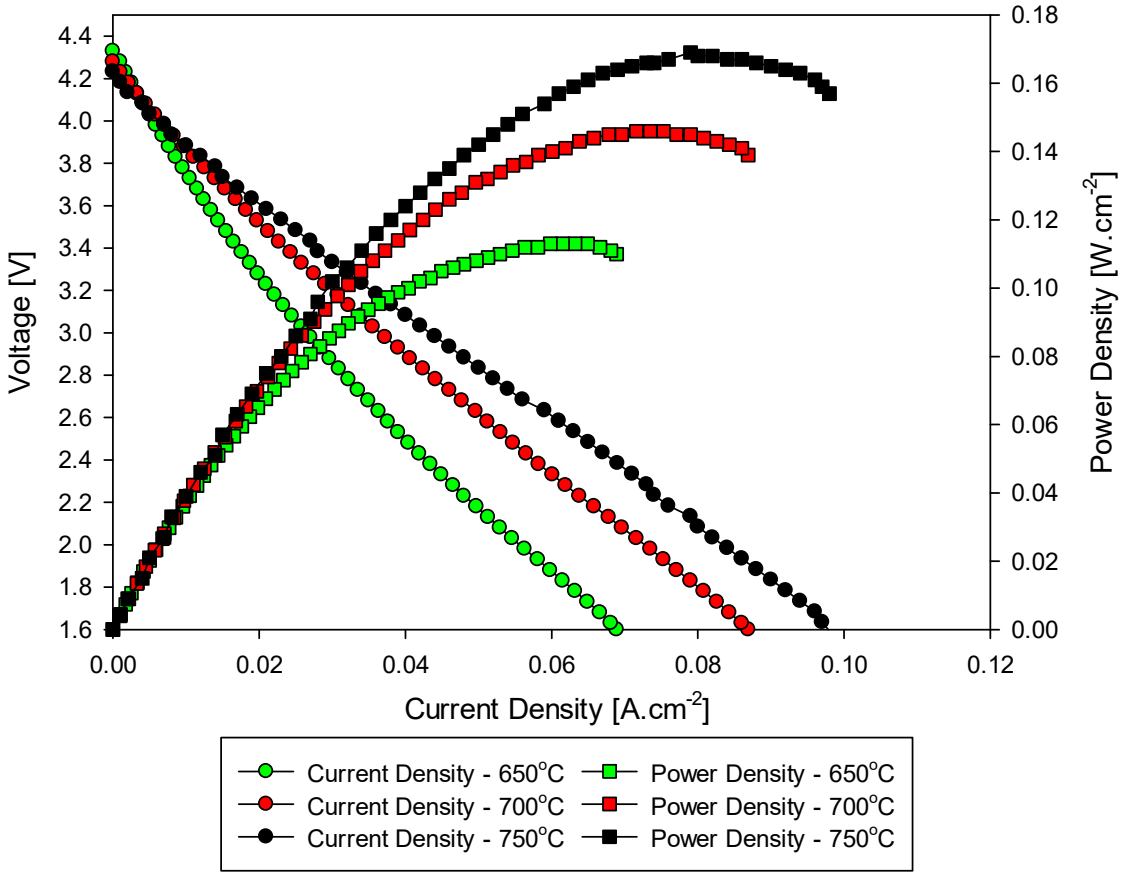

Figure 8.38 - Polarisation and power density plot of the 4-cell stack with central nickel and hiTRAN MPD combined current collection, tested with an 800 ml.min^{-1} H_2 total flow at 650°C, 700°C and 750°C.

The polarisation and power density plot of the stack presented in Figure 8.38 is presented broken down into a single cell within the stack, a 2-cell stack, 3-cell stack and the 4-cell stack at 750°C. When the stack was up to operating temperature and the dataset was being acquired, it was observed that the performance was lower was expected and so the stack was shut-down and the wiring inspected with a multi-meter to look for any short circuits that might have developed since the stack had been checked for short circuits upon assembly. The stack was first split into two 2-cell stacks. The two stacks then underwent the start-up procedure. One of the stacks had a serious short-circuit and produced negligible current and so the data was not presented. The other stack functioned well and is seen in Figure 8.39. The wiring of the poorly performing 2-cell stack was inspected and appeared to be intact without any obvious short-circuiting. The wiring of each cathode section (that was dissected by the central anode current collector) was split to further inspect the source of any short-circuiting in each active region. A portion of one of the cells was suspected to be at fault, although the problem persisted when the cathode wiring was removed and the anode wires isolated. It was suspected that

the porous silver ink used for the cathode current collector had penetrated the cathode and caused short-circuiting.

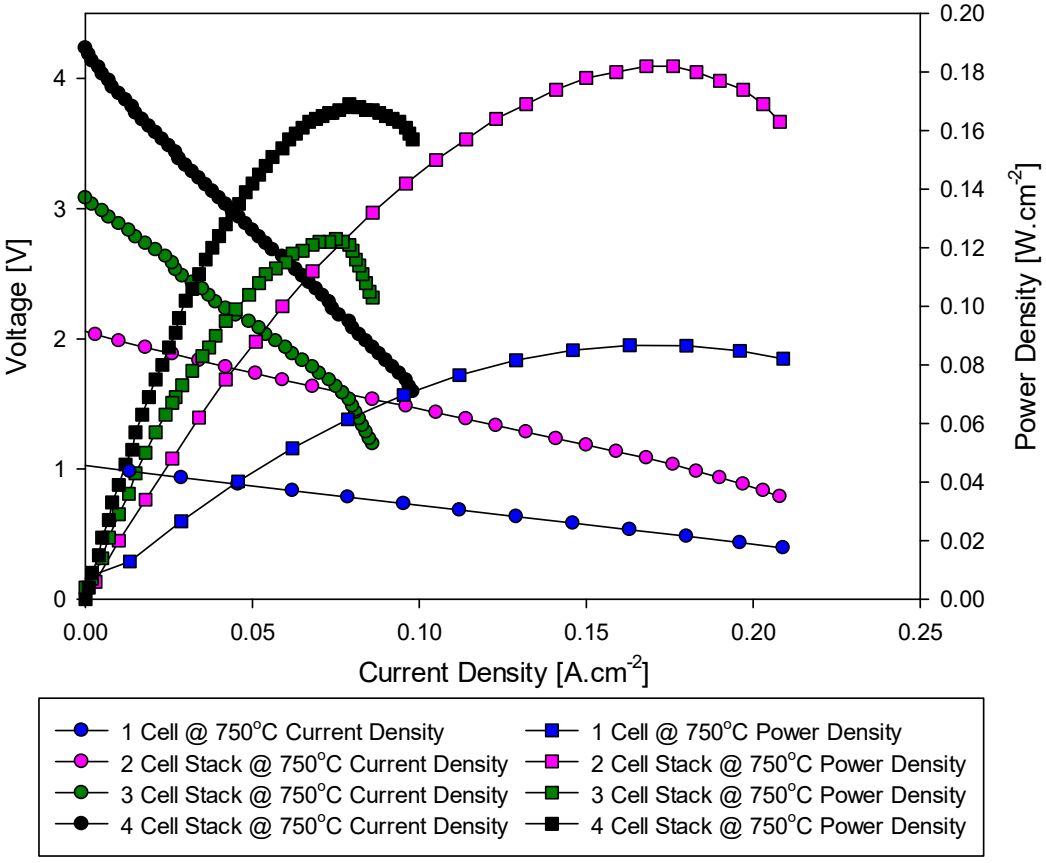

Figure 8.39 - Polarisation and power density plot of hiTRAN and central nickel single cell in a stack, 2 cells within the stack, 3 cells within the stack and 4-cell stack, tested with an 800 ml.min^{-1} H_2 total flow at 750°C.

The current density at 0.7 V of the 'first' cell within the stack was 0.106 A.cm^{-2}, the peak power density was 0.087 W.cm^{-2} and the ASR was 2.98 Ω.cm^2. The 2-cell stack had a current density at 1.4 V (nominal voltage of 0.7 V per cell) of 0.11 A.cm^{-2}, a peak power density of 0.182 W.cm^{-2} and an ASR of 5.56 Ω.cm^2. The 3-cell stack had a current density at 2.1 V (each cell at 0.7 V equivalent) of 0.014 A.cm^{-2}, a peak power density of 0.123 W.cm^{-2}, and an ASR of 17.9 Ω.cm^2. The ASR of the 3-cell stack was 3.2 times higher than the 2-cell stack indicated a severe wiring issue between the 2nd and 3rd cell. The 4-cell stack had a current density at 2.8 V (each cell at 0.7 V equivalent) of 0.051 A.cm^{-2}, the peak power density was 0.169 W.cm^{-2} and the ASR was 24.24 Ω.cm^2. The high OCV of each cell confirmed that the poor performance was not a fueling issue but an interconnection issue. The cell spacing was sufficient to conduct post-fabrication wiring inspections but the fragility of the stack after thermal cycling made maintenance near impossible difficult.

The complexity of the anode wiring with a combined central and hiTRAN MPD, in addition to the anode wiring being in close proximity to the cathode current collector, was a cumbersome design that presented a high risk of short-circuiting. The resulting difficulty in current collector troubleshooting led to the use of the simpler hiTRAN only stack design being favoured for future work.

8.6.2 4-Cell Stack – hiTRAN MPD

Four cells were prepared with BNi-2 inert brazed hiTRAN only current collectors. The hiTRAN anode slots were sealed around the hiTRAN tail with Ceramabond and dried in air before curing in the furnace as per the standard method. Once cool, Schott glass sealant was then applied to the covered slot, covering the relatively porous Ceramabond to provide hermeticity. With the cells positioned in the plastic manifold, they were connected in series. The hiTRAN tails leaving the anode of the first cell was lined up to the cathode of the second cell and sized to sit along the entire active area length. All of the tails used for interconnecting or as the main current output wire (end cell) were covered in dense silver paste and then air dried for 1 hour. The tie wires securing the hiTRAN tail were silver and prepared and attached in the standard way as described in Section 3.2.4. An additional voltage wire was also added on the 'first' cell to allow for performance measurement of a single cell within the stack. The assembled stack was then positioned in the centre of the furnace on a ceramic support. The stack was spaced above the support with ceramic tiles to ensure there was sufficient supply to the cells nearest the support. All of the wires were then insulated. The wires were connected to the measurement system and the manifolds attached to the gas supply as described in Chapter 3. The 4-cell stack with BNi-2 inert brazed hiTRAN is seen in Figure 8.40.

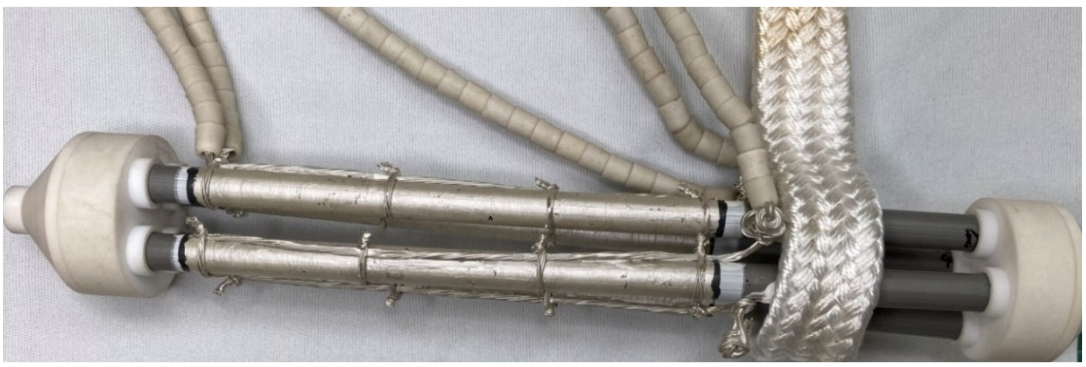

Figure 8.40 - 4 cell stack with hiTRAN-only current collection.

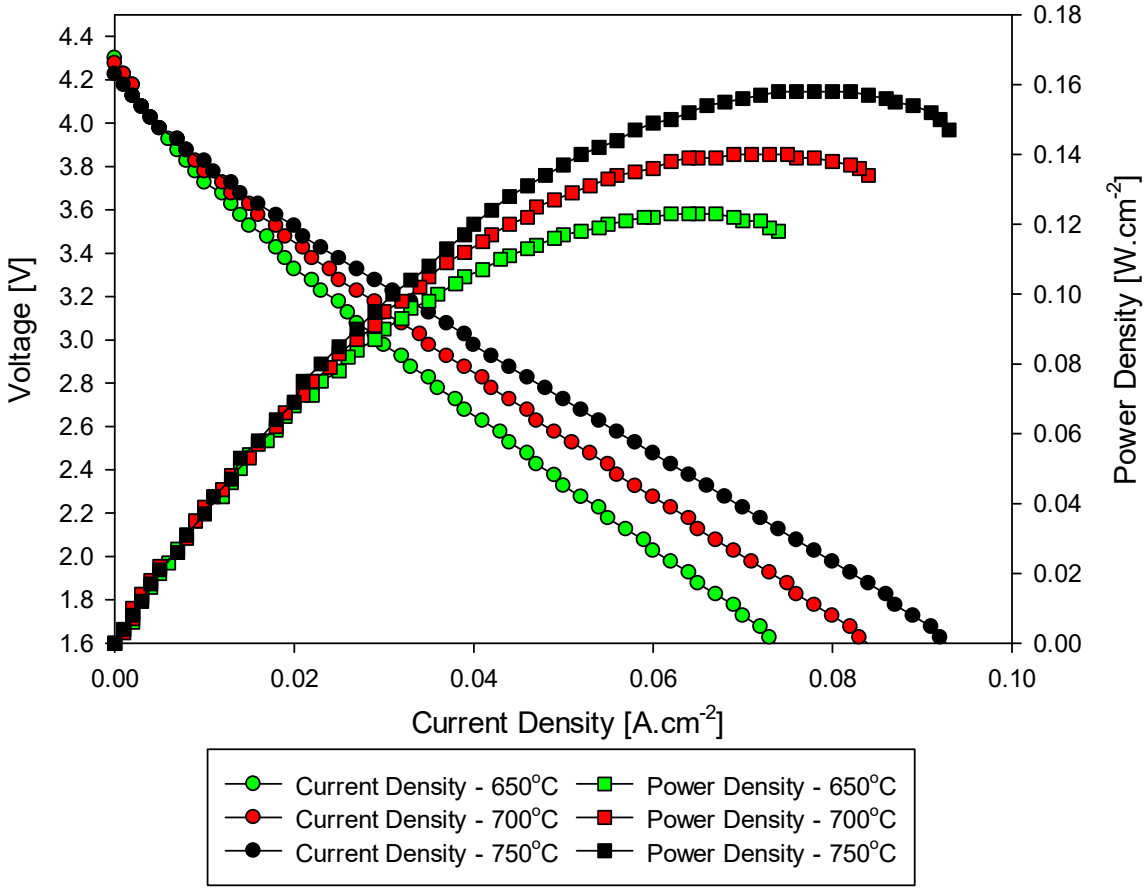

Figure 8.41 - Polarisation and power density plots of the 4-cell stack with BNi-2 inert brazed hiTRAN-only current collection with an 800 ml.min^{-1} H_2 total flow at 650°C, 700°C and 750°.

The polarisation and power density plots for the 4-cell stack are seen in Figure 8.41. The stack current density at 2.8 V (nominal voltage of 0.7 V per cell) was 0.036 A.cm^{-2}, 0.042 A.cm^{-2} and 0.047 A.cm^{-2} at 650°C, 700°C and 750°C, respectively. The peak power density was 0.123 W.cm^{-2}, 0.140 W.cm^{-2} and 0.158 W.cm^{-2} at 650°C, 700°C and 750°C, respectively. This corresponded to a stack power of 9.9 W, 11.2 W and 12.7 W, respectively. The ASR estimated from the gradient between 2.4 V and 3.2 V was 33.33 Ω.cm^2, 28.57 Ω.cm^2 and 25.81 Ω.cm^2 at 650°C, 700°C and 750°C, respectively. As with the previous stack, at a flow of 800 ml.min^{-1} H_2, the OCV of the stack was above 4 V at each temperature, indicating that the electrolytes of all cells were intact with minimal to no fuel leakage, and the manifold design was proficient in equally distributing fuel to each cell. The OCV decreased as temperature increased as per the temperature dependent Nernst equation, changing from 4.35 V at 650°C to 4.30 V at 700°C and to 4.25 V at 750°C.

The ohmic polarisation, electrode polarisation, total resistance and ASR at OCV of the 4-cell BNi-2 inert brazed hiTRAN stack at 650°C, 700°C and 750°C are seen in Figure 8.42. Both the ohmic

polarisation and electrode polarisation decreased with increasing temperature meaning the total resistance and ASR followed the same trend. The ASR decreased from 79 Ω.cm^2 to 66 Ω.cm^2 and 53 Ω.cm^2 at 650°C, 700°C and 750°C, respectively. The performance data is summarised in Table 8.3.

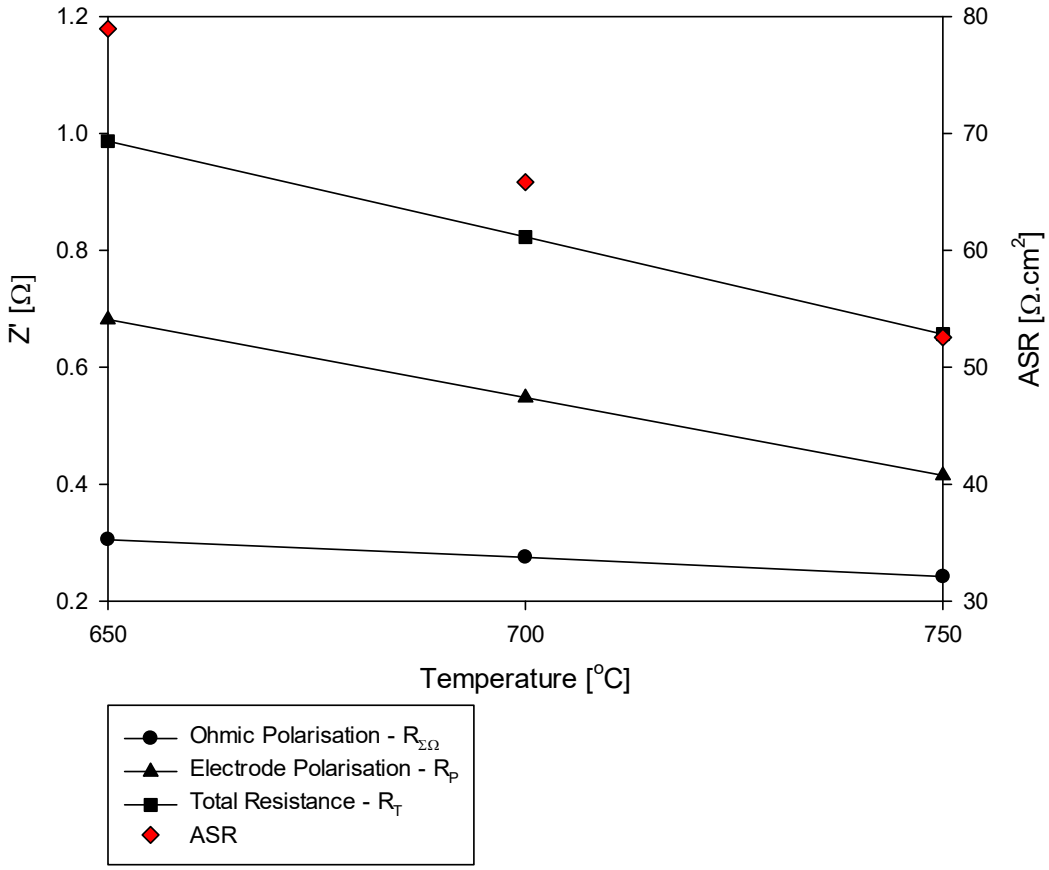

Figure 8.42 - Ohmic polarisation, electrode polarisation, total resistance and ASR at OCV of the 4-cell stack with BNi-2 inert brazed hiTRAN-only current collection, tested with an 800 ml.min^{-1} H_2 total flow at 650°C, 700°C and 750°C.

Table 8.3 - Performance data at 750°C and a total flow of 800 ml.min^{-1} H_2 for the 4-cell hiTRAN-only stack at 650°C,700°C and 800°C.

Operating Temperature [°C]	OCV [V]	Current Density at 2.8 V [A.cm^{-2}]	Peak Power Density [W.cm^{-2}]	Stack Power Output [W]	ASR (IV) [Ω.cm^2]	ASR (EIS) [Ω.cm^2]
650	4.12	0.036	0.123	9.9	33.33	79
700	4.17	0.042	0.140	11.2	28.57	66
750	4.23	0.047	0.158	12.7	25.81	53

The impedance close to OCV was measured at the start of each day of testing at 750°C. The Nyquist plot was deconstructed into the ohmic polarisation, electrode polarisation and total resistance with the latter multiplied by the 80 cm^2 stack area to give the ASR plotted in Figure 8.43. Day 1 was the first day of testing and the data are the same as plotted in Figure 8.42. The ASR increased by 23% during the first day of testing from 53 $\Omega.cm^2$ to 65 $\Omega.cm^2$. Over the remaining days of testing the ASR increased by less than 4% per day. The expected initial drop during the first day was due to the sintering of the stack as indicated by the ASR trend showing a strong correlation to the electrode polarisation. The intensive initial testing of the stack during the first day put the cells under strain which would have an additional contribution to the initial ASR drop observed.

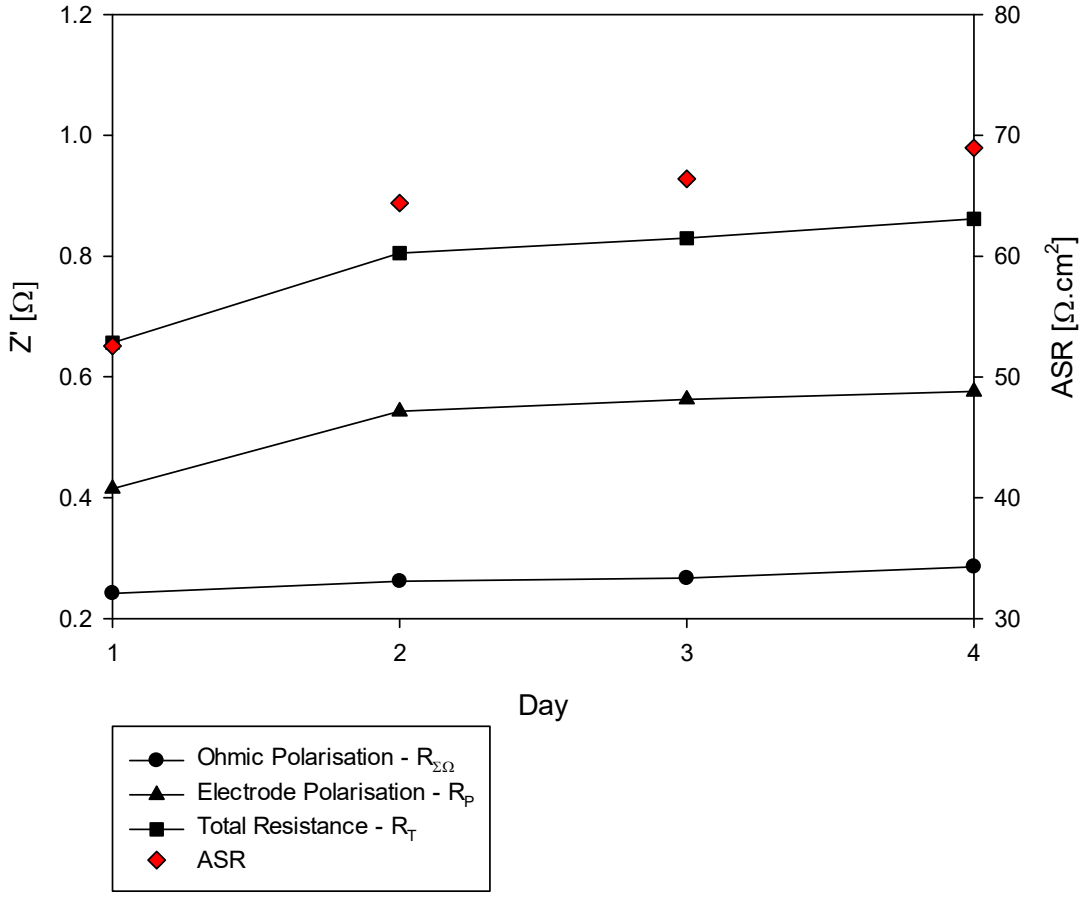

Figure 8.43 - Ohmic polarisation, electrode polarisation, total resistance and ASR at OCV versus operating time of the 4-cell stack with BNi-2 inert brazed hiTRAN-only current collection, tested with an 800 ml.min^{-1} H_2 total flow at 750°C.

Once polarisation data and impedance data were obtained at the start of each day of testing, the stack was held at a constant potential. The potentiostatic hold was at 2.8 V (nominal voltage of 0.7 V per cell) which would be a typical operating potential of the stack for high efficiency with the

flexibility to respond to load changes. The average degradation rate for each hour of the potentiostatic hold measured in $mA.h^{-1}$ is seen in Figure 8.44. Over the 4 days of operation, the cumulative potentiostatic hold time was 83 hours. The start and end of each day of testing are indicated by the green and red data point, respectively. The average degradation rate was between 0.048 $mV.h^{-1}$ and 0.043 $mV.h^{-1}$ for the duration of operation with values within 11% of each other. During the first day of testing the degradation was at its highest and was 0.048 $mV.h^{-1}$ for the first four hours decreasing by 6% to 0.045 $mV.h^{-1}$ at the 13^{th} hour of operation. During the 18 hours of potentiostatic hold on day 2, the degradation rate dropped from 0.045 $mV.h^{-1}$ during the first hour to a stable 0.044 $mV.h^{-1}$ during the remaining period. The average degradation rate on the first 3 hours of day 3 was 0.044 $mV.h^{-1}$, decreasing to 0.043 $mV.h^{-1}$ for the remaining 20 hours of potentiostatic hold. The initial drop during the first day of operation was due to the initial running-in of the stack which was expected. During this period the stack is sintered, in particular, the glass sealant and the nickel in the anode. In addition, the first cells were under more strain due to the more intensive data acquisition, in particular when producing polarisation plots. The potentiostatic holds were only interrupted to take polarisation data, otherwise, the breaks in the data were due to the unfortunate freezing or erroneous shutdown of the Solartron and software. During these interruptions, the cell remained at the temperature and flow operating conditions.

The initial polarisation and power plots from the 'first cell' in each stack at 750°C with a total H_2 flow of 800 $ml.min^{-1}$ are seen in Figure 8.45. The OCV of the cell with a combined central nickel and hiTRAN current collector was 1.05 V while the hiTRAN-only cell had an OCV of 1.11 V which was attributed to the better condition of the electrolyte in the latter given that no cutting or sealing was required for preparing the central current collector. The key data from Figure 8.45 and the data from the hiTRAN-only averaged single cell data presented in Figure 7.19 are presented in Table 8.4. The current density and peak power density of the hiTRAN-only 'first cell' was 38% and 31% higher, respectively, than the 'first cell' in the hiTRAN and central nickel stack. The ASR of the hiTRAN-only 'first cell' was 79% of the hiTRAN and central nickel 'first cell'. The superior performance of the hiTRAN-only design was attributed to the reduced number of wiring joints such as the hiTRAN-central current collector joint which were a source of increased contact resistance and ASR. The peak power density on the hiTRAN-only 'first cell' was 76% of the hiTRAN-only single cell average value. The difference was attributed to the complexity of a stack design, namely the manifold setup and additional interconnection wiring. Decreasing this difference in performance would be a target for future research.

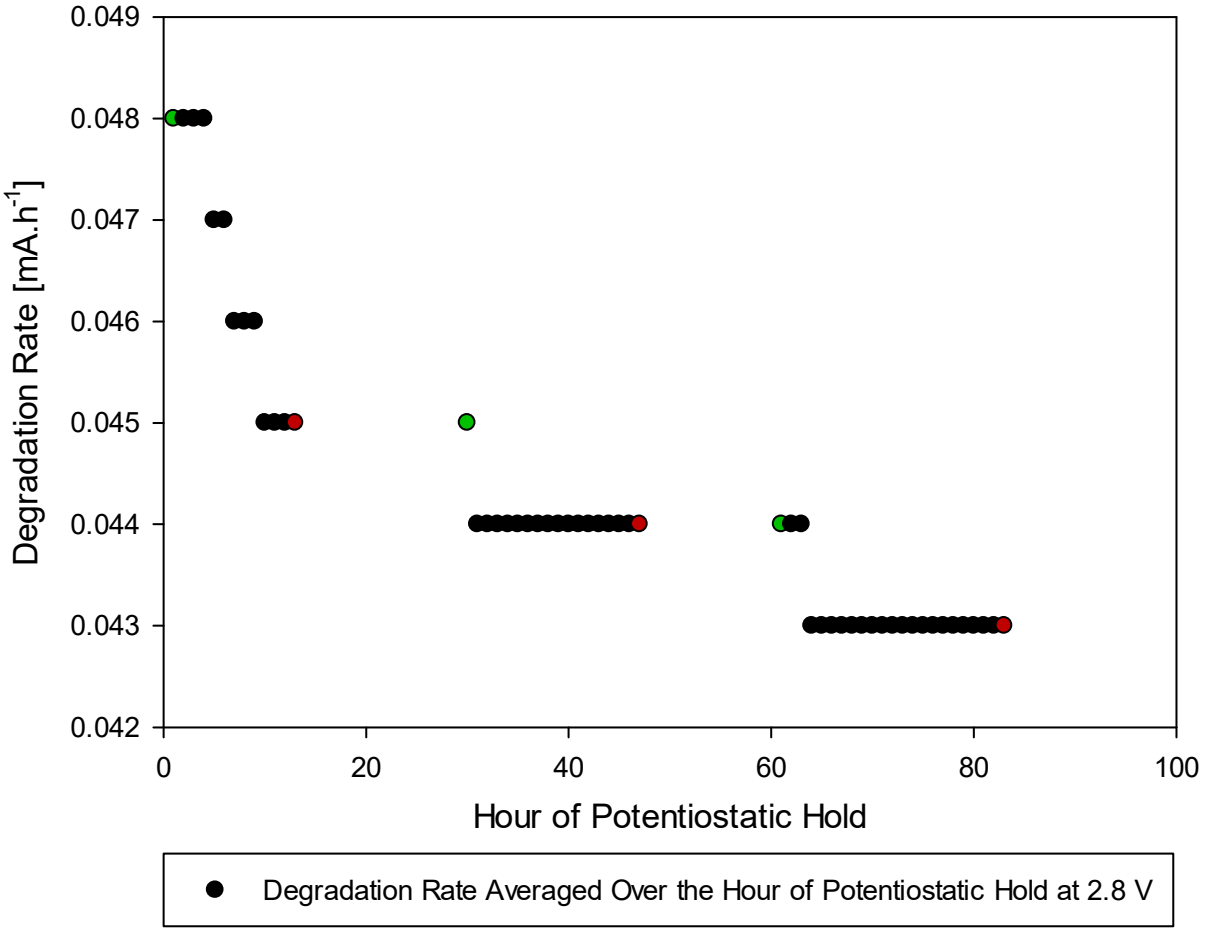

Figure 8.44 - Averaged hourly degradation rate at a 2.8 V potentiostatic hold, tested with an 800 ml.min^{-1} H_2 total flow 750°C.

Table 8.4 - Performance data at 750°C and a flow of 200 ml.min^{-1} H_2 (approx. for stack) for hiTRAN-only average single cell test, hiTRAN-only 'first' cell in the stack and for the 'first' cell in the hiTRAN and central nickel stack.

Cell Configuration	OCV [V]	Current Density at 0.7 V [A.cm^{-2}]	Peak Power Density [W.cm^{-2}]	ASR (IV) [Ω.cm^2]
hiTRAN-only single cell test average	1.15	0.19	0.15	1.82
hiTRAN-only 'first' cell in the stack	1.11	0.146	0.114	2.53
hiTRAN & central nickel 'first' cell in the stack	1.05	0.106	0.087	3.2

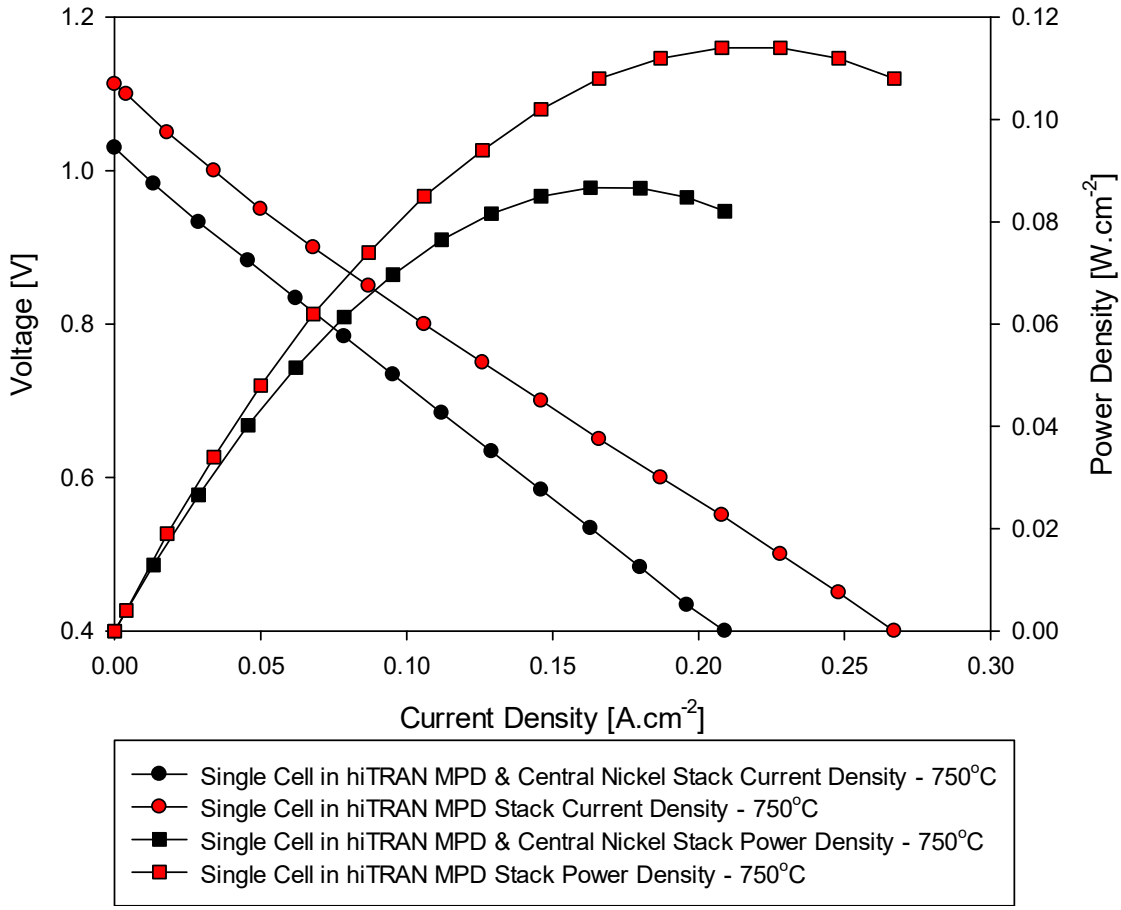

Figure 8.45 - Polarisation and power plots of a single cell in the hiTRAN & central nickel stack and hiTRAN-only stack operating on 800 ml.min^{-1} of H_2 at 750°C.

8.7 Summary

A fuel inlet and fuel outlet manifold was designed for stacking four µT-SOFC with hiTRAN current collection. The stack design was translated into CAD and analysed with CFD. Solving for the conservation of momentum, it was determined that the design of the manifolds was effective in providing an equal distribution of fluid to and from each cell, a fundamental objective of a manifold design. A canister was added to the CFD geometry of the stack, the canister was primarily representative of a typical canister used in real µT-SOFC stacks, and somewhat representative of the furnace used in testing. The model solved for the conservation of momentum and energy and described the air flow around the stack and the temperature throughout. The heat production at peak current density of a cell with BNi-2 brazed hiTRAN current collector was estimated from polarisation data and fed into the model as a heat source. The air inlet velocity was based on the air utilisation of the same polarisation data. Base case data of velocity distribution and temperature

throughout the stack was obtained. Parametric optimisation was then conducted to reduce the peak stack temperature to below 910°C, which was defined as the maximum temperature for a safe level of operation.

The CAD manifold design was fabricated using additive manufacturing in plastic. The 3D printed plastic manifold was used for final design adjustments and mock assembly. The final design was machined in Macor. Two stack designs using inert BNi-2 brazed hiTRAN were fabricated, the first with a parallel-connected central nickel and hiTRAN current collector design and the latter design with hiTRAN as the sole current collector. Cells in each stack were connected in series. The interconnection of the first stack design was cumbersome and led to short-circuiting issues. Polarisation and power density data were obtained at three operating temperatures, but performance was lower than expected. The hiTRAN-only design did not have short-circuiting issues, required no cutting of fuel cell layers, no loss of active area and was less effort concerning assembly time and material cost. Polarisation and power density data as well as impedance data were obtained at three operating temperatures. Potentiostatic data and impedance data were obtained over 100 hours of stack operation with a degradation rate between 0.048 $mV.h^{-1}$ and 0.043 $mV.h^{-1}$ at 750°C. The total power produced by the stacks were similar, the former achieving 13.3 W and the latter 12.7 W at 750°C. The design with hiTRAN as the sole current collector was favoured for its simpler design for cell preparation, wiring, assembly, weight and cost. The final stack design appeared suitable for reliable operation of a portable µT-SOFC stack.

Chapter 9 Conclusions and Further work

This chapter highlights the key findings from the study on µT-SOF current collection, the development of a novel, brazed internal current collector and subsequent implementation in a CFD optimised µT-SOFC stack. Scope for future work is discussed in brief.

9.1 Summary of Conclusions and Novelty

9.1.1 Current Collection

Long electron conduction pathways in µT-SOFCs have long been described in literature as a weak point of the tubular design and a bottleneck for commercialisation. The current study was conducted to find the effect of varying anode current collector position, the number of current collectors and collector material on cell performance. It was found through an empirical study and numerical analysis that a central current collector position outperformed an inlet or outlet current collector. It was concluded that the difference in performance was due to a reduction in the average conduction path length. Increasing the number of current collector positions decreased the conduction pathways and resulted in increased cell performance. However, for a given cell length, increasing the number of external anode current collectors resulted in a loss of available active area. A solution was proposed to collect current from the cell interior. A novel brush-like internal current collector called hiTRAN, originally designed as a flow turbuliser for tubular heat exchangers, was adapted for use as a current collector. The hiTRAN collected current internally from multiple contact points along the 100 mm current generating portion of the anode without the need to sacrifice active area of the cathode. The hiTRAN performed as a current collector but not as well as expected. This was determined to be due to a high contact resistance at the contact points between the hiTRAN and the anode. Changes to the base material and coating of the hiTRAN were explored to reduce the contact resistance. While both methods reduced the contact resistance and improved the efficiency of hiTRAN as a current collector, the mismatch in CTE between the hiTRAN and anode led to fracture of the contact points. The separation resulted in an increased ASR and necessitated the physical joining of the anode and hiTRAN.

9.1.2 Brazing

Brazing was identified as a suitable candidate for current collector-anode contacting and a study on the development of brazing materials and environment, temperature profile and application of the braze on the hiTRAN for joining hiTRAN and anode was presented. Two braze materials were successfully used to contact the anode and hiTRAN at multiple nodes along the cell interior. A novel braze and braze application technique using electroless plating suitable for mass production was presented. Mechanical testing data was presented of the hiTRAN-anode joint, finding that the post-tested joint strength after thermal cycling was 9 times higher than the un-brazed hiTRAN, suitable for withstanding the impact likely incurred in portable μT-SOFC operation. Electrochemical data was presented of cells with two braze materials in two environments. The novel braze and braze application achieved a peak power density 2.35 times of the un-brazed value. The data for the optimised setup using a BNi-2 (nickel-based) braze in an inert brazing environment exhibited a peak power density 2.5 times the un-brazed hiTRAN value. It was shown that brazing considerably improved the performance of the hiTRAN as an internal current collector. While brazing in this study was limited to contacting, the proficiency of brazing for sealing purposes was highlighted. For both purposes, it was determined that anode side brazing favours a reducing environment while cathode side brazing should be in an inert environment. Brazing of a stack incorporating brazing for current collector contacting and sealing purposes could be done in a combined step favouring a low cost, manufacturing time and complexity. More research must be undertaken to reduce the impact of brazing on the electrode polarisation, looking into new braze materials, further optimising the brazing environment and lowering brazing temperature below 1000°C.

9.1.3 Interconnection and Stacking

CAD and CFD results were shown for a 4-cell inlet and outlet manifold with a successful distribution of fuel to and extraction from each cell. The manifolds were integrated into a 4-cell stack model including the μT-SOFC and air canister and the results from a parametric optimisation study. The model used the heat produced and flow requirements from the finalised BNi-2 inert brazed single cell tests. The performance and durability data from electrochemical testing of two 4-cell stacks, both implementing BNi-2 inert brazed hiTRAN with two anode current collection/interconnection methods, was presented. A final 4-cell stack using solely hiTRAN as the anode current collector produced 13 W with a reliable power delivery over 100 hours of continuous operation.

9.1.4 Further Work

Based on the findings described above, further work in completing a µT-SOFC portable system design should address the following:

- Combine the methods of reducing hiTRAN-anode contact resistance by plating with optimised brazes and identify the key sources of ohmic polarisation when interconnecting hiTRAN; minimise contact resistance by optimising geometrical design, materials choices and brazing process, possibly embedding the contacting element into the anode substrate;

- Further develop and optimise braze materials, braze application, and geometry of the hiTRAN and consider protective coatings for long-term stable operation;

- Conduct a CFD optimisation study for a 6-cell stack with integrated cooling seen in Figure 9.1 before fabricating the finalised design to produce a stack with a power output of above 20 W at 5 V; design, optimise and test sub-modules considering more than 6 cells;

- Combine sub-modules into stack units of up to 500 W electrical output.

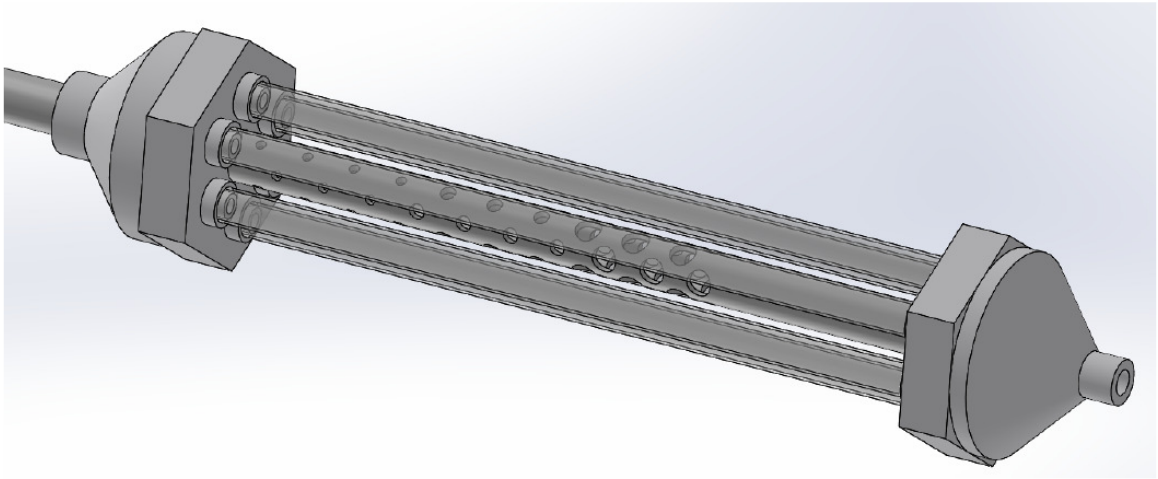

Figure 9.1 - 6-cell stack with integrated cooling (tapered holes) CAD design.

References

[1] P. Lemke, J.F. Ren, I. Allison, J.F. Carrasco, Observations: Changes in Snow, Ice and Frozen Ground., in: Cambridge University Press, Cambridge, 2007.

[2] H. Ritchie, M. Roser, CO2 and Greenhouse Gas Emissions, (2019). https://ourworldindata.org/co2-and-other-greenhouse-gas-emissions (accessed August 20, 2020).

[3] IPCC, Climate Change 2014: Mitigation of Climate Change, Cambridge University Press, 2014.doi:10.1017/CBO9781107415416.

[4] J.G.J. Olivier, M.M. Greet Janssens-Maenhout, J.A.H.W. Peters, Trends in global CO2 emissions 2016, PBL Netherlands Environmental Assessment Agency, 2016.

[5] S.H. Schneider, Greenhouse Effect: Science and Policy, Science (80-.). 243 (1989).doi:10.1126/science.243.4892.771.

[6] E. Rosa, T. Dietz, Human drivers of national greenhouse-gas emissions, Nat. Clim. Chang. 2 (2012) 581–586.doi:10.1038/NCLIMATE1506.

[7] European Commission - URNA, EU Energy In Figures - Statistical Pocketbook 2016, Publications Office of the European Union, Luxembourg, 2016.doi:10.2832/91509.

[8] Arabella Advisors, The Global Fossil Fuel Divestment and Clean Energy Investment Movement, Washington, DC, 2016.

[9] A. Azapagic, S. Perdan, R. Clift, Sustainable Development in Practice: case studies for engineers and scientists, John Wiley & Sons, 2004.doi:10.1002/0470014202.

[10] N. Stern, The Economics of Climate Change, Cambridge University Press, Cambridge, 2006.doi:10.1257/aer.98.2.1.

[11] United Nations, Kyoto Protocol To the United Nations Framework Kyoto Protocol To the United Nations Framework, 1998.doi:10.1111/1467-9388.00150.

[12] United Nations, Paris Agreement - Chapter XXVII Environment, 27 (2016) 1–38. https://treaties.un.org/doc/Publication/MTDSG/Volume II/Chapter XXVII/XXVII-7-d.en.pdf (accessed January 5, 2020).

[13] UNFCCC. V, Adoption of the Paris Agreement. Proposal by the President., in: Paris Clim. Chang. Conf. - Novemb. 2015, COP 21, 2015: p. 32.doi:FCCC/CP/2015/L.9/Rev.1.

[14] Bloomberg New Energy Finance, Global Trends in Renewable Energy Investment, Frankfurt, 2017.

[15] B. Looney, Statistical Review of World Energy 2020, London, 2020. https://www.bp.com/content/dam/bp/business-sites/en/global/corporate/pdfs/energy-economics/statistical-review/bp-stats-review-2020-full-report.pdf.

[16] P. Haldi, D. Favrat, Methodological aspects of the definition of a 2 kW society, Energy. 31 (2006) 3159–3170.doi:10.1016/j.energy.2006.02.011.

[17] J. Larmine, A. Dicks, Fuel Cell Systems Explained, John Wiley & Sons, Chichester, England, 2006.

[18] M. van der Hoeven, Technology Roadmap Hydrogen and Fuel Cells, 2015.doi:10.1007/SpringerReference_7300.

[19] G. Marbán, T. Valdés-Solís, Towards the hydrogen economy?, Int. J. Hydrogen Energy. 32 (2007) 1625–1637.doi:10.1016/j.ijhydene.2006.12.017.

[20] M. Rabuni, N. Vatcharasuwan, T. Li, K. Li, High performance micro-monolithic reversible solid oxide electrochemical reactor, J. Power Sources. 458 (2020) 228026.doi:10.1016/j.jpowsour.2020.228026.

[21] T. Isaac, HyDeploy: The UK's First Hydrogen Blending Deployment Project, 3 (2019) 114–125.doi:10.1093/ce/zkz006.

[22] M.M. Mench, Fuel Cell Engines, John Wiley & Sons, Hoboken, USA, 2008.

[23] J. Andujar, F. Segura, Fuel cells: History and updating. A walk along two centuries, Renew. Sustain. Energy Rev. 13 (2009) 2309–2322.doi:https://doi.org/10.1016/j.rser.2009.03.015.
[24] R. O'Hayre, S.-W. Cha, W. Celella, F.B. Prinz, Fuel Cell Fundamentals, Second, John Wiley & Sons, New York, USA, 2009.
[25] K. Kendall, M. Kendall, M. Cassidy, P.A. Connor, J.T.S. Irvine, C.D. Savaniu, Anodes, in: High-Temperature Solid Oxide Fuel Cells 21st Century, 2016: pp. 133–160.doi:10.1016/B978-0-12-410453-2.00005-1.
[26] J.W. Fergus, R. Hui, X. Li, Solid Oxide Fuel Cells - Materials Properties and Performance, 2016.
[27] O.Z. Sharaf, M.F. Orhan, An overview of fuel cell technology: Fundamentals and applications, Renew. Sustain. Energy Rev. 32 (2014) 810–853.doi:10.1016/j.rser.2014.01.012.
[28] W. Chen, Mobile applications: cars, trucks, locomotives, marine vehicles, and aircraft, Elsevier Inc., 2020.doi:10.1016/b978-0-12-815253-9.00012-4.
[29] S.C. Singhal, Solid oxide fuel cells for stationary, mobile, and military applications, Solid State Ionics. 153 (2002) 405–410.
[30] D. Hart, F. Lehner, S. Jones, J. Lewis, The Fuel Cell Industry Review 2019, London, 2019. www.FuelCellIndustryReview.com. (accessed May 1, 2020).
[31] C. Watanabe, Ene-Farms Use Hydrogen to Power Homes but Don't Come Cheap, Bloom. Technol. (2015). https://www.bloomberg.com/news/articles/2015-01-15/fuel-cells-for-homes-japanese-companies-pitch-clean-energy (accessed August 1, 2020).
[32] Plug Power, GENDRIVE Fuel Cells, (2017). http://www.plugpower.com/products/gendrive/ (accessed May 8, 2017).
[33] Intelligent Energy, Intelligent Energy's fuel cells stacks to be used in Met Police zero emission scooter trial, Intell. Energy. (2017). http://www.intelligent-energy.com/news-and-events/company-news/2017/02/07/intelligent-energys-fuel-cells-stacks-to-be-used-in-met-police-zero-emission-scooter-trial/ (accessed May 8, 2017).
[34] S. Barley, Hydrogen bus launched on London tourist route, Guard. (2010). https://www.theguardian.com/environment/2010/dec/10/hydrogen-bus-london (accessed August 5, 2020).
[35] Hyundai, Hyundai ix35 Hydrogen Fuel Cell Vehicle, (2017). http://www.hyundai.co.uk/about-us/environment/hydrogen-fuel-cell (accessed May 8, 2017).
[36] Toyota, Mirai - Bringing the future into the present, (n.d.). https://www.toyota.co.uk/new-cars/new-mirai/landing.json (accessed May 8, 2017).
[37] M.D. Fernandes, S.T. de, V.N. Bistritzki, R.M. Fonseca, L.G. Zacarias, H.N.C. Gonçalves, A.F. de Castro, R.Z. Domingues, T. Matencio, SOFC-APU systems for aircraft: A review, Int. J. Hydrogen Energy. 43 (2018) 16311–16333.doi:10.1016/j.ijhydene.2018.07.004.
[38] P. Li, L. Schaefer, M.K. Chyu, Multiple Transport Processes in Solid Oxide Fuel Cells, Dev. HEAT Transf. 19 (2005) 1.
[39] W.W. Pulkrabek, Engineering Fundamentals of the Internal Combustion Engine, J. Chem. Inf. Model. 53 (2013) 1689–1699.doi:10.1017/CBO9781107415324.004.
[40] R. Bove, S. Ubertini, Modeling Solid Oxide Fuel Cells. Methods, Procedures and Techniques, Springer, 2008.
[41] K. Kendall, M. Kendall, S.B. Adler, Sources of cell and electrode polarisation losses in SOFCs, in: High-Temperature Solid Oxide Fuel Cells 21st Century, Elsevier, London, England, 2016: pp. 357–381.doi:10.1016/B978-0-12-410453-2.00011-7.
[42] D.J.L. Brett, A. Atkinson, N. Brandon, S.J. Skinner, Intermediate temperature solid oxide fuel cells, Chem.Soc.Rev. 37 (2008) 1568–1578.doi:10.1039/b612060c.
[43] K. Kendall, M. Kendall, N.Q. Minh, Cell and stack design, fabrication and performance, in: High-Temperature Solid Oxide Fuel Cells 21st Century, Elsevier, London, England, 2016: pp. 255–282.
[44] E.D. Wachsman, K. Lee, Lowering the Temperature of Solid Oxide Fuel Cells, Sci. 334. 6058

(2011) 935–939.doi:10.1126/science.1204090.
[45] W.Z. Zhu, S.C. Deevi, Development of interconnect materials for solid oxide fuel cells, Mater. Sci. Eng. A. 348 (2003) 227–243.doi:10.1016/S0921-5093(02)00736-0.
[46] L.M. Rodriguez-Martinez, M. Rivas, L. Otaegi, N. Gomez, M.A. Alvarez, E. Sarasketa-Zabala, J. Manzanedo, N. Burgos, F. Castro, A. Laresgoiti, I. Villarreal, Tubular Metal Support Solid Oxide Fuel Cell Manufacturing and Characterization, ECS Trans. (2011) 445–450.doi:10.1149/1.3570021.
[47] B.A. Haberman, A.J. Marquis, A Numerical Investigation Into the Interaction Between Current Flow and Fuel Consumption in a Segmented-in-Series Tubular SOFC, J. Fuel Cell Sci. Technol. 6 (2009).doi:10.1115/1.3005386.
[48] K. Kendall, M. Kendall, L. Niewolak, F. Tietz, W.J. Quadakkers, Interconnects, in: High-Temperature Solid Oxide Fuel Cells 21st Century, Elsevier, London, England, 2016: pp. 195–254.
[49] S.D. Vora, SECA Program at Siemens Westinghouse, Presented at SECA Annual Workshop and Peer Review Meeting, (2004). https://www.osti.gov/scitech/servlets/purl/834189#page=41 (accessed August 20, 2020).
[50] M. Kendall, A.D. Meadowcroft, K. Kendall, Microtubular Solid Oxide Fuel Cells (mSOFCs), ECS Trans. 57 (2013).doi:10.1149/05701.0123ecst.
[51] K. Kendall, Introduction to SOFCs, in: High-Temperature Solid Oxide Fuel Cells 21st Century, Elsevier, London, England, 2016: pp. 1–24.
[52] Y. Sin, K. Galloway, B. Roy, N.M. Sammes, J. Song, The properties and performance of micro-tubular (less than 2.0 mm O.D.) anode suported solid oxide fuel cell (SOFC), Int. J. Hydrogen Energy. 36 (2011) 1882–1889.doi:10.1016/j.ijhydene.2009.12.167.
[53] C. Ren, Y. Gan, C. Yang, M. Lee, X. Xue, Fabrication and Characterization of Direct Methane Fueled Thin Film SOFCs Supported by Microchannel-Structured Microtubular Substrates, ACS Appl. Energy Mater. 3 (2020) 1831–1841.doi:10.1021/acsaem.9b02271.
[54] W. Bujalski, C.M. Dikwal, K. Kendall, Cycling of three solid oxide fuel cell types, J. Power Sources. 171 (2007) 96–100.doi:10.1016/j.jpowsour.2007.01.029.
[55] K. Kendall, A. Meadowcroft, Improved ceramics leading to microtubular Solid Oxide Fuel Cells (mSOFCs), in: Int. J. Hydrogen Energy, 2013.doi:10.1016/j.ijhydene.2012.08.094.
[56] S. Mukerjee, R. Leah, M. Selby, G. Stevenson, N.P. Brandon, Life and Reliability of Solid Oxide Fuel Cell-Based Products : A Review, in: Solid Oxide Fuel Cell Lifetime Reliab., Elsevier Ltd, 2017: pp. 173–192.doi:10.1016/B978-0-08-101102-7.00009-X.
[57] D. Hart, F. Lehner, R. Rose, J. Lewis, M. Klippenstein, The Fuel Cell Industry Review 2015, in: E4Ttech, London, 2015.
[58] Kraftwerk, Kraftwek, (2017). https://www.kickstarter.com/projects/ezelleron/kraftwerk-highly-innovative-portable-power-plant (accessed April 4, 2017).
[59] C. Hatchwell, N.. Sammes, K. Kendall, Cathode current-collectors for a novel tubular SOFC design, J. Power Sources. 1 (1998) 85–90.doi:10.1016/S0378-7753(97)02693-1.
[60] C. Hatchwell, N.M. Sammes, I.W.M. Brown, K. Kendall, Current collectors for a novel tubular design of solid oxide fuel cell, J. Power Sources. (1999) 64–68.
[61] I.P. Kilbride, Preparation and properties of small diameter tubular solid oxide fuel cells for rapid start-up, J. Power Sources. 61 (1996) 167–171.doi:10.1016/S0378-7753(96)02362-2.
[62] K. Kendall, M. Palin, A small solid oxide fuel cell demonstrator for microelectronic applications, J. Power Sources. 71 (1998) 268–270.
[63] T. Suzuki, T. Yamaguchi, Y. Fujishiro, M. Awano, Improvement of SOFC Performance Using a Microtubular, Anode-Supported SOFC, J. Electrochem. Soc. 153 (2006) 925–928.doi:10.1149/1.2185284.
[64] T. Suzuki, T. Yamaguchi, Y. Fujishiro, M. Awano, Fabrication and characterization of micro tubular SOFCs for operation in the intermediate temperature, J. Power Sources. 160 (2006)

73–77.doi:10.1016/j.jpowsour.2006.01.037.
[65] A. Dhir, K. Kendall, Microtubular SOFC anode optimisation for direct use on methane, J. Power Sources. 181 (2008) 297–303.doi:10.1016/j.jpowsour.2007.11.005.
[66] A. Dhir, Improved microtubular solid oxide fuel cells. Doctoral Thesis, University of Birmingham, 2008.
[67] A. Dhir, K. Kendall, Improving Reliability of Microtubular SOFCs for Direct Use on Methane, ECS Tran. 7 (2007) 823–828.doi:10.1149/1.2729171.
[68] K. Kendall, Progress in solid oxide fuel cell materials, Int. Mater. Rev. 50 (2005) 257.doi:10.1179/174328005X41131.
[69] Y. Fu, M.Z. Bazant, Theoretical and Experimental Study of Solid Oxide Fuel Cell (SOFC) Using Impedance Spectra. Doctoral Thesis, MASSACHUSETTS INSTITUTE OF TECHNOLOGY, 2014.
[70] J. Wu, X. Liu, Recent development of SOFC metallic interconnect, J. Mater. Sci. Technol. 26 (2010) 293–305.doi:10.1016/S1005-0302(10)60049-7.
[71] J.W. Fergus, Metallic interconnects for solid oxide fuel cells, Mater. Sci. Eng. A. 397 (2005) 271–283.doi:10.1016/j.msea.2005.02.047.
[72] M. Bianco, M. Linder, Y. Larring, F. Greco, J. Van herle, Lifetime Issues for Solid Oxide Fuel Cell Interconnects, Elsevier Ltd, 2017.doi:10.1016/B978-0-08-101102-7.00007-6.
[73] W. Kong, J. Li, S. Liu, Z. Lin, The influence of interconnect ribs on the performance of planar solid oxide fuel cell and formulae for optimal rib sizes, J. Power Sources. 204 (2012) 106–115.doi:10.1016/j.jpowsour.2012.01.041.
[74] J.W. Fergus, Lanthanum chromite-based materials for solid oxide fuel cell interconnects, Solid State Ionics. 171 (2004) 1–15.doi:10.1016/j.ssi.2004.04.010.
[75] S.P.. Badwal, J.. Zhang, Interaction between chromia forming alloy interconnects and air, Solid State Ionics. 99 (1997).doi:.doi.org/10.1016/S0167-2738(97)00247-6.
[76] L.S.S. M. Brandner, C. Bienertb, S. Megela, M. Kusnezoffa, N. Trofimenkoa, V. Sauchuka, A. Venskutonisb, W. Krausslerb, A. Michaelis, Long Term Performance of Stacks with Chromium-based Interconnects (CFY), ECS Trans. 57 (2013) 2235–2244.
[77] L. Niewolak, E. Wessel, L. Singheiser, W.J. Quadakkers, Potential suitability of ferritic and austenitic steels as interconnect materials for solid oxide fuel cells operating at 600◦C, J. Power Sources. 195 (2010) 7600–7608.doi:10.1016/j.jpowsour.2010.06.007.
[78] M. Casteel, Hybrid Materials Design For SOFC Interconnect Applications. Doctoral Thesis, Rensselaer Polytechnic Institute, 2012.
[79] J.E. Hammer, S.J. Laney, R.W. Jackson, K. Coyne, F.S. Pettit, The Oxidation of Ferritic Stainless Steels in Simulated Solid-Oxide Fuel-Cell Atmospheres, Oxid. Met. 67 (2007) 1–38.doi:10.1007/s11085-006-9041-y.
[80] P.D. Jablonski, D.E. Alman, Oxidation resistance and mechanical properties of experimental low coefficient of thermal expansion (CTE) Ni-base alloys, Int. J. Hydrogen Energy. 32 (2007) 3705–3712.doi:10.1016/j.ijhydene.2006.08.019.
[81] M. Linder, T. Hocker, L. Holzer, K.A. Friedrich, B. Iwanschitz, A. Mai, J.A. Schuler, Model-based prediction of the ohmic resistance of metallic interconnects from oxide scale growth based on scanning electron microscopy, J. Power Sources. 272 (2014) 595–605.doi:10.1016/j.jpowsour.2014.08.098.
[82] P. Blennow, J. Hjelm, T. Klemensø, S. Ramousse, A. Kromp, A. Leonide, A. Weber, Manufacturing and characterization of metal-supported solid oxide fuel cells, J. Power Sources. 196 (2011) 7117–7125.doi:10.1016/j.jpowsour.2010.08.088.
[83] F. Zhao, A. V. Virkar, Dependence of polarization in anode-supported solid oxide fuel cells on various cell parameters, J. Power Sources. 141 (2005) 79–95.doi:10.1016/j.jpowsour.2004.08.057.
[84] M. Finsterbusch, Degradation Mechanisms of Solid Oxide Fuel Cell Cathodes. Doctoral Thesis, Technische Universität Ilmenau, 2011.

[85] J. Froitzheim, S. Canovic, M. Nikumaa, R. Sachitanand, L.G. Johansson, J.E. Svensson, Long term study of Cr evaporation and high temperature corrosion behaviour of Co coated ferritic steel for solid oxide fuel cell interconnects, J. Power Sources. 220 (2012) 217–227.
[86] P. Singh, Z. Yang, V. Viswanathan, J.W. Stevenson, Observations on the Structural Degradation of Silver During Simultaneous Exposure to Oxidizing and Reducing Environments, J. Mater. Eng. Perform. 13 (2004) 287–294.doi:10.1361/10599490419261.
[87] J. Wu, C.D. Johnson, R.S. Gemmen, X. Liu, The performance of solid oxide fuel cells with Mn-Co electroplated interconnect as cathode current collector, J. Power Sources. 189 (2009) 1106–1113.doi:10.1016/j.jpowsour.2008.12.079.
[88] S. Mukerjee, K. Haltiner, R. Kerr, L. Chick, V. Sprenkle, C. Lu, J.Y. Kim, K.S. Weil, Solid Oxide Fuel Cell Development : Latest Results, ECS Trans. 7 (2007) 59–65.doi:10.1149/1.2729074.
[89] N.Q. Minh, Ceramic Fuel Cells, J. Am. Ceram. Soc. 76 (1993) 563–88.
[90] O. Aydin, H. Nakajima, T. Kitahara, Processes Involving in the Temperature Variations in Solid Oxide Fuel Cells In-Situ Analyzed through Electrode-Segmentation, 163 (2016) 216–224.doi:10.1149/2.0701603jes.
[91] C. Compson, C. Songho, H. Abermathy, Y.-M. Choi, L. Meilin, Stability and performance of silver in an SOFC interconnect environment, in: 31st Int. Conf. Adv. Ceram. Compos., 2008: pp. 301–312.
[92] N. Akhtar, S.P. Decent, K. Kendall, Structural stability of silver under single-chamber solid oxide fuel cell conditions, Int. J. Hydrogen Energy. 34 (2009) 7807–7810.doi:10.1016/j.ijhydene.2009.07.079.
[93] A.J. Majewski, A. Dhir, Application of silver in microtubular solid oxide fuel cells, Mater. Renew. Sustain. Energy. (2018) 1–13.doi:10.1007/s40243-018-0123-y.
[94] Cambridge Press, Materials Data Book, 2003 Editi, Cambridge University Engineering Department, 2003.
[95] J. Ding, X. Zhou, Q. Liu, G. Yin, Development of tubular anode-supported solid oxide fuel cell cell and 4-cell- stack based on lanthanum gallate electrolyte membrane for mobile application, J. Power Sources. 401 (2018) 336–342.doi:10.1016/j.jpowsour.2018.08.089.
[96] H. Zhu, R.J. Kee, V.M. Janardhanan, O. Deutschmann, D.G. Goodwin, Modeling Elementary Heterogeneous Chemistry and Electrochemistry in Solid-Oxide Fuel Cells, J. Electrochem. Soc. (2005).doi:10.1149/1.2116607.
[97] J. Sudagar, J. Lian, W. Sha, Electroless nickel, alloy, composite and nano coatings - A critical review, 2013.doi:https://doi.org/10.1016/j.jallcom.2013.03.107.
[98] R. Parkinson, Properties and applications of electroless nickel, Nickel Dev. Inst. 37 (1997). https://www.nickelinstitute.org/media/1769/propertiesandapplicationsofelectrolessnickel_10081_.pdf (accessed February 5, 2020).
[99] L. Curtis, Electroforming - Jewellery Handbooks, Bloomsbury Publishing PLC, n.d.
[100] P. Fan, G. Li, Y. Zeng, X. Zhang, Numerical study on thermal stresses of a planar solid oxide fuel cell, Int. J. Therm. Sci. 77 (2014) 1–10.doi:10.1016/j.ijthermalsci.2013.10.008.
[101] N. Mahato, A. Banerjee, A. Gupta, S. Omar, K. Balani, Progress in material selection for solid oxide fuel cell technology: A review, Prog. Mater. Sci. 72 (2015) 141–337.doi:10.1016/j.pmatsci.2015.01.001.
[102] J.H. Zhu, H. Ghezel-Ayagh, Cathode-side electrical contact and contact materials for solid oxide fuel cell stacking: A review, Int. J. Hydrogen Energy. 42 (2017) 24278–24300.doi:10.1016/j.ijhydene.2017.08.005.
[103] C. Lin, T. Chen, Y. Chyou, L. Chiang, Thermal stress analysis of a planar SOFC stack, J. Power Sources. 164 (2007) 238–251.doi:10.1016/j.jpowsour.2006.10.089.
[104] ThyssenKrupp, Crofer 22 APU - Material Data Sheet No. 4046, ThyssenKrupp VDM. (2010).
[105] R. Ottersted, Electrolyte for cost-effective, electrolyte-supported high-temperature fuel cell having high performance and high mechanical strength, US Patent 9,136,553 B2, 2015.

[106] Haynes International, HAYNES® 230® alloy, Data Sheet. (2020). http://haynesintl.com/docs/default-source/pdfs/new-alloy-brochures/high-temperature-alloys/brochures/230-brochure.pdf (accessed January 1, 2020).
[107] S. Linderoth, P. V. Hendriksen, M. Mogensen, N. Langvad, Investigations of metallic alloys for use as interconnects in solid oxide fuel cell stacks, J. Mater. Sci. 31 (1996) 5077–5082.doi:10.1007/BF00355908.
[108] H. Greiner, Chromium based Alloys for High Temperature SOFC Applications, ECS Proc. Vol. 1995–1 (1995) 879–888.doi:10.1149/199501.0879pv.
[109] N.M. Sammes, Y. Du, R. Bove, Design and fabrication of a 100 W anode supported micro-tubular SOFC stack, J. Power Sources. 145 (2005) 428–434.doi:10.1016/j.jpowsour.2005.01.079.
[110] The Alloys Network, Properties, Fabrication and Applications of Commercially Pure Nickel, (2020). https://www.nickel-alloys.net/article/commercially-pure-properties.html (accessed September 18, 2020).
[111] S.P. Jiang, J.G. Love, L. Apateanu, Effect of contact between electrode and current collector on the performance of solid oxide fuel cells, Solid State Ionics. 160 (2003) 15–26.doi:10.1016/S0167-2738(03)00127-9.
[112] K. Kendall, M. Kendall, K. Kendall, Portable early market SOFCs, in: High-Temperature Solid Oxide Fuel Cells 21st Century, Elsevier, London, England, 2016: pp. 329–356.
[113] A. Hornes, M. Torrell, A. Morata, M. Kendall, K. Kendall, A. Tarancon, P.H. Road, Towards a high fuel utilization and low degradation of micro-tubular solid oxide fuel cells, Int. J. Hydrogen Energy. 42 (2017) 13889–13901.doi:10.1016/j.ijhydene.2016.12.106.
[114] K. Kendall, M. Kendall, T. Kawada, T. Horita, Cathodes, in: High-Temperature Solid Oxide Fuel Cells 21st Century, 2016: pp. 161–193.
[115] J. Durango-petro, J. Usuba, H. Valle, G. Abarzua, H. Flies, R. Udayabhaskar, R. V Mangalaraja, Ascendable method for the fabrication of micro-tubular solid oxide fuel cells by ram-extrusion technique, Ceram. Int. 46 (2020) 2602–2611.doi:10.1016/j.ceramint.2019.08.252.
[116] M.A. Laguna-Bercero, H. Monzon, A. Larrea, V.M. Orera, Improved stability of reversible solid oxide cells with a nickelate-based oxygen electrode, J. Phys. Chem. A. 4 (2016) 1446–1453.doi:10.1039/c5ta08531d.
[117] M. Laguna-Bercero, H. Luebbe, J. Silva, J. Van herle, Electrochemical Performance of NdNiO Cathode supported Microtubular Solid Oxide Fuel Cells, Fuel Cells. 15 (2015) 98–104.doi:10.1002/fuce.201400071.
[118] D. Panthi, B. Choi, A. Tsutsumi, Direct methane operation of a micro-tubular solid oxide fuel cell with a porous zirconia support, J. Solid State Electrochem. (2017) 1–8.doi:10.1007/s10008-016-3366-5.
[119] D. Panthi, B. Choi, A. Tsutsumi, A Novel Micro-Tubular Solid Oxide Fuel Cell with a Porous Zirconia Support for Intermediate-Temperature Operation, ECS Trans. 68 (2015) 2259–2265.
[120] K. Zhao, B.H. Kim, Q. Xu, Y. Du, B.G. Ahn, Redox cycling performance of inert-substrate-supported tubular single cells with nickel anode current collector, J. Power Sources. 293 (2015) 336–342.doi:10.1016/j.jpowsour.2015.05.089.
[121] K. Kikuta, K. Yasue, M. Suzuki, S. Kanehira, S. Kirihara, Design and fabrication of micro close end tubular SOFC with internal conduction layer, J. Ceram. Soc. Japan. 124 (2016).
[122] T. Li, Z. Wu, K. Li, A dual-structured anode/Ni-mesh current collector hollow fibre for micro-tubular solid oxide fuel cells (SOFCs), J. Power Sources. 251 (2014) 145–151.doi:10.1016/j.jpowsour.2013.11.043.
[123] K. Kendall, M. Slinn, J. Preece, Formulating liquid ethers for microtubular SOFCs, J. Power Sources. 157 (2006) 750–753.doi:10.1016/j.jpowsour.2006.01.061.
[124] C. Liu, J. Pu, X. Chen, Z. Ma, X. Ding, J. Zhou, S. Wang, Influence of anode's microstructure on electrochemical performance of solid oxide direct carbon fuel cells, Int. J. Hydrogen Energy.

45 (2020) 11784–11790.doi:10.1016/j.ijhydene.2020.02.119.
[125] A.R. Hanifi, S. Paulson, A. Torabi, A. Shinbine, M.C. Tucker, V. Birss, T.H. Etsell, P. Sarkar, Slip-cast and hot-solution infiltrated porous yttria stabilized zirconia (YSZ) supported tubular fuel cells, J. Power Sources. 266 (2014) 121–131.doi:10.1016/j.jpowsour.2014.05.001.
[126] B. Park, R. Song, S. Lee, T. Lim, S. Park, W. Jung, J. Lee, Conformal bi-layered perovskite / spinel coating on a metallic wire network for solid oxide fuel cells via an electrodeposition-based route, J. Power Sources. 348 (2017) 40–47.doi:10.1016/j.jpowsour.2017.02.080.
[127] M.A. Laguna-Bercero, A.R. Hanifi, T.H. Etsell, P. Sarkar, V.M. Orera, Microtubular solid oxide fuel cells with lanthanum strontium manganite infiltrated cathodes, Int. J. Hydrogen Energy. 40 (2015) 5469–5474.doi:10.1016/j.ijhydene.2015.01.060.
[128] M.Z. Khan, R.H. Song, A. Hussain, S.B. Lee, T.H. Lim, J.E. Hong, Effect of applied current density on the degradation behavior of anode-supported flat-tubular solid oxide fuel cells, J. Eur. Ceram. Soc. 40 (2020) 1407–1417.doi:10.1016/j.jeurceramsoc.2019.11.017.
[129] D. Cui, Y. Ji, C. Chang, Z. Wang, X. Xiao, Influence of fuel flow rate on the performance of micro tubular solid oxide fuel cell, Int. J. Hydrogen Energy. 45 (2020) 1–10.doi:10.1016/j.ijhydene.2020.03.042.
[130] C. Chen, Y. Dong, L. Li, Z. Wang, M. Liu, B.H. Rainwater, Y. Bai, Electrochemical properties of micro-tubular intermediate temperature solid oxide fuel cell with novel asymmetric structure based on BaZr0.1Ce0.7Y0.1Yb0.1O3-δ proton conducting electrolyte, Int. J. Hydrogen Energy. 44 (2019) 16887–16897.doi:10.1016/j.ijhydene.2019.04.264.
[131] J. Banhart, Manufacture, characterisation and application of cellular metals and metal foams, Prog. Mater. Sci. 46 (2001) 559–632.doi:10.1016/S0079-6425(00)00002-5.
[132] I.-S. Lee, M.-H. Park, J.-H. Jun, C.-R. Park, B.-S. Kim, C.-W. Lee, S.-H. Choi, Cathode current collector for solid oxide fuel cell, and solid oxide fuel cell compromising same, US Patent 2017/0005345 A1, 2017.
[133] W. Huang, C. Finnerty, R. Sharp, K. Wang, B. Balili, High-Performance 3D Printed Microtubular Solid Oxide Fuel Cells, Adv. Mater. Technol. 2 (2017) 1–5.doi:10.1002/admt.201600258.
[134] L. Troskialina, A. Dhir, R. Steinberger-Wilckens, Improved Performance and Durability of Anode Supported SOFC Operating on Biogas, ECS Trans. 68 (2015) 2503–2513.
[135] X.Z. Fu, J. Melnik, Q.X. Low, J.L. Luo, K.T. Chuang, A.R. Sanger, Q.M. Yang, Surface modified Ni foam as current collector for syngas solid oxide fuel cells with perovskite anode catalyst, Int. J. Hydrogen Energy. 35 (2010) 11180–11187.doi:10.1016/j.ijhydene.2010.07.038.
[136] N. Yan, X.Z. Fu, J.L. Luo, K.T. Chuang, A.R. Sanger, Ni-P coated Ni foam as coking resistant current collector for solid oxide fuel cells fed by syngas, J. Power Sources. 198 (2012) 164–169.doi:10.1016/j.jpowsour.2011.09.068.
[137] A. Crumm, Q. Shuck, J. Rice, Solid Oxide Fuel Cell with Improved Current Collection, US Patent 8,343,689 B2, 2013.
[138] Á. Helgadóttir, S. Lalot, F. Beaubert, H. Pálsson, Mesh twisting technique for swirl induced laminar flow used to determine a desired blade shape, Appl. Sci. 8 (2018).doi:10.3390/app8101865.
[139] S. Naga Sarada, K.K. Radha, A.V.S. Raju, Experimental investigations in a circular tube to enhance turbulent heat transfer using mesh inserts, J. Eng. Appl. Sci. 4 (2009) 53–60.
[140] M. Rahimi, B. Aghel, A.A. Alsairafi, Chemical Engineering and Processing : Process Intensification Experimental and CFD studies on using coil wire insert in a proton exchange membrane fuel cell, Chem. Eng. Process. Process Intensif. 49 (2010) 688–695.doi:10.1016/j.cep.2009.11.003.
[141] R. De la Torre, V. Sglvado, Fabrication of Innovative Compliant Current Collector- Supported Microtubular Solid Oxide Fuel Cells, Int. J. Appl. Ceram. Technol. 6 (2011) 1–6.doi:10.1111/j.1744-7402.2011.02676.x.
[142] R. De La Torre, H.J. Avila-Paredes, V.M. Sglavo, Comparative performance analysis of anode-

supported micro-tubular SOFCs with different current-collection architectures, Fuel Cells. 13 (2013) 729–732.doi:10.1002/fuce.201300010.
[143] R. De la Torre García, Production of Micro-Tubular Solid Oxide Fuel Cells. Doctoral Thesis, University of Trento, 2011.
[144] M. Casarin, V.M. Sglavo, Effect of the current collector on performance of anode-supported microtubular solid oxide fuel cells, J. Fuel Cell Sci. Technol. 12 (2015) 1–6.doi:10.1115/1.4029875.
[145] A.N. Celik, Three-dimensional multiphysics model of a planar solid oxide fuel cell using computational fluid dynamics approach, Int. J. Hydrogen Energy. 43 (2018) 19730–19748.doi:10.1016/j.ijhydene.2018.08.212.
[146] D.H. Jeon, A comprehensive CFD model of anode-supported solid oxide fuel cells, Electrochim. Acta. 54 (2009) 2727–2736.doi:10.1016/j.electacta.2008.11.048.
[147] M. Navasa, C. Graves, C. Chatzichristodoulou, T. Løye, B. Sund, A three dimensional multiphysics model of a solid oxide electrochemical cell : A tool for understanding degradation, Int. J. Hydrogen Energy. 43 (2018) 11913–11931.doi:10.1016/j.ijhydene.2018.04.164.
[148] Y. Bai, C. Wang, C. Jin, J. Liu, Anode Current Collecting Efficiency of Tubular Anode-supported Solid Oxide Fuel Cells, Fuel Cells. 11 (2011) 465–468.doi:10.1002/fuce.201000053.
[149] A. Meadowcroft, K. Howe, A. Dhir, R. Steinberger-Wilckens, Connection Optimisation for Micro-Tubular Solid Oxide Fuel Cells (A1507), in: 11th Eur. SOFC SOE Forum, Lucerne Switzerland, 2014.
[150] A. Shimizu, H. Nakajima, T. Kitahara, Current Distribution Measurement of a Microtubular Solid Oxide Fuel Cell, ECS Trans. 57 (2013) 727–732.doi:10.1149/05701.0727ecst.
[151] C. Jin, J. Liu, L. Li, Y. Bai, Electrochemical properties analysis of tubular NiO–YSZ anode-supported SOFCs fabricated by the phase-inversion method, J. Memb. Sci. 341 (2009) 233–237.doi:10.1016/j.memsci.2009.06.012.
[152] C.M. Jones, J. Persky, R. Datta, Exploring Conditions That Enhance Durability and Performance of a Tubular Solid Oxide Fuel Cell Fed with Simulated Biogas, Energy Fuels. 31 (2017) 12875–12892.doi:10.1021/acs.energyfuels.7b02362.
[153] K.M. Paciejewska, Y. Yu, S. Kühn, A. Weber, M. Kleber, Adjustment of GDC layer microstructure and its influence on the electrochemical properties of microtubular SOFCs, J. Ceram. Soc. Japan. 123 (2015) 171–177.
[154] M.A. Morales-Zapata, A. Larrea, M.A. Laguna-Bercero, Reversible operation performance of microtubular solid oxide cells with a nickelate-based oxygen electrode, Int. J. Hydrogen Energy. 45 (2020) 5535–5542.doi:10.1016/j.ijhydene.2019.05.122.
[155] R.J. Milcarek, H. Nakamura, T. Tezuka, K. Maruta, J. Ahn, Investigation of microcombustion reforming of ethane/air and micro-Tubular Solid Oxide Fuel Cells, J. Power Sources. 450 (2020) 227606.doi:10.1016/j.jpowsour.2019.227606.
[156] R.J. Milcarek, H. Nakamura, T. Tezuka, K. Maruta, J. Ahn, Microcombustion for micro-tubular flame-assisted fuel cell power and heat cogeneration, J. Power Sources. 413 (2019) 191–197.doi:10.1016/j.jpowsour.2018.12.043.
[157] A.M. Soydan, O. Omer Yıldız, Abdullatif Dur gun, A.A. Yagız Akduman, Production, performance and cost analysis of anode-supported NiO-YSZ micro-tubular SOFCs, Int. J. Hydrog. Energ Y. 4 (2019) 1–9.doi:10.1016/j.ijhydene.2019.09.156.
[158] R.J. Milcarek, M.J. Garrett, K. Wang, J. Ahn, Micro-tubular flame-assisted fuel cells running methane, Int. J. Hydrogen Energy. 41 (2016) 20670–20679.doi:10.1016/j.ijhydene.2016.08.155.
[159] H. Monzón, M.A. Laguna-Bercero, Highly stable microtubular cells for portable solid oxide fuel cell applications, Electrochim. Acta. 222 (2016) 1622–1627.doi:10.1016/j.electacta.2016.11.150.

[160] Ö. Aydin, T. Koshiyama, H. Nakajima, T. Kitahara, In-situ diagnosis and assessment of longitudinal current variation by electrode-segmentation method in anode-supported microtubular solid oxide fuel cells, J. Power Sources. 279 (2015) 218–223.doi:10.1016/j.jpowsour.2014.12.156.
[161] R.J. Milcarek, J. Ahn, Micro-tubular flame-assisted fuel cells running methane , propane and butane : On soot , efficiency and power density, Energy. 169 (2019) 776–782.doi:10.1016/j.energy.2018.12.098.
[162] S. Vafaeenezhad, N.K. Sandhu, A.R. Hanifi, T.H. Etsell, P. Sarkar, Development of proton conducting fuel cells using nickel metal support, J. Power Sources. 435 (2019) 226763.doi:10.1016/j.jpowsour.2019.226763.
[163] C. Chen, Y. Dong, L. Li, Z. Wang, M. Liu, B.H. Rainwater, High performance of anode supported BaZr0.1Ce0.7Y0.1Yb0.1O3-δ proton- conducting electrolyte micro-tubular cells with asymmetric structure for IT- SOFCs, J. Electroanal. Chem. 844 (2019) 49–57.doi:10.1016/j.jelechem.2019.05.001.
[164] Y. Dong, C. Chen, M. Liu, B.H. Rainwater, Y. Bai, Enhancement of Electrochemical Properties, Impedance and Resistances of Micro-tubular IT-SOFCs with Novel Asymmetric Structure Based on Conducting Electrolyte, Fuel Cells. 20 (2020) 70–79.doi:10.1002/fuce.201900130.
[165] D. Panthi, Y. Du, Tubular solid oxide fuel cells fabricated by a novel freeze casting method, J. Am. Ceram. Soc. 1 (2019) 1–11.doi:10.1111/jace.16781.
[166] M.J. López-Robledo, M.A. Laguna-Bercero, A. Larrea, V.M. Orera, Reversible operation of microtubular solid oxide cells using La0.6Sr0.4Co0.2Fe0.8O3-Δ-Ce0.9Gd0.1O2-Δ oxygen electrodes, J. Power Sources. 378 (2018) 184–189.doi:10.1016/j.jpowsour.2017.12.035.
[167] Y.-X. Liu, S.-F. Wang, Y.-F. Hsu, P. Jasinski, Characteristics of La0.8Sr0.2Ga0.8Mg0.2O3-δ-supported micro-tubular solid oxide fuel cells with LaCo0.4Ni0.6-xCuxO3-δ cathodes, Int. J. Hydrogen Energy. (2018).doi:10.1016/j.ijhydene.2018.01.170.
[168] H. Yoon, T. Kim, S. Park, N. Mark, Stable LSM / LSTM bi-layer interconnect for flat-tubular solid oxide fuel cells, Int. J. Hydrogen Energy. 43 (2017) 363–372.doi:10.1016/j.ijhydene.2017.11.024.
[169] M.J. López-Robledo, M.A. Laguna-Bercero, J. Silva, V.M. Orera, A. Larrea, Electrochemical performance of intermediate temperature micro-tubular solid oxide fuel cells using porous ceria barrier layers, Ceram. Int. 41 (2015) 7651–7660.doi:10.1016/j.ceramint.2015.02.093.
[170] S.Y. Park, J.H. Ahn, C.W. Jeong, C.W. Na, R.H. Song, J.H. Lee, Ni-YSZ-supported tubular solid oxide fuel cells with GDC interlayer between YSZ electrolyte and LSCF cathode, Int. J. Hydrogen Energy. 39 (2014) 12894–12903.doi:10.1016/j.ijhydene.2014.06.103.
[171] D. Panthi, A. Tsutsumi, Micro-tubular solid oxide fuel cell based on a porous yttria-stabilized zirconia support, Sci. Rep. 4 (2014) 1–6.doi:10.1038/srep05754.
[172] M.A. Laguna-Bercero, A.R. Hanifi, H. Monzón, J. Cunningham, T.H. Etsell, P. Sarkar, High performance of microtubular solid oxide fuel cells using Nd 2NiO4+δ-based composite cathodes, J. Mater. Chem. A. 2 (2014) 9764–9770.doi:10.1039/c4ta00665h.
[173] A. Slodczyk, M. Torrell, A. Hornés, A. Morata, K. Kendall, A. Tarancón, Understanding longitudinal degradation mechanisms of large-area micro-tubular solid oxide fuel cells, Electrochim. Acta. 265 (2018) 232–243.doi:10.1016/j.electacta.2018.01.184.
[174] A.F. Omar, M.H.D. Othman, C.N. Gunaedi, S.M. Jamil, M.H. Mohamed, J. Jaafar, M.A. Rahman, A.F. Ismail, Performance analysis of hollow fibre-based micro-tubular solid oxide fuel cell utilising methane fuel, Int. J. Hydrogen Energy. 44 (2019) 30754–30762.doi:10.1016/j.ijhydene.2018.03.107.
[175] Z. Tan, T. Ishihara, Reversible Operation of Tubular Type Solid Oxide Fuel Cells Using LaGaO3 Electrolyte Porous Layer on Dense Film Prepared by Dip-Coating Method, J. Electrochem. Soc. 164 (2017) 1690–1696.doi:10.1149/2.1491714jes.
[176] Z. Tan, T. Ishihara, Sr(La)TiO3 Anode Substrate for Low Ni Diffusion in Sr- and Mg-Doped

LaGaO3 Film Prepared with Co-Sintering Method for Intermediate Temperature Tubular Type Solid Oxide Fuel Cells, J. Electrochem. Soc. 164 (2017) 815–820.doi:10.1149/2.0821707jes.
[177] A. Murat, O. Yagiz, A. Durgun, Evaluation of the sintering regime on the mechanical and physical properties of the NiO e YSZ anode support tubes, Int. J. Hydrogen Energy. 42 (2017) 26933–26942.doi:10.1016/j.ijhydene.2017.06.022.
[178] A.D. A. J. Majewski, Direct Utilization of Methane in Microtubular-SOFC, Electrochem. Soc. Direct. 68 (2015) 2189–2198.
[179] M. Torrell, A. Morata, P. Kayser, M. Kendall, K. Kendall, Performance and long term degradation of 7 W micro-tubular solid oxide fuel cells for portable applications, J. Power Sources J. 285 (2015) 439–448.doi:10.1016/j.jpowsour.2015.03.030.
[180] W. Huang, C. Finnerty, K. Wang, R. Sharp, B. Balili, Operation of micro tubular solid oxide fuel cells integrated with propane reformers, Int. J. Hydrogen Energy. 44 (2019).doi:10.1016/j.ijhydene.2019.10.061.
[181] M. Morales, M.A. Laguna-bercero, Influence of Anode Functional Layers on Electrochemical Performance and Mechanical Strength in Microtubular Solid Oxide Fuel Cells Fabricated by Gel-casting, ACS Appl. Energy Mater. 1 (2018) 2024–2031.doi:doi.org/10.1021/acsaem.8b00115.
[182] H. Sumi, T. Yamaguchi, H. Shimada, Y. Fujishiro, M. Awano, Development of a Portable SOFC System with Internal Partial Oxidation Reforming of Butane and Steam Reforming of Ethanol, ECS Trans. 80 (2017).
[183] H. Sumi, T. Yamaguchi, T. Suzuki, H. Shimada, K. Hamamoto, Y. Fujishiro, Development of Micro Power Generator Using LPG-Fueled Microtubular Solid Oxide Fuel Cells, ECS Trans. 68 (2015) 201–208.doi:10.1149/06801.0201ecst.
[184] H. Sumi, S. Nakabayashi, T. Kawada, Y. Uchiyama, N. Uchiyama, K. Ichihara, Demonstration of SOFC Power Sources for Drones (UAVs; Unmanned Aerial Vehicles), ECS Trans. 91 (2019) 149–157.doi:10.1149/09101.0149ecst.
[185] T.I. Z. Tan, A. Takagakia, Infiltration of Rare Earth Oxide into NiO-YSZ Anode Substrate for the High Performance Micro-tubular SOFC Using LSGM Electrolyte film, ECS Trans. 91 (2019) 1807–1814.doi:10.1149/09101.1807ecst.
[186] S. Jamil, M. Hilmi, M. Ridhwan, M.A. Rahman, J. Jaafar, A. Fauzi, A novel single-step fabrication anode / electrolyte / cathode triple-layer hollow fiber micro-tubular SOFC, Int. J. Hydrogen Energy. 43 (2018) 18509–18515.doi:10.1016/j.ijhydene.2018.08.010.
[187] H. Sumi, T. Yamaguchi, H. Shimada, K. Hamamoto, T. Suzuki, S.A. Barnett, Direct Butane Utilization on Ni-(Y2O3)0.08(ZrO2)0.92-(Ce0.9Gd0.1)O1.95 Composite Anode-Supported Microtubular Solid Oxide Fuel Cells, Electrocatalysis. 8 (2017) 288–293.doi:10.1007/s12678-017-0369-7.
[188] S. Shimizu, T. Yamaguchi, T. Suzuki, Y. Fujishiro, Fabrication and Properties of Honeycomb-type SOFCs Accumulated with Multi Micro-cells, ECS Trans. 7 (2007) 651–656.doi:10.1149/1.2729149.
[189] S. Jamil, M. Ha, D. Othman, M.A. Rahman, J. Jaafar, A. Fauzi, S. Honda, Y. Iwamoto, Properties and performance evaluation of dual-layer ceramic hollow fiber with modified electrolyte for MT-SOFC, Renew. Energy. 134 (2019).doi:10.1016/j.renene.2018.09.071.
[190] S. Jamil, M. Hafiz, D. Othman, M.A. Rahman, J. Jaafar, A. Fauzi, Anode supported micro-tubular SOFC fabricated with mixed particle size electrolyte via phase- inversion technique, Int. J. Hydrogen Energy. 42 (2016) 9188–9201.doi:10.1016/j.ijhydene.2016.05.016.
[191] Y. Wang, Y. Shi, N. Cai, X. Ye, S. Wang, Performance Characteristics of a Micro-tubular Solid Oxide Fuel Cell Operated with a Fuel-rich Methane Flame, ECS Trans. 68 (2015) 2237–2243.doi:10.1149/06801.2237ecst.
[192] K.N. Grew, W.K.S. Chiu, A review of modeling and simulation techniques across the length scales for the solid oxide fuel cell, J. Power Sources. 199 (2012) 1–

13.doi:10.1016/j.jpowsour.2011.10.010.
[193] R.J. Boersma, N.M. Sammes, C.J. Fee, Losses resulting from in-plane electricity conduction in tubular solid oxide fuel cells, Solid State Ionics. 135 (2000) 493–502.
[194] H. Zhu, R.J. Kee, The influence of current collection on the performance of tubular anode-supported SOFC cells, J. Power Sources. 169 (2007) 315–326.doi:10.1016/j.jpowsour.2007.03.047.
[195] D. Chen, Y. Xu, B. Hu, C. Yan, L. Lu, Investigation of proper external air flow path for tubular fuel cell stacks with an anode support feature, Energy Convers. Manag. 171 (2018) 807–814.doi:10.1016/j.enconman.2018.06.036.
[196] A. Mohammadzadeh, S. Kiana, N. Zadeh, M.H. Saidi, M. Sharifzadeh, Chapter 3. Mechanical engineering of solid oxide fuel cell systems: geometric design, mechanical configuration, and thermal analysis, Elsevier Inc., 2020.doi:10.1016/B978-0-12-815253-9.00003-3.
[197] K.S. Howe, G.J. Thompson, K. Kendall, Micro-tubular solid oxide fuel cells and stacks, J. Power Sources. 196 (2011) 1677–1686.doi:10.1016/j.jpowsour.2010.09.043.
[198] W. Zimmerman, Process Modelling and Simulation with Finite Element Methods, World Scientific Publishing, Sheffileld, UK, 2004.
[199] M. Peksen, L. Blum, D. Stolten, A 3D CFD model for predicting the temperature distribution in a full scale APU SOFC short stack under transient operating conditions, Appl. Energy. 135 (2014) 539–547.doi:10.1016/j.apenergy.2014.08.052.
[200] D. Bhattacharyya, R. Rengaswamy, A Review of Solid Oxide Fuel Cell (SOFC) Dynamic Models, Ind. Eng. Chem. Res. 48 (2009) 6068–6086.
[201] R. Pryor, Multiphysics modeling using COMSOL: A first principles approach, Jones and Bartlett Publishers, 2009.doi:10.1109/MCSE.2005.51.
[202] V. Lawlor, S. Griesser, G. Buchinger, A.G. Olabi, S. Cordiner, D. Meissner, Review of the micro-tubular solid oxide fuel cell Part I . Stack design issues and research activities, J. Power Sources. 193 (2009) 387–399.doi:10.1016/j.jpowsour.2009.02.085.
[203] M. Peksen, 3D transient multiphysics modelling of a complete high temperature fuel cell system using coupled CFD and FEM, Int. J. Hydrogen Energy. 39 (2014) 5137–5147.doi:10.1016/j.ijhydene.2014.01.063.
[204] J.W. Norman F. Bessette II, William J. Wepfer, A Mathematical Model of a Solid Oxide Fuel Cell, J. Electrochem. Soc. 142 (1995) 3792–3800.
[205] A. V. Virkar, F.F. Lange, M.A. Homel, A simple analysis of current collection in tubular solid oxide fuel cells, J. Power Sources. 195 (2010) 4816–4825.doi:10.1016/j.jpowsour.2010.02.041.
[206] K. Wang, D. Hissel, M.C. Pera, N. Steiner, D. Marra, M. Sorrentino, C. Pianese, M. Monteverde, P. Cardone, J. Saarinen, A Review on solid oxide fuel cell models, Int. J. Hydrogen Energy. 36 (2011) 7212–7228.doi:10.1016/j.ijhydene.2011.03.051.
[207] P. Li, K. Suzuki, Numerical Modeling and Performance Study of a Tubular SOFC, J. Electrochem. Soc. (2004) 548–557.doi:10.1149/1.1647569.
[208] R.J. Kee, B.L. Kee, J.L. Martin, Radiative and convective heat transport within tubular solid-oxide, J. Power Sources. 195 (2010) 6688–6698.doi:10.1016/j.jpowsour.2010.04.010.
[209] M. Zeng, J. Yuan, J. Zhang, B. Sundén, Q. Wang, Investigation of thermal radiation effects on solid oxide fuel cell performance by a comprehensive model, J. Power Sources. 206 (2012) 185–196.doi:10.1016/j.jpowsour.2012.01.130.
[210] F. Calise, M. Dentice d'Accadia, G. Restuccia, Simulation of a tubular solid oxide fuel cell through finite volume analysis: Effects of the radiative heat transfer and exergy analysis, Int. J. Hydrogen Energy. 32 (2007) 4575–4590.doi:10.1016/j.ijhydene.2007.05.040.
[211] S. Kakaç, A. Pramuanjaroenkij, X.Y. Zhou, A review of numerical modeling of solid oxide fuel cells, Int. J. Hydrogen Energy. 32 (2007) 761–786.doi:10.1016/j.ijhydene.2006.11.028.
[212] S.A. Hajimolana, M.A. Hussain, M. Soroush, W.M.A. Wan Daud, M.H. Chakrabarti, Modeling of a tubular-SOFC: The effect of the thermal radiation of fuel components and coparticipating in

the electrochemical process, Fuel Cells. 12 (2012).doi:10.1002/fuce.20120005.
[213] A. Bertei, J. Mertens, C. Nicolella, Electrochemical Simulation of Planar Solid Oxide Fuel Cells with Detailed Microstructural Modeling, Electrochim. Acta. 146 (2014) 151–163.doi:10.1016/j.electacta.2014.08.120.
[214] A. Bertei, C. Nicolella, Common inconsistencies in modeling gas transport in porous electrodes : The dusty-gas model and the Fick law, J. Power Sources. 279 (2015) 133–137.doi:10.1016/j.jpowsour.2015.01.007.
[215] X. Lu, O.O. Taiwo, A. Bertei, T. Li, K. Li, D.J.L. Brett, P.R. Shearing, Multi-length scale tomography for the determination and optimization of the effective microstructural properties in novel hierarchical solid oxide fuel cell anodes, J. Power Sources. 367 (2017) 177–186.doi:10.1016/j.jpowsour.2017.09.017.
[216] A. Bertei, V. Yu, F. Tariq, N.P. Brandon, A novel approach for the quantification of inhomogeneous 3D current distribution in fuel cell electrodes A novel approach for the quantification of inhomogeneous 3D current distribution in fuel cell electrodes, J. Power Sources. 396 (2018) 246–256.doi:10.1016/j.jpowsour.2018.06.029.
[217] F. Tariq, E. Ruiz-trejo, A. Bertei, P. Boldrin, N.P. Brandon, Microstructural Degradation : Mechanisms , Quantification , Modeling and Design Strategies to Enhance the Durability of Solid Oxide Fuel Cell Electrodes, Elsevier Ltd, 2017.doi:10.1016/B978-0-08-101102-7.00005-2.
[218] R. Suwanwarangkul, E. Croiset, M.W. Fowler, P.L. Douglas, E. Entchev, M.A. Douglas, Performance comparison of Fick ' s , dusty-gas and Stefan – Maxwell models to predict the concentration overpotential of a SOFC anode, J. Power Sources. 122 (2003) 9–18.doi:10.1016/S0378-7753(02)00724-3.
[219] H. Yakabe, M. Hishinuma, M. Uratani, Y. Matsuzaki, I. Yasuda, Evaluation and modeling of performance of anode-supported solid oxide fuel cell, J. Power Sources. 86 (2000) 423–431.doi:10.1016/S0378-7753(99)00444-9.
[220] D. Bhattacharyya, R. Rengaswamy, C. Finnerty, Dynamic modeling and validation studies of a tubular solid oxide fuel cell, Chem. Eng. Sci. 64 (2009) 2158–2172.doi:10.1016/j.ces.2008.12.040.
[221] D. Bhattacharyya, R. Rengaswamy, C. Finnerty, Isothermal models for anode-supported tubular solid oxide fuel cells, Chem. Eng. Sci. 62 (2007) 4250–4267.doi:10.1016/j.ces.2007.04.020.
[222] U. Pasaogullari, C. Wang, Computational Fluid Dynamics Modeling of Solid Oxide Fuel Cells, Electrochem. Soc. Proc. 7 (2003) 1403–1412.doi:10.1243/095765005X7583.
[223] W. Kong, H. Zhu, Z. Fei, Z. Lin, A modified dusty gas model in the form of a Fick ' s model for the prediction of multicomponent mass transport in a solid oxide fuel cell anode, J. Power Sources. 206 (2012) 171–178.doi:10.1016/j.jpowsour.2012.01.107.
[224] T. Suzuki, T. Yamaguchi, Y. Fujishiro, M. Awano, Current collecting efficiency of micro tubular SOFCs, J. Power Sources. 163 (2007) 737–742.doi:10.1016/j.jpowsour.2006.09.071.
[225] T. Suzuki, Y. Funahashi, T. Yamaguchi, Anode-supported micro tubular SOFCs for advanced ceramic reactor system, J. Power Sources. 171 (2007) 92–95.doi:10.1016/j.jpowsour.2007.01.003.
[226] D. Cui, L. Liu, Y. Dong, M. Cheng, Comparison of different current collecting modes of anode supported micro-tubular SOFC through mathematical modeling, J. Power Sources. 174 (2007) 246–254.doi:10.1016/j.jpowsour.2007.08.094.
[227] D. Cui, M. Cheng, Numerical Analysis of Thermal and Electrochemical Phenomena for Anode Supported Microtubular SOFC, Mater. INTERFACES, Electrochem. Phenom. 55 (2009).doi:10.1002/aic.
[228] J. Otomo, J. Oishi, K. Miyazaki, S. Okamura, K. Yamada, Coupled analysis of performance and costs of segmented-in-series tubular solid oxide fuel cell for combined cycle system, Int. J. Hydrogen Energy. 42 (2017) 19190–19203.doi:10.1016/j.ijhydene.2017.06.031.

[229] X. Lu, A. Bertei, T.M.M. Heenan, Y. Wu, D. Jl, P.R. Shearing, Multi-length scale microstructural design of micro-tubular Solid Oxide Fuel Cells for optimised power density and mechanical robustness, J. Power Sources. 434 (2019) 226744.doi:10.1016/j.jpowsour.2019.226744.
[230] S. Amiri, R.E. Hayes, P. Sarkar, Transient simulation of a tubular micro-solid oxide fuel cell, J. Power Sources. 407 (2018) 63–69.doi:10.1016/j.jpowsour.2018.10.062.
[231] X. Jin, M. Guo, R.E. White, K. Huang, Computational Analysis of Dynamic Tubular SOFC with a Built-in Chemical Iron Bed, ECS Trans. 78 (2017) 2683–2698.
[232] Ö. Aydin, H. Nakajima, T. Kitahara, Reliability of the numerical SOFC models for estimating the spatial current and temperature variations, Int. J. Hydrogen Energy. 41 (2016) 15311–15324.doi:10.1016/j.ijhydene.2016.06.194.
[233] D. Cui, B. Tu, M. Cheng, Effects of cell geometries on performance of tubular solid oxide fuel cell, J. Power Sources. 297 (2015) 419–426.doi:10.1016/j.jpowsour.2015.08.013.
[234] D. Cui, M. Cheng, Design for segmented-in-series solid oxide fuel cell through mathematical modeling, J. Power Sources. 195 (2010) 1435–1440.doi:10.1016/j.jpowsour.2009.09.020.
[235] M.F. Serincan, U. Pasaogullari, N.M. Sammes, Effects of operating conditions on the performance of a micro-tubular solid oxide fuel cell (SOFC), J. Power Sources. 192 (2009) 414–422.doi:10.1016/j.jpowsour.2009.03.049.
[236] H. Feng, L. Chen, Z. Xie, F. Sun, Constructal optimization for a single tubular solid oxide fuel cell, J. Power Sources. 286 (2015) 406–413.doi:10.1016/j.jpowsour.2015.03.162.
[237] H. Sumi, T. Yamaguchi, K. Hamamoto, T. Suzuki, Y. Fujishiro, Experimental and Simulated Evaluations of Current Collection Losses in Anode-Supported Microtubular Solid Oxide Fuel Cells, J. Electrochem. Soc. 160 (2013) 1232–1236.doi:10.1149/2.031311jes.
[238] T. Suzuki, Y. Funahashi, T. Yamaguchi, Y. Fujishiro, M. Awano, Y. Funahcishi, T. Yamaguchi, Y. Fujishiro, M. Awano, New stack design of micro-tubular SOFCs for portable power sources, Fuel Cells. 8 (2008) 381–384.doi:10.1002/fuce.200800047.
[239] A.G. Sabato, G. Cempura, D. Montinaro, A. Chrysanthou, M. Salvo, E. Bernardo, M. Secco, F. Smeacetto, Glass-ceramic sealant for solid oxide fuel cells application: Characterization and performance in dual atmosphere, J. Power Sources. 328 (2016) 262–270.doi:10.1016/j.jpowsour.2016.08.010.
[240] T. Yamaguchi, S. Shimizu, T. Suzuki, Y. Fujishiro, M. Awano, Fabrication and evaluation of a novel cathode-supported honeycomb SOFC stack, Mater. Lett. 63 (2009) 2577–2580.doi:10.1016/j.matlet.2009.09.009.
[241] J. Ding, J. Liu, A novel design and performance of cone-shaped tubular anode-supported segmented-in-series solid oxide fuel cell stack, J. Power Sources. 193 (2009) 769–773.doi:10.1016/j.jpowsour.2009.04.049.
[242] K.S. Weil, B.J. Koeppel, Comparative finite element analysis of the stress – strain states in three different bonded solid oxide fuel cell seal designs, J. Power Sources. 180 (2008) 343–353.doi:10.1016/j.jpowsour.2008.01.093.
[243] C. Chao, C. Chu, Y. Fuh, R. Hsu, S. Lee, Y. Cheng, Joint strength of Ag – 9Pd – 9Ga brazed interconnect and anode-supported electrolyte for solid-oxide fuel cell applications, J Mater. Des. Appl. 0 (2016) 1–12.doi:10.1177/1464420716647077.
[244] J.H. Kim, R.H. Song, D.R. Shin, Joning of metallic cap and anode-supported tubular solid oxide fuel cell by induction brazing process, J. Fuel Cell Sci. Technol. 6 (2009) 0310121–0310126.doi:10.1115/1.3006344.
[245] L. Correas, V.M. Orera, Long-Term Stability Studies of Anode- Supported Microtubular Solid Oxide Fuel, Fuel Cells. 13 (2013) 1116–1122.doi:10.1002/fuce.201300063.
[246] T. Zhang, Q. Zou, J. Zhang, D. Tang, H. Yang, Development of ceramic sealant for solid oxide fuel cell application: Self-healing property, mechanical stability and thermal stability, J. Power Sources. 204 (2012) 122–126.doi:10.1016/j.jpowsour.2012.01.022.
[247] A. Meadowcroft, S.R. Howroyd, K. Kendall, M. Kendall, Testing microtubular SOFCs in

unmanned air vehicles (UAVs), ECS Trans. 57 (2013) 451–457.doi:10.1149/05701.0451ecst.
[248] T. Alston, K. Kendall, M. Palin, M. Prica, P. Windibank, A 1000-cell SOFC reactor for domestic cogeneration, J. Power Sources. 71 (1998) 271–274.
[249] A. Meadowcroft, K. Gulia, K. Kendall, 3D Printing and Prototyping Manifolds for Microtubular Solid Oxide Fuel Cells (mSOFCs), Int. J. Sci. Res. 4 (2015) 709–712.doi:10.21275/v4i11.nov151168.
[250] N.M. Sammes, R. Bove, Y. Du, Assembling Single Cells to Create a Stack : The Case of a 100 W Microtubular Anode-Supported Solid Oxide Fuel Cell Stack, J. Mater. Eng. Perform. 15 (2006) 463–467.doi:10.1361/105994906X117314.
[251] T. Suzuki, Y. Funahashi, T. Yamaguchi, Cube-type micro SOFC stacks using sub-millimeter tubular SOFCs, J. Power Sources. 183 (2008) 544–550.doi:10.1016/j.jpowsour.2008.05.026.
[252] T. Suzuki, Y. Funahashi, T. Yamaguchi, Y. Fujishiro, M. Awano, Fabrication and characterization of micro tubular SOFCs for advanced ceramic reactors, J. Alloys Compd. 451 (2008) 632–635.doi:10.1016/j.jallcom.2007.04.149.
[253] M.A. T. Suzuki, Y. Funahashi, T. Yamaguchi, Y. Fujishiro, Fabrication of Micro-Tubular SOFC Stack Using Ceramic Manifold, ECS Trans. 7 (2007) 477–482.
[254] T. Suzuki, Y. Funahashi, T. Yamaguchi, Y. Fujishiro, M. Awano, Effect of the Fuel Flow Rate on the Performance of the Chip-Type SOFC Module, J. Electrochem. Soc. 155 (2008) B1296.doi:10.1149/1.2990722.
[255] M. Mehran, S. Park, J. Kim, J. Hong, S. Lee, S. Park, R. Song, Performance characteristics of a robust and compact propane-fueled 150 W-class SOFC power-generation system, Int. J. Hydrogen Energy. 44 (2019) 6160–6171.doi:10.1016/j.ijhydene.2019.01.076.
[256] U. Mushtaq, M. Taqi, S. Kim, T. Lim, S. Asad, A. Naqvi, J. Lee, S. Lee, S. Park, R. Song, Evaluation of steady-state characteristics for solid oxide carbon fuel cell short-stacks, Appl. Energy. 187 (2017) 886–898.doi:10.1016/j.apenergy.2016.11.015.
[257] J.E. Hong, M. Usman, S.B. Lee, R.H. Song, T.H. Lim, Thermally self-sustaining operation of tubular solid oxide fuel cells integrated with a hybrid partial oxidation reformer using propane, Energy Convers. Manag. 189 (2019) 132–142.doi:10.1016/j.enconman.2019.04.001.
[258] M.K. K. Kendall, J. Newton, Adelan, Microtubular SOFC (mSOFC) System in Truck APU Application, Electrochem. Soc. 68 (2015) 187–192.doi:10.1149/06801.0187ecst.
[259] K. Kendall, B. Liang, M. Kendall, Microtubular SOFC (mSOFC) System in Mobile Robot Applications, ECS Trans. 78 (2017) 237–242.doi:10.1149/07801.0237ecst.
[260] N. Watanabe, T. Ooe, T. Ishihara, Design of thermal self supported 700 W class, solid oxide fuel cell module using, LSGM thin film micro tubular cells, J. Power Sources. 199 (2012) 117–123.doi:10.1016/j.jpowsour.2011.10.071.
[261] S.-B. Lee, T.-H. Lim, R.-H. Song, D.-R. Shin, S.-K. Dong, Development of a 700 W anode-supported micro-tubular SOFC stack for APU applications, Int. J. Hydrogen Energy. (2008).doi:10.1016/j.ijhydene.2008.02.034.
[262] R.J. Milcarek, V.P. DeBiase, J. Ahn, Investigation of startup, performance and cycling of a residential furnace integrated with micro-tubular flame-assisted fuel cells for micro-combined heat and power, Energy. 196 (2020) 117148.doi:10.1016/j.energy.2020.117148.
[263] H. Zeng, S. Gong, Y. Shi, Y. Wang, N. Cai, Micro-tubular solid oxide fuel cell stack operated with catalytically enhanced porous media fuel-rich combustor, Energy. 179 (2019) 154–162.doi:10.1016/j.energy.2019.04.125.
[264] R.J. Milcarek, M.J. Garrett, T.S. Welles, J. Ahn, Performance investigation of a micro-tubular flame-assisted fuel cell stack with 3000 rapid thermal cycles, J. Power Sources. 394 (2018) 86–93.doi:10.1016/j.jpowsour.2018.05.060.
[265] R.J. Milcarek, M.J. Garrett, J. Ahn, Micro-tubular flame-assisted fuel cell stacks, Int. J. Hydrogen Energy. 41 (2016) 21489–21496.doi:10.1016/j.ijhydene.2016.09.005.
[266] H.K. Jung, J.-E. Hong, Preliminary Results on a 5W Portable Butane MT-SOFC Stack As a

Battery Charger, Electrochem. Soc. (2015).doi:https://doi.org/10.1149/MA2015-03/1/40.
[267] T.S. and Y.F. Hirofumi Sumi, Toshiaki Yamaguchi, Koichi Hamamoto, Development of Portable SOFC System Using Microtubular Cells, ECS Trans. 56 (2014) 63–69.doi:https://doi.org/10.1149/05601.0063ecst.
[268] X.F. Ye, C. Yuan, Y.P. Chen, C.Y. Zhong, Z.L. Zhan, S.R. Wang, Micro-tubular Solid Oxide Fuel Cells and Their Stacks Running on Direct Ethanol Fuels, ECS Trans. 57 (2013) 351–358.
[269] A.M. Ferriz, M.A. Laguna-Bercero, M. Ruperez, J. Mora, L.C. Correas, Modelling and performance of a microtubular YSZ-based anode supported solid oxide fuel cell stack and power module, Energy Procedia. 29 (2012) 166–176.doi:10.1016/j.egypro.2012.09.021.
[270] Y.F. T. Yamaguchi, H. Sumi, T. Suzuki, Fabrication and Evaluation of Micro-Tubular SOFC Stack, ECS Trans. 45 (2012) 531–534.doi:https://doi.org/10.1149/1.3701345.
[271] T. Suzuki, Y. Funahashi, T. Yamaguchi, Y. Fujishiro, M. Awano, Performance of the Micro-SOFC Module Using Submillimeter Tubular Cells, J. Electrochem. Soc. 156 (2009) B318.doi:10.1149/1.3046159.
[272] Y. Funahashi, T. Shimamori, T. Suzuki, Y. Fujishiro, M. Awano, New Fabrication Technique for Series- Connected Stack With Micro Tubular SOFCs, Fuel Cells. 9 (2009) 711–716.doi:10.1002/fuce.200900004.
[273] M. Lockett, M.J.H. Simmons, K. Kendall, CFD to predict temperature profile for scale up of micro-tubular SOFC stacks, J. Power Sources. 131 (2004) 243–246.doi:10.1016/j.jpowsour.2003.11.082.
[274] B. Hari, J.P. Brouwer, A. Dhir, R. Steinberger-Wilckens, A computational fluid dynamics and finite element analysis design of a microtubular solid oxide fuel cell stack for fixed wing mini unmanned aerial vehicles, Int. J. Hydrogen Energy. 44 (2019) 8519–8532.doi:10.1016/j.ijhydene.2019.01.170.
[275] B. Hari, A. Dhir, R. Steinberger-Wilckens, A Thermo Fluid and Thermo Mechanical Modelling of a Microtubular Solid Oxide Fuel Cell Stack for Unmanned Aerial Vehicles, ECS Trans. 68 (2015) 3133–3141.doi:10.1149/06801.3133ecst.
[276] P. Pianko-Oprych, T. Zinko, Z. Jaworski, Numerical analysis of thermal stresses in a new design of microtubular stack, Open Chem. 13 (2015) 1045–1062.doi:10.1515/chem-2015-0116.
[277] P. Pianko-Oprych, Z. Jaworski, T. Zinko, M. Palus, A review of the numerical studies on planar and tubular solid oxide fuel cells within four EU projects of the 7th framework programme, Chem. Process Eng. - Inz. Chem. I Proces. 39 (2018) 377–393.doi:10.24425/122958.
[278] M. Hering, J. Brouwer, W. Winkler, Dynamic model of a micro-tubular solid oxide fuel cell stack including an integrated cooling system, J. Power Sources. 342 (2017) 504–514.doi:10.1016/j.jpowsour.2016.11.070.
[279] M. Hering, J. Brouwer, W. Winkler, Evaluation and optimization of a micro-tubular solid oxide fuel cell stack model including an integrated cooling system, J. Power Sources. 303 (2016) 10–16.doi:10.1016/j.jpowsour.2015.09.036.
[280] K. Howe, Design Improvements of Micro-Tubular Solid Oxide Fuel Cells for Unmanned Aircraft Applications. Doctoral Thesis, University of Birmingham, 2013.
[281] Aremco, Aremco Ceramabond ™ 552 High Temperature Ceramic Adhesive/Paste, Alumina Filled, (2019). http://www.matweb.com/search/datasheet.aspx?matguid=e6b75c1c0a4f46ec8a4f3bff3bc828e3&ckck=1 (accessed September 1, 2020).
[282] Shanghai Research Insititute of Synthetic Resins Co.,LTD. Certificate of Analysis -Y02018008 DAD-87 COA, (2018).
[283] SPI, PROPERTIES AND TECHNICAL NOTES, (2019) 1–4. https://www.2spi.com/catalog/documents/5001-5002-AB_Silver_Paint-v2.pdf (accessed March 24, 2020).
[284] Insulcon, Ecomab® braided specialty glass fibre sleeving – 1200°C, (2019) 13082007.

https://www.insulcon.com/products/textile-products-industrial/sleevings/ (accessed March 1, 2020).
[285] SCHOTT AG, SCHOTT Glass and Glass-Ceramic Sealants for Technical Ceramics in High-Temperature Applications SCHOTT Glass and Glass-Ceramic Sealants for Technical Ceramics in High-Temperature Applications, 530 (2019). https://www.schott.com/d/epackaging/bb967de5-a550-4e8f-85c5-b337021f2e11/1.4/schott-cerajoin-sealing-glass-ceramic-sealant-for-high-temperatures_eng.pdf (accessed March 24, 2020).
[286] M. Pihlatie, A. Kaiser, P.H. Larsen, M. Mogensen, Dimensional Behavior of Ni–YSZ Composites during Redox Cycling, J. Electrochem. Soc. 156 (2009) B322.doi:10.1149/1.3046121.
[287] X. Pan, Why do commercial CT scanners still employ traditional, filtered back-projection for image reconstruction?, Inverse Probl. 25 (2009).doi:10.1088/0266-5611/25/12/123009.
[288] Y. Zou, J. Malzbender, Development and optimization of porosity measurement techniques, Ceram. Int. 42 (2016) 2861–2870.doi:10.1016/j.ceramint.2015.11.015.
[289] COMSOL, COMSOL Multiphysics® Reference Manual v.5.5, (2018). https://doc.comsol.com/5.5/doc/com.comsol.help.comsol/COMSOL_ReferenceManual.pdf (accessed September 1, 2020).
[290] R.B. Bird, W. Stewart, E. Lightfoot, Transport Phenomena, Second Edi, Wiley, Vicksburg, USA, 2007.
[291] E.N. Fuller, P.D. Schettler, J.C. Giddings, A new method for prediction of binary gas-phase diffusion coefficients., Ind. Eng. Chem. 16 (1966) 551.doi:10.1016/0042-207X(66)90400-3.
[292] P. Costamagna, P. Costa, V. Antonucci, Micro-modelling of solid oxide fuel cell electrodes, Electrochim. Acta. 43 (1998) 375–394.doi:10.1016/S0013-4686(97)00063-7.
[293] J.I. Sandells, M.M. Hussain, X. Li, I. Dincer, Mathematical modeling of planar solid oxide fuel cells, J. Power Sources. 161 (2006) 1012–1022.doi:10.1016/j.jpowsour.2006.05.055.
[294] P. Costamagna, K. Honegger, Modeling of Solid Oxide Heat Exchanger Integrated Stacks and Simulation at High Fuel Utilization, J. Electrochem. Soc. 145 (1998) 3995.doi:10.1149/1.1838904.
[295] J.H. Nam, D.H. Jeon, A comprehensive micro-scale model for transport and reaction in intermediate temperature solid oxide fuel cells, Electrochim. Acta. 51 (2006) 3446–3460.doi:10.1016/j.electacta.2005.09.041.
[296] M. Mogensen, The Kinetics of Hydrogen Oxidation on a Ni-YSZ SOFC Electrode at 1000°C, ECS Proc. Vol. 1993–4 (1993) 484–493.doi:10.1149/199304.0484pv.
[297] M. Mogensen, S. Skaarup, Kinetic and geometric aspects of solid oxide fuel cell electrodes, Solid State Ionics. 86–88 (1996) 1151–1160.doi:10.1016/0167-2738(96)00280-9.
[298] K.S. T. Yonekuraa, Y. Tachikawa, T. Yoshizumia, Y. Shiratoria, K. Ito, Exchange Current Density of Solid Oxide Fuel Cell Electrodes, ECS Trans. 35 (2011) 1007–1014.
[299] K. Zouhri, S.Y. Lee, Tubular SOFC air electrode ohmic overpotential: Parametric and exergy study, Energy Convers. Manag. 121 (2016) 1–12.doi:10.1016/j.enconman.2016.04.098.
[300] N. Akhtar, S.P. Decent, K. Kendall, Numerical modelling of methane-powered micro-tubular, single-chamber solid oxide fuel cell, J. Power Sources. 195 (2010) 7796–7807.doi:10.1016/j.jpowsour.2010.01.084.
[301] J. Murray, Pressure loss and heat transfer for single-phase turbulent flow in tubes fitted with wire-matrix inserts. Doctoral Thesis, University of Birmingham, 2009.
[302] P. Drogemuller, The Use of hiTRAN Wire Matrix Elements to Improve the Thermal Efficiency of Tubular Heat Exchangers in Single and Two-Phase Flow, Chem. Ing. Tech. 81 (2015) 188–202.doi:10.1002/cite.201400081.
[303] G.O. Brown, The History of the Darcy-Weisbach Equation for Pipe Flow Resistance, Environ. Water Resour. Hist. (2003) 34–43.doi:10.1061/40650(2003)4.
[304] Daily Metal Prices, (2020).

https://www.dailymetalprice.com/metalpricecharts.php?c=cu&u=lb&d=20 (accessed August 1, 2020).
[305] Wires.co.uk, (2020). https://www.wires.co.uk/ (accessed July 1, 2020).
[306] X. Si, J. Cao, S. Liu, X. Song, J. Qi, Y. Huang, J. Feng, Fabrication of 3D Ni nanosheet array on Crofer22APU interconnect and NiO-YSZ anode support to sinter with small-size Ag nanoparticles for low-temperature sealing SOFCs, Int. J. Hydrogen Energy. 43 (2018) 2977–2989.doi:10.1016/j.ijhydene.2017.12.132.
[307] D. Sekulic, Advances in Brazing: Science, Technology and Applications, Woodhead Publishing, 2013.
[308] S.J. Hitchcock, N.T. Carroll, M.G. Nicholas, Some effects of substrate roughness on wettability, J. Mater. Sci. 16 (1981) 714–732.doi:10.1007/BF02402789.
[309] J.Y. Kim, J.S. Hardy, S. Weil, Dual-atmosphere tolerance of Ag – CuO-based air braze, Int. J. Hydrogen Energy. 32 (2007) 3655–3663.doi:10.1016/j.ijhydene.2006.08.054.
[310] J.Y. Kim, J.-P. Choi, K.S. Weil, Mechanical properties and dual atmosphere tolerance of Ag – Al based braze, Int. J. Electrochem. Sci. 33 (2008) 3952–3961.doi:10.1016/j.ijhydene.2007.12.043.
[311] K.M. Erskine, A.M. Meier, S.M. Pilgrim, Brazing perovskite ceramics with silver / copper oxide braze alloys, J. Mater. Sci. 37 (2002) 1705–1709.
[312] VBC Group, VBC Alloy 4776, (2010) 4776. https://www.vbcgroup.com/brazing-products/base-metal-brazing-alloys/ (accessed January 8, 2020).
[313] VBC Group, VBC Alloy 4777, (2010). https://www.vbcgroup.com/brazing-products/base-metal-brazing-alloys/ (accessed January 8, 2020).
[314] VBC Group, VBC Alloy 4770, (2010) 4770. https://www.vbcgroup.com/brazing-products/base-metal-brazing-alloys/ (accessed January 8, 2020).
[315] Aufhauser Corporation, AUFHAUSER Ni-80, (1950) 201912. https://www.brazing.com/Pdf/NickelAlloy/Ni-80_datasheet.pdf (accessed August 20, 2020).
[316] T. Paper, M. Weinstein, T.S. Manager, L. Lee, L. Johnson, T.S. Engineer, A. Battenbough, T.S. Manager, Properties of Selected Nickel and Iron Based Brazing Filler Metals, 2015.
[317] G. Cui, N. Li, D. Li, J. Zheng, Q. Wu, The physical and electrochemical properties of electroless deposited nickel – phosphorus black coatings, Surf. Coat. Technol. 200 (2006) 6808–6814.doi:10.1016/j.surfcoat.2005.10.015.
[318] V. Molkov, Fundamentals of Hydrogen Safety Engineering I, Bookboon.com, 2012.
[319] Omegascope, Table of Total Emissivity, 212 (2000) 88–90. https://web.archive.org/web/20090711135115/http://www.monarchserver.com/TableofEmissivity.pdf (accessed July 7, 2020).
[320] Precision Ceramics, Macor Data Sheet, 44 (2020). https://www.precision-ceramics.co.uk/wp-content/uploads/2016/04/macor.pdf (accessed November 7, 2020).